

CMS-HIN-23-011

CERN-EP-2024-057  
2025/04/09

# Overview of high-density QCD studies with the CMS experiment at the LHC

The CMS Collaboration<sup>\*</sup>

## Abstract

We review key measurements performed by CMS in the context of its heavy ion physics program, using event samples collected in 2010–2018 with several collision systems and energies. These studies provide detailed macroscopic and microscopic probes of the quark-gluon plasma (QGP) created at the LHC energies, a medium characterized by the highest temperature and smallest baryon-chemical potential ever reached in the laboratory. Numerous observables related to high-density quantum chromodynamics (QCD) were studied, leading to some of the most impactful and qualitatively novel results in the 40-year history of the field. Using a dedicated high-multiplicity trigger in the first pp run, CMS discovered that small collision systems can exhibit signs of collectivity, a generic phenomenon with significant implications and presently understood to affect essentially all soft physics processes. This observation opened new paths to understand how fluidity and plasma properties emerge in QCD matter as a function of system size. Measurements of jet quenching have reached a completely new level of detail by directly assessing, for the first time, the medium modification of parton showers, as opposed to simply observing leading hadrons or di-hadrons. The first fully reconstructed beauty hadron and heavy-flavor jet nuclear modifications were also measured. The large size of the event samples, the precision of the measurements, and the extension of the probed kinematical phase space, allowed many other hard probes of the QGP medium to be explored in detail, leading to multiple groundbreaking findings. In particular, the seminal measurements of bottomonium suppression patterns answer fundamental questions that have been actively pursued, both theoretically and experimentally, by the community since the mid-1980s. We conclude by outlining the opportunities offered by the continuation of this physics program at the LHC.

*Published in Physics Reports as doi:10.1016/j.physrep.2024.11.007.*



## Contents

|      |   |     |
|------|---|-----|
| 1    | Introduction . . . . .  | 3   |
| 1.1  | Evolution of the field: From first studies to CMS . . . . .                                       | 4   |
| 1.2  | HI operation at the LHC . . . . .   | 5   |
| 1.3  | CMS detector design and implementation . . . . .  | 7   |
| 1.4  | Initial physics goals of the CMS heavy ion program . . . . .                                      | 9   |
| 1.5  | Major achievements of the CMS heavy ion physics program . . . . .                                 | 10  |
| 2    | Experimental challenges . . . . .   | 12  |
| 2.1  | The CMS detector . . . . .  | 12  |
| 2.2  | Luminosity measurement techniques and luminosity-dependent corrections . . . . .                  | 14  |
| 2.3  | Online event selection . . . . .  | 15  |
| 2.4  | Minimum bias event selection . . . . .  | 17  |
| 2.5  | Centrality determination in nucleus-nucleus collisions . . . . .                                  | 19  |
| 2.6  | Event classification methods in pp and pPb collisions . . . . .                                   | 22  |
| 2.7  | Tracking and vertex reconstruction . . . . .  | 23  |
| 2.8  | Muon reconstruction . . . . .   | 24  |
| 2.9  | High- $E_T$ electron and photon reconstruction . . . . .  | 26  |
| 2.10 | Jet reconstruction . . . . .  | 27  |
| 2.11 | Treating the underlying event in physics object reconstruction . . . . .                          | 28  |
| 2.12 | Heavy-flavor hadron reconstruction and identification . . . . .                                   | 31  |
| 3    | The initial state of the collisions . . . . .   | 33  |
| 3.1  | Constraining nuclear parton distribution functions with hard probes . . . . .                     | 33  |
| 3.2  | Tests of the Glauber model and $N_{\text{coll}}$ scaling using electroweak bosons . . . . .       | 38  |
| 3.3  | Small- $x$ nuclear structure . . . . .  | 41  |
| 3.4  | Photoproduction of vector mesons . . . . .  | 46  |
| 3.5  | Summary of results for the initial state . . . . .  | 51  |
| 4    | Bulk properties and novel phenomena . . . . .   | 53  |
| 4.1  | Initial-state entropy and energy densities . . . . .  | 53  |
| 4.2  | The paradigm of a nearly perfect liquid . . . . .   | 55  |
| 4.3  | System space-time evolution via femtoscopy . . . . .  | 65  |
| 4.4  | Searches for chiral magnetic effects and early-stage short-lived electromagnetic fields . . . . . | 70  |
| 4.5  | Summary of results for bulk properties and novel phenomena . . . . .                              | 76  |
| 5    | Hard probes in heavy ion collisions and sensitivity to quark-gluon plasma . . . . .               | 78  |
| 5.1  | Observations of parton quenching . . . . .  | 78  |
| 5.2  | Strength of energy loss . . . . .   | 86  |
| 5.3  | Medium modifications to jet substructure and fragmentation . . . . .                              | 94  |
| 5.4  | Studying wavelength behavior by varying parton flavor . . . . .                                   | 104 |
| 5.5  | Studies of in-medium hadronization . . . . .  | 106 |
| 5.6  | Quarkonium production and suppression in PbPb collisions . . . . .                                | 110 |
| 5.7  | Summary of hard probes in the QGP . . . . .   | 116 |
| 6    | Studies of high-density QCD in small collision systems . . . . .                                  | 118 |

|     |  |     |
|-----|--|-----|
| 6.1 | Particle production and hadronization . . . . .  | 118 |
| 6.2 | Studies of collectivity in small systems . . . . .   | 121 |
| 6.3 | Modification of quarkonium production in small systems . . . . .   | 130 |
| 6.4 | Searches for jet quenching in small systems . . . . .  | 131 |
| 6.5 | Summary of results for small systems . . . . .   | 134 |
| 7   | Tests of the electroweak sector and searches for new physics . . . . .                                   | 135 |
| 7.1 | The QED production of an exclusive muon pair . . . . .   | 136 |
| 7.2 | The QED production of an exclusive electron-positron pair . . . . .                                      | 138 |
| 7.3 | Light-by-light scattering and $\tau$ lepton pair production . . . . .                                    | 140 |
| 7.4 | Exclusion limits on axion-like particle production and anomalous $\tau$ lepton magnetic moment . . . . . | 144 |
| 7.5 | Summary of QED results and BSM searches with UPC . . . . .   | 145 |
| 8   | Summary . . . . .  | 147 |
| 8.1 | Discoveries and insights from the CMS heavy-ion physics program . . .                                    | 147 |
| 8.2 | Future physics opportunities at CMS for high-density QCD measurements                                    | 149 |
| A   | Glossary . . . . .   | 154 |
| B   | The CMS Collaboration . . . . .  | 201 |

## 1 Introduction

The Compact Muon Solenoid (CMS) detector [1], optimized for studies of high transverse-momentum ( $p_T$ ) particle production in high-luminosity proton-proton (pp) collisions at the CERN Large Hadron Collider (LHC), has proven to be a versatile tool with significant potential in other areas of research. From the very beginning [2], it was realized that its muon acceptance and calorimetric  $4\pi$  coverage, along with appropriate adaptations of its data acquisition system and online event filtering, could lead to significant contributions in the field of ultrarelativistic heavy ion (HI) collisions. In particular, the CMS detector is capable of performing detailed investigations [3, 4] of the thermodynamic and transport properties of the quark-gluon plasma (QGP), a deconfined state of quarks and gluons [5, 6] formed in such collisions. These studies are based on numerous experimental probes measured in an extended  $p_T$  range from about 0.3 GeV up to a few TeV. Along with the ALICE [7], ATLAS [8] and LHCb [9] experiments, CMS results cover a very broad range of experimental studies of ultrarelativistic HI collisions at the LHC.

The study of proton-nucleus (pA) interactions, which are intermediate in terms of the system size between pp and HI collisions, was initially considered a means to provide a baseline of “cold nuclear matter”, a non-QGP system considered to be formed in such collisions, to better understand the observations made in HI collisions [10]. Studies of pA and high multiplicity pp collisions have since become a fascinating area of research in their own right. It has become increasingly evident that the likely partonic systems produced in pA collisions and in very high multiplicity events formed in pp collisions offer valuable information and play a crucial role in unraveling the small-size limit of the QGP. Additionally, the capabilities of the CMS detector have allowed research into numerous non-QGP-related physics phenomena, such as photon-photon ( $\gamma\gamma$ ) and photon-nucleus ( $\gamma N$ ) interactions.

This article provides a comprehensive overview of the multiyear efforts undertaken by the CMS Collaboration in the field of HI physics, summarizing the key physics results and discoveries. It delves into the partonic structure of the nuclei and properties of the QGP, the unexpected QGP-like effects observed in small collision systems, and other important findings. The article concludes with possible future directions for the CMS experiment to address open questions in the field in a unique or complementary way. The article is organized as follows.

- This Introduction presents the physics motivations behind studying HI collisions at LHC energies, and in particular how data from the CMS detector can be used to address fundamental questions related to the high-density matter that is created in these strong interactions, governed by quantum chromodynamics (QCD).
- Section 2 outlines the experimental challenges associated with the overall data-taking strategy and the subsequent reconstruction of HI events. It also describes the various detectors, filters (triggers), and offline software techniques used to select the events of interest and to provide data samples for physics analysis.
- Section 3 focuses on studies of the initial state of the collisions, in particular on constraints of nuclear parton distribution functions (nPDFs), and on searches for gluon saturation phenomena at small values of parton fractional momenta (Bjorken  $x$ ), by means of particles produced in processes with a large squared momentum transfer  $Q^2$  (“hard probes”) and diffractive photoproduction of vector mesons.
- Section 4 describes the bulk observables that provide information on the geometry, entropy, energy density, and other collective properties of the medium produced in HI collisions for various collision systems and LHC energies. Searches for chiral

symmetry restoration are also discussed.

- Section 5 presents the interesting physics in the high- $Q^2$  realm, in particular how hadrons, jets, and particles containing heavy quarks can act as “tomographic” probes of the medium formed in the HI reactions.
- Section 6 highlights the paradigm-shifting findings made by CMS in studies of small collision systems, such as the emergence of collectivity for unidentified, light- and heavy-flavor hadrons.
- Section 7 details the results related to photon-induced processes in electromagnetic (EM) nucleus-nucleus (AA) interactions.
- Finally, Section 8 provides a comprehensive summary of the results obtained by CMS in the first two LHC runs and discusses an outlook for future discoveries using the CMS detector.
- Appendix A contains a glossary defining all of the acronyms used in this review.

## 1.1 Evolution of the field: From first studies to CMS

Soon after the demonstration of asymptotic freedom as a fundamental property of QCD gauge theory, it was realized that strongly interacting matter at finite temperature and/or net-baryon density can exist in different thermodynamic phases [11, 12]. Early predictions based on finite-temperature simulations of QCD on the lattice [13] indicated a transition to a new phase of QCD matter, the QGP [14], in which the quarks and gluons are no longer confined in hadrons and chiral symmetry, a global symmetry of QCD, is restored. More recently, lattice QCD calculations considering realistic light-quark masses have shown that chiral symmetry is restored in a crossover transition at a vanishingly small net-baryon density and at a precisely determined “pseudocritical” temperature (as opposed to a critical temperature in fixed order transitions) of  $T_c = 156\text{--}158\text{ MeV}$  [15, 16]. These same calculations estimated that the critical energy density at  $T_c$  is  $\epsilon_c = 0.3\text{--}0.4\text{ GeV/fm}^3$ .

It had already been conjectured in Ref. [14] that this regime of the QCD phase transition could be accessible by investigating high-energy HI collisions, where extremely hot and dense QCD matter could be produced by concentrating a substantial amount of energy in the center-of-mass overlap region of the two nuclei. For center-of-mass energies larger than 5 GeV (achieved at the AGS accelerator at BNL), the initial energy density in a large overlap area of two heavy nuclei is expected to significantly exceed  $\epsilon_c \approx 0.4\text{ GeV/fm}^3$  [17]. Studying collisions of nuclei at high energies looked attractive for at least two reasons: i) the large amount of energy liberated in the collision of highly Lorentz-contracted nuclei is distributed over a very small volume, as defined by their transverse size, and ii) these interactions are expected to provide very high densities of soft partons. From pA and AA interactions at high energies, one may therefore gain insight into many aspects of the strong interaction in the QCD framework. Despite the fact that QCD theory remains unchallenged since the discovery of asymptotic freedom [17], a complete and deep understanding of the nature of its phase transitions is still lacking.

Almost four decades of experimental and theoretical research have followed a scientific strategy aimed at the discovery and characterization of the QGP. Significant progress in the experimental field was made in the early period using fixed-target experiments at the BNL AGS [18] and the CERN SPS [19]. The BNL RHIC, a dedicated HI collider that provides interactions up to a center-of-mass energy per nucleon pair (NN) of  $\sqrt{s_{_{\text{NN}}}} = 200\text{ GeV}$ , started operating in the year 2000. With their much higher achievable center-of-mass energies, HI colliders are better suited to provide the appropriate conditions for the study of highly excited quark-gluon matter. An integral part of the CERN LHC experimental program has been devoted to HI collisions,

such as lead-lead (PbPb) and proton-lead (pPb) collisions up to  $\sqrt{s_{\text{NN}}}$  of 5.36 and 8.16 TeV, respectively. Since the inauguration of RHIC and the LHC (year 2009), these facilities and their experiments have continuously upgraded their capabilities, collecting a wealth of data across a wide range of collision energies and various colliding systems [20, 21].

Although the experimental conditions in HI collisions are tailored to create a hot and dense system, this medium cannot be formed under controlled thermodynamical conditions (such as the formation of water vapor from liquid water), but rather follows a dynamical trajectory across the temperature and net-baryon density axes of the QCD phase diagram [22]. Contrary to what was initially believed, the medium produced in HI collisions has been shown to not be a nearly free gas of quarks and gluons [6, 23–25]. Instead, a “strongly coupled” quark-gluon plasma was discovered [26–29], exhibiting properties akin to conventional (electromagnetic) plasmas [30]. These plasmas often demonstrate liquid or solid-like behavior, characterized by inter-particle potential energies exceeding the particles’ kinetic energy. Within a time of the order of 1 fm (in natural units), the conditions that prevail in a HI collision lead to the formation of a strongly coupled liquid with a nonuniform energy density, which then evolves according to the laws of viscous relativistic hydrodynamics [31]. Hydrodynamics converts initial spatial anisotropies into momentum space via pressure gradients [32]. These anisotropies persist because of the small specific viscosity of the QGP [33]. The observation of a strong anisotropy known as “elliptic flow”, in which final-state hadrons exhibit preferential emission with respect to a specific azimuthal angle, not only contributed to shedding light on the existence of the QGP but also characterized it as “the most perfect fluid known” [34]. A wealth of experimental data, such as unidentified particle and heavy-flavor quark  $p_{\text{T}}$  distributions, as well as two-particle and multiparticle correlations, have elucidated the “bulk” properties of this medium across a variety of energy- and volume-dependent colliding systems [35–37]. The strongly coupled nature of the QGP is also investigated on a wide range of length scales by taking advantage of the rapid “energy loss” by highly energetic partons traversing it (more accurately, a redistribution of energy to the surrounding medium) [38, 39].

Over the past few years, experiments at RHIC and the LHC, including CMS, performed increasingly precise “soft” (low- $Q^2$  processes) and hard (high- $Q^2$  processes) measurements of the bulk properties and jet modifications in HI collisions. Concurrently, advances in both the macroscopic (long-wavelength dynamical description) and microscopic (short-wavelength dynamical description) theories of interactions within the QGP are beginning to transform the abundant data into insights regarding the structure and properties of this state of matter. Notable success has been achieved in data-to-theory comparisons, particularly within well-defined frameworks in subfields such as the physics of soft probes [31–33, 40]. These achievements guide ongoing and future studies of the QGP nature, on a wide range of length scales [41]. Such an exploration is facilitated by the extensive nuclear data sets currently available or to be collected in the near future.

## 1.2 HI operation at the LHC

In most years since the start of its operations in 2009, the LHC has been reconfigured for a month-long HI run [42]. The first two PbPb collision runs were performed during LHC Run 1 (years 2010–2013) at  $\sqrt{s_{\text{NN}}} = 2.76$  TeV in 2010 [43] and 2011 [44].

Following these initial runs, the LHC HI physics community requested that the next run during this one-month period provide pPb collisions. Asymmetric collisions were not included in the LHC design, and are nontrivial since the “2-in-1” magnet design requires the two beams to have identical rigidity. This leads to unequal beam energies in the laboratory frame, since

the ratio of the atomic over mass numbers for the lead nucleus,  $Z/A$ , is only about 40% of that for protons. The original physics case [10] was based on a target luminosity of  $1.15 \times 10^{29} \text{ cm}^{-2} \text{ s}^{-1}$  at a beam energy of  $7Z \text{ TeV}$  ("design" parameters). However, to better match  $\sqrt{s_{\text{NN}}}$  for future PbPb runs, a value of  $4Z \text{ TeV}$  was chosen, with the exact number determined by accelerator requirements. Following a feasibility test and pilot physics fill in October 2011 and September 2012, respectively, the first pPb run took place in January 2013. This one month data-taking period provided the four major LHC experiments with approximately  $36 \text{ nb}^{-1}$  of pPb integrated luminosity at  $\sqrt{s_{\text{NN}}} = 5.02 \text{ TeV}$  [45]. This first pPb run represented a gain of about a factor of 25 in collision energy compared to previous asymmetric collisions studied at RHIC, one of the largest energy leaps in the history of particle accelerators. Together with a "reference" pp run at  $\sqrt{s} = 2.76 \text{ TeV}$  (i.e., at the same  $\sqrt{s_{\text{NN}}}$  as the previously collected PbPb data), these runs were the last physics operations before the first LHC shutdown in years 2013 and 2014.

The LHC Run 2 (2015–2018) operational period with HI collisions started with a reference pp run with beams of  $2.51 \text{ TeV}$  to obtain the same center-of-mass energy as in the pPb run of 2013 ( $\sqrt{s_{\text{NN}}} = 5.02 \text{ TeV}$ ). For the same reason, the ensuing PbPb operation in November–December 2015 was carried out at  $\sqrt{s_{\text{NN}}} = 5.02 \text{ TeV}$ , that is, an energy of  $6.37Z \text{ TeV}$  [46] (slightly less than the maximum possible value at that time of  $6.5Z \text{ TeV}$ ). A second pPb run at  $\sqrt{s_{\text{NN}}} = 5.02 \text{ TeV}$  occupied part of the period devoted to HI physics in November–December 2016.

Based on a range of crucial physics questions that emerged from the earlier pPb data, as well as the opportunity to measure various heavy elementary particles, the remainder of the 2016 pPb run was at a higher  $\sqrt{s_{\text{NN}}}$ . Despite the complex strategy for repeated recommissioning and operation of the LHC, a plan to satisfy most requirements was implemented [47] by successfully exploiting the different beam lifetimes at two  $\sqrt{s_{\text{NN}}}$  values of  $5.02$  and  $8.16 \text{ TeV}$ . In the latter case, the peak luminosity surpassed the design value by a factor of almost 8.

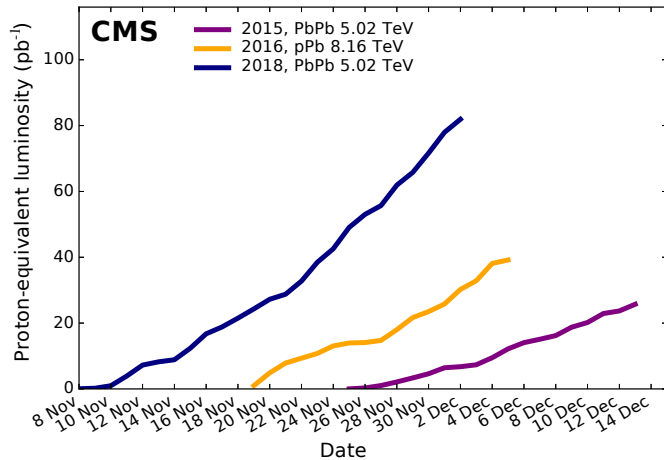


Figure 1: Integrated luminosity delivered to the CMS experiment with PbPb and pPb collisions at  $\sqrt{s_{\text{NN}}} = 5.02$  [48] and  $8.16 \text{ TeV}$  [49], respectively, as a function of time during the LHC Run 2 period. The years of data collection shown correspond to 2015 (purple), 2016 (orange), and 2018 (navy blue). This plot shows the proton-equivalent luminosity, i.e., the values for the PbPb data have been scaled by  $A^2 = 208^2$  and the values for the pPb data by  $A = 208$ .

As shown in Fig. 1, the subsequent 2018 PbPb run [50] provided more than three times the integrated luminosity than was collected in 2015, bringing the LHC one step closer to its high-luminosity era (HL-LHC) with heavy ions. A series of improvements, both in the LHC and in its injector chain, including an increase in the average colliding bunch intensity and a decrease

in the nominal bunch spacing, resulted in reaching about six times higher instantaneous luminosity than the design value of  $1.0 \times 10^{27} \text{ cm}^{-2} \text{ s}^{-1}$ , and delivering to the CMS experiment an integrated luminosity of  $1.89 \text{ nb}^{-1}$  of PbPb data (note the multiplicative factor mentioned in the caption of Fig. 1).

### 1.3 CMS detector design and implementation

The CMS detector [1] is one of the two general-purpose detectors at the LHC and is located at interaction point 5 (IP5). It has an overall length of 22 m, a diameter of 15 m, and weighs 14 000 tons. The detector uses a right-handed coordinate system, with the origin at the nominal interaction point, the  $x$  axis pointing to the center of the LHC ring, the  $y$  axis pointing up (perpendicular to the LHC plane) and the  $z$  axis along the counterclockwise beam direction. The azimuthal angle  $\phi$  is measured in the  $x$ – $y$  plane, with  $\phi = 0$  along the positive  $x$  axis, and  $\phi = \pi/2$  along the positive  $y$  axis. The radial coordinate in this plane is denoted by  $r$ , while the polar angle  $\theta$  is defined in the  $r$ – $z$  plane with respect to the  $z$  axis. The pseudorapidity is given by  $\eta = -\ln(\tan(\theta/2))$ . For particles whose momentum and  $p_T$  are much higher than their invariant mass,  $\eta \approx y$ , where  $y = \frac{1}{2} \ln \frac{E+p_z}{E-p_z}$  is the rapidity and  $E$  and  $p_z$  the energy and the particle momentum parallel to the  $z$  axis, respectively. The shape of any distribution as a function of  $y$  is invariant under Lorentz boosts in the beam direction. The component of the momentum transverse to the  $z$  axis is denoted by  $p_T$ , whereas the missing transverse momentum  $p_T^{\text{miss}}$  is the vectorial sum of the undetectable transverse momenta of the particles. The transverse energy is defined as  $E_T = E \sin \theta$ .

The key elements of the detector are as follows.

- A large solenoidal magnetic field magnetic field of 3.8 T to measure the momentum of charged particles and to separate the calorimeter energy deposits of charged and neutral particles.
- A fine-grained tracker providing efficient reconstruction of charged particle trajectories.
- A highly segmented electromagnetic calorimeter (ECAL) allowing energy deposits of charged hadrons, neutral hadrons, and photons to be clearly separated from each other. The ECAL combines efficient photon identification with high resolution in both energy and position.
- A hermetic hadron calorimeter (HCAL) with modest energy resolution and coarse segmentation but sufficient to separate charged and neutral hadron energy deposits.
- A muon tracking system delivering efficient and high-purity muon identification, regardless of the surrounding particle density.
- Two forward subdetectors, the Centauro And STrange Object Research (CASTOR) and Zero Degree Calorimeter (ZDC), enhance the hermeticity of the CMS detector during HI data-taking periods.

Figure 2 displays a simplified sketch of the acceptance of the various components of the CMS detector in  $\eta$ – $\phi$  coordinates. The characteristics of the CMS subdetectors are described in more detail in Section 2.

The CMS general-purpose detector is designed to explore the standard model (SM) and to search for physics beyond the SM (BSM) at the TeV scale. In addition, it is equally capable of studying the properties of strongly interacting matter produced in nuclear collisions at the highest energy densities ever reached in the laboratory. The detector subsystems were designed

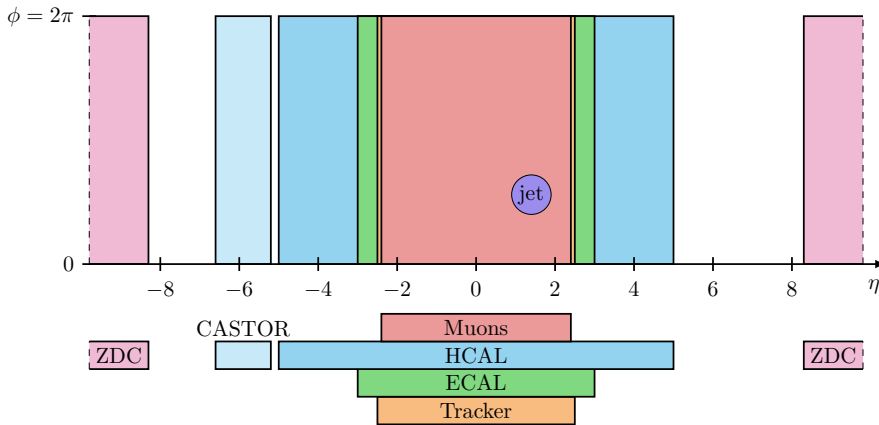


Figure 2: A simplified sketch of the acceptance in  $\eta$  and  $\phi$  for the tracking, calorimetry (ECAL, HCAL, CASTOR, and ZDC) and muon identification (“Muons”) components of the CMS detector. In the lower section, the central elements (that is, excluding ZDC and CASTOR) are arranged based on their proximity to the beam, with the tracker being the closest element of the central detectors, and the muon detectors positioned farthest away. The size of a jet cone with  $R = 0.5$  (to be discussed in Section 2.10) is also depicted for illustration. (Figure adapted from Ref. [4].)

with a resolution and granularity adapted to cope with the high number of simultaneous collisions per bunch crossing that occur during high-luminosity pp running. As a result, the detector is also able to deal with the very large charged particle multiplicities that can be created in a single PbPb collision. Therefore, CMS provides a range of remarkable capabilities, some of which are unique, to the HI effort at the LHC [4].

- Acceptance: Broad coverage near midrapidity ( $|\eta| < 2.5$ , full  $\phi$  coverage) for layered detection of charged and neutral hadrons as well as muons, electrons, and photons, over a wide range of  $p_T$  (from about 100 MeV to hundreds of GeV).
- Resolution: Exceptional dimuon mass resolution, leading to a clean separation of the various heavy quarkonium states and an improved signal-over-background ratio, also coupled with excellent charged particle momentum resolution over a wide  $p_T$  and  $\eta$  range. At  $|\eta| \approx 0$ , the relative dimuon mass resolution is 0.6%, or 20 MeV for the  $J/\psi$  and 70 MeV for the  $Y(1S)$ . Integrated over the rapidity ranges used in the analyses reported in this paper, it becomes around 1.3%, in pp and PbPb collisions (even in the most central collisions) [51].
- Calorimetry: Full electromagnetic and hadronic calorimetry for complete jet triggering and reconstruction over a very large solid angle, leading to large event samples for measurements of individual jets (discussed in Section 2.10) and jet + X channels along with the recoiling  $p_T$  in them, where X could be another jet, an electroweak (EW) boson, etc.
- Forward coverage: Excellent forward physics and global event capabilities thanks to the forward hadronic (HF) calorimeters ( $3 < |\eta| < 5$ ), CASTOR ( $-6.6 < \eta < -5.2$ ), and the ZDCs ( $|\eta| > 8.3$ ).
- Optimized online and offline operation: The data acquisition (DAQ) system is capable of delivering almost every PbPb event to a two-tier trigger system, allowing maximum flexibility to select “bulk” and rare probes.

## 1.4 Initial physics goals of the CMS heavy ion program

This section presents a concise historical overview, both experimental and phenomenological, of the observables that were considered to be essential measurements for CMS prior to the inauguration of the LHC. Capitalizing on previous discoveries, the LHC experimental program with PbPb and pPb collisions has significantly advanced the state of the art in both the soft- and hard-physics sectors. Sections 3–7 describe in detail the physics analyses motivated by the priorities introduced here, as well as significant extensions that far surpassed these initial goals.

At the LHC, the pPb and PbPb center-of-mass energies exceed those at RHIC by factors of roughly 25, thereby accessing a completely uncharted regime. Initial expectations were primarily driven by the fact that this regime could be characterized by the following properties.

- An initial state dominated by high-density parton distributions. The relevant range of the parton momentum fraction  $x$  reaches as low as  $\sim 10^{-4}$  (at midrapidity) for values of the squared momentum transfer  $Q^2$  as large as  $Q^2 \approx 10^6 \text{ GeV}^2$ . This small- $x$  range, where the gluon density becomes so high that perturbation theory breaks down even for a small coupling constant, is expected to be dominated by nonlinear gluon dynamics [52] governed by a characteristic saturation scale that is a factor of 2–3 times larger than that probed at RHIC [53]. Important aspects of particle production and the early time evolution of the system were expected to be governed by classical chromodynamics, as described, e.g., in the color-glass condensate (CGC) framework [54], an approximation of the quantum theory (“effective field theory”) of the dense initial-state partonic wavefunctions.
- Since the initial energy density, temperature, volume, and lifetime of the QGP were expected to be much larger than those at RHIC, parton dynamics were expected to drive the evolution of the medium [55, 56]. Partonic degrees of freedom should thus dominate the QGP expansion and the collective features of the resulting hadronic final state.
- The higher yield of hard probes (e.g., prompt EW bosons, jets produced by hard-scattered partons, high- $p_T$  hadrons, heavy-flavor hadrons) should provide direct information on the nPDFs of the colliding ions. Since their production cross sections can be calculated with high accuracy using perturbative QCD (pQCD), these probes provide a “calibrated” reference for final-state interactions in the medium. Any observed attenuation would give precise “tomographic” information about the QGP and its eventual disintegration into hadrons.
- Because of the very large electric charge of the Pb ions, the induced EM processes provide unique possibilities for studying high-energy  $\gamma\gamma$  and  $\gamma A$  interactions in unexplored regions of phase space, thus complementing the QCD physics aspects listed above.

The initial emphasis was placed on measurements that could assist in clarifying some of the previously unresolved issues. For example, before the start up of RHIC, predictions for the charged-particle multiplicity per unit of rapidity at midrapidity  $dN/dy|_{y=0}$  (largely based on extrapolations of SPS measurements) varied widely. This observable is related to the entropy density produced in the collision, which impacts the global properties of the medium. The initial predictions for RHIC were mostly overestimates. The expected values for the maximum design energy of the LHC (5.5 TeV) were later refined to  $dN/d\eta|_{\eta=0} \approx 1.5 \times 10^3$  [55, 56] for the most central PbPb collisions. These lower particle multiplicities at the LHC would be more

easily manageable by the CMS detector.

Measurements of the properties of momentum anisotropies in PbPb collisions at the LHC were deemed of primary importance to confirm or reject the interpretation of the fluid-like state found at RHIC. At LHC energies, the contribution from the QGP phase to the collective momentum anisotropy was expected to be more dominant than at RHIC. Consequently, interpretations of the properties of the QGP might be less dependent on the details of the later hadronic phase.

Among the most exciting results of the RHIC physics program was the observation of a large suppression of the yields of high- $p_T$  hadrons in head-on AuAu collisions, compared to the expectations from an incoherent superposition of pp collisions [57]. The capability to fully reconstruct jets at the LHC was expected to result in a better understanding of the mechanisms leading to high- $p_T$  hadron suppression. The measurement of jets recoiling opposite prompt EW bosons as well as performing high-precision studies in the heavy-flavor sector (using both jets and identified particles) were also of utmost importance. These observations could both clarify some apparently conflicting results at RHIC (e.g., on the energy loss flavor dependence) and also provide accurate information on the transport properties of the QCD matter. The LHC measurements were also crucial for resolving surprising findings, such as the similar amount of  $J/\psi$  yield modification observed at SPS and RHIC energies [58, 59], and the rapidity dependence of that modification [60]. In addition, the more abundant production of particles containing bottom quarks, including the  $Y$  states, at LHC energies, coupled with the excellent reconstruction capabilities of the CMS detector, would enable a unique opportunity to extend the study of the behavior of heavy quarks in the QGP.

Forward coverage was considered crucial for measuring low- $x$  PDFs, particularly the gluon densities, in protons and nuclei. Initial studies in pp collisions involving perturbative probes, such as Drell–Yan and jet production within and beyond the HF acceptance, laid the groundwork for extending measurements to other hard probes, including inclusive high- $p_T$  hadron or photon production in nuclear collisions, where gluon saturation effects are expected to be more pronounced. Additionally, hadron production at forward rapidity in nuclear collisions at LHC energies presented interesting connections to cosmic-ray physics, providing data necessary for calibrating the models used to study ultra-high energy cosmic ray interactions in the upper atmosphere. To complement the physics program in the baryon-free midrapidity region, the unique design of the CASTOR detector was implemented to further investigate exotic (“Centauro”) cosmic-ray events.

Finally, the high “photon fluxes” produced by the large electric charge of the relativistic Pb nuclei [61, 62] also opened up possibilities for  $\gamma\gamma$  as well as  $\gamma A$  studies, reaching energies that had not been explored at colliders prior to the LHC [63–65]. Interesting physics within the SM, including both QCD and quantum electrodynamics (QED) studies, would thus be possible [66–68]. Additionally, states with high invariant mass could be explored, where the detection of new particles could potentially fall within the phase space region probed by CMS. In general, events with far-grazing collisions, so-called “ultraperipheral collisions” (UPC), characterized by relatively small outgoing particle multiplicities and a small background, offered a very wide range of possibilities [69–80].

## 1.5 Major achievements of the CMS heavy ion physics program

The heavy ion physics program of CMS, based on analyses of data collected from 2010 to 2018 across various collision systems and energies, has provided groundbreaking insights into high-density QCD, in general, and the nature of the QGP state, in particular. These discoveries,

briefly summarized in this section, have fundamentally advanced the field, setting new benchmarks for the study of QCD matter.

- **Collective behavior in small collision systems**

A groundbreaking discovery by CMS was the observation of collective behavior in small collision systems, such as pp and pPb collisions. This phenomenon, known as “collectivity”, had previously only been associated with larger systems, such as PbPb collisions. This breakthrough, supported by measurements made in many different classes of observables, suggests that fluidity and plasma properties may emerge in QCD matter in systems with very different sizes, opening new paths for theoretical and experimental studies aimed at understanding the origins of these collective effects.

- **Properties of the quark-gluon plasma**

Several analyses of CMS data provided both a macroscopic and a microscopic characterization of the highest temperature and smallest baryon-chemical potential QCD medium ever produced in a laboratory setting. Thanks to the unprecedented precision of these measurements, the results have significantly advanced the understanding of the QGP’s thermodynamical and transport properties, including its fluid-like behavior and the dynamics of its formation and evolution.

- **Jet quenching and medium modification of parton showers**

The direct observation of jet quenching established new standards in the field, significantly extending previous studies beyond the leading hadrons and di-hadrons to assess the medium modification of entire parton showers. The results reveal the intricate mechanisms by which the QGP alters the energy and structure of high-energy jets passing through it, offering deep insights into the interactions between hard probes and the QCD medium.

- **Heavy-flavor hadron and jet nuclear modifications**

CMS conducted pioneering studies of fully reconstructed beauty hadrons and of heavy-flavor jets (i.e., jets containing charm or bottom quarks). These measurements, performed for the first time in the harsh environment produced in nucleus-nucleus collisions, provide critical information on the interactions of heavy quarks with the QGP and on how they lose energy or are scattered by the medium, shedding light on the role of the quark mass in quark energy loss mechanisms.

- **Suppression patterns of five S-wave quarkonium states**

For the first time, CMS measured the centrality dependence of the nuclear suppression of all five S-wave quarkonia, including the elusive  $\Upsilon(3S)$ , showing that the suppression patterns follow a sequential hierarchy reflecting the binding energies of the quarkonium states: the more strongly bound is the considered meson, the hotter must be the medium before we see its suppression. Interestingly, the loosely-bound  $\psi(2S)$  meson is significantly suppressed even in the most peripheral PbPb collisions probed by the CMS data. Using the distance between the dimuon vertex and the primary collision vertex, we could also measure the suppression pattern of nonprompt charmonia, an indirect measurement of the effects of the QCD medium on B mesons.

## 2 Experimental challenges

Experimental measurements in ultrarelativistic HI collisions have reached a precision era. As shown in Sections 3–7, in order to effectively discriminate between the various theoretical models attempting to describe the phenomena at play in these collisions, there are two experimental challenges. First, it is important to collect large samples of very specific types of events in order to reduce the statistical uncertainties. Second, large event samples and improved analysis techniques are needed to minimize the systematic uncertainties in these measurements. Accomplishing both of these goals is required to perform quantitative data-theory comparisons. Of particular importance in HI physics is to carry out multiple differential analyses in bins of centrality (defined in Section 2.5).

This section describes the hardware and techniques used by the CMS Collaboration to select and classify events, detect the properties of the produced particles, and extract various physics observables. These tasks are particularly difficult in the extremely high particle multiplicity environment of HI collisions at LHC energies, as illustrated by the event display shown in Fig. 3.

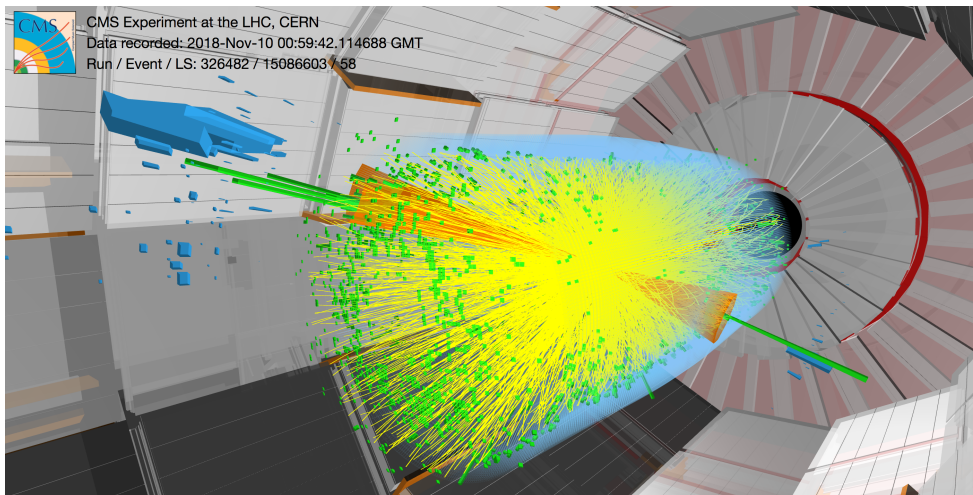


Figure 3: An almost head-on collision event selected from the 2018 PbPb data set. The yellow lines show the huge number of charged-particle tracks and the two cones show nearly back-to-back candidate jets originating from bottom quarks. (Figure adapted from Ref. [81].)

### 2.1 The CMS detector

The central feature of the CMS apparatus is a superconducting solenoid of 6 m internal diameter, providing a magnetic field of 3.8 T. Within the solenoid volume, as shown in Fig. 2, are a silicon pixel and strip tracker, a lead tungstate crystal ECAL, and a brass and scintillator HCAL, each composed of a barrel and two endcap sections. Hadron forward (HF) calorimeters, made of steel and quartz-fibers, extend the pseudorapidity coverage provided by the barrel and endcap detectors. Muons are measured in gas-ionization detectors embedded in the steel flux-return yoke outside the solenoid. The procedure followed for aligning the detector is described in Ref. [82]. A more detailed description of the CMS detector can be found in Ref. [1].

The silicon tracker used until 2016 measured charged particles within the range  $|\eta| < 2.5$ . For nonisolated particles of  $1 < p_T < 10$  GeV and  $|\eta| < 1.4$ , the track resolutions were typically 1.5% in  $p_T$  and 25–90 (45–150)  $\mu\text{m}$  in the transverse (longitudinal) impact parameter [83]. At the start of 2017, a new pixel detector was installed [84]; the upgraded tracker measured particles up to  $|\eta| < 3.0$  with typical resolutions of 1.5% in  $p_T$  and 20–75  $\mu\text{m}$  in the transverse impact

parameter [85] for nonisolated particles of  $1 < p_T < 10 \text{ GeV}$ . More details about the tracking algorithms are discussed in Section 2.7.

In the region  $|\eta| < 1.74$ , the HCAL cells have widths of 0.087 in pseudorapidity and 0.087 in azimuth ( $\phi$ ). In the  $\eta$ – $\phi$  plane, and for  $|\eta| < 1.48$ , the HCAL cells map on to  $5 \times 5$  arrays of ECAL crystals to form calorimeter towers projecting radially outwards from close to the nominal interaction point. For  $1.74 < |\eta| < 3.0$ , the coverage of the towers increases progressively to a maximum of 0.174 in  $\Delta\eta$  and  $\Delta\phi$ . Within each tower, the energy deposits in ECAL and HCAL cells are summed to define the calorimeter tower energies, which are used as inputs to the jet-finding algorithms determining the energies and directions of hadronic jets.

The two halves of the HF calorimeter are located 11.2 m from the interaction region, one on each end, and together they provide coverage in the range  $3.0 < |\eta| < 5.2$ . They also serve as luminosity monitors. Two subdetectors, CASTOR and ZDC, enhanced the hermeticity of the CMS detector during the HI data-taking periods by extending the rapidity coverage. The single CASTOR detector, a Cherenkov sampling calorimeter with no segmentation, was located 14.37 m from IP5 and about 1 cm from the beam line, covering the region  $-6.6 < \eta < -5.2$ . The two ZDCs, made of quartz fibers and plates embedded in tungsten absorbers, are installed at  $0^\circ$  relative to the beam direction at the interaction point and between the two beam lines 140 m away from IP5. Their location behind the first bending magnets of the LHC allows for detecting neutrons from nuclear dissociation events in the range  $|\eta| > 8.3$ . The first section of each ZDC is segmented into 5 vertical slices, giving some information about particle direction.

Muons are measured in the pseudorapidity range  $|\eta| < 2.4$ , with four detection planes made using three technologies: drift tubes (DT), cathode strip chambers (CSC), and resistive-plate chambers (RPC). The reconstruction of muon tracks is described in Section 2.8. During Run 1, matching muons to tracks measured in the silicon tracker results in a relative transverse momentum resolution, for muons with  $20 < p_T < 100 \text{ GeV}$ , of 1.3–2.0% in the barrel and better than 6% in the endcaps. The  $p_T$  resolution in the barrel is better than 10% for muons with  $p_T$  up to 1 TeV [86]. For Run 2, the corresponding numbers are  $p_T$  resolutions of 1% in the barrel and 3% in the endcaps for muons with  $p_T$  up to 100 GeV and better than 7% in the barrel for muons with  $p_T$  up to 1 TeV [87].

The global event reconstruction (also called particle-flow (PF) event reconstruction [88]) aims to reconstruct and identify each individual particle in an event, with an optimized combination of all subdetector information. In this process, the identification of the particle type (photon, electron, muon, charged hadron, neutral hadron) plays an important role in the determination of the particle direction and energy. Photons (e.g., coming from  $\pi^0$  decays or from electron bremsstrahlung) are identified as ECAL energy clusters not linked to the extrapolation of any charged-particle trajectory to the ECAL. Electrons (e.g., coming from photon conversions in the tracker material or from b hadron semileptonic decays) are identified as a primary charged-particle track, and potentially several ECAL energy clusters corresponding to this track extrapolation to the ECAL and to possible bremsstrahlung photons emitted along the way through the tracker material. Muons (e.g., from quarkonium and EW boson decays) are identified as tracks in the central tracker consistent with either a track or several hits in the muon system, and associated with calorimeter deposits compatible with the muon hypothesis. Charged hadrons are identified as charged-particle tracks neither identified as electrons, nor as muons. Finally, neutral hadrons are identified as HCAL energy clusters not linked to any charged-hadron trajectory, or as a combined ECAL and HCAL energy excess with respect to the expected charged hadron energy deposit. Details on how the PF objects are used as input in jet reconstruction can be found in Section 2.10.

The energy of photons is obtained from the ECAL measurement. The energy of electrons is determined from a combination of the track momentum at the main interaction vertex, the corresponding ECAL cluster energy, and the energy sum of all bremsstrahlung photons attached to the track. The energy of charged hadrons is determined from a combination of the track momentum and the corresponding ECAL and HCAL energies, corrected for the response function of the calorimeters to hadronic showers. Finally, the energy of neutral hadrons is obtained from the corresponding corrected ECAL and HCAL energies. Details about the methods to reconstruct and identify electrons and photons can be found in Section 2.9.

During Run 1, the barrel section of the ECAL achieved an energy resolution of about 1% for unconverted or late-converting photons in the tens of GeV energy range. The energy resolution of the remaining barrel photons is about 1.3% up to  $|\eta| = 1$ , increasing to about 2.5% at  $|\eta| = 1.4$ . In the endcaps, the energy resolution is about 2.5% for unconverted or late-converting photons, and between 3 and 4% for photons converting in the tracker material before reaching the ECAL [89].

For Run 2, the electron momentum is estimated by combining the energy measurement in the ECAL with the momentum measurement in the tracker. The momentum resolution for electrons with  $p_T \approx 45$  GeV from  $Z \rightarrow ee$  decays ranges from 1.6 to 5%. It is generally better in the barrel region than in the endcaps, and also depends on the bremsstrahlung energy emitted by the electron as it traverses the material in front of the ECAL [90, 91].

Jets are reconstructed offline from the energy deposits in the calorimeter towers or PF objects, clustered using the anti- $k_T$  algorithm [92–95] with a distance parameter of 0.4 (discussed in Section 2.10). When combining information from the entire detector, the jet energy resolution in pp collisions amounts typically to 15–20% at 30 GeV, 10% at 100 GeV, and 5% at 1 TeV [96].

## 2.2 Luminosity measurement techniques and luminosity-dependent corrections

For many analyses of the HI program performed at the LHC, a precise knowledge of the integrated luminosity is essential to achieve the high-precision cross sections needed to both test and, in many cases, improve relevant theory calculations. Although a key parameter for any particle collider, the task of calibrating the absolute scale of the luminosity has proven to be particularly challenging at hadron colliders. Knowing the instantaneous luminosity during data acquisition is also essential to monitor the beam condition and accelerator performance.

To determine the absolute luminosity, a technique based on varying the separation of the two LHC beams is used, the so-called “van der Meer scans” [97]. These scans allow for a determination of the luminosity per colliding bunch pair directly from the machine parameters. With the exception of special, reference proton and HI runs, these scans are performed either under carefully controlled conditions, with tailored beam parameters, or during normal physics operation. In both cases, the target precision is set to  $\mathcal{O}(1\text{--}2\%)$  [97].

The CMS experiment used a system consisting of up to five detectors to monitor and measure the luminosity delivered by the LHC during LHC Runs 1 and 2. Real-time monitoring of the luminosity was achieved with three of them: the fast beam conditions monitor, HF, and pixel luminosity telescope detectors, each with its own high-rate data acquisition system. Two additional systems, the silicon pixel detector and the drift tube chambers, feature very low occupancy and good stability over time. The absolute luminosity is determined by integrating the subdetector rate of these two systems as a function of beam separation, which corresponds to an approximate van der Meer scan precision of  $\mathcal{O}(1\%)$ . The dominant uncertainty in the absolute luminosity is typically related to how well the beam bunch density profiles

can be factorized. For the measurements highlighted in this report, a small total uncertainty of  $\mathcal{O}(1.5\text{--}2.0\%)$  [48, 49, 98, 99] was achieved, including the time stability of the van der Meer calibrated subdetector response.

### 2.3 Online event selection

During Runs 1 and 2, the CMS detector was used to collect a large quantity of data for the different colliding systems provided by the LHC as part of its HI program. A beam of Pb nuclei in one LHC ring collided with either a second counterrotating Pb beam or with a proton beam. A small event sample of colliding xenon (Xe) nuclei was also collected. The resulting integrated luminosities ( $\mathcal{L}$ ) are summarized in Table 1. A comparison of the integrated luminosity delivered by the LHC (5<sup>th</sup> column) to that collected by the CMS detector (last column) shows that the detector acquired more than 95% of the available data (with the exception of the very first run in 2010, for which the fraction was 90%).

Table 1: Summary of HI data-taking periods during Runs 1 and 2.

| LHC Run | Year | Colliding system | $\sqrt{s_{\text{NN}}}$ (TeV) | Delivered $\mathcal{L}$ ( $\text{nb}^{-1}$ ) | Recorded $\mathcal{L}$ ( $\text{nb}^{-1}$ ) |
|---------|------|------------------|------------------------------|--|---|
| Run 1   | 2010 | PbPb             | 2.76                         | $9.69 \times 10^{-3}$                        | $8.70 \times 10^{-3}$                       |
|         | 2011 | PbPb             | 2.76                         | 0.184  | 0.174                                       |
|         | 2013 | pPb              | 5.02                         | 36.14  | 35.5  |
| Run 2   | 2015 | PbPb             | 5.02                         | 0.59   | 0.56  |
|         | 2016 | pPb              | 5.02                         | 0.530  | 0.509                                       |
|         | 2016 | pPb              | 8.16                         | 188.3  | 180.2                                       |
|         | 2017 | XeXe             | 5.44                         | $3.50 \times 10^{-3}$                        | $3.42 \times 10^{-3}$                       |
|         | 2018 | PbPb             | 5.02                         | 1.89   | 1.79  |

Table 2: Summary of reference pp data-taking periods during Runs 1 and 2. To compare with the nucleon-nucleon-equivalent luminosities from Table 1, it is important to note that the listed integrated luminosities should be divided by factors of either  $A^2$  (for the PbPb case) or  $A$  (for the pPb case), where  $A = 208$  is the Pb mass number.

| LHC Run | Year | $\sqrt{s}$ (TeV) | Recorded $\mathcal{L}$ ( $\text{pb}^{-1}$ ) |
|---------|------|------------------|---|
| Run 1   | 2011 | 2.76             | 0.200                                       |
|         | 2013 | 2.76             | 5.40  |
| Run 2   | 2015 | 5.02             | 27.4  |
|         | 2017 | 5.02             | 304   |

In addition to the HI runs shown in Table 1, special pp runs were required by the HI program in order to provide the so-called “pp reference data” for comparison to the HI results. They are listed in Table 2 and were taken with detector conditions similar to those used in the HI runs, and with the same colliding energy per nucleon pair (which is lower than that used in the high-energy pp program). In addition, pp data were collected under conditions that yielded a very small number ( $\ll 1$ ) of concurrent interactions in the same bunch crossing (pileup, PU). These low-PU data were required for studies searching for the possible existence of a hot and dense medium in events which produced a very large number of charged particles, the so-called “high-multiplicity events.” Table 3 summarizes the integrated luminosities collected for the low-PU pp collisions.

Table 3: Summary of low-PU pp data-taking periods during Runs 1 and 2.

| LHC Run | Year  | $\sqrt{s}$ (TeV) | Recorded $\mathcal{L}$ ( $\text{pb}^{-1}$ ) |
|---------|-------|------------------|---|
| Run 1   | 2010  | 7                | 6.2   |
|         | 2015  | 5.02             | 1.0   |
|         | Run 2 | 13               | 2.0   |
|         |       | 13               | 1.3   |
|         |       | 13               | 10.2  |

To deal with the large amount of data delivered by the LHC, online event selection is performed by the CMS trigger system [100] that was developed to quickly and precisely select the events of interest. The trigger operates in two stages, the first of which (level-1 or L1) is a hardware-based trigger that examines every collision using a set of event selections implemented directly in the firmware. The L1 trigger uses energy deposited in the towers of the calorimetry system and signals from the muon detectors to construct various physics objects, and then uses that information to make the initial event selection. In order to suppress noncollision-related noise, cosmic rays, prefiring triggers [101], and beam backgrounds, the L1 trigger is required to accept events in coincidence with the presence of both colliding ion bunches in the interaction region. The next stage is the high-level trigger (HLT), a software-based trigger running on a computer farm composed of  $\approx 30$  k computer central processing units (CPUs). The HLT uses information from the L1 trigger and performs additional event filtering using sophisticated computer algorithms executed similarly to those used for the offline physics analyses. This processing in the HLT takes  $\approx 250$  ms and  $\approx 350$  ms on average for pp and PbPb events, respectively. In pp collisions, the L1 trigger reduces the event rate from 40 MHz to 100 kHz, while the HLT further reduces the rate from 100 kHz to around 2 kHz on average in pp collisions. In PbPb and pPb collisions on average the rates are reduced to 8 kHz and 20 kHz, respectively. During Run 2, event rates of around 30 kHz were delivered for PbPb collisions, while around 100 kHz were delivered for both pp reference and pPb collisions. The trigger system output rates are optimized to fill as much bandwidth as the DAQ can support (around 6 GB/s maximum during Run 2) [102]. Between Runs 1 and 2, the L1 trigger system was updated significantly and restructured [103].

In order to optimize the performance of the trigger system in HI collisions, several modifications and additions are made to the L1 and HLT setups used for pp collisions [104–106]. In HI collisions, minimum bias (MB) triggers require at least one channel in both sides of HF to have deposited energies that exceed a certain threshold. By triggering on the total energy deposited in the HF calorimeters, events can be selected with different centrality. The rate of the MB triggers in 2018 PbPb collisions were around 6 kHz, where one out of three MB events were recorded. In addition, ultraperipheral events, where one of the colliding nuclei remains intact, can be triggered by requiring activity on only one side of the HF. The jet background subtraction at L1 is optimized for triggering on jets in the higher multiplicity HI environment. To suppress the influence of underlying event (UE) fluctuations, the average UE contribution to the jet energy is estimated by summing the energy over full calorimeter  $\phi$ -rings sharing the jet position in  $\eta$ . The sum is rescaled by the number of towers in the jet compared to the number of towers in the calorimeter  $\phi$ -ring and then subtracted from the jet energy [107]. For the electron/photon triggers, the isolation and selections were relaxed and the shape requirements were bypassed at L1 to maintain a high efficiency in the high-occupancy environment of HI collisions. Figure 4 shows the efficiency of the 50 GeV single-jet and 15 GeV photon triggers during Run 1 PbPb data taking. In the HLT configuration for HI collisions, the track selection

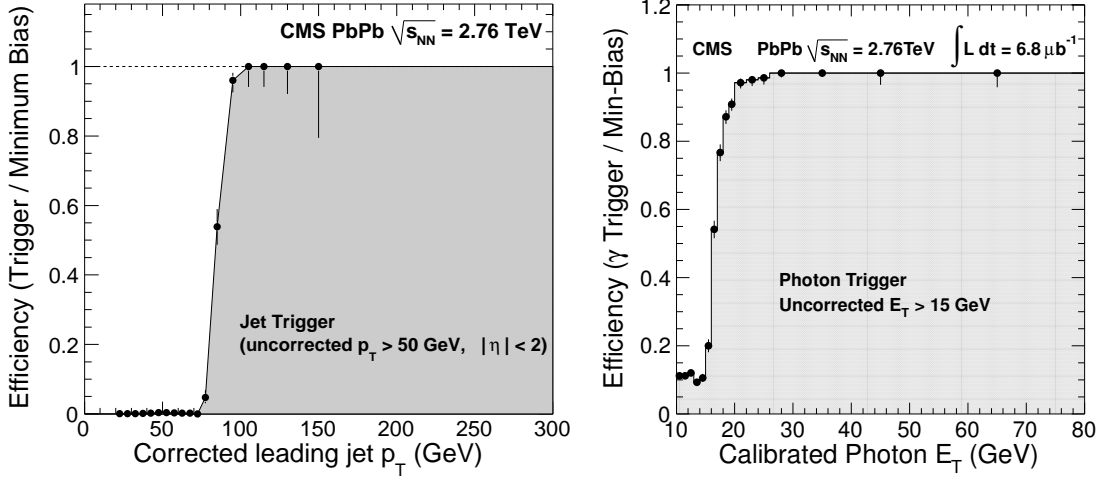


Figure 4: Left: Efficiency for the 50 GeV single-jet trigger as a function of the corrected leading jet transverse momentum in PbPb collisions at 2.76 TeV. Right: Efficiency for the 15 GeV photon trigger as a function of the corrected photon transverse energy in PbPb collisions at 2.76 TeV. (Figure adapted from Refs. [108, 109].)

requirements are loosened to be the same as the offline ones in order to reach higher efficiency for the triggers using track reconstruction (described in Section 2.7). Changes are also made for the muon triggers, where only outside-in tracking (Section 2.8) is implemented, and for the heavy-flavor triggers, in which the selection criteria are tightened to reduce the processing time. The typical  $p_T$  thresholds of the jet, photon, electron, and muon triggers in PbPb collisions were 100, 40, 20, and 12 GeV, respectively.

With the goal of studying the properties of high-multiplicity pPb and pp collisions (discussed in Section 6.2), dedicated triggers were designed and implemented to capture the rare events with a large number of produced particles. An L1 trigger which filters on the scalar sum of total transverse momentum over the calorimeters (ETT, including both ECAL and HCAL) is used to select events. Those events are passed to the HLT where track reconstruction is performed using the pixel tracker and the number of found pixel tracks is used to select high-multiplicity events. Figure 5 shows the L1 and HLT trigger efficiencies as functions of the number of tracks reconstructed offline ( $N_{\text{trk}}^{\text{offline}}$ ) for 5.02 TeV pPb collision data taken in 2013.

## 2.4 Minimum bias event selection

Hadronic interactions of HIs can occur over a broad range of overlaps of the two nuclei, from head-on collisions (most central) to just barely grazing (most peripheral). Investigating the full range of possibilities requires a MB event sample. The selection procedure for this sample includes both an online trigger (discussed in Section 2.3) as well as offline quality criteria. The optimal selection maximizes the overall efficiency for the total inelastic hadronic cross section, while mitigating contamination from non-hadronic collision sources, including beam-gas collisions and electromagnetic interactions in peripheral and ultraperipheral collisions (UPC). The first three filters listed below, namely the primary vertex (PV), cluster compatibility, and HF coincidence filters were used as standard event selection for PbPb Run 2 analyses.

### 2.4.1 Primary vertex filter

The definition of MB interactions is limited to only those events in which at least one PV containing at least two reconstructed tracks is found. Track reconstruction and vertex finding are

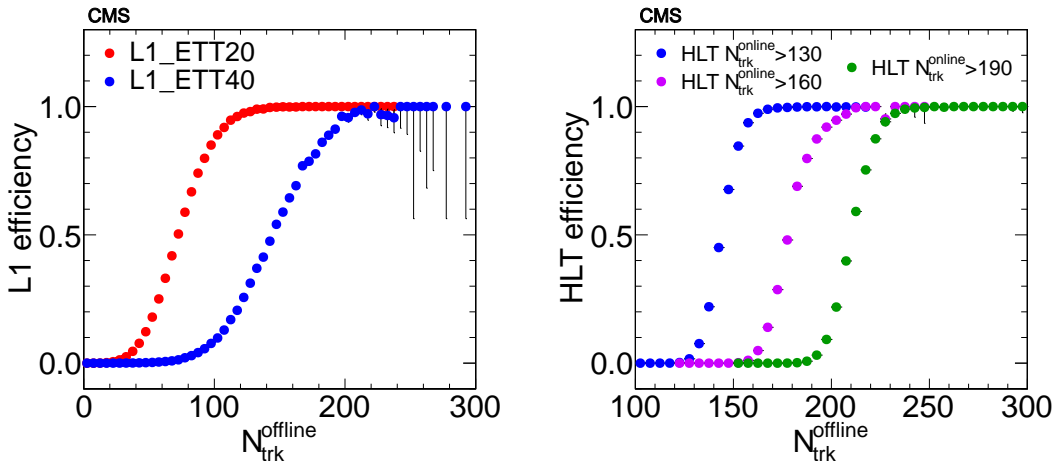


Figure 5: The L1 and HLT trigger efficiencies for the high-multiplicity triggers as functions of  $N_{\text{trk}}^{\text{offline}}$  for 5.02 TeV pPb collision data taking in the year of 2013. (Figure adapted from Ref. [110].)

detailed in Section 2.7, whereas the centrality description is given in Section 2.5. For most of the events, only tracks satisfying the high-purity quality criterion [83], with the additional restrictions  $p_{\text{T}} > 0.7 \text{ GeV}$  and  $d_0 < 2 \text{ mm}$  (where  $d_0$  is the transverse impact parameter of a track with respect to the beam), are included in the PV filter. In more peripheral events, all reconstructed tracks are used because the high-purity selection is too restrictive. For the most central collisions, the minimum  $p_{\text{T}}$  requirement was increased to  $p_{\text{T}} > 1.0 \text{ GeV}$ . These restrictions keep the maximum number of fitted tracks less than about 40–60, thereby ensuring a time-efficient reconstruction. The requirement of an accepted vertex removes a large fraction of the background events, especially beam-gas interactions, which can have large HF energy deposits but very few pixel hits.

#### 2.4.2 Cluster compatibility filter

A particle traversing a pixel module at some angle leaves a cluster with a width proportional to its angle of incidence. That angle, and hence the expected width of the cluster, can be determined by the particle pseudorapidity and the position of the collision vertex along the beam direction ( $z$ ). This information can be used to determine the number of clusters in an event that have a width compatible with particles originating from the vertex position. Alternatively, this compatibility can be investigated without a predetermined vertex by scanning the  $z$  axis to determine how many clusters are compatible with a vertex at each value of  $z$ . This technique can be used to locate the most likely  $z$  position of the collision without the need for any reconstructed tracks or, instead, to determine if the collision likely occurred outside the interaction region. The cluster size is proportional to  $|\sinh \eta|$ , where the  $\eta$  of the cluster is computed with respect to the reconstructed vertex. A selection on this variable is performed as a function of  $\eta$  [111].

#### 2.4.3 Other filters

The HF coincidence filter requires at least two towers in both of the HF calorimeters (one on each side of the interaction point) with a deposited energy above 4 GeV. This requirement removes approximately 99% of the UPC events (discussed in Section 2.4.5).

Finally, the beam scintillation counter (BSC) [112] is a set of large-area scintillators mounted in front of HF to provide beam halo information. A dedicated filter excluded events where any of

the BSC halo L1 trigger bits were set. This filter was only used for the Run 1 data samples.

#### 2.4.4 MB event selection efficiency

Along with the unwanted background, the event selection criteria described above also remove some valid hadronic collision events. The selection efficiency is defined as the fraction of valid events that pass the MB criteria applied to the data, and is found using a method based on Monte Carlo (MC) simulations. The distribution in data, either the total energy deposited in the HF calorimeters (which is not saturated in the more peripheral events) or the number of pixel hits which pass the cluster size requirement, is compared to the respective distribution found using simulated events. The two distributions are normalized in the higher-multiplicity region and any differences at lower multiplicity are indicative of selection inefficiencies. The uncertainty in this estimate is determined by varying the MC simulation parameters, particularly those affecting the average multiplicity, and also by varying the normalization range. The overall trigger and event selection efficiency for MB HI collisions is estimated to be  $97 \pm 3\%$  in PbPb collisions at 2.76 TeV (Run 1) [108] using events from the AMPT 1.26t5 simulation [113], and  $97 \pm 1.5\%$  in PbPb collisions at 5.02 TeV (Run 2) using HYDJET 1.9 simulations [114].

#### 2.4.5 Electromagnetic contamination

When two nuclei pass each other with transverse impact parameters larger than the sum of their nuclear radii, their hadronic interaction cross section is vanishingly small, but the nuclei can still interact through their large EM fields. The EM interactions occurring in the UPC events induce a level of contamination that is studied by using generated events from STARLIGHT 2.2 + DPMJET 3.0 [115, 116] or STARLIGHT +PYTHIA8.2 [115, 117], passing them through a simulation of the CMS detector response based on GEANT4 [118], and then applying the same reconstruction procedure as for the data. In order to estimate this contamination in the MB sample, the number of events surviving different event selections are determined. Event rates obtained by applying the PV plus cluster compatibility filters are used as a baseline. The HF coincidence filter is then applied in data and simulations, but with varying requirements on the number of towers and their energies. This variation is needed because the simulations do not include UPC events. Any differences seen between the data and MC distributions with the varying HF filters imply the presence of remaining UPC contamination in the MB sample. This allows for the determination of the best HF coincidence filter to remove the overwhelming majority of the UPC events and also to estimate the remaining EM contamination. A STARLIGHT sample simulating photoproduction events (including only single photon events) was used for the efficiency determination. For Run 2 PbPb collisions, only 0.8% of the EM events survive the selection criteria. The total expected photoproduction cross section in PbPb collisions at 5.02 TeV is 34 b, implying an EM contamination cross section of 0.27 b. Using the MB event selection efficiency of 98%, combined with the hadronic cross section of 7.7 b, gives 7.5 b of hadronic events. The ratio of the 0.27 b of EM contamination and the total hadronic plus EM cross section of 7.77 b implies that the EM contamination in the selected MB sample is about 3.5%.

### 2.5 Centrality determination in nucleus-nucleus collisions

The degree of overlap of two colliding nuclei (called “centrality”), or equivalently their transverse impact parameter ( $b$ ), is a critical component in the study of HI collisions. Many properties of the interaction vary significantly with centrality. These include the shape of the overlap region (varying from lenticular for peripheral collisions to roughly spherical for central ones) and its size (or equivalently the number of participating nucleons,  $N_{\text{part}}$ ). Other quantities of

interest include the average distance each nucleon traverses while passing through the other nucleus, from which one can calculate the average number of interactions per nucleon and the total number of binary nucleon-nucleon (NN) collisions,  $N_{\text{coll}}$ . The nuclear overlap function,  $T_{\text{AA}}$ , is then defined as  $N_{\text{coll}}$  divided by the inelastic NN cross section  $\sigma_{\text{NN}}^{\text{inel}}$ . The value of  $T_{\text{AA}}$  can be interpreted as equivalent to the NN integrated luminosity per HI collision. These quantities are essential for comparing data from different collision systems or different experiments, and also for comparing data to theoretical calculations. The quantitative measure of centrality is defined as the percentage of the total inelastic hadronic nucleus-nucleus cross section, with 0% corresponding to full overlap and 100% corresponding to the nuclei just barely missing each other. Values of  $b$ ,  $N_{\text{part}}$ , and  $N_{\text{coll}}$  cannot be experimentally measured, and so they need to be deduced from the data using Glauber MC models [119, 120]. To obtain these values, experiments rely on other observables, such as the multiplicity of outgoing particles (or the energy in the forward region), which are roughly proportional to  $N_{\text{part}}$ .

### 2.5.1 Glauber Monte Carlo model

The Glauber MC model estimates geometric quantities such as  $N_{\text{part}}$ ,  $N_{\text{coll}}$ , and the impact parameter. This method is used by experiments at both RHIC and the LHC [120] and is related to, but distinct from, the original so-called “Glauber model”, which first used a variation of the optical model of scattering theory to analytically derive the properties of collisions of protons with nuclei (as described in Ref. [119] and references therein). The Glauber MC model first assumes that, at ultrarelativistic energies, individual nucleons in one nucleus carry enough momentum to not be deflected as they traverse the other colliding nucleus. The collisions are assumed to happen over such a short time scale that there is no movement within the nuclei, so the constituent nucleons move in independent linear trajectories parallel to the beam direction. Finally, nucleons from opposite nuclei are assumed to interact if their relative transverse distance is less than the “ball diameter”, i.e.,  $D = \sqrt{\sigma_{\text{NN}}^{\text{inel}}/\pi}$ , where  $\sigma_{\text{NN}}^{\text{inel}}$  is the inelastic hadronic NN cross section at the NN center of mass energy. With these hypotheses, a MC model can be used to find values for the interaction cross section of the two nuclei, as well as  $N_{\text{part}}$  and  $N_{\text{coll}}$ , in terms of the basic NN interaction. Individual events in the MC involve randomly distributing the nucleons within each nucleus and then following their trajectories.

The probability density used to place the nucleons is based on Woods–Saxon distributions (i.e., Fermi–Dirac distributions applied to describe the nuclear density),

$$\rho(r) = \rho_0 \frac{1 + w(r/R)^2}{1 + \exp(\frac{r-R}{a})}, \quad (1)$$

where  $\rho_0$  is the nucleon density in the center of the nucleus,  $R$  is the nuclear radius,  $a$  is the skin depth, and  $w$  represents the deviation of the nucleus from a spherical shape. For  $^{208}\text{Pb}$  nuclei, the parameter  $\rho_0$  is an overall normalization and  $w$  is equal to zero. The impact parameter of the collisions is distributed by using  $dN/db \approx b$ , considering a  $b_{\text{max}}$  around 20 fm. A new parameter is introduced to require a minimum inter-nucleon distance between the centers of the nucleons. Specifically, nucleons are distributed on a uniform 3-dimensional lattice with a minimum nodal separation  $d_{\text{node}} = 0.4$  fm. In this way, the position of each nucleon is determined stochastically, event-by-event, and the geometric quantities are estimated by averaging over multiple events.

### 2.5.2 Centrality determination

The primary detector for centrality determination is the HF, which covers the forward rapidities  $3 < |\eta| < 5.2$ , as described in Section 2.1. The transverse energies on both sides of this

detector are summed to give a variable that is monotonically increasing with charged-particle multiplicity.

This sum of transverse energy  $E_T$  in the HF calorimeters was the default centrality variable during Runs 1 and 2 [108]. A set of  $E_T$  boundaries was determined, which divided the full HF distribution into 200 centrality bins, corresponding to centrality classes of width 0.5% of the total inelastic hadronic cross section. The bin boundaries are calculated from a sample of MB events with the trigger and event selections applied. To consider the event selection efficiency and possible EM and UPC contamination, a HYDJET MC simulation [114] was used for events with HF  $E_T$  less than a threshold, above which the HF  $E_T$  distributions for the data and HYDJET MC have identical shapes. The MC distribution is scaled to match that of the data in the high  $E_T$  (central collision) region by minimizing the  $\chi^2$  goodness-of-fit. This scaled MC distribution can then be used to determine centrality bins in the low- $E_T$  (peripheral collision) region, where inefficiencies and/or EM contamination can distort the distribution in data. The centrality class for a selection of events is given as a range in percentage of the total inelastic hadronic cross section.

The dependence of the charged-particle multiplicity density at midrapidity on the centrality class is shown in Fig. 6. As expected, the multiplicity increases monotonically with increasing overlap of the two nuclei (i.e., decreasing centrality percentage). Note the logarithmic scale for the  $y$  axis, indicating that the multiplicity increases more rapidly as the collisions get more central.

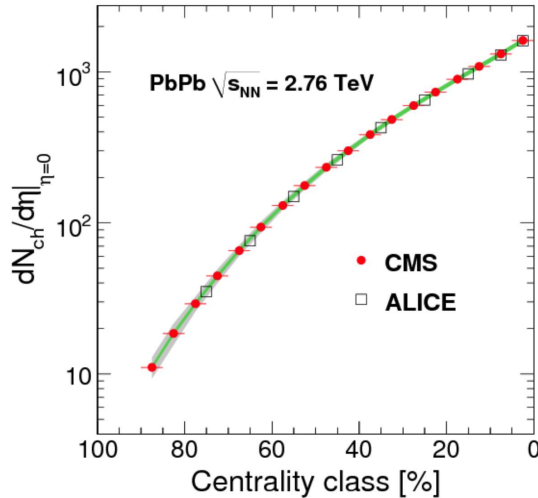


Figure 6: Charged hadron multiplicity density at mid-rapidity ( $dN_{ch}/d\eta|_{\eta=0}$ ) as a function of centrality class in PbPb collisions at  $\sqrt{s_{NN}} = 2.76$  TeV from the CMS (solid circles) and ALICE [121] (open squares) experiments. The inner green band shows the measurement uncertainties affecting the scale of the measured distribution, while the outer grey band represents the full systematic uncertainty, i.e., affecting both the scale and the slope. (Figure adapted from Ref. [111].)

The number of pixel hits is also considered in the centrality determination. Having the same monotonic dependence as the energy measured in the HF, this quantity provides a good cross-check. In addition, the ZDC detector is used to test the quality of both variables. The total energy in the ZDC is correlated to the number of spectator neutrons released in the interaction, thus providing a variable that is correlated (anti-correlated) with the multiplicity of events in peripheral (more central) events [119].

### 2.5.3 Uncertainties in the centrality determination

The two major contributions to the centrality uncertainties are from the Glauber model parameters and the estimate of the event selection efficiency. The uncertainties in the Glauber parameters are extracted by using the procedure described in Ref. [120], where Glauber MC samples were produced with varying values of the parameters. The systematic uncertainties in the four input parameters to the Glauber MC calculation are shown in Tables 4 and 5 for PbPb collisions at 5.02 TeV, whereas similar conclusions hold for the other  $\sqrt{s_{\text{NN}}}$  values.

Table 4: Input parameters and their uncertainties for the PbPb 5.02 TeV Glauber MC [122].

| Glauber parameter                  | Value and uncertainty |
|------------------------------------|-----------------------|
| $R$ (nuclear radius)               | $6.68 \pm 0.02$ fm    |
| $a$ (skin depth)                   | $0.447 \pm 0.01$ fm   |
| $d_{\text{node}}$                  | $0.4 \pm 0.4$ fm      |
| $\sigma_{\text{NN}}^{\text{inel}}$ | $67.6 \pm 0.6$ mb     |

Table 5: Geometric quantities and their systematic uncertainties averaged over centrality ranges in PbPb collisions at 5.02 TeV.

| Centrality interval | $\langle N_{\text{coll}} \rangle$ | $\langle N_{\text{part}} \rangle$ | $\langle T_{\text{AA}} \rangle$ (mb $^{-1}$ ) |
|---------------------|-----------------------------------|-----------------------------------|---|
| 0–5%                | $1737 \pm 32$ (1.8%)              | $382.3 \pm 1.5$ (0.4%)            | $25.70 \pm 0.47$ (1.8%)                       |
| 5–10%               | $1379 \pm 27$ (2.0%)              | $331.5 \pm 1.2$ (0.4%)            | $20.40 \pm 0.40$ (2.0%)                       |
| 0–10%               | $1558 \pm 28$ (1.8%)              | $356.9 \pm 0.9$ (0.3%)            | $23.05 \pm 0.42$ (1.8%)                       |
| 10–20%              | $973 \pm 21$ (2.1%)               | $262.3 \pm 1.3$ (0.5%)            | $14.39 \pm 0.30$ (2.1%)                       |
| 20–30%              | $595 \pm 15$ (2.5%)               | $188.2 \pm 1.4$ (0.8%)            | $8.80 \pm 0.22$ (2.5%)                        |
| 30–40%              | $346 \pm 11$ (3.1%)               | $131.0 \pm 1.4$ (1.1%)            | $5.12 \pm 0.16$ (3.1%)                        |
| 40–50%              | $187.7 \pm 7.2$ (3.8%)            | $87.2 \pm 1.3$ (1.5%)             | $2.78 \pm 0.11$ (3.8%)                        |
| 50–80%              | $50.4 \pm 2.5$ (5.0%)             | $33.8 \pm 0.8$ (2.4%)             | $0.745 \pm 0.037$ (5.0%)                      |
| 0–100%              | $382 \pm 27$ (2.0%)               | $113.7 \pm 0.8$ (0.7%)            | $5.65 \pm 0.12$ (2.2%)                        |

## 2.6 Event classification methods in pp and pPb collisions

For pp and pPb collision data, an event selection similar to that described for PbPb events was adopted. The integrated values for the combined trigger and event selection efficiency for pPb collisions at 5.02 TeV are 90.7% based on EPOS LHC [123] simulations, and 95.0% when using HIJING v2.1 [124], both with a systematic uncertainty of 3%.

In pp collisions, the events are characterized by bins in  $N_{\text{trk}}^{\text{offline}}$ , which is the multiplicity of high-purity quality tracks within  $|\eta| < 2.4$  and  $p_{\text{T}} > 0.4$  GeV. To mitigate effects from backgrounds, a reconstructed track was considered as a primary-track candidate if the transverse impact parameter significance (the value divided by its uncertainty) and the significance of the separation between the track and the best reconstructed PV along the beam direction both have an absolute value less than 3. In order to remove tracks with poor momentum estimates, the relative uncertainty of the momentum measurement was required to be less than 10%.

For pPb collisions, the HF calorimeters could, in principle, be used for a centrality measurement in the same way as was done for PbPb collisions. However, this is not particularly useful since simulations show that the correlation between the HF energy and the number of participating nucleons is extremely broad [125]. So, data for pPb collisions are, for the most part, also binned in  $N_{\text{trk}}^{\text{offline}}$ . The average multiplicity values,  $\langle N_{\text{trk}}^{\text{offline}} \rangle$  and  $\langle N_{\text{trk}}^{\text{corrected}} \rangle$ , where the latter are corrected for efficiency and acceptance, are listed in Table 6 for each  $N_{\text{trk}}^{\text{offline}}$  interval. A

Table 6: Fraction of MB triggered events after event selections in each multiplicity bin, and the average multiplicity of reconstructed tracks per bin with  $|\eta| < 2.4$  and  $p_T > 0.4$  GeV, before ( $N_{\text{trk}}^{\text{offline}}$ ) and after ( $N_{\text{trk}}^{\text{corrected}}$ ) acceptance and efficiency corrections, for pPb and PbPb collisions at 5.02 and 2.76 TeV, respectively [110].

| $N_{\text{trk}}^{\text{offline}}$ bin | Fraction           | pPb data at 5.02 TeV                              |   | PbPb data at 2.76 TeV                            |   |   |
|---------------------------------------|--------------------|---|---|--|---|---|
|                                       |                    | $\langle N_{\text{trk}}^{\text{offline}} \rangle$ | $\langle N_{\text{trk}}^{\text{corrected}} \rangle$ | $\langle \text{Centrality} \rangle$<br>± RMS (%) | $\langle N_{\text{trk}}^{\text{offline}} \rangle$ | $\langle N_{\text{trk}}^{\text{corrected}} \rangle$ |
| 0–∞                                   | 1.00               | 40  | $50 \pm 2$  |  |   |   |
| 0–20                                  | 0.31               | 10  | $12 \pm 1$  | $92 \pm 4$                                       | 10  | $13 \pm 1$  |
| 20–30                                 | 0.14               | 25  | $30 \pm 1$  | $86 \pm 4$                                       | 24  | $30 \pm 1$  |
| 30–40                                 | 0.12               | 35  | $42 \pm 2$  | $83 \pm 4$                                       | 34  | $43 \pm 2$  |
| 40–50                                 | 0.10               | 45  | $54 \pm 2$  | $80 \pm 4$                                       | 44  | $55 \pm 2$  |
| 50–60                                 | 0.09               | 54  | $66 \pm 3$  | $78 \pm 3$                                       | 54  | $68 \pm 3$  |
| 60–80                                 | 0.12               | 69  | $84 \pm 4$  | $75 \pm 3$                                       | 69  | $87 \pm 4$  |
| 80–100                                | 0.07               | 89  | $108 \pm 5$   | $72 \pm 3$                                       | 89  | $112 \pm 5$   |
| 100–120                               | 0.03               | 109   | $132 \pm 6$   | $70 \pm 3$                                       | 109   | $137 \pm 6$   |
| 120–150                               | 0.02               | 132   | $159 \pm 7$   | $67 \pm 3$                                       | 134   | $168 \pm 7$   |
| 150–185                               | $4 \times 10^{-3}$ | 162   | $195 \pm 9$   | $64 \pm 3$                                       | 167   | $210 \pm 9$   |
| 185–220                               | $5 \times 10^{-4}$ | 196   | $236 \pm 10$  | $62 \pm 2$                                       | 202   | $253 \pm 11$  |
| 220–260                               | $6 \times 10^{-5}$ | 232   | $280 \pm 12$  | $59 \pm 2$                                       | 239   | $299 \pm 13$  |
| 260–300                               | $3 \times 10^{-6}$ | 271   | $328 \pm 14$  | $57 \pm 2$                                       | 279   | $350 \pm 15$  |
| 300–350                               | $1 \times 10^{-7}$ | 311   | $374 \pm 16$  | $55 \pm 2$                                       | 324   | $405 \pm 18$  |

number of analyses have attempted to compare pPb and PbPb results for similar system “size” by using identical bins in  $N_{\text{trk}}^{\text{offline}}$ . Table 6 also shows the corresponding average PbPb collision centrality (as determined by the total energy deposited in the HF calorimeters), as well as the same average multiplicities in bins of  $N_{\text{trk}}^{\text{offline}}$ .

## 2.7 Tracking and vertex reconstruction

The CMS Collaboration uses two approaches for offline reconstruction of charged particles in HI collisions. One employs an iterative approach based on the combinatorial Kalman filter (CKF), resulting in a set of tracks called “general tracks” [83], whereas the other method uses a single iteration based on the pixel detector only, known as “pixel detector tracks” [126]. The first method, similar to the one applied in pp collisions, considers both strips and pixel detectors, and covers the charged-particle transverse momentum region above a few hundreds of MeV. The pixel detector tracking is designed to reach the lowest possible transverse momentum. It accomplishes this by having a very reduced rate of misreconstructed tracks as compared to the general tracks, even in events with very high charged-particle multiplicities.

For PbPb data taken during Runs 1 and 2, the total efficiency  $\epsilon_{\text{eff}}$  of the general tracks (track reconstruction, and track selection), folded with the detector acceptance, varied as a function of the collision centrality and the transverse momentum of the particles in the range 10–75% (lower values in central collisions and the low- $p_T$  region down to 0.5 GeV). Similar trends are observed for pixel tracking with total efficiency in the range 15–70% for  $0.3 < p_T < 1.0$  GeV. For misreconstructed tracks, the general tracks have  $\epsilon_{\text{misID}}$  values (ratio between the number of reconstructed tracks that do not share more than 75% of their hits with a generator-level track and the total number of reconstructed tracks) in the range 1–20% (higher in central collisions and the low- $p_T$  region down to 0.5 GeV). Again, the results for pixel detector tracking are

similar, with  $\epsilon_{\text{misID}}$  values in the range 2–10% for  $0.3 < p_{\text{T}} < 1.0 \text{ GeV}$ . The performance for pp, pPb, and XeXe data samples is similar, especially when comparing events with similar track multiplicity, as described in Refs. [83, 127].

In Run 1, the general track collection in PbPb collisions was built using a variation of the iterative tracking procedure used for pp data, including modified code and a different number of steps in the algorithm, as described in Ref. [128]. As described in Ref. [83], the analyses in Run 2 used the same code for track reconstruction for all colliding systems, as well as almost the same number of iterations. An exception to this similarity is the algorithm dedicated to reconstructing tracks whose origin was significantly displaced from the PV, e.g., particles created in heavy-flavor hadron decay. However, the PbPb collision environment is considerably different from that found in “typical” pp collisions with an average PU of 20, being much denser in number of tracks (details are given in Sections 2.6 and 4.1). Therefore, the tracking parameters used in the algorithms shared with pp analysis needed to be tuned for PbPb collisions in order to have a good performance in terms of CPU time, storage, tracking efficiency, and the rate of misreconstructed tracks. The sharing of algorithms between the various colliding systems is very important because now all the developments implemented for pp collisions are generally incorporated for PbPb data taking and vice-versa. This commonality will become increasingly important since a central PbPb collision has a track density similar to that which will be created by PU in pp collisions in future high-luminosity LHC running.

The offline PV reconstruction used in CMS analysis is based on a two-step procedure: vertex finding using a deterministic annealing algorithm to produce clusters of tracks coming from the same interaction vertex, followed by vertex fitting using the adaptive vertex fit to compute the best estimate of the vertex position and the corresponding parameters of its associated tracks [83]. The main challenge in the vertexing procedure is to avoid vertex merging and splitting (combining two independent vertices into one, or generating two separate vertices out of a single collision). Compared to the method used for pp collisions, an additional track  $p_{\text{T}}$  requirement ( $p_{\text{T}} > 1 \text{ GeV}$ ) was applied for the 20% most central PbPb collisions, with no additional selections added for other centrality classes. This requirement was used to reduce vertex merging and splitting in central PbPb collisions, while maintaining high vertex reconstruction efficiency in peripheral collisions.

## 2.8 Muon reconstruction

Final states containing muons are important components of many HI physics analyses, including studies of quarkonia and electroweak bosons. The excellent performance of the CMS muon detection system enables the reconstruction and identification of muons with high efficiency and accuracy over a wide momentum range [86, 87, 129]. Details regarding the performance of CMS muon reconstruction across collision systems during Run 2 can be found in Ref. [51]. This section summarizes the main findings related to offline muon reconstruction, stressing the challenges arising in the high-multiplicity HI collision environment.

Similar tracking algorithms [87] are employed for all collision systems in Runs 1 and 2 as mentioned in Section 2.7. Based on the output of track reconstruction in the silicon tracker (“tracker track”) and in the muon system (“standalone muon track”) independently, muons are reconstructed following two complementary approaches. In the “tracker muon” reconstruction, muons correspond to extrapolated tracker tracks matching at least one segment (local tracks built within each CSC or DT chamber) in the muon system; while the “global muon” reconstruction combines standalone muon tracks with hits from tracker tracks via an outside-in fit procedure [86, 87]. Muon candidates are then fed into the PF algorithm [88] for a complete

description of all individual particles per event, as discussed in Section 2.1. The nominal muon detection acceptance of the CMS apparatus is defined by the minimum momentum needed to traverse the material in front of the first muon detector layer. As shown in Fig. 7, the  $p_T$  threshold is about 3.2 GeV for  $|\eta| \lesssim 1$  and decreases to about 0.5 GeV for  $2.0 \lesssim |\eta| < 2.4$ .

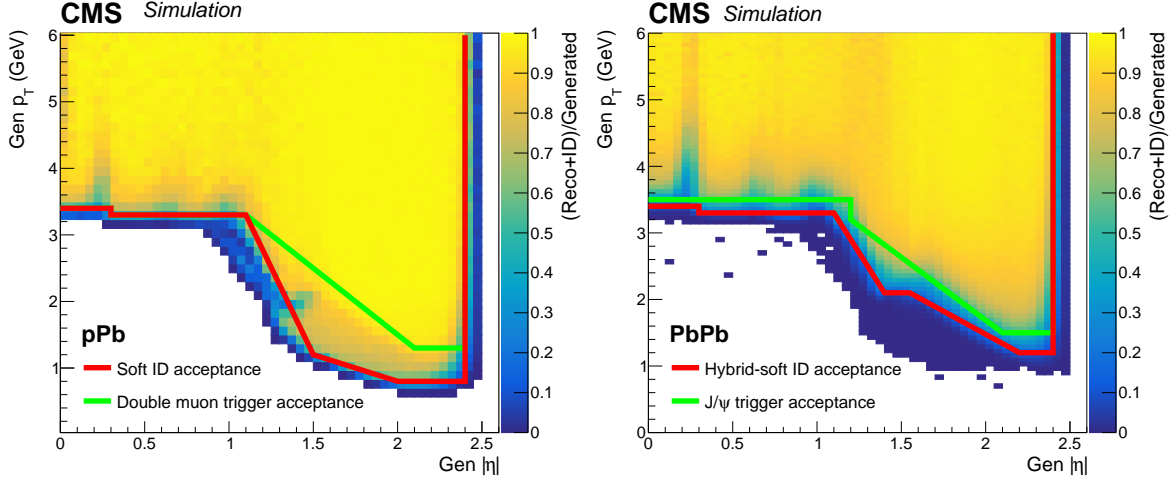


Figure 7: Muon reconstruction and identification efficiencies as functions of the simulated muon pseudorapidity and  $p_T$  in pPb (left) and PbPb (right) collisions. The lines delimit the acceptance regions used for physics analyses: the red curves for measurements not relying on a dedicated muon trigger while the green ones are for analyses using the muon trigger information, i.e., for most of the quarkonia results presented in this paper. (Figure adapted from Ref. [51].)

Muon reconstruction is found to be highly efficient from pp to pPb to PbPb collisions, with the exception of the highest multiplicity PbPb events, particularly those with more than about 1000 tracks [51]. The tracker muon approach is inherently more efficient than the global one at low momentum since the latter starts from a standalone track reconstructed with segments in two or more muon detector layers. However, the inside-out approach has disadvantages that are amplified in HI events. Because all of the tracker tracks are propagated to the muon system as potential muon candidates, the reconstruction efficiency—including the matching with muon detector segments—degrades with the occupancy in the silicon tracker layers. Moreover, most of low- $p_T$  muons only reach the innermost station and thus only match one segment. This increases the probability of misidentification from charged hadrons either produced promptly in the collision or by hadron showers developed within the HCAL. These effects are dramatically enhanced with the large number of pions produced in nucleus-nucleus collisions. For Run 1 and 2 analyses of PbPb collision data, this misidentification rate was partially mitigated by selecting muon objects reconstructed as global muon tracks, at the cost of a reduced fiducial region for the measurements, as shown in the right panel of Fig. 7. This selection is complemented by a set of identification criteria called *hybrid-soft muon ID*, a version of the *soft muon ID* optimized for HI events [51]. Those two sets differ mainly in the addition of the global muon requirement and the removal of the selection of high-purity quality tracks [83] for hybrid-soft ID. The physics analyses use the soft muon identification to select low- $p_T$  ( $< 20$  GeV) muons in pp, pPb, and ultraperipheral PbPb collisions, and the hybrid-soft version for hadronic PbPb events.

## 2.9 High- $E_T$ electron and photon reconstruction

Electrons are found by combining information from the ECAL with charged-particle tracks. Photons are found using only ECAL information, but tracking information is also used to reject electrons or other sources of misidentified photon candidates.

### 2.9.1 Electron reconstruction

The electron reconstruction uses information from the pixel and strip tracker as well as the ECAL. Electrons traversing the silicon tracker can emit bremsstrahlung photons, which can also deposit energy in the ECAL. This causes a significant spread of the signals in the azimuthal direction. An algorithm for creating superclusters, which are clusters of signals from all particles passing through the ECAL, is used to estimate the proper energy of electrons and photons in the HI environment [109].

For Run 1 data, a Gaussian-sum filter algorithm, which combines ECAL superclusters with information from the pixel and strip tracker considering the bremsstrahlung emissions, is used to reconstruct electrons [130]. Standard algorithms and identification criteria [131] were used for pp and pPb data, resulting in a reconstruction efficiency larger than 95%. For PbPb collisions, the electron reconstruction efficiency is smaller, approximately 85% for electrons from  $Z$  boson decays with  $p_T > 20\text{ GeV}$  and  $|\eta| < 1.44$ , because the tracking algorithm optimized for high-multiplicity events has a lower track reconstruction efficiency than that used for pp collisions [132]. The requirements used to reduce background (Ref. [131] contains the variable definitions) include selections on: the energy-momentum combination between the supercluster and the track, the  $\eta$  and  $\phi$  spatial matching between the track and the supercluster, the supercluster shower shape width, the hadronic leakage (the ratio of energy deposited in the HCAL and ECAL,  $H/E$ ), and a transverse distance of the closest approach to the measured PV. These selections eliminate most of the background while reducing the single-electron efficiency by only about 10 (5)% in PbPb (pp) collisions.

For Run 2 PbPb data, electrons are identified as ECAL superclusters [133] matched in position and energy to tracks reconstructed in the tracker, using the PF algorithm as discussed in Section 2.1. The electrons must have  $p_T > 20\text{ GeV}$  and their supercluster must be within the acceptance of the trigger,  $|\eta| < 2.1$ . The reconstruction efficiency is  $>95\%$ , whereas a multivariate discriminant, optimized using the TMVA package [134], selects electrons with a working point corresponding to 90% identification efficiency and 80% rejection of misreconstructed electrons [133].

### 2.9.2 Photon reconstruction

In analyses using Run 1 and Run 2 data, photons are reconstructed offline in PbPb collisions using an island energy clustering algorithm [109] that is optimized for high-multiplicity HI events. The island algorithm builds ECAL superclusters in two steps:

- Defines clusters by adding energy of adjacent reconstructed hits in the ECAL using some building stopping criteria (e.g., if the corrected energy of reconstructed hits is below some threshold or if the hits were already included in other clusters);
- Combines the clusters from previous step into superclusters. The criterion for merging the clusters requires a minimum value of its transverse energy of 1 GeV and the clusters should be located in a spatial strip of  $\Delta\eta = 0.07$  and  $\Delta\phi = 0.8$ .

The photon momentum is calculated with respect to the location of the reconstructed primary interaction vertex. If multiple vertices are reconstructed, the vertex with the largest scalar sum

of the transverse momenta of the associated tracks is selected. For pp data, the island algorithm is used for Run 1, while the global event description (GED) algorithm [89] is used for Run 2. The GED uses a similar idea as the island method to build the superclusters [133]. It uses additional variables with respect to the discrimination between converted and unconverted photons. In addition, there are considerable differences in the procedure for applying corrections to the energy of the clusters.

Additional criteria to reject electrons that are misidentified as photons and misidentified photons caused by highly ionizing particles interacting directly with the silicon avalanche photodiodes in the ECAL barrel readout are applied following the procedure described in Ref. [109]. Several additional criteria are applied: corrections for UE contamination and the effects from the material in front of the ECAL, selections to eliminate high- $p_T$  hadron contamination, and an isolation ( $I$ ) requirement [135]. The latter one is defined as the sum of transverse energies in the ECAL and HCAL (excluding the photon component) and the transverse momenta of all reconstructed tracks with  $p_T > 2$  GeV inside the cone  $\Delta R = \sqrt{(\Delta\eta)^2 + (\Delta\phi)^2} = 0.4$ . The efficiency to detect isolated photons as a function of their transverse energy ( $E_T^\gamma$ ), extracted from MC simulations, is shown in Fig. 8.

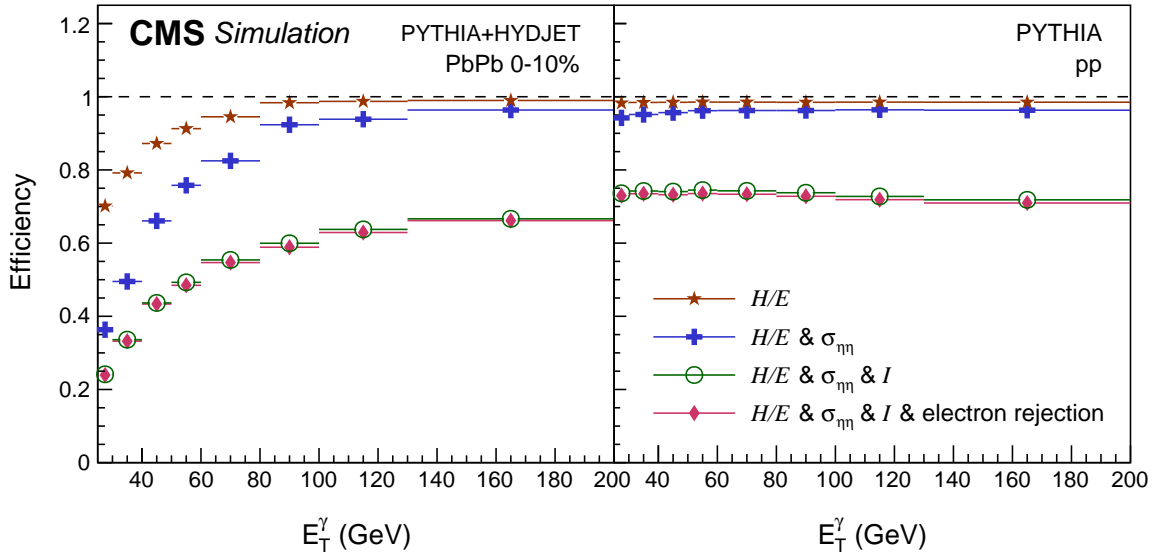


Figure 8: Isolated photon detection efficiency in  $|\eta| < 1.44$  as a function of  $E_T^\gamma$  obtained from MC simulations. Left: PbPb collisions in the 0–10% centrality range. Right: pp collisions. Both the PbPb and pp collisions are at 5.02 TeV. The different colors represent efficiencies reached for successive application of the listed selection criteria: ratio of HCAL over ECAL energies  $H/E < 0.1$ , EM shower shape variable  $\sigma_{\eta\eta} < 0.01$ , isolation variable  $I < 1$  GeV, and electron rejection criterion. (Figure adapted from Ref. [135].)

## 2.10 Jet reconstruction

Jet reconstruction for CMS data takes PF objects as the input set of constituents for the iterative recombination algorithms encoded in the FASTJET software package [93, 136]. The algorithm can combine either the PF objects themselves or, instead, a set of objects modified by subtraction of their UE contributions. The subtraction method used for HI collision data, which differs from the approach taken for high-PU pp collisions, is detailed in Section 2.11.1.

The iterative recombination family of jet-finding algorithms takes as a starting point a set of particles or particle “proxies” (such as calorimeter towers or PF objects). The algorithm

proceeds through all combinations of two entries in the list of input objects and determines whether or not to merge a given pair by finding the minimum values of  $d_{ij}$  and  $d_{iB}$ , defined as

$$d_{ij} = \min((p_{T,i})^{2p}, (p_{T,j})^{2p}) \frac{\Delta R_{ij}^2}{R^2} \quad d_{iB} = (p_{T,i})^{2p} \quad (2)$$

where  $p_{T,i}$  is of particle  $i$ ,  $\Delta R_{ij} = \sqrt{(y_i - y_j)^2 + (\phi_i - \phi_j)^2}$  is the 2-dimensional distance between the two objects in rapidity and azimuthal angle,  $R$  is the so-called “distance” parameter, and the parameter  $p$  typically takes values of  $p = 1$ ,  $p = 0$ , or  $p = -1$ . If  $\min(d_{ij}) < \min(d_{iB})$ , the  $i$ -th and  $j$ -th objects are combined in a 4-vector sum, the resulting combination replaces the two particles in the list, and the list of objects is scanned again. Otherwise, if  $\min(d_{iB}) < \min(d_{ij})$ , object  $i$  is removed from the list as a final-state jet. Iterations continue until the list is exhausted, and the set of objects removed using the  $d_{iB}$  criterion contains the resulting jets.

The typical choices for the value of parameter  $p$ ,  $p = 1$ ,  $p = 0$ , and  $p = -1$ , correspond to the  $k_T$ , Cambridge–Aachen, and anti- $k_T$  algorithms, respectively. The  $k_T$  algorithm preferentially clusters soft particles nearby in  $\eta$  and  $\phi$ , the Cambridge–Aachen one clusters the closest particles irrespective of their momentum, and the anti- $k_T$  choice preferentially clusters the hardest particles with all nearby particles. As a result, anti- $k_T$  jets have a regular, cone-like shape. For experimental reasons relating to background subtraction and energy calibration, anti- $k_T$  is the preferred choice for jet reconstruction in HI data. In specific studies of jet substructure (discussed in Section 5.3.3), jets originally clustered with the anti- $k_T$  may have their resulting constituent set reclustered using another algorithm but, outside of this exception, the anti- $k_T$  algorithm is used.

## 2.11 Treating the underlying event in physics object reconstruction

Compared to pp collisions, one of the primary additional challenges faced by HI analyses is the large UE produced by the many binary NN collisions that occur when nuclei collide. As one example, in order to extract the properties of the fragmenting hard-scattered parton generating a jet, corrections must be made for the significant additional energy the UE can add to the reconstructed jet. A similar problem occurs in pp collisions because of the high rates of PU, requiring correction for the additional event activity produced. However, in PbPb collisions, the additional activity/underlying event to be subtracted is

1. typically a much larger fraction of the signals of interest,
2. anisotropic in azimuthal angle due to collective flow (as discussed in Section 4.2),
3. originates from a volume comparable to the diameter of a Pb nucleus ( $\approx 10$  fm), as opposed to being spread out across many vertices along the beam direction, which is the case for PU in pp.

As a result of these three differences, techniques developed to correct for the UE contributions in pp data, such as vertexing techniques for the removal of PU contributions to jet energy, are frequently ineffective in the HI environment. The following subsections detail how physics object reconstruction is modified to account for these differences.

### 2.11.1 Correcting for the underlying event in jet reconstruction

As discussed in Section 2.10, jets are typically reconstructed using PF objects as discussed in Section 2.1. In pp collisions, the additional activity energy primarily comes from PU collisions

which are separable by longitudinal vertex position. The PF objects not originating from the vertex of the hard-scattering that produced the jets can be identified and removed prior to clustering. This technique is called charged-hadron subtraction [137]. In HI events, both the hard scattering and the additional energy from the UE share a single vertex and there is no possibility of determining which PF objects come from the hard scattering. As a result, a two-part approach to correcting for UE energy contributions is typically employed for HI collision data. A determination of the UE contribution as a function of  $\eta$ ,  $\phi$ , and centrality is followed by an algorithm by which the UE is subtracted.

The first half of this two-part approach follows the iterative pedestal PU subtraction procedure [138] modified to account for the azimuthal modulation introduced by hydrodynamic flow (introduced in Section 1.1 and discussed in detail in Section 4.2), and is similar to the ALICE event-by-event fitting method [139]. This procedure first estimates the energy from the UE by taking the average energy in  $\eta$  strips defined by the HCAL tower geometry. As this estimator is known to be biased by the presence of jets, jet finding and correction is performed using the biased estimator, and regions identified as containing jets are excluded for a second iteration of determining the UE contribution. Because the HI UE is asymmetric in  $\phi$  due to the presence of hydrodynamic flow, a  $\phi$ -dependence is added to this  $\eta$ -dependent UE estimation via event-by-event fits of track multiplicities in  $\phi$  following the ALICE example. Note that this  $\phi$ -dependent correction was added to jet reconstruction late in the Run 2 period, and therefore many analyses detailed in this document do not include this step.

The second half of the UE correction procedure follows the jet-by-jet constituent subtraction method (CS) [140, 141]. In this approach, “ghost” particles, or four-vectors of infinitesimally small energies, are randomly distributed in  $\eta$ - $\phi$  space and the number that are included in a particular jet is used to calculate its area. These ghosts can be clustered into the jets without modifying their kinematics. Once this clustering is complete, the ghosts are assigned an UE energy (found using the estimator in step one) according to their  $\eta$ - $\phi$  position, and that energy is removed from the jets they are part of. If the total energy of the ghosts exceeds the total jet energy, the jet is removed rather than being assigned a negative energy, as it is taken to be a misidentified jet coming from the UE.

The resulting performance of this hybrid iterative pedestal/CS subtraction is documented in Ref. [142]. Figure 9 (left and right panels) shows the full subtraction as applied to a single central PbPb event. As PF objects do not have well-defined areas, they have first been combined into pseudotowers in this illustration, with their  $E_T$  sums restricted in  $\eta$ - $\phi$  as defined by the HCAL tower geometry. Figure 10 shows the distribution of UE energy per unit area ( $\rho$ ) as a function of the centrality class. Here,  $\rho$  is estimated by averaging the energy over an area spanning a central- $\eta$  strip corresponding to four HCAL tower widths and covering the full detector in  $\phi$ . The increasing value of  $\rho$  with centrality is illustrative of the difficulty of accounting for the UE contributions in the most central PbPb events. Figure 11 is adapted from Ref. [143] and shows the resulting jet energy scale and resolution after the application of this UE subtraction procedure for both small and large jet distance parameters,  $R = 0.2$  and  $R = 1.0$ . The performance degrades as the distance parameter  $R$  increases, as the greater transverse area of the jet cone increases the contribution of the UE. To mitigate this degrading performance, jets with large  $R$  are only studied at higher  $p_T$  values, thereby reducing the fractional contribution of the UE.

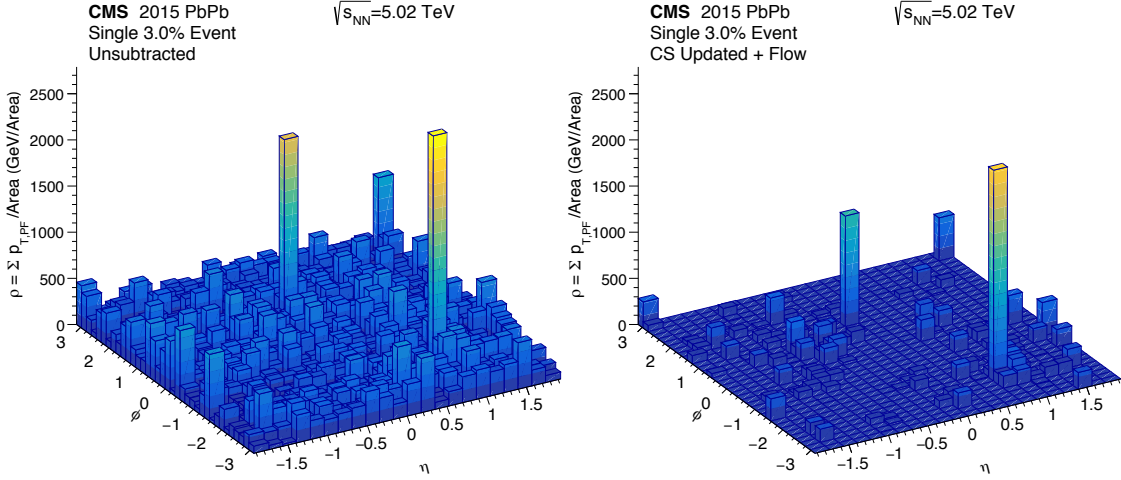


Figure 9: Left: Distribution of PF pseudotowers in  $\eta$ - $\phi$  in a single central (top 3%) event in PbPb collisions before subtraction, with the  $z$  axis showing the corresponding tower energy per unit tower area. Right: The same event after full subtraction with flow modulation is applied. (Figure adapted from Ref. [142].).

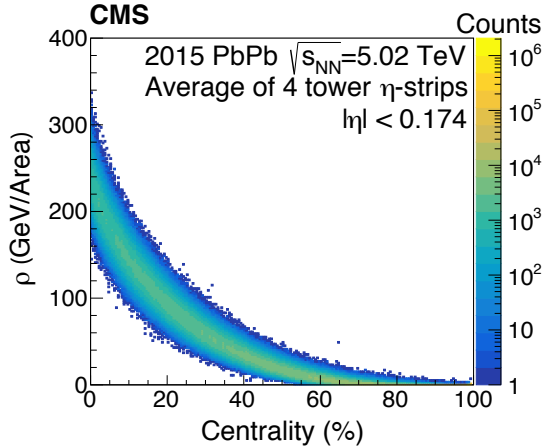


Figure 10: Distribution of  $\rho$ , the UE energy per unit area, as a function of centrality, found using the central- $\eta$  strip of PF pseudotowers. (Figure adapted from Ref. [142].).

### 2.11.2 Correcting for the UE in photon isolation

High-energy isolated photons are produced mostly in hard quark-gluon scatterings (in contrast to nonisolated ones which arise from hadron decays and parton fragmentation) [144], and are identified by the absence of other particles produced within a cone surrounding the photon candidate. The presence of a large UE in PbPb collisions poses a challenge because of the presence of many other soft processes. To determine the UE contribution around a photon candidate, the local surroundings within a cone in pseudorapidity and azimuthal angle around the centroid of the photon is examined to identify any hadronic activity that surpasses a specific veto threshold (typically 5 GeV for isolated photon analyses).

When measuring  $I$  (Section 2.9) in PbPb data, the UE contribution is removed by subtracting the average value of the energy in a rectangular area with a length of  $2\Delta R$  in the  $\eta$ -direction around a photon candidate and a width of  $2\pi$  in the  $\phi$ -direction. However, no UE correction is applied in pp data.

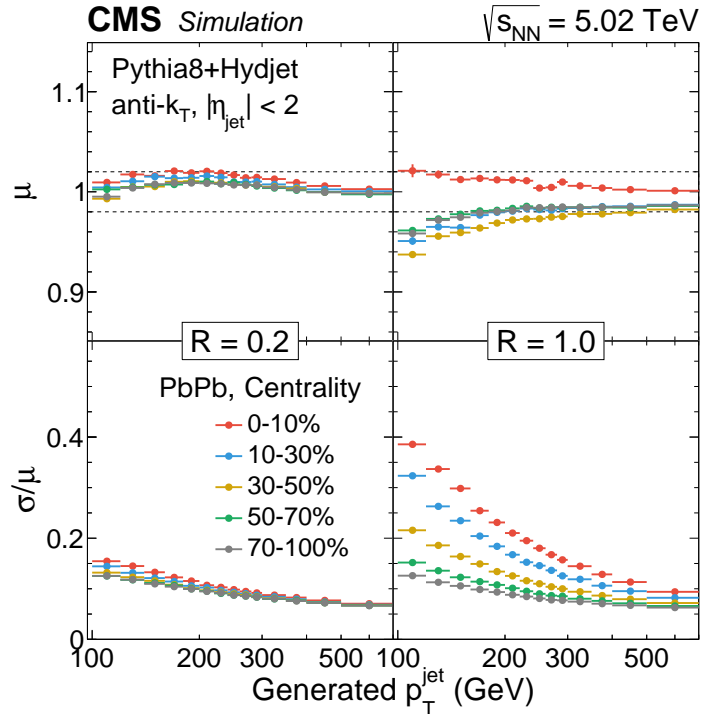


Figure 11: Performance of jet reconstruction in the HI environment for jet distance parameters of  $R = 0.2$  (left) and  $R = 1.0$  (right). The jet energy scale is shown in the upper panels, while the jet energy resolution is plotted in the lower panels. (Figure adapted from Ref. [143].)

## 2.12 Heavy-flavor hadron reconstruction and identification

In HI collisions, heavy-flavor hadrons can be identified in several decay modes involving charged hadrons (pions, kaons, and protons) and/or leptons. During Run 1, these heavy-flavor hadrons were identified by performing a reconstruction step to identify a secondary vertex (SV) that was the origin of the decay particles (without identifying them as pions, kaons, or protons). This was followed by simple selections on individual topologically motivated variables. These included the impact parameter of the reconstructed momentum vector of the decaying hadron with respect to the PV, as well as the angle between that momentum vector and a line connecting the PV and SV [145].

For Run 2, machine learning approaches started to be incorporated into the identification procedure. The primary method uses boosted decision trees (trained using simulations) from the TMVA package. Unfortunately, systematic uncertainties in final results are dominated by uncertainties from these ML procedures [146–148], primarily because the MC simulations used in the training do not describe well the kinematics of heavy-flavor hadrons.

Similarly to heavy-flavor hadrons, the identification of  $b$  jets is based on kinematic variables related to the relatively long lifetime and large mass of  $b$  hadrons. Indeed, heavy-flavor jet identification techniques exploit the properties of the hadrons in the jet to discriminate between jets originating from bottom or charm quarks and those originating from light-flavor quarks or gluons. Several improvements have been made in heavy-flavor jet identification algorithms for Run 2 data, including multivariate analysis developments. For jets with  $p_T$  in the range found in simulated top quark pair events, an efficiency of 70% for the correct identification of a  $b$  jet, along with a probability of 1% of misidentifying a light-flavor jet, was achieved. The improvement in relative efficiency is about 15% (at the same misidentification probability) compared

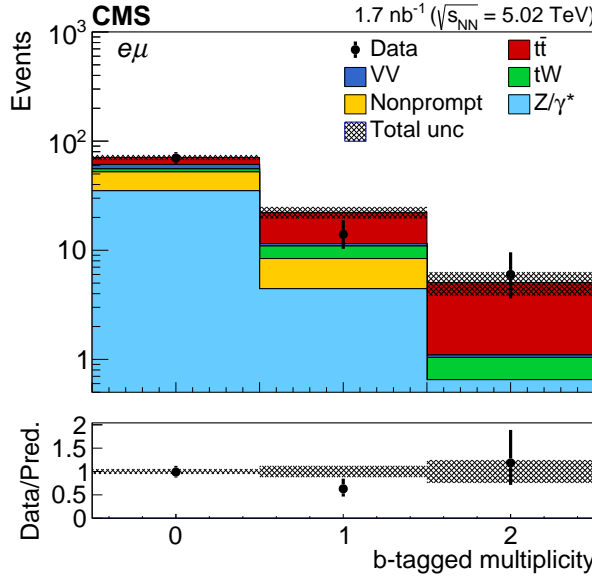


Figure 12: Multiplicity distribution of the b-tagged jets in a top quark pair enriched final state using PbPb collisions. The distribution of the main background is taken from the data. Backgrounds and  $t\bar{t}$  signal are shown with the filled histograms and data are shown with the markers. The vertical bars on the markers represent the statistical uncertainties in data. The hatched regions show the uncertainties in the sum of  $t\bar{t}$  signal and backgrounds. The lower panel displays the ratio of the data to the predictions with bands representing the uncertainties in the predictions. (Figure adapted from Ref. [149].)

to previous algorithms [150]. Figure 12 shows the number of jets “tagged” as originating from b quarks (referred to as “b-tagged jets”) in events progressively enriched with top quarks, i.e., going from no b-tagged jets up to a b-tagged jet multiplicity of 2 [149]. The application of sophisticated b-tagging algorithms is therefore found to enhance the signal (depicted in red in Fig. 12) over background ratio in PbPb collisions, as is the case for standard pp analyses.

### 3 The initial state of the collisions

This section discusses a number of measurements by the CMS Collaboration that constrain our understanding of the initial state in pp, pPb, and PbPb collisions. The initial state comprises the spacetime (or energy-momentum) distribution of parton and nucleon constituents just before a collision. The large number of nucleons present in a HI, such as lead, gives rise to interesting emergent properties of the initial state in high energy collisions. For example, a proposed saturation of the parton density may have measurable consequences at energies achievable at current accelerator facilities using HI probes. While the initial state of an isolated nucleon, or a nucleon that exist within a nucleus, is of interest in its own right, this state has a profound influence on the evolution of a nuclear collision, including the formation and properties of the QGP created in PbPb collisions at the LHC.

Many CMS Run 1 and 2 measurements have helped define the initial-state properties relevant for experiments at the LHC. Of particular interest are the small- and high- $x$  partonic distributions in protons and nuclei. These measurements have also provided a test of the Glauber model that is used to simulate the initial geometry of heavy ion collisions. Here, we highlight the diverse experimental program, including a wide range of measurements designed to access the properties of the initial state, extending from heavy EW boson and high- $p_T$  jet production in hadronic collisions to heavy-flavor photoproduction in UPCs.

#### 3.1 Constraining nuclear parton distribution functions with hard probes

Parton distribution functions (PDFs) are key quantities used in the description of the initial state of a hadronic collisions. They describe the fraction  $x$  of the total momentum of an isolated nucleon that each parton carries. When the nucleon resides within a nucleus, these distributions are known as nPDFs. Calculation of nPDFs from first principles is challenging because of their intrinsic nonperturbative nature, so experimental input is required to establish reference points at different values of  $x$  and of the momentum transfer scale,  $Q^2$ . Global fits of these reference data and the Dokshitzer–Gribov–Lipatov–Altarelli–Parisi (DGLAP) evolution equations [151–153] can then be employed to infer the values of nPDFs at a given value of  $x$  and  $Q^2$ . The accuracy of these fits and extrapolations is largely dictated by the precision and  $(x, Q^2)$  coverage of the input experimental data, meaning that high-quality precision measurements in a large kinematic range are extremely valuable. Studies of EW boson production are examples of such measurements.

Massive EW bosons, i.e., W and Z bosons, have lifetimes on the order of 0.1 fm and can decay to final states that include highly energetic leptons. These leptons do not have a QCD color charge and, consequently, do not interact strongly with other particles. Thus, massive EW bosons and their decay products should be relatively unmodified by the existence of any hot nuclear medium. Consequently, they encode information about the earliest stages of a HI collision and can be used to constrain the corresponding nPDFs and, by extension, the collision’s initial conditions.

The pPb collision system is an ideal environment to carry out measurements of nPDFs using EW bosons. One advantage of using proton-lead collisions is that one can use the better known PDF of the proton to cleanly probe the “target” nuclear PDF. In PbPb collisions, a mixture of two unknown nuclear PDFs is used, which makes the nPDF constraint less strong. The asymmetric collision system provides access to two different regions of initial parton  $x$  for a given value of  $|\eta|$ , greatly expanding the  $x$  coverage of several measurements as compared to a symmetric collision system. We adopt the convention that positive  $\eta$  values indicate the proton-going, or “forward”, side of the detector, i.e., the side that preferentially selects low- $x$  partons

in the target Pb nucleus. Similarly, negative  $\eta$  values denote the lead-going, or “backward”, side which preferentially measures high- $x$  partons in the target nucleus. During pPb collisions at the LHC, there is an asymmetry in the per-nucleon energy in each beam that causes an offset of 0.465 units of rapidity between the laboratory and nucleon-nucleon center-of-mass reference frames. Results are presented as functions of the pseudorapidity  $\eta_{\text{CM}}$  and rapidity  $y_{\text{CM}}$  calculated in the center-of-mass frame. An additional benefit of pPb collisions is that they typically have less event activity than AA collisions at a similar center-of-mass energy, allowing more precise lepton identification and reconstruction.

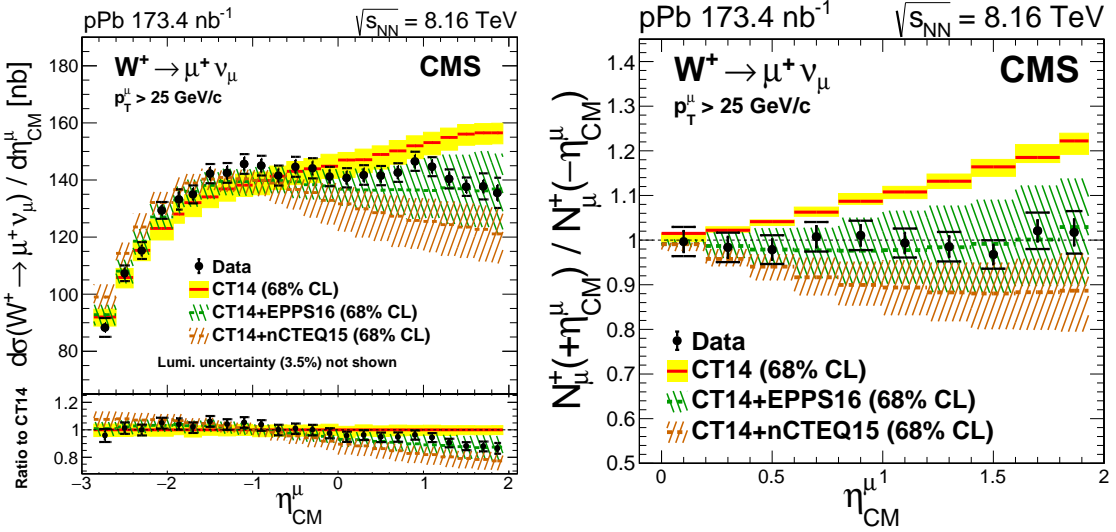


Figure 13: The differential cross sections (left) and forward-backward ratio for decay muon yields (right) for the process  $W^+ \rightarrow \mu^+ \nu_\mu$  versus muon pseudorapidity in the center-of-mass frame ( $\eta_{\text{CM}}$ ). Black horizontal lines above and below the data points represent the quadrature sum of statistical and systematic uncertainties, whereas the vertical bars show the statistical uncertainties only. The NLO calculations with CT14 PDF, and CT14+nCTEQ15 and CT14+EPPS16 nPDFs are displayed, including their 68% confidence interval uncertainty bands. The ratios of data, CT14+nCTEQ15 and CT14+EPPS16 with respect to CT14 are shown in the lower left panel. A global integrated luminosity uncertainty of 3.5% in the cross section is not shown. (Figure compiled from Ref. [154].)

At leading order (LO) in perturbation theory,  $W$  bosons are produced primarily through the annihilation of quarks and antiquarks, e.g.,  $u\bar{d} \rightarrow W^+$  and  $d\bar{u} \rightarrow W^-$ . Thus, measurements of the  $W$  boson production can give access to the light quark and antiquark nPDFs. Additionally, the charge asymmetry of  $W$  boson production enables disentangling of the  $u$  and  $d$  quark nPDF contributions individually. The left panel of Fig. 13 shows a measurement of the differential cross section of  $W$  boson production in  $\sqrt{s_{\text{NN}}} = 8.16$  TeV pPb collisions as a function of the decay lepton  $\eta_{\text{CM}}$  [154]. The result is for the  $W^+ \rightarrow \mu^+ \nu_\mu$  process. Also shown, as shaded bands, are next-to-leading order (NLO) pQCD MC predictions calculated with the MCFM v8.0 [155] program interfaced with the CT14 [156] free proton PDF, as well as the combined CT14+EPPS16 [157] and CT14+nCTEQ15 [158] nPDFs. In general, the data agree better with the predictions using nPDFs than with those using the free proton PDFs, with a slight enhancement in the backward region and a suppression in the forward region. These trends correspond to the “antishadowing” and “shadowing” [159] regions of the nPDF, respectively. The results are consistent with earlier CMS analyses of  $W$  boson production in pPb collisions at the lower collision energy of  $\sqrt{s_{\text{NN}}} = 5.02$  TeV [160].

A more precise test of the nPDF predictions was performed by taking forward-backward ratios

of the yields of muons resulting from  $W$  boson decays to enable cancellation of systematic uncertainties. This quantity is shown in the right panel of Fig. 13 for  $W^+$  bosons. The data clearly favor models containing nuclear effects. Similar conclusions were reached with  $W^-$  bosons. The comparison of this measurement to various models is the first clear demonstration of the nuclear modification of quark PDFs using EW bosons in nuclear collisions [154]. Because of the unprecedented precision of these measurements (as can be seen by comparing the measurement uncertainties to the model uncertainties in the right panel of Fig. 13), state-of-the-art nPDF models such as EPPS21 [161], nCTEQ15WZ [162], nNNPDF2.0 [163], nNNPDF3.0 [164], and TUJU21 [165] have all incorporated these results into their global fits to extract the parton densities in heavy nuclei.

The production of oppositely charged lepton pairs via  $q\bar{q}$  annihilation in the  $s$ -channel through the exchange of a  $Z$  boson or virtual photon  $\gamma^*$  is known as the neutral Drell–Yan (DY) process. Like  $W$  boson production, this process is sensitive to quark nPDFs. The upper panel of Fig. 14 shows a measurement of the differential cross section of DY dimuons as a function of their invariant mass for  $p\text{Pb}$  collisions at  $\sqrt{s_{\text{NN}}} = 8.16 \text{ TeV}$  [166]. This measurement probes a large range of invariant mass from 15 to 600 GeV. A clear peak in the data can be seen, corresponding to the  $Z$  boson mass. For DY dimuons in this mass range, a measurement of the cross section as a function of the dimuon rapidity shows features similar to those observed for  $W$  bosons, i.e., enhancement compared to the CT14 PDF in the backward antishadowing region and suppression in the shadowing region. The forward-backward ratio of this cross section as a function of dimuon rapidity  $|y_{\text{CM}}|$  is shown in the lower right panel of Fig. 14 for a mass selection around the  $Z$  boson peak ( $60 < m_{\mu^+\mu^-} < 120 \text{ GeV}$ ). The error bars represent the total measurement uncertainties. Theoretical predictions from the POWHEG NLO [167, 168] generator using the CT14 [156] free proton PDF, as well as the CT14+EPPS16 [157] and CT14+nCTEQWZ [162] nPDFs, are shown by blue, red, and green boxes, respectively. The data strongly deviate from the CT14 prediction for large values of  $|y_{\text{CM}}|$  but are consistent with the nPDF models. Similar trends were observed in earlier CMS measurements of  $Z$  boson production in 5.02 TeV  $p\text{Pb}$  collisions [169]. The precision of the measurement is better than the nPDF model uncertainties, including the nCTEQWZ model, which was already updated to include the previously discussed CMS  $W$  boson data. Thus, the DY data are expected to further improve the understanding of quark and antiquark nPDFs.

At lower invariant masses, the dynamics of the DY process are increasingly dictated by virtual photon exchange and, therefore, probe a region of lower  $x$  and energy scale  $Q^2$  compared to the production of  $Z$  or  $W$  bosons. For the first time in collisions of nuclei, similar cross section and forward-backward ratio measurements were performed in a lower mass region of  $15 < m_{\mu^+\mu^-} < 60 \text{ GeV}$ , as shown in the lower left panel of Fig. 14. Although the precision of the measurement does not currently allow for strong constraints of the various models, these measurements represent an important step towards expanding the kinematic region in which the DY process can be used to understand nPDF effects. For example, Ref. [165] found that the inclusion of next-to-NLO (NNLO) corrections can significantly increase the ability of nPDF models to describe these low-mass data.

The production of top quark pairs in nuclear collisions probes the gluon nPDFs at high- $x$ , and is therefore complementary to EW boson measurements primarily probing quark PDFs [170]. The first observation and evidence of top quark production in  $p\text{A}$  and  $\text{AA}$  collisions, respectively, was performed by the CMS collaboration [149, 171]. As displayed in Fig. 15, the measured cross section is consistent with the expectations from scaled pp data, as well as pQCD calculations at NNLO, with soft gluon resummation at next-to-next-to-leading logarithmic (NNLL) accuracy [172–174]. The difference in the inclusive cross section computed with the PDF for

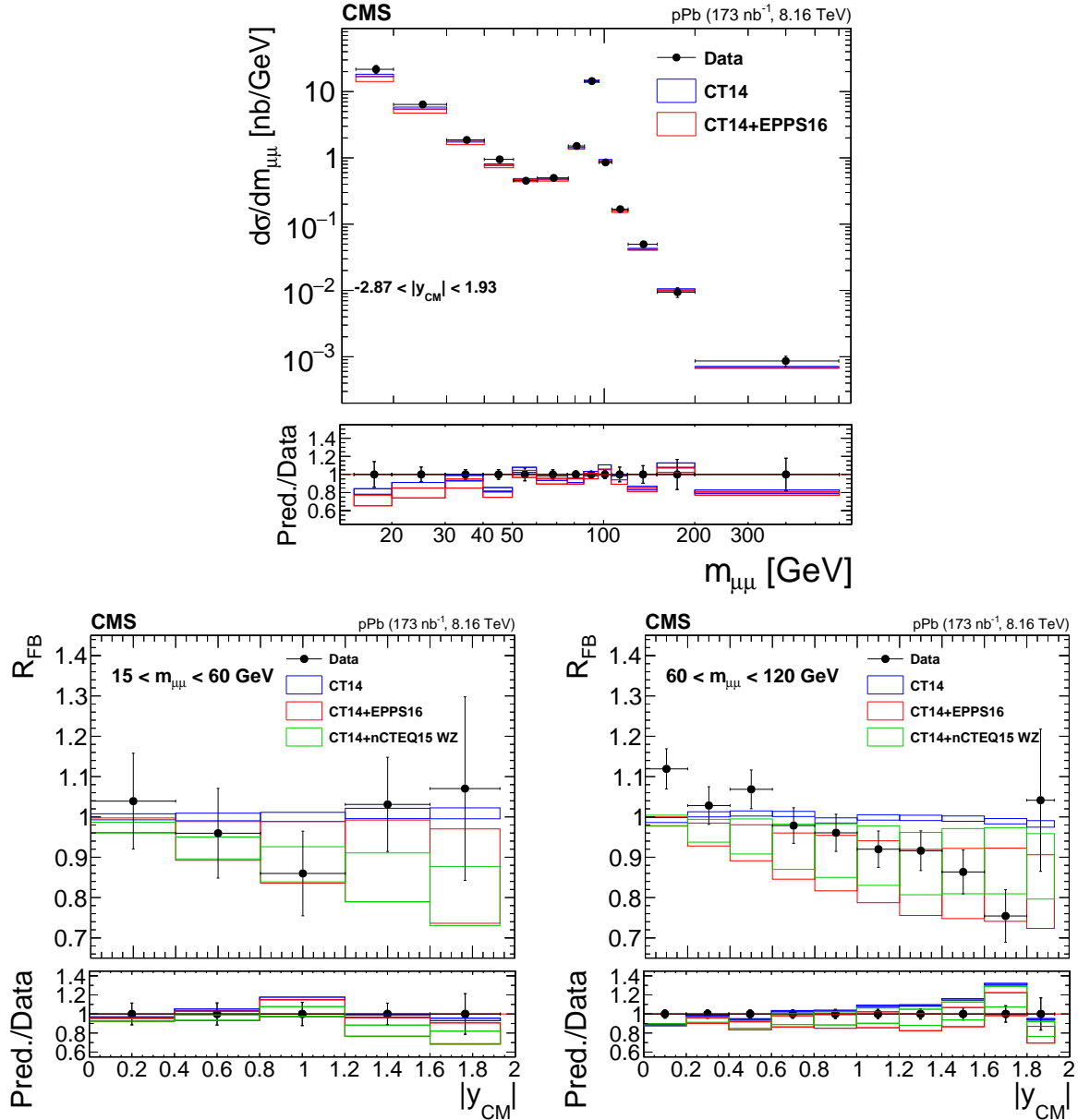


Figure 14: Differential cross section for the Drell-Yan process measured in the muon channel as a function of the dimuon invariant mass (upper) and the forward-backward ratios for  $15 < m_{\mu^+\mu^-} < 60$  GeV (lower left) and  $60 < m_{\mu^+\mu^-} < 120$  GeV (lower right). Error bars represent the total measurement uncertainty. Theory predictions from the POWHEG NLO generator using the CT14 PDF (blue), or the CT14+EPPS16 (red) or CT14+nCTEQ15WZ (green) nPDF sets are shown. The standard deviation of the nPDF uncertainties are shown by the boxes. Ratios of theory predictions over data are shown in the lower panels. (Figure adapted from Ref. [166].)

free protons and for bound nucleons is small. A net overall enhancing (antishadowing) effect increases the total top quark pair cross section by approximately 5% in pPb relative to pp collisions. Such a difference is too small to be observed in the data with the current experimental uncertainties. However, this first measurement paves the way for future detailed investigations of top quark production in nuclear interactions. In particular, top quark pair production provides a new tool for studying the strongly interacting matter created in AA collisions [149] (as discussed in Section 5.2.4).

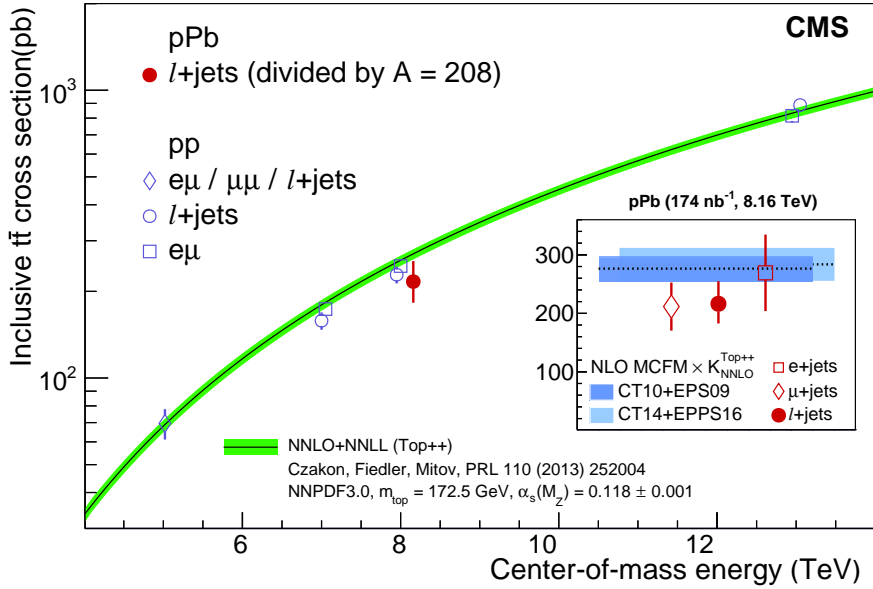


Figure 15: Top quark pair production cross section in pp and pPb collisions as a function of the center-of-mass energy per nucleon pair; the CMS results at different center-of-mass energies in the dilepton and semileptonic channels. The measurements are compared to the NNLO+NNLL QCD theory predictions [172–174]. (Figure adapted from Ref. [171].)

Another well-known probe of nPDFs is the production of high transverse momentum jets. Both quark and gluon nPDFs can be studied over a wide range of  $x$  values based on jet production. For the  $p_T$  range of 50–200 GeV probed in pPb collisions, it is expected that jets at central rapidity mostly constrain gluon nPDFs at mid- to high- $x$ . This helps cover swathes of phase space that are more challenging to constrain with  $W$  or  $Z$  boson production in pPb collisions. Unlike EW bosons, jets can be produced via processes involving only QCD interactions. This is advantageous because it leads to jet events being produced quite copiously at the LHC. However, jet observables come with experimental challenges as well; the CMS detector resolution in jet  $p_T$  and pointing angle tends to be larger than for other objects. This means that a careful assessment of the bin-to-bin migration effects, and their corrections, are required.

Measurements of the inclusive dijet pseudorapidity spectra at 5.02 TeV have been performed by the CMS Collaboration [125, 177], with the most recent measurement shown in Fig. 16. To make potential nPDF effects more visible, the result is presented as a ratio between the pPb and pp data. The measurements, which are differential in dijet pseudorapidity,  $\eta_{\text{dijet}} = (\eta_{\text{jet 1}} + \eta_{\text{jet 2}})/2$ , and in average dijet transverse momentum,  $p_T^{\text{ave}}$ , help constrain nPDFs for a wide range of  $x$  and  $Q^2$ . The measurements show tension with the nPDF sets that were available when they were first presented, as can be seen in the ratios of theoretical predictions to the data from Ref. [177] in Fig. 17. In particular, discrepancies were observed for values of  $\eta_{\text{dijet}} > 1.5$  and  $\eta_{\text{dijet}} < -0.5$ , which correspond to low  $x$  and intermediate  $x$  suppression of the nPDF relative to the proton PDF (known as the shadowing and the EMC [178] regions of nPDFs, respectively). This measurement was also the first-ever evidence that *gluons* in the nuclei featured antishadowing (an enhancement of the nPDF at  $x \approx 0.1$ ) compared to the proton densities [161, 179]. Previous measurements of the antishadowing and EMC effects had only probed nuclear quark densities. Before these measurements, nPDFs did not have input from dijet data at LHC energies. In recent years, the PDF collaborations have incorporated these data sets [161, 164], which has significantly improved the gluon PDFs across a wide  $x$  range, demon-

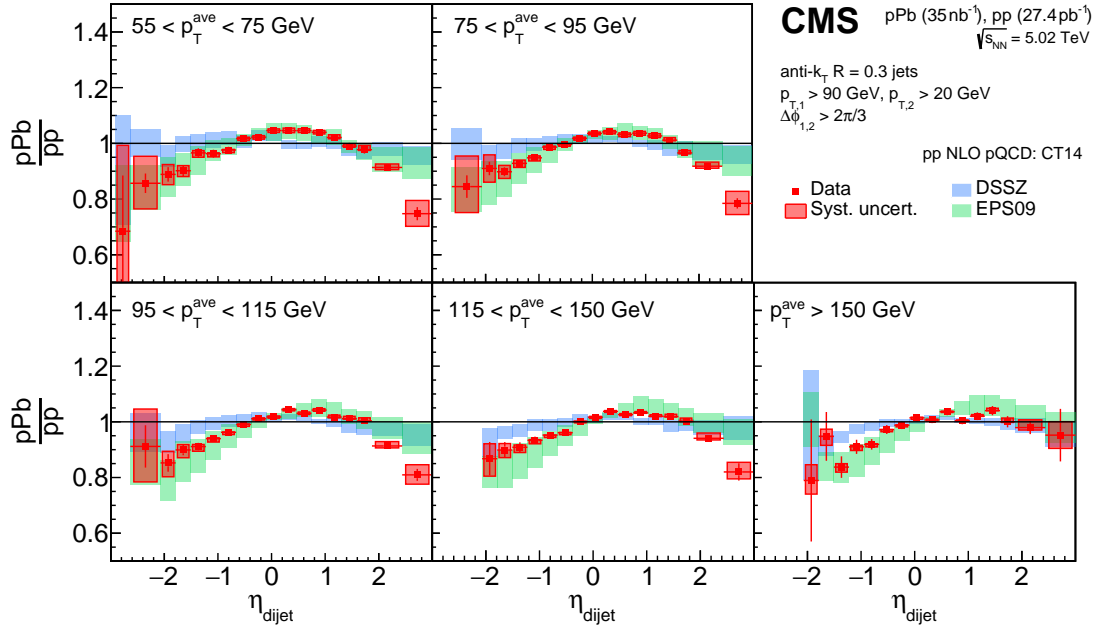


Figure 16: The ratio of the dijet  $\eta$  spectra for pPb and pp data in a selection of  $p_T^{\text{ave}}$  ranges. Theoretical predictions are from the NLO pQCD calculations of DSSZ [175] and EPS09 [176] are shown. Red boxes and bars indicate the systematic and statistical uncertainties in data, respectively. Green and blue boxes represent nPDF uncertainties. (Figure adapted from Ref. [177].)

strating the unique constraining power of these measurements. The  $x$  and  $Q^2$  two-dimensional regions constrained by the CMS measurements of dijets and electroweak bosons are presented in Fig. 18.

### 3.2 Tests of the Glauber model and $N_{\text{coll}}$ scaling using electroweak bosons

The nuclear modification factor  $R_{\text{AA}}$  is a common observable that is used when studying the QGP produced in AA collisions. It is defined as

$$R_{\text{AA}} = \frac{1}{\langle T_{\text{AA}} \rangle} \frac{dN_{\text{AA}}/dp_T}{d\sigma_{\text{pp}}/dp_T} = \frac{1}{\langle N_{\text{coll}} \rangle} \frac{dN_{\text{AA}}/dp_T}{dN_{\text{pp}}/dp_T}, \quad (3)$$

where  $N_{\text{AA}}$  is the corresponding yield of the particle species of interest in AA collisions, and  $N_{\text{pp}}$  ( $\sigma_{\text{pp}}$ ) is the corresponding yield (cross section) in pp collisions. The average values of the nuclear overlap function  $\langle T_{\text{AA}} \rangle$  and  $\langle N_{\text{coll}} \rangle$  are typically calculated for a given centrality range with a Glauber MC model [120, 180, 181], which uses parameters such as the nuclear radius, deformation, and skin depth as input (as discussed in Section 2.5). A typical interpretation of the nuclear modification factor is that an  $R_{\text{AA}}$  value of unity indicates the absence of nuclear effects, i.e., that the collision at a given centrality can be treated as a superposition of  $N_{\text{coll}}$  independent nucleon-nucleon collisions. This expectation is known as  $N_{\text{coll}}$  scaling.

As previously discussed, the EW bosons (photons, W, and Z bosons) do not interact strongly with a QGP, and the W and Z bosons decay to leptons in the earliest stages of the collision. Additionally, nPDF effects on EW boson production in PbPb collisions are fairly well understood and expected to be relatively small (of the order of 5% or less at midrapidity) compared to the nuclear modifications observed for color-charged particles [165]. These factors make EW bosons ideal probes to test the  $N_{\text{coll}}$  scaling hypothesis and, by extension, the Glauber model used to calculate  $N_{\text{coll}}$  and  $T_{\text{AA}}$  values.

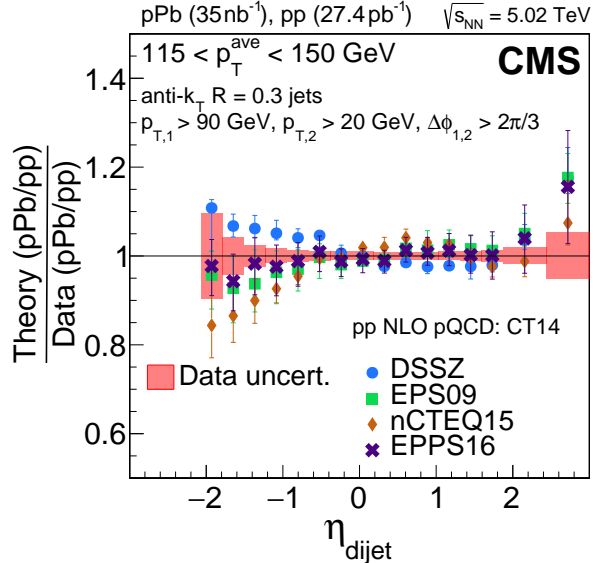


Figure 17: The ratio of theoretical predictions to CMS data for the ratio of the pPb to pp dijet  $\eta$  spectra for  $115 < p_T^{\text{ave}} < 150 \text{ GeV}$ . Theoretical predictions are from the NLO pQCD calculations of DSSZ [175], EPS09 [176], nCTEQ15 [158], and EPPS16 [157] nPDFs, using CT14 [156] as the baseline PDFs. Red boxes indicate the total uncertainties in data and the error bars on the points represent nPDF uncertainties. (Figure adapted from Ref. [177].)

Figure 19 shows a measurement of the midrapidity ( $|\eta| < 1.44$ ) isolated photon  $R_{\text{AA}}$  as a function of the photon transverse energy  $E_T^\gamma$  in four PbPb centrality ranges using 5.02 TeV PbPb and pp data [135]. For the measured range  $25 < E_T^\gamma < 200 \text{ GeV}$ ,  $R_{\text{AA}}$  is consistent with unity, supporting the  $N_{\text{coll}}$  scaling hypothesis. An earlier analysis of 2.76 TeV PbPb data reached a similar conclusion [109]. The 5.02 TeV data are found to be consistent with NLO calculations from the JETPHOX version 1.3.1.4 [182] MC generator, indicating a solid understanding of isolated photon production in AA collisions.

Measurements of massive EW bosons complement measurements of isolated photons because they can access similar information about the initial state without being sensitive to photon reconstruction effects,  $\pi^0$  and  $\eta$  decay contamination, and fragmentation photon backgrounds. Figure 20 shows a measurement of W bosons in  $\sqrt{s_{\text{NN}}} = 2.76 \text{ TeV}$  PbPb collisions [183]. The quantity displayed is the yield of W bosons divided by the  $T_{\text{AA}}$  value calculated for the centrality range of interest (i.e., per NN integrated luminosity,  $1/T_{\text{AA}}$ , at a given PbPb impact parameter), which is then scaled by the muon  $\eta$  acceptance ( $\Delta\eta = 4.2$ ). The measurements are plotted as a function of  $N_{\text{part}}$  for five centrality selections, shown by the solid markers, with an inclusive selection plotted with open markers around  $N_{\text{part}} = 120$ . For comparison, the same quantity for pp collisions at the same collision energy is shown by the open markers at  $N_{\text{part}} = 2$ . For all centrality selections in PbPb collisions, the results for  $W^+$  and  $W^-$  bosons are consistent with each other. This is not the case for pp collisions, where  $W^+$  bosons are produced at nearly twice the rate of  $W^-$  bosons. This difference is attributed to the combination of two effects. Because of isospin, the presence of neutrons within the lead nucleus affects the production of  $u\bar{d} \rightarrow W^+$  and  $d\bar{u} \rightarrow W^-$ . In addition, conservation of angular momentum results in preferential emission of  $W^+ \rightarrow l^+ \nu_l$  and  $W^- \rightarrow l^- \bar{\nu}_l$  toward midrapidity and more forward rapidities, respectively. When summing over both W charge states, the normalized yields in PbPb collisions are consistent with those in pp collisions for all centrality selections. The measured centrality-inclusive  $R_{\text{AA}}$  value for W bosons is determined to be  $1.04 \pm 0.07 \text{ (stat)} \pm 0.12 \text{ (syst)}$ , a value which strongly supports the assumption of binary scaling

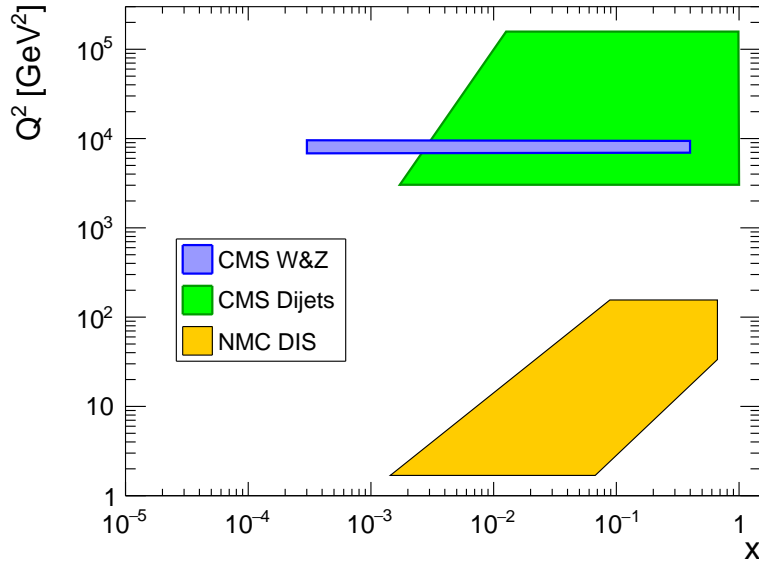


Figure 18: Schematic representation of the phase space regions, in the  $x$  and  $Q^2$  plane, covered by the CMS measurements of dijets (green area) and electroweak bosons (blue area). They cover a much higher  $Q^2$  region than previous measurements from fixed-target experiments also included in the EPPS21 analysis [161] (orange area).

of the production of hard probes.

Early analyses of Z boson production at  $\sqrt{s_{\text{NN}}} = 2.76$  TeV [132, 184] produced similar conclusions to those from the W boson and photon measurements. However, these measurements had large uncertainties, which prevented detailed examination of peripheral (50–100%) collisions. The larger integrated luminosities achieved for 5.02 TeV PbPb collisions during the LHC Run 2 enabled much more precise studies of these peripheral events. Figure 21 shows the per-event yields normalized per NN integrated luminosity for Z bosons decaying to two muons or electrons in 5.02 TeV PbPb collisions [185]. The data points in the 0–40% centrality range are consistent with the inclusive centrality selection, supporting the  $N_{\text{coll}}$  scaling hypothesis in this centrality region. However, the increased precision of the measurement, as compared to previous measurements, reveals a falling trend in the 40–90% centrality range. In particular, the data for the 40–90% and 70–90% centrality ranges deviate from inclusive 0–90% data point by 1.6 and 2.2 standard deviations, respectively. The green boxes show a prediction from the HG-PYTHIA model [186], which agrees with the measurement. This model incorporates the  $N_{\text{coll}}$  scaling hypothesis, but accounts for additional event selection effects and correlations between the centrality calibration and the hard process being measured when predicting  $R_{\text{AA}}$  for a hard, colorless probe, such as the Z boson. The agreement of these data with HG-PYTHIA implies that, even if binary scaling of hard probes production is correct, the absence of final-state effects does not guarantee an  $R_{\text{AA}}$  of unity for very peripheral collisions, which in turn could affect the interpretation of similar measurements of color-charged particles. Therefore, this deviation from unity cannot be interpreted as violation of binary scaling, but instead points to additional selection effects in peripheral collisions which must be accounted for in addition to  $N_{\text{coll}}$  scaling [181].

Figure 22 shows a comparison of the CMS 5.02 TeV PbPb collision Z boson data with EW boson measurements from the ATLAS [188] and ALICE [187] Collaborations at the same collision energy. To remove overall scale and isospin effects and to allow for comparison of the centrality

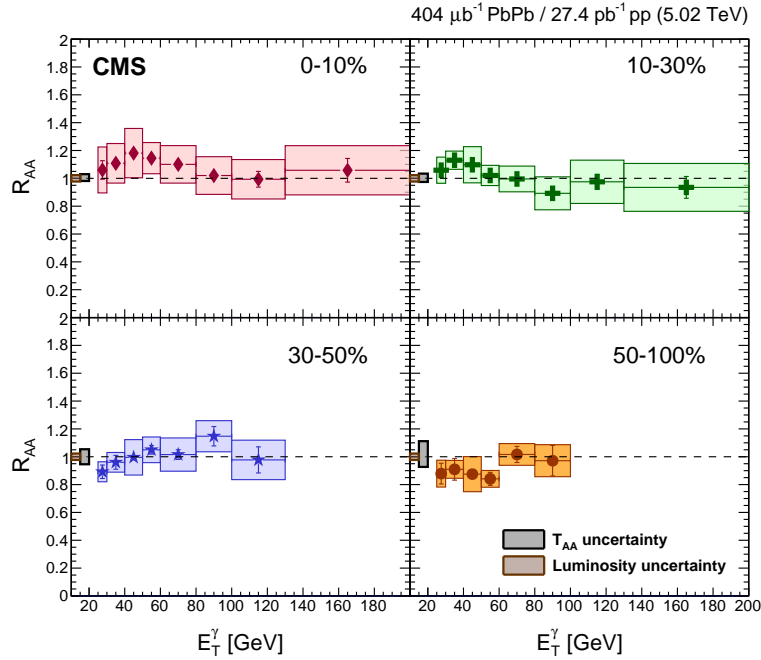


Figure 19: The photon  $R_{AA}$  versus photon  $E_T^\gamma$  in four centrality ranges for 5.02 TeV PbPb collisions. The error bars indicate the statistical uncertainties and the systematic uncertainty, excluding  $T_{AA}$  uncertainties, are shown by the colored boxes. The  $T_{AA}$  uncertainties are common to all points in a given centrality range, and are indicated by a gray box on the left side of each panel. Similarly, a 2.3% pp collision integrated luminosity uncertainty is shown with a brown box. (Figure adapted from Ref. [135].)

dependence of the measurements, each data set has been normalized such that the most central point equals unity. A scale uncertainty common to all points in a data set, resulting from the normalization by the most central data point, is not shown on the figure. These uncertainties are 3.7% (CMS  $Z/\gamma^*$ ), 3.2% (ATLAS  $Z/\gamma^*$ ), 4.1% (ATLAS  $W^+$ ), 3.9% (ATLAS  $W^-$ ), 9.6% (ALICE  $W^+$ ), and 7.5% (ALICE  $W^-$ ). For the data shown here,  $T_{AA}$  values calculated with TGLAUBERMC v3.2 (as opposed to the earlier v2.4) are used by all experiments to ensure a fair comparison. A difference in the trends of the CMS  $Z$  [185], and ATLAS  $Z$  and  $W$  data is apparent. The rising trend in the peripheral ATLAS data has been interpreted as a shadowing of the total NN cross section [189], which is a key input parameter in MC Glauber simulations. This interpretation is not consistent with the CMS  $Z$  and ALICE  $W$  boson results.

In summary, from these measurements of EW bosons it is clear that the  $N_{\text{coll}}$ -scaling hypothesis, which is a key component of interpreting observables such as  $R_{AA}$ , is well supported in the 0–40% centrality range. In the 40–90% centrality range the situation appears to be more complex. Although the  $N_{\text{coll}}$  scaling hypothesis cannot be definitely refuted in this centrality region, a combination of  $N_{\text{coll}}$  scaling, as well as selection and centrality effects such as those included in HG-PYTHIA may be needed to adequately describe the data.

### 3.3 Small- $x$ nuclear structure

As a first approximation, the small- $x$  evolution of the nuclear wave function is dominated by gluon splitting  $g \rightarrow gg$ . The gluon splitting contribution is incorporated in the DGLAP evolution equations of pQCD [151–153], which resum at all-orders all diagrams that lead to logarithmic enhancements with the four-momentum transfer of the collision. While the DGLAP evolu-

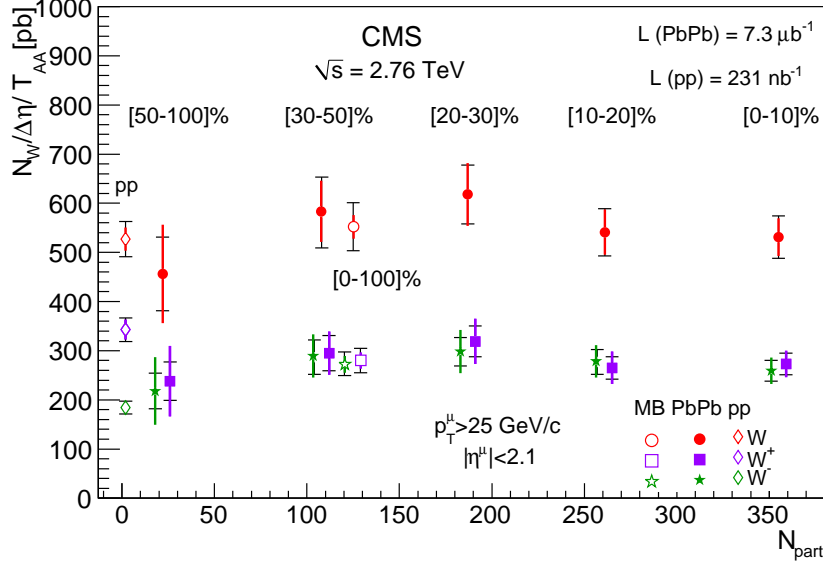


Figure 20: Normalized yields (per NN integrated luminosity and per unit rapidity) of  $W \rightarrow \mu\nu$  production in 2.76 TeV PbPb collisions, shown for inclusive  $W$  (red),  $W^+$  (violet), and  $W^-$  (green). The open symbols at  $N_{\text{part}} = 120$  represent values for MB collisions. At  $N_{\text{part}} = 2$  the corresponding cross sections, divided by the muon pseudorapidity acceptance  $\Delta\eta$ , for pp collisions at the same energy are displayed. For clarity the  $W^+$  and  $W^-$  points are slightly shifted horizontally. Error bars represent statistical uncertainties and horizontal lines show systematic uncertainties. (Figure adapted from Ref. [183].)

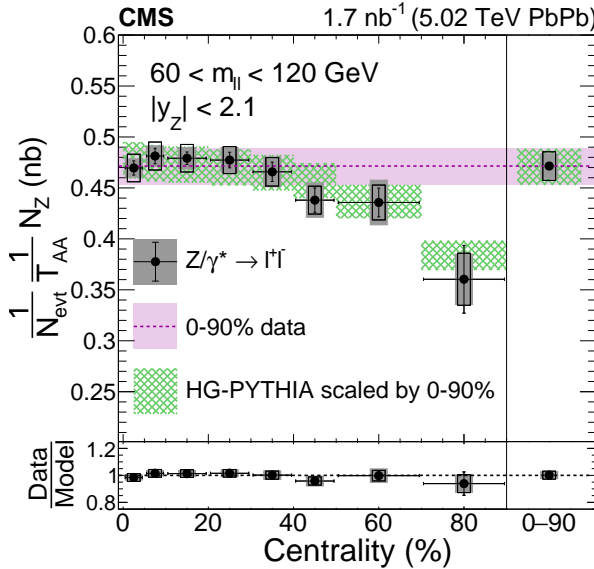


Figure 21: The  $T_{\text{AA}}$ -normalized yields of  $Z$  bosons versus centrality for 5.02 TeV PbPb collisions. The error bars, open boxes, and solid gray boxes represent the statistical, systematic, and  $T_{\text{AA}}$  uncertainties, respectively. The value of the 0–90% data (pink) and the scaled HG-PYTHIA model (green) are displayed. The width of the bands represents the contribution from the total 0–90% data point uncertainty. (Figure adapted from Ref. [185].)

tion equations capture some of the dominant contributions that compensate for the small value of the strong coupling constant  $\alpha_S$  via logarithms of  $1/x$ , a dedicated resummation is needed to

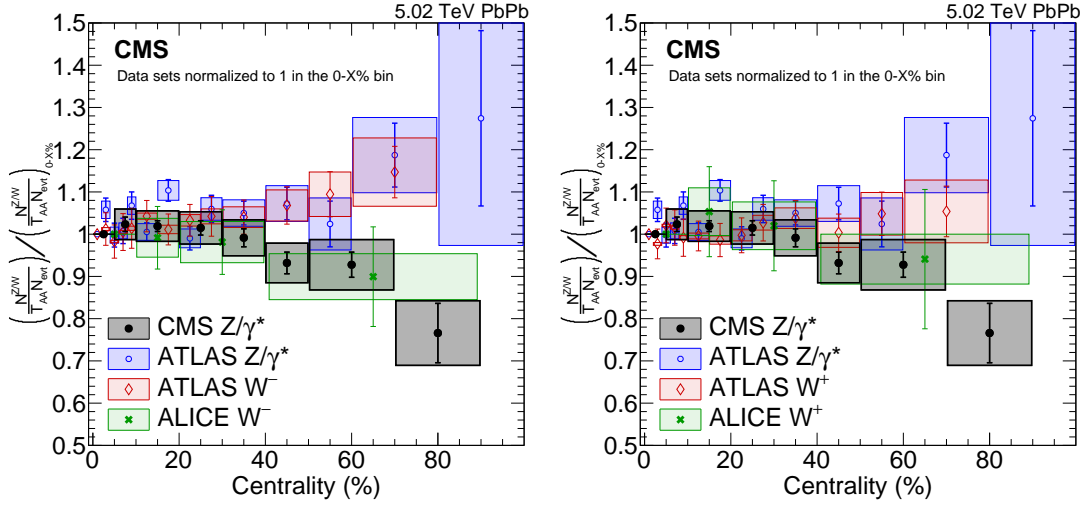


Figure 22: A comparison of results from the ALICE [187], ATLAS [188], and CMS [185] Collaborations for Z and W production in PbPb collisions. The data have been normalized so that the most central data point equals unity to enable comparison of the shape of the distribution. The left (right) panel shows data for  $W^-$  ( $W^+$ ) and Z bosons. For the ATLAS W data, the error bars represent the combined statistical and systematic uncertainty, while the boxes show  $T_{AA}$ -related uncertainties. For all other data sets, the error bars display statistical uncertainties and the boxes show combined systematic and  $T_{AA}$  uncertainties.

properly account for these logarithmically-enhanced terms at small- $x$ . This can be done using the Balitsky–Fadin–Kuraev–Lipatov (BFKL) [190–193] evolution equations of pQCD, which resum terms of the form  $\alpha_S \ln(1/x)$  to all orders in the perturbative expansion. One of the key predictions from the BFKL equation is that the gluon density grows at small- $x$ , following a power law, with the exponent given by the running of  $\alpha_S$ . Since both BFKL and DGLAP equations incorporate parton splitting contributions, it is predicted that the gluon densities should only increase at smaller  $x$ . Thus, gluon splitting alone leads to unitarity violation for cross sections. However, at high enough gluon occupancy numbers, it is expected that gluon recombination  $gg \rightarrow g$  also plays a role. The evolution equations that incorporate both splitting and recombination in the nuclear wave function are the Balitsky–Kovchegov (BK) evolution equations [194–197]. The characteristic energy scale at which both the splitting and recombination mechanisms are in balance is known as the parton saturation scale. Since the initial state of the collision is a crucial ingredient for predictions in HI collisions, it is imperative to measure the splitting and recombination behavior at small- $x$  in controlled environments. Establishing the existence of parton saturation effects is a long-standing problem in hadronic physics, since it relates to the quantum mechanical behavior of gluons at high density. Parton saturation effects are expected to be universal, and are expected to manifest in both the structure of protons and nuclei at small- $x$ . However, the advantage of studying this effect with HIs is that their parton density is much larger than that in protons, and therefore the critical energy scale below which gluon saturation manifests itself is larger, and thus more accessible experimentally.

A natural way of constraining the small- $x$  gluon nPDFs is by extending the measurements discussed in previous sections to the forward rapidity region. In particular, forward jets with low  $p_T$  offer insights into the parton densities and their evolution at small  $x$  because at lowest order in  $\alpha_S$ , the  $\eta$ - and  $p_T$ -dependences of jets are correlated to the momentum fraction  $x$  carried by the incoming parton, which can be estimated with  $x \approx (p_T/\sqrt{s}) \exp(\pm\eta)$ . The nominal acceptance for jet reconstruction in CMS extends over the range  $|\eta| < 5.2$ , limited by the acceptance

of the HF calorimeters. However, the acceptance for forward particle production has been extended to  $-6.6 < \eta < -5.2$  using the CASTOR calorimeter during special runs. This detector allows for the detection and reconstruction of jets with a minimum  $p_T$  of approximately 3 GeV. Therefore, the study of jets using CASTOR provides an opportunity to explore the low- $x$  regime and examine perturbative nonlinear parton evolution effects. In pPb collisions where the incoming Pb ion is in the direction pointing to CASTOR, the jets detected in the acceptance range of that detector allow for measurements highly sensitive to the small- $x$  region of the Pb nucleus down to  $x \sim 10^{-6}$ . The most challenging aspect of this measurement is the calibration of the forward jets detector in CASTOR. An energy-dependent correction factor is used to account for the noncompensating behavior of the detector. These energy-dependent calibration functions are obtained from simulation by matching particle-level jets (with a particle-level jet isolation requirement) to the detector-level jets. More details of the jet calibration and reconstruction are presented in Ref. [198].

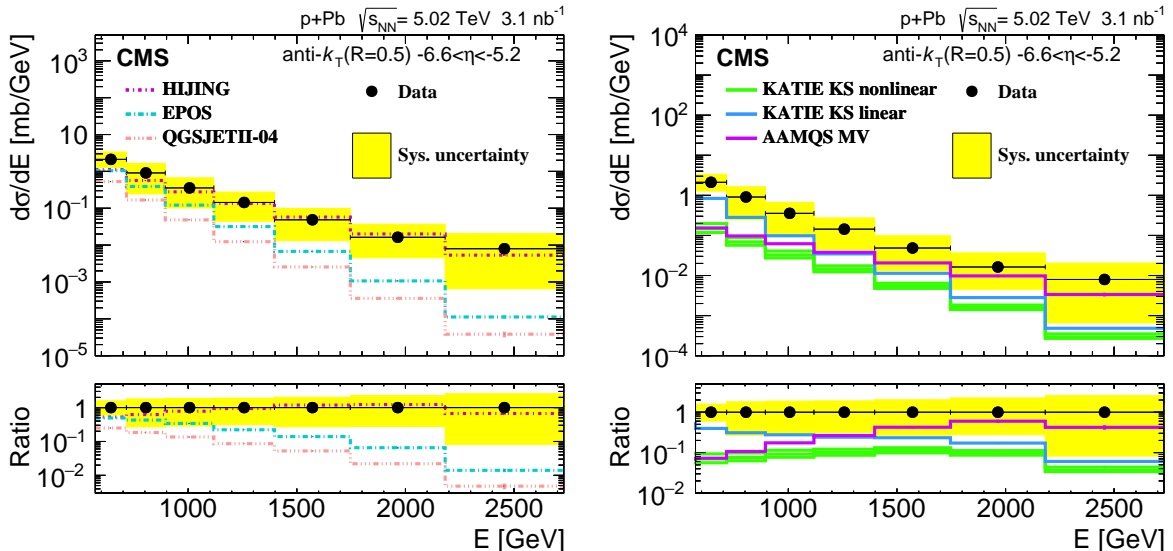


Figure 23: Forward jet differential cross section, where forward jet is in the proton-going direction, as a function of jet energy in pPb collisions at 5.02 TeV. The kinematics of the collision allows us to probe the small- $x$  wave function in the Pb nucleus with a high- $x$  parton from the proton. This measurement is compared with different Monte Carlo event generators, EPOS-LHC [123], HIJING [124], and QGSJETII-04 [199] (left) and predictions of the KATIE [200] and AAMQS [201] saturation models (right). (Figures adapted from Ref. [202].)

The CMS experiment has measured differential cross sections for inclusive forward jet production in pPb collisions at a center-of-mass energy of  $\sqrt{s_{\text{NN}}} = 5.02 \text{ TeV}$  using the CASTOR detector [202]. This measurement was performed as a function of jet energy in hadronic, non-diffractive pPb collisions, as presented in Figs. 23 and 24. The experimental uncertainty of this measurement is dominated by the jet energy scale calibration for jets in CASTOR. Also, since CASTOR lacks segmentation in  $\eta$ , other effects add to the uncertainty, such as the merging of particles from beam-beam remnants or two jets merged into a single jet at the detector level. The comparisons with numerous MC event generators presented in Fig. 23, excluding (left panel) or including (right panel) parton saturation effects, show that none of the models studied can describe all the features observed in the experimental data. The MC predictions including saturation effects are consistent with the data within the uncertainties in the absolute cross sections (this is for small- $x$  evolution for the proton). Data obtained with the reversed beam (“Ppb”) configuration are compared to EPOS LHC, HIJING, and QGSJETII-04 in Fig. 24 (left). This

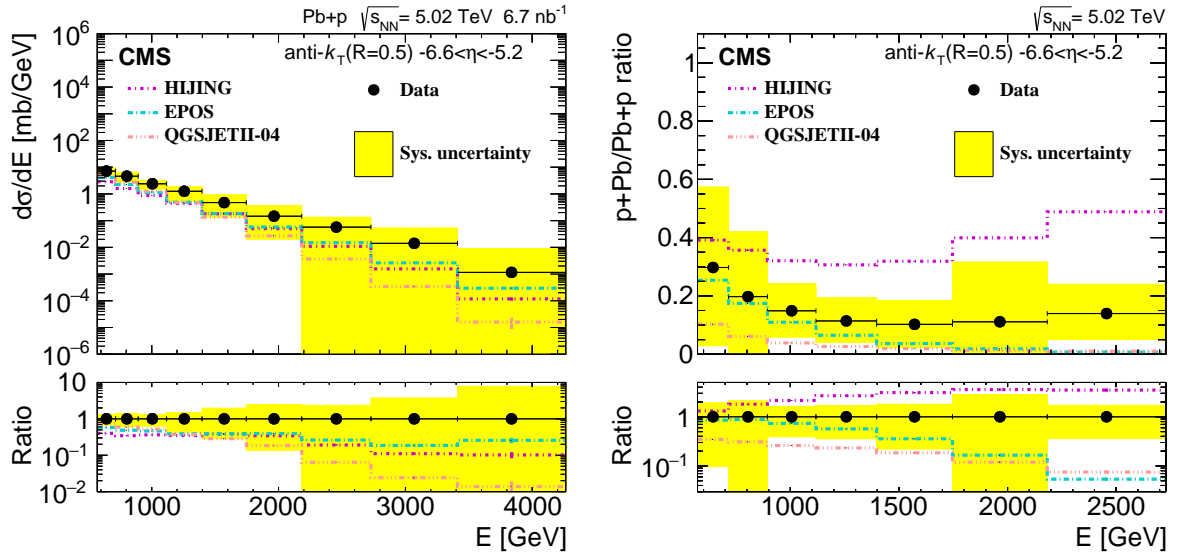


Figure 24: (Left) Forward jet differential cross section, where the forward jet is in the Pb-going direction, as a function of the jet energy in pPb collisions at 5.02 TeV. The kinematic properties of the collision probe the small- $x$  wave function of the proton with a high- $x$  parton from the Pb nucleus. The data are compared with different Monte Carlo event generators: EPOS-LHC [123], HIJING [124], and QGSJETII-04 [199]. (Right) The ratio of the inclusive jet cross sections; the numerator (denominator) of the ratio corresponds to the case where the jet is measured in the proton-going (Pb-going) direction. (Figure adapted from Ref. [202].)

is the region with significant contributions from nuclear remnants. The EPOS LHC and HIJING models describe the shape of the distribution reasonably well, but are too low in normalization. The QGSJETII-04 model yields a spectrum that is too soft. Since the measurement is dominated by experimental uncertainties, the ratio of the pPb and Pb+p systems is also reported in the right panel of Fig. 24. This ratio allows for large cancellations of correlated experimental uncertainties, with the trade-off that one is comparing systems with different rapidity boosts with respect to the laboratory frame. With this in mind, one can readily see that the predictions from MC-generated events cannot simultaneously describe the cross section ratio and the absolute cross sections. After the publication of this measurement, the theory interpretation has been further refined. In Ref. [203], an updated set of predictions were presented. Such a set of predictions includes the contribution of virtual  $1 \rightarrow 2$  splittings in the forward region, as well as an improved modeling of forward jets from multiple parton-parton interactions. The jets from those mechanisms merge with the forward jets from the hard scattering in the forward region due to the coarse calorimeter granularity of CASTOR, so accounting for them has an important numerical effect in the prediction. This is all in addition to small- $x$  nonlinear evolution of interest. As seen in Fig. 25, where the theory predictions from Ref. [203] are compared to the data, the prediction with these additional contributions lead to a better agreement with the pPb data.

The advantage of measuring jets in the forward region is that it allows for the use of similar experimental techniques as previously employed in dijet studies at central pseudorapidity. From the theory point of view, the use of collinear PDFs (i.e., PDFs with impact parameter and momentum degrees of freedom integrated) is also well justified. The challenge in the very forward region comes from the contribution from other higher-order corrections and nonperturbative corrections that are not related to the initial state in order to arrive at a clean theoretical conclusion, as discussed in the previous paragraph. Thus, additional probes of small- $x$  nuclear structure are needed. A complementary study involves measuring exclusive final states, as

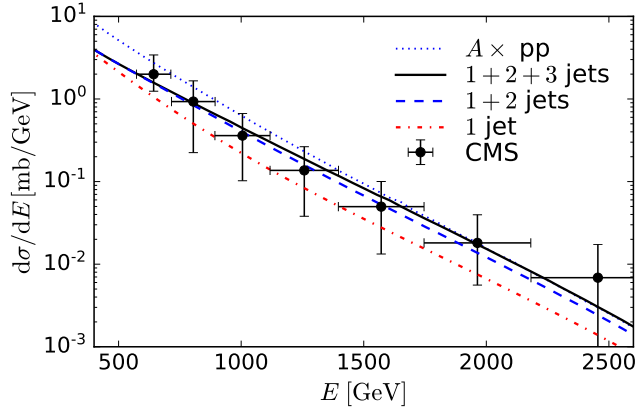


Figure 25: Forward jet differential cross section, where the forward jet ( $-6.6 < \eta < -5.2$ ) is in the p-going direction, as a function of the jet energy in pPb collisions at 5.02 TeV. The kinematics of the collision allows us to probe the small- $x$  wave function of the Pb nucleus with a high- $x$  parton from the proton. The data points are from Ref. [202], with the error bars denoting the total uncertainty in the measurement. (Figure adapted from Ref. [203].)

discussed in the next section.

### 3.4 Photoproduction of vector mesons

In ultraperipheral collisions (UPCs) of HI collisions, where the impact parameter of the two colliding nuclei is greater than the sum of the two nuclear radii, hadronic interactions are highly suppressed compared to central collisions and the strong electromagnetic fields surrounding the nuclei give rise to  $\gamma\gamma$  and  $\gamma A$  interactions. Such electromagnetic fields are highly Lorentz-contracted and can be treated as linearly polarized quasi-real photons with a flux that depends on the square of the electric charge of the emitting nucleus [204, 205]. These quasi-real photons can fluctuate into a quark-antiquark pair, essentially a color dipole, that interacts with the target nucleus or proton via two-gluon color-singlet exchange. The quark-antiquark pair eventually hadronizes into a vector meson (VM). These interactions are usually classified depending on whether the projectile photon interacts with the target ion as a whole (coherently) or if it interacts with a single nucleon inside the ion (incoherently). Coherent photoproduction of heavy VM is of particular interest given that at lowest order in pQCD, the cross section is directly proportional to the square of the gluon PDF of the target at small  $x$  [206, 207]. The mass of VMs sets an energy scale large enough to be studied in the framework of pQCD. In addition, at LHC energies, coherent photoproduction of VMs opens a special window to the poorly known low- $x$  region, allowing studies of shadowing effects towards the high energy limit of QCD.

To probe the internal structure of the proton at small  $x$ , one can study the exclusive photoproduction of VMs, using the lead ion electromagnetic field as a source of quasi-real photons. The CMS experiment has studied the exclusive photoproduction of  $Y(nS)$  and  $\rho^0$  mesons in pPb collisions at  $\sqrt{s_{NN}} = 5.02$  TeV [208, 209]. The advantage of using different VMs is that they give different effective sizes of the color dipoles probing the structure of the proton (or nucleus), which have different sensitivities to potential nonlinear evolution effects at small- $x$  and low  $Q^2$ . If nonlinear evolution effects are present, they are expected to also depend on the probe. Thus, they should manifest differently for a variety of VMs as well. The general analysis strategy relies on the identification of the two oppositely-charged particles from the VM decay in an otherwise empty detector. Additional exclusivity criteria are also applied using the HF calorimeters, requiring energy deposits to be below noise thresholds in order to suppress

contributions from nondiffractive hadronic interactions. The signal is separated from the main background (for example, the QED continuum) by fitting the dimuon invariant mass distribution of two charged particles. These raw signal yields contain contributions from different processes, such as coherent (where the emitted photon interacts with the whole nuclear “target”) and incoherent (where the  $\gamma$  interacts with individual nucleons) photoproduction of VM, and also VM resulting from resonance decay feed-down. The coherent (incoherent) photoproduction have characteristically low (high) dimuon transverse momentum distributions, so their individual yields can be separated by means of multidimensional template fits.

The advantage of using asymmetric pPb collisions for these measurements is that one can (to a large extent) unambiguously unfold the cross section in the laboratory frame to the cross section in the photon-proton center-of-mass frame. The center-of-mass energy of the photon-proton system,

$$W_{\gamma p} = \sqrt{\sqrt{s}_{\text{NN}} M_{\text{VM}} \exp(\pm y)},$$

with  $y$  the rapidity of the vector meson, is strongly correlated with the parton momentum fraction  $x$ : smaller (larger)  $W_{\gamma p}$  corresponds to high  $x$  (small  $x$ ). This mapping allows for more direct comparisons between measurements at the DESY HERA in electron-proton collisions with those at the LHC in pPb collisions.

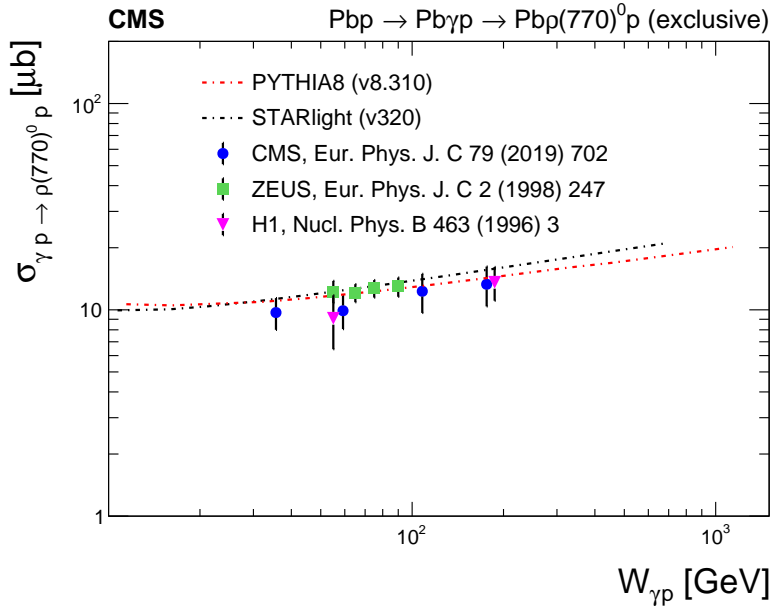


Figure 26: The cross section in the  $\gamma p$  center-of-mass frame  $\sigma(\gamma^* p \rightarrow \rho(770)^0 p)$  for exclusive  $\rho(770)^0$  VM photoproduction as a function of  $W_{\gamma p}$ . CMS measurements during Run 2 extend up to  $W_{\gamma p} = 1$  TeV. The CMS data points are from Ref. [209]. The H1 and ZEUS data in electron-proton collisions are shown in the same panel. The data points are compared to predictions from PYTHIA8 [117] and STARLIGHT [115]. (Figure adapted from Ref. [209].)

Figures 26 and 27 compare the photoproduction cross sections at HERA and the LHC. Notably, this is one of the few instances where one can compare cross sections from completely different colliding configurations in the same plots. It is observed that the CMS measurements complement the kinematical reach of the ones by HERA and from the LHCb experiment. The measurements have been compared with calculations based on BFKL, DGLAP, and BK evolution equations. It seems that, within the experimental sensitivity, no clear distinction between the nonlinear and linear evolution can be established with these measurements alone. These

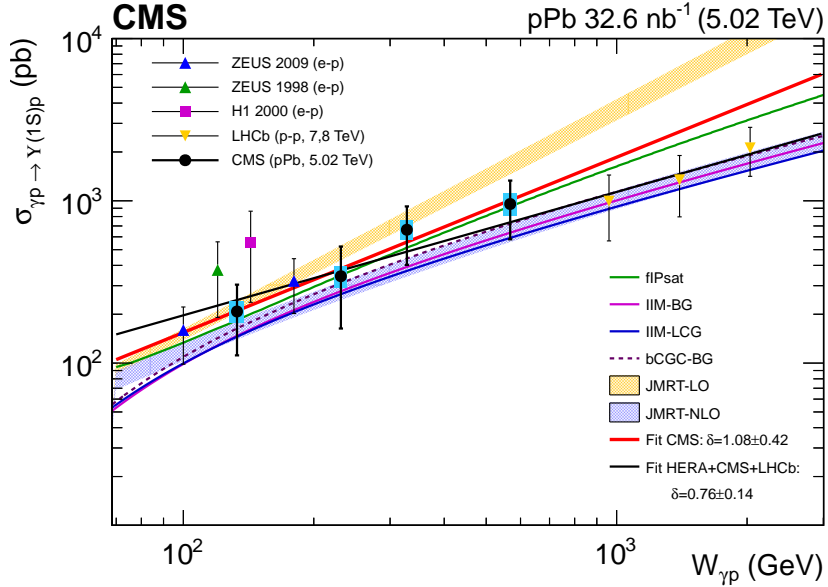


Figure 27: Photoproduction cross section in the photon-proton center-of-mass frame  $\sigma(\gamma^* p \rightarrow Y(1S)p)$  for exclusive  $Y(1S)$  VM photoproduction as a function of  $W_{\gamma p}$ . The data are compared with different calculations with different implementations of nonlinear evolution in the parton distributions. (Figure adapted from Ref. [208].)

data in principle can be used as input for global collinear PDF fits [210]. They are expected to constrain the small- $x$  gluon distribution in the  $Q^2 \approx m_{\text{VM}}^2$  region, complementary to the small- $x$  reach at HERA. Information about the distribution of gluons in impact parameter space can be obtained via the  $p_T$  distribution of the VM, as the two variables are Fourier conjugates. Thus, this process can be used not only to learn about small- $x$  evolution, but also how such evolution is linked with the spatial distribution of partons within the proton or the nucleus.

A more promising way to establish if there is a manifestation of nonlinear evolution is by using nuclei as targets instead of protons. As mentioned earlier in this section, the advantage of the use of HIs is that the manifestation of nonlinear evolution effects can occur at lower collision energies than what is expected in proton-proton collisions. Figure 28 shows the CMS results for exclusive  $J/\psi$  production in  $\text{PbPb}$  collisions at  $\sqrt{s_{\text{NN}}} = 2.76$  TeV [213]. The calculation labeled “impulse approximation” simply scales the prediction for  $\gamma p$  collisions by the number of nucleons, without any nuclear modification effects. The experimental cross sections are significantly smaller than this simple prediction, demonstrating the presence of strong nuclear modification effects that suppress the cross section relative to pure scaling expectations. The CMS acceptance in rapidity for low- $p_T$   $J/\psi$  particle production is complementary to that of the ALICE experiment [211, 212]. This measurement demonstrates that there is a suppression relative to calculations that include pure scaling due to the larger number of nucleons in  $\text{PbPb}$  collisions. However, in order to establish if this shadowing is a result of nonlinear evolution at small- $x$ , one has to do the mapping from the laboratory-frame cross sections to the  $\gamma A$  center-of-mass frame. Unfortunately, unlike the asymmetric  $\text{pPb}$  collisions case, in a symmetric  $\text{PbPb}$  collision either ion can be the emitter or the target nucleus, hence it is (at face value) not possible to identify the contributions from low- and high-energy photons. One can make educated guesses in certain kinematical regions (for example, at central rapidities one can extract an average of the high energy and low energy photon contributions). However, if we want to do a comparison as is done for  $\gamma p$  collisions, some additional input is needed.

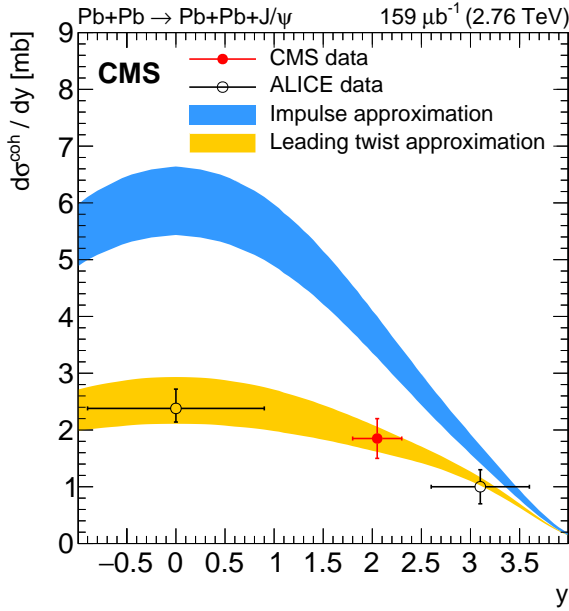


Figure 28: Differential  $J/\psi$  meson photoproduction cross section as a function of rapidity in  $Pb+Pb \rightarrow Pb+Pb+J/\psi$  collisions at  $\sqrt{s_{NN}} = 2.76$  TeV measured by ALICE [211, 212] and CMS [213]. Data are compared with the leading twist [214] and the impulse approximation [214, 215] predictions. The leading twist approximation is a perturbative QCD calculation that takes into account nuclear shadowing effects from multinucleon interference. (Figure adapted from Ref. [213].)

Indeed, it was proposed in Refs. [214, 216] that one can set additional constraints in a way that makes it possible to obtain cross sections in the  $\gamma A$  frame. Such additional constraints are obtained by detecting forward neutrons emitted by virtue of the deexcitation of giant dipole resonances of the Pb nuclei [217]. These giant dipole resonances take place as a consequence of additional soft-photon interactions between colliding ions, which are absorbed by the HI. When the excited HI relaxes, it is accompanied by the emission of forward collinear neutrons. This phenomenon is well-known from low-energy nuclear physics, and it turns out that it can be exploited in order to tag certain geometrical configurations of the colliding lead ions at the LHC. Indeed, the more “central” (smaller impact parameter) the UPC is, the more likely it is to have additional soft-photon emissions. Thus, by directly counting the number of neutrons in the forward region, one is effectively filtering UPCs in a way analogous to the centrality classification in conventional head-on  $PbPb$  collisions. To detect these forward neutrons, dedicated calorimeters are installed in  $PbPb$  collisions, known as the Zero Degree Calorimeters (ZDCs) with an acceptance of  $|\eta| > 8.3$ , with a ZDC located on either side of the interaction point. The neutron multiplicity is determined by the energies deposited in the ZDCs [218]. For single neutrons, the relative energy resolution of each ZDC is 22–26%, while the detection efficiency is close to 100% in simulated events [219]. Based on neutron peaks observed in the total ZDC energy distribution, as shown in Fig. 29, coherent  $J/\psi$  meson photoproduction events are classified as having no neutrons (0n) or with at least one neutron ( $Xn$ ,  $X \geq 1$ ) in each ZDC.

The measured coherent  $J/\psi$  meson photoproduction differential cross sections with and without neutron selection over the rapidity range  $1.6 < |y| < 2.4$  are reported in the left and right panels of Fig. 30, respectively [221]. Theoretical results based on the leading twist approximation (LTA) [216] and color dipole models [220] are also shown for comparison. The leading twist approximation [216] is a pQCD calculation that accounts for nuclear shadowing effects using multinucleon interference. In each neutron multiplicity class, the LTA predictions tend to

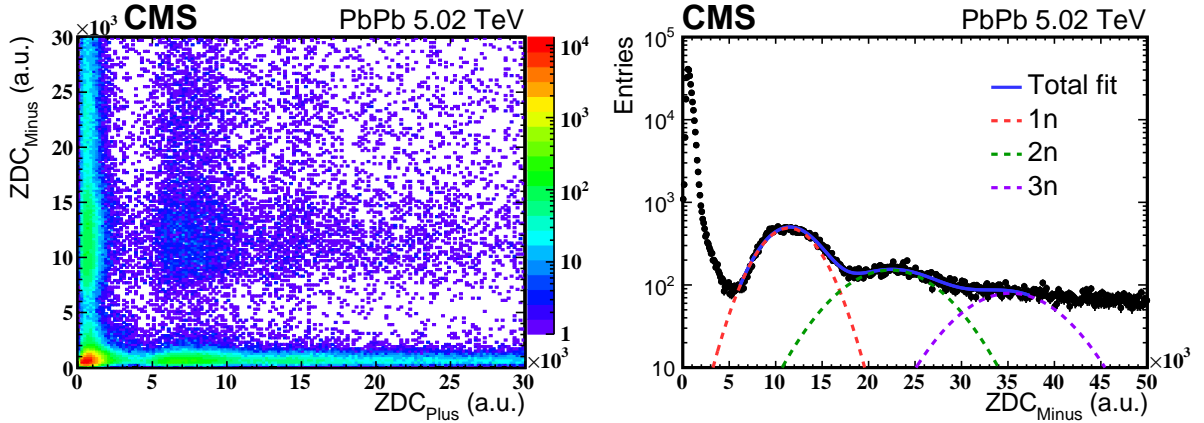


Figure 29: The left panel shows the correlation between energy distributions of the Minus and Plus ZDC detectors (one entry per event), while the right panel shows a multi-Gaussian function fit to the Minus ZDC energy distribution. The different “peaks” in the ZDC energy distribution can be assigned to different forward neutron multiplicities, the first peak is detector noise, which corresponds to no detected neutrons, the second peak can be associated with one neutron, and so on. (Figures adapted from Ref. [218].)

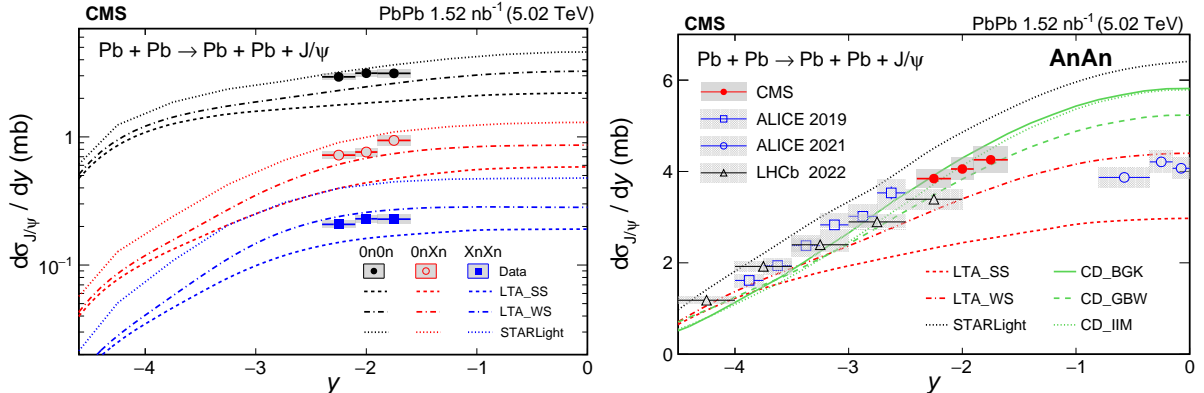


Figure 30: The differential coherent  $J/\psi$  meson photoproduction cross section as a function of rapidity, in different neutron multiplicity classes (left): 0n0n, 0nXn and XnXn ( $X \geq 1$ ); (right): AnAn (inclusive in the number of neutrons detected in the ZDC). The small vertical bars and shaded boxes represent the statistical and systematic uncertainties, respectively. The horizontal bars represent the bin widths. Theoretical predictions from LTA weak/strong shadowing [216], color dipole models (CD\_BGK, CD\_BGW, and CD\_IIM) [220], and STARLIGHT [115] are shown. (Figures adapted from Ref. [221].)

be lower than the CMS results. For the case of no neutron selection (AnAn), the data follow the trend of the forward-rapidity measurements of ALICE [222], but over a new  $y$  region. None of the models describe the results with or without neutron selection over the full rapidity range, which may indicate that there are key ingredients missing from the theoretical understanding of high-energy  $\gamma A$  scattering processes.

The measured coherent  $J/\psi$  meson photoproduction cross section as a function of  $\gamma N$  energy ( $W_{\gamma N}^{\text{Pb}}$ ) up to  $\approx 400$  GeV is shown in Fig. 31, after decomposing the two-way ambiguity with the differential cross sections split in different neutron multiplicity classes. The results show that the coherent  $J/\psi$  meson photoproduction cross section as a function of  $W_{\gamma N}^{\text{Pb}}$  increases, as it does for the  $\gamma p$  case, but the slope of the cross section quickly changes at energies around 40–100 GeV, at which point the growth occurs at a different rate. This follows the qualitative

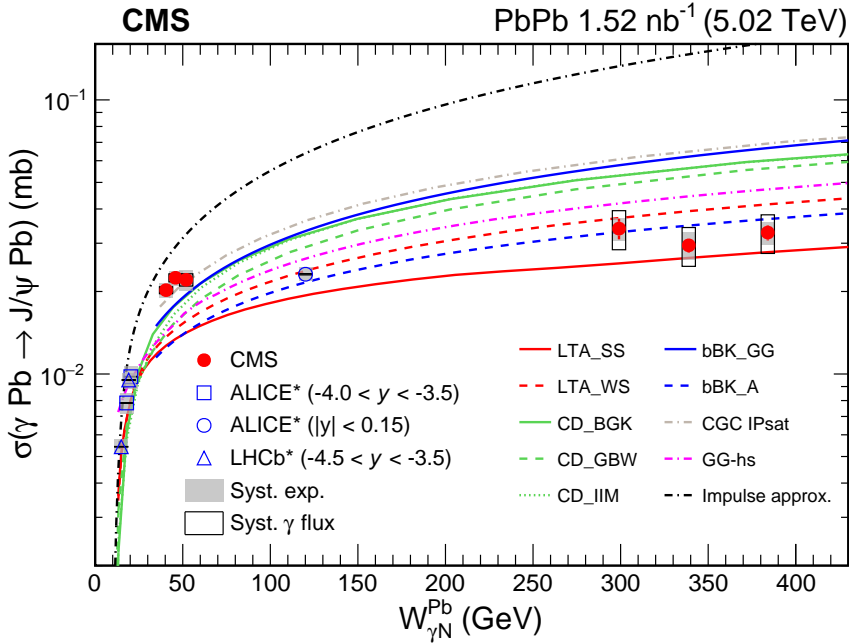


Figure 31: Total coherent  $J/\psi$  meson photoproduction cross section as a function of  $W_{\gamma N}^{\text{Pb}}$  in  $\text{PbPb}$  UPCs at  $\sqrt{s_{\text{NN}}} = 5.02 \text{ TeV}$ . The vertical bars and the shaded and open boxes represent the statistical, experimental, and theoretical (photon flux) uncertainties, respectively. The predictions from various theoretical calculations [214, 216, 220, 223–225] are shown by the curves. (Figure adapted from Ref. [221].)

expectation that at smaller  $x$ , the fast growth slows down due to nonlinear evolution effects. None of the theoretical predictions are able to reproduce the trends at high or small  $x$ . While the predictions qualitatively predict a change of shape as is observed in data, none of the theoretical predictions agree with the data in the full range explored in the measurement. To establish if this is due to genuine small  $x$  nonlinear evolution effects, it is important to continue exploring these measurements for other vector mesons. Indeed, nonlinear evolution effects are expected to be universal, and thus they should not depend strongly on the VM used to probe the nuclear structure. Since different vector mesons have different masses, which can be related to the effective size of their color dipoles, they will have different sensitivities to the properties of high partonic densities at small  $x$ . Also, significant advances have been made on the theoretical side. Notably, in recent years, the fixed-order next-to-leading order corrections to the hard scattering have been provided for exclusive quarkonium production in  $\text{PbPb}$  collisions [226–228]. It is found that the quark-antiquark channel has a nonnegligible contribution, and large cancellations between the real and virtual contributions for the two-gluon channel are found for  $J/\psi$  meson production. For the data to be used in global nPDF fits, an understanding of these corrections, as well as additional measurements using other VMs, will be important.

### 3.5 Summary of results for the initial state

During LHC Runs 1 and 2, the CMS Collaboration used pPb data to make significant strides in constraining nPDFs, particularly through the study of EW gauge bosons, dijets, and top quark pairs. These measurements have provided crucial input for nPDF models and have resulted in substantial improvements in accurately reproducing experimental results, especially at medium and high Bjorken- $x$  values. Furthermore, studies of EW bosons in  $\text{PbPb}$  collisions have confirmed that colorless hard probes, such as photons and  $Z$  bosons, are not significantly modified by the QGP in central collisions, offering the potential opportunity to use these probes

for improved event selection and centrality calibration, especially in peripheral collisions.

For the low- $x$  regions, measurements at LHC energies have primarily focused on the evolution of gluon nPDFs. Forward inclusive jet cross sections in pPb collisions, along with exclusive VM production in both pPb and PbPb collisions, have been instrumental in constraining models that incorporate gluon recombination alongside gluon splitting within their small- $x$  perturbative QCD evolution. Notably, very forward jet measurements by the CASTOR detector probe the phase space in a region with exceptionally low  $x$  ( $\approx 10^{-5}$ ) and  $Q^2$  ( $\approx 10 \text{ GeV}^2$ ). These measurements have shown that existing predictions, which also apply to cosmic ray physics, severely underestimate jet cross sections by factors of 10–100, underscoring the potential of these data to refine theoretical models.

Exclusive VM production has demonstrated that pPb collisions can effectively function as  $\gamma p$  colliders, providing valuable constraints on gluon PDFs for protons in the small- $x$  region at low  $Q^2$ . Similarly, PbPb collisions offer the opportunity to constrain gluon nPDFs in comparable kinematic regimes. However, analyzing exclusive VM production in symmetric PbPb collisions presents a unique challenge because of the ambiguity in identifying which nucleus emits the quasireal photon and which the pomeron. The use of the ZDCs has been pivotal in resolving this ambiguity by distinguishing between low- and high-energy photon contributions, enabling the determination of the exclusive VM cross section in the  $\gamma A$  center-of-mass frame for the first time.

The energy dependence of exclusive VM production in the  $\gamma A$  frame reveals a marked suppression compared to the scaling behavior expected from  $\gamma p$  cross sections, consistent with parton saturation effects. However, the overall trend is not fully captured by current theoretical models, suggesting that further research is necessary to definitively attribute this nuclear suppression to the expected short-distance mechanism of gluon recombination.

## 4 Bulk properties and novel phenomena

Understanding the bulk thermodynamic and hydrodynamic properties of the QGP formed in ultrarelativistic heavy ion collisions is crucial for gaining insights into the fundamental degrees of freedom of this medium and its transport dynamics. This section reviews studies of the bulk properties of the QGP by the CMS Collaboration. The results are based on measurements that use the large pseudorapidity coverage of the CMS detector. Charged-hadron densities and the correlations among particles widely separated in pseudorapidity are presented and discussed in context of the initial-state geometry. Measurements employing femtoscopy techniques of the size and shape of particle emitting sources at the last stage of the system evolution are also performed for different collision systems and LHC energies. Searches for novel phenomena related to chiral anomalous transport effects are also reviewed.

### 4.1 Initial-state entropy and energy densities

The multiplicity and energy distributions of the primary charged particles (discussed in Section 2.1) that emerge from HI collisions are basic observables that inform on the initial entropy and energy density and the medium evolution. At lower energies, these rapidity distributions are generally consistent with Landau hydrodynamics [229]. The LHC experiments can test if a hydrodynamic description continues to be valid at TeV energies. In an early measurement, CMS established the  $\eta$  dependence of charged-particle production in PbPb collisions at  $\sqrt{s_{\text{NN}}} = 2.76$  TeV [111]. For the 5% most central collisions, a charged-particle density per unit of pseudorapidity ( $dN_{\text{ch}}/d\eta$ ) of  $1612 \pm 55$  was found. This value is consistent with a similar measurement by the ALICE Collaboration [121], and is twice the value found at RHIC [230].

The top panels of Fig. 32 show, for different centrality ranges, the  $\eta$  dependence of the charged-particle densities  $dN_{\text{ch}}/d\eta$  in PbPb (left) and XeXe (right) collisions, the former case scaled by  $N_{\text{part}}/2$ , where  $N_{\text{part}}$  is the number of nucleons that participate in the collisions. The  $\eta$  dependence of the results is weak, varying by less than 10% over the range  $|\eta| < 2.4$ . The slight dip at  $\eta = 0$  is a trivial (Jacobian) kinematic effect resulting from the use of  $\eta$  rather than rapidity  $y$  for the independent variable. This dip is absent in the  $dE_{\text{T}}/d\eta$  distribution (bottom panel of Fig. 32), where  $E_{\text{T}}$  is the measured transverse energy. This latter distribution can be described by a Gaussian function of width  $\sigma_{\eta} = 3.4 \pm 0.1$  for central collisions, which is larger than predicted by Landau hydrodynamics. Indeed, none of the standard LHC event generators, including AMPT, HYDJET, and EPOS, have been able to fully describe either the measured charged-particle multiplicity or the transverse energy distributions [111, 231, 232]. That means that the new LHC results provide important constraints on models and generators that characterize multiparticle production in HI collisions at high energies.

In order to further study the system size dependence of particle density distributions, we have measured  $dN_{\text{ch}}/d\eta$  values in the smaller XeXe system [231]. The per-participant multiplicities for XeXe and PbPb collisions with similar  $\langle N_{\text{part}} \rangle$ , and consequently corresponding to different centrality classes, are inconsistent in the two collision systems, as shown in Fig. 33 (left). This is most apparent for  $\langle N_{\text{part}} \rangle \approx 236$ . However, as shown in Fig. 33 (right), where  $\langle N_{\text{part}} \rangle/2A$  is used as a proxy for centrality, the per-participant charged-hadron multiplicities for different colliding nuclei are equal within uncertainties when the geometry (centrality) and energy of the compared systems are the same. This mirrors a lower-energy result obtained at RHIC that the particle production is dependent on the collision geometry in addition to the system size and collision energy [233].

Figure 34 shows the dependence on the center-of-mass energy per nucleon pair  $\sqrt{s_{\text{NN}}}$  of the charged-particle multiplicities (left panel) at midrapidity ( $\eta = 0$ ). The AA results from CMS,

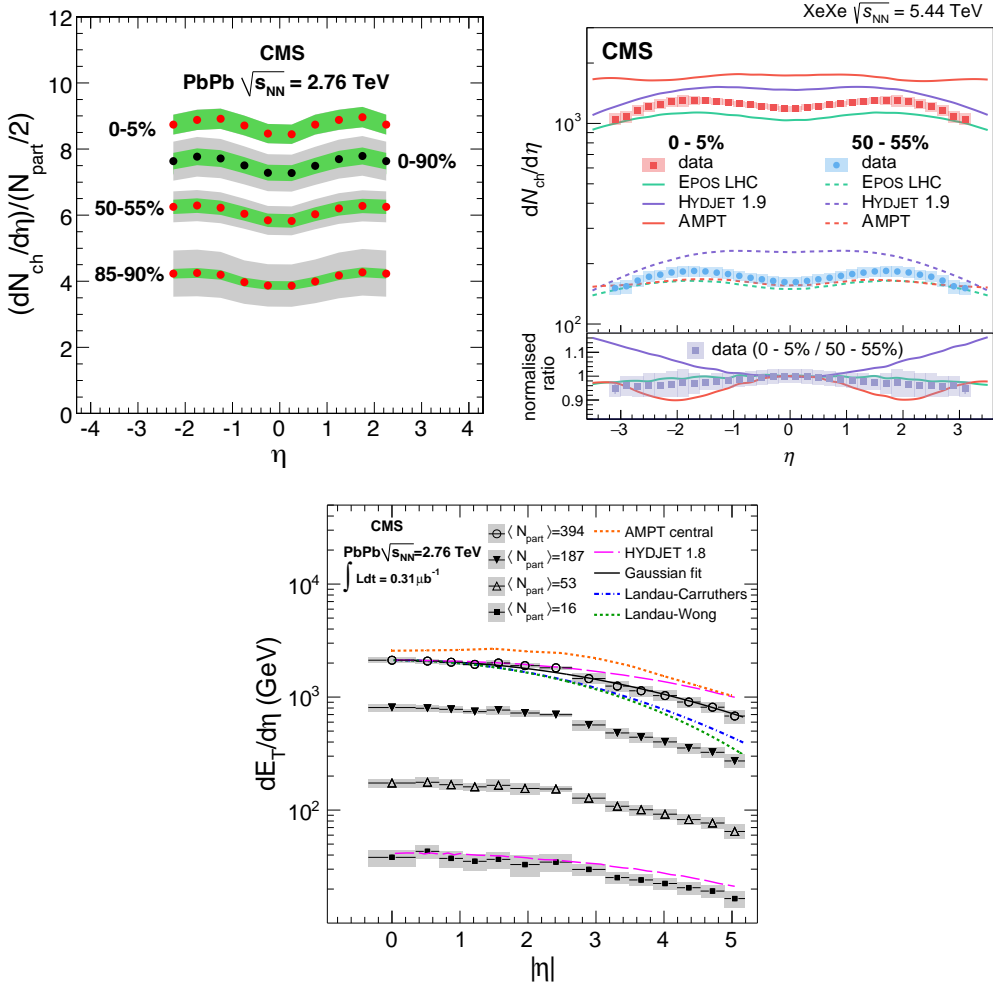


Figure 32: Distributions  $(dN_{ch}/d\eta)/(N_{part}/2)$  in 2.76 TeV PbPb (top left) and  $dN_{ch}/d\eta$  in 5.44 TeV XeXe (top right) collisions, and  $dE_T/d\eta$  in 2.76 TeV PbPb collisions (bottom) as functions of  $\eta$  in various centrality bins. The inner green band in the left panel shows the measurement uncertainties affecting the scale of the measured distribution, while the outer gray band shows the full systematic uncertainty, i.e. affecting both the scale and the slope. (Figures adapted from Refs. [111, 231, 232].)

ALICE [121], PHENIX [230], and PHOBOS [234], and the non-single-diffractive (NSD) pp results (excluding events with significantly high particle density on one rapidity side only) from CMS [235, 236], ALICE [237], UA5 [238], and UA1 [239] experiments, are shown. The dependence is modeled by a power-law function  $a + s_{NN}^n$ , with observed value  $n = 0.13$  for PbPb and  $n = 0.10$  for NSD pp events. This shows that the multiplicity increases more rapidly with the center-of-mass energy than the logarithmic dependence used to describe data up to  $\sqrt{s_{NN}} = 200$  GeV [230]. A similar study has been performed for the transverse energy distribution (right panel), where  $n \approx 0.2$ , showing that the transverse energy density increases faster with collision energy than the charged-particle multiplicity. Furthermore, for the 5% most central collisions, CMS has measured the transverse energy per charged-particle at  $\eta = 0$  of  $1.25 \pm 0.08$  GeV at  $\sqrt{s_{NN}} = 2.76$  TeV. The corresponding value at  $\sqrt{s_{NN}} = 200$  GeV was found to be  $0.88 \pm 0.07$  GeV [230], indicating a significant increase of transverse energy per particle at the higher beam energy. This increase reflects a higher initial energy density at the LHC, compared to RHIC, as transverse energy is closely related to the energy deposited in the medium.

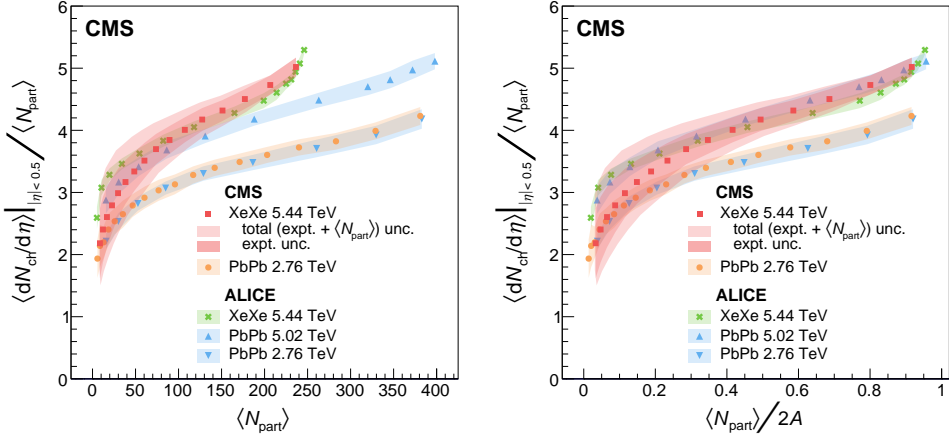


Figure 33: Average  $dN_{\text{ch}}/d\eta$  at midrapidity normalised by  $\langle N_{\text{part}} \rangle$ , shown as a function of  $\langle N_{\text{part}} \rangle$  (left) and  $\langle N_{\text{part}} \rangle / 2A$  (right), where  $A$  is the mass number of the nuclei. (Figures adapted from Ref. [231].)

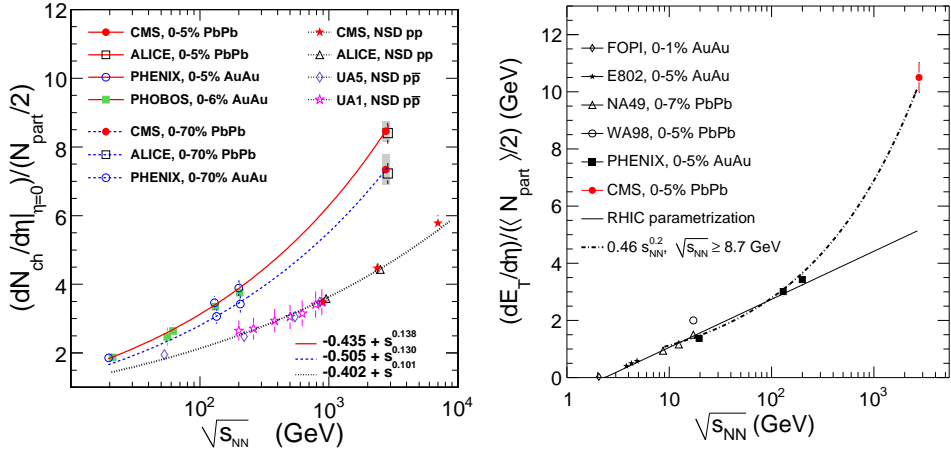


Figure 34: Normalized charged-particle pseudorapidity (left, figure adapted from Ref. [111]) and transverse energy density (right, figure adapted from Ref. [232]) at  $\eta = 0$  as functions of center-of-mass energy, from various experiments. The fits to power-law functions are shown by lines.

## 4.2 The paradigm of a nearly perfect liquid

In a noncentral HI collision, the overlap region has a lenticular initial shape, and the interacting nucleons in this region are known as “participants”. The “participant plane” is defined by the beam direction and the short axis of the participating nucleon distribution. Because of fluctuations that arise from the finite number of nucleons, the impact parameter vector typically does not coincide with the short axis of this lenticular region. Strong partonic rescatterings of the system may lead to local thermal equilibrium and the build-up of anisotropic pressure gradients, driving a collective expansion that is anisotropic with a faster expansion along the short axis of the lenticular overlap region. As a result, the eccentricity of the initial collision geometry translates in an anisotropic azimuthal distribution of the final-state particles. This final-state anisotropy is typically characterized by the Fourier harmonic coefficients ( $v_n$ ) in the azimuthal angle ( $\phi$ ) distribution of the hadron yield,

$$dN/d\phi \propto 1 + 2 \sum_n v_n \cos[n(\phi - \Psi_N)], \quad (4)$$

where  $\Psi_N$  is the event-by-event azimuthal angle of the event plane, defined as the direction of maximum final-state particle density. The second-order Fourier component ( $v_2$ ) is known as the “elliptic flow” harmonic, and its event plane angle  $\Psi_2$  corresponds, approximately, to the short axis direction of the lenticular region. Because of event-by-event fluctuations, higher-order eccentricities can also arise, leading to higher-order Fourier harmonics ( $v_n$ ,  $n \geq 3$ ) in the final state with respect to their corresponding event plane angles,  $\Psi_N$  [32]. In hydrodynamic models, the  $v_n$  coefficients are related to the response of the QGP medium to the initial geometry and its fluctuations [32]. As such, these Fourier components can provide insight into the fundamental transport properties of the medium.

A wide  $\eta$  coverage gives the CMS Collaboration an opportunity to correlate particles with large  $\eta$  difference and thus significantly suppress short-range correlations. Taking this advantage extensive studies have been performed of the particle anisotropy developed through collective flow using several techniques based on particle correlations over a wide phase space [128, 240–244] to extract the  $v_n$  coefficients. These techniques include using correlations of two-particle pairs over long ranges in  $\eta$  [240, 241, 243, 244] and the scalar-product or, in earlier studies, event plane method that correlates individual particles in one region of phase with an event plane angle  $\Psi_N$  established in another [128, 242]. Correlations among multiple particles (four or more), known as the “cumulants,” have also been studied. These multiparticle correlations are particularly sensitive to event-by-event fluctuations of the  $v_n$  coefficients [128, 242]. Measurements of event-by-event  $v_2$  probability distributions provide a direct means to constrain the elliptic-flow fluctuations [245]. Collectively, the particle correlation studies have played a vital role in constraining the initial state and transport properties of the QGP medium, leading to the paradigm of a nearly perfect QCD liquid formed in ultrarelativistic nuclear collisions.

#### 4.2.1 Transport properties and ripples in the QGP

Two-particle correlations provide a powerful quantitative tool to study the collective anisotropy of final-state particles from HI collisions. In this section we review results based on two-particle correlations to demonstrate how transport properties of the QGP can be constrained by experimental data. Each pair of particles can have its constituents chosen from the same or different  $p_T$  ranges, denoted as  $p_T^{\text{trig}}$  (or “trigger”) and  $p_T^{\text{assoc}}$  (or “associated”), within the CMS tracker acceptance of  $|\eta| < 2.5$ . The two-dimensional (2D) two-particle correlations as functions of the relative pseudorapidity ( $\Delta\eta$ ) and azimuthal angle ( $\Delta\phi$ ) between the two particles of a pair is given by

$$\frac{1}{N_{\text{trig}}} \frac{d^2N^{\text{pair}}}{d\Delta\eta\,d\Delta\phi} = B(0,0) \frac{S(\Delta\eta,\Delta\phi)}{B(\Delta\eta,\Delta\phi)}, \quad (5)$$

where  $N_{\text{trig}}$  is the number of trigger particles in an event and  $N^{\text{pair}}$  is the total number of hadron pairs for the event. The signal distribution,  $S(\Delta\eta,\Delta\phi)$ , is constructed by taking particle pairs from the same event, while the background distribution,  $B(\Delta\eta,\Delta\phi)$ , is obtained by pairs of particles taken from different events with similar topology. The ratio  $B(0,0)/B(\Delta\eta,\Delta\phi)$  represents the correction for pair-acceptance effects.

Figure 35 (left) shows the two-particle correlation function for both particles with  $1 < p_T < 3$  GeV in 0–0.2% central PbPb events at  $\sqrt{s_{\text{NN}}} = 2.76$  TeV. On the near side ( $\Delta\phi \sim 0$ ) of the correlation function, a long-range structure extending over the entire  $\Delta\eta$  region is evident. This feature of long-range rapidity correlations has been observed across multiple centrality ranges [240, 241], corresponding to different initial size and geometry of the system. The one-dimensional (1D)  $\Delta\phi$  correlation function is shown in Fig. 35 (right) with a requirement of  $|\Delta\eta| > 2$  to exclude noncollective effects from other sources of correlations, such as jet frag-

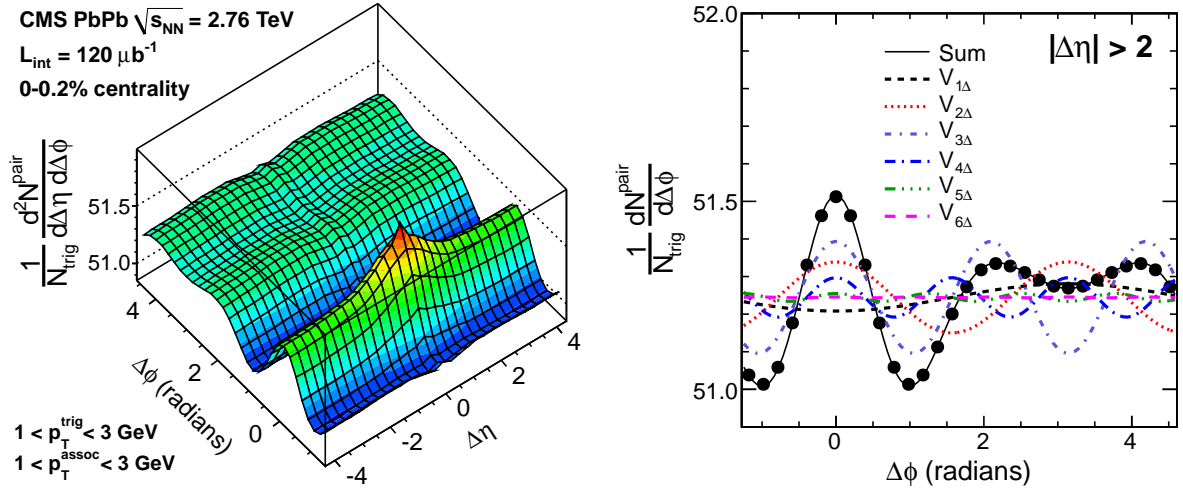


Figure 35: The 2D (left) and 1D  $\Delta\phi$  (right) two-particle correlation functions for  $1 < p_{\text{T}} < 3$  GeV in 0–0.2% central PbPb collisions at  $\sqrt{s_{\text{NN}}} = 2.76$  TeV. (Figures adapted from Ref. [243].)

mentation. By fitting the 1D  $\Delta\phi$  correlation function by a Fourier series (as indicated by dashed curves),

$$\frac{1}{N_{\text{trig}}} \frac{dN^{\text{pair}}}{d\Delta\phi} \propto 1 + \sum_{n=1}^{\infty} 2V_{n\Delta}(p_{\text{T}}^{\text{trig}}, p_{\text{T}}^{\text{assoc}}) \cos(n\Delta\phi), \quad (6)$$

where  $V_{n\Delta}(p_{\text{T}}^{\text{trig}}, p_{\text{T}}^{\text{assoc}})$  are the two-particle Fourier coefficients. Assuming that  $V_{n\Delta}(p_{\text{T}}^{\text{trig}}, p_{\text{T}}^{\text{assoc}})$  can be factorized into a product of single-particle, global  $v_n$  coefficients (as defined in Eq. (4)), as both particles share a common event plane  $\Psi_N$  [246],

$$V_{n\Delta} = v_n(p_{\text{T}}^{\text{trig}}) v_n(p_{\text{T}}^{\text{assoc}}). \quad (7)$$

Hence, the anisotropy flow coefficients as functions of  $p_{\text{T}}$  can be extracted.

The single-particle azimuthal anisotropy coefficients, from  $v_2$  to  $v_6$ , as functions of  $p_{\text{T}}$  extracted in 0–0.2% central PbPb collisions at  $\sqrt{s_{\text{NN}}} = 2.76$  TeV, are shown in Fig. 36 (left). Different orders of  $v_n$  harmonics show very different dependences on  $p_{\text{T}}$ . At low  $p_{\text{T}}$  ( $p_{\text{T}} < 1$  GeV), the  $v_2$  harmonic coefficient that corresponds to an elliptical anisotropy has the greatest magnitude. However, this coefficient becomes smaller than the  $v_3$  coefficient at  $p_{\text{T}} \approx 1$  GeV, and even smaller than the  $v_5$  coefficient for  $p_{\text{T}} > 3$  GeV. This intriguing  $p_{\text{T}}$  dependence can be used to quantitatively constrain hydrodynamics models of HI collisions with fluctuating initial conditions.

The  $p_{\text{T}}$ -averaged  $v_n$  values from 0.3 to 3.0 GeV are presented in Fig. 36 (right) as functions of  $n$  up to  $n = 7$ , and compared with hydrodynamic model calculations [247]. As the collisions are extremely central, the initial eccentricities for all orders are mostly driven by event-by-event participant fluctuations and are of similar values [247]. Therefore, the diminishing  $v_n$  values towards higher orders reflects damping effects of viscous dissipation (typically characterized by the shear viscosity to entropy density ratio,  $\eta/s$ , which is a dimensionless quantity [32]) that tends to suppress higher-order deformations more strongly. As shown in Fig. 36 (right), the CMS  $v_n$  data for all orders except for  $n = 2$  lie between the two hydrodynamic calculations with only differences in initial-state models (MC-Glauber and MC-KLN) and  $\eta/s$  values (0.08 and 0.2). The ‘tension’ for  $n = 2$  has been largely resolved in more recent calculations with improved modeling of the initial state [40]. Therefore, these studies have imposed a stringent constraint on the allowed  $\eta/s$  value for the QGP. The observed value, in the range 0.08–0.2,

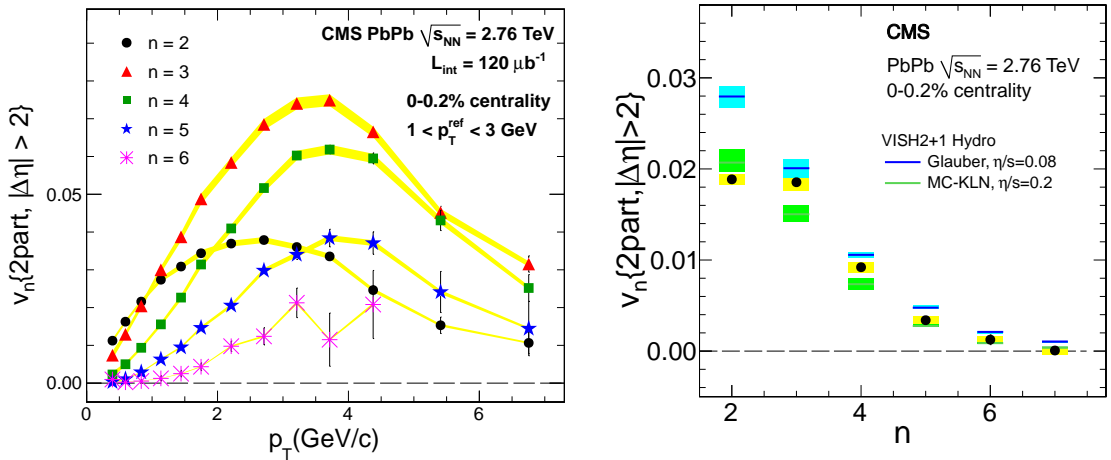


Figure 36: Left: the  $v_2$  to  $v_6$  values as functions of  $p_T$  in 0–0.2% central PbPb collisions at  $\sqrt{s_{\text{NN}}} = 2.76$  TeV. Right: Comparison of  $p_T$ -integrated (0.3–3.0 GeV)  $v_n$  data with VISH2+1D hydrodynamic calculations for Glauber initial condition with  $\eta/s = 0.08$  (blue) and MC-KLN initial condition with  $\eta/s = 0.2$  (green), in 0–0.2% central PbPb collisions at  $\sqrt{s_{\text{NN}}} = 2.76$  TeV. Error bars denote the statistical uncertainties, while the shaded color bands correspond to the systematic uncertainties. (Figures adapted from Ref. [243].)

suggests that the QGP behaves like a nearly perfect liquid (close to the theoretical lower bound by quantum fluctuations of  $\eta/s = 1/4\pi$  [248]) with little frictional momentum dissipation.

#### 4.2.2 Direct constraints on initial-state fluctuations

As a consequence of the initial geometry fluctuations, flow harmonic magnitudes vary significantly event-by-event. This is also the case for the elliptic flow  $v_2$  coefficient that, for noncentral events, has its origin in the shape of the overlapping area of the colliding nuclei. The second-order eccentricity  $\epsilon_n$  of the medium responsible for the azimuthal particle density asymmetry is affected by fluctuations of participant positions in the colliding nuclei which, in turn, results in fluctuations in the observed  $v_2$  values. Different methods for measuring azimuthal anisotropy, which essentially have different ways of averaging anisotropy over many events, give different  $v_2$  values. Comparison of flow coefficients measured by different methods is a direct probe of the initial-state conditions.

The CMS Collaboration has directly studied the probability distribution functions of the magnitudes of the  $v_n$  values,  $p(v_n)$ , through an unfolding technique [245]. The particles within an event are used to construct the “observed”  $p(v_2^{\text{obs}})$  distributions, while residual contributions from multiplicity-related fluctuations and nonflow effects are estimated and subtracted by considering  $p(v_n)$  difference between two symmetric subevents based on pseudorapidity. This difference should not contain “real” flow, given that  $v_2(\eta)$  is symmetric about  $\eta = 0$ , on average, for the symmetric PbPb system.

Figure 37 shows the  $p(v_2)$  distribution in PbPb collisions for three centrality classes. In addition,  $p(v_2^{\text{obs}})$  distributions are plotted for each centrality to illustrate the statistical resolution effects present prior to unfolding. The elliptic power and Bessel-Gaussian parametrizations are used to fit the data (a discussion of the parameterizations can be found in Ref. [249]). The elliptic power  $\chi^2/\text{dof}$  values vary between 0.8 and 1.5 from central to peripheral collisions, while the Bessel-Gaussian  $\chi^2/\text{dof}$  values vary between 3 and 9. Both models assume linear response between eccentricity and flow, with  $p(\epsilon_2) = k_2 p(v_2)$ , but only the elliptic power function al-

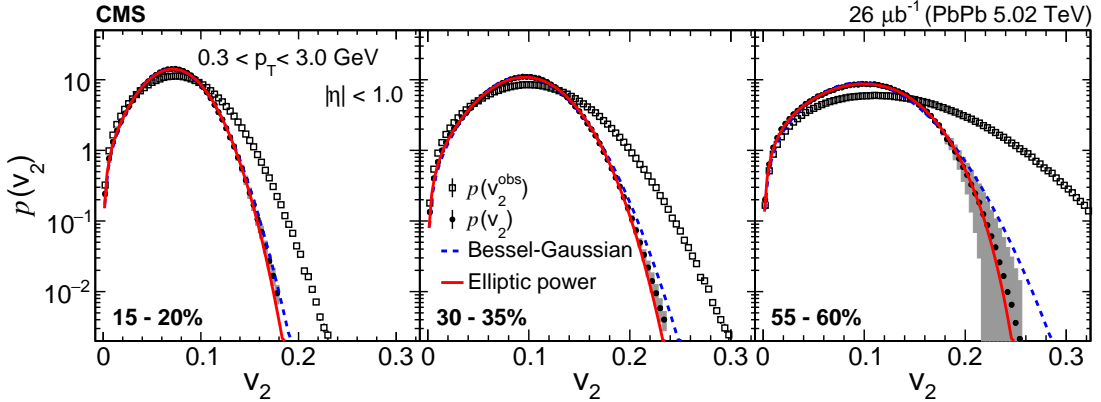


Figure 37: Representative final unfolded  $p(v_2)$  distributions (closed black circles) in three centrality bins (15–20%, 30–35%, and 55–60%). Respective observed  $p(v_2^{\text{obs}})$  distributions (open black squares) are shown to illustrate the statistical resolution present in each centrality bin prior to unfolding. Distributions are fitted with Bessel-Gaussian and elliptic power functions to infer information on the underlying  $p(\varepsilon_2)$  distributions. (Figure adapted from Ref. [245].)

lows for a nonzero skewness (asymmetry of the distribution), hence being able to better fit the data. The  $k_2$  parameter of the elliptic power function is expected to have only a weak dependence on the initial conditions and the measured value is consistent with the hydrodynamic calculation with Glauber initial conditions and an  $\eta/s$  value of 0.19 [249].

In addition to PbPb results, a short run with Xe nuclei in 2017 gave the LHC experiments a chance to probe the scaling of the hydrodynamics and initial-state effects with system size. Fluctuations of the initial state are proportional to  $A^{-1/2}$ , where  $A$  is the atomic mass, and, therefore, one can expect a larger fluctuation component for XeXe collisions than for PbPb collisions [250]. However, the viscosity, which tends to decrease the azimuthal anisotropy, is thought to be proportional to  $A^{-1/3}$  [251] and is, therefore, also expected to be larger for XeXe collisions. Also, the quadrupole deformation of the Xe nuclei can cause two colliding systems in the same centrality class to have different geometries.

Figure 38 compares the spectrum-weighted  $v_2$ ,  $v_3$ , and  $v_4$  values with  $0.3 < p_T < 3.0 \text{ GeV}$  for the XeXe and PbPb systems. For all three harmonics, the XeXe values are higher in central collisions, while the PbPb results become larger for more peripheral events. The ordering of the measured harmonics between the two systems is consistent with participant fluctuations having a dominant role in central collisions, and viscosity effects becoming more important for mid-central and peripheral collisions. The largest difference between the two systems is found for the  $v_2$  coefficients corresponding to the most central events, where the XeXe results are larger by a factor of about 1.3. The hydrodynamic model calculations with Trento initial conditions [254] for both spherical and deformed Xe shape, performed for the  $p_T$  range  $0.2 < p_T < 5.0 \text{ GeV}$ , are shown in the lower panel. The xenon nuclear deformation is found to only have a significant effect on the model  $v_2$  values for the most central collisions, where the calculation with deformed nuclei is closer to the data. For all measured harmonics, the model values lie below the experimental results, although qualitatively the behavior is similar.

#### 4.2.3 A new window to the full (3+1)-dimensional space-time and dynamical evolution

It was thought originally that the factorization relation in Eq. (7) holds for correlations arising from collective hydrodynamic flow, where emitted particles share a common event plane  $\Psi_N$ . However, in a first analysis of its kind, the CMS Collaboration has observed and studied the

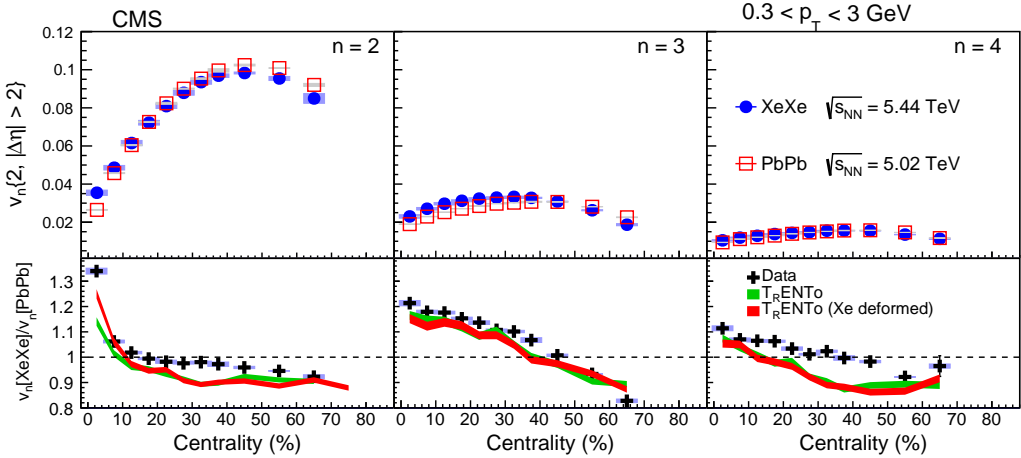


Figure 38: Centrality dependence of the  $v_2$ ,  $v_3$ , and  $v_4$  harmonic coefficients from two-particle correlations method for  $0.3 < p_T < 3.0$  GeV for XeXe collisions at  $\sqrt{s_{NN}} = 5.44$  TeV and PbPb collisions at 5.02 TeV. The lower panels show the ratio of the results for the two systems. Theoretical predictions from Ref. [252] are compared to the data. The model calculation is done for the  $p_T$  range  $0.2 < p_T < 5.0$  GeV. (Figure adapted from Ref. [253].)

factorization breaking in anisotropic flow measurements using two-particle correlations [241]. Because of initial-state local fluctuations, the final-state event plane depends on the particle kinematics, instead of being a global property of the phase space [255, 256]. Comprehensive studies were conducted in Ref. [244], where the  $p_T$ -dependent factorization ratio,

$$r_n = \frac{V_{n\Delta}(p_T^a, p_T^b)}{\sqrt{V_{n\Delta}(p_T^a, p_T^a)V_{n\Delta}(p_T^b, p_T^b)}}, \quad (8)$$

served as a quantitative measure of the factorization breaking. This ratio probes the relative fluctuations of flow vectors with particles from two different  $p_T$  ranges [255, 256], denoted  $a$  and  $b$ . Hence, if the factorization holds exactly, this ratio is expected to be unity. However, with the presence of  $p_T$ -dependent flow fluctuations, this ratio typically becomes smaller than 1.

Figure 39 shows  $r_n$  results for  $2.5 < p_T^a < 3.0$  GeV and  $0.3 < p_T^b < 0.5$  GeV in pPb and PbPb collisions as functions of event multiplicity (the corresponding centrality scale for PbPb events is shown by the upper  $x$  axis) [244]. Factorization breaking is clearly observed for both the second and third harmonic. The  $r_2$  value deviates from unity by 2–5% for midcentral and peripheral events, but suddenly increases to  $\approx 20\%$  for 0–0.2% centrality events. The  $r_3$  value, in comparison, stays at a 2–3% level for the entire centrality range. For a similar multiplicity range, the  $r_2$  value in pPb collisions is slightly higher than for PbPb collisions, but with the two values within statistical uncertainties. An  $r_3$  value larger than 1, as found for low-multiplicity pPb events, corresponds to the presence of nonflow effects. Alternative hydrodynamic model calculations in PbPb collisions, using either MC-Glauber or MC-KLN [257] initial conditions, are also shown. Neither set of initial conditions leads to quantitative agreement with the data over the entire centrality range, although the qualitative trend is reproduced.

For very central events, where the factorization breaking effect is the strongest, the calculations using different values of  $\eta/s$  are compared to the data in Fig. 40 [244]. For each initial-state model, the  $r_2$  values are found to be largely insensitive to different values of  $\eta/s$ . This observation, as well as the centrality dependence of the  $r_2$  values, is consistent with the flow

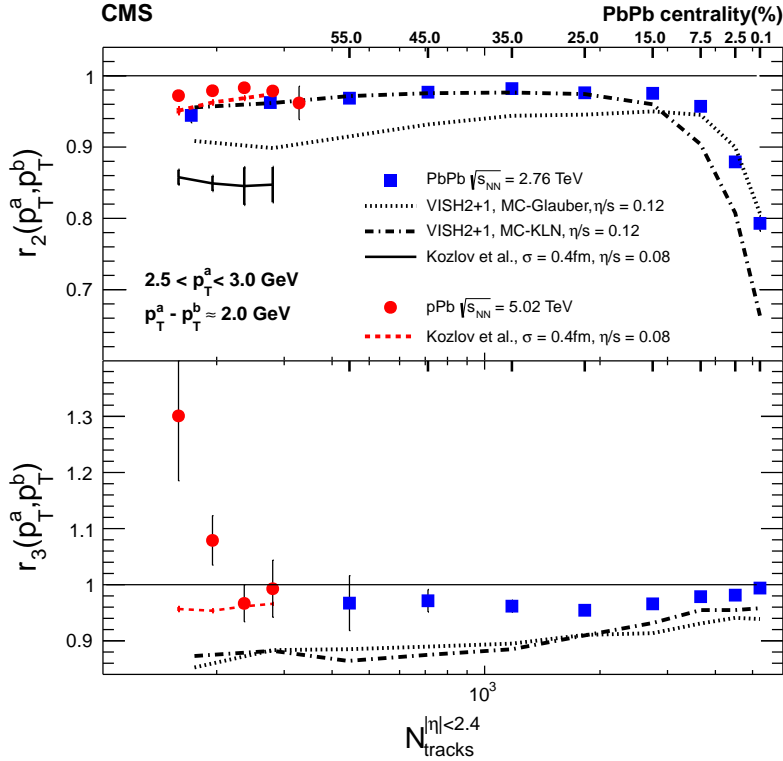


Figure 39: The  $p_T$ -dependent factorization ratios,  $r_2$  and  $r_3$ , as functions of event multiplicity in pPb and PbPb collisions. The lines represent different hydrodynamics calculations. (Figure adapted from Ref. [244].)

fluctuations in  $p_T$  being driven primarily by local fluctuations in the initial energy density distribution. Thus,  $r_n$  measurements can provide unique constraints on the initial-state modeling.

An equivalent approach for studying the  $p_T$ -dependence of the event plane and factorization breaking is the principal component analysis, where measured two-particle Fourier coefficients as functions of  $p_T^a$  and  $p_T^b$  can be expressed in terms of an orthogonal basis of leading and subleading flow modes, as detailed in Ref. [258].

Most of the earlier studies on collective flow have focused on the transverse expansion in the midrapidity region. Leveraging the wide coverage of the CMS detector, the CMS Collaboration has now explored the longitudinal dynamics of the QGP to establish, for the first time, a full three-dimensional picture of the system evolution. By studying the decorrelation of flow harmonic vectors measured at different rapidities, the CMS Collaboration aims to address two key questions related to the (3+1)D dynamics of a QGP: (1) How is the initial entropy deposited in 3-D space, and how does it fluctuate event-by-event? (2) What is the role of the longitudinal pressure gradient?

A rapidity-dependent event plane twist decorrelation has been predicted, as illustrated in Fig. 41 (left). Based on a “wounded” nucleon model [259], particles in the forward rapidity regions are predominantly produced from one of the projectile nuclei. As a result, the flow orientation angle (or event plane) at forward and backward rapidities can be slightly twisted event-by-event, creating a torqued QGP along the rapidity direction. Additionally, in the color glass condensate model [260], fluctuating granularity of the gluon field at different rapidities can also lead to rapidity-correlated flow fluctuations.

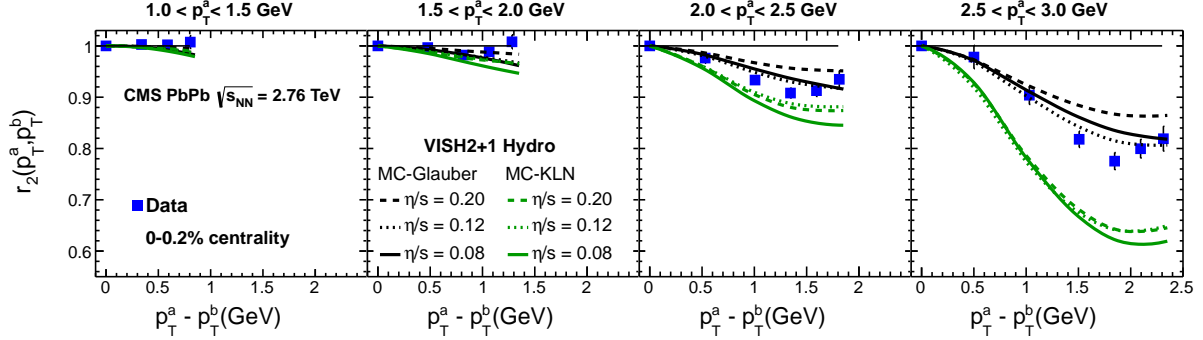


Figure 40: The  $p_T$ -dependent factorization ratios,  $r_2(p_T)$ , in very central (0–0.2% centrality) PbPb collisions. The lines represent hydrodynamics calculations for different initial conditions and different values of  $\eta/s$ . (Figure adapted from Ref. [244].)

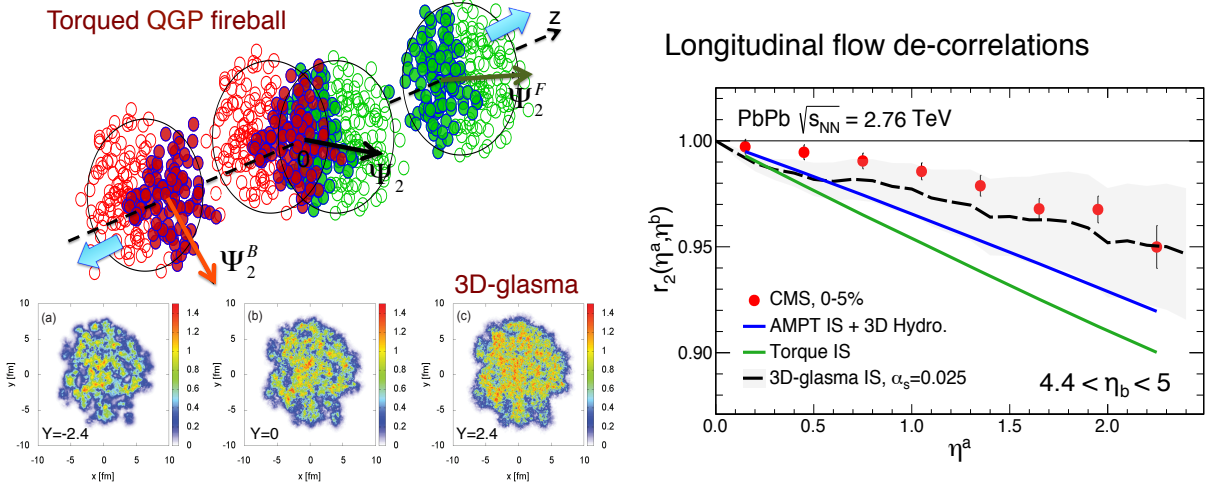


Figure 41: Left: illustration of flow event plane decorrelations as functions of rapidity in the wounded nucleon picture (or ‘torqued QGP fireball’) [259] and 3D color glass condensate model [260]. Right: measurement of elliptic flow decorrelations as functions of pseudorapidity in 0–5% central PbPb collisions at 2.76 TeV from CMS [244], with comparison to theoretical calculations [259, 260].

Rapidity-dependent flow decorrelations have been observed by the CMS Collaboration using a novel observable based on two flow vectors,  $\vec{V}_n(\eta^a) = v_n(\eta^a) \exp(-in\Psi_n(\eta^a))$  and  $\vec{V}_n(\eta^b) = v_n(\eta^b) \exp(-in\Psi_n(\eta^b))$ , measured in different rapidity regions,

$$r_n \equiv \frac{\left\langle \vec{V}_n(-\eta^a) \vec{V}_n^*(\eta^b) \right\rangle}{\left\langle \vec{V}_n(\eta^a) \vec{V}_n^*(\eta^b) \right\rangle}. \quad (9)$$

This  $r_n$  ratio is similar to that used to measure the  $p_T$  dependent decorrelation, but now designed to approximate the decorrelation between two event plane angles separated by a large gap of  $2\eta_a \langle \cos n [\Psi_n(\eta^a) - \Psi_n(-\eta^a)] \rangle$ , as shown in Fig. 41 (right) for elliptic flow in 0–5% central PbPb collisions, while avoiding the contamination of short-range nonflow correlation. The data are compared to several initial-state models, including the torqued QGP model, the AMPT initial state followed by a (3+1)D hydrodynamics, and the 3D CGC glasma model. All of the initial state models are able to qualitatively reproduce the data. It is worth noting that almost all of the rapidity decorrelation effect is determined by the initial state. The addition of

(3+1)D hydrodynamic evolution is found to have little impact on the  $r_n$  ratio. This underlines the importance of incorporating a rapidity-dependent modeling of initial-state fluctuations in hydrodynamic calculations.

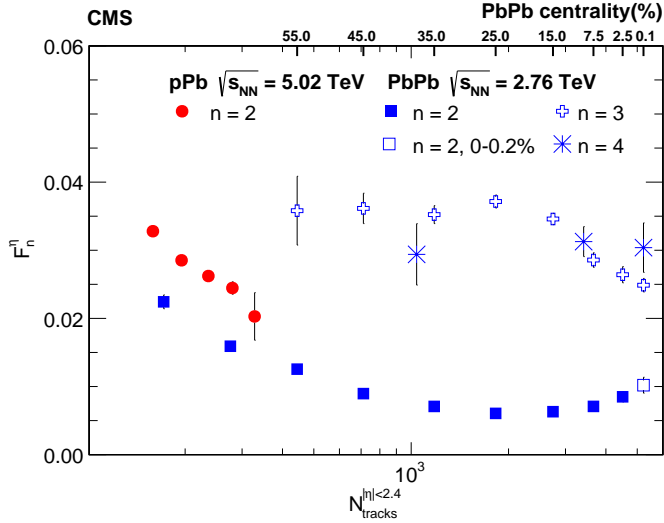


Figure 42: The  $F_N^\eta$  parameter as a function of event multiplicity in PbPb collisions at  $\sqrt{s_{NN}} = 2.76$  TeV for  $n = 2$ –4 and pPb collisions at  $\sqrt{s_{NN}} = 5.02$  TeV for  $n = 2$ . (Figure adapted from Ref. [244].)

The slope in the  $\eta$  dependence of the  $r_n$  ratio, parameterized as  $F_N^\eta$ , is plotted as a function of event multiplicity in Fig. 42 for pPb collisions with  $n = 2$  and for PbPb collisions with  $n = 2$ –4. For PbPb collisions, the  $F_2^\eta$  value reaches its minimum value near  $\sim 20\%$  centrality (i.e., midcentral events), and increases significantly for more peripheral or central PbPb events and also for pPb events, where flow fluctuations become more dominant [242]. At a similar multiplicity, the magnitude of the  $F_2^\eta$  parameter is significantly larger for pPb collisions than for PbPb collisions. In PbPb collisions, a much stronger  $\eta$ -dependent factorization breakdown is seen for higher-order harmonics than for the second-order harmonic, as shown by the  $F_3^\eta$  and  $F_4^\eta$  parameters. There is little centrality dependence for  $n = 3$ , except for the most central 0–20% PbPb collisions.

#### 4.2.4 Nonlinear evolution and novel hydrodynamic observables

Developing precise constraints for the transport properties of the QGP is one of the principal goals of the HI physics programs. While the  $v_2$  and  $v_3$  flow coefficients reflect the transport properties, their values also depend on the initial-state geometry and its fluctuations. Additional observables are needed to disentangle the various contributions to these coefficients.

Higher-order flow coefficients  $v_n$  with  $n \geq 4$  can arise from initial-state anisotropies in the same-order harmonic (linear response) or can be induced by lower-order harmonics (nonlinear response) [261–263]. Based on the notation of Eq. (4), complex anisotropic flow coefficients can be defined for different harmonics  $n$ , with  $V_n = v_n \exp(in\Psi_n)$ . The  $V_n$  coefficients should not be confused with the previously defined two-particle Fourier coefficients  $V_{n\Delta}$ . Expressed in

terms of their linear- and nonlinear-response components [261, 262],

$$\begin{aligned}
 V_4 &= V_{4L} + \chi_{422} V_2^2, \\
 V_5 &= V_{5L} + \chi_{523} V_2 V_3, \\
 V_6 &= V_{6L} + \chi_{624} V_2 V_{4L} + \chi_{633} V_3^2 + \chi_{6222} V_2^3, \\
 V_7 &= V_{7L} + \chi_{725} V_2 V_{5L} + \chi_{734} V_3 V_{4L} + \chi_{7223} V_2^2 V_3,
 \end{aligned} \tag{10}$$

where  $V_{nL}$  denotes the part of  $V_n$  that is not induced by lower-order harmonics [263–265], and the  $\chi$  are the nonlinear-response coefficients. Each nonlinear-response coefficient has its associated mixed harmonic, which is  $V_n$  measured with respect to the lower-order symmetry plane angle. The  $V_{nL}$  component can be obtained by subtracting the nonlinear term from  $V_n$ .

As one can see from Eq. (10), the nonlinear-response coefficients are dimensionless values that are ratios of different flow coefficients. To illustrate, taking  $V_5$  as an example, if we multiply both sides of the equation  $V_5 = V_{5L} + \chi_{523} V_2 V_3$  by the complex conjugate terms  $V_2^* V_3^*$ , and assume that the two terms on the right-hand side of this equation are uncorrelated [261],  $\chi_{523}$  can be expressed as  $V_5 V_2^* V_3^* / (V_2^2 V_3^2)$ . Therefore, the nonlinear-response coefficients are not strongly sensitive to the initial-state anisotropies [261, 262, 265, 266]. As a result, their experimental values can serve as unique and robust probes of hydrodynamic behavior of the QGP [265].

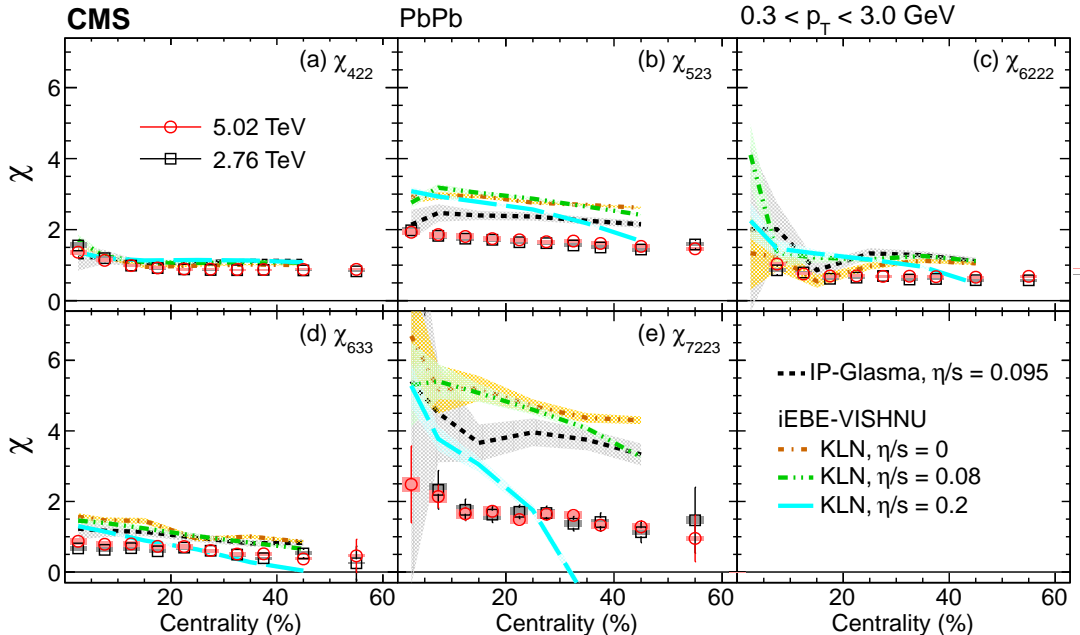


Figure 43: Nonlinear-response coefficients,  $\chi_{422}$ ,  $\chi_{523}$ ,  $\chi_{6222}$ ,  $\chi_{633}$ , and  $\chi_{7223}$  at 2.76 and 5.02 TeV, as functions of centrality. The results are compared with predictions from a hydrodynamics + hadronic cascade hybrid approach with the IP-Glasma initial conditions using  $\eta/s = 0.095$  [267] at 5.02 TeV and from iEBE-VISHNU hydrodynamics with the KLN initial conditions using  $\eta/s = 0, 0.08$ , and  $0.2$  [262] at 2.76 TeV. (Figure adapted from Ref. [268].)

The nonlinear-response coefficients,  $\chi_{422}$ ,  $\chi_{523}$ ,  $\chi_{6222}$ ,  $\chi_{633}$ , and  $\chi_{7223}$  at 2.76 and 5.02 TeV are presented as functions of centrality in Fig. 43. The results are also compared with the predictions from a hybrid model of hydrodynamics and a hadronic cascade that uses IP-Glasma initial conditions with  $\eta/s = 0.095$  [267] at 5.02 TeV and from iEBE-VISHNU hydrodynamics with the KLN initial conditions using  $\eta/s = 0, 0.08$ , and  $0.2$  [262] at 2.76 TeV. All calculations

describe the  $\chi_{422}$  centrality dependence well, but none of them give a good description of the  $\chi_{523}$  and  $\chi_{7223}$  centrality dependences. The model calculations of  $\chi_{7223}$  vary for the different initial conditions and  $\eta/s$  values, which suggests that the measurement of  $\chi_{7223}$  could provide strong constraints on models.

### 4.3 System space-time evolution via femtoscopy

Femtoscopy is a powerful tool to infer the shape and size of the particle emitting region formed in high-energy collisions by measuring two-particle correlation functions in terms of the momentum difference of particle pairs [269]. The method reflects the quantum statistics governing identical particles, i.e., Bose–Einstein correlations (BEC) for bosons (the situation for almost all cases discussed in this section), or Fermi–Dirac correlations for fermions. Nevertheless, it is also sensitive to final-state interactions, e.g., the Coulomb interaction for charged particles or the strong force between emitted hadrons. This technique, originally proposed for estimating stellar dimensions [270–272], was accidentally discovered in high-energy collisions in 1960 [273] and has since been applied to a multitude of different high-energy analyses, both for small colliding systems, such as  $e^+e^-$ , pp, and for AA collisions, with the measurements covering a wide energy spectrum. It was early thought that BEC data could provide a signature of QGP formation [274] and this signature was searched for at the AGS, SPS, and RHIC [269]. In 2010, at the beginning of the LHC era, CMS made the first BEC correlation measurement for pp collisions at  $\sqrt{s} = 0.9$  and 2.36 TeV in terms of the 1D invariant relative momentum of particle pairs,  $q_{\text{inv}} = \sqrt{-(p_1 - p_2)^\mu (p_1 - p_2)_\mu}$ , with  $p_{1,2}$  being the individual four-momenta of the particles in the pair, to establish the invariant radius  $R_{\text{inv}}$  [275].

In high-energy collisions, the femtoscopic correlation function can be defined by a single ratio (SR) of signal over reference pair distributions,  $C(q) = [dN_{\text{sig}}(q)/dq]/[dN_{\text{ref}}(q)/dq] = SR$ , with  $[dN_{\text{sig}}(q)/dq]$  constructed by pairing same-sign (SS) particles from the same event, and  $[dN_{\text{ref}}(q)/dq]$  built as a reference sample (ideally containing all pair correlations that are present in the signal sample, except for those arising from femtoscopic effects, such as quantum statistics and final-state interactions). The most common form of defining this reference distribution is by pairing particles from different events. In principle, the SR would yield a correlation function containing femtoscopic effects only. In case of correlations involving charged pairs, the Coulomb final-state interaction has to be taken into account. For pp collisions, the approximation represented by the Gamow factor [275–277] can be employed to the final-state charged hadrons. In addition, other effects may still distort the signal, such as minijets or resonances, generically called background contributions [277], requiring additional techniques for removing such spurious correlations. In CMS, several techniques have been adopted for this purpose, with details given in Refs. [275–279].

For extracting the information about the effective source sizes revealed by the femtoscopic technique, a function is fitted to the pair correlation function, which can be parametrized by a generic Lévy stable distribution [280], as employed in Refs. [275–278],

$$C_{\text{BE}}(q_{\text{inv}}) = C[1 + \lambda e^{-(q_{\text{inv}} R_{\text{inv}})^\alpha}] (1 + \epsilon q_{\text{inv}}). \quad (11)$$

In Eq. (11),  $C_{\text{BE}}(q_{\text{inv}})$  refers to the two-particle Bose–Einstein correlation,  $C$  is a constant;  $R_{\text{inv}}$  and  $\lambda$  are the radius (also called the length of homogeneity) and intercept (correlation intensity) parameters, respectively. The exponent  $\alpha$  is the Lévy index of stability satisfying  $0 < \alpha \leq 2$ . If treated as a free parameter in the fit,  $\alpha$  usually returns a number between the value characterizing an exponential function ( $\alpha = 1$ ) and that for a Gaussian distribution ( $\alpha = 2$ ). More details can be found in Ref. [280]. The additional term, linear in  $q_{\text{inv}}$  and proportional to a fitting constant  $\epsilon$ , is introduced to account for possible long-range nonfemtoscopic correlations.

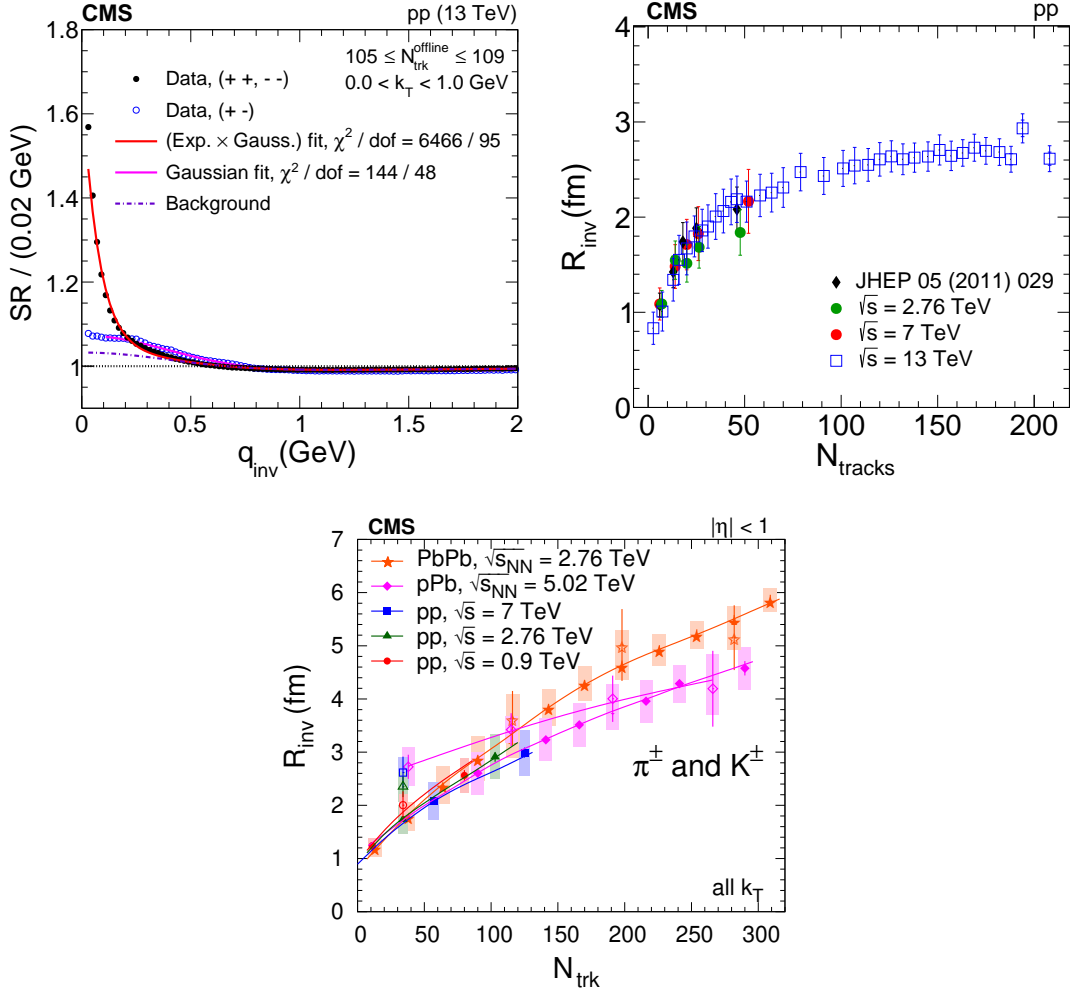


Figure 44: Top left: Illustration of a typical BEC as functions of  $q_{\text{inv}}$ , for pp collisions at 13 TeV, for opposite-sign pairs (no BEC), used to estimate the background contribution, and for same-sign pairs, together with the fits to both cases. Top right: Results for femtoscopic correlations of unidentified charged hadrons from pp collisions at various LHC energies and in different multiplicity ranges. Bottom: The plot shows results for identified pions (filled markers) and kaons (open markers) for different colliding systems and at several LHC energies. The error bars correspond to the statistical uncertainties, the colored boxes to the systematic uncertainties. The lines are cubic spline interpolations, added to guide the eye. (Figure adapted from Refs. [276–278].)

An example of a typical correlation function versus  $q_{\text{inv}}$  is shown in Fig. 44 (top left) for high-multiplicity pp events at 13 TeV. This illustrates the Gaussian-type fit to the opposite-sign (OS) (background-type contribution) correlation function and the exponential+background fit to the SS correlation function that contains the BECs.

The results for the invariant source radius  $R_{\text{inv}}$  from a follow up measurement conducted in 2010 in pp collisions at 7 TeV [276] are shown in Fig. 44 (top right). The abscissa is the particle multiplicity of the events,  $N_{\text{tracks}}$ , after correction for the detector acceptance and efficiency. Figure 44 (top right) also shows the results from another analysis performed years later, employing the same analysis framework in terms of the 1D correlation function versus  $q_{\text{inv}}$ , using data from pp collisions at 2.76 TeV and a significantly larger sample of new data at 7 TeV [277].

The data show a steady rise as the number of produced tracks increases, with no clear dependence on the collision energy.

Simultaneously, another analysis was conducted, in pp collisions at different LHC energies, as well as in pPb and peripheral PbPb collisions at  $\sqrt{s_{\text{NN}}} = 5.02$  and 2.76 TeV, respectively, using a special tracker condition that allowed for identifying pions and kaons with high purity [277]. The resulting femtoscopic correlations of identified pions and kaons in different colliding systems and energies are shown in Fig. 44 (bottom). A continuous rise with multiplicity can also be seen in this case, in a larger range of multiplicity in pPb and peripheral PbPb collisions.

More recently, an additional 1D analysis was performed for pp collisions at  $\sqrt{s} = 13$  TeV that covered a very wide range of particle multiplicities [278]. Tracks with  $p_T > 0.4$  GeV were selected for events with multiplicities ranging from only a few tracks and up to  $\langle N_{\text{tracks}} \rangle \sim 250$  charged particles. This is a range of event activity similar to that for pPb and peripheral PbPb collisions. Recording such a large range in  $N_{\text{tracks}}$  in pp collisions was made possible with the help of very efficient high-multiplicity triggers available at CMS [281]. The main motivation for this study was to investigate if a continuous increase with  $N_{\text{tracks}}$  would be observed for the femtoscopic radius  $R_{\text{inv}}$ , as expected from hydrodynamical models, or if the rise would saturate at some point, as suggested by the CGC theory [282, 283]. Three different techniques were employed to guarantee the independence of the results on the adopted analysis method, all three returning compatible values for  $R_{\text{inv}}$  [278]. The results, illustrated using values from one of the methods, are shown in Fig. 44 (top right) by the blue square markers. The values of  $R_{\text{inv}}$  increase with multiplicity and seem to saturate at higher values of  $N_{\text{tracks}}$ , as suggested by the CGC model [282, 283], although a continuous rise, as suggested by hydrodynamics, cannot be dismissed.

The 1D investigation on the behavior of the invariant radius parameter was also conducted for  $R_{\text{inv}}$  as a function of the average transverse momentum of the pair,  $\vec{k}_T = (\vec{p}_{T,1} + \vec{p}_{T,2})/2$ . This study is important to explore the dynamics involved in the system evolution: a static system is not expected to show a  $k_T (= |\vec{k}_T|)$  dependence, whereas such a dependence would be expected for an expanding system subjected to flow. The results are shown in Fig. 45 for some of the systems and energies mentioned above.

Figure 45 (left) shows results of  $R_{\text{inv}}$  as a function of  $k_T$  for pp collisions at 2.76, 7, and 13 TeV. In this plot the data points are shown at the average values of  $k_T$ , taken in each bin of variable width. The latter is shown for two ranges of multiplicity: the lower values corresponding to events with multiplicity smaller than 80 tracks and the higher values to multiplicities greater than 80 tracks. The results for identified pions from pPb collisions  $\sqrt{s_{\text{NN}}} = 5.02$  TeV are shown in Fig. 45 (right). In this plot the data points are shown at the bin center. In all cases we see that the values of  $R_{\text{inv}}$  decrease with  $k_T$ , a behavior normally seen in data and more clearly illustrated by the results from pp at 13 TeV. This behavior indicates that the system expands before decoupling.

In addition, an extension of the previous analyses was developed for investigating the source in three different directions (3D case), in terms of the Bertsch–Pratt variables ( $R_S, R_L, R_O$ ) [269], where  $R_L$  is the component along the beam (longitudinal) direction,  $R_O$  is transverse to  $R_L$  and parallel to the direction of  $k_T$  and reflects different emission times, and  $R_S$  is transverse to the directions of both  $R_L$  and  $R_O$ . The results for these variables as functions of multiplicity are shown in Fig. 46 for both unidentified charged hadrons from pp collisions (left) and for charged pions from pPb collisions (middle). These radial components, in general, show similar behavior as functions of  $N_{\text{tracks}}$  as in the 1D case. The right panel of Fig. 46 also illustrates the behavior of  $(R_S, R_L, R_O)$  versus  $k_T$  (the data points are shown at the average values of  $k_T$ , taken

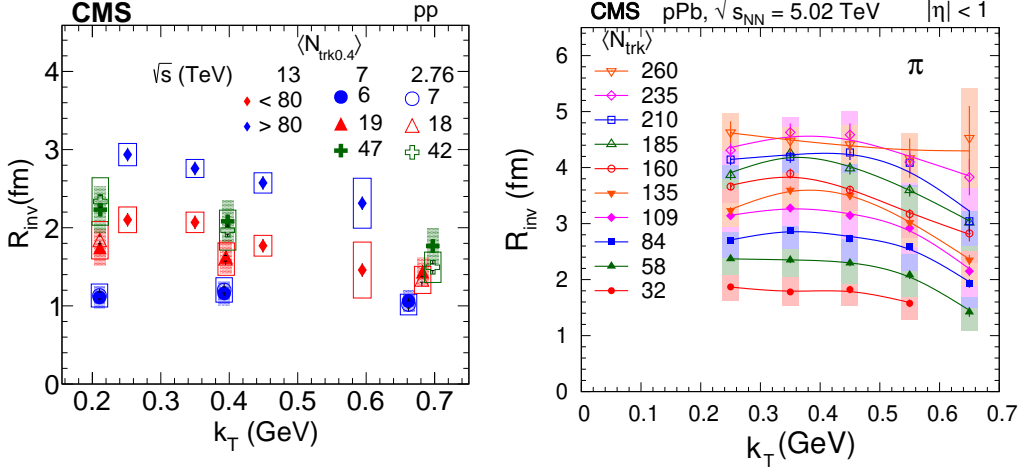


Figure 45: Left: Results for  $R_{\text{inv}}$  are shown as a function of  $k_T$  for pp collisions at different energies and multiplicity ranges. (Figure adapted from Refs. [277, 278].) Right: Similarly,  $R_{\text{inv}}$  values versus  $k_T$  are shown for pPb collisions at 5.02 TeV. The error bars correspond to the statistical uncertainties, the colored boxes to the systematic uncertainties. The lines are cubic spline interpolations, added to guide the eye. (Figure adapted from Ref. [277].)

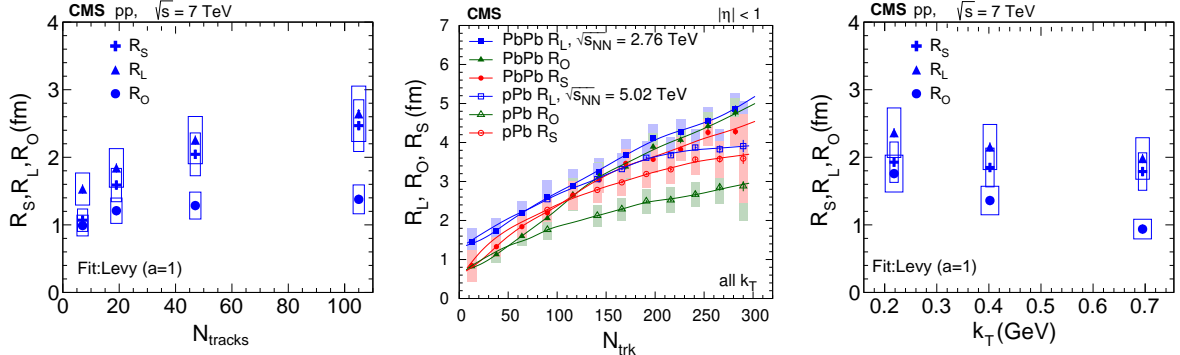


Figure 46: Left: The femtoscopic Bertsch-Pratt radius components in different directions ( $R_S$ ,  $R_L$ ,  $R_O$ ) are shown as functions of multiplicity for charged hadrons from pp collisions at 7 TeV. Middle: The three variables are shown for pions from the pPb and PbPb systems at 2.76 and 5.02 TeV, respectively. The lines are cubic spline interpolations, added to guide the eye. A similar tendency of increasing radius parameters with multiplicity is seen in each of the three directions, for all cases. Right: The variation of these components with  $k_T$  is shown for charged hadrons from pp collisions at 7 TeV. (Figures adapted from Ref. [277]).

in each bin of variable width). All three components tend to decrease with  $k_T$ , as expected for expanding sources.

Furthermore, the results for  $(R_S, R_L, R_O)$  were found to be similar for pp and pPb collisions, with  $R_L > R_S > R_O$  in both cases [277]. However, in PbPb collisions, a different relation is observed, showing similar values for the three variables, i.e.,  $R_L \approx R_S \approx R_O$  [277]. In other words, the shape of the system formed in pp and pPb collisions is elongated in the longitudinal direction, whereas the system formed in PbPb collisions is more spherical in shape.

The findings from femtoscopic correlation measurements performed in pp collisions at  $\sqrt{s} = 13$  TeV demonstrate the complex and complementary behavior of the systems formed in such collisions: under certain conditions they behave similarly to systems formed in high-energy

$e^+e^-$  collisions. This is reflected in an anticorrelation (values of  $C_{BE}$  below unity) seen in the 1D double ratios away from the BEC peak, which is more pronounced in the lower multiplicity ranges [276–278]. This anticorrelation is usually quantified in terms of a model ( $\tau$  model [284, 285]), in which particle production has a broad distribution in proper time and the phase space distribution of the emitted particles is dominated by strong correlations of the space-time coordinate and momentum components. The depth of the anticorrelation has been quantified [276–278] and shown to decrease with increasing  $\langle N_{\text{tracks}} \rangle$  and  $k_T$  (except for large values of multiplicities, in the latter case). Although this observation in minimum bias pp collisions suggests that such a structure could be associated with small systems, another investigation [286] reveals a linear relation between the fitted  $R_{\text{inv}}^{-2}$  values and the transverse mass of the pair,  $m_T = \sqrt{m^2 + k_T^2}$ , with a slope proportional to the square of a Hubble constant divided by the system freeze-out temperature (assumed to be  $T_{\text{fo}} \sim 500$  MeV) [278]. This result matches expectations from hydrodynamics: the formed system undergoes a strong expansion characterized by a Hubble-type flow, as found in high-energy nuclear collisions. The analogy with cosmology is made because hydrodynamical calculations show a behavior compatible with the Hubble law,  $v = Hr$ , where  $v$  is the fluid velocity at the fluid position  $r$  and  $H = \dot{R}/R$  is the Hubble constant,  $R$  being a scale parameter. Towards the end of the fluid expansion, when the acceleration coming from pressure gradients is negligible,  $\dot{R}$  tends to a constant value and  $R \sim \dot{R}t$ , so that  $H \sim 1/t$ , with  $t$  representing time [286]. From the slope of  $R_{\text{inv}}^{-2}$  versus  $m_T$ , the Hubble constant of the collision has been determined in two multiplicity ranges [278, 286],  $H_{\text{MB}} = 0.298 \pm 0.004 \text{ (stat)} \text{ fm}^{-1}$  for minimum bias events ( $N_{\text{tracks}} \lesssim 80$ ) and  $H_{\text{HM}} = 0.17 \pm 0.04 \text{ (stat)} \text{ fm}^{-1}$  for high-multiplicity events ( $N_{\text{tracks}} \gtrsim 80$ ). These values are compatible with those obtained for peripheral and central AuAu collisions at RHIC [287–290], respectively, implying that the expansion is faster in peripheral collisions than in more central ones. These values correspond to a directionally-averaged Hubble constant. A detailed discussion can be found in Ref. [278].

More recently, two-particle BEC functions have been measured in PbPb collisions at  $\sqrt{s_{\text{NN}}} = 5.02$  TeV in different centrality and transverse momentum classes [279], and compared to theoretical models based on parametric Lévy sources, incorporating the Coulomb effect [291]. The value of the  $\alpha$  parameter, describing the source shape, was found to be approximately 50% larger than that found in 200 GeV AuAu collisions at RHIC [292]. This difference in the  $\alpha$  values found at RHIC and LHC may stem from a larger mean free path at lower collision energies, reflecting a larger deviation from normal diffusion (whose processes lead to a Gaussian distribution) in systems formed at lower energies, resulting in a heavy tail; the further the deviation, the heavier the tail, and the smaller is the  $\alpha$  value. This is consistent with the observed centrality dependence of  $\alpha$ : it is closer to 2 in case of the most central collisions, and decreases to values close to 1.6 for peripheral collisions. Moreover, it was found that the  $R$  parameter (describing the homogeneity length, similarly to  $R_{\text{inv}}$ , and representing the final state) scales as the cube root of the average number of participating nucleons in the collision, a proxy for the initial size. Furthermore, a linear dependence of  $1/R^2$  on the pair transverse mass  $m_T$  was observed. This is consistent with a hydrodynamic scaling, predicted for Gaussian sources. From this linear dependence, the Hubble constant of the collisions was determined to increase from 0.11 to 0.18  $\text{fm}^{-1}$  from central to peripheral collisions, comparable to those values found at RHIC [292] or in high-multiplicity pp collisions at  $\sqrt{s} = 13$  TeV [278], as mentioned above. Taken together, these results can be interpreted as the hadron emitting source having a shape consistent with a Lévy distribution in 5.02 TeV PbPb collisions.

Besides revealing valuable insights on the space-time dimensions of particle-emitting sources created in high-energy collisions, as discussed above, femtoscopy has also been used in high-

energy experiments to extract parameters related to Coulomb and strong force final-state interactions [269]. In particular, the strong force interaction scattering parameters, such as the scattering length and effective range, can be extracted with this technique. For instance, femtoscopy of strange  $\Lambda$  baryons can add significant information about baryon-baryon interactions and, depending on the values found for the scattering length and effective range, could indicate the potential formation of exotic bound states, such as the H-dibaryon [293]. In addition, studies of  $K_S^0 K_S^0$  and  $\Lambda \Lambda$  correlations offer information about the interactions of strange hadrons, thus providing valuable guidance to model the composition of neutron stars [294–296]. Different fitting functions and analysis procedures are adopted in this case (as discussed in Ref. [297]). The CMS Collaboration conducted  $K_S^0 K_S^0$ ,  $\Lambda K_S^0$ , and  $\Lambda \Lambda$  femtoscopy studies using PbPb collision data at  $\sqrt{s_{\text{NN}}} = 5.02$  TeV [296]. The  $K_S^0 K_S^0$  correlation is measured in six centrality bins, covering the 0–60% range [297]. The source size extracted from the  $K_S^0 K_S^0$  correlation shows the expected decreasing trend from central to peripheral collisions. The negative scattering length extracted from  $\Lambda K_S^0$  correlations indicates that the strong interaction between  $\Lambda$  and  $K_S^0$  is repulsive. On the other hand, the positive scattering length extracted from  $\Lambda \Lambda$  correlations indicates that the interaction between  $\Lambda$  particles is attractive and disfavors the existence of a possible bound H-dibaryon state.

#### 4.4 Searches for chiral magnetic effects and early-stage short-lived electromagnetic fields

An object is *chiral*, either left- or right-handed, if it is not invariant under the parity ( $P$ ) transformation. In a chiral system, the imbalance of right- and left-handed objects can be characterized by a chiral chemical potential ( $\mu_5$ ). It has been predicted that in a system of charged chiral fermions with a finite  $\mu_5$  value, an electric current density ( $\vec{J}_e$ ) can be induced when an external magnetic field ( $\vec{B}$ ) is applied, with the current density along the direction of the magnetic field,

$$\vec{J}_e \propto \mu_5 \vec{B}. \quad (12)$$

This phenomenon is known as the chiral magnetic effect (CME) [298, 299].

In relativistic nuclear collisions, the chiral symmetry is expected to be restored in a QGP, rendering nearly massless or chiral quarks. If the topological solutions of the SU(3) gauge group of QCD are chiral, they can transfer chirality to quarks via a chiral anomaly, forming local chiral domains with finite  $\mu_5$  values in the initial stage (more details in Ref. [300] and references therein). Within each domain, there is an imbalance of right- and left-handed chiral quarks. Meanwhile, extremely strong magnetic fields ( $B \sim 10^{15}$  T) can be formed in noncentral HI events, mostly by energetic spectator protons. The presence of the parity-even  $\vec{B}$  field and parity-odd  $\mu_5$  is predicted to lead to an electric current along the direction of  $\vec{B}$ , namely the CME. Observing a CME signal in nuclear collisions would have profound impacts on many aspects of fundamental physics, including the topological phases of QCD, chiral symmetry restoration, and QGP evolution with strong electromagnetic fields. The CME and related phenomena, such as the chiral magnetic wave, emerge when applying a fluid dynamics description to a combined QED+QCD system influenced by the chiral anomaly. While the theoretical basis for these effects is well established, the potential magnitude of a CME signal is highly model-dependent, as it is significantly affected by the initial conditions, which are not well known.

In this section, we review the progress in searching for the CME in high-energy nuclear collisions made by the CMS Collaboration.

#### 4.4.1 Searches for chiral magnetic effects

The charge separation induced by the CME can be manifested as the first parity-odd ( $P$ -odd) sine term ( $a_1$ ) in a Fourier decomposition of the charged-particle azimuthal distribution [301],

$$\frac{dN}{d\phi} \propto 1 + 2 \sum_n \{ v_n \cos[n(\phi - \Psi_{\text{RP}})] + a_n \sin[n(\phi - \Psi_{\text{RP}})] \}, \quad (13)$$

where  $\phi - \Psi_{\text{RP}}$  represents the particle azimuthal angle with respect to the reaction plane angle  $\Psi_{\text{RP}}$  (determined by the impact parameter and beam axis), and  $v_n$  and  $a_n$  denote the  $P$ -even and  $P$ -odd Fourier coefficients, respectively. Experimentally, the  $\Psi_{\text{RP}}$  is approximated by the second-order event plane,  $\Psi_2$ , of the elliptic flow. As any  $P$ -odd term will vanish after averaging over events, the most commonly investigated observable is an azimuthal three-particle correlator,  $\gamma_{112}$ , which measures  $\langle a_1^2 \rangle$  [301],

$$\gamma_{112} \equiv \langle \cos(\phi_\alpha + \phi_\beta - 2\Psi_2) \rangle = \langle \cos(\phi_\alpha - \Psi_2) \cos(\phi_\beta - \Psi_2) \rangle - \langle \sin(\phi_\alpha - \Psi_2) \sin(\phi_\beta - \Psi_2) \rangle. \quad (14)$$

Here,  $\alpha$  and  $\beta$  denote particles with the same or opposite electric charge sign and the angle brackets reflect an averaging over particles and events. The first term on the right-hand side of Eq. (14) becomes  $\langle v_{1,\alpha} v_{1,\beta} \rangle$ , which is generally small and independent of the charge [302], while the second term is sensitive to the charge separation and can be expressed as  $\langle a_{1,\alpha} a_{1,\beta} \rangle$ . By taking a difference between OS (where  $\alpha$  and  $\beta$  have OS electric charge) and SS (where  $\alpha$  and  $\beta$  have SS electric charge)  $\gamma$  correlators,

$$\Delta\gamma \equiv \gamma^{\text{OS}} - \gamma^{\text{SS}}, \quad (15)$$

all charge-independent effects are canceled.

Despite having a relatively simple observable, the existence of the CME in nuclear collisions remained inconclusive after more than a decade of experimental searches. While observations were consistent with the existence of a CME, these could also be interpreted as resulting from background contributions, such as local charge conservation from resonance decays embedded in an elliptic-flow background. Because of the nonperturbative nature of background processes, theory is not able to provide a quantitative estimate of their importance. By applying an approach based on control samples in data to control the signal strength, while keeping the backgrounds constant, CMS has made two key contributions that have convincingly demonstrated that the CME signal at LHC energies, even if it exists, is too small to observe.

High-multiplicity pp and pPb collisions have been shown to generate large final-state azimuthal anisotropies, comparable to those in AA collisions [36, 110, 303–308]. However, the CME contribution to any charge-dependent signal is expected to be negligible in a high-multiplicity pPb collision. As illustrated in Fig. 47 (left) based on MC Glauber calculations [180], while the angle between the magnetic field direction, which is given approximately by the direction of the reaction plane (red arrow in the figure), and the event plane of elliptic anisotropy (black arrow in figure) is strongly correlated in PbPb collisions, it is expected to be mostly random in pPb collisions. Figure 47 (right) shows the correlation between the reaction plane angle ( $\Psi_{\text{RP}}$ ) and participant plane angle ( $\Psi_{\text{PP}}$ , approximating the event plane) in terms of the distribution of  $\cos(2(\Psi_{\text{RP}} - \Psi_{\text{PP}}))$  for pPb and PbPb collisions. The event-averaged value of  $\cos(2(\Psi_{\text{RP}} - \Psi_{\text{PP}}))$  is consistent with zero for pPb collisions, while a significant correlation is observed for PbPb collisions. With a random field orientation, the CME contribution to any charge-dependent signal is expected to be small in pPb collisions.

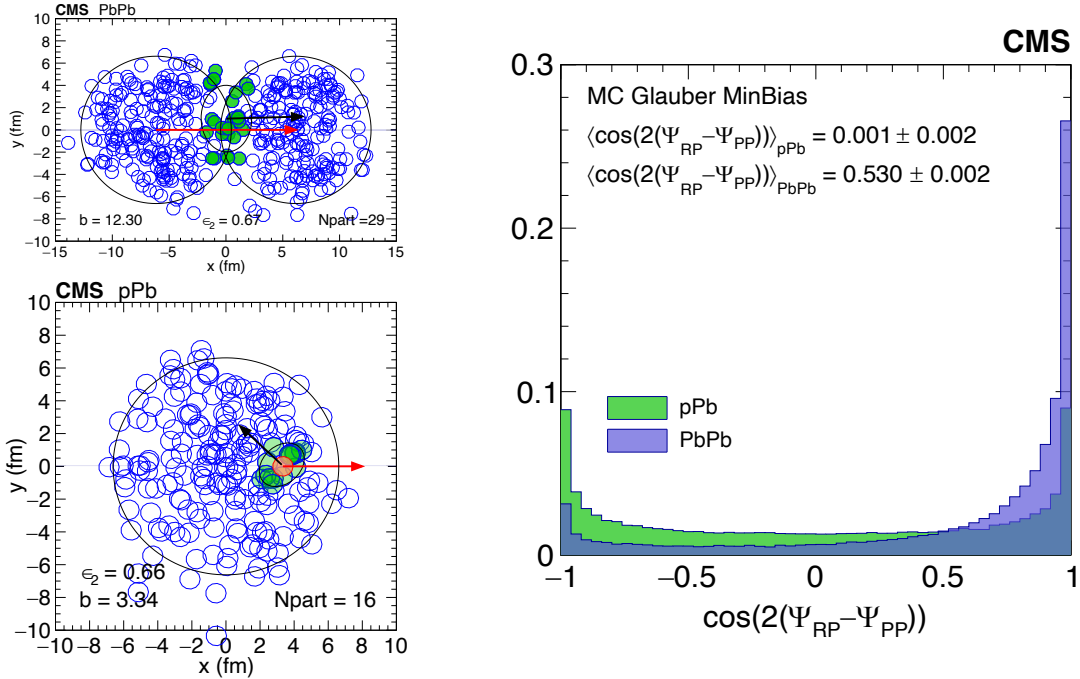


Figure 47: Left: Event geometry of one peripheral PbPb and one central pPb event using MC Glauber simulation at  $\sqrt{s_{\text{NN}}} = 5.02$  TeV. The red and black arrows point in the direction of the reaction and participant plane angle, respectively. Right: The cosine of the relative angle between the reaction plane and the participant plane. (Figures adapted from Ref. [309].)

The high-multiplicity pPb data sample collected by CMS gives access to multiplicities comparable to those in peripheral PbPb collisions, allowing for a direct comparison of the two systems with very different CME contributions. Figure 48 (left) shows the difference of the charge-dependent three-particle correlator for the OS and SS cases, as a function of multiplicity for pPb and PbPb collisions at  $\sqrt{s_{\text{NN}}} = 5.02$  TeV. Within uncertainties, the pPb and PbPb data show nearly identical values. The striking similarity in the observed charge-dependent azimuthal correlations strongly suggests a common physical origin. In PbPb collisions, it was suggested that the charge dependence of the three-particle correlator is an indication of the charge separation effect due to the CME signal [302, 310]. However, as argued earlier, a strong charge separation signal from the CME is not expected in a very high-multiplicity pPb collision. Therefore, the similarity seen between high-multiplicity pPb and peripheral PbPb collisions presents a significant challenge to the attribution of the observed charge-dependent correlations to the CME.

Furthermore, the charge separation effect from the CME is only expected along the direction of the induced magnetic field normal to the reaction plane, approximated by the second-order event plane,  $\Psi_2$ . As the symmetry plane of the third-order Fourier term (“triangular flow” [312]),  $\Psi_3$ , is expected to have a weak correlation with  $\Psi_2$  [313], the charge separation effect with respect to  $\Psi_3$  is also expected to be negligible. By constructing a charge-dependent correlator with respect to the third-order event plane,

$$\gamma_{123} \equiv \langle \cos(\phi_\alpha + 2\phi_\beta - 3\Psi_3) \rangle, \quad (16)$$

charge-dependent background effects unrelated to the CME can be explored. In particular, in the context of the local charge conservation mechanism, the  $\gamma_{123}$  correlator is also expected to have a background contribution, similar to that for the  $\gamma_{112}$  correlator, but proportional to  $v_3$ ,

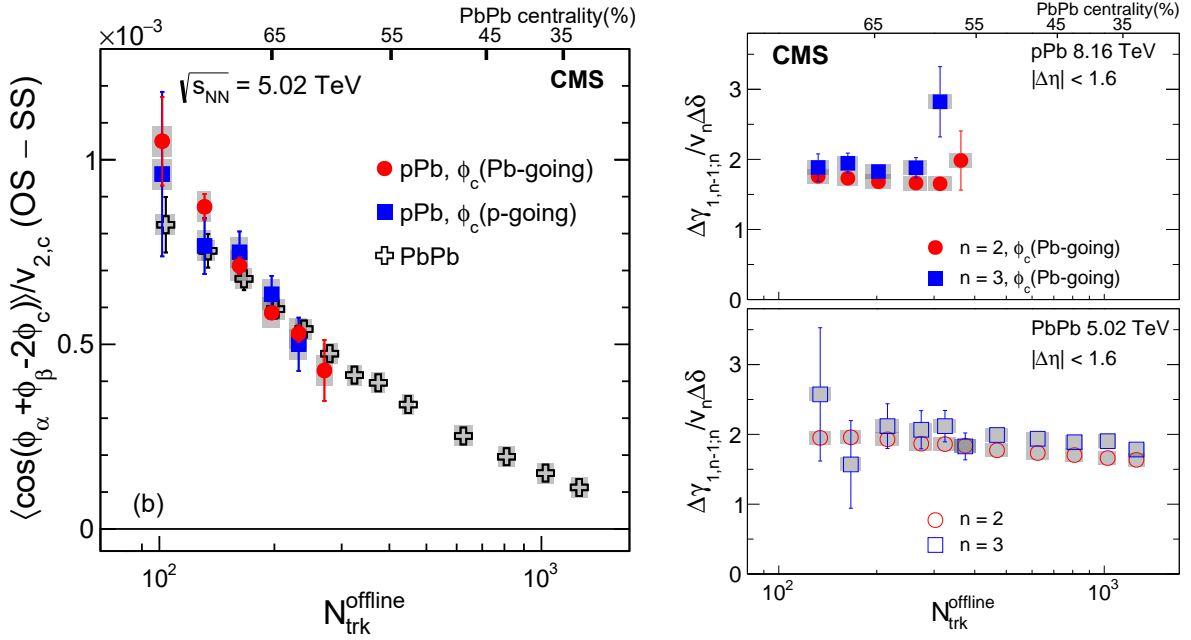


Figure 48: Left: the difference of the opposite sign (OS) and same sign (SS) three-particle correlators as a function of  $N_{\text{trk}}^{\text{offline}}$  in pPb and PbPb collisions at  $\sqrt{s_{\text{NN}}} = 5.02 \text{ TeV}$ . (Figure adapted from Ref. [309].) Right: ratio of  $\Delta\gamma_{112}$  and  $\Delta\gamma_{123}$  to the product of  $v_n$  and  $\delta$  in pPb collisions for the Pb-going direction at  $\sqrt{s_{\text{NN}}} = 8.16 \text{ TeV}$  and PbPb collisions at 5.02 TeV. (Figure adapted from Ref. [311].)

instead of  $v_2$ . After scaled by  $v_2$  and  $v_3$ , respectively, the  $\gamma_{112}$  and  $\gamma_{123}$  correlators are expected to be similar, largely independent of harmonic event plane orders, as shown in Fig. 48 (right). This similarity, seen in high-multiplicity pPb and peripheral PbPb collisions for both  $\Delta\gamma_{112}$  and  $\Delta\gamma_{123}$ , again challenges the attribution of the observed charge-dependent correlations to the CME.

To set a quantitative limit on the existence of the CME signal, CMS has applied the event shape engineering (ESE) technique [314]. This technique involves establishing a direct link between the  $\gamma$  correlators and  $v_n$  coefficients. By applying ESE in a specific range of centrality or multiplicity, where the magnetic field remains relatively constant, events are further categorized based on the magnitude of the  $v_n$  coefficient measured in the forward rapidity region. In each event category, measurements of  $\gamma$  correlators and  $v_n$  values are compared to assess the linear relationship, and observed dependence is extrapolated to the  $v_n = 0$  region. A non-zero value of the  $\gamma$  correlators at that point would reflect the strength of the CME.

Based on the assumption of a nonnegative CME signal, the upper limit of the  $v_2$ -independent fraction  $f_{\text{norm}}$  in the  $\Delta\gamma_{112}$  correlator is obtained with the measured statistical and systematic uncertainties. In Fig. 49, the upper limit of  $f_{\text{norm}}$  is presented at 95% confidence level (CL) as a function of event multiplicity. The combined limits from all presented multiplicities and centralities are also shown in pPb and PbPb collisions. An upper limit on the  $v_2$ -independent fraction of the three-particle correlator, or possibly the CME signal contribution, is estimated to be 13% in pPb and 7% in PbPb collisions, at 95% CL.

The data presented here provide new stringent constraints on the nature of the background contribution to the charge-dependent azimuthal correlations, and establish a new baseline for the search for the CME in HI collisions.

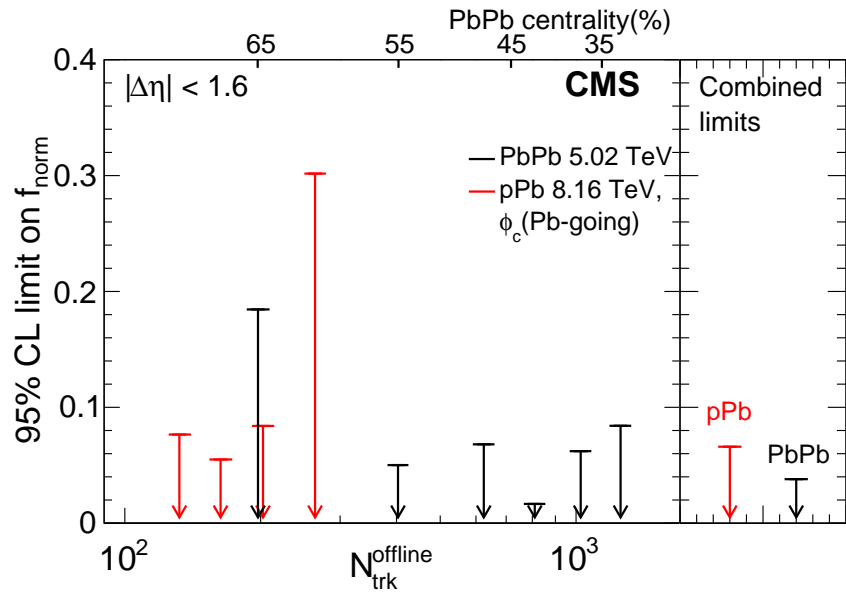


Figure 49: Upper limits of the fraction of  $v_2$ -independent  $\gamma_{112}$  correlator component as a function of  $N_{\text{trk}}^{\text{offline}}$  in pPb collisions at  $\sqrt{s_{\text{NN}}} = 8.16$  TeV and PbPb collisions at 5.02 TeV. (Figure adapted from Ref. [311].)

#### 4.4.2 Searches for chiral magnetic waves

The chiral magnetic wave (CMW) is a phenomenon similar to the CME. The chiral separation effect (CSE) is a process where the separation of the chiral charges along the magnetic field will be induced by a finite density of the initial net electric charges [315]. The coupling of electric and chiral charge densities and currents leads to a long-wavelength collective excitation, known as the chiral magnetic wave [316]. It is worth noting that a lack of experimental evidence for the CME [309, 311] does not necessarily imply the absence of the CMW effect, as the CME requires an initial chirality imbalance from topological QCD charges, whereas a CMW only requires an initial net electric charge density [315, 316]. Therefore, the CME and CMW deserve independent experimental investigations.

The propagation of the CMW leads to an electric quadrupole moment, where additional positive (negative) charges are accumulated away from (close to) the reaction plane [315]. Following a hydrodynamic evolution of the medium formed in AA collisions, this electric quadrupole moment is expected to result in a charge-dependent variation of the second-order anisotropy coefficient ( $v_2$ ) in the Fourier expansion of the final-state particle azimuthal distribution. More specifically, the  $v_2$  coefficient will exhibit a linear dependence on the observed event charge asymmetry [315],  $A_{\text{ch}} \equiv (N_+ - N_-)/(N_+ + N_-)$ , where  $N_+$  and  $N_-$  denote the number of positively and negatively charged hadrons in each event,

$$v_{2,\pm} = v_{2,\pm}^{\text{base}} \mp r A_{\text{ch}}. \quad (17)$$

Here  $v_{2,\pm}^{\text{base}}$  represents the value in the absence of a charge quadrupole moment from the CMW for positively (+) and negatively (-) charged particles, and  $r$  denotes the slope parameter. In the presence of a CMW, the difference of  $v_2$  values between positively and negatively charged particles would be proportional to  $A_{\text{ch}}$ . Similar charge-dependent effects from the CMW are not expected for the third-order anisotropy coefficient ( $v_3$ ) [317].

The normalized  $v_3$  difference,  $(v_3^- - v_3^+)/ (v_3^- + v_3^+)$ , is derived as a function of true event charge asymmetry ( $A_{\text{ch}}^{\text{true}}$ ), obtained by correcting the observed value for the detector accep-

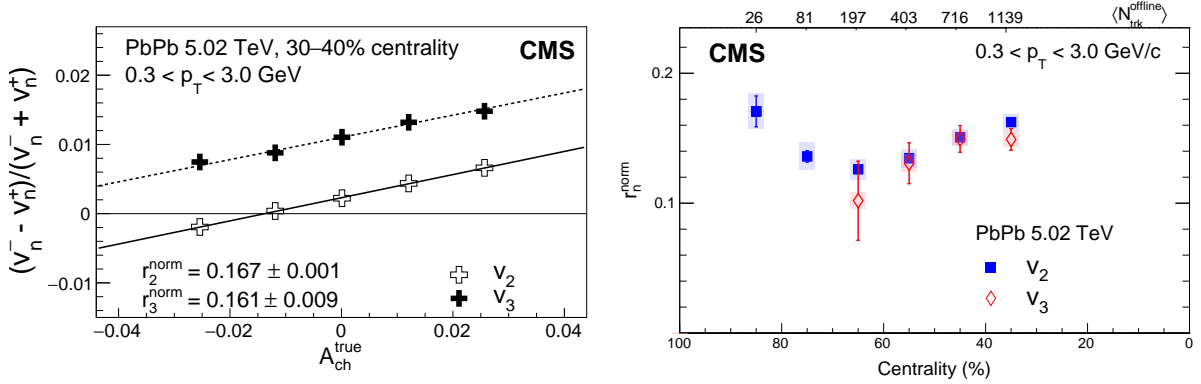


Figure 50: Left: The normalized difference in  $v_n$ ,  $(v_n^- - v_n^+)/v_n$ , for  $n = 2$  and  $3$ , as a function of true event charge asymmetry for the 30–40% centrality class in PbPb collisions at  $\sqrt{s_{\text{NN}}} = 5.02 \text{ TeV}$ . Right: The linear slope parameters,  $r_2^{\text{norm}}$  and  $r_3^{\text{norm}}$ , as functions of the centrality class in PbPb collisions. (Figures adapted from Ref. [318].)

tance and tracking efficiency, in PbPb collisions and compared with that for  $v_2$  in Fig. 50 (left). The normalized slope parameter of  $v_3$ ,  $r_3^{\text{norm}}$ , agrees well with  $r_2^{\text{norm}}$  within statistical uncertainties. Once normalized, no difference is observed for the  $A_{ch}^{\text{true}}$  dependence between the charge-dependent  $v_2$  and  $v_3$  values.

The  $r_2^{\text{norm}}$  and  $r_3^{\text{norm}}$  values of PbPb collisions at  $\sqrt{s_{\text{NN}}} = 5.02 \text{ TeV}$  are shown in Fig. 50 (right), as functions of centrality in the range 30–90%. As found for  $r_2^{\text{norm}}$ , a moderate centrality dependence of  $r_3^{\text{norm}}$  is observed. Over the centrality range studied in this analysis, the  $r_2^{\text{norm}}$  and  $r_3^{\text{norm}}$  slope parameters are consistent with each other within uncertainties. The CMW effect is expected with respect to the reaction plane, which is approximated by the second-order event plane in AA collisions, but highly suppressed with respect to the third-order event plane [317]. The observation of the harmonic-order independence, reflected in the similar  $r_2^{\text{norm}}$  and  $r_3^{\text{norm}}$  values, indicates an underlying physics mechanism unrelated to the CMW effect and, instead, can be qualitatively explained by late local-charge conservation [319].

#### 4.4.3 Searches for the electromagnetic conductivity in QGP

Very strong and short-lived EM fields might be created in the early stages of relativistic HI collisions. The configuration of these electromagnetic fields is not trivial to predict because they receive contributions from several sources that involve the spectators and participants in the collision. In some theoretical predictions, the net magnetic or Coulomb fields are expected to generate significant rapidity-odd (rapidity-even) contributions to  $v_n$  coefficients, with  $n$  odd (even) [320]. The lifetime of the EM fields is expected to depend on the electric conductivity of the medium [321]. Therefore, measuring such effects in the  $v_n$  coefficients as functions of rapidity would not only point to the existence of strong EM fields created in the collisions, but also constrain the properties of the QGP, such as its electric conductivity.

Heavy-flavor quarks are expected to be produced primarily in the initial stages of a collision (order of  $\sim 0.1 \text{ fm}$ ) and to pass through the medium with a lower probability of annihilation as compared to light-flavor quarks [322, 323]. The EM fields are, at least in some theoretical approaches, expected to have a maximum magnitude on a time scale below  $0.2 \text{ fm}$ . As a consequence, the impact of EM fields on  $v_n$  values as a function of rapidity is predicted to be much stronger for  $D^0$  mesons (containing charm quarks) than for the abundantly produced charged hadrons [324].

In light of these predictions, the CMS Collaboration measured the  $v_2$  difference ( $\Delta v_2$ ) between

$D^0$  and  $\bar{D}^0$  mesons as a function of rapidity to search for the effect of a possible strong Coulomb field created by the collision participants [146]. The results, with an average value of  $\Delta v_2^{\text{avg}} = 0.001 \pm 0.001 \text{ (stat)} \pm 0.003 \text{ (syst)}$ , are shown in Fig. 51. The expected magnitude for charged hadrons is  $\Delta v_2 \sim -0.001$  [320], i.e., with the same magnitude, but with a different sign. Given the present uncertainties, the measurement sensitivity is not sufficient to clarify if charm hadron collective flow is affected or not by the strong Coulomb field created in ultrarelativistic heavy ion collisions. Significant improvements in both statistical and systematic uncertainties for the  $\Delta v_2$  measurement are expected with future large data samples made possible with the upgraded CMS detector.

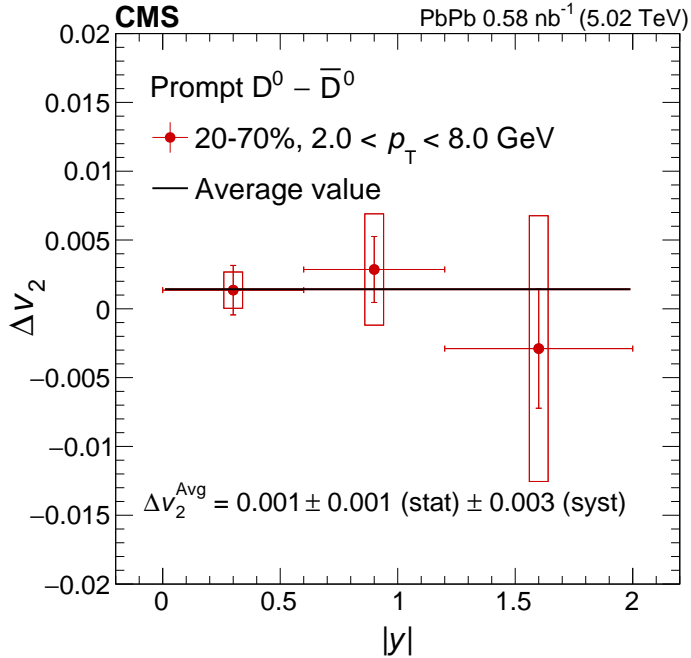


Figure 51: Difference of  $v_2$  between  $D^0$  and  $\bar{D}^0$  mesons as a function of rapidity. The average value ( $\Delta v_2^{\text{Avg}}$ ) is extracted by fitting the data considering the statistical uncertainties only. The systematic uncertainty of the  $\Delta v_2^{\text{Avg}}$  is estimated by shifting the each point up and down by its systematic uncertainty. (Figure adapted from Ref. [146].)

#### 4.5 Summary of results for bulk properties and novel phenomena

The CMS Collaboration has leveraged the extensive phase space coverage of its detector to explore QGP properties and to probe fundamental aspects of the strong force. The full coverage in  $\phi$  and the large  $\eta$  range of the CMS detector have enabled precise measurements of particle densities and correlations, offering deep insights into the behavior of the QGP.

In the most central PbPb collisions at the LHC, the charged-particle density and average transverse energy per particle are significantly higher than those observed at RHIC. This suggests that the QGP formed at the LHC is denser, hotter, and longer-lived, while reaffirming the notion of a “nearly perfect liquid” with minimal viscosity. Detailed studies of azimuthal correlations, particularly the elliptic and higher-order Fourier coefficients, have constrained the shear viscosity to entropy density ratio ( $\eta/s$ ) to within 0.08–0.2, close to the theoretical lower bound.

Data from CMS have also been used to challenge the assumption that two-particle correlations can be factorized with respect to a common event plane. The observed  $p_T$ - and  $\eta$ -dependent

factorization breaking provides new insights into initial-state fluctuations and the longitudinal dynamics of the QGP, enabling a three-dimensional view of the medium evolution. Nonlinear response coefficients, derived from high-order Fourier analyses, offer robust probes of the QGP's hydrodynamic behavior, independent of initial-state anisotropies.

Femtoscopy techniques have revealed that the size and shape of particle-emitting sources vary with collision system and energy. In PbPb collisions, the sources are more spherical, while in pp and pPb collisions, they are elongated along the longitudinal direction. The Levy-type shape observed in PbPb collisions at 5.02 TeV suggests a shorter mean free path and a closer approach to normal diffusion at LHC energies, compared to the more Gaussian-like distributions at RHIC energies. These findings are supported by the similarity in the measured Hubble constant between low-multiplicity pp events and peripheral AuAu collisions at RHIC. Investigations using femtoscopy to study the interactions between strange hadrons have provided valuable data on these interactions, further enriching our understanding of QGP dynamics.

In the search for CME and CMW signals, CMS has pioneered the development of a series of new observables and their application to small systems to set unique constraints on background contributions to the CME and CMW measurements. The results show unambiguously that the CME and CMW signals in relativistic nuclear collisions are too small to be observed at LHC energies with the current data set. The most stringent upper limit to date has been set on these signals.

## 5 Hard probes in heavy ion collisions and sensitivity to quark-gluon plasma

In ultrarelativistic HI collisions, rare hard scatterings of the parton constituents of the nucleons can produce a suite of energetic final states, known collectively as “hard probes”. Heavy-flavor quarks, jets, photons, weak bosons, and even top quarks are all hard probes measured by CMS during Runs 1 and 2 in PbPb and pPb collisions, as well as in pp collision data at the same energy as the other two systems to be used as a reference. Produced predominantly during the initial collision prior to the formation of the QGP, the production mechanisms and vacuum propagation of these particles are strongly constrained by studies in the experimentally cleaner pp collision environment, with theoretical control via pQCD calculations. As a result, hard probes can be used to tag the initial momentum scale of a hard scattering (in the case of photons and similarly colorless probes), to determine the strength and nature of the medium interactions (in the case of QCD color-charge carriers such as quarks and gluons), and thoroughly map the QCD medium interactions across a suite of topologies and kinematic extremes (via jet substructure, the more-massive top quarks, and the highest- $p_T$  jets). The following sections will provide detailed information about these and other phenomena, as studied with CMS data.

### 5.1 Observations of parton quenching

The current section details the first observations of partonic energy loss, manifesting experimentally as “quenching”, using inclusive jet production dominated by hard-scattered light quarks and gluons. Observations of enhanced dijet asymmetry, transverse momentum imbalance, and the suppression of both jet and high- $p_T$  hadron spectra with respect to pp data are discussed.

#### 5.1.1 Dijet asymmetry and relative energy loss

The suppression of high- $p_T$  hadrons, indicating modifications to hard-scattered partons induced by the QGP, was initially observed at RHIC by both the PHENIX and STAR experiments [325, 326]. With the start of beams at the LHC and data taking by general-purpose experiments with nearly  $4\pi$  calorimetric coverage, the study of partonic energy loss with fully reconstructed jets became possible. The first observations by ATLAS [327] and CMS [108] were of a substantial, centrality-dependent enhancement of dijet asymmetry ( $A_J$ ), defined as

$$A_J = \frac{p_{T,1} - p_{T,2}}{p_{T,1} + p_{T,2}}, \quad (18)$$

where  $p_{T,1}$  corresponds to the highest  $p_T$  jet (“leading jet”) in the event and  $p_{T,2}$  corresponds to the second-highest  $p_T$  jet (“subleading jet”) in the event.

In pp collisions,  $A_J$  is typically used for jet energy calibration and observed dijet pairs with significant transverse momentum asymmetry, after accounting for effects such as finite jet energy resolution and initial-state/final-state radiation, typically indicate the presence of a third jet to conserve the transverse momentum of the system [328]. However, as shown in calorimeter event displays, such as the example in Fig. 52, frequently there is no such compensating third jet present in PbPb collisions. Instead, an energetic leading jet is observed back-to-back in azimuthal angle with a substantially less energetic subleading jet, and no third jet is visible in the event display by inspection.

Subsequent studies of dijet pairs produced in PbPb collisions quantified the magnitude and centrality dependence (Section 2.5) of the observed enhancement in  $A_J$ . Figure 53 shows  $A_J$  as

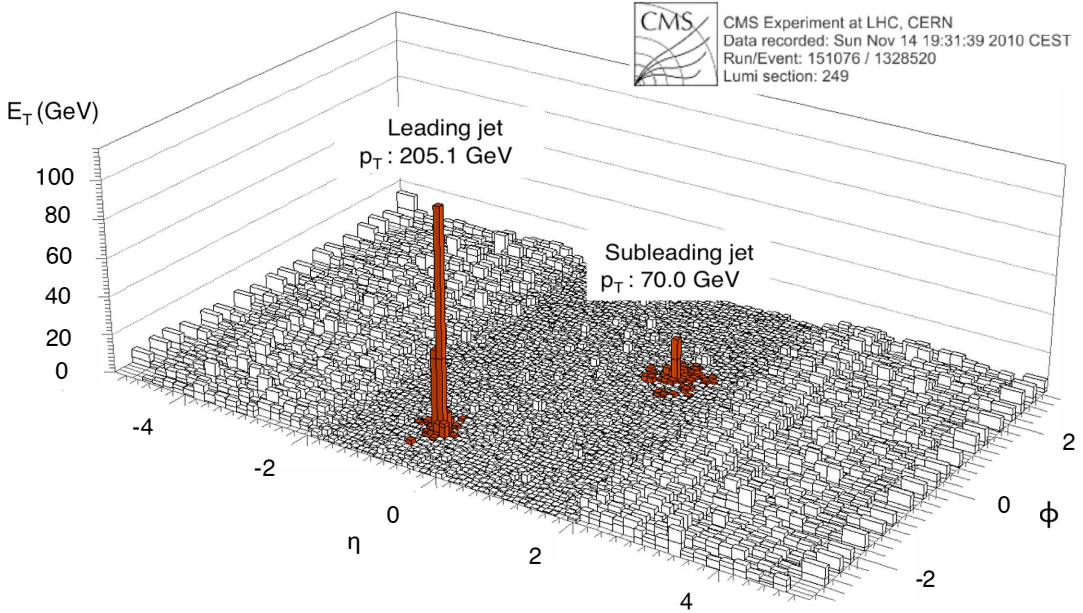


Figure 52: An “unrolled” calorimeter display of energy deposition in an event containing an unbalanced dijet pair in a  $\sqrt{s_{\text{NN}}} = 2.76$  TeV PbPb collision, as recorded by the CMS detector in 2010. The tower-by-tower transverse energy sum combining the measurement in electromagnetic and hadronic calorimeters is plotted as a function of  $\eta$  and  $\phi$ . The fully corrected transverse momenta of the unbalanced dijet pair are labeled and their position in  $\eta$ - $\phi$  indicated with the red-highlighted constituent towers. (Figure adapted from Ref. [108].)

a function of centrality class for PbPb data and PYTHIA+HYDJET simulation, with  $A_J$  in pp collisions shown in the first panel only [329]. All systems correspond to  $\sqrt{s_{\text{NN}}} = 2.76$  TeV, and both the pp data and the PYTHIA+HYDJET simulations act as a reference for what the  $A_J$  distribution would be in the absence of parton-medium interactions. In addition, the PYTHIA+HYDJET simulation includes the impact of the broadening of the measured energy distribution as a result of the degrading jet energy resolution caused by the underlying event background increasing as a function of event centrality. In the peripheral centrality selection of 70–100%, the PbPb data is qualitatively consistent with both the pp data and the simulations. However, moving from peripheral to more central selections increases the observed dijet  $A_J$  value in data beyond the expected changes from energy resolution effects modeled in PYTHIA+HYDJET, with the greatest observed discrepancy occurring in the 0–10% centrality class. Similar trends were also observed for inclusive dijets produced at the higher collision energy of  $\sqrt{s_{\text{NN}}} = 5.02$  TeV [330].

The observed enhancement in dijet asymmetry is interpreted as a signature of differential jet-energy loss, whereby the leading jet has lost less energy to parton-medium interactions than the subleading jet. There are multiple possible causes of the jet energy loss being differential between leading and subleading jets; a few examples include a difference in path-length through the QGP, a color-charge factor governing interactions differently for quark- and gluon-initiated jets, or the highly stochastic nature of parton-medium interactions resulting in significant biases when selecting final-state leading and subleading jets (the  $p_T$ -dependent studies of  $A_J$  in Ref. [329] suggest this last option). Independently of the underlying mechanism, one can additionally characterize the energy loss with a missing transverse momentum observable ( $\not{p}_T^{\text{miss}}$ ), defined as

$$\not{p}_T^{\text{miss}} = - \sum_i p_T^i \cos(\phi_i - \phi_{\text{leadingJ}}), \quad (19)$$

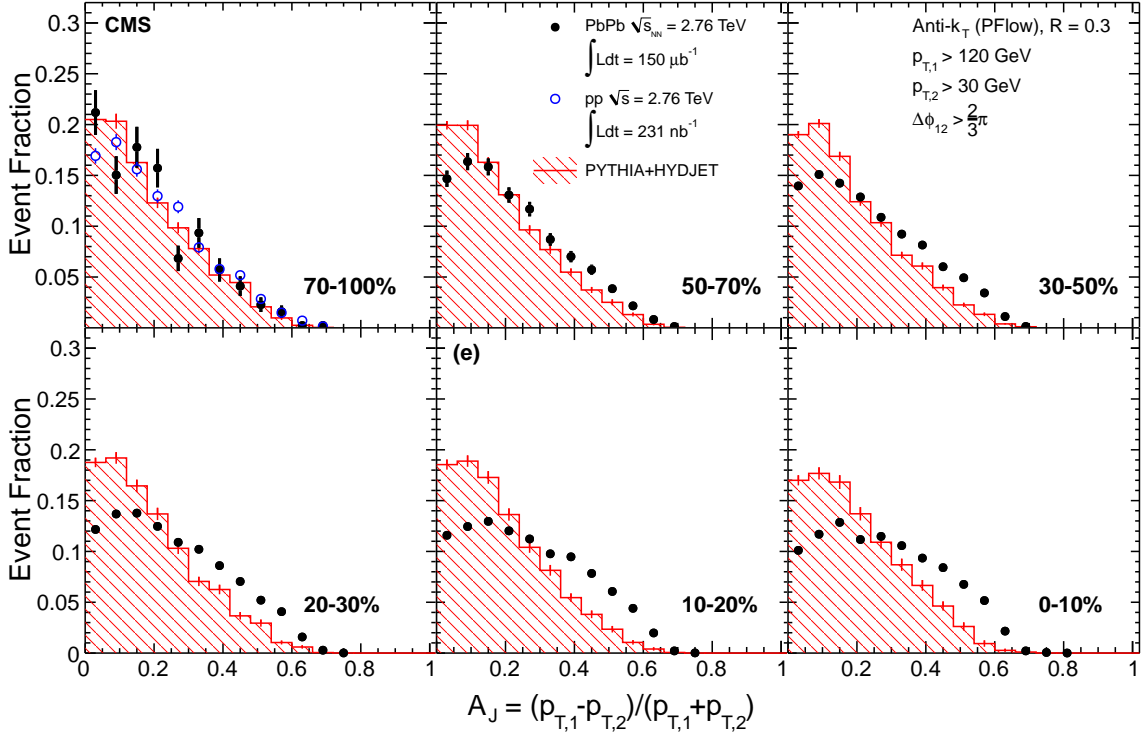


Figure 53: The  $A_J$  distributions for jet pairs with a leading jet of  $p_{T,1} > 120$  GeV and subleading jet of  $p_{T,2} > 30$  GeV, presented for different event centrality classes. The dijet pair is required to fulfill a back-to-back requirement in azimuthal angle of  $\Delta\phi_{1,2} > 2\pi/3$ . Black filled points represent the PbPb data, while the red hatched histogram shows the PYTHIA+HYDJET simulation results. The open blue circles in the upper left panel are the results from  $\sqrt{s} = 2.76$  TeV pp collisions, acting as an unquenched reference in conjunction with the simulations. Vertical bars represent statistical uncertainties only. (Figure adapted from Ref. [329].)

where the index  $i$  is the  $i^{\text{th}}$  reconstructed track in the event,  $p_T^i$  its transverse momentum,  $\phi_i$  its azimuthal position, and  $\phi_{\text{leadingJ}}$  is the azimuthal position of the leading jet. Note that by this definition, particles in the direction of the leading jet will have a negative contribution.

The average of the  $\not{p}_T^{\parallel}$  observable over events passing back-to-back dijet selections,  $\langle \not{p}_T^{\parallel} \rangle$ , is related to the relative distribution of energy in the leading and subleading jet hemispheres. This average is shown in Fig. 54 as a function of  $A_J$  for two different centrality classes (30–100% and 0–30%). The color-filled histograms show the  $\langle \not{p}_T^{\parallel} \rangle$  contributions for track  $p_T$  ranges of 0.5–1.0, 1.0–2.0, 2.0–4.0, 4.0–8.0, and greater than 8.0 GeV. From the figure, in both PYTHIA+HYDJET simulations and PbPb data, the leading jet dominates the greater than 8.0 GeV  $p_T$  bin (red histogram, negative  $y$  axis contributions). However, relative to the simulations, which lack a quenching mechanism, the balancing spectra of particles corresponding to those in the sub-leading jets direction (positive  $y$  axis contributions) are softer in PbPb data. A substantial excess of particles is observed in the 0.5–1.0 and 1.0–2.0 GeV  $p_T$  ranges (light-blue and yellow histograms). Furthermore, this excess increases with the  $A_J$  category, here used as a proxy for the strength of the relative energy lost to the medium between the jets of the dijet pair. Finally, there is an observable depletion in the relative contribution of the semi-hard category of particles of 4.0–8.0 GeV in central PbPb events compared to both peripheral PbPb events and central simulations. Later studies performed by CMS using a data set 25 times larger reached similar conclusions and were able to establish that these trends hold for a variety of jet distance parameters from  $R = 0.2$  to  $0.5$  [331], as long as particles up to an  $\eta$ - $\phi$  distance of 2.0 in  $\Delta R$  from

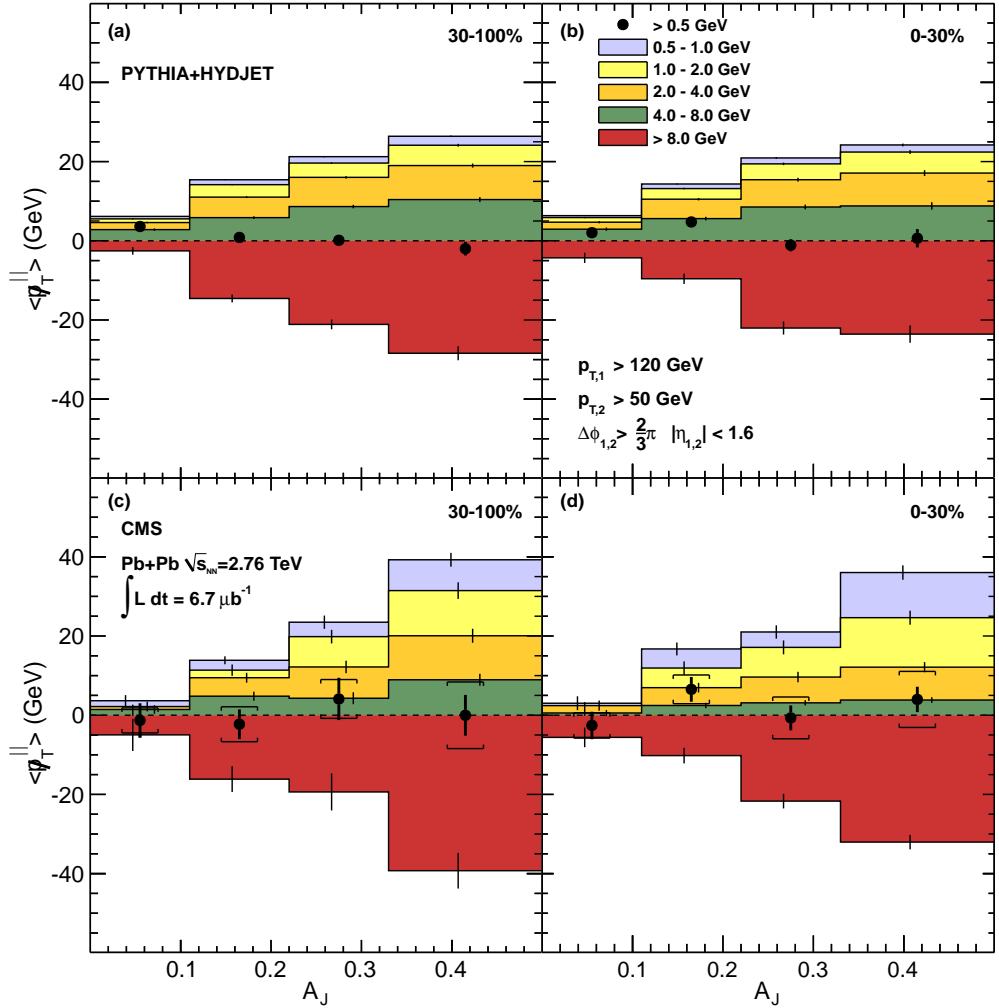


Figure 54: The  $\langle \not{p}_T \rangle$  values as a function of  $A_J$  for tracks with  $p_T > 0.5$  GeV. Dijets are selected with  $p_{T,1} > 120$  GeV,  $p_{T,2} > 50$  GeV, and  $\Delta\phi_{1,2} > 2\pi/3$ . The left panels are for peripheral, 30–100% centrality events, and the right panels are for central, 0–30% events. The upper row shows the results in PYTHIA+HYDJET simulation (lacking quenching) while the lower row shows the result in PbPb data. Both data and simulation are for  $\sqrt{s_{NN}} = 2.76$  TeV. Solid circles show the total average  $\langle \not{p}_T \rangle$  while individual color-filled histograms show contributions from particles of  $p_T$  ranging from 0.5–1.0 GeV to larger than 8.0 GeV. Vertical bars represent statistical uncertainties while the horizontal bars surrounding the solid black circles represent systematic uncertainties. (Figure adapted from Ref. [108].)

the jet axis are included. In summary, studies of dijet asymmetry indicate differential jet energy loss, with a depletion of hard particles in subleading jets and a corresponding enhancement of soft constituent particles.

### 5.1.2 Suppression of jet spectra in PbPb collisions

While the measurements described in Section 5.1.1 firmly establish that parton-medium interactions modify both the energy and radiation patterns of final-state jets, the observables  $A_J$  and  $\langle \not{p}_T \rangle$  are constructed so that all such statements can only be made *relatively*, i.e., the quenching effects are only seen comparing a subleading jet to a leading jet. Both jets however are poten-

tially quenched, as both are produced prior to medium formation and traverse the medium over some path length. Therefore, to observe energy loss in absolute terms for inclusive jet production, CMS and other HI experiments use the nuclear modification factor  $R_{AA}$ , as defined by Eq. (3) in Section 3.2. In the absence of medium effects, hard probes, such as jets and high- $p_T$  tracks, are expected to scale with the number of binary nucleon-nucleon collisions and therefore give an  $R_{AA}$  of one. An  $R_{AA}$  larger than unity, such as that observed from anti-shadowing effects in pPb (as discussed in Section 6.4), indicates enhancement, while an  $R_{AA}$  smaller than unity indicates suppression.

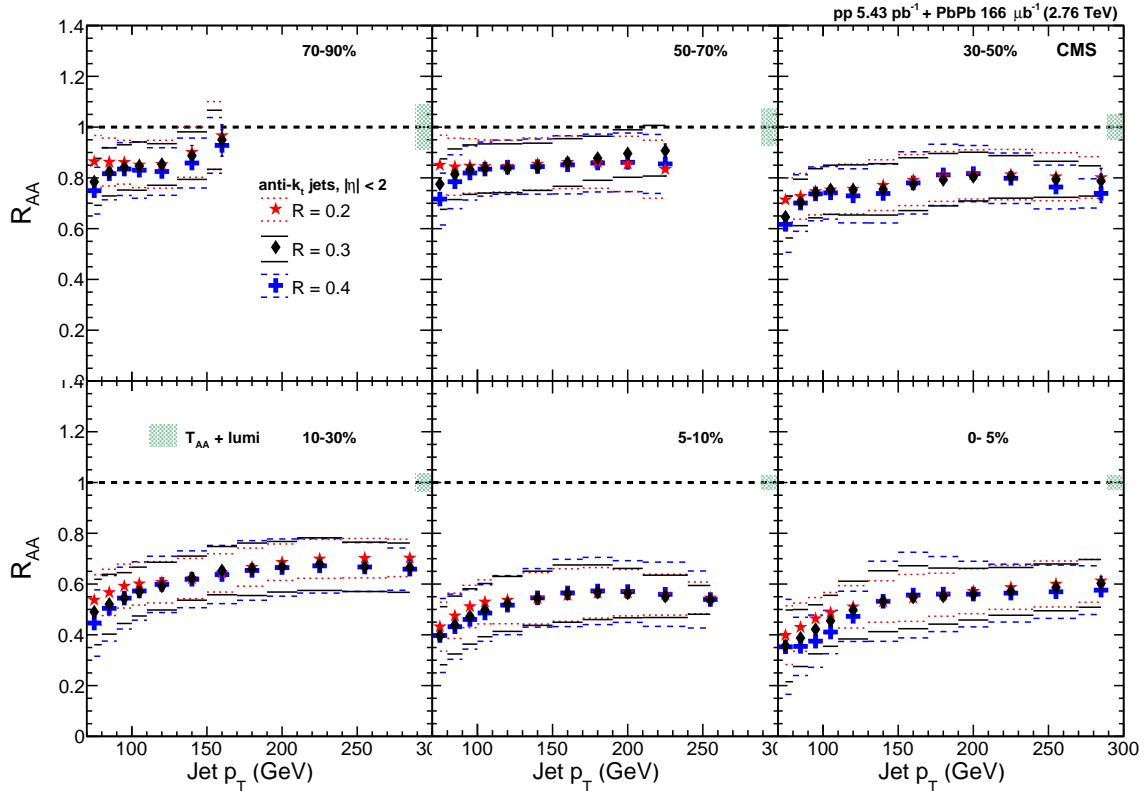


Figure 55: Inclusive jet  $R_{AA}$  plotted as a function of the jet  $p_T$  for  $|\eta| < 2.0$ . Each panel corresponds to a different centrality class (upper left) 70–90%, (upper middle) 50–70%, (upper right) 30–50%, (lower left) 10–30%, (lower middle) 5–10%, and (lower right) 0–5%. Results for three jet distance parameters,  $R = 0.2, 0.3$ , and  $0.4$ , are overlaid as red stars, black diamonds, and blue crosses, respectively. Vertical bars (typically smaller than the markers) represent the statistical uncertainty, while horizontal bars around each point are the nonglobal systematic uncertainties. Finally, the combined global systematic uncertainty coming from  $T_{AA}$  and the integrated luminosity measurement is plotted as a shaded green bar on the horizontal black-dashed unity line. (Figure adapted from Ref. [332].)

The first measurement of inclusive jet  $R_{AA}$  by CMS [332] observed a significant suppression for jets produced in PbPb collisions at  $\sqrt{s_{NN}} = 2.76$  TeV for three jet distance parameters ( $R = 0.2, 0.3$ , and  $0.4$ ), spanning a jet  $p_T$  range of 70–300 GeV and in six centrality classes covering 70–90% through 0–5%, as shown in Fig. 55. A strong centrality dependence is observed, with largest suppression occurring in the 0–5% centrality class with an  $R_{AA}$  of 0.35 at a jet  $p_T$  value of 70 GeV. However, as functions of jet  $R$ , the central values for  $R_{AA}$  are consistent within the reported uncertainties across all centrality classes. The lack of  $R$  dependence is curious given the expectation that some fraction of the observed lost jet energy is recoverable when looking beyond the jet cone, as observed in the initial and subsequent  $\langle p_T^{\parallel} \rangle$  studies discussed

in Section 5.1.1 [108, 331].

The paired observations of  $\langle \psi_T^{\text{ll}} \rangle$  recovery at large  $\Delta R$  angular distances from the jet axis [331] and the jet  $R_{\text{AA}}$  insensitivity to the distance parameter  $R$  for  $R \leq 0.4$  [332] motivated a study of jets with even larger jet distance parameters. In addition, partonic quenching models, such as JEWEL [333], show a jet  $R_{\text{AA}}$  dependence at large  $R$  that is subject to assumptions on how the missing jet energy is deposited into the larger medium, making such studies a model-dependent test of the response of the medium [334].

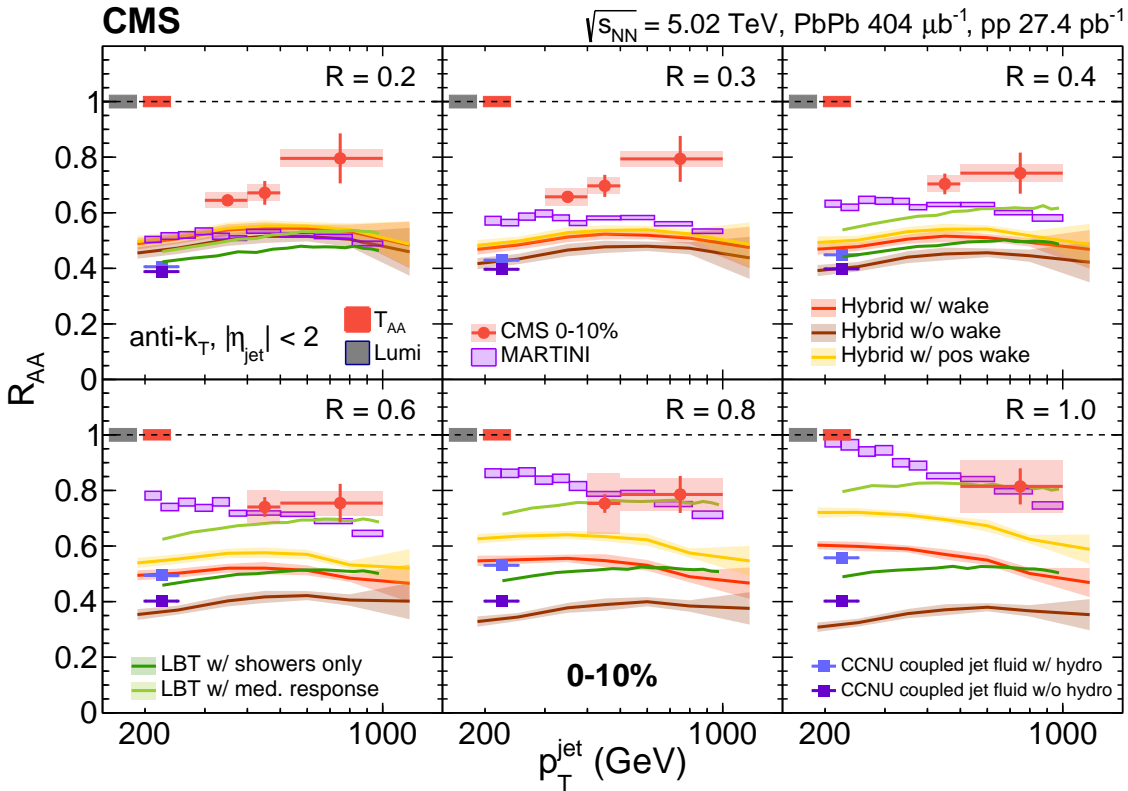


Figure 56: Jet  $R_{\text{AA}}$  in the 0–10% centrality class as a function of jet  $p_T$  for jets with  $|\eta| < 2.0$ . Each panel corresponds to a different distance parameter  $R$ , as indicated. Filled red circle markers represent the data, with vertical red lines representing statistical uncertainties and horizontal red lines representing bin widths. The shaded red boxes around the points represent systematic uncertainties. Integrated luminosity (for pp collisions) and  $\langle T_{\text{AA}} \rangle$  (for PbPb collisions) global uncertainties are shown as shaded boxes around the dashed horizontal line for  $R_{\text{AA}} = 1$ . Predictions for the HYBRID [335, 336], MARTINI [337], LBT [338], and CCNU [339–341] models are plotted for comparison. (Figure adapted from Ref. [143].)

The CMS Collaboration has reconstructed jets up to an  $R$  parameter of 1.0, for the first time in HI collisions, using the 5.02 TeV PbPb (corresponding to an integrated luminosity of  $404 \mu\text{b}^{-1}$ ) and pp reference ( $27.4 \text{ pb}^{-1}$ ) data sets collected in 2015. The  $R_{\text{AA}}$  values are determined as a function of jet  $p_T$ . To mitigate the growing impact and associated uncertainties arising from the underlying event background on jet energy as the jet  $R$  parameter is increased, stringent thresholds are implemented on the minimum  $p_T$  of the jets considered, with respect to  $R$ . Specifically, for  $R = 1.0$ , only jets with  $p_T > 500 \text{ GeV}$  are taken into consideration. The results for six  $R$  values in the centrality class 0–10% are plotted in Fig. 56. All six  $R_{\text{AA}}$  values for the highest jet  $p_T$  bin are close to 0.8, with no significant dependence on  $R$ , within systematic uncertainties, even

after accounting for the correlated uncertainties. There is no indication that  $R_{AA}$  approaches unity, even for  $R = 1$ , the largest  $R$  analyzed using Run 2 data, as would be expected if the quenched energy transported to large angles is fully recovered.

Figure 56 also compares a number of jet quenching models to the experimental results. While the models encode different assumptions about the physics of parton-medium and jet quenching interactions, one interesting detail is how assumptions regarding the medium response affect the results. In the context of jet quenching, medium response is the collective motions and modes induced by the jet energy deposited in parton-medium interactions, resulting in nontrivial structures such as a wake of energetic and depleted regions. Both the HYBRID and LBT models allow for alternative assumptions of the medium response. As an example, the HYBRID model provides three different curves: a red curve corresponding to the full model of the medium wake, a brown curve corresponding to zero medium wake, and a golden yellow curve that only includes positive contributions and ignores energy depletion resulting from the medium wake [336]. While each of these curves roughly match within reported systematic uncertainties for small jet  $R$  (0.2–0.4), at large  $R$  there are significant differences. The CMS data indicates a preference for the HYBRID implementation featuring a positive wake, while it is worth highlighting that all curves exhibit a tendency to underestimate the measured values. Likewise, of the two curves provided by the LBT model, the prediction with showers only is disfavored and the prediction incorporating a medium response is favored [338]. The prediction from MARTINI does not include alternative assumptions for the medium response effect and, therefore, no comment on the medium impact can be made [337]. Finally, the CCNU prediction is restricted to a jet  $p_T$  below what was measured for large  $R$  [339–341]. These observations motivate future jet measurements, at low  $p_T$  and using a large  $R$  parameter, similar to the one reported in Ref. [342], to further constrain the modeling of the medium response.

### 5.1.3 Suppression of high- $p_T$ hadron production

High- $p_T$  hadrons are produced via fragmentation and hadronization mechanisms initiated by the same partonic hard scatterings that result in final-state jets. Thus, high- $p_T$  hadron spectra can also be used to probe the strength of parton energy loss in the QGP medium. As compared to jet spectra, theoretical predictions of hadron spectra (and the resulting  $R_{AA}$  values) are more sensitive to details of the fragmentation and hadronization model used. However, high- $p_T$  charged hadrons are produced in larger numbers than jets and can have their  $p_T$  measured with excellent resolution. These experimental considerations have made the  $R_{AA}$  of charged hadrons a touchstone measurement of parton energy loss effects for over two decades, and was key to the discovery of jet quenching at RHIC [325, 326].

Figure 57 shows a compilation comparing CMS measurements of the charged-particle  $R_{AA}$  at  $\sqrt{s_{NN}} = 2.76\text{ TeV}$  [350] (red points) and  $5.02\text{ TeV}$  [351] (black points) to other experimental results [343–349]. The CMS 5.02 TeV data spans nearly three orders of magnitude of  $p_T$ , revealing an oscillating structure having a local minimum around 7 GeV. For  $p_T$  values under 3 GeV, where effects such as parton energy loss, initial-state effects, and radial flow can all have significant contributions, an approximate ordering with collision energy is observed. The 17.3 GeV SPS data has higher values than the 200 GeV RHIC data, which are in turn higher than the TeV-scale LHC data. For higher  $p_T$  values, parton energy loss is expected to be the dominant effect, resulting in a strong suppression that is remarkably similar at RHIC and the LHC around  $p_T = 7\text{ GeV}$ , despite the order of magnitude difference in collision energy. This similarity can be explained by the shape of the underlying hadron spectra. Flatter spectra, which are observed at higher collision energies, demand a greater absolute energy loss to achieve similar  $R_{AA}$  suppression values. This implies that energy loss effects are stronger at higher collision

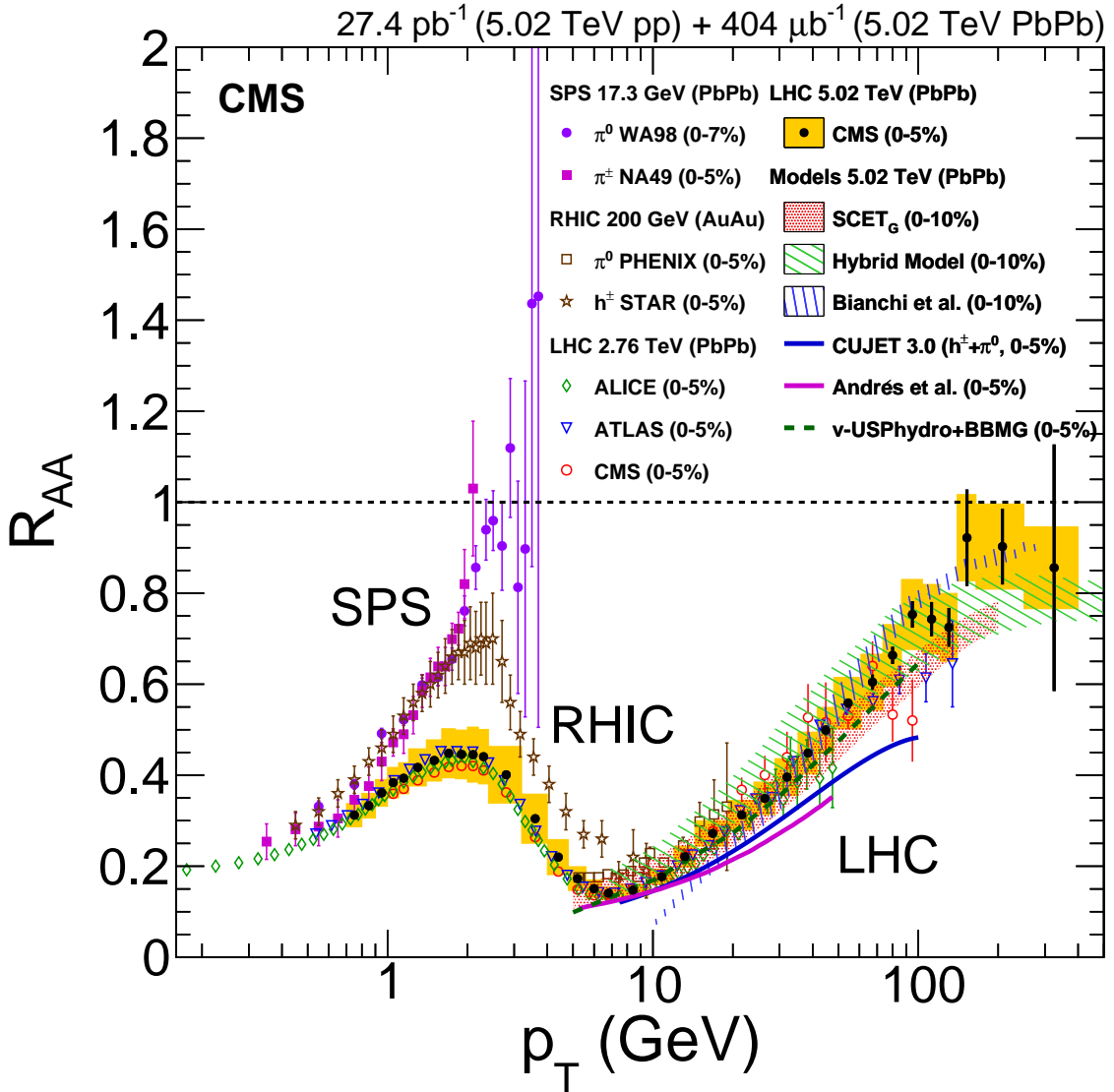


Figure 57: Measurements of  $R_{AA}$  in central heavy ion collisions at four different center-of-mass energies, for neutral pions (SPS, RHIC), charged hadrons ( $h^\pm$ ) (SPS, RHIC), and charged particles (LHC). Data are taken from Refs. [343–351]. Predictions of six models for  $\sqrt{s_{NN}} = 5.02$  TeV PbPb collisions are shown [41, 335, 352–355]. The error bars represent the statistical uncertainties and the yellow boxes around the 5.02 TeV CMS data show systematic uncertainties. The  $T_{AA}$  uncertainties, which are small, are not shown. (Figure adapted from Ref. [351].)

energies.

As  $p_T$  increases,  $R_{AA}$  becomes less suppressed, and at  $p_T$  values above 150 GeV,  $R_{AA}$  is consistent with unity. This contrasts with the trend observed for the inclusive jet  $R_{AA}$  shown in Fig. 55, which is nearly independent of jet  $p_T$  for jet  $p_T > 150$  GeV. One potential explanation for the difference between the jet and the charged-particle  $R_{AA}$  trends is related to selection effects coming from the requirement of a high- $p_T$  hadron being present in the event. Color coherence effects tend to reduce radiative energy loss as parton energy increases [356], because of the Landau–Pomeranchuk–Migdal (LPM) mechanism (in which consecutive gluon emissions in the parton shower exhibit quantum interference) and because the effective number of radiating color sources is suppressed in the parton shower [357]. The requirement for a high- $p_T$

hadron in an event could preferentially select configurations where the LPM effect is stronger than average for a jet at any given  $p_T$ . Six theoretical predictions of the charged-hadron  $R_{AA}$  are also overlaid with the data in Fig. 57 [41, 335, 352–355]. Most of the models are able to accurately predict the strong suppression observed at the local minimum of  $R_{AA}$ , but the models predict a large range of values at higher  $p_T$ . Thus, these data can be used to constrain energy loss models for events containing hard jet fragmentation patterns that result in a very energetic hadron and are complementary to measurements of the inclusive jet  $R_{AA}$ , which are not strongly biased towards any particular fragmentation pattern.

## 5.2 Strength of energy loss

This section details the Run 1 and 2 measurements by CMS that quantify the strength of interactions between color-charge carriers and the QGP through studies of the path-length dependence of parton energy loss, measurements of the absolute (as opposed to relative) energy loss of jets, and the QCD color-charge dependence of parton energy loss effects. Also discussed is the first measurement of top quarks in HI collisions, which may lead to new methods for probing the energy loss of partons at different stages of the QGP evolution.

### 5.2.1 Path-length dependence of energy loss

The amount of energy lost by a parton in the QGP is thought to depend on its path length through the medium. Although the average energy lost is expected to increase as the average path length increases, a quantitative understanding of this dependence can provide insight into the relative strengths of collisional and radiative energy loss. Collisional energy loss is expected to scale linearly with the path length  $L$  in a static medium. Because radiated gluons can also lose energy, radiative energy loss processes are expected to scale with an approximately  $L^2$  dependence in a static medium [358]. Although additional effects such as the expansion of the medium, the LPM effect, and color coherence effects can reduce the power of the anticipated path-length dependence, in general radiative energy loss is expected to scale faster with  $L$  compared to collisional energy loss. Multiple experimental techniques are available to explore this topic.

The first technique involves studying the strength of the energy loss by hard probes traveling through different volumes of QGP. One way of experimentally varying the volume of the QGP produced in HI collisions is to collide different ion species. The left panel of Fig. 58 shows a comparison of the charged-hadron  $R_{AA}$  for central PbPb collisions at  $\sqrt{s_{NN}} = 5.02$  TeV [351], collected in 2015, and  $R_{AA}^*$  for XeXe collisions at  $\sqrt{s_{NN}} = 5.44$  TeV [127], collected in 2017. The asterisk in  $R_{AA}^*$  indicates that a MC-based extrapolation procedure was used to adjust a measured 5.02 TeV pp reference spectrum to the appropriate reference energy of 5.44 TeV for the XeXe measurement. As discussed in Section 5.1.3, the relatively small difference in collision energy of these two systems is not expected to strongly affect the magnitude of the  $R_{AA}$  suppression. However, the radius of the Xe nucleus is  $\approx 5.4$  fm, while that of the Pb nucleus is  $\approx 6.6$  fm [359]. Thus, a smaller volume of QGP is produced in collisions of XeXe compared to collisions of PbPb at the same centrality. The values of the XeXe charged-hadron  $R_{AA}^*$  in the range  $p_T > 5$  GeV, where energy loss effects dominate, are clearly less suppressed than those of PbPb collisions, which is consistent with partons experiencing less energy loss in the smaller collision system. These data have been used to estimate that the path-length dependence of energy loss scales as  $L^{1.3 \pm 0.5}$  [360].

The right panel of Fig. 58 displays the charged-hadron  $R_{AA}$  and  $R_{AA}^*$  for these two collision systems near the local minimum of  $R_{AA}$  at  $6.4 < p_T < 7.2$  GeV as a function of the average  $N_{\text{part}}$ . The data from the two collision systems seem to follow a common decreasing trend. A value of

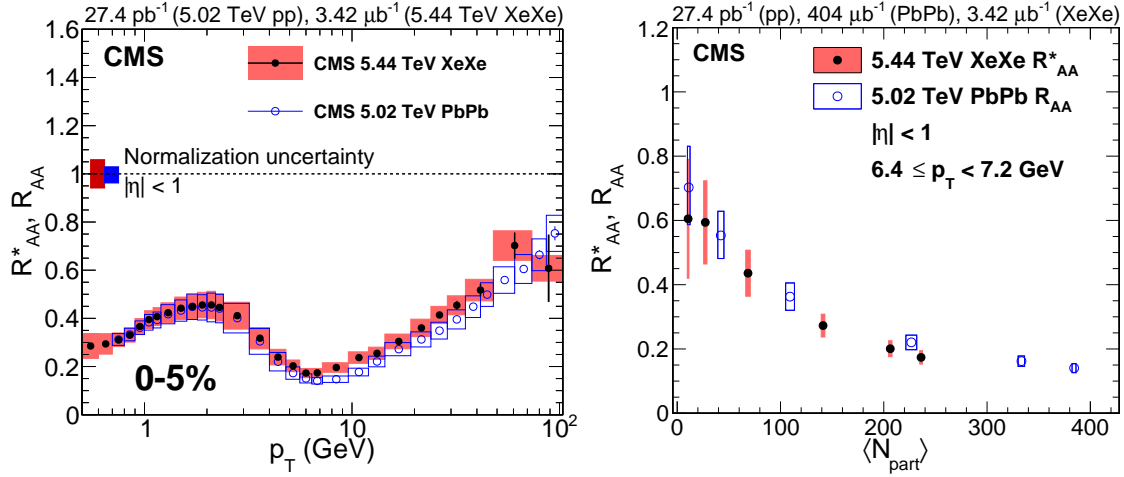


Figure 58: The charged-particle  $R_{AA}^*$  for XeXe collisions at  $\sqrt{s_{NN}} = 5.44$  TeV [127] and  $R_{AA}$  for PbPb collisions at 5.02 TeV [351]. The asterisk in  $R_{AA}^*$  indicates that the 5.44 TeV pp reference has been calculated by extrapolating a measured 5.02 TeV pp spectrum. The solid pink and open blue boxes represent the systematic uncertainties of the XeXe and PbPb data, respectively. The left panel shows the result as a function of particle  $p_T$  for a 0–5% centrality selection. In the right panel, the results for the  $6.4 < p_T < 7.2$  GeV range are plotted as functions of average  $N_{\text{part}}$ . (Figures adapted from Refs. [127, 351].)

$\langle N_{\text{part}} \rangle \approx 230$  corresponds to the most central (0–5%) XeXe collisions and semicentral (10–30%) PbPb collisions. Still, for this  $N_{\text{part}}$  value, the two systems have very similar  $R_{AA}$  and  $R_{AA}^*$  values. This implies, that at a given center-of-mass energy, systems containing similar volumes of QGP produce similar values of energy loss for hard probes, regardless of the initial colliding ion species or impact parameter. Interestingly, both the PbPb and XeXe data show a significant suppression in the most peripheral events examined (around  $\langle N_{\text{part}} \rangle \approx 10$ ). The values of  $R_{AA}$  and  $R_{AA}^*$  are consistent with the suppression observed for color-neutral  $Z$  bosons produced in 5.02 TeV PbPb collisions, as discussed in Section 3.2. Therefore, the  $R_{AA}$  suppression observed in this centrality region cannot be interpreted as a signature of parton energy loss. Other potential event selection or centrality calibration effects may fully explain this observation [186]. Such effects are expected to be negligible for central and semicentral collisions and therefore do not strongly affect any conclusions regarding energy loss in larger volumes of QGP.

Another technique for assessing the path-length dependence of parton energy loss makes use of inherent spatial anisotropies within the initial state of HI collisions. The initial partons resulting from a hard scattering are not expected to have any preferred azimuthal direction. Because of the initial-state geometry of HI collisions, the overlapping transverse area between the two ions, where the QGP is expected to form, typically has a nonzero eccentricity that is related to the impact parameter, and therefore the collision centrality. This is important because the relatively large transverse eccentricities present in semicentral HI collisions can give rise to substantially different path lengths for partons traveling parallel and transverse to the direction of the collision impact parameter. Furthermore, comparable effects may arise even in events lacking significant initial-state eccentricity due to the influence of fluctuations of the initial-state geometry. Given that partons encountering a greater path length within the medium are expected to experience comparatively higher energy loss on average, this phenomenon can induce an azimuthal anisotropy of final-state high- $p_T$  particles. This anisotropy can be expressed in terms of Fourier coefficients  $v_n$  (as shown by Eq. (4) in Section 4.2). We note that this picture of path length dependent energy loss does not account for possible large jet-by-jet

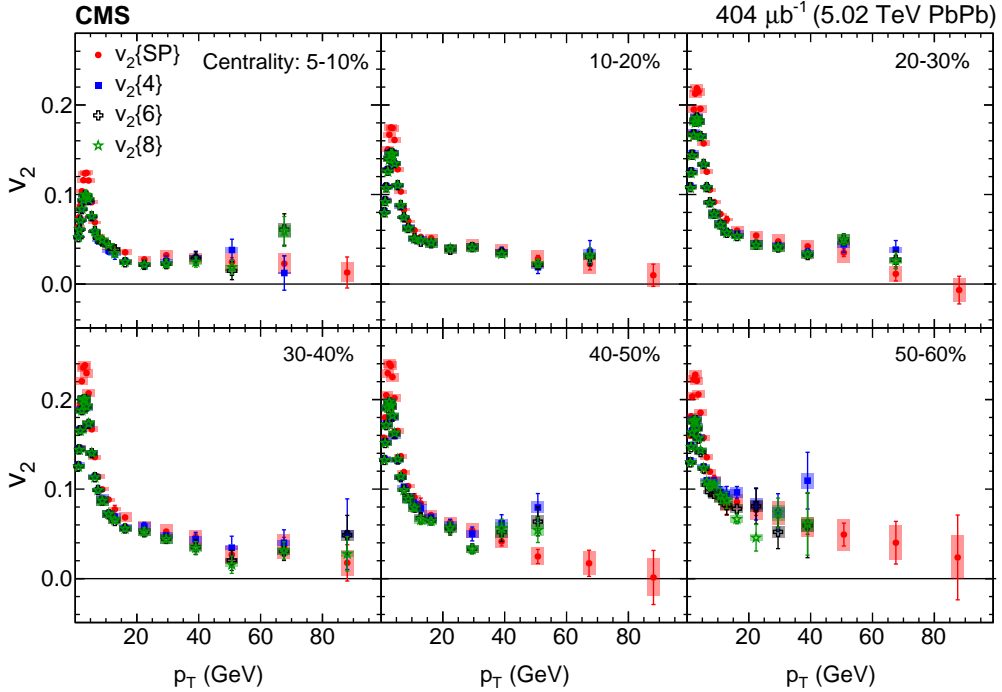


Figure 59: Comparison between charged-hadron  $v_2$  results from various methods as a function of  $p_T$  in six centrality selections from 0–5% to 50–60%. The vertical bars represent the statistical uncertainties, while the shaded boxes represent systematic uncertainties. (Figure adapted from Ref. [361].)

fluctuations in energy loss, as discussed in Section 5.1.1.

Figure 59 shows a measurement of the  $v_2$  coefficient as a function of  $p_T$  for charged hadrons in 5.02 TeV PbPb collisions [361]. For low  $p_T$  values (i.e.,  $p_T < 3$  GeV), hydrodynamic flow is believed to dominate multiparticle correlations, with the  $v_2$  value reflecting the eccentricity of the particle-emitting region. Four different methods for determining  $v_2$  values are shown, including the scalar-product method  $v_2\{\text{SP}\}$  and four, six, and eight particle correlators  $v_2\{4\}$ ,  $v_2\{6\}$ ,  $v_2\{8\}$ , respectively (Section 4.1 presents the methods). The method originally used for bulk particle production has been adapted and modified for the high- $p_T$  regime. Specifically, the  $v_2\{8\}(80\text{ GeV})$  is not derived from the correlation of eight particles with  $p_T$  around 80 GeV, but rather from correlating one 80 GeV particle with softer particles. Significant positive  $v_2$  values are observed up to  $p_T = 80$  GeV for most centrality selections investigated. Furthermore, the  $v_2$  values in the range  $10 < p_T < 50$  GeV tend to be larger for centrality selections containing a larger average initial-state eccentricity, as indicated by the magnitude of the  $v_2$  values at low  $p_T$ . These results do not seem to strongly depend on the method used to extract the  $v_2$  values. In particular, the results using multiparticle correlation methods, which tend to suppress non-flow contributions to the  $v_2$  values, strongly imply a connection between  $v_2$  and the initial-state geometry and its event-by-event fluctuations. A similar conclusion was reached when analyzing 2.76 TeV PbPb collision data [362]. In the analysis of 5.02 TeV collisions, positive values of  $v_3$  were also observed up to  $p_T$  values of around 20 GeV, but were found to be consistent with zero for higher  $p_T$  values.

A similar measurement of  $v_2$  using fully reconstructed dijets in 5.02 TeV PbPb collisions is shown in Fig. 60 [363]. The results are calculated by correlating each jet in a dijet pair with hadrons having large  $\eta$  separation from the jet. A significant positive  $v_2$  is observed in all three centrality selections examined, with the magnitude of  $v_2$  increasing as the average initial-state

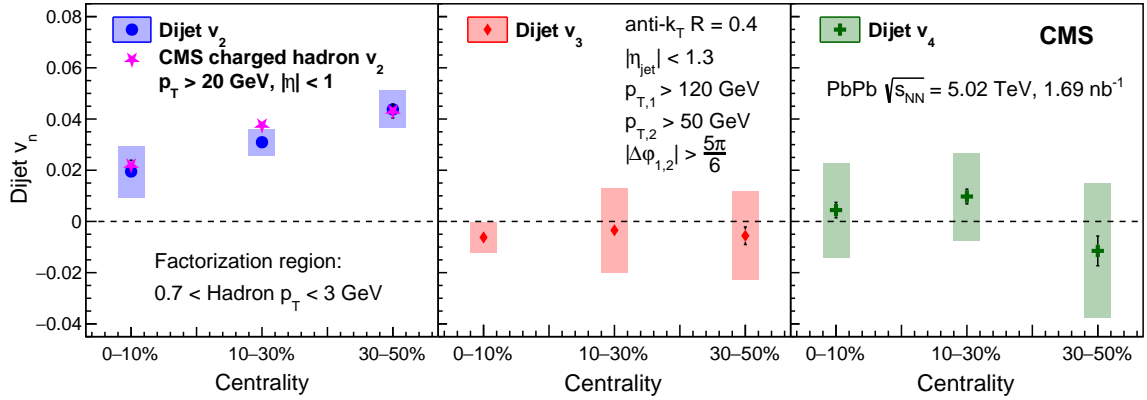


Figure 60: The dijet  $v_2$  (left),  $v_3$  (middle), and  $v_4$  (right) measured as functions of collision centrality in 5.02 TeV PbPb collisions. The dijet  $v_2$  results are compared to CMS high- $p_T$  hadron  $v_2$  results. The shaded boxes represent systematic uncertainties, while the vertical bars show statistical uncertainties. (Figure adapted from Ref. [363].)

eccentricity increases. This indicates more jets are observed in the azimuthal direction parallel to the event plane, as compared to the perpendicular direction. The results for the  $v_2$  of dijets are compatible with those for individual high- $p_T$  charged hadrons. These results strongly imply a path-length dependence of parton energy loss and can be used to constrain parton energy loss models. Measurements of dijet  $v_3$  and  $v_4$  were also performed, but the values were found to be consistent with zero, implying that jets are not strongly affected by event-by-event initial-state geometry fluctuations.

### 5.2.2 Measurements of absolute jet energy loss

As noted in Section 5.1.2, many of the initial observations of jet quenching relied on observables, such as the dijet  $A_J$ , where both jets were quenched. To determine the total amount of energy a color-charge carrying parton loses to medium interactions in the QGP, as opposed to its relative energy loss, it is necessary to determine the initial parton energy. This can be done by studying rarer hard-scattering processes with a boson + jet in the final state, such as the LO processes depicted in Fig. 61. The boson, typically a photon or  $Z$  boson for the purposes of these studies, is colorless and therefore is not modified by strong interactions in the medium. Thus, the boson can be used to determine the initial energy of the companion parton that eventually results in a jet. By comparing the jet energies tagged in this manner with those similarly tagged in pp reference collisions, the absolute impact of medium interactions on partons is observable.

Such studies were carried out with the limited integrated luminosity of Run 1 with photon-tagged jets [109] and with the cleaner but statistically limited  $Z$ -tagged jets with Run 2 data from 2015 [365]. The currently most precise measurement of absolute jet energy loss by CMS uses photon-tagged jets taken at  $\sqrt{s_{NN}} = 5.02$  TeV in 2015 with integrated luminosities of  $404 \mu\text{b}^{-1}$  for PbPb collisions and  $27.4 \text{ pb}^{-1}$  for the pp reference collisions [364]. Photons are required to be isolated, as discussed in Section 2.11.2, reducing contributions from photons produced in fragmenting jets or from resonance decays. In each centrality class (50–100%, 30–50%, 10–30%, 0–10%), photons are correlated with all jets opposite in azimuthal angle and for each photon-jet pair the balancing observable  $x_J \gamma$ , defined as  $x_J \gamma = p_T^{\text{jet}} / p_T \gamma$ , is calculated. The distributions are then normalized by the number of photons found in each centrality class (and in the pp reference). The result of this measurement is shown in Fig. 62.

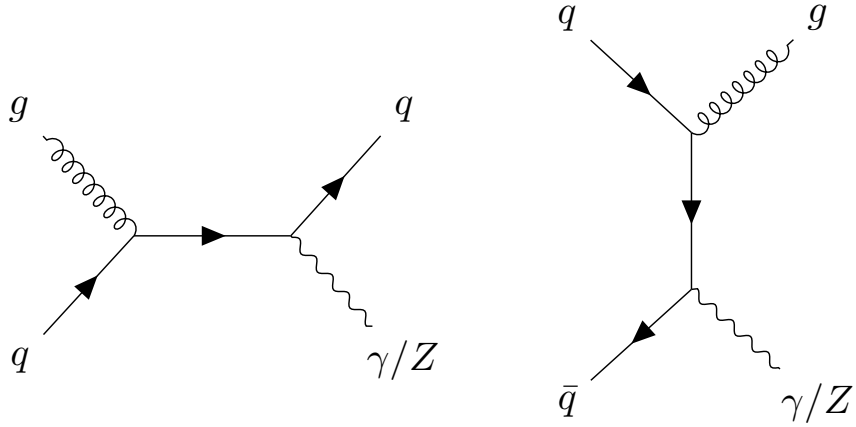


Figure 61: Feynman diagrams depicting two leading-order processes producing a photon or a Z boson with a jet balancing the transverse momentum in the final state. The first diagram shows the outgoing jet to be initiated by a quark, while the other shows the outgoing jet to be initiated by a gluon. These rare hard scatterings have been used to study jet quenching in a number of CMS analyses [364].

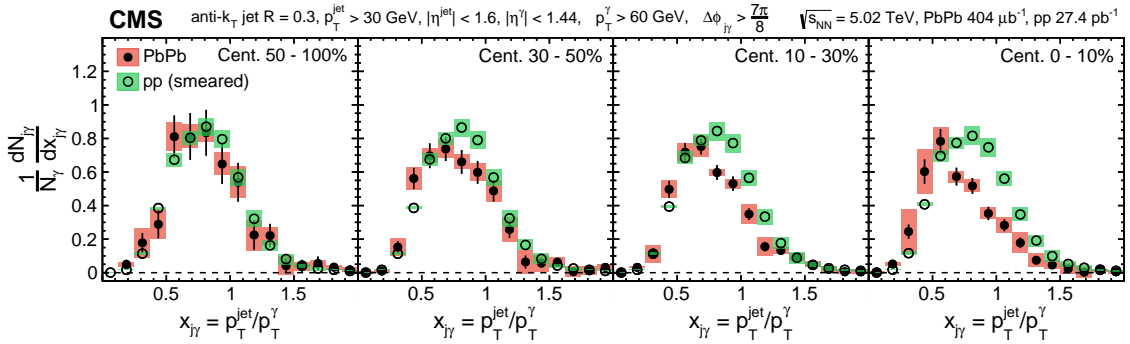


Figure 62: The  $p_T$  balancing observable  $x_{J\gamma}$  for  $\gamma +$  jet pairs is plotted as a function of centrality class panel-by-panel, with the leftmost panel corresponding to the 50–100% peripheral selection, progressing to the 0–10% central selection in the rightmost panel. The distribution is normalized by the number of photons in a pp reference (open markers) and PbPb (full markers) data, per centrality class. Vertical lines display the statistical uncertainties while the shaded bars around the points (red for PbPb, green for pp) show the systematic uncertainties. The statistical uncertainties of the pp data are smaller than the markers for many data points. (Figure adapted from Ref. [364].)

On inspection, it is clear that quenching effects do not modify the  $x_{J\gamma}$  distribution in the peripheral 50–100% centrality class compared to the pp reference spectrum beyond the currently reported uncertainties. For this comparison the pp reference spectrum is modified to have a similar resolution as the PbPb distribution, i.e., “smeared”. However, moving to a semiperipheral selection of 30–50% centrality already shows a modest depletion in balanced photon-jet configurations, corresponding to  $x_{J\gamma}$  larger than 0.75. Going to the semicentral 10–30% centrality selection, the observed depletion of balanced configurations increases substantially, and in the central 0–10% selection even extends down to  $x_{J\gamma} \approx 0.6$ . While there are hints of a corresponding enhancement for  $x_{J\gamma} < 0.6$ , this enhancement is at the edge of the reach allowed by the statistical and systematic uncertainties. The integral areas of the PbPb distributions decrease as collisions become more central, resulting from a relatively larger fraction of jets quenched below the  $p_T^{jet}$  threshold of 30 GeV.

### 5.2.3 Color-charge dependence of energy loss

For the hard probes sector, specifically jets, constraints based on control samples in data are provided by CMS for theoretical calculations of jet transport coefficients, energy loss parametric dependencies, and in-medium shower evolution. The interactions in the QGP medium are expected to vary with the color charge of the energetic parton traversing it; gluons will interact more strongly than quarks given their larger Casimir color factor [366, 367]. Thus, significant efforts have been made to develop observables that preserve sensitivity in the final state to the identity of the parton initiating the observed process.

Aside from small contributions from heavy-flavor quarks, the overwhelming majority of jets from HI collision data represent a mix of light-quark and gluon contributions, with no identification of partonic origin possible on a per-jet basis. Even statistical discrimination methods for light-quark and gluon jet tagging remain challenging. Several standard tagging tools are used as light-quark versus gluon jet discriminators. These tools include jets produced in coincidence with EW bosons as discussed in Section 5.2.2, and the jet charge that serves as a proxy for the electric charge of the parent parton.

It is important to note that within the framework of common searches for hot nuclear effects, where a specific measurement from AA collisions is compared to a pp reference, none of the aforementioned discriminators allows the *isolation* of color-charge effects in jet quenching studies. Instead, they provide various combinations of potential selection biases. For example, the photon-tagged jet sample used in previously discussed studies of absolute energy loss has a significant fraction of initial quark jets, as illustrated using a MC generator in Fig. 63 [364], which is higher than the initial quark jet fraction of an inclusive jet sample. Additionally, in the QGP medium, the requirement of a nonstrongly interacting boson as a “trigger” potentially alters the survival (or surface) bias of the studied jets. Thus, future comparisons of boson-tagged jet samples against inclusive jet samples may yield insights about the interplay between these selection effects and the different energy loss behavior of the various light-parton flavors.

For the jet charge (or other jet constituent-based observables), complications may arise from

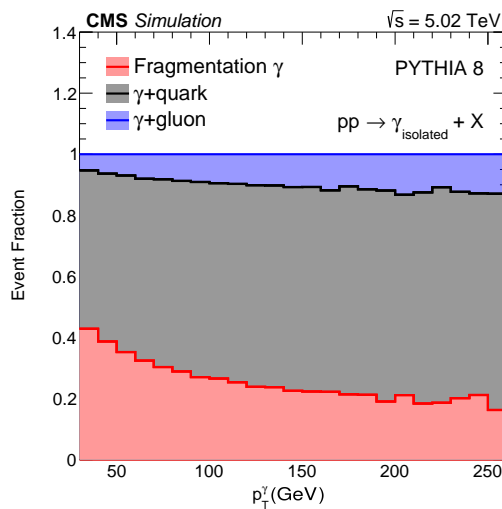


Figure 63: Relative contributions of fragmentation (red), photon+quark jet (grey), and photon+gluon jet (blue) processes to the production of isolated photons in PYTHIA8 events. The requirement of an isolated photon in the event increases the fraction of quark-initiated jets relative to an inclusive jet sample. (Figure adapted from Ref. [364].)

the medium response that is inevitably reconstructed as part of the jet shower; additionally, the jet charge is not infrared- or collinear-safe. Despite its potential limitations, the jet charge is an experimentally available observable that enables the evaluation of the quark-gluon composition of the jet sample, albeit relying on MC modeling. Introduced in the 1970s as one of the earliest jet substructure observables, the measurement of the jet charge has served as a method for measuring the electric charge of a quark [368]. The technique was first used in deep inelastic scattering experiments at Fermilab [369, 370], CERN [371–374], and Cornell University [375]. The jet charge is defined as the transverse momentum-weighted sum of the charges of particles within the jet cone, and experiments have used a variation of weight exponents and momentum thresholds to maximize its discriminating power. While initially used to study the substructure of nucleons, it has been suggested that the jet charge may also yield insights into the properties of the QGP [376].

CMS has conducted a measurement of jet charge distributions in HI collisions using 5.02 TeV PbPb data [377]. Surprisingly, the investigation revealed no significant differences from what is observed in pp collisions. The widths, average values, and fractions of gluon-like jets, obtained through MC-based template fits, remained consistent with the reference pp collision sample from peripheral to central PbPb collisions. This stability is illustrated in Fig. 64, which displays the gluon-like jet fraction as a function of the track  $p_T$  threshold used in the measurement. Assuming that medium-induced effects remain charge-neutral on average and that gluon-initiated jets suffer more energy loss than quark-initiated jets on average, it could be expected that fewer gluon-like jets, as measured using the jet charge, might be observed in a sample at a given jet  $p_T$  when compared to a pp reference. This result shows no evidence for such an effect and therefore calls for careful examination of possible selection biases in this (and other) measurements featuring quark or gluon tagging. Conversely, if no such biases are present, this observable may provide a way of enhancing the fraction of quark- or gluon-initiated jets in a sample on a statistical basis without being sensitive to medium effects.

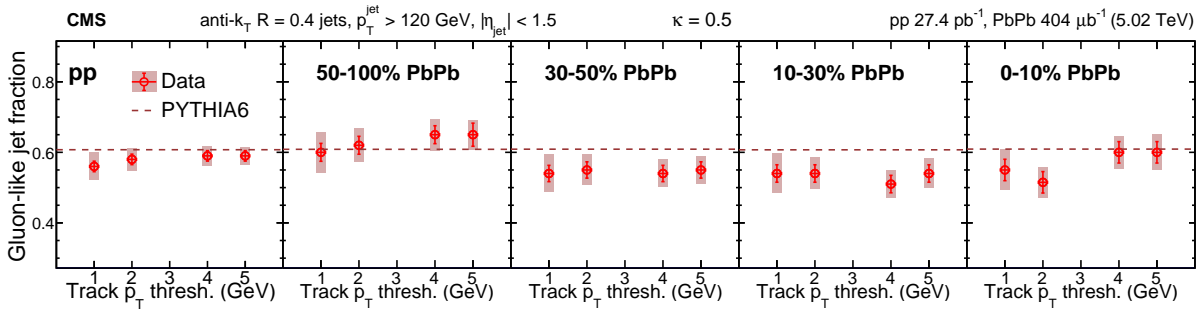


Figure 64: Results for the gluon-like jet fractions in pp and PbPb data shown for different track  $p_T$  threshold values and event centrality selections in PbPb collisions. The systematic and statistical uncertainties are represented by the shaded regions and vertical bars, respectively. The predictions for the gluon jet fractions from PYTHIA 6 are shown in dashed red lines. (Figure adapted from Ref. [377].)

Heavy-flavor jets are rarer than light-flavor or gluon jets, but can provide a more unambiguous tag of the flavor of the parton that initiates a jet. In particular, a selection of dijets in which both jets are “b tagged”, i.e., have a displaced secondary vertex or tracks displaced from the primary vertex that most likely results from the decay of a b hadron, can heavily suppress gluon-initiated jet contributions. A measurement of the average  $p_T$  imbalance,  $\langle x_J \rangle$ , of b dijets [330] is shown in Fig. 65, where  $x_J$  is defined as

$$x_J = p_{T,2}/p_{T,1}. \quad (20)$$

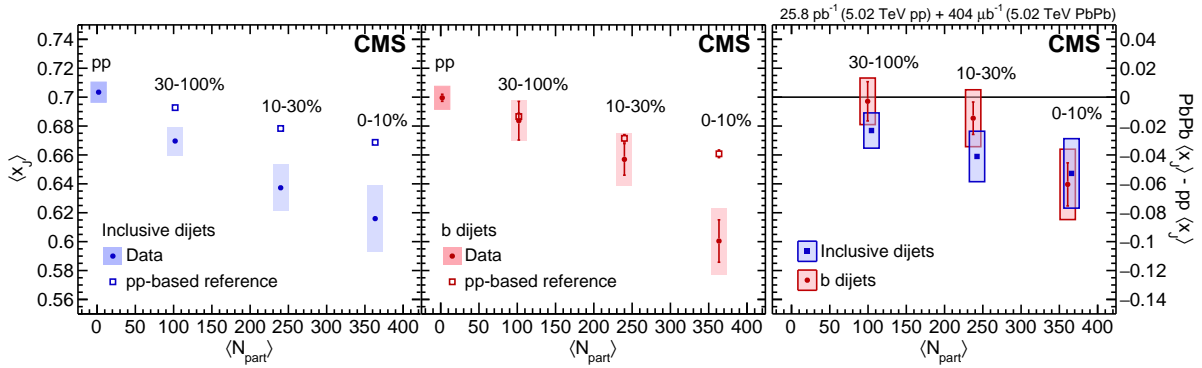


Figure 65: Dijet imbalance for inclusive (left) dijets and b dijets (center) in pp collisions and for different centrality selections of 5.02 TeV PbPb collisions. The right panel shows the difference in the  $\langle x_j \rangle$  values between PbPb and the smeared pp reference. Systematic uncertainties are shown as shaded boxes and statistical uncertainties are displayed as vertical lines. (Figure adapted from Ref. [330].)

The imbalance is found to increase as a function of collision centrality for both an inclusive dijet (left panel) and b dijet (middle panel) selection. The comparison of the two selections (right panel) reveals no significant differences between them, given the current measurement uncertainties. Although inclusive b jet measurements are expected to exhibit larger contributions from processes such as gluon splitting ( $g \rightarrow b\bar{b}$ ), when compared to b dijets, previous CMS measurements of the inclusive b jet  $R_{\text{AA}}$  in 2.76 TeV PbPb collisions are consistent with the  $R_{\text{AA}}$  of inclusive jets [378]. Both of these measurements, as well as the ATLAS  $\gamma$  and b jet measurements [379, 380], indicate that any potential differences between samples of light-quark or gluon initiated jets and b quark jets in the range  $80 < p_{\text{T}} < 250$  GeV are small when compared to the sensitivity of current measurements. Extending these measurements to lower jet  $p_{\text{T}}$  values, where flavor-dependent differences are expected to be larger but also where high rates of fake jets make the measurements difficult, may allow a clear distinction to be drawn between the dynamics of heavy-quark and light-quark or gluon initiated jets.

#### 5.2.4 Prospects for measuring energy loss across various stages of QGP evolution

All parton energy loss observables described so far are only sensitive to the properties of the QGP integrated over its lifetime of  $\sim 10^{-23}$  s, as the hard scattered partons are produced during the initial stages of the collision. In contrast, the top quark, the heaviest elementary particle known (and accessible in nucleus-nucleus collisions at the LHC), can provide complementary insights into the time structure of the QGP. Indeed, and as noted in Ref. [381], hadronically decaying W bosons, produced in top quark decays, provide a well calibrated “time delay” between the moment of the collision (when the top quarks are produced) and the moment when the W boson decay daughters start interacting with the QGP medium. The magnitude of the time delay can be determined by implementing a selection based on the reconstructed  $p_{\text{T}}$  of the top quark. Using such a procedure, and the event samples expected to be collected by the end of the HL-LHC running period, we should be able to probe lifetime scales at the 1 fm level.

As an initial step toward conducting these types of investigations, CMS has presented the first evidence of top quark production in AA collision systems. This evidence is derived from 5.02 TeV PbPb collision data [149]. In particular, two methods are used to measure the cross section for top quark pair production via the decay into charged leptons (electrons or muons, leading to  $e^{\pm}\mu^{\mp}$ ,  $\mu^+\mu^-$ , and  $e^+e^-$  final states) and b quarks (separated into 0b-, 1b-, and 2b-

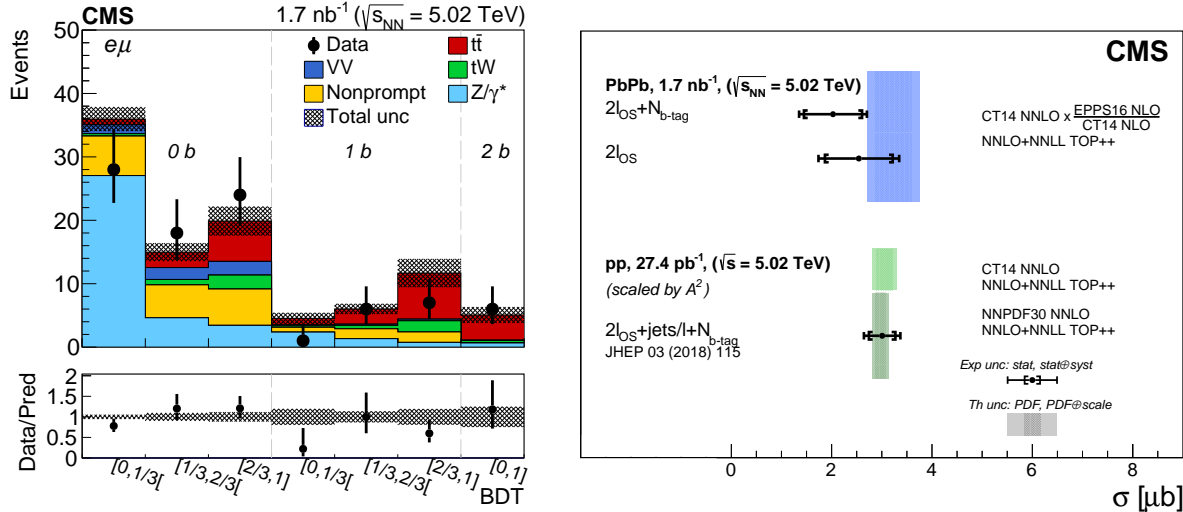


Figure 66: Left: Observed and postfit predicted BDT discriminator distributions in the  $e^\pm\mu^\mp$  final state separately in the 0b-, 1b-, and 2b-tagged jet multiplicity categories. The data are shown with markers, and the signal and background processes with filled histograms. The vertical bars on the markers represent the statistical uncertainties in data. The hatched regions show the uncertainties in the sum of  $t\bar{t}$  signal and backgrounds. The lower panel displays the ratio between the data and the predictions, including the  $t\bar{t}$  signal, with bands representing the uncertainties in the postfit predictions. Right: Inclusive  $t\bar{t}$  cross sections measured with two methods in the combined  $e^\pm\mu^\mp$ ,  $\mu^+\mu^-$ , and  $e^+\mu^-$  final states in  $PbPb$  collisions at  $\sqrt{s_{NN}} = 5.02$  TeV, and  $pp$  results at  $\sqrt{s} = 5.02$  TeV (scaled by  $A^2$ ). The measurements are compared with theoretical predictions at NNLO+NNLL accuracy in QCD. The inner (outer) experimental uncertainty bars include statistical (statistical and systematic, added in quadrature) uncertainties. The inner (outer) theoretical uncertainty bands correspond to nPDF or PDF (PDF and scale, added in quadrature) uncertainties. (Figures adapted from Ref. [149].)

tagged jet multiplicity categories). One method relies on the leptonic information alone, while the other one exploits, in addition, the presence of b quarks. For both the dilepton-only and dilepton plus b-tagged jets methods, a boosted decision tree classifier is trained on the simulated  $t\bar{t}$  signal versus the overall  $Z/\gamma^*$  background (Fig. 66, left). This classifier is based exclusively on leptonic quantities to minimize effects from the imprecise knowledge of the jet properties in the HI environment. For both methods, the measured cross sections are compatible with, though somewhat lower than, the expectations from scaled  $pp$  data and QCD predictions (Fig. 66, right). This measurement serves as a proof of concept for using the top quark as a novel probe, potentially enabling the investigation of energy loss and QGP dynamics at various stages during the temporal evolution of the system.

### 5.3 Medium modifications to jet substructure and fragmentation

Jets, as final-state multiscale composite objects initiated by hard-scattered partons, are characterized both by macroscopic quantities (such as their energy and direction) and by microscopic quantities that describe their internal structure. Therefore, the jet quenching phenomenon should be understood not only as a single overall medium-induced energy loss, but also as more detailed modifications to internal jet characteristics. Simultaneous measurements of jet properties at the macroscopic and microscopic scales can disentangle model scenarios with fundamentally different approaches to parton-medium interactions. These measurements should include characteristics such as the jet mass, angularity, and net charge, together with the longitudinal and transverse constituent distributions in the shower. Such an all-encompassing

approach is necessary, realizing that using a jet to probe the medium is not equivalent to using a single parton that has a set (hard) perturbative scale. Rather, a jet is instead a continuous-scale dynamical process involving momentum exchanges with variable couplings. The following sections describe CMS studies of jet fragmentation functions (Section 5.3.1), shapes (Section 5.3.2), and substructure (Section 5.3.3).

### 5.3.1 Longitudinal structure of jets: fragmentation functions

Implicit in the iterative recombination algorithms employed for jet identification is the notion of a jet constituent, which refers to the individual physics objects (such as PF or generator-level particles) clustered together within the resultant jet in the final state. One method to study the internal jet structure is to simply count the number of constituents within a jet according to their relative contribution to the overall jet energy,

$$z = \frac{p_{\parallel}^{\text{track}}}{p_{\text{jet}}}, \quad \xi = \ln \frac{1}{z}, \quad (21)$$

where  $p_{\parallel}^{\text{track}}$  is the track momentum projected onto the axis of the jet into which it is clustered and  $p_{\text{jet}}$  is the momentum of the jet. The distribution of this final state constituent-by-constituent energy fraction for a given initiating parton energy, evaluated over an ensemble, is the fragmentation function. All tracks with  $\Delta R$  less than the jet distance parameter  $R = 0.3$  are used, where  $\Delta\phi$  the difference in  $\phi$  between track and jet and  $\Delta\eta$  is the corresponding difference in  $\eta$ .

Figure 67 shows a high-precision measurement of inclusive jet fragmentation functions as the number of tracks in bins of  $\xi$  normalized by bin width and per jet in 2.76 TeV PbPb collisions, for a jet  $p_{\text{T}}$  selection of 150–300 GeV and track  $p_{\text{T}} > 1$  GeV [382]. The upper panels show fragmentation functions for PbPb collisions, plotted in four centrality classes, along with their corresponding pp reference data. The lower panels show the ratio between the two, which can be used to study possible medium-induced modifications of the fragmentation functions. In the leftmost panel, which corresponds to the most peripheral centrality selection of 50–100%, the ratio displayed in the lower panel remains consistent with unity within one standard deviation after accounting for both statistical and systematic uncertainties. This suggests that there is no significant change to the fragmentation functions resulting from interactions between jets and the plasma for these peripheral collisions. However, starting with the 30–50% centrality class there is an observable enhancement in the high  $\xi$  (or low track  $p_{\text{T}}$ ) region. This is consistent with  $\not{p}_{\text{T}}^{\parallel}$  measurements, detailed in Section 5.1.1, which show enhancement of soft particle production in the subleading (more quenched) jet direction. For the 10–30% selection, in addition to the enhancement of low- $p_{\text{T}}$  tracks, there is also an observable trend of depletion in the intermediate track  $p_{\text{T}}$  range ( $\xi$  1.5–3.0). The lowest  $\xi$  point suggests an upward trend, but remains consistent with unity. For the most central events (0–10% shown in the rightmost panels), the trends closely resemble those observed in the 10–30% centrality range. The increased systematic uncertainty observed in this centrality range primarily stems from the significant correction needed for UE contributions.

The deviations observed in the fragmentation functions measured in PbPb collisions relative to the reference pp data can be attributed to several potential causes. First, it is expected from QCD that quarks and gluons have different color charge factors regulating the strength of parton-medium interactions. Consequently, it is likely that gluons will experience more energy loss while traversing the QGP than quarks. As quarks and gluons are known to have different fragmentation patterns in vacuum, any change in inclusive jet q/g fraction as a result

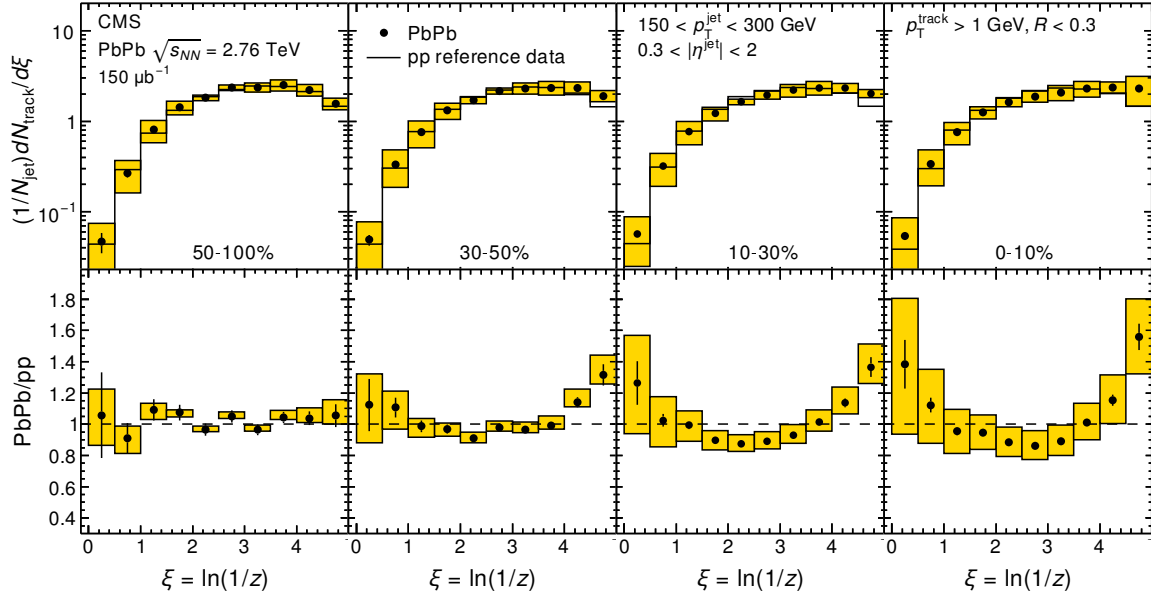


Figure 67: Upper: Fragmentation functions as a function of  $\xi$  in bins of PbPb centrality (left-to-right: 50–100%, 30–50%, 10–30%, and 0–10%) with the result from pp reference data overlaid. Lower: Ratios of the PbPb fragmentation functions over those for the pp reference. Jets are selected in the  $p_T$  range 150 to 300 GeV and tracks with  $p_T > 1$  GeV. Vertical bars and shaded boxes represent the statistical and systematic uncertainties, respectively. (Figure adapted from Ref. [382].)

of quenching would cause changes to the fragmentation functions. In addition to this, parton-medium interactions can either modify the parton showers or induce a medium response that remains confined to the vicinity of the jet itself, consequently imitating an altered fragmentation pattern. Distinguishing between these three possibilities in a rigorous, systematic manner requires extensive study beyond the inclusive jet system.

This initial study measured inclusive jets in both PbPb and pp reference data at  $\sqrt{s_{\text{NN}}} = 2.76$  TeV taken during Run 1. Similarly sized samples of  $\gamma$ -tagged jets in PbPb and pp collisions at  $\sqrt{s_{\text{NN}}} = 5.02$  TeV were recorded during Run 2. As discussed in Section 5.2.2, one use of these samples is to explore the absolute energy loss of jets by using the photon energy as a proxy for the energy of the initial hard scattering. These events can also be used to study fragmentation functions for cases in which both the initial- and final-state energies of the jet are tagged. For the inclusive jet fragmentation functions shown in Fig. 67, the  $p_T$  selection ( $150 < p_T^{\text{jet}} < 300$  GeV) is applied to the jets in the final state, i.e., after quenching has changed the jet population substantially as compared to the pp reference data. In contrast,  $\gamma$ -tagged jet samples avoid this bias by selecting on the  $p_T$  of the colorless photon. Using these tagged events, fragmentation functions can be extracted using both the traditional observable  $\xi$  (renamed to  $\xi_T^{\gamma}$  in the results shown below) as well as a new observable  $\xi_T^{\gamma}$ , defined as

$$\xi_T^{\gamma} = \ln \frac{-|\vec{p}_T^{\gamma}|^2}{\vec{p}_T^{\text{trk}} \cdot \vec{p}_T^{\gamma}}, \quad (22)$$

where  $\vec{p}_T^{\gamma}$  and  $\vec{p}_T^{\text{trk}}$  are the transverse momentum vectors of the photons and tracks, respectively. The quantity  $\xi_T^{\gamma}$  is similar to  $\xi^{\text{jet}}$ , except that the track momentum is now projected onto a direction opposite to that of the photon (presumably the unmodified jet direction).

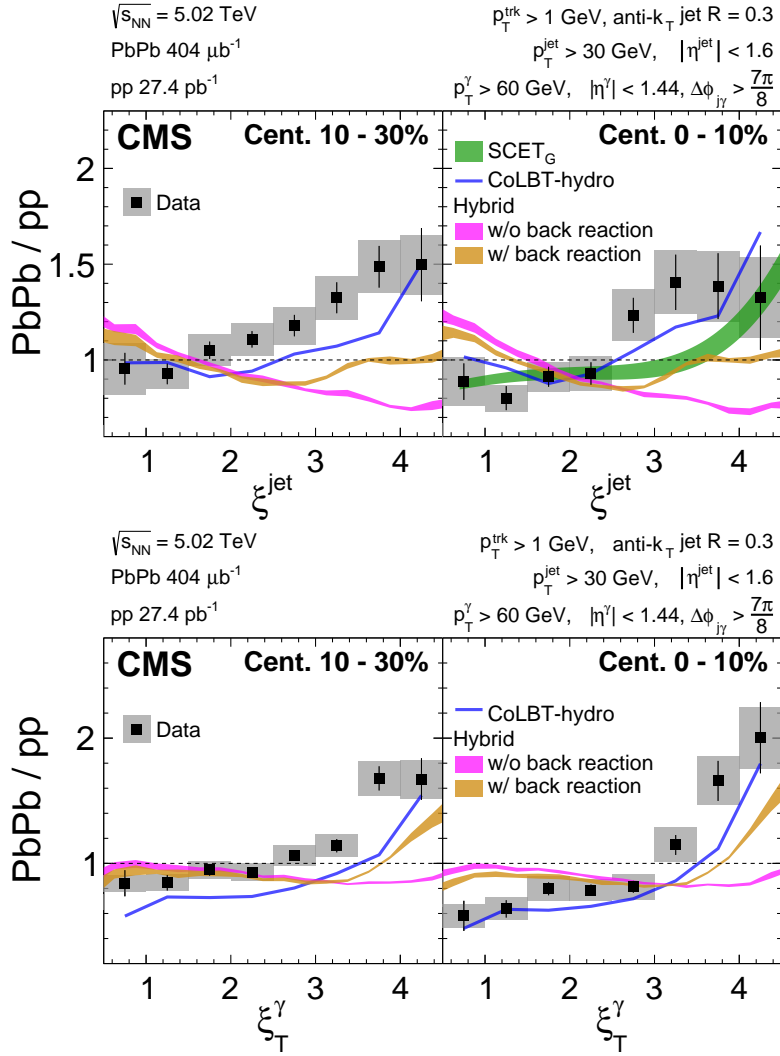


Figure 68: Comparison of  $\gamma$ -tagged fragmentation functions in centrality bins 10–30% (left) and 0–10% (right) as a function of the observables  $\xi^{\text{jet}}$  (upper), defined in Eq. (21), and  $\xi_T^\gamma$  (lower), defined in Eq. (22). For comparison, curves from the theoretical models SCETG [352], CoLBT-hydro [383–385], and HYBRID [386] are overlaid. The widths of the bands represent variations of the coupling strength in the SCETG case and of the dimensionless parameter  $\kappa$  in the HYBRID case. Vertical bars and shaded boxes represent the statistical and systematic uncertainties, respectively. (Figures adapted from Ref. [387].)

Figure 68 shows fragmentation functions in terms of both  $\xi^{\text{jet}}$  (upper panels) and  $\xi_T^\gamma$  (lower panels) in  $\gamma$ -tagged jet events [387]. Results are presented for both semicentral (10–30%, left panels) and central (0–10%, right panels) events. The conventional fragmentation functions using  $\xi^{\text{jet}}$  display only a minor enhancement of soft particles alongside a corresponding reduction of hard particles (at large and small  $\xi^{\text{jet}}$ , respectively). In contrast, those using  $\xi_T^\gamma$  demonstrate that once the influence of jet energy loss is eliminated, these effects become notably more pronounced, exhibiting a clear centrality dependence. Theory curves are plotted for the SCETG [352], CoLBT-hydro [383–385], and HYBRID [386] models. Of particular interest is the HYBRID model, which only describes the data qualitatively well when incorporating the medium response (labeled HYBRID with back reaction). This is an example of a model that can describe the energy loss of partons in the QGP without accounting for the response of the medium if we only consider what happens at the scale of the full jet but fail to do so at a

smaller scale (at the jet substructure level), where the response of the medium needs to be taken into consideration. Nevertheless, this evidence for the existence of medium response remains indirect and model-dependent.

### 5.3.2 Transverse structure of jets: jet shapes

In this section, a review of the measurements for the transverse shower profiles, known as “jet shapes,” is presented, complementing the CMS results on the modification of longitudinal jet substructure discussed in Section 5.3.1. The same jet definitions and angular track associations are used as in the previous section.

Measurements of the jet shape,  $\rho(\Delta r)$ , are obtained by identifying the jet constituents and examining the distribution of charged-particle tracks in rings around the jet axis, with each particle weighted by its corresponding track transverse momentum value  $p_T^{\text{trk}}$ . Typically, shower particles are separated from those of the underlying event on a statistical basis. The transverse momentum profile  $P(\Delta r)$  of the jet is then defined as

$$P(\Delta r) = \frac{1}{\delta r} \frac{1}{N_{\text{jets}}} \sum_{\text{jets}} \sum_{\text{tracks} \in (\Delta r_a, \Delta r_b)} p_T^{\text{trk}}, \quad \Delta r < 1, \quad (23)$$

where  $\Delta r_a$  and  $\Delta r_b$  define the annular edges of  $\Delta r$ , and  $\delta r = \Delta r_b - \Delta r_a$ . The jet profile, which is normalized to unity within  $\Delta r = 1$ , is related to the  $P(\Delta r)$  distribution, with the jet shape definition

$$\rho(\Delta r) = \frac{P(\Delta r)}{\sum_{\text{jets}} \sum_{\text{tracks}} p_T^{\text{trk}}}. \quad (24)$$

The  $\rho(\Delta r)$  and  $P(\Delta r)$  distributions are sensitive to subsequent parton emissions by the initial hard-scattered parton. These distributions have been used historically in high-energy physics to provide robust tests of parton showering calculations in QCD. Together with calculations of hadronization and underlying event contributions, the  $\rho(\Delta r)$  and  $P(\Delta r)$  distributions are also used for tuning MC event generators that account for parton showering effects. Jet shapes have been measured in elementary collisions (ep,  $p\bar{p}$ , pp) at HERA [388, 389], the Tevatron [390, 391], and the LHC [392].

In a HI collision environment, the jet shape measurements are particularly challenging given the high multiplicities encountered. Significant correlations with the underlying event lead to difficulties in differentiating the shower constituents from particles produced through other processes. The CMS Collaboration has addressed these issues in the first measurement of jet shapes using data from the LHC Run 1 PbPb collisions at  $\sqrt{s_{\text{NN}}} = 2.76$  TeV [393]. With this measurement, modifications of jet shower profiles while passing through the QGP medium were determined by comparing the measurements at different centralities of PbPb data and pp reference data. A clear modification of the in-cone ( $\Delta r < 0.3$ ) jet constituent distributions was observed in the PbPb data. As compared to the pp reference, a greater fraction of the jet’s transverse momentum is measured at a large  $\Delta r$ . This modification was shown to become stronger from peripheral to central collisions. However, these in-cone modifications were insufficient to explain the previously reported dijet momentum imbalance [329], which does not account for a significant amount of the  $\not{p}_T^{\parallel}$ . Instead, the observed trends in the PbPb to pp jet shapes ratios suggested that the modifications are not limited to the small cone size used in the measurements. This cone size was chosen to have better control over the fluctuating background. Measurements of energy redistribution between the entire hemispheres of dijet-containing events [108, 331] have shown that the energy flow is globally modified in HI events as a result of jet quenching and that the energy “splash” is felt at very large angles from the axis of a dijet.

Extending measurements of jet profiles to large angles was crucial to properly determine the dominant jet energy-loss mechanisms in various kinematic domains. The extended profiles are also needed to clearly establish the response of the QGP medium to the evolving jet. CMS has since performed a series of such studies [394–397], extending the angular range of jet constituent measurements with respect to a jet axis through a jet-track correlation technique. In this technique, tracks are classified by  $p_T$  and proximity to the jet axis in  $\Delta\eta$  and  $\Delta\phi$ . They are also corrected for acceptance affects, tracking inefficiencies, uncorrelated backgrounds, and jet reconstruction biases.

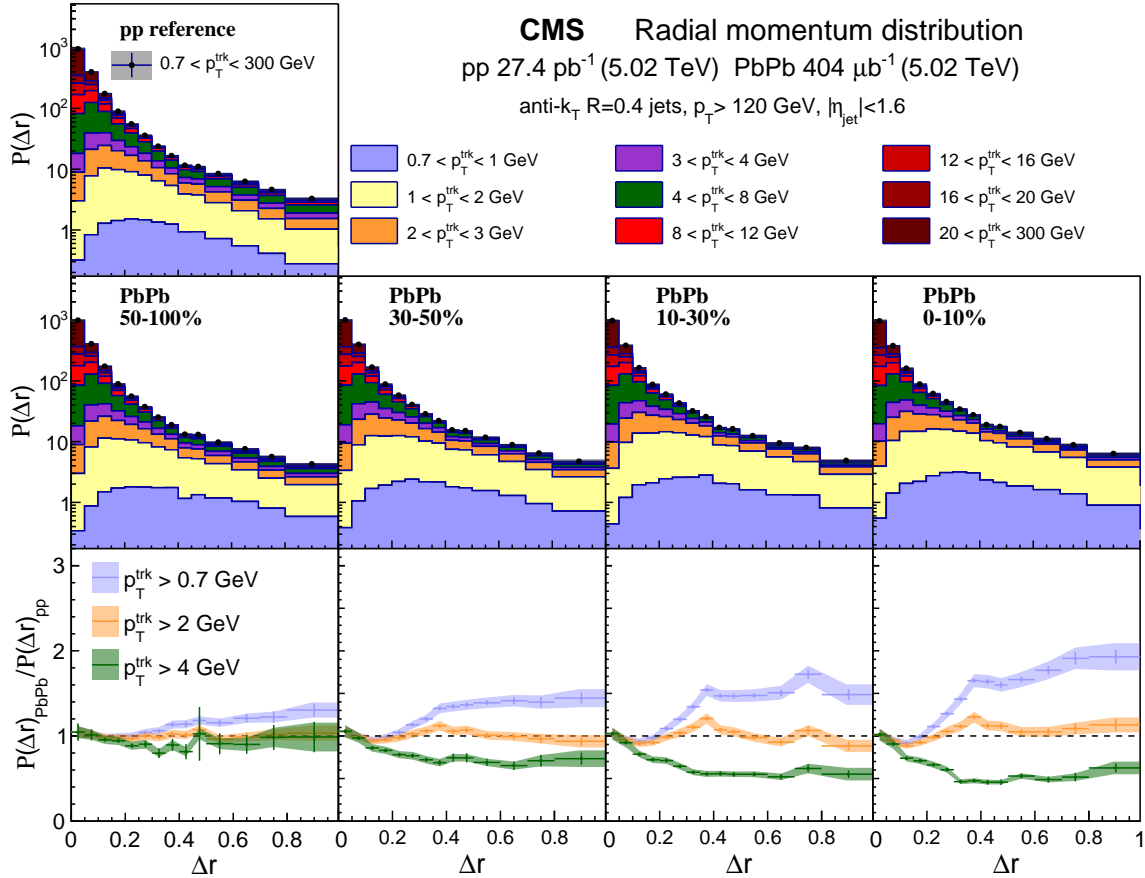


Figure 69: The angular jet momentum distribution  $P(\Delta r)$  of jets in pp (upper) and PbPb (middle) collisions. The PbPb results are shown for different centrality regions. The lower row shows the ratio between PbPb and pp data for the indicated intervals of  $p_T^{\text{trk}}$ . The shaded bands show the total systematic uncertainties. (Figure adapted from Ref. [396].)

The findings from these studies are illustrated in Fig. 69, which shows measurements of transverse momentum profiles for inclusive jets from 5.02 TeV pp and PbPb collisions. The upper panel presents reference measurements using pp data, detailing relative transverse momentum contributions of jet constituents at various distances from the jet axis. The second panel shows the same results for several centrality ranges of the PbPb collision data. To facilitate the comparison, the lower panel shows ratios between PbPb and pp results for the indicated  $p_T^{\text{trk}}$  intervals. The CMS jet shape measurements consistently demonstrate a redistribution of the jet energy inside and outside typical cone sizes. A significant excess of soft particles in PbPb events relative to pp events at intermediate to large angles from the jet axis is seen most prominently in central collisions, compensated for by a relative depletion at all track angles at high  $p_T^{\text{trk}}$ .

This two-sided modification has been argued to result from a combination of jet quenching in the medium and the medium response (or back reaction) to the propagating jet. The details of these interpretations remain nontrivial. For example, the narrowing of the hard “core” of the jet could be an artifact of a selection bias. At the same reconstructed momentum, a jet from a PbPb collision is more likely to have originated from a higher initial energy parton than in a pp event, where fragmentation occurs in vacuum. Alternatively, the hardening could arise from a selection bias caused by having a higher fraction of quark-initiated jets in the HI sample because of the expected color-charge effects on the energy loss [398, 399]. Regarding the broadening or enhancement of the soft components within the jets, although models exhibit variations in the details of the jet-medium interactions, it has become evident that only models integrating medium feedback can replicate the significant excesses at very large  $\Delta r$  in the momentum profiles, particularly the substantial low- $p_T^{\text{trk}}$  excesses [334, 400].

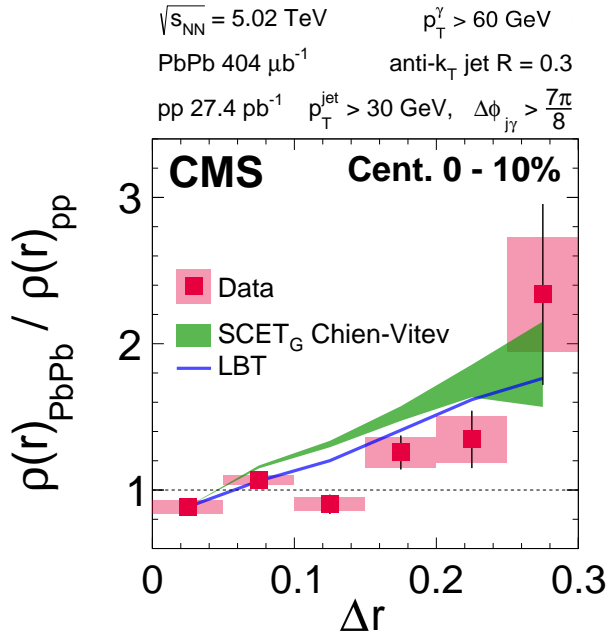


Figure 70: Ratio of the differential jet shape for jets associated with an isolated photon for 5.02 TeV 0–10% PbPb collisions and pp reference data. The measurement is performed using jets having  $p_T^{\text{jet}} > 30 \text{ GeV}$  and tracks with  $p_T^{\text{trk}} > 1 \text{ GeV}$ . (Figure adapted from Ref. [401].)

It is important to understand if the observed modifications are induced by the presence of the quark-gluon plasma or by a selection bias. CMS has explored a variety of experimental means to constrain possible selection biases in jet quenching studies. As discussed in Section 5.2.2, some biases can be alleviated by using jets produced in conjunction with an EW probe, such as a photon or Z boson. Photon-jet events have substantially lower cross sections than inclusive jet production, and the reconstruction of an *isolated* photon (as discussed in Section 2.11.2) required for such studies is experimentally challenging. The CMS Collaboration has successfully measured the fragmentation functions (as discussed in Section 5.3.1) and the jet shapes for photon-jet events at 5.02 TeV in pp and PbPb collisions. Figure 70 illustrates the modifications of the differential jet shape for jets associated with an isolated photon found in the 10% most central PbPb events [401]. The momentum carried by charged particles with  $p_T^{\text{trk}} > 1 \text{ GeV}$  for jets with  $p_T^{\text{jet}} > 30 \text{ GeV}$ , tagged by an isolated photon of  $p_T, \gamma > 60 \text{ GeV}$ , is redistributed towards larger angular distances from the jet axis. Minimal, if any, suppression is seen at the low/intermediate angles, where it stood more prominently for inclusive jet results. Similar measurements of events producing high- $p_T$  hadrons in association with a Z boson have been

used to study this redistribution over an ever larger angular range [402]. In central events, the redistribution of momentum carried by particles with  $p_T^{\text{trk}} > 1 \text{ GeV}$  appears to extend somewhat uniformly across nearly the full range of azimuthal angles with respect to the Z boson. These boson-tagged measurements on one side establish unambiguously the broadening of the shape of the corresponding jets. Yet, the narrowing of the jet core is not strongly evident in the measurement. This could be explained by the intrinsically higher quark content of a boson-tagged jet sample as compared to the inclusive jet sample. Alternatively, the differences in the steepness of the transverse profile, which complicate the direct comparison of the jet shape ratio between different samples, could potentially explain the deviations in boson-tagged and inclusive jet samples.

As mentioned, selection bias is one of the main difficulties for interpreting the existing experimental results. “Survival bias”, another form of selection bias, is also a significant issue for comparing the PbPb and pp results. This bias is an unavoidable consequence of jet quenching itself: selected with any given momentum threshold, any sample of HI collision jets will always be biased towards those least quenched. To “dig deeper” into the medium, a set of jet shape measurements has been performed for dijets using the dijet momentum asymmetry as a quenching control parameter [397]. This study found that both sides of a dijet (the leading and subleading) appear to be modified through interactions with the QGP medium. Even for the most asymmetric scenario considered, the leading jets shape was modified compared to a reference from pp collisions. Overall, the jet shape distributions for leading jets are the widest for events with balanced jet momenta. A possible interpretation, consistent with these observations, is that the leading jets traversing the largest average in-medium path lengths come from momentum-balanced events. In contrast, for subleading jets, the widest distributions were observed for the most unbalanced dijets. The relatively wider subleading jet shape distributions can be explained by this relationship between path length and survival bias. Alternative explanations are subject to active developments, with several recent works indicating that the dijet momentum asymmetry, dijet jet shape modifications, and even high- $p_T v_2$ , as discussed in Section 5.2.1, could also result, at least in part, from energy loss fluctuations [403, 404].

### 5.3.3 Parton-level substructure

A key feature of jet substructure is that the underlying physics can be factorized into a convolution of a pQCD-like probabilistic parton shower and non-pQCD effects including hadronization. This results in jets with a variety of topologies. In particular, jet substructure might be different in vacuum compared to jets in the QGP, where one expects a range of parton energy-loss effects. Variations in energy loss resulting from the possible impact of the in-medium path length and from fluctuations can result in jet modifications. The use of advanced algorithms that enable us to reconstruct the partonic structure of a jet can help in untangling these various processes, which is crucial for understanding the dependence of the jet topology on energy loss. The clustering tree of a reconstructed jet can be analyzed in more detail to get information about the parton splitting history. Recently, this sort of analysis has grown into an active area of research in both the experimental and theoretical regimes.

Such studies emphasize the importance of quantifying the energy loss of jets as a function of their momentum and angular scales. Observables related to jet substructure typically start with the constituents of the jet (tracks or calorimeter towers in an experiment, particles in a theoretical study) originally found via the anti- $k_T$  algorithm, followed by a reclustering with an alternative algorithm. The most common reclustering uses the Cambridge–Aachen algorithm, which enforces angular ordering in the pairing. Thus, in vacuum, one can directly associate specifically identified hard splittings found at later stages of the reclustering with wide-angle

and early-time emissions in the parton shower. The process by which a particular hard splitting is selected is termed “grooming”, which iteratively proceeds backwards through the clustering tree (i.e., declusters the jet) and requires some criterion to select a specific splitting. From a phenomenological standpoint, observables found using these groomed jets have a reduced contribution from soft, wide-angle radiation, particles from the underlying event, and multi-parton interactions, all of which are theoretically more challenging to describe. Thus, we can compare the data more accurately with theoretical calculations.

The first algorithm used to measure the groomed jet substructure in HI collisions was the soft-drop [406] groomed momentum sharing, which uses the observable  $z_g$ , defined as the momentum fraction of the first soft branch in the declustering satisfying the condition,

$$z_g = \frac{\min(p_{T,1}, p_{T,2})}{p_{T,1} + p_{T,2}} > z_{\text{cut}} \left( \frac{R_{12}}{R} \right)^\beta, \quad (25)$$

where the indices 1 and 2 identify the two branches in the clustering tree, and  $z_{\text{cut}}$  and  $\beta$  are the soft-drop parameters. The quantity  $R_{12}$  is the angle between the two branches and  $R$  is the jet distance parameter. The groomed jet distance parameter  $R_g$  is defined similarly as the angle between two such branches. For this very first HI study,  $\beta$  was set to zero and  $z_{\text{cut}}$  was set to 0.1, meaning that only the momentum fraction was required to select the first hard branch. Using data gathered in 2015 by the CMS experiment, this analysis involved PbPb and pp data samples, both obtained at  $\sqrt{s_{\text{NN}}} = 5.02$  TeV [405]. The measured ratio of the  $z_g$  distribution in the most central PbPb collisions compared to a pp reference is shown in Fig. 71, where each panel shows a different jet  $p_T$  selection. Compared to expectations based on pp data, the PbPb

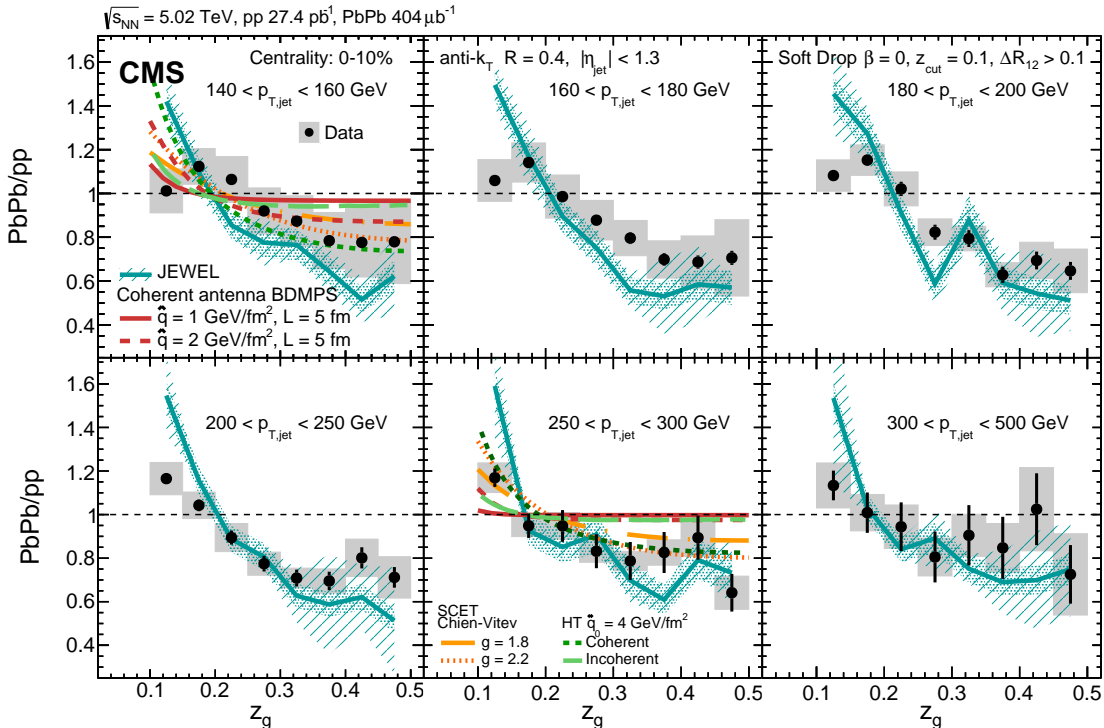


Figure 71: Distribution of the ratio of the groomed jet splitting fraction in central PbPb data compared to a pp reference. Each panel corresponds to a different jet  $p_T$  range and the different colored lines and bands are predictions from MC models. Statistical and systematic uncertainties in the data are shown by vertical bars and shaded boxes, respectively. (Figure adapted from Ref. [405].)

data show a marked suppression for jets with a larger  $z_g \approx 0.5$  and an enhancement at smaller values,  $z_g \approx 0.1$ . The ratios are also compared to different calculations and MC models, which are found to qualitatively describe the trend of the suppression. The enhancement of jets with more asymmetric splittings is consistent with expectations from jet energy loss, where jets with a single hard cluster are found more often than jets where the energy is more equally shared among multiple subclusters.

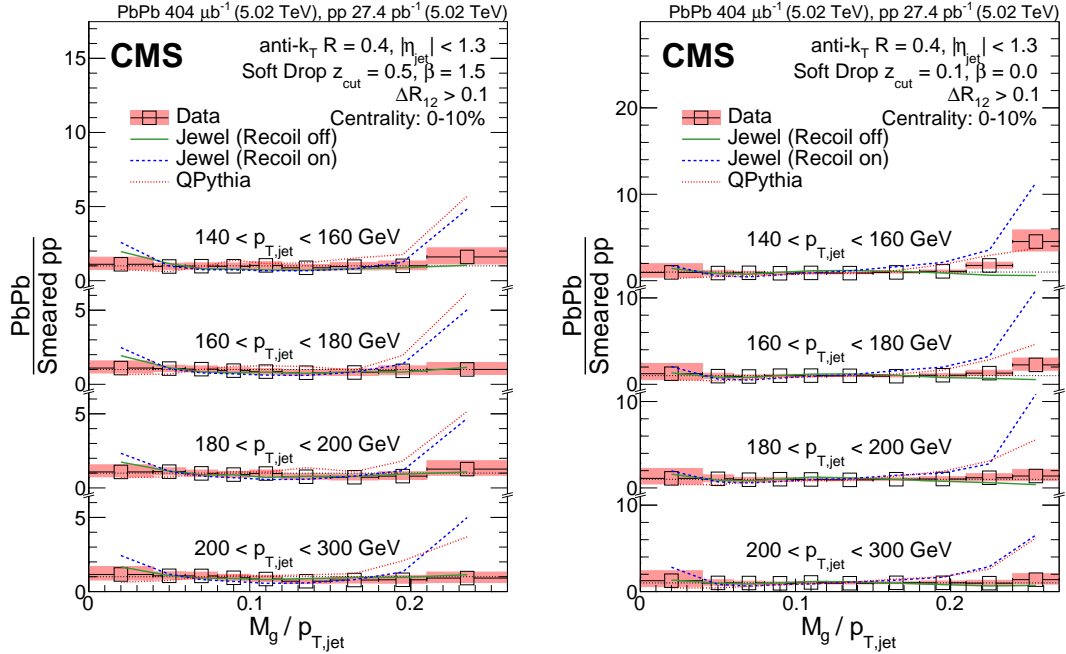


Figure 72: Distribution of the ratio of the groomed jet mass,  $M_g$ , in central PbPb data compared to the pp reference for two different grooming criteria in four ranges of jet  $p_T$ . The left panel shows more stringent grooming criteria, while the right panel shows the same measurement for the default grooming requirements. The different lines represent MC predictions; they show deviations from the data at larger masses. Statistical and systematic uncertainties in the data are shown by vertical bars and shaded boxes, respectively. (Figure adapted from Ref. [407].)

The next study of jet substructure performed using CMS data varied the grooming procedure by employing a stronger angular-dependent grooming ( $z_{\text{cut}} = 0.5, \beta = 1.5$ ) compared to the softer grooming previously used ( $z_{\text{cut}} = 0.1, \beta = 0$ ) [407]. Figure 72 shows the differential measurement of the groomed jet mass,  $M_g$ , defined as the invariant mass of the system consisting of the two subjets (normalized by the jet  $p_T$ ) for PbPb data compared to a pp reference, for jets in different ranges of  $p_T$ . The  $M_g$  variable is sensitive to both the parton splitting function and the opening angle between the two outgoing partons. The results are compared to the predictions of the JEWEL and QPYTHIA event generators. In the case of stronger grooming, no significant modification of the groomed jet mass is observed; however, there is a slight indication of enhancement for jets with larger masses in the context of weaker grooming. The indication of enhancement appears for configurations where the opening angle between the two subjets is large and one subjet has significantly more momentum than the other. The MC predictions qualitatively follow the trends in the data but significantly overestimate the enhancement effect. Note that, in contrast to what was observed for  $z_g$ , any possibility of small modifications is only present for lower- $p_T$  jets, and essentially disappears for jets of higher  $p_T$ . This is significant since the mass is an observable which convolutes both the momentum and angular scales, with sensitivity to the virtuality, where competing effects from both scales affect the distribution.

## 5.4 Studying wavelength behavior by varying parton flavor

As discussed in previous sections, high- $p_T$  jets are used to investigate the quenching of energetic partons traversing the medium, and varying flavors of the probe partons enables the study of the processes that dominate in different kinematic regions. Because their mass is larger than the QCD perturbative scale,  $m_{HQ} \gg \Lambda_{QCD}$ , as well as the typical temperature reached in HI experiments,  $m_{HQ} \gg T_{QGP}$ , heavy quarks (charm and bottom) are mainly produced by hard scatterings. This feature provides sensitivity to transport properties of the QGP across a broad  $p_T$  range, and the comprehensive coverage of phase space offers distinctive insights into various structures within the QCD medium. In this section, the role of parton flavors, their dominant processes in different  $p_T$  regions, and the corresponding implications on the nature of the QGP are discussed.

### 5.4.1 Mass dependence of energy loss

From intermediate to high  $p_T$ , within the framework of perturbative QCD, heavy quarks experience considerable energy loss through gluon radiation, similar to the situation observed for high- $p_T$  light quarks; however, the magnitude of this effect is expected to vary depending on the quark mass. First, gluons have larger color charge than quarks and are therefore expected to experience stronger energy loss. In addition, the emission of gluons is predicted to be suppressed inside an angle proportional to the ratio of the quark mass to its energy, denoted as  $m/E$  [408]. The color-charge effect and the “dead-cone” effect lead to a hierarchy of parton energy loss, where  $\Delta E_g > \Delta E_\ell > \Delta E_c > \Delta E_b$ . This flavor dependence of energy loss is studied by comparing  $R_{AA}$  of hadrons containing light and heavy quarks.

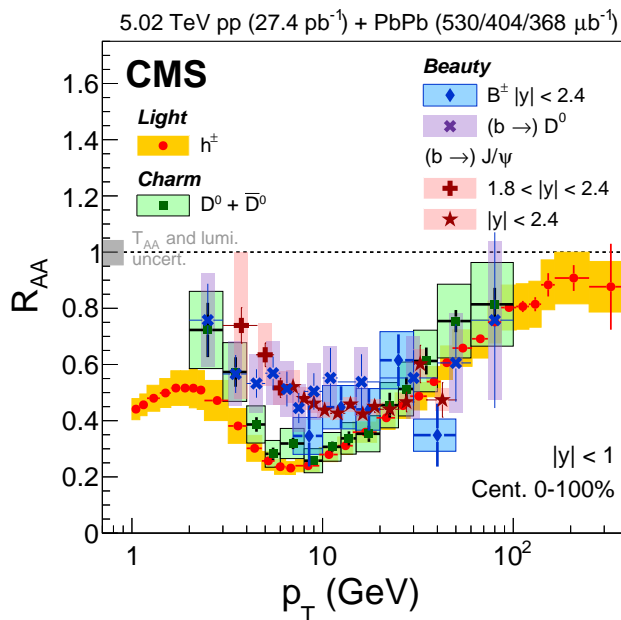


Figure 73: Nuclear modification factors of inclusive charged particles, prompt D $^0$  and B $^+$ , and nonprompt D $^0$  and J/ $\psi$  mesons, as a function of their  $p_T$  in PbPb collisions. (Figure adapted from Refs. [351, 409–412].)

As shown in Fig. 73, the nuclear modification factor ( $R_{AA}$ ) of charged particles, D $^0$  mesons, and B $^+$  mesons, as well as D $^0$  and J/ $\psi$  mesons originating from B hadron decays (nonprompt), have been measured by CMS. For  $p_T > 20$  GeV, the  $R_{AA}$  values for all particle species are similar and noticeably smaller than unity. This result suggests that both light and heavy quarks are

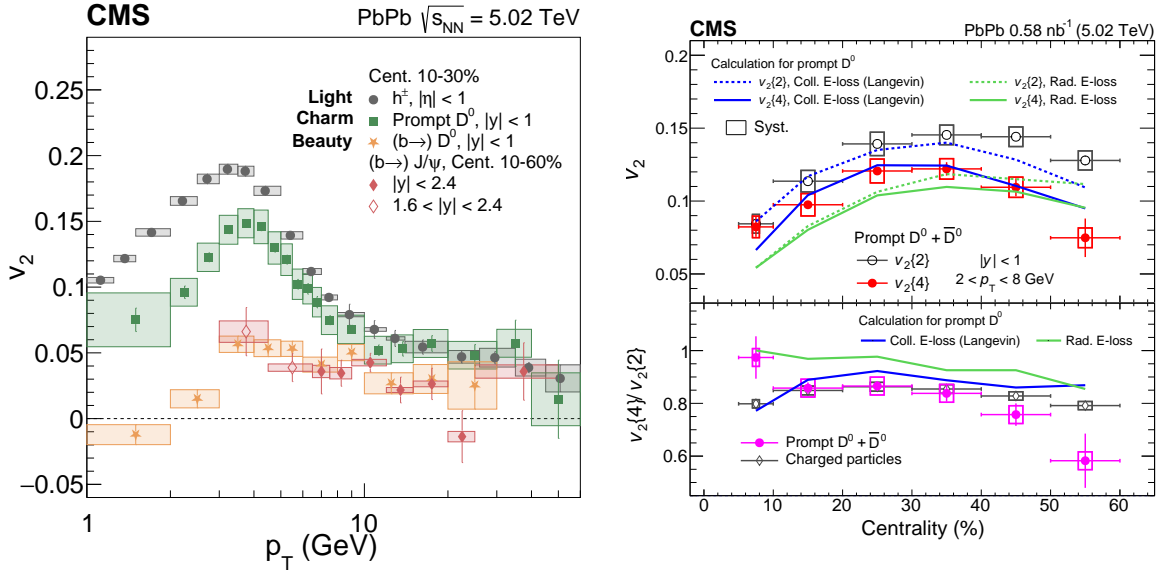


Figure 74: Left: Azimuthal anisotropy coefficient  $v_2$  of inclusive charged particles, prompt  $D^0$ , and nonprompt  $D^0$  and  $J/\psi$  mesons as a function of  $p_T$  in  $\text{PbPb}$  collisions. Right: Prompt  $D^0$  meson  $v_2\{2\}$ ,  $v_2\{4\}$  and their ratio as functions of centrality. (Figure adapted from Refs. [146–148, 361, 413].)

suppressed within the QGP, and the impact of quark mass becomes less pronounced when  $p_T$  greatly exceeds the parton mass. This behavior aligns with the expected outcome in the context of radiative energy loss. As shown in the left panel of Fig. 74, the  $v_2$  values of hadrons with different flavors at high  $p_T$  are also similar. One possible interpretation is that the diminishing effect of the parton mass on energy loss at high  $p_T$  affects not only the overall magnitude of inclusive suppression but also the dependence on path length. However, in the intermediate- $p_T$  range, the  $R_{AA}$  of nonprompt  $J/\psi$  mesons is notably larger than that of  $D^0$  mesons and charged particles, implying a less pronounced suppression of bottom quarks compared to charm and light quarks.

#### 5.4.2 Elastic energy loss and diffusion

In addition to gluon radiation, partons can also lose energy through elastic collisions with medium partons. Radiative and collisional energy loss effects dominate at high and low  $p_T$ , respectively, while intermediate- $p_T$  values serve as a transition region. Therefore, the measurement of the  $D^0$  meson  $R_{AA}$  values over a wide  $p_T$  range, as shown in Fig. 73, is ideal for studying the underlying mechanisms of parton energy loss. Theoretical models incorporating collisional energy loss can qualitatively describe the shape of the  $D^0 R_{AA}$  distribution at low  $p_T$ , while the models that do not consider radiative energy loss fail to replicate the experimental results at high  $p_T$ . Therefore, the relative significance of both contributions is determined by varying the  $p_T$ . In addition to examining the average suppression, the fluctuations of energy loss can also be studied using  $v_2$  measurements. For light-flavor particles, event-by-event geometry fluctuations have been shown to result in a difference in  $v_2$  values based on two-particle correlations and those determined using multiparticle correlations [414, 415]. This difference is shown for charged particles and prompt  $D^0$  mesons in the right panel of Fig. 74. For heavy quarks, an additional contribution coming from energy-loss fluctuations has been suggested [416].

With a large number of elastic collisions in the medium, low- $p_T$  heavy quarks can undergo

thermalization. On the one hand, thermalization of heavy quarks is delayed by effects related to the heavy quark mass  $m_{HQ}$ . This results in a relaxation time that is comparable to the lifetime of the QGP medium produced in HI collisions. Hence, the extent of thermalization of heavy quarks when the QGP medium ceases to exist becomes an indicator of their coupling strength. On the other hand, since the mass of heavy quarks is larger than the typical temperature of the expanding medium, the momentum exchange between heavy quarks and medium partons remains limited. As a consequence, their behavior is similar to “Brownian motion” and can be described by the Fokker-Planck equation [417]. The transport properties of the QGP are encoded in the coefficients that vary with temperature and momentum. In particular, the spatial diffusion coefficient  $D_s$  characterizes the long-wavelength behavior of heavy quarks and can be directly translated into the fundamental properties of the medium, such as shear viscosity (a review can be found in Ref. [418]). This theoretical insight implies a strong coupling of heavy quarks with the expanding medium, allowing them to behave collectively. Moreover, at low  $p_T$ ,  $v_2$  exhibits a distinct flavor hierarchy. This observation indicates that heavy quarks do not completely undergo thermalization and retain sensitivity to the microscopic transport properties. The spatial diffusion coefficient  $D_s$  has been constrained using measurements of the  $D^0$  meson  $R_{AA}$  and  $v_2$  carried out by multiple experiments and using various transport models [39, 419]. For instance, the obtained  $D_s$  values from a Langevin model-based Bayesian analysis in Ref. [420] rule out the pQCD calculations that characterize the weak coupling limit, but align with the predictions from lattice QCD and AdS/CFT calculations, the latter representing the strong-coupling limit for a scale-invariant gauge theory using the conjectured equivalence between a weakly coupled gravitational and conformal field theory [418]. This consistency confirms the sensitivity of charm quarks to the non-perturbative structure of the QGP.

The radial distribution of  $D^0$  mesons relative to jet axes was also studied to examine the alteration of heavy quarks. As shown in Fig. 75, there is a subtle hint that  $D^0$  mesons in the intermediate  $p_T$  range of 4–20 GeV that are associated with jets may be slightly farther away from the jet axes in PbPb collisions than in pp collisions [421]. Such measurements can provide further constraints on the role of charm quark diffusion in the QGP medium.

## 5.5 Studies of in-medium hadronization

The correct interpretation of experimental data requires a thorough understanding of both the in-medium interactions and the subsequent hadronization processes. Parton fragmentation [423] is expected to be the form of hadronization in pp collisions. In HI collisions, hadrons can be produced not only through parton fragmentation but also through other mechanisms, such as coalescence of partons inside or at the boundary of the QGP medium [424, 425]. The production of hadrons through coalescence is predicted to be most prominent for the regions of low and intermediate  $p_T$ , where the density is highest for the precursor partons and decreases with increasing hadron  $p_T$ . At high  $p_T$ , the fragmentation process is anticipated to dominate hadron production. The coalescence effect is anticipated to be more visible for heavy-flavor hadrons containing strange quarks owing to the strangeness enhancement in the QGP medium [426]. To study the heavy quark hadronization, comprehensive measurements of both charm and bottom hadrons were conducted at CMS using data taken during Runs 1 and 2 [422, 427–431]. Some of the findings are highlighted in this section.

Measurements of  $\Lambda_c^+$  baryons via the  $\Lambda_c^+ \rightarrow p K^- \pi^+$  channel [422] are presented in Fig. 76. The left panel displays the  $\Lambda_c^+/D^0$  ratio as a function of  $\Lambda_c^+ p_T$  in pp collisions at 5.02 TeV. The right panel shows the same pp data points, compared with PbPb results at the same collision energy. For  $p_T > 10$  GeV, the  $\Lambda_c^+/D^0$  ratios for pp and PbPb collisions are consistent with each other, suggesting that the coalescence process does not significantly affect  $\Lambda_c^+$  baryon produc-

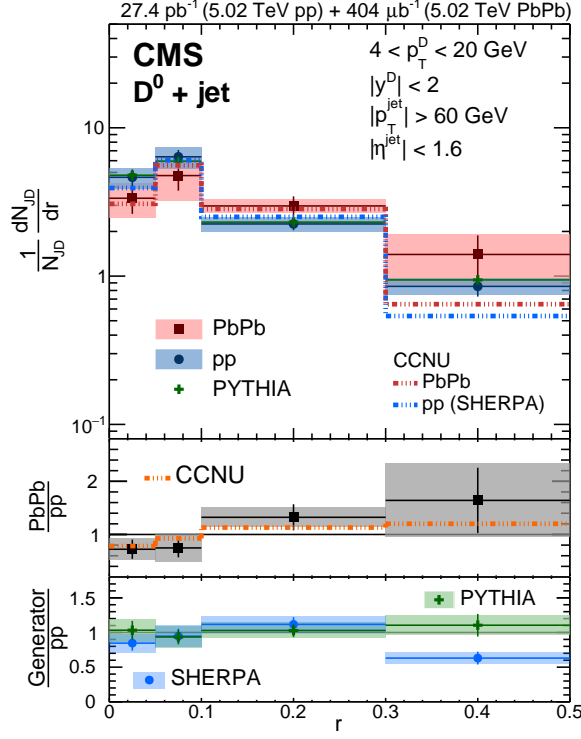


Figure 75: Distributions of  $D^0$  mesons in jets, as a function of the distance from the jet axis. The ratios of the  $D^0$  meson radial distributions in  $\text{PbPb}$  and  $\text{pp}$  data are shown in the middle panel, whereas in the lower panel the ratios of the  $D^0$  meson radial distributions of  $\text{pp}$  over the two MC event generators are presented. (Figure adapted from Ref. [421].)

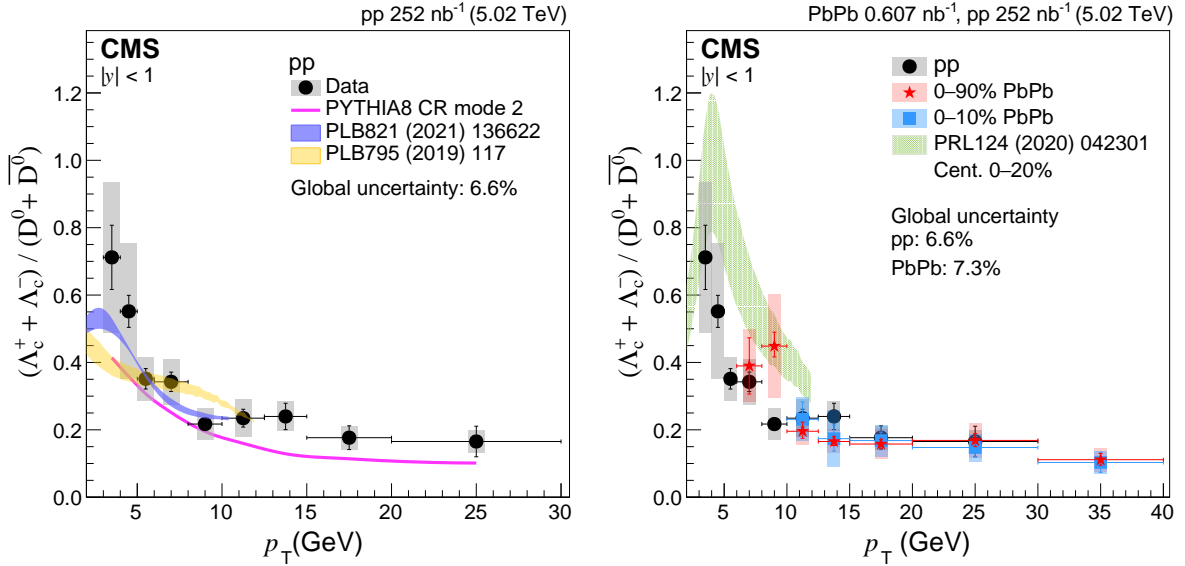


Figure 76: The ratio of the production cross sections of prompt  $\Lambda_c^+$  to prompt  $D^0$  versus  $p_T$  from  $\text{pp}$  collisions. The data are compared to various models (left) and to similar measurements in  $\text{PbPb}$  collisions (right). (Figure adapted from Ref. [422].)

tion in this  $p_T$  region. The  $\Lambda_c^+/\bar{D}^0$  ratio in all collision systems are observed to be much higher than that in  $e^+e^-$  collisions for  $p_T < 30 \text{ GeV}$ , which is around 0.1 with mild  $p_T$  dependence. To further understand the implications of the measurements for  $\Lambda_c^+$  production, the results are

compared with predictions of various models. The color reconnection mechanism [432] implemented in PYTHIA8 enhances baryon-to-meson ratios in pp collisions by considering the string fragmentation to be color connected in a way that the total string length becomes as short as possible. This prediction (shown by the CR2 prediction displayed as a purple line in the left panel of Fig. 76) is consistent with the pp measurement for  $p_T < 10$  GeV, but is systematically lower than the data at higher  $p_T$ . A model involving both coalescence and fragmentation in pp collisions [433], shown by the blue band, describes the pp measurements well after it is tuned using previous CMS measurements [430]. It is worth mentioning that the Catania model [433] assumes the formation of a QGP medium in pp collisions. Another model, displayed as a yellow and green band in the left and right panels, respectively, adopts a statistical hadronization approach and takes into account decays of excited charm baryon states [434, 435]. It provides a reasonable description of the measurements in pp and PbPb collisions for  $p_T < 12$  GeV.

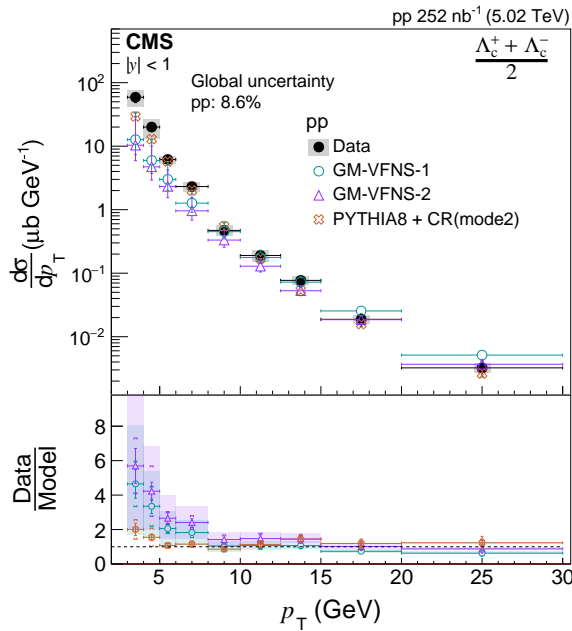


Figure 77: The  $p_T$ -differential cross sections for prompt  $\Lambda_c^+$  baryon production in pp collisions, together with model calculations. (Figure adapted from Ref. [422].)

Figure 77 shows the  $p_T$ -differential cross sections for prompt  $\Lambda_c^+$  production in pp collisions [422]. In addition to the previously discussed model of PYTHIA8 with color reconnection, the results are compared to calculations using the general-mass variable-flavor-number scheme (GM-VFNS) [436, 437]. The GM-VFNS calculations use fragmentation functions derived from fits to measurements from the OPAL and Belle experiments. While these calculations accurately describe the  $D^0$  cross section [409], they significantly underestimate the  $\Lambda_c^+ / D^0$  ratios measured in pp collisions. The  $\Lambda_c^+$  baryon yield in pp collisions is also considerably higher than the GM-VFNS calculation, indicating a breakdown of the universality of charm quark fragmentation functions.

CMS has performed extensive studies of flavor-identified B hadrons, including the first observation of  $B_s^0$  and  $B^+$  production, and evidence of  $B_c^+$  meson production, in PbPb collisions. Measurements of  $B_s^0$ ,  $B^+$ , and  $B_c^+$  mesons [429] in PbPb collisions are presented in Fig. 78. The left panel displays the  $B_s^0 / B^+$  yield ratio as a function of  $p_T$  in PbPb collisions, together with the LHCb measurements in pp collisions at 7 TeV [438], scaled by the branching fraction ratio serving as a baseline for PbPb results. The PbPb measurement is consistently above the pp result; however, due to substantial uncertainties, no significant dependence on  $p_T$  and centrality

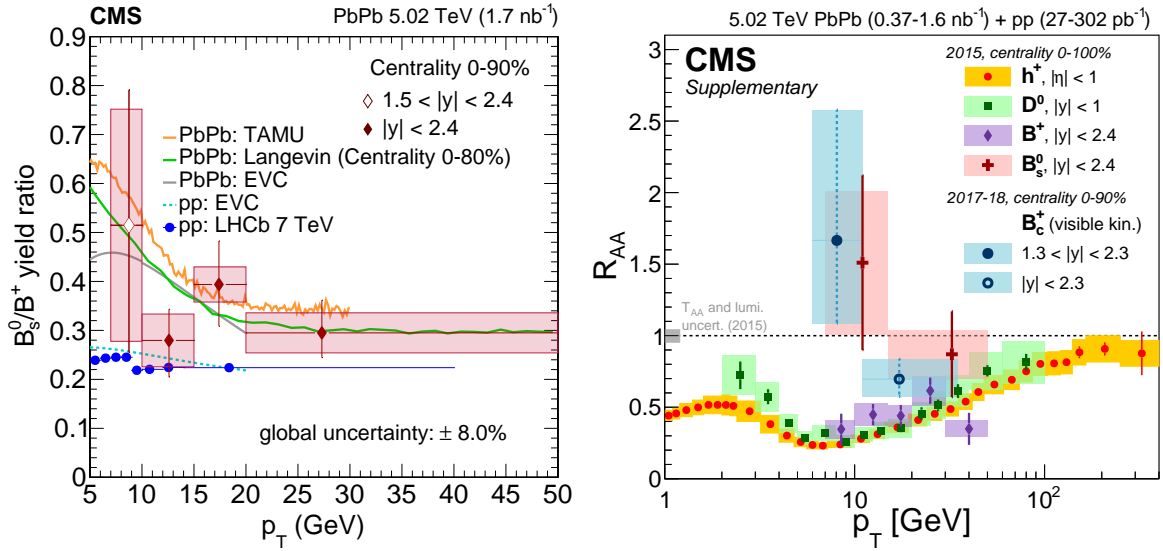


Figure 78: Left: The ratio of  $B_s^0$  and  $B^+$  production yields as a function of  $p_T$  in pp and PbPb collisions, together with model calculations. Right: The nuclear modification factor of  $B_c^+$  and other hadrons in PbPb collisions. (Figure adapted from Refs. [428, 429].)

can be established. It should be noted that the pp ratio at forward rapidity, as measured by LHCb, may be different from that at mid-rapidity. The results are compared with several models, including a transport model based on a Langevin equation that incorporates collisional energy loss and heavy quark diffusion in the medium [439], an advanced Langevin hydrodynamic model [440], and a quark combination model using the equal-velocity combination approximation [441]. All models predict a significant enhancement at low  $p_T$  attributed to the coalescence contribution to  $B_s^0$  production and are in agreement with the data. The right panel of Fig. 78 displays the nuclear modification factor of  $B_c^+$  meson in PbPb collisions in comparison with other hadrons. The  $B_c^+$  meson, composed of a charm quark and a bottom antiquark, bridges the gap between the ground states of charmonia and bottomonia in size and binding energy. The modification of the  $B_c^+$  meson production in PbPb collisions can offer additional insights into the interaction of heavy quarks with the medium. Due to the small production cross section of the  $B_c^+$  meson, the coalescence contribution could potentially be more significant. Although the suppression levels of  $B_c^+$  and  $B_s^0$  production align with those of other hadrons in the high- $p_T$  region, both of them show a reduced level of suppression at low  $p_T$ . This consistency suggests an enhancement in their production through coalescence. To draw more conclusive insights into the B meson hadronization process, future measurements with increased precision are needed.

To study the coalescence effect with a larger number of valence quarks, CMS has presented the first evidence for  $X(3872)$  production in HI collisions, using the  $J/\psi \pi^+ \pi^-$  decay channel [431]. Although it is generally agreed that the  $X(3872)$  state—the first discovered exotic hadron—is composed of four valence quarks, its internal structure remains under discussion and several options have been proposed for its composition, including charm-anticharm quark pairs, charm meson molecules, tetraquarks, and their mixtures. In HI collisions, the production yield of the  $X(3872)$  state, which is affected by the rate of coalescence and dissociation, should depend on its internal structure [442–444]. Figure 79 depicts the ratio between the prompt  $X(3872)$  and the  $\psi(2S)$  production yields in PbPb collisions, alongside the pp results [445–447]. The measurement suggests that, in PbPb collisions, either the  $X(3872)$  state is not suppressed with respect to its pp production yield or it is suppressed at a level similar to that of the  $\psi(2S)$ .

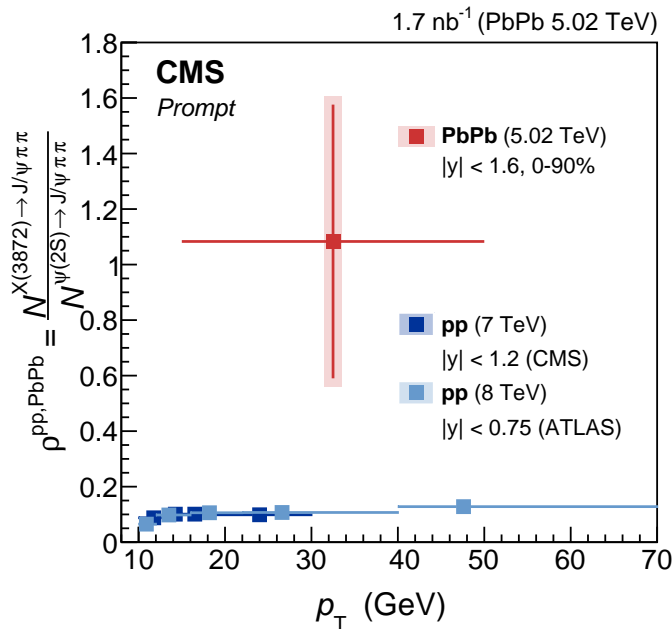


Figure 79: The yield ratio  $\rho^{\text{PbPb}}$  of prompt  $X(3872)$  over  $\psi(2S)$  production in pp and PbPb collisions as a function of  $p_T$ . (Figure adapted from Ref. [431].)

## 5.6 Quarkonium production and suppression in PbPb collisions

The suppression of quarkonium states in high-energy HI collisions was first proposed as a signature of QGP formation in a famous paper published by T. Matsui and H. Satz in 1986 [448]. The basic idea is rather simple: heavy quarkonium states (i.e., bound states of the charmonium and bottomonium families) should be produced less frequently as we move from small-system collisions (such as pp, pPb, or peripheral PbPb collisions) to increasingly central HI collisions because the color-charge distribution of the created QGP screens away the potential that binds together the two heavy quarks. This conjecture leads to a definite and characteristic prediction: for a given medium temperature, the level of suppression should be different for the various quarkonium states and follow a sequential hierarchy, reflecting the different values of binding energy (i.e., the difference between the mass of the particle and twice the mass of the lightest corresponding open-flavor meson) [449, 450]. In other words, the more strongly bound the considered quarkonium state is, the hotter must be the medium before we start seeing signs of its suppression. This means, in particular, that the more loosely bound states should be suppressed already in relatively peripheral HI collisions, while the states with the largest binding energies should only show signs of being suppressed in the most head-on nucleus-nucleus collisions.

While the prediction that deconfinement produces a sequential suppression of the quarkonium states is intuitively straightforward and potentially translates into qualitatively well-defined production patterns, in practice there are many challenges that need to be overcome before it can be reliably and cleanly compared with experimental measurements.

### 5.6.1 Quarkonium suppression: context and challenges

The first hurdle, already faced when interpreting the first charmonium suppression measurements from the SPS experiments NA38, NA50, and NA60 [451–453], is that the quarkonium production yields also decrease in the absence of a QGP medium. For example, the production

of  $J/\psi$  mesons has been firmly established in pA collisions [454–456] to increase at a rate that is less than linear with the mass number of the target nucleus. This behavior can seemingly be attributed to a range of cold nuclear matter (CNM) effects, which include nuclear modifications of parton densities, multiple collisions of the final-state resonance with nucleons of the target nuclei resulting in the disintegration of the meson, and effects of energy loss and transverse momentum broadening. These CNM effects vary with the rapidity and  $p_T$  of the produced meson, as well as with the center-of-mass energy of the collision. Additionally these effects act distinctively on different quarkonium states, leading to a more pronounced absorption of the more loosely bound states. For example, the  $\psi(2S)$  meson production has been observed to experience a greater reduction than  $J/\psi$  production, even in the absence of a QGP medium [454–460].

Another important challenge is that we do not yet know sufficiently well, even for the most copiously produced ground states,  $J/\psi$  and  $Y(1S)$  mesons, and for the baseline reference pp collisions, the fraction of the observed yields corresponding to *directly* produced mesons, as opposed to those created in feed-down decays of heavier quarkonia. This aspect is of critical importance in any endeavor to interpret the quarkonium suppression measurements. For the sake of illustration, let us consider a scenario in which only 50% of the observed  $Y(1S)$  yield in pp collisions can be attributed to direct production. This reasonable assumption is supported by LHCb measurements at forward rapidity [461] and trends extrapolated from midrapidity LHC cross sections [462, 463]. Additionally, let us further restrict this scenario to the limiting case where the heavier (S- and P-wave [464]) states, accounting for the other half of the  $Y(1S)$  yield through feed-down decays, are no longer produced in central PbPb collisions because they dissociate in the QGP (given their weaker binding). Then, we would only observe 50% of the  $Y(1S)$  yield and might be tempted to wrongly infer that there is a very strong suppression of the direct  $Y(1S)$  production, contradicting expectations based on its relatively large binding energy. Therefore, a reliable interpretation of the experimental results must carefully account for how the QCD medium impacts not only the directly produced particle under examination but also all the relevant feed-down sources, each with their specific characteristics.

One further complication affecting the theory-to-data comparisons has to do with the polarizations assumed for the different quarkonium states. In fact, there is a correlation between the assumed polarizations and the measured feed-down fractions. We can realistically assume, for example, that around 25% of the observed (promptly produced)  $J/\psi$  mesons come from decays of the  $\chi_{c1}$  and  $\chi_{c2}$  states [465, 466]. However, this assumption arises from measurements of the  $(\chi_{c1} + \chi_{c2}) / J/\psi$  cross section ratio, and these results depend on the polarizations assumed for these three states, which affect the calculation of the detection acceptances. Reasonable variations in the assumed polarization scenarios, including nonnegligible changes as a function of  $p_T$  (e.g., from longitudinal to transverse polarizations when  $p_T$  increases) can easily lead to  $\chi_c$  feed-down fractions significantly different from 25%.

It should be clear by now that it is challenging to achieve compelling experimental evidence that confirms (or rules out) the existence of a sequential suppression mechanism. A crucial element in the path to reliably probe that prediction is to collect high-precision data, both in pp and in HI collisions, of as many quarkonium states as possible, including not only the S-wave vector states ( $J/\psi$ ,  $\psi(2S)$ ,  $Y(1S)$ ,  $Y(2S)$ , and  $Y(3S)$ ) but also the  $\chi_{c1}$  and  $\chi_{c2}$  states, and the corresponding  $\chi_{bJ}(nP)$  states in the bottomonium family. To set the baseline reference, we need to measure, in pp collisions, the double-differential cross sections, in rapidity and  $p_T$ , as well as the corresponding polarizations, for as many states as possible. This will allow us to define a detailed matrix with all of the feed-down fractions and polarizations. We also need, naturally, detailed measurements of quarkonium production yields in PbPb collisions, as

functions of collision centrality, also paying attention to the explored kinematics phase space. Measurements made with pPb collisions should help in understanding the relevance of the CNM effects mentioned above.

Lastly, to probe the existence of the sequential quarkonium suppression signal, it is important to restrict the theory-to-data comparisons to events that are not substantially affected by background processes. In particular, low- $p_T$  charmonia should be excluded from our investigations because they might be dominated by mesons composed of quarks produced in uncorrelated nucleon-nucleon collisions, a phenomenon known as coalescence, recombination, or regeneration [467, 468].

In the remainder of this section, we will present a selection of the CMS measurements that we consider as important milestones in the challenging path just mentioned. More specifically, we summarize the  $R_{AA}$  patterns that CMS measured for the  $J/\psi$ ,  $\psi(2S)$ ,  $Y(1S)$ ,  $Y(2S)$ , and  $Y(3S)$  quarkonia, for PbPb collisions at  $\sqrt{s_{NN}} = 5.02$  TeV, as a function of collision centrality. These suppression patterns, together with the feed-down and polarization inputs mentioned above, are the most crucial inputs for global analyses [469] testing whether the binding energy hierarchy at the core of the sequential suppression conjecture provides a reliable explanation of the experimental data. In addition, pioneering, high-precision  $v_2$  measurements of various quarkonium states and results on the fragmentation of  $J/\psi$  mesons in jets are also discussed, providing crucial information about quarkonium formation.

### 5.6.2 Measurements of quarkonium suppression in PbPb collisions

The most recent CMS publication on charmonium production and suppression in PbPb collisions [412] provides a rather complete and diversified set of  $R_{AA}$  measurements based on pp and PbPb data collected in 2015. Measurements are reported for the promptly produced  $J/\psi$  mesons (directly produced or coming from feed-down decays of heavier charmonia) as well as for the nonprompt mesons, originating from decays of b hadrons. The two components can be resolved thanks to the separation of the  $J/\psi \rightarrow \mu^+ \mu^-$  decay vertex from the primary collision vertex. We can see, in particular, how the  $R_{AA}$  changes with the collision centrality (using the  $N_{part}$  variable), as well as with the meson's  $p_T$  and rapidity, for both prompt and nonprompt  $J/\psi$  mesons. Among the more differential results, the CMS measurements include dependences with  $p_T$  and  $N_{part}$  for two rapidity ranges, as well as with  $p_T$  for several  $N_{part}$  ranges and vice-versa, both for central and forward rapidity.

Particularly interesting for the studies of sequential suppression, the  $\psi(2S)$  and  $J/\psi$   $R_{AA}$  patterns are reported as a function of  $N_{part}$  for  $p_T > 6.5$  GeV, in the central rapidity range  $|y| < 1.6$ , as shown in the upper left panel of Fig. 80. The  $\psi(2S)$   $R_{AA}$  values are derived by using the  $\psi(2S)/J/\psi$  double ratio previously reported in Ref. [471] and shown in the lower left panel. No significant dependence on rapidity is observed, in the  $|y| < 2.4$  range. Also the dependence on  $p_T$  is rather mild, at least in the  $6.5 < p_T < 20$  GeV range. Instead, we see a rather strong centrality dependence, the production yields being increasingly suppressed as the collisions become more central, for both the prompt  $J/\psi$  and  $\psi(2S)$  cases, as well as for the nonprompt  $J/\psi$  mesons. Most crucially for the investigation of sequential suppression, it is evident that the yield of  $\psi(2S)$  mesons is notably more suppressed than that of the  $J/\psi$  mesons, with this stronger suppression becoming apparent even in the most peripheral PbPb collisions covered by the collected data.

The upper right panel of Fig. 80 shows the centrality-dependent  $R_{AA}$  patterns for the  $Y(1S)$ ,  $Y(2S)$ , and  $Y(3S)$  states. Contrary to the charmonium results, the  $Y(nS)$   $p_T$  reach starts at  $p_T = 0$  GeV. This arises from the higher  $Y(nS)$  mass, which enables the muons to reach the

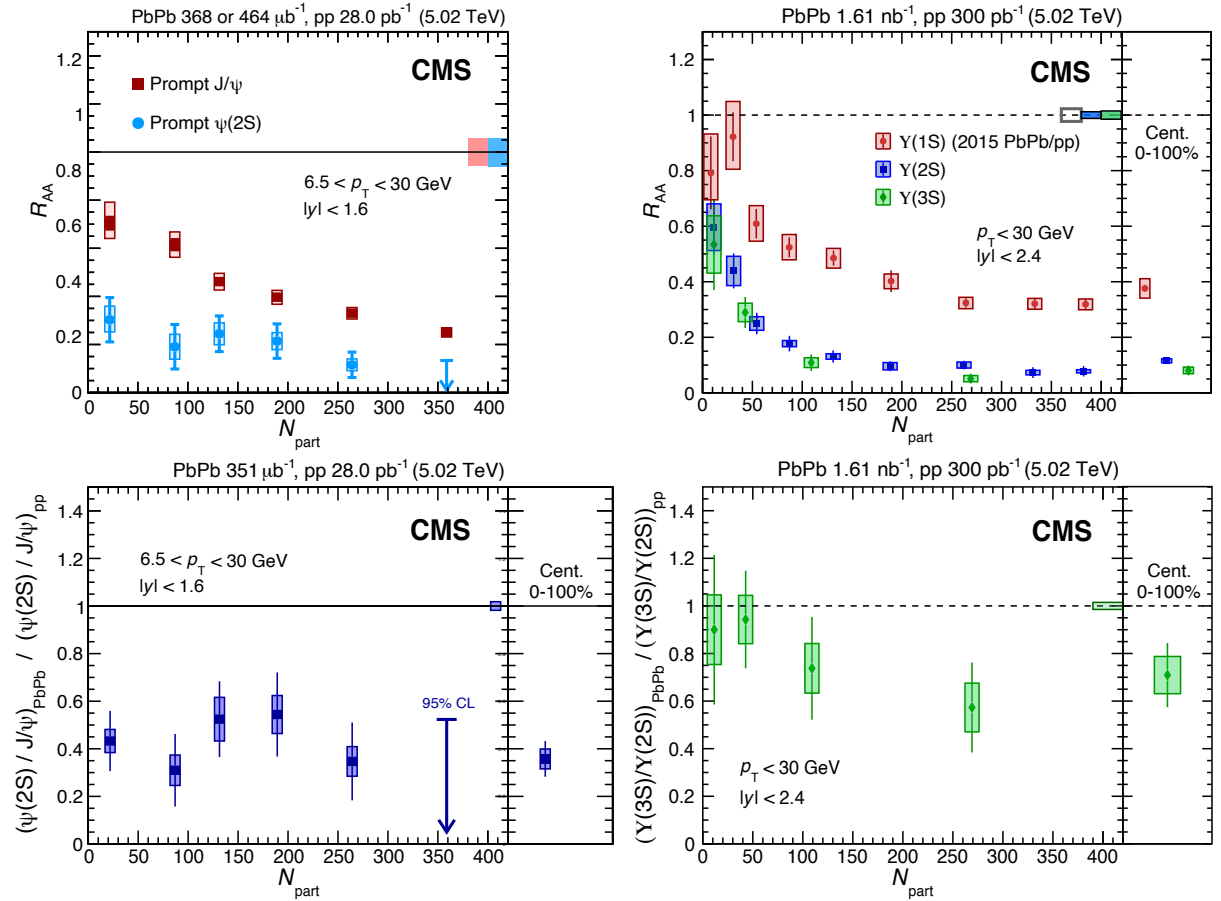


Figure 80: Upper: Nuclear modification factors, as a function of the mean number of participants, for the promptly-produced  $J/\psi$  and  $\psi(2S)$  mesons (left), as well as for the  $Y(1S)$ ,  $Y(2S)$ , and  $Y(3S)$  (right), as measured from pp and PbPb data at 5.02 TeV. Lower: Corresponding  $\psi(2S)/J/\psi$  (left) and  $Y(3S)/Y(2S)$  (right) double-ratios. (Figure adapted from Refs. [412, 470, 471].)

CMS muon detectors even if their parent particle is generated at rest. It is to be noted that the likelihood of more than one pair of beauty quarks being produced in each PbPb collision remains quite low, even at LHC collision energies, so that our results should be essentially unaffected by the coalescence process, even in the low- $p_T$  region, which is more likely to influence the charmonium case.

It is worth emphasizing here that the measurement of  $Y(3S)$  production represents a remarkable *tour de force*, given its small production rate. In a previous CMS publication [472], the  $R_{AA}$  of the  $Y(1S)$  and  $Y(2S)$  states could be properly studied, while only upper limits were reported for the  $Y(3S)$  state. Benefiting from the larger luminosity recorded in 2018 (Table 1), the new analysis [470] succeeds in observing the  $Y(3S)$  peak in the dimuon mass distribution with a significance well above five standard deviations, as shown in Fig. 81, thanks to a state-of-the-art analysis method that uses boosted decision trees to reduce the large yield of background muon pairs and, hence, obtain a signal-enriched dimuon sample. Another important aspect that makes this measurement feasible is the rather good dimuon mass resolution (0.6% at midrapidity), enabling the observation of well-resolved invariant mass peaks for the  $Y(2S)$  and  $Y(3S)$  excited states. Finally, we should not forget that the bottomonium production cross sections are much smaller than those of the charmonium states, so that their studies also require large integrated luminosities, efficient triggers, and the allocation of suitable DAQ

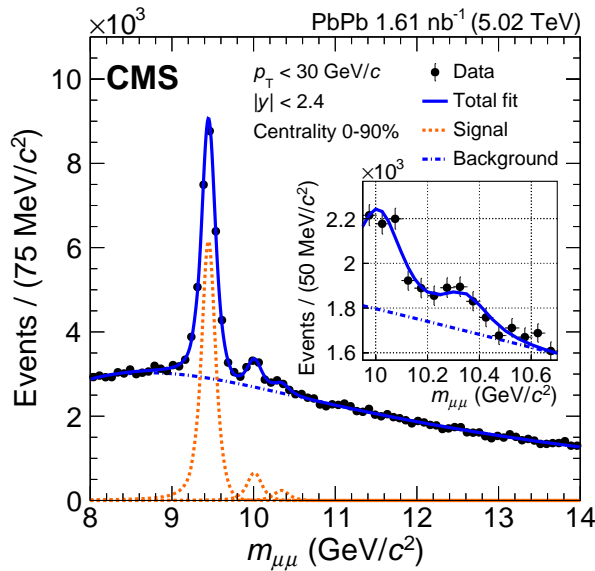


Figure 81: The dimuon invariant mass distribution measured in PbPb collisions when integrating over the full kinematic range of  $p_T < 30$  GeV and  $|y| < 2.4$ . The solid curves show the fit results, and the orange dashed and blue dash-dotted curves display the three Y states and the background, respectively. The inset shows the region around the Y(3S) meson mass. (Figure adapted from Ref. [470].)

(permanent storage) bandwidths. All of the above points explain why CMS is particularly well suited, among the LHC experiments, to probe the physics of bottomonium production in HI collisions. An additional challenge in the observation of the Y(2S) and Y(3S) states in PbPb collisions is that their production rates are considerably suppressed, much more than the Y(1S) state, with respect to the linear scaling with  $N_{\text{coll}}$  from pp collisions. This is especially true for the Y(3S) state and is most pronounced in the most central PbPb collisions, as shown in the lower right panel of Fig. 80.

Looking at all the patterns shown in Fig. 80 allows us to clearly see that the  $\psi(2S)$  meson is particularly fragile, not surprisingly if we consider that it is the most weakly bound state, with a binding energy of only 44 MeV, barely 1% of the meson's mass [464]. On the other hand, the  $J/\psi$  and Y(1S) states are the least suppressed ones, presumably also related to their much larger binding energies of 633 and 1099 MeV, respectively. As previously mentioned, a thorough examination of the  $R_{\text{AA}}$  patterns of the five quarkonia can only be made by also accounting for the presence of poorly known feed-down decays stemming from S- and P-wave quarkonium states, and their respective binding energies. Nevertheless, the present measurements provide a strong indication that we indeed see signs of nuclear suppression effects that have a stronger (sequential) effect on the more weakly bound states.

### 5.6.3 Other $J/\psi$ production measurements

To understand quarkonium production, it is also important to know if there is a parton shower contribution, in addition to the standard (mostly gluon fusion) production term. For such studies, CMS measured distributions of the jet fragmentation variable  $z$ , the ratio of the  $J/\psi$   $p_T$  to the jet  $p_T$ , in both pp and PbPb collisions. The normalized  $z$  distribution of prompt  $J/\psi$  in pp collisions is shown in Fig. 82. Unlike what is seen from a sample of prompt  $J/\psi$  particles generated with PYTHIA8 (red line), where the mesons are produced in the initial-state partonic scattering, the measured distribution (black squares) shows a larger yield at low  $z$

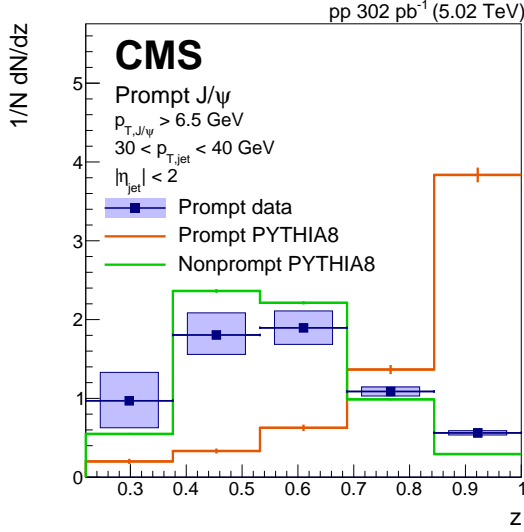


Figure 82: Normalized  $z$  distribution of  $J/\psi$  mesons in jets measured in pp collisions at 5.02 TeV, compared to prompt and nonprompt  $J/\psi$  in PYTHIA8. (Figure adapted from Ref. [473].)

values, where the surrounding jet activity is more important. The  $z$  distribution in data more closely resembles that of the nonprompt  $J/\psi$  PYTHIA8 simulation (green line), which contains a larger jet-like component from fragmentation, as well as other products of the  $b$ -hadron decay. This suggests a significant parton shower contribution to  $J/\psi$  production, indicating that parton energy loss in the QGP should also contribute to the suppression of the observed quarkonium yield.

Moreover, insights into the comparison between open and hidden charm particles are sought by examining the prompt  $J/\psi$  and  $D^0$   $R_{AA}$  values. As shown in the left panel of Fig. 83, the prompt  $J/\psi$  and  $D^0$  mesons have similar  $R_{AA}$  patterns as a function of  $p_T$ , suggesting a similar jet quenching mechanism. The  $R_{AA}$  values of the prompt  $J/\psi$  mesons as a function of  $z$ , shown

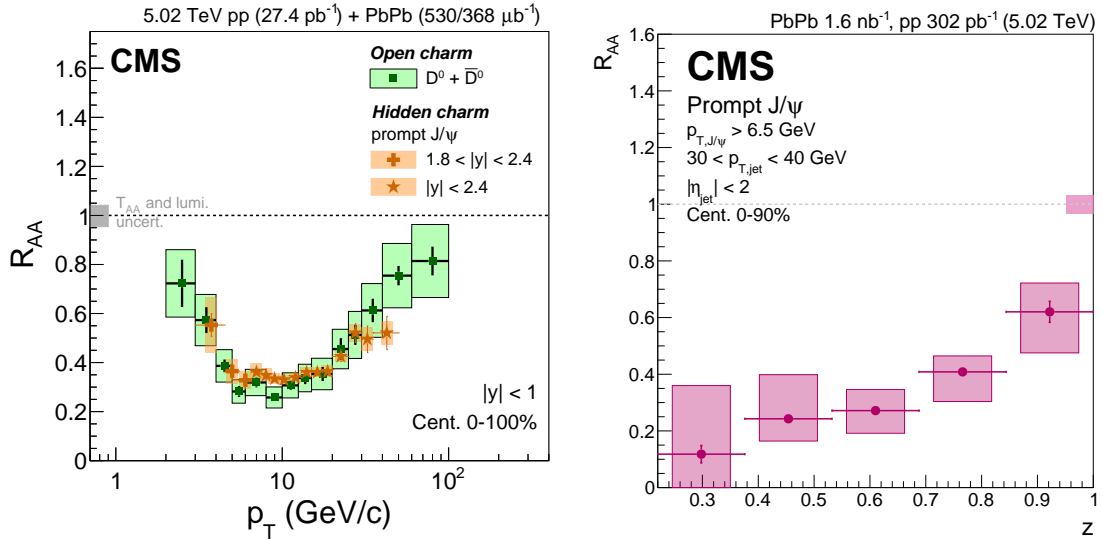


Figure 83: Nuclear modification factors  $R_{AA}$  for the promptly-produced  $J/\psi$ , as a function of  $p_T$ , compared with  $D^0$  mesons (left) and as a function of  $z$  (right), as measured from pp and PbPb data at 5.02 TeV. (Figure adapted from Refs. [409, 412, 473].)

in the right panel of Fig. 83, present a consistent picture: the suppression is stronger at small  $z$ , where the large parton multiplicity is expected to result in a large degree of interaction with the QGP.

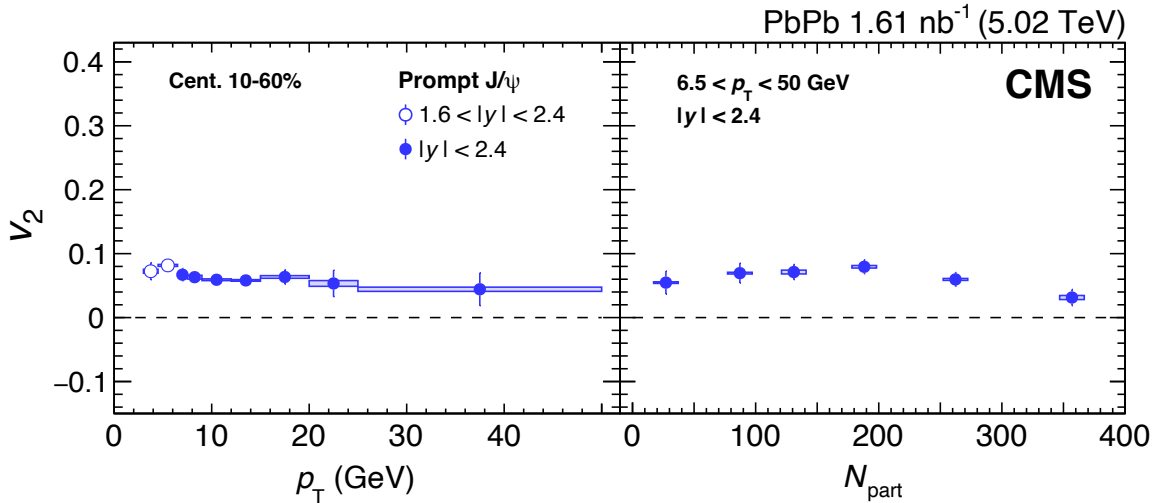


Figure 84: The prompt  $\text{J}/\psi$   $v_2$  as a function of  $p_{\text{T}}$  (left) and  $N_{\text{part}}$  (right), in  $\text{PbPb}$  collisions at 5.02 TeV. (Figure adapted from Ref. [413].)

Figure 84 shows that prompt  $\text{J}/\psi$  mesons have significant and positive  $v_2$  values, over a wide kinematic range. At low  $p_{\text{T}}$ , the  $\text{J}/\psi$   $v_2$  values can be attributed to collective hydrodynamic flow, as found for charged hadrons, while at high  $p_{\text{T}}$ , where the hydrodynamical effects are expected to vanish, the non-zero  $v_2$  values suggest a source of path-length-dependent parton energy loss.

## 5.7 Summary of hard probes in the QGP

The CMS Collaboration has used hard scatterings in HI collisions as a powerful toolset for probing the QGP at short length scales. High- $p_{\text{T}}$  objects such as jets, hadrons, electroweak bosons, and heavy-flavor quarks, along with more complex event types such as dijets, heavy-flavor jets, and photon-jet pairs, have been instrumental in revealing the intricate dynamics of the QGP. The extensive data collected during LHC Runs 1 and 2, combined with the broad tracking and calorimeter coverage of the CMS detector, have facilitated a comprehensive exploration of these hard probes.

Early results using data from LHC Run 1 for  $\text{PbPb}$  collisions identified significant dijet  $p_{\text{T}}$  asymmetries and suppressed jet and hadron nuclear modification factors, confirming the presence of and expanding the available data related to jet quenching in the QGP. Subsequent studies have deepened our understanding of the path-length dependence of parton energy loss, although a clear observation of the color-charge dependence of jet quenching remains elusive. Events with back-to-back electroweak boson-jet pairs have allowed the determination of absolute jet energy loss, while also highlighting potential selection biases when comparing jets in pp and  $\text{PbPb}$  collisions.

The internal structure of jets is heavily modified by the QGP, as revealed by measurements of jet fragmentation functions and shapes. These results suggest that jet quenching not only reduces jet energy, but also redistributes it from high- $p_{\text{T}}$  constituents to softer particles and from small to large angles relative to the jet axis. Newer jet grooming techniques have offered insights into the earliest stages of parton shower evolution within the QGP, indicating that the groomed jet

mass remains relatively unmodified, potentially linking jet evolution to initial parton splittings.

The CMS Collaboration has systematically studied the mass dependence of quark energy loss, comparing  $R_{AA}$  and  $v_2$  for light, charm, and beauty hadrons across a wide  $p_T$  range. At high  $p_T$ , these hadrons exhibit similar suppression, consistent with radiative energy loss processes. However, at lower  $p_T$ , a flavor hierarchy emerges, indicating increased quark diffusion and elastic collisions. Heavy-flavor hadronization has been investigated through ratios of baryon to meson yields, revealing that coalescence effects are minimal for  $p_T > 6$  GeV, although beauty mesons with strange or charm quarks show slightly enhanced  $R_{AA}$  values, hinting at possible coalescence effects.

Quarkonium suppression studies have provided crucial insights into the sequential suppression conjecture, which links quarkonium suppression in the QGP to their binding energies. Significant suppression of  $\psi(2S)$  and  $Y(3S)$  mesons, even in peripheral PbPb collisions, highlights their fragility, while  $J/\psi$  and  $Y(1S)$  states exhibit milder suppression because of their stronger binding. These findings advance our understanding of how quarkonium binding energies influence suppression in high-energy nuclear collisions.

The ongoing increase in LHC luminosity will enable more detailed studies of hard probes, particularly in quarkonium production, for which the CMS detector is exceptionally well-suited. The hard scales associated with these probes provide vital connections to pQCD theory, aiding in the theoretical interpretation of the observables and enhancing our understanding of high-density QCD.

## 6 Studies of high-density QCD in small collision systems

Before the first LHC data became available, the primary objective of studying small collision systems, such as pp and pA collisions, was to provide essential reference measurements that represent interactions in the absence of QGP formation. The data obtained from pp collisions offered valuable insights into particle production and hadronization without the complexities introduced by a nuclear initial state. Similarly, pA reference data were used to extract information about CNM effects by comparing them to results from pp collisions. However, in 2010, the CMS experiment made an unexpected breakthrough. By analyzing two-particle correlations in pp collisions with high multiplicities using a specially designed trigger, a long-range near-side ridge signal was found. This discovery challenged the prevailing understanding of pp collisions and suggested the potential existence of collective behavior within these systems (discussed in Refs. [474, 475]). Moreover, the observation of collectivity in pPb collisions, using multiparticle correlations, has significantly broadened the scope of flow-like correlation studies. The comprehensive exploration of collectivity signals in various small systems revealed a remarkable similarity between high-multiplicity pp, pPb, and PbPb collisions.

These groundbreaking discoveries demonstrated the emergence of collectivity in small collision systems and offered possible indications of QGP formation. This unexpected connection between high-multiplicity pp, pPb, and PbPb collisions led to a substantial paradigm shift in our understanding of the prerequisites for QGP formation. The investigations of flow-like phenomena with CMS expanded to smaller systems like  $\gamma p$  in UPC pPb collisions. These studies were complemented by examining archived ALEPH data for similar phenomena in  $e^+e^-$  collisions, where recent claims suggest possible indications of flow-like effects, and in eA collisions at HERA. Nonetheless, no definitive collectivity signal has been detected in these latter searches.

This section summarizes CMS results in small collision systems, detailing first the particle production and hadronization studies, followed by investigations into collectivity with soft probes, analysis of quarkonia production in pp and pPb collisions, and finally a discussion of the search for jet quenching signals.

### 6.1 Particle production and hadronization

The CMS Collaboration has conducted several measurements and comparisons in pp and pPb collisions at the LHC. For the studies of inclusive particle production in small collision systems, pseudorapidity distributions of primary charged hadrons have been measured in pp, pPb, XeXe, and PbPb collisions at various collision energies. These measurements are intriguing not only for the insights they provide about particle production but also for their vital role in calibrating other physics objects, such as jets and isolated photons.

As shown in Fig. 85, the pseudorapidity spectra in pPb collisions feature an asymmetrical shape with a higher density in the lead-going direction. Although all theoretical models largely capture the asymmetric shape, the magnitude is better described by KLN, EPOS LHC, and HIJING 2.1 with shadowing. The comparison to the HIJING generator underscores the importance of including the shadowing effect. The pseudorapidity density normalized by the number of participating nucleons in pPb collisions can be compared to pp and AA data. The non-single-diffractive pPb results at 5.02 and 8.16 TeV align with the results from inclusive pp collisions, which are significantly lower than the NSD pp and AA results. The data illustrate that AA collisions have a higher efficiency in converting energy into charged particles than pp and pPb collisions.

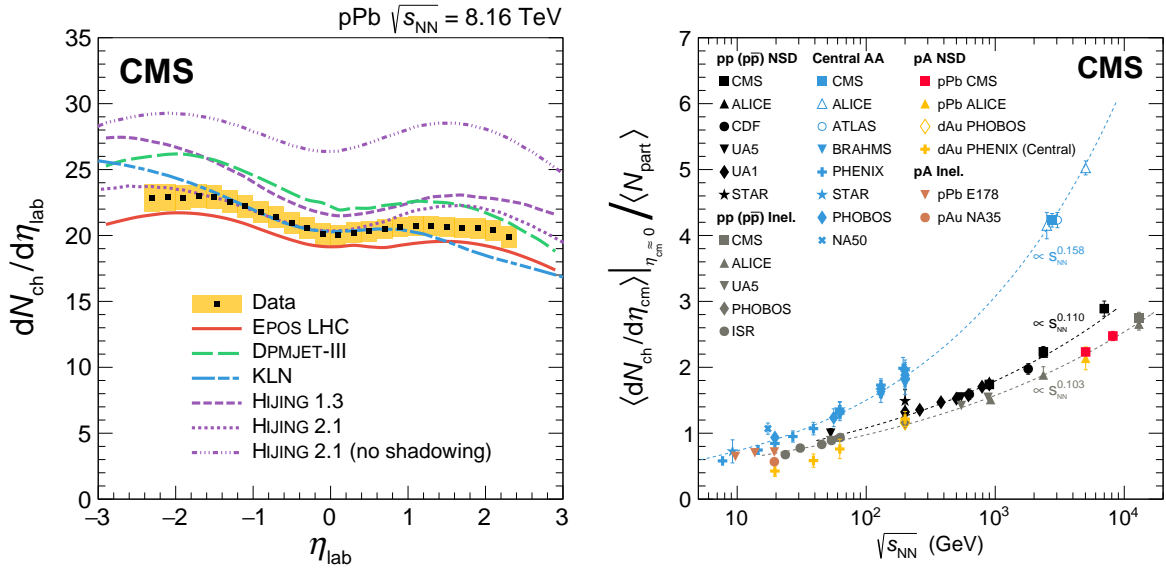


Figure 85: Left: Pseudorapidity density of charged hadrons in the range  $|\eta_{lab}| < 2.4$  in pPb collisions at 8.16 TeV. The results are compared to predictions from the MC event generators EPOS LHC [123, 476] (v3400), HIJING [124] (versions 1.3 [477] and 2.1 [478]), and DPMJET-III [479], as well as from the KLN model [257]. The shaded boxes around the data points indicate their systematic uncertainties. The proton beam goes in the positive  $\eta_{lab}$  direction. Right: Comparison of the measured density at midrapidity, scaled by  $N_{part}$  in pPb [480, 481], pAu [482], dAu [483–485] and central heavy ion collisions [111, 234, 484, 486–497], as well as NSD [235, 236, 238, 239, 497–499] and inelastic [234, 237, 238, 500, 501] pp collisions. The dashed curves, included to guide the eye, are from Refs. [237, 494].

To explore the system size dependence of particle production, characterized by the final state particle multiplicity, spectra of identified charged hadrons were measured in pPb collisions at 5.02 TeV. As shown in Fig. 86, the average  $p_T$  was observed to increase with particle mass and charged particle multiplicity, with heavier hadrons exhibiting a more pronounced increase. Comparisons with MC event generators revealed that EPOS LHC, which incorporates additional hydrodynamic evolution of the created system, could reproduce most of the data features, unlike HIJING and AMPT. The study also conducted comparisons of the pPb  $p_T$  spectra and integrated yields to those in pp and PbPb collisions, revealing an intriguing similarity between different collision systems at the same particle multiplicity.

The  $E_T$  distribution was also measured in pPb collisions at 5.02 TeV, using the hermetic coverage of the CMS detector [505]. The study covered a wide pseudorapidity range and leveraged the presence of the CASTOR calorimeter. The results demonstrated a strong centrality dependence, characterized by a significantly greater increase of  $dE_T/d\eta$  in more central events on the lead-going side compared to the proton-going side. Predictions from EPOS LHC, QGSJET II [199], and HIJING were compared to the data, but none could fully encompass all aspects of the  $\eta$  and centrality dependence.

Measurements of transverse momentum spectra of strange hadrons ( $K_S^0$ ,  $\Lambda + \bar{\Lambda}$ , and  $\Xi^- + \bar{\Xi}^+$ ) in pp, pPb, and PbPb collisions at different collision energies have been performed with CMS [504], extending the measurements beyond studies with light-flavor hadrons. These measurements are sensitive to medium-induced modifications of the final-state particle composition. Figure 87 summarizes the ratio of  $p_T$  spectra for  $\Lambda/2K_S^0$  in pp, pPb, and PbPb collisions as a function of  $p_T$ . In a radial flow picture, we expect the  $\Lambda$  baryon, which contains three con-

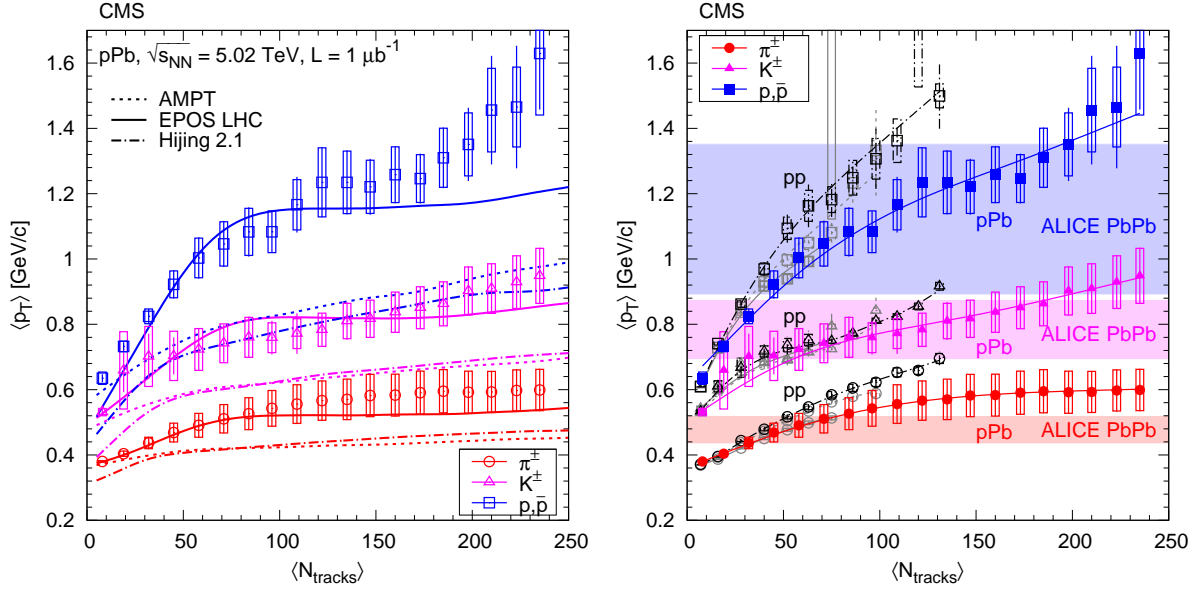


Figure 86: Average transverse momentum of identified charged hadrons in the range  $|y| < 1$  as a function of the corrected track multiplicity for  $|\eta| < 2.4$ , for pp collisions (open symbols) at several energies [502] and for pPb collisions (filled symbols) at  $\sqrt{s_{NN}} = 5.02$  TeV. Left: Results compared to predictions from event generators. Right: Comparison of pp, pPb, and PbPb data. The ranges of  $\langle p_T \rangle$  values measured by ALICE in various centrality PbPb collisions at  $\sqrt{s_{NN}} = 2.76$  TeV [503] are indicated with horizontal bands.

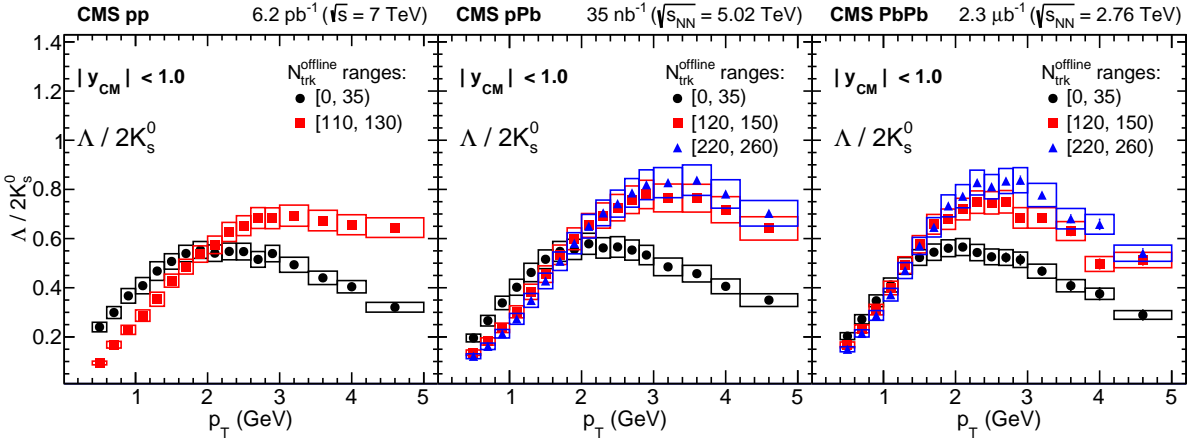


Figure 87: Ratios of  $p_T$  spectra for  $\Lambda/2K_S^0$  in the center-of-mass rapidity range  $|y_{cm}| < 1.0$  for pp collisions at  $\sqrt{s} = 7$  TeV (left), pPb collisions at  $\sqrt{s} = 5.02$  TeV (middle), and PbPb collisions at  $\sqrt{s_{NN}} = 2.76$  TeV (right). Two (for pp) or three (for pPb and PbPb) representative multiplicity intervals are presented. (Figure adapted from Ref. [504].)

stituent quarks, to receive a larger boost, in transverse momentum, compared to the  $K_S^0$  meson, resulting in the kind of modification pattern that we see in the high multiplicity data. An enhancement of the ratio is observed in all collision systems at intermediate to high  $p_T$  and high multiplicity, indicating a similarity in the multiplicity and  $p_T$  dependence of the ratio.

The average transverse kinetic energy ( $\langle KE_T \rangle$ ) of strange hadrons is observed to rise with multiplicity, with a more pronounced increase noted for heavier particles across all collision systems. Furthermore, when comparing results at similar multiplicities, the difference in  $\langle KE_T \rangle$

among various strange-particle species is more substantial in pp and pPb events than in PbPb events. In pPb collisions, the average transverse kinetic energy is slightly larger in the Pb-going direction than in the p-going direction for events featuring high particle multiplicities.

In conclusion, the observed patterns, especially the mass-dependent rise in  $\langle KE_T \rangle$  and the enhanced  $\Lambda/2K_S^0$  ratio, align with expectations from radial flow, suggesting additional evidence of collectivity in these systems.

## 6.2 Studies of collectivity in small systems

### 6.2.1 Exploring small-system collectivity using light-flavor particles

Well before the LHC began operating, the presence of collectivity in AA collisions at RHIC and elsewhere had been well established. Flow coefficients were extracted using a variety of methods, including measurements of the azimuthal anisotropy of particle yields with respect to the event plane and measurements of two-particle and multiparticle correlations [506]. The dominant source of the second order coefficient  $v_2$  was understood as hydrodynamic flow driven by the asymmetric shape of the overlap region of the two nuclei. Higher order harmonics were also understood by that time as resulting from asymmetries created by fluctuations in the collision geometry [312].

The LHC started its operation with pp collisions, in which collectivity was not expected to exist. However, it was speculated that for sufficiently high charged particle multiplicities, collectivity might be observed if fluctuations in the collision geometry could also create initial-state anisotropies in these collisions. As a measure of the necessary multiplicities, the values of  $dN_{ch}/d\eta$  for AuAu collisions at 200 GeV in the 60–70% and 70–80% centrality ranges are  $45 \pm 3$  and  $22 \pm 2$ , respectively [497]. Clear  $v_2$  signals were observed in both of these AA collision cases [507].

Even at LHC energies, the average  $dN_{ch}/d\eta$  for MB pp collisions is much smaller than these values. However, during the first pp run, the CMS Collaboration developed a way to trigger on high-multiplicity pp events. Using this trigger in pp collisions at 7 TeV, the average number of charged particles with  $p_T > 0.4$  GeV and  $|\eta| < 2.4$  corrected for tracking efficiency,  $N_{trk}^{\text{corrected}}$ , was about 136 for events selected with the number of observed tracks reconstructed offline  $N_{trk}^{\text{offline}} \geq 110$  [303]. This corresponds to  $dN_{ch}/d\eta \approx 28$  with  $p_T > 0.4$  GeV, which is comparable to the values mentioned above for peripheral AuAu collisions. In two-particle correlations (as described in Section 4.2.1), a striking long-range ( $|\Delta\eta| > 2$ ) ridge-like structure was observed on the near-side ( $\Delta\phi \approx 0$ ) for  $1 < p_T < 3$  GeV with  $N_{trk}^{\text{offline}} > 110$ , as shown in the upper left panel of Fig. 88. This discovery motivated further studies of small collision systems at RHIC, as well as pp, pPb, and peripheral PbPb collisions at the LHC. This section describes some of the CMS analyses of small systems using various flow analysis techniques, including multiparticle correlations, and new observables such as cumulant ratios and symmetric cumulants.

To further understand the origins of the ridge, the  $p_T$  and multiplicity dependence of its yield, as well as flow coefficients,  $v_n$ , were studied using two-particle correlations. Panels (a), (b), and (c) of Fig. 88 compare 2D two-particle correlation functions for pairs of charged particles with  $1 < p_T < 3$  GeV for pp at 7 TeV with  $N_{trk}^{\text{offline}} \geq 110$ , pPb at 5.02 TeV with  $N_{trk}^{\text{offline}} \geq 110$ , and peripheral PbPb collisions at 2.76 TeV with  $220 \leq N_{trk}^{\text{offline}} < 260$ , respectively. To investigate the long-range, near-side correlations in detail, 1D distributions in  $\Delta\phi$  are found by averaging the two-dimensional distributions over  $2 < |\Delta\eta| < 4$ . The ridge yield is then calculated by integrating over the region  $|\Delta\phi| < 1.2$ , with the results for the three systems shown in panel (d)

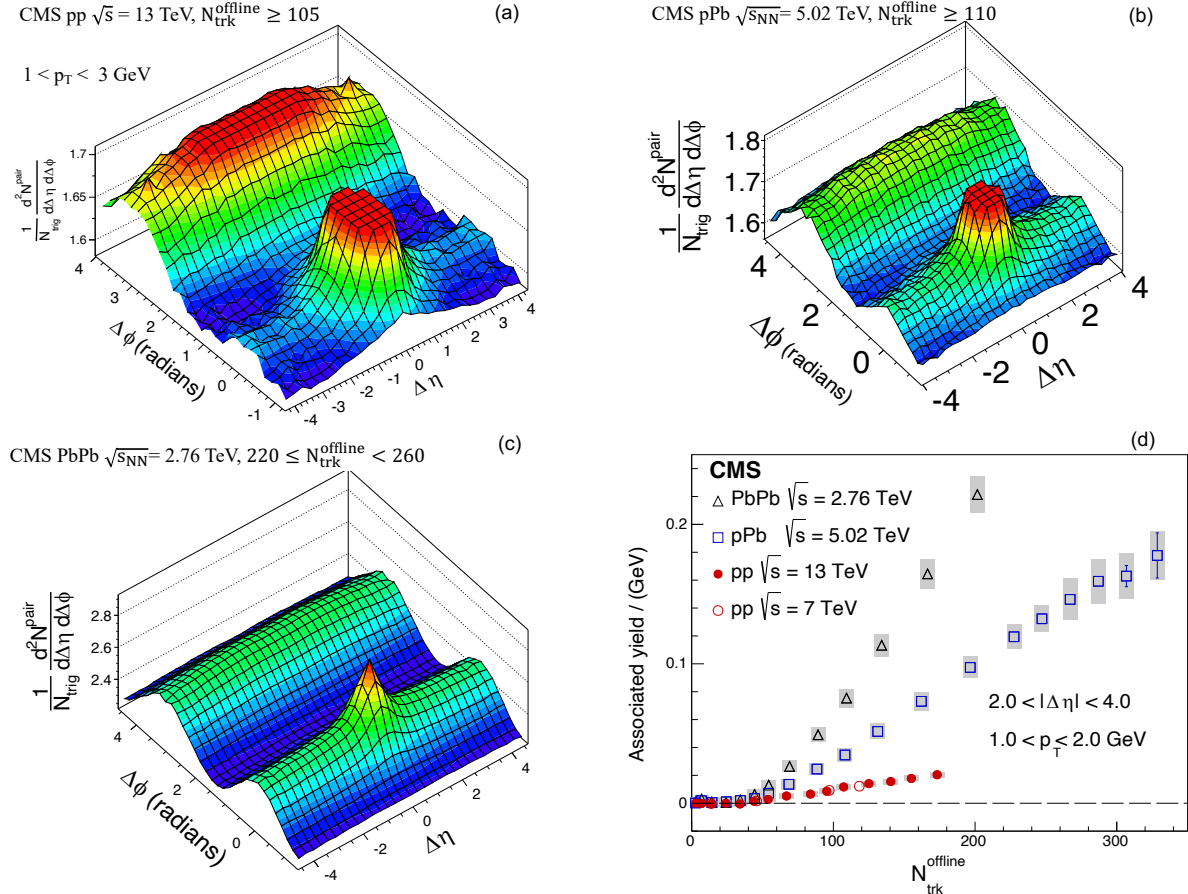


Figure 88: Panels (a), (b), and (c) show the 2D two-particle correlation functions for pairs of charged particles with  $1 < p_T < 3$  GeV for high multiplicity events in pp at 7 TeV and pPb at 5.02 TeV, as well as peripheral PbPb collisions at 2.76 TeV. Panel (d) displays the ridge yield as a function of multiplicity in pp, pPb, and PbPb collisions. The vertical bars and shaded boxes denote the statistical and systematic uncertainties, respectively. (Figure adapted from Refs. [110, 303, 304, 306].)

of Fig. 88 as a function of multiplicity. The ridge yields show an approximately linear increase for  $N_{\text{trk}}^{\text{offline}} \gtrsim 40$ , which corresponds to  $N_{\text{trk}}^{\text{corrected}} \gtrsim 53$ . Although the shape of the multiplicity dependence is qualitatively similar for pp, pPb, and PbPb collisions, a significantly higher yield per trigger particle is seen in PbPb than for pPb collisions, which is itself larger than for pp collisions at a given multiplicity.

Flow coefficients can be extracted via a Fourier decomposition of the long-range two-particle  $\Delta\phi$  correlation function described in Section 4.2.1. However, back-to-back nonflow correlations, which are more significant for pp and pA than in AA collisions, are still present in the away-side region of these long-range distributions. This contribution can be suppressed by performing low-multiplicity subtractions [110]. The  $v_2$  values before and after this subtraction,  $v_2\{2, |\Delta\eta| > 2\}$  and  $v_2^{\text{sub}}\{2, |\Delta\eta| > 2\}$ , are shown as a dot-dash line and red circles, respectively, in Fig. 89. At lower multiplicity, the nonflow contributions increase and a reliable extraction of the flow signal becomes model-dependent.

Another way to suppress nonflow effects is to use multiparticle correlation methods [110, 305, 308]. The flow coefficient values from 4-, 6-, and 8-particle cumulants,  $v_2\{4\}$ ,  $v_2\{6\}$ , and  $v_2\{8\}$ , as well as all-particle correlations,  $v_2\{\text{LYZ}\}$ , are also shown in Fig. 89. Within experimental un-

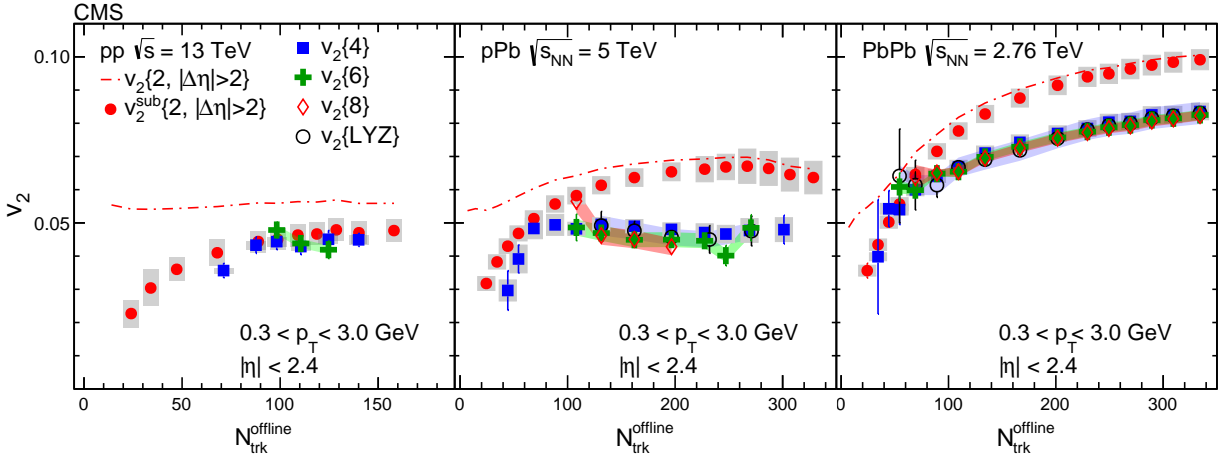


Figure 89: Left: The  $v_2\{2, |\Delta\eta| > 2\}$ ,  $v_2^{\text{sub}}\{2, |\Delta\eta| > 2\}$ ,  $v_2\{4\}$ , and  $v_2\{6\}$  values as functions of  $N_{\text{trk}}^{\text{offline}}$  for charged particles, averaged over  $0.3 < p_{\text{T}} < 3.0$  GeV and  $|\eta| < 2.4$ , in pp collisions at 13 TeV. Middle: The  $v_2\{2, |\Delta\eta| > 2\}$ ,  $v_2^{\text{sub}}\{2, |\Delta\eta| > 2\}$ ,  $v_2\{4\}$ ,  $v_2\{6\}$ ,  $v_2\{8\}$ , and  $v_2\{\text{LYZ}\}$  values in pPb collisions at 5 TeV. Right: The  $v_2\{2, |\Delta\eta| > 2\}$ ,  $v_2^{\text{sub}}\{2, |\Delta\eta| > 2\}$ ,  $v_2\{4\}$ ,  $v_2\{6\}$ ,  $v_2\{8\}$ , and  $v_2\{\text{LYZ}\}$  values in PbPb collisions at 2.76 TeV. The vertical bars and shaded boxes for  $v_2^{\text{sub}}\{2, |\Delta\eta| > 2\}$  and  $v_2\{4\}$  denote the statistical and systematic uncertainties, respectively, with the former generally being smaller than the symbols. For  $v_2\{6\}$ ,  $v_2\{8\}$ , and  $v_2\{\text{LYZ}\}$ , vertical bars show statistical uncertainties and systematic uncertainties are shown by green, red, and gray shaded bands, respectively. (Figure adapted from Ref. [305].)

certainties, the  $v_2$  values from all of the multiparticle correlation methods are consistent with each other. This provides strong evidence for the collective nature of the long-range correlations observed in these small systems.

The differences between cumulants of different orders originate from fluctuations in the eccentricity distribution in the initial state [508]. To further investigate whether the flow coefficients in small systems are directly related to the geometry of the initial stage, as is the case for larger AA systems, the ratios  $v_2\{6\}/v_2\{4\}$  and  $v_2\{8\}/v_2\{6\}$  as functions of the ratio  $v_2\{4\}/v_2\{2\}$  are measured. These values can then be compared with the same ratios found using initial-state eccentricities resulting from geometry fluctuations. Figure 90 shows these comparisons for pPb collisions at 5.02 and 8.16 TeV. The agreement of the calculations with the data shows that the differences found among the multiparticle cumulant results for the  $v_2$  values can be described by initial-state fluctuations [508]. These results confirm the hypothesis that multiparticle correlations originate from the multiplication of single-particle correlations with respect to symmetry planes. These single-particle correlations stem from source fluctuations related to the overall collision geometry, similar to what is observed in larger collision systems [509].

The values of the initial-state eccentricities  $\epsilon_2$  and  $\epsilon_3$  quantify the degree to which the initial state of an event has an elliptic or triangular geometry, respectively. Assuming that the flow coefficients  $v_2$  and  $v_3$  are proportional to these eccentricities, the event-by-event correlation between  $v_2$  and  $v_3$  should be negative, so long as the hydrodynamic evolution of the system maintains this proportionality. One technique to extract this correlation is by measuring the symmetric cumulant  $SC(n, m)$ , which correlates the Fourier coefficients of order  $m$  and  $n$ ,

$$SC(n, m) = \langle v_n^2 v_m^2 \rangle - \langle v_n^2 \rangle \langle v_m^2 \rangle, \quad (26)$$

where  $\langle \dots \rangle$  denotes the average over all events. To remove nonflow effects,  $SC(n, m)$  can be measured using different subevent methods [281, 510, 511]. In the subevent approach, every

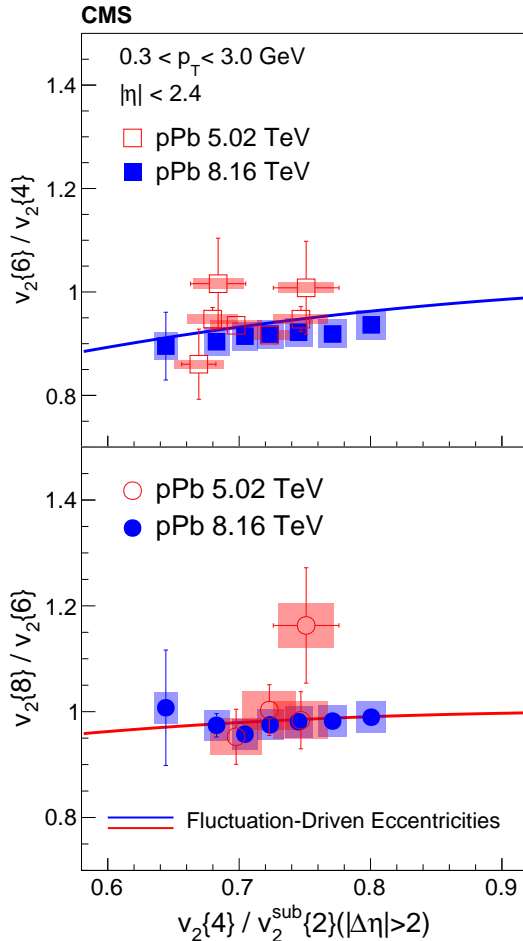


Figure 90: Cumulant ratios  $v_2\{6\} / v_2\{4\}$  (upper) and  $v_2\{8\} / v_2\{6\}$  (lower) as functions of  $v_2\{4\} / v_2^{\text{sub}}\{2\}$  in pPb collisions at 5.02 and 8.16 TeV. The solid curves show the expected behavior based on a hydrodynamics-motivated study of the role of initial-state fluctuations [508]. (Figure adapted from Ref. [509].)

event is subdivided into multiple subevents, each of which spans a distinct rapidity range. A negative correlation between  $v_2$  and  $v_3$  has been observed in large collision systems [512, 513]. Figure 91 shows  $SC(2,3)$  (left panel) and  $SC(2,4)$  (right panel) as functions of  $N_{\text{trk}}^{\text{offline}}$  using no, 2, 3, and 4 subevents for pPb at 8.16 TeV. Nonflow contributions are suppressed by using multiple subevents. A clear anticorrelation is observed between the single-particle anisotropy harmonics  $v_2$  and  $v_3$ , while  $v_2$  and  $v_4$  are positively correlated. These results provide further evidence for the onset of long-range collective behavior in high multiplicity events in small systems.

Significant progress has been made, both theoretically and experimentally, towards understanding collectivity in small systems [36, 37]. In addition to explanations using hydrodynamic models, there are alternative interpretations such as parton scattering [514, 515] and initial-state momentum correlation [516, 517]. Several additional observables have been proposed to distinguish between the various interpretations, including correlating  $v_2$  and mean  $p_T$  values [518] and studying QCD collectivity in a single-parton system propagating in vacuum [519]. Future experiments, and possibly new observables, are expected to further enhance our understanding of the origins of azimuthal correlations and collectivity in small collision systems.

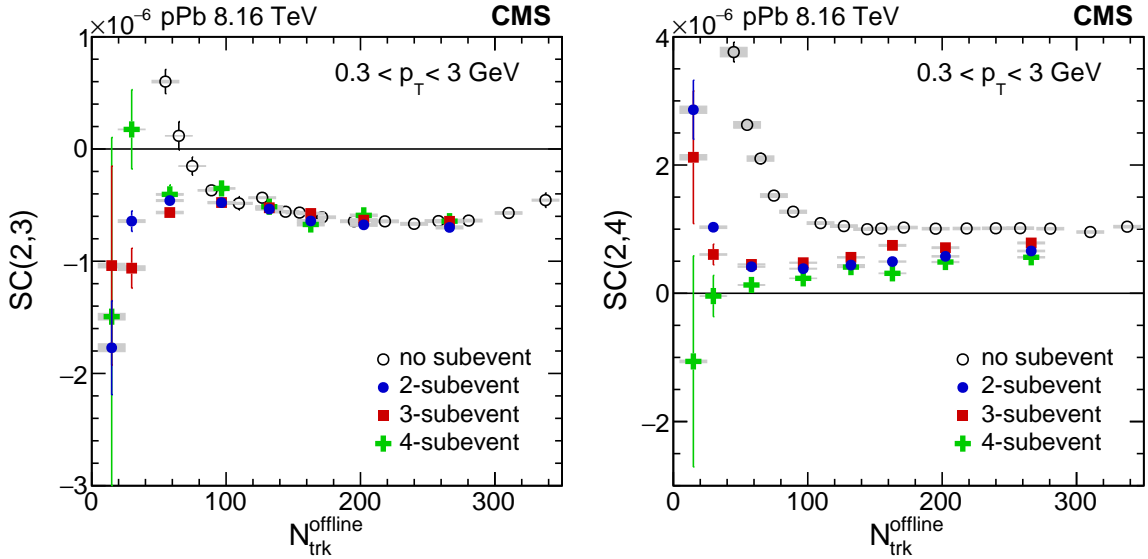


Figure 91: The  $SC(2,3)$  (left panel) and  $SC(2,4)$  (right panel) distributions as functions of  $N_{\text{trk}}^{\text{offline}}$  from methods using no (open black circles), 2 (full blue circles), 3 (red squares), and 4 (green crosses) subevents for pPb at 8.16 TeV. Statistical and systematic uncertainties are shown by vertical bars and shaded boxes, respectively. (Figure adapted from Ref. [510].)

### 6.2.2 Exploring small system collectivity using heavy-flavor particles

As a consequence of their large masses, heavy quarks (charm and bottom) are primarily produced in the early stages of collisions. If a QGP is formed, heavy-quark interactions with the medium will probe its entire evolution [322]. Flow measurements for heavy-flavor mesons in HI collisions at RHIC [520] and the LHC [145, 521, 522] suggest that charm quarks develop a strong collective behavior, similar to that for light-flavor particles, which are primarily produced from the bulk of the QGP. In small systems, collective flow of heavy-flavor mesons, and especially the comparison to results for light hadrons, can impose further constraints on interpretations of the origin of the observed collectivity.

Collective flow measurements have been performed for  $D^0$  and  $J/\psi$  mesons using CMS data of pPb collisions at  $\sqrt{s_{\text{NN}}} = 8.16$  TeV in 2016 [523, 524] and of pp collisions at  $\sqrt{s} = 13$  TeV in 2017 and 2018 [525]. Because of the asymmetric beam energies in pPb collisions at  $\sqrt{s_{\text{NN}}} = 8.16$  TeV (6.5 TeV for the protons and 2.56 TeV per nucleon for the lead nuclei), particles selected with the laboratory rapidity  $y_{\text{lab}}$  have a corresponding nucleon-nucleon center-of-mass frame rapidity  $y_{\text{cm}} = y_{\text{lab}} - 0.46$ . The upper panel of Fig. 92 shows elliptic flow results after subtracting jet correlations ( $v_2^{\text{sub}}$ ) for prompt  $J/\psi$  mesons at forward rapidities ( $-2.86 < y_{\text{cm}} < -1.86$  and  $0.94 < y_{\text{cm}} < 1.94$  combined), as well as for  $K_S^0$  and  $\Lambda$  hadrons and prompt  $D^0$  mesons at midrapidity ( $-1.46 < y_{\text{cm}} < 0.54$ ), for high-multiplicity ( $185 \leq N_{\text{trk}}^{\text{offline}} < 250$ ) pPb collisions, as a function of  $p_{\text{T}}$  from 0.2 to 10 GeV. Positive  $v_2^{\text{sub}}$  values are observed for prompt  $D^0$  and  $J/\psi$  mesons, with an initial increase up to  $p_{\text{T}} \approx 4$  GeV, and then a slow decrease toward higher  $p_{\text{T}}$ . Over the full  $p_{\text{T}}$  range, the  $v_2^{\text{sub}}$  values for these two mesons are consistent with each other within uncertainties, and are smaller than those for  $K_S^0$  and  $\Lambda$  hadrons. This observation indicates that charm quarks develop a collective response to the bulk medium in this small system, albeit weaker than that for light quarks.

A recent model calculation of  $J/\psi$  meson  $v_2$  in pPb collisions, based on final-state interactions between produced charm quarks and a QGP medium, predicts far smaller values than seen in the data [526]. This calculation suggests that additional contributions, e.g., those from initial-

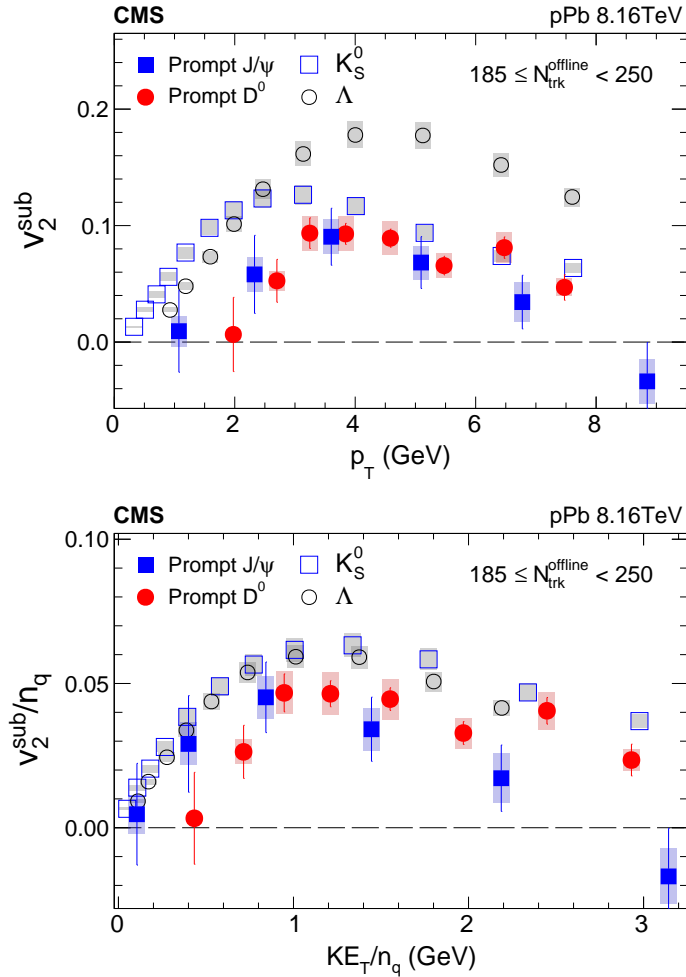


Figure 92: Upper: The  $v_2^{\text{sub}}$  values for prompt  $J/\psi$  mesons at forward rapidities ( $-2.86 < y_{\text{cm}} < -1.86$  or  $0.94 < y_{\text{cm}} < 1.94$ ), as well as for  $K_S^0$  and  $\Lambda$  hadrons, and prompt  $D^0$  mesons at midrapidity ( $-1.46 < y_{\text{cm}} < 0.54$ ), as a function of  $p_T$  for pPb collisions at  $\sqrt{s_{\text{NN}}} = 8.16$  TeV with  $185 \leq N_{\text{trk}}^{\text{offline}} < 250$ . Lower: The  $n_q$ -normalized  $v_2^{\text{sub}}$  results. The vertical bars correspond to statistical uncertainties, while the shaded boxes denote the systematic uncertainties. (Figure adapted from Ref. [524].)

state interactions, may be needed to account for the observed  $v_2$  signal for prompt  $J/\psi$  mesons in high-multiplicity pPb events.

Motivated by the quark coalescence model [424, 527, 528], collective flow at the partonic level is investigated by studying the scaling properties of  $v_2^{\text{sub}}$  divided by the number of constituent quarks ( $n_q$ ), as a function of the transverse kinetic energy per constituent quark ( $KE_T/n_q$ , where  $KE_T = \sqrt{m^2 + p_T^2} - m$ ). The lower panel of Fig. 92 shows the same data as the upper panel, but now as a function of  $KE_T$  with both  $v_2^{\text{sub}}$  and  $KE_T$  normalized by  $n_q$ . The observed similarity of  $n_q$ -normalized  $v_2^{\text{sub}}$  values for the  $K_S^0$  meson and  $\Lambda$  baryon is known as number-of-constituent-quark (NCQ) scaling [307, 529–531], indicating that collective behavior is first developed among the partons, which later recombine into final-state hadrons. The values of  $(v_2^{\text{sub}}/n_q)$  for prompt  $D^0$  mesons are consistently smaller than those for the  $K_S^0$  meson and  $\Lambda$  baryon. For  $J/\psi$  mesons,  $v_2^{\text{sub}}/n_q$  values are consistent with those of  $K_S^0$  and  $\Lambda$  hadrons within statistical uncertainties at lower  $KE_T/n_q$ , while for  $KE_T/n_q \gtrsim 1$  GeV, the results are consistently

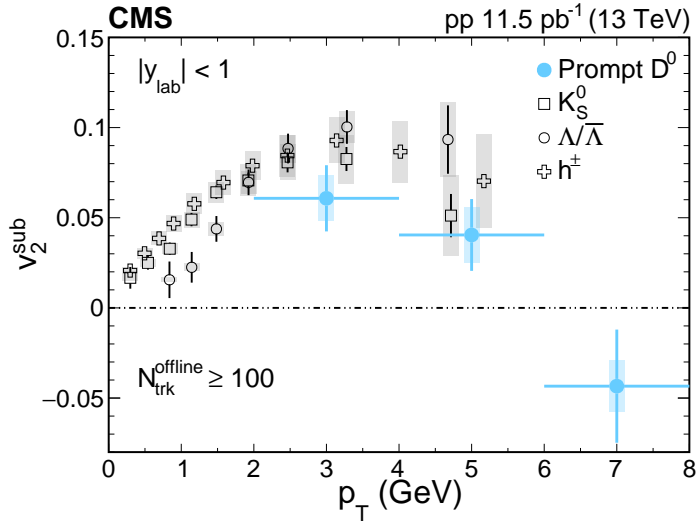


Figure 93: Results of  $v_2^{\text{sub}}$  for prompt  $D^0$  mesons, as a function of  $p_T$  for  $|y_{\text{lab}}| < 1$ , with  $N_{\text{trk}}^{\text{offline}} \geq 100$  in pp collisions at  $\sqrt{s} = 13$  TeV. The results for charged particles,  $K_S^0$  mesons, and  $\Lambda$  baryons are shown for comparison. Vertical bars correspond to the statistical uncertainties, while the shaded boxes denote the systematic uncertainties. The horizontal bars represent the width of the  $p_T$  bins for prompt  $D^0$  mesons. (Figure adapted from Ref. [525].)

smaller than those for the other two particles.

To investigate whether collective behavior of heavy-flavor quarks exists in even smaller systems, similar measurements have been performed for prompt  $D^0$  mesons from pp collisions at  $\sqrt{s} = 13$  TeV, with the  $v_2^{\text{sub}}$  distribution presented in Fig. 93 as a function of  $p_T$  for  $D^0$  rapidity  $|y_{\text{lab}}| < 1$  and event multiplicity  $N_{\text{trk}}^{\text{offline}} \geq 100$ . The positive  $v_2$  signal ( $0.061 \pm 0.018 \text{ (stat)} \pm 0.013 \text{ (syst)}$ ) over a  $p_T$  range of  $\sim 2\text{--}4$  GeV (with a declining trend toward higher  $p_T$ ) provides an indication of collectivity for charm quarks in pp collisions. The  $v_2$  magnitude for prompt  $D^0$  mesons is found to be compatible with that for light-flavor hadron species, which suggests that collectivity is comparable (or slightly weaker) for charm hadrons than that for light-flavor hadrons in high-multiplicity pp collisions.

To further investigate the possible system size dependence of collectivity for charm hadrons in small colliding systems,  $v_2$  for prompt  $D^0$  mesons in pPb and pp collisions are measured in different multiplicity classes. The prompt  $D^0$  meson  $v_2$  as a function of event multiplicity for three different  $p_T$  ranges:  $2 < p_T < 4$  GeV,  $4 < p_T < 6$  GeV, and  $6 < p_T < 8$  GeV are presented in Fig. 94. At similar multiplicities of  $N_{\text{trk}}^{\text{offline}} \sim 100$ , the prompt  $D^0$   $v_2$  values are found to be comparable within uncertainties in pp and pPb systems. For  $2 < p_T < 4$  GeV, the measurement for prompt  $D^0$  mesons provides indications of positive  $v_2$  down to  $N_{\text{trk}}^{\text{offline}} \sim 50$  with a significance of more than 2.4 standard deviations, while for  $6 < p_T < 8$  GeV clearly positive signals are only present in the higher-multiplicity region. Because of the large uncertainties, especially at low multiplicities, no clear multiplicity dependence can be determined for pp results.

Figure 95 adds  $v_2^{\text{sub}}$  values for nonprompt  $D^0$  mesons from bottom hadron decays to the results shown in the upper panel of Fig. 92 for pPb collisions at 8.16 TeV with  $185 \leq N_{\text{trk}}^{\text{offline}} < 250$ . At low  $p_T$ , the nonprompt  $D^0$   $v_2$  is consistent with zero, while at high  $p_T$ , a hint of a positive  $v_2$  value for  $D^0$  mesons from b hadron decays is suggested. At  $p_T \sim 2\text{--}5$  GeV, the nonprompt  $D^0$  meson  $v_2$  from bottom hadron decays is observed to be smaller than that for prompt  $D^0$  mesons with a significance of 2.7 standard deviations, suggesting a flavor hierarchy of the collectivity signal that tends to diminish for the heavier bottom hadrons. This is qualitatively consistent

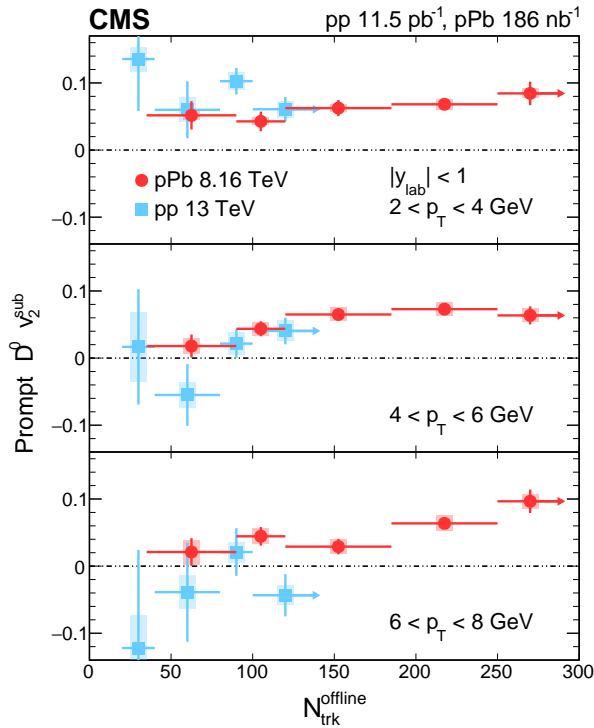


Figure 94: Results of  $v_2^{\text{sub}}$  for prompt  $D^0$  mesons, as a function of event multiplicity for three different  $p_T$  ranges, with  $|y_{\text{lab}}| < 1$  in pp collisions at  $\sqrt{s} = 13$  TeV, and pPb collisions at  $\sqrt{s_{\text{NN}}} = 8.16$  TeV. The vertical bars correspond to statistical uncertainties, while the shaded boxes denote the systematic uncertainties. Vertical bars extending beyond the y-axis are symmetric with respect to the central values. The horizontal bars represent the width of the  $N_{\text{trk}}^{\text{offline}}$  bins. The right-most points with right-hand arrows correspond to  $N_{\text{trk}}^{\text{offline}} \geq 100$  for pp collisions and  $N_{\text{trk}}^{\text{offline}} \geq 250$  for pPb collisions. (Figure adapted from Ref. [525].)

with the scenario of  $v_2$  being generated via final-state rescatterings, where heavier quarks tend to develop a weaker collective  $v_2$  signal [419].

Correlations at the initial stage of the collision between partons originating from projectile protons and dense gluons in the lead nucleus are able to generate sizable elliptic flow in the CGC framework [36, 532, 533]. These CGC calculations of  $v_2$  signals for prompt  $J/\psi$  mesons, as well as prompt and nonprompt (from  $b$  hadron decay)  $D^0$  mesons, are also shown in Fig. 95. Note that the parameterizations used in the CGC model in Ref. [533] are unable to describe  $v_2$  for the full  $J/\psi$  meson  $p_T$  spectrum. The qualitative agreement between data and theory suggests that initial-state effects may play an important role in the generation of collectivity for these particles in pPb collisions.

### 6.2.3 Search for collective behavior in the smallest system limit

Fourier coefficients ( $V_{n\Delta}$ ) of the azimuthal distributions of charged hadrons emitted in photon-proton ( $\gamma p$ ) interactions were measured using pPb UPCs at  $\sqrt{s_{\text{NN}}} = 8.16$  TeV. Lead ions produce a flux of photons that interact with oncoming protons. This  $\gamma p$  system provides a unique set of initial conditions with a multiplicity lower than that in photon-lead collisions but comparable to recent electron-positron and electron-proton data [534–539].

Figure 96 shows the  $N_{\text{trk}}^{\text{offline}}$  spectra for the  $\gamma p$ -enhanced and MB data samples along with simulations from the PYTHIA8 and HIJING event generators. The  $N_{\text{trk}}^{\text{offline}}$  average is 2.9 for the

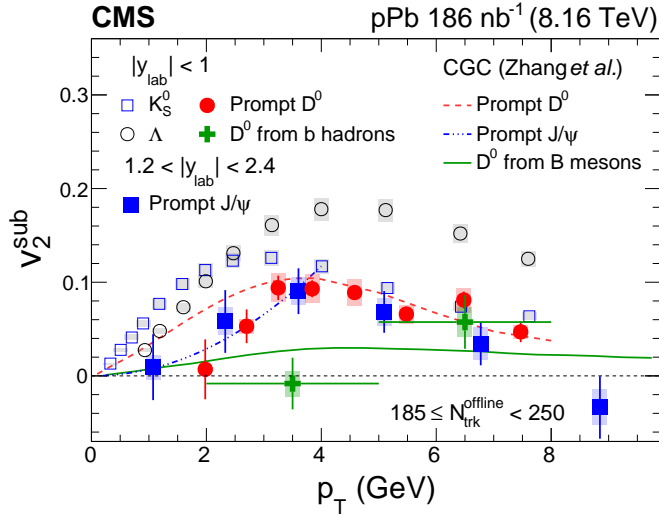


Figure 95: Results of  $v_2^{\text{sub}}$  for prompt and nonprompt  $D^0$  mesons, as well as  $K_S^0$  mesons,  $\Lambda$  baryons for  $|y_{\text{lab}}| < 1$ , and prompt  $J/\psi$  mesons for  $1.2 < |y_{\text{lab}}| < 2.4$ , as a function of  $p_T$  with  $185 \leq N_{\text{trk}}^{\text{offline}} < 250$  in  $p\text{Pb}$  collisions at  $\sqrt{s_{\text{NN}}} = 8.16$  TeV. The vertical bars correspond to statistical uncertainties, while the shaded boxes denote the systematic uncertainties. The horizontal bars represent the width of the nonprompt  $D^0$   $p_T$  bins. The red dashed, blue dash-dotted, and green solid lines show the theoretical calculations for prompt  $D^0$ ,  $J/\psi$ , and nonprompt  $D^0$  mesons, respectively, within the CGC framework [532, 533]. (Figure adapted from Ref. [525].)

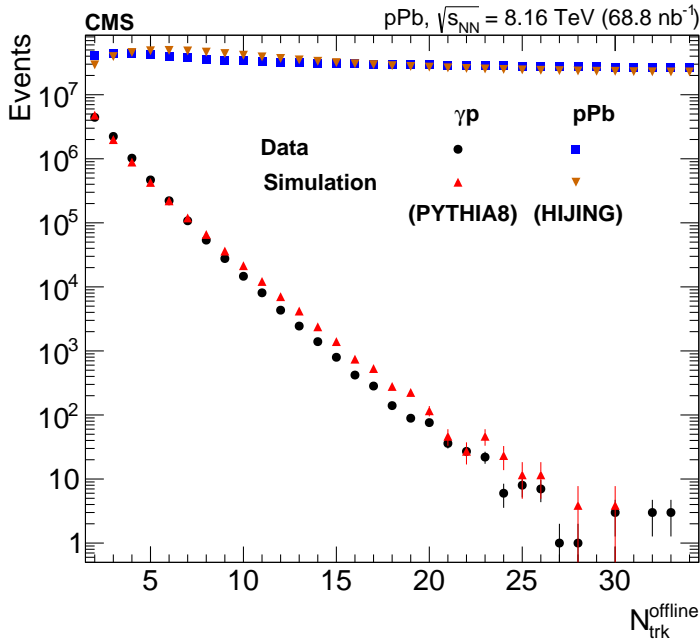


Figure 96: The  $N_{\text{trk}}^{\text{offline}}$  spectra for  $\gamma p$  and minimum bias  $p\text{Pb}$  samples. The simulated  $N_{\text{trk}}^{\text{offline}}$  distribution for  $\gamma p$  events has been normalized to the same event yield as the  $\gamma p$ -enhanced data sample.

$\gamma p$  sample and 16.6 for the  $p\text{Pb}$  sample. For a given multiplicity range, the mean  $p_T$  of charged particles is smaller in  $\gamma p$  than in  $p\text{Pb}$  collisions. For both the  $\gamma p$  and  $p\text{Pb}$  samples,  $V_{1\Delta}$  is negative,  $V_{2\Delta}$  is positive, and  $V_{3\Delta}$  is consistent with 0.

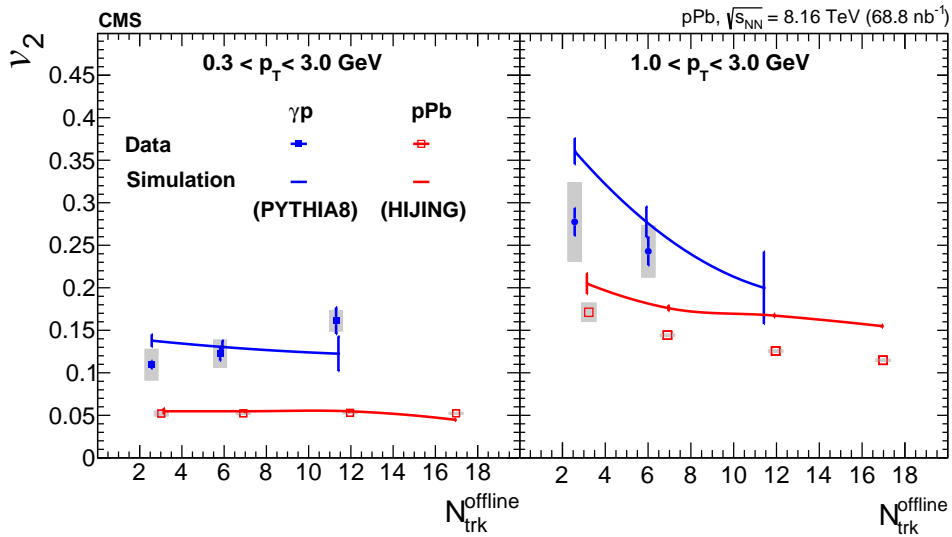


Figure 97: Single-particle azimuthal anisotropy  $v_2$  versus  $N_{\text{trk}}^{\text{offline}}$  for  $\gamma p$ -enhanced and  $p\text{Pb}$  samples in two  $p_{\text{T}}$  regions. The systematic uncertainties are shown by the shaded bars in the two panels. Predictions from the PYTHIA8 and HIJING generators are shown for the  $\gamma p$  and MB  $p\text{Pb}$  samples respectively. For the  $\gamma p$  events, the same  $N_{\text{trk}}^{\text{offline}}$  bin arrangement as in Fig. 96 is kept, while for  $p\text{Pb}$  the bins [2, 5), [5, 10), [10, 15), and [15, 20) are used.

Figure 97 shows the single-particle  $v_2 = \sqrt{V_{2\Delta}}$  as a function of  $N_{\text{trk}}^{\text{offline}}$  and two  $p_{\text{T}}$  regions for both  $\gamma p$  and MB data sets. For  $0.3 < p_{\text{T}} < 3.0 \text{ GeV}$ , the MB results are consistent with the previously published CMS results [281]. Predictions from the PYTHIA8 and HIJING generators are also shown for  $\gamma p$  and MB  $p\text{Pb}$  interactions, respectively. None of the models incorporates collective effects. An increase of  $v_2$  with  $p_{\text{T}}$  is evident in both the data measurements and the simulations, as shown in Fig. 97. However, both generators slightly exceed the data at higher  $p_{\text{T}}$ . It is noticeable that, for a given  $p_{\text{T}}$  and  $N_{\text{trk}}^{\text{offline}}$ ,  $v_2$  is larger for  $\gamma p$  than for  $p\text{Pb}$  interactions.

The  $\gamma p$  data are consistent with model predictions that do not have collective effects. This suggests that the data are dominated by noncollective effects, e.g., back-to-back dijet production. Within the scope of the current experimental sensitivity, no substantial signal of collectivity is observed.

### 6.3 Modification of quarkonium production in small systems

As discussed in Section 5.6, quarkonium states are powerful probes of the QGP that span its dynamic evolution from the early stage onward. The interaction of heavy quarks with the QGP generated in  $\text{PbPb}$  collisions alters the yields of quarkonium states, depending on their binding energies. Understanding the initial- and final-state CNM effects is essential for interpreting the  $\text{PbPb}$  data. To address this issue, the CMS Collaboration has conducted studies on quarkonium production in  $p\text{Pb}$  collisions. For charmonia, as depicted in the left panel of Fig. 98, CMS identified differences in the suppression levels between the excited and ground states in the backward (lead-going) rapidity region [540]. One interpretation posits that, as the charmonia are surrounded by more comoving particles (as is the case with the higher  $dN/d\eta$  in the backward direction) and the interaction probability rises, there is enhanced dissociation of the excited states. In contrast, in the forward (proton-going) region, these CNM effects diminish, and the nuclear modifications to both the ground and excited states are more similar. An analogous observation was made for bottomonia nuclear modification factors [541], as shown in the right panel of Fig. 98. These results suggest the presence of final-state effects in  $p\text{Pb}$  collisions,

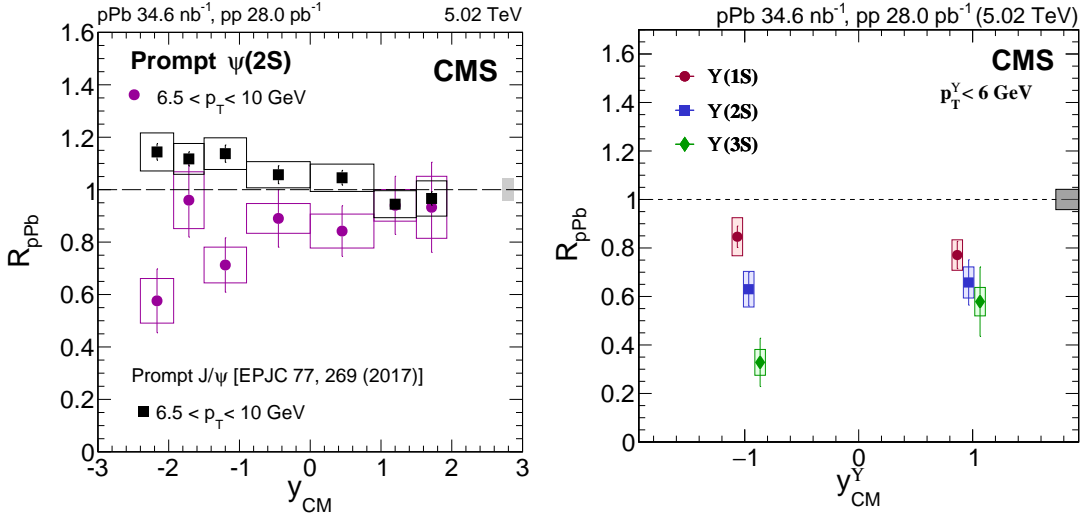


Figure 98: Left: Rapidity dependence of  $R_{pPb}$  for prompt  $\psi(2S)$  meson in the  $p_T$  range  $6.5 < p_T < 10$  GeV. For comparison, the prompt  $J/\psi$  meson nuclear modification factor is also shown. (Figure adapted from Refs. [540, 541].) Right: Nuclear modification factor of  $Y(1S)$  (red dots),  $Y(2S)$  (blue squares), and  $Y(3S)$  (green diamonds) at forward and backward rapidity [541]. For both panels, statistical and systematic uncertainties are represented with vertical bars and boxes, respectively. The fully correlated global uncertainty of 4.2%, affecting both charmonia equally, is displayed as the gray box around  $R_{pPb} = 1$ .

in line with predictions of models that include disintegration of bound quarkonium states via interactions with comoving particles from the underlying event.

In addition to these studies using inclusive pPb collisions, the production cross section ratios of the excited  $Y(2S)$  and  $Y(3S)$  mesons relative to the  $Y(1S)$  ground state have been examined as a function of the number of charged particles in pp collisions at 7 TeV [542]. These ratios were observed to decrease as the particle multiplicity increases, especially at low meson  $p_T$  values. Events including a  $Y(1S)$  meson exhibited a multiplicity higher than that for the excited states, a discrepancy that cannot be solely attributed to feed-down contributions. Events were also categorized by sphericity, with high sphericity indicating a uniform, sphere-like emission and low sphericity indicating a narrow, jet-like emission. For  $Y(nS)$  mesons with  $p_T > 7$  GeV, ratios of their production relative to that for  $Y(1S)$  were seen to be independent of multiplicity in jet-like events (which have small sphericity). Furthermore, in jet-like events, the average number of charged particles per event remained consistent across all three  $Y$  states, suggesting that the variation in associated particle counts is not directly tied to mass differences between these states.

These measurements illustrate that interpreting the sequential disappearance of quarkonia in HI collisions requires a deep understanding of their elementary production processes and of the effect of the surrounding multiplicity in small systems.

## 6.4 Searches for jet quenching in small systems

In Section 5, studies of jet quenching, a phenomenon sensitive to the formation of a QGP, were discussed for HI collisions. As detailed in Section 6.2, analyzing particle correlations in small collision systems revealed a significant flow-like signal, similar to observations that have been linked to QGP formation in larger systems. Moreover, measurements of quarkonium  $R_{pA}$ , presented in Section 6.3, suggest final-state effects in pPb collisions. Consequently, these observa-

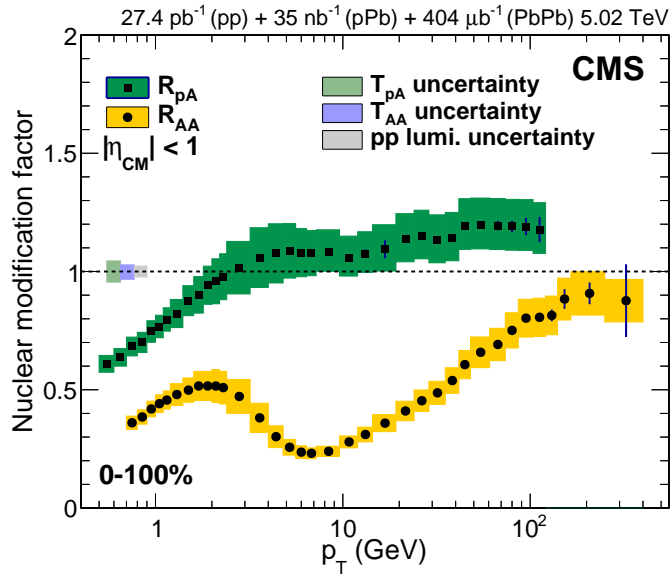


Figure 99: Nuclear modification factors versus  $p_T$  for an inclusive centrality selection for both PbPb and pPb collisions. The green and orange boxes show the systematic uncertainties for  $R_{pA}$  and  $R_{AA}$ , respectively, while the  $T_{pA}$ ,  $T_{AA}$ , and pp integrated luminosity uncertainties are shown as grey boxes around unity at low  $p_T$ . Statistical uncertainties are shown as vertical bars. (Figure adapted from Ref. [351].)

tions have motivated the investigation of the presence of jet quenching in small systems [543].

The simplest observable used to study jet quenching is the inclusive charged-particle nuclear modification factor, denoted as  $R_{pA}$ . Figure 99 shows both  $R_{AA}$  and  $R_{pA}$  for events integrated in all centralities as functions of  $p_T$  [351]. The observation of an  $R_{pA}$  smaller than unity at  $p_T < 2$  GeV can be attributed to initial-state effects, such as the nuclear shadowing and saturation effects discussed in Section 3. On the other hand, at high  $p_T$  the charged-particle  $R_{pA}$  is above unity, consistent with mild antishadowing effects in the intermediate- $x$  region [543]. Since the data are consistent with models that include only initial-state effects, these results show no indication of jet quenching within uncertainties in inclusive hadronic pPb collisions at 5.02 TeV. Moreover, this finding reinforces the conclusion that the smaller than unity charged-particle  $R_{AA}$  observed in PbPb collisions is primarily due to jet quenching in the QGP.

Additionally, dijet  $p_T$  asymmetry studies in pPb collisions at 5.02 TeV [125] have been performed to explore the possibility of larger dijet  $p_T$  asymmetry than in the pp reference, as observed in PbPb collisions (discussed in Section 5.1). The dijet  $p_T$  balance  $x_j$ , which is the ratio of the subleading ( $p_{T,1}$ ) to leading ( $p_{T,2}$ ) jet  $p_T$ , is sensitive to differences between the jet quenching effects on the leading and subleading jets in the event. Selected MB and dijet events were divided into HF activity classes according to the raw transverse energy measured in the HF detectors within the pseudorapidity interval  $4.0 < |\eta| < 5.2$ , denoted as  $E_T^{4 < |\eta| < 5.2}$ . This pseudorapidity interval is chosen to separate the event class selection and dijet measurements by a pseudorapidity gap of at least one unit ( $3.0 < |\eta| < 4.0$ ). For all  $E_T^{4 < |\eta| < 5.2}$  classes, no significant modification of  $x_j$  has been detected. In Fig. 100, the mean of  $x_j$  in different event activity classes is compared to a PYTHIA+HIJING reference with no jet quenching effect. Even for events with the largest  $E_T^{4 < |\eta| < 5.2}$ , no significant deviation from the PYTHIA+HIJING reference is observed. This result provides valuable insights into the allowed size of any quenching effects. Furthermore, studies of jet fragmentation functions, as well as inclusive and charm

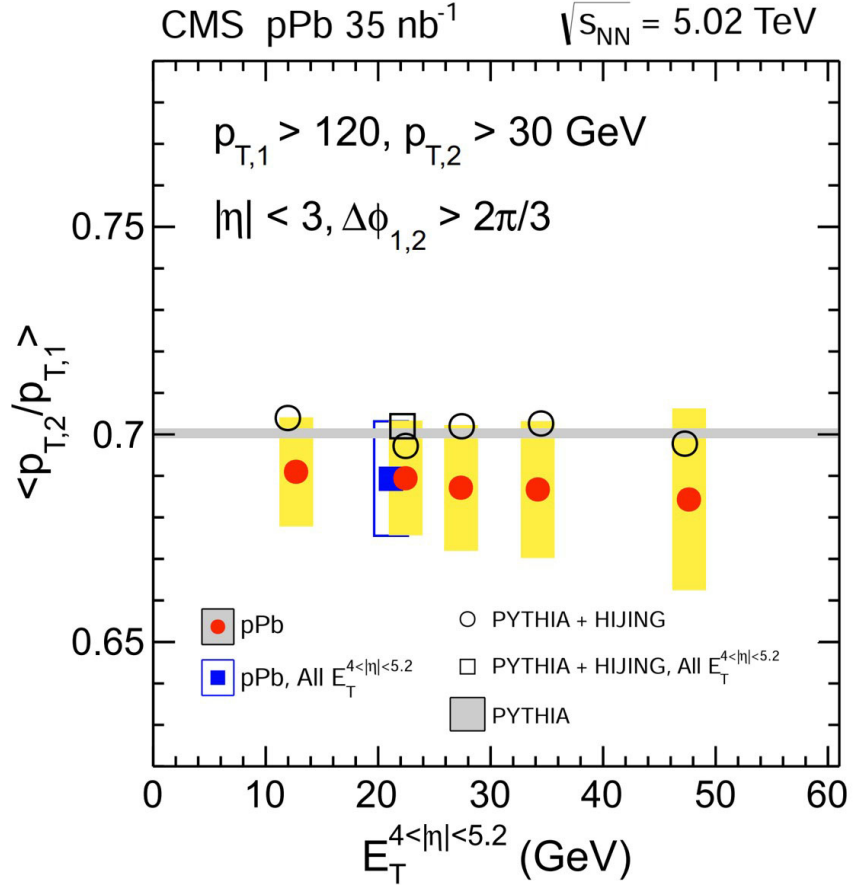


Figure 100: Average ratios of jet transverse momenta as a function of  $E_T^{4 < |\eta| < 5.2}$ . The inclusive HF activity results for pPb and PYTHIA+HIJING are shown as blue solid and black empty squares, respectively. The systematic (statistical) uncertainties are indicated by the yellow, grey, and blue boxes (vertical bars). Various theoretical calculations are shown by the open square and circles and the grey band at about 0.7. (Figure adapted from Ref. [125].)

jet nuclear modification factors in pPb collisions, indicate no significant nuclear modifications when compared to pp references [544, 545]. This consistency indicates that, within the current experimental uncertainties, no significant modifications are observed in the jet fragmentation patterns in pPb collisions.

An alternative approach to investigate jet quenching involves studying the azimuthal angle anisotropy of high- $p_T$  hadrons through two-particle correlation functions. Nevertheless, it is crucial to acknowledge that measuring the high- $p_T$   $v_2$  in pPb collisions presents challenges as a result of significant nonflow contributions. To address this issue, various techniques, such as selecting events with large rapidity gaps and subtracting low multiplicity events, have been employed to mitigate the impact of nonflow effects. Using these techniques, the CMS analysis reveals positive high- $p_T$   $v_2$  values up to  $p_T = 8$  GeV, as depicted in Fig. 95. These findings suggest possible room for jet quenching effect in pPb collisions at high  $p_T$ . However, it is important to note that the magnitude of  $v_2$  heavily depends on the nonflow subtraction method, which currently hinders reaching a conclusion when using  $v_2$  measurements in the search for jet quenching in small systems. In summary, the reported high- $p_T$  jet and hadron results for pPb collisions do not exhibit clear indications of jet quenching, setting important constraints on the size of any such effects.

## 6.5 Summary of results for small systems

Studies of inclusive particle production across pp, pPb, and PbPb collisions have demonstrated that the PbPb system, at the same  $\sqrt{s_{\text{NN}}}$ , converts energy into charged particles more efficiently than either the pp or pPb systems. In high-multiplicity pPb collisions, transverse energy distributions and the mean  $p_{\text{T}}$  of charged particles are better described by the EPOS LHC generator, which incorporates hydrodynamical evolution, than by models without hydrodynamics. This underscores the importance of hydrodynamic effects in these systems.

The CMS Collaboration has observed long-range correlations indicative of charged-hadron collectivity in high-multiplicity pp and pPb collisions (and with some indication in low-multiplicity pp collisions), similar to those seen in HI collisions. Multiparticle correlation analyses across pp, pPb, and PbPb collisions provide strong evidence of collectivity. These studies have been extended to the  $\gamma$ Pb system using UPCs, where the data align with models excluding collective effects, highlighting the varying nature of collectivity in different collision systems.

Heavy-flavor meson collectivity has also been explored, with measurements of prompt  $D^0$  and  $J/\psi$  mesons in pPb and pp collisions suggesting a weaker collectivity signal for charm quarks compared to light quarks. Charm quarks exhibit positive elliptic flow even in low-multiplicity pPb collisions, while bottom hadrons show weaker collective signals (albeit better measurements are needed to confirm this indication), pointing to a mass hierarchy in quark collectivity.

In the realm of quarkonia, CMS has identified distinct final-state interactions in pPb collisions, particularly in the suppression patterns of excited versus ground states of  $c\bar{c}$  and  $b\bar{b}$  systems. These suppression patterns are more pronounced in the lead-going rapidity region, likely a consequence of increased interactions with comoving particles leading to greater dissociation of excited states. In contrast, the forward (proton-going) region shows similar suppression for both states, aligning with studies of  $Y$  mesons, where particle multiplicity influences the production ratios of excited-to-ground states. Additionally, in high-multiplicity pp collisions, events with ground state  $Y(nS)$  mesons tend to have more charged-particle tracks than those with excited states, suggesting that factors beyond feed-down contributions affect particle production.

Lastly, CMS has conducted searches for jet quenching in small collision systems. Studies using various observables, including inclusive charged-particle  $R_{\text{pA}}$  and jet fragmentation functions, have shown no detectable jet quenching in pPb collisions at high  $p_{\text{T}}$ . However, more precise measurements are needed to clarify, with improved significance, if jet quenching is completely absent or simply below the levels that can be probed with the current samples of pPb collisions.

## 7 Tests of the electroweak sector and searches for new physics

In addition to the nuclear hadronic interactions discussed in previous sections, EM interactions can also be studied using the CMS detector. In UPCs that occur at large separations of the colliding nuclei in the transverse plane (i.e., such that the strong interaction does not dominate the collision dynamics), very large EM fields are possible [66–68]. In HI collisions, the field of each ion can interact with that of the other ion, leading to particle production via  $\gamma\gamma$  and  $\gamma A$  interactions.

Two-photon interactions are fundamental processes that have previously been studied, in particular, at HERA and LEP [546]. In general,  $\gamma\gamma$  measurements using UPC at the LHC have focused on QED processes and probing new physics phenomena. In HI collisions, studies of QED processes with strong EM fields benefit from a background-free environment due to the dominance of the  $\gamma\gamma$  process over central diffraction, both of which are characterized by substantial rapidity gaps [547]. Many final states have been measured in UPC  $\gamma\gamma$  interactions of proton and/or lead beams at the LHC, as described in Refs. [218, 548, 549] and references therein, including lepton pair production ( $\gamma\gamma \rightarrow e^+e^-, \mu^+\mu^-, \tau^+\tau^-$ ). In combination with the identification of interactions in which at least one of the lead nuclei is excited, based on neutrons detected by the ZDC detectors (discussed in Section 3.4), these processes are studied over a wide range of nuclear impact parameters. More specifically, these effects may be enhanced in events with a higher number of neutrons emitted or depleted in events with a lower number of emitted neutrons [71]. At higher photon energies, where the photon flux is large, QCD two-photon processes are also of great interest, e.g., double vector meson production [550], which complements multiparton scattering studies in pp, pPb, and PbPb collisions [551], and investigations of charmonium states to constrain their decay widths [552, 553]. Since UPC calculations can be extended to include collisions with partial nuclear overlap, where dynamics related to the strong interaction is present,  $\gamma\gamma$  interactions have also been studied in peripheral nuclear collisions, as discussed in Ref. [554] and references therein.

In the case of ultraperipheral pA collisions, the proton can also interact with the EM field generated by the heavy ion. The pA measurements extend the energy range accessible in photoproduction studies at HERA for several important processes. As discussed in Section 3, the non-linear QCD dynamics in heavy nuclei at small- $x$  gluon densities can be studied through heavy quark production by photon-gluon fusion when the gluon originates from the nucleus, or via diffractive dynamics when the gluon comes from a Pomeron [555]. Although these studies are also important for understanding the AA collision dynamics in the framework of collinear factorization at NLO in pQCD [226, 556] and in the dipole picture [227], this section focuses on interesting  $\gamma\gamma$  interaction processes in PbPb collisions.

Stronger experimental limits on increasingly larger masses of BSM particles have made the potential discovery of these particles in  $\gamma\gamma$  processes at the LHC more challenging [557]. Still, there are interesting regions of parameter space for BSM production that can be explored. At the LHC, higher  $\gamma\gamma$  invariant masses are accessible with pp collisions and lower masses can be explored with PbPb collisions [558, 559]. In pp collisions, protons that have lost a few percent of their energy can be tagged [560], which makes it possible to study processes involving, for example, EW bosons ( $\gamma\gamma \rightarrow W^+W^-, ZZ, \gamma\gamma$ ) [561]. Although the  $\gamma$  spectrum falls less rapidly for smaller charges—favoring proton over nuclear beams in the production of large invariant mass diphoton systems—each photon flux scales with the squared charge of the hadron,  $Z^2$ , such that the effective  $\gamma\gamma$  luminosities are significantly enhanced for ion beams (e.g., in the case of PbPb collisions, the enhancement factor is  $Z^4 = 5 \times 10^7$ ). The Lorentz factor of the Pb beam at the LHC dictates the maximum quasireal photon energy of approximately 80 GeV,

leading to  $\gamma\gamma$  collisions of energies up to  $\sqrt{s} \approx 160$  GeV. This is comparable to the center-of-mass energy achieved at LEP [562] but with  $Z^4$  enhanced production cross sections.

Therefore, a wide range of processes can be studied using  $\gamma\gamma$  interactions in UPCs. In the following, some examples of photon-induced processes using PbPb UPC are described, including exclusive high-mass dilepton ( $m_{1+1-} \gtrsim 5$  GeV) production (Sections 7.1 and 7.2), the rare processes of light-by-light (LbL) scattering and  $\tau$  lepton production (Section 7.3), and BSM searches, e.g., for axion-like particles (ALPs, Section 7.4). The final-state signature of these studies is exceptionally clean. Figure 101, as an example, shows the interaction  $\text{PbPb} \rightarrow \gamma\gamma \rightarrow \text{Pb}^{(*)}\tau^+\tau^-\text{Pb}^{(*)}$ , with a leptonic  $\tau$  decay (red),  $\tau \rightarrow \mu\bar{\nu}_\mu\nu_\tau$ , and a hadronic  $\tau$  decay (yellow),  $\tau \rightarrow \pi^\pm\pi^\mp\pi^\pm\nu_\tau$ . Otherwise, the central part of the detector is empty. Typically, outgoing Pb ions survive the interaction, whereas neutrons originating from a potential electromagnetic excitation (denoted by the superscript “(\*)”) are detected at very high  $|\eta|$ . Interestingly, the  $\gamma\gamma \rightarrow e^+e^-$  production process, in which the electron is captured in a bound state with one of the ions (“bound-free pair production”), is the dominant beam-physics effect restricting the maximum PbPb luminosity at the LHC [563].

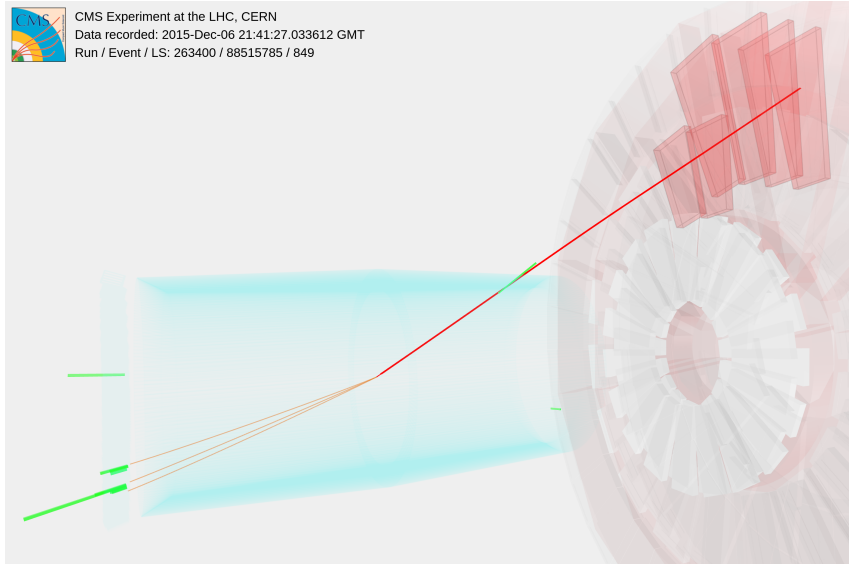


Figure 101: Event display of a candidate  $\gamma\gamma \rightarrow \tau^+\tau^-$  event measured in a PbPb UPC at CMS. The event is reconstructed as corresponding to a leptonic  $\tau$  decay (red),  $\tau \rightarrow \mu\bar{\nu}_\mu\nu_\tau$ , and a hadronic  $\tau$  decay (yellow),  $\tau \rightarrow \pi^\pm\pi^\mp\pi^\pm\nu_\tau$ . (Figure adapted from Ref. [549].)

## 7.1 The QED production of an exclusive muon pair

An experimental handle is essential to determine the impact parameter dependence of lepton pair production in UPCs [564]. As discussed in Section 3.4, the impact parameter of the UPC can be controlled by using forward-emitted neutron multiplicities from the electromagnetic dissociation (EMD) of one or both of the Pb ions. In this way, we can disentangle possible contributions from initial-state (associated with the QED field strength) and final-state (e.g., multiple scattering in the QGP) effects that are both strongly dependent on the impact parameter. More specifically, a broadening of lepton pair azimuthal angle correlations (or, equivalently, an increase in the lepton pair  $p_T$ ) is observed in hadronic collisions compared to those from UPCs. Alternative origins of this modification have been proposed, including final-state EM modifications of lepton pairs within a QGP medium [554, 565] or an impact parameter dependence of the initial photon  $p_T$  value [566–568], or both processes combined.

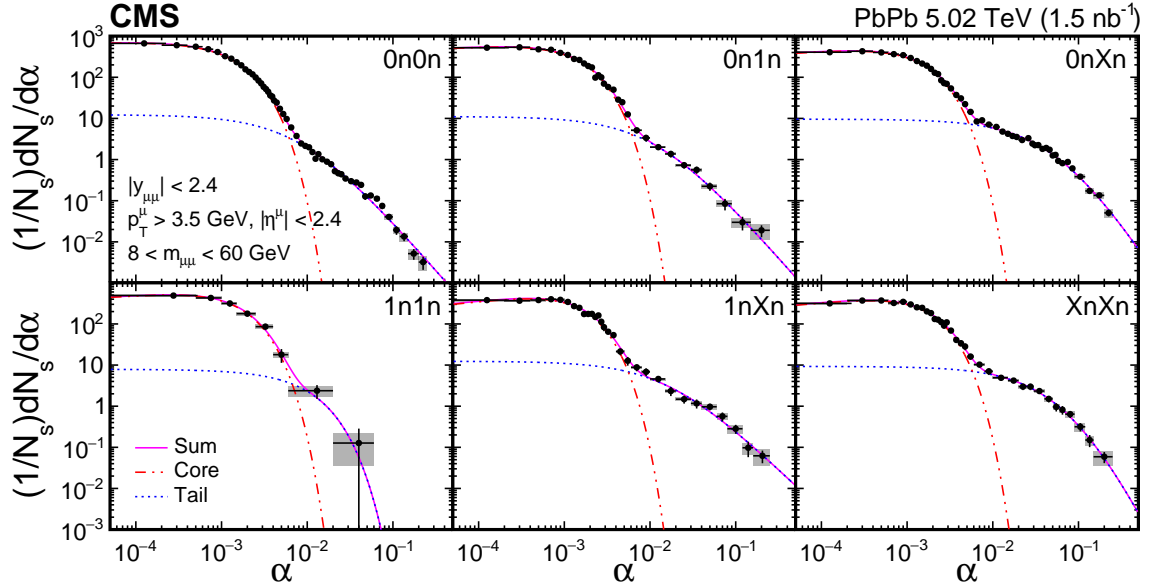


Figure 102: Neutron multiplicity dependence of acoplanarity distributions from  $\gamma\gamma \rightarrow \mu^+\mu^-$  in ultraperipheral PbPb collisions at  $\sqrt{s_{\text{NN}}} = 5.02$  TeV. The  $\alpha$  distributions are normalized to unit integral over their measured range. The dot-dot-dashed and dotted lines indicate the core and tail contributions, respectively. The vertical lines on data points depict the statistical uncertainties, while the systematic uncertainties and horizontal bin widths are shown as gray boxes. (Figure adapted from Ref. [218].)

Figure 102 shows the distributions of the acoplanarity,  $\alpha = 1 - |\phi^+ - \phi^-|/\pi$ , of  $\mu^+\mu^-$  pairs for six neutron multiplicity classes in PbPb UPCs at  $\sqrt{s_{\text{NN}}} = 5.02$  TeV. Here,  $\phi^\pm$  represents the azimuthal angle of the positive and negative muons in the laboratory frame, so  $\alpha$  characterizes the deviation from back-to-back azimuthal separation of the muon pair. The 0n0n class corresponds to no Coulomb breakup of either nucleus, and the 1nXn ( $X \geq 2$ ) class corresponds to one neutron emitted from one nucleus and at least two neutrons emitted from the other nucleus. Each  $\alpha$  distribution is characterized by a narrow core close to zero (note the logarithmic horizontal scale) and a long tail. The core component originates mainly from LO  $\gamma\gamma \rightarrow \mu^+\mu^-$  scattering. In the tail component, however, higher order processes dominate, e.g., extra photon radiation from the produced lepton(s), multiple-photon interactions, and scattering of (one or both) photons emitted from one of the protons inside the nucleus [569, 570].

To investigate a possible dependence of the initial photon  $p_T$  value on the impact parameter, the core contribution to the  $\alpha$  distribution is decoupled from the tail contribution using a two-component empirical fit function [218]. The average acoplanarity of  $\mu^+\mu^-$  pairs from the core component ( $\langle\alpha^{\text{core}}\rangle$ ) is then determined using the fit function. The neutron multiplicity dependence of  $\langle\alpha^{\text{core}}\rangle$  for  $\mu^+\mu^-$  pairs is shown in Fig. 103 (upper). A strong neutron multiplicity dependence of  $\langle\alpha^{\text{core}}\rangle$  is clearly observed, while  $\langle\alpha^{\text{core}}\rangle$  predicted by the STARLIGHT MC generator [115], shown as the dot-dashed line in Fig. 103 (upper), is almost constant. In contrast, the  $\langle\alpha^{\text{core}}\rangle$  value in the data increases as the multiplicity of neutrons emitted increases. A constant value of  $\langle\alpha^{\text{core}}\rangle$  as a function of the neutron multiplicity is rejected with a  $p$  value corresponding to 5.7 standard deviations. A LO QED calculation [571], which incorporates an impact parameter dependence of the initial photon  $p_T$ , can qualitatively describe the increasing trend of  $\langle\alpha^{\text{core}}\rangle$ , as shown by the dashed line in Fig. 103 (upper). This observation suggests that the  $p_T$  values of the initial photons producing  $\mu^+\mu^-$  pairs have a significant dependence on the impact parameter, which affects both the  $p_T$  and the acoplanarity of the muon pairs in the

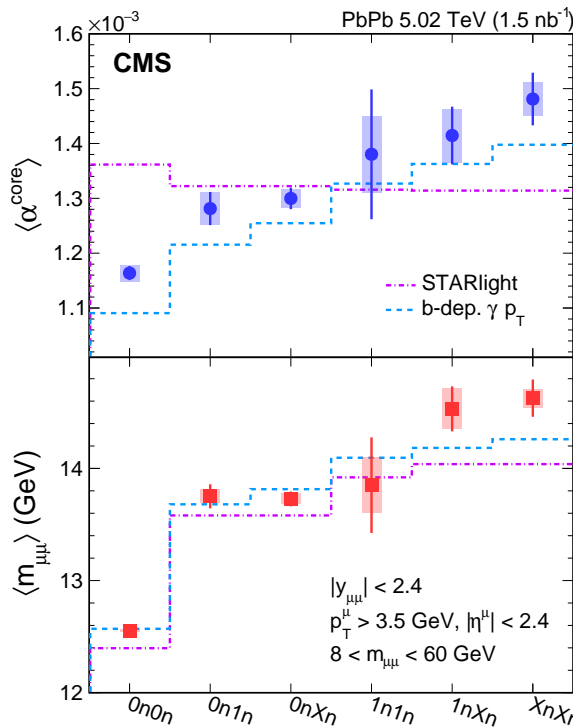


Figure 103: Neutron multiplicity dependence of the (upper) average acoplanarity  $\langle \alpha^{\text{core}} \rangle$  and (lower) average invariant mass  $\langle m_{\mu\mu} \rangle$  of  $\mu^+\mu^-$  pairs in ultraperipheral PbPb collisions at  $\sqrt{s_{\text{NN}}} = 5.02 \text{ TeV}$ . The vertical lines on data points depict the statistical uncertainties while the systematic uncertainties of the data are shown as shaded areas. The dot-dashed line shows the STARLIGHT MC prediction and the dashed line corresponds to the LO QED calculation of Ref. [571]. The calculation incorporating Sudakov radiative corrections is also compared to data in Ref. [218], leading to an overall better agreement. (Figure adapted from Ref. [218].)

final state. This initial-state contribution must be properly taken into account when exploring possible final-state EM effects arising from a hot QGP medium formed in hadronic heavy ion collisions [554, 565].

In Fig. 103 (lower), the average invariant mass  $\langle m_{\mu\mu} \rangle$  of muon pairs is shown as a function of the neutron multiplicity. A clear neutron multiplicity dependence of  $\langle m_{\mu\mu} \rangle$  is observed, with the  $\langle m_{\mu\mu} \rangle$  value measured in  $XnXn$  events being greater than that in  $0n0n$  events with a significance exceeding 5 standard deviations. This trend of  $\langle m_{\mu\mu} \rangle$  can be qualitatively described by both model calculations. As the muon pair invariant mass is largely determined by the initial photon energy, this observation suggests that the energy of the photons is, on average, larger in collisions with a smaller impact parameter, a conclusion similar to that previously drawn for the initial photon  $p_T$  value.

## 7.2 The QED production of an exclusive electron-positron pair

One of the possible backgrounds in the  $\gamma\gamma \rightarrow \gamma\gamma$  final state (shown schematically in Fig. 104, left) is the QED production of an exclusive electron-positron pair (Fig. 104, center) and the gluon-induced central exclusive production (CEP) (Fig. 104, right). Exclusive  $\gamma\gamma \rightarrow e^+e^-$  events can be misidentified as  $\gamma\gamma \rightarrow \gamma\gamma$  scattering in the case that neither electron track is reconstructed or when both electrons undergo hard bremsstrahlung. Given that the cross section for the  $\gamma\gamma \rightarrow e^+e^-$  process is four to five orders of magnitude larger than that for  $\gamma\gamma \rightarrow \gamma\gamma$  scattering, and its identification relies on physics objects (electrons) that closely resemble those

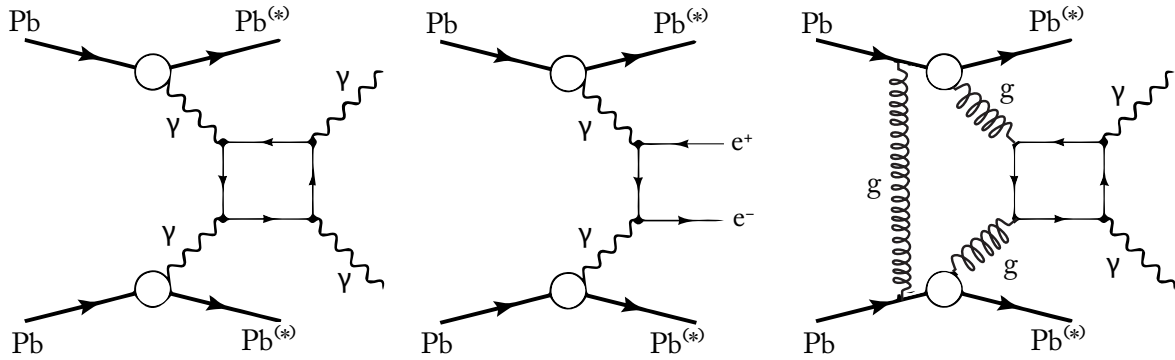


Figure 104: Schematic diagrams of light-by-light scattering ( $\gamma\gamma \rightarrow \gamma\gamma$ , left), QED dielectron ( $\gamma\gamma \rightarrow e^+e^-$ , center), and central exclusive diphoton ( $gg \rightarrow \gamma\gamma$ , right) production in ultraperipheral PbPb collisions. The “(\*)” superscript indicates a potential electromagnetic excitation of the outgoing ions. (Figure adapted from Ref. [548].)

of the signal ( $\gamma$ ), a thorough analysis of the exclusive dielectron background is undertaken. This aims not only to estimate event-level efficiencies that are common for the dielectron and diphoton final states, but also to determine a  $\gamma\gamma \rightarrow \gamma\gamma / \gamma\gamma \rightarrow e^+e^-$  production cross section ratio with reduced common uncertainties.

In addition to the low- $p_T$  (low- $E_T$ ) online event selection and to the selection of physics objects (discussed in Section 2), the offline analysis includes a series of additional requirements to increase the signal component coming from exclusive  $\gamma\gamma$  production. More specifically, the so-called “neutral and charged exclusivity” selection criteria are applied to reject events that have additional activity in the  $|\eta| < 5.2$  range. For the neutral exclusivity criteria, events must have no activity in the calorimeters above energy noise thresholds, with noise thresholds determined from no- or single-bunch crossing events and separately in the barrel and endcap regions (discussed in Section 2.1). For the charged exclusivity criteria, events with additional reconstructed charged-particle tracks above a certain low- $p_T$  threshold (e.g., 0.1 GeV) are removed from further consideration. To further eliminate nonexclusive backgrounds, characterized by a final state with a larger vector sum of the  $p_T$  values and larger diphoton acoplanarities  $A_\phi = (1 - \Delta\phi^{e^+e^-} / \pi)$  than the back-to-back exclusive events, the transverse momentum and acoplanarity of the reconstructed systems are required to satisfy  $p_T^{e^+e^-} < 1$  GeV and  $A_\phi < 0.01$ . These values are motivated by initial phenomenological studies [572] and further optimized based on similar CMS studies of exclusive dilepton production [573, 574].

Figure 105 shows the  $e^+e^-$  acoplanarity distribution measured in the data, compared to MC expectations. The curve is a binned  $\chi^2$  fit of the data to the sum of two exponential functions, representing the exclusive QED  $e^+e^-$  production plus any residual background in the high- $A_\phi$  tail. It should be noted that using the 2015 PbPb data set (Table 1 in Section 2.3) approximately ten thousand dielectron events are reconstructed in the signal-dominated region of  $A_\phi < 0.01$  with a purity of almost unity (as obtained from the ratio of amplitudes of the two exponential functions fitted to the data). The yellow histogram shows the same distribution, obtained directly from a LO QED MC simulation. A small difference is found between the average  $A_\phi$  value obtained from the data and the MC prediction, resulting from the higher experimental yields for events with  $A_\phi > 0.01$ . This is probably the result of  $\gamma\gamma \rightarrow e^+e^-$  events where one (or both) electrons radiate an extra soft photon, which are not explicitly simulated with LO MC event generators, and/or any residual background surviving the event selection. When inte-

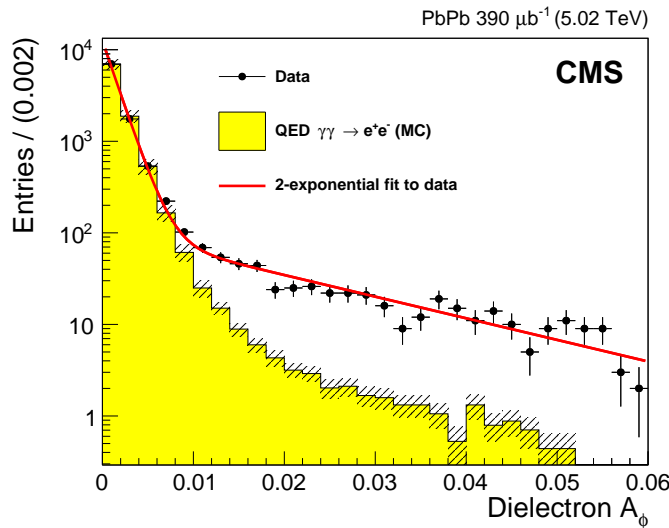


Figure 105: Acoplanarity distribution of exclusive  $e^+e^-$  events measured in data (circles), compared to the expected QED  $e^+e^-$  spectrum in a LO MC simulation (histogram). The curve shows a  $\chi^2$  fit to the sum of two exponential distributions, corresponding to exclusive  $e^+e^-$  plus any residual (nonacoplanar) background pairs. The error bars represent statistical uncertainties while the hashed bands around the histogram represent the systematic and MC statistical uncertainties added in quadrature. The horizontal bars indicate the bin size. (Figure adapted from Ref. [548].)

grated over the whole range of the distributions, these discrepancies modify the measurements below the current level of precision, and hence do not significantly alter the interpretation of the data. However, their influence on the accuracy of the extracted cross sections will gradually increase with the accumulation of a larger amount of luminosity. Some recent progress has been reported towards understanding higher-order QED corrections in more detail, particularly those resulting from final-state photon radiation from the leptons [575].

Some corresponding kinematic distributions of the selected  $\gamma\gamma \rightarrow e^+e^-$  events in the  $A_\phi < 0.01$  region are shown in Fig. 106, together with the corresponding MC predictions. Good agreement between data and simulations is found, thereby confirming the MC predictions for exclusive particle production in PbPb UPCs at the LHC, as well as illustrating the quality of the EM particle reconstruction and the exclusive event selection criteria in CMS.

### 7.3 Light-by-light scattering and $\tau$ lepton pair production

As indicated in Fig. 104 (left), the elastic LbL scattering that occurs in HI collisions is a purely quantum-mechanical process that, to LO in the QED coupling constant  $\alpha$ , proceeds via virtual box diagrams [572, 576]. The QED box diagram involves contributions from either charged fermions or the  $W^\pm$  bosons. The direct observation of LbL scattering in the laboratory has remained elusive until recently due to a very suppressed production cross section, proportional to  $\alpha^4 \approx 3 \times 10^{-9}$ . However, based on PbPb collision data recorded in 2015, both the ATLAS [577] and CMS [548] Collaborations have found direct evidence of LbL scattering. The ATLAS Collaboration subsequently analyzed a larger PbPb data sample, obtained in 2018 [578]. More recently, an aggregate analysis was performed [579], further improving the experimental uncertainty by approximately 10% compared to the individual analyses.

The LbL signal is extracted by applying the same selection criteria, including full exclusivity, as described above for the QED  $e^+e^-$  events, with the main requirement corresponding to

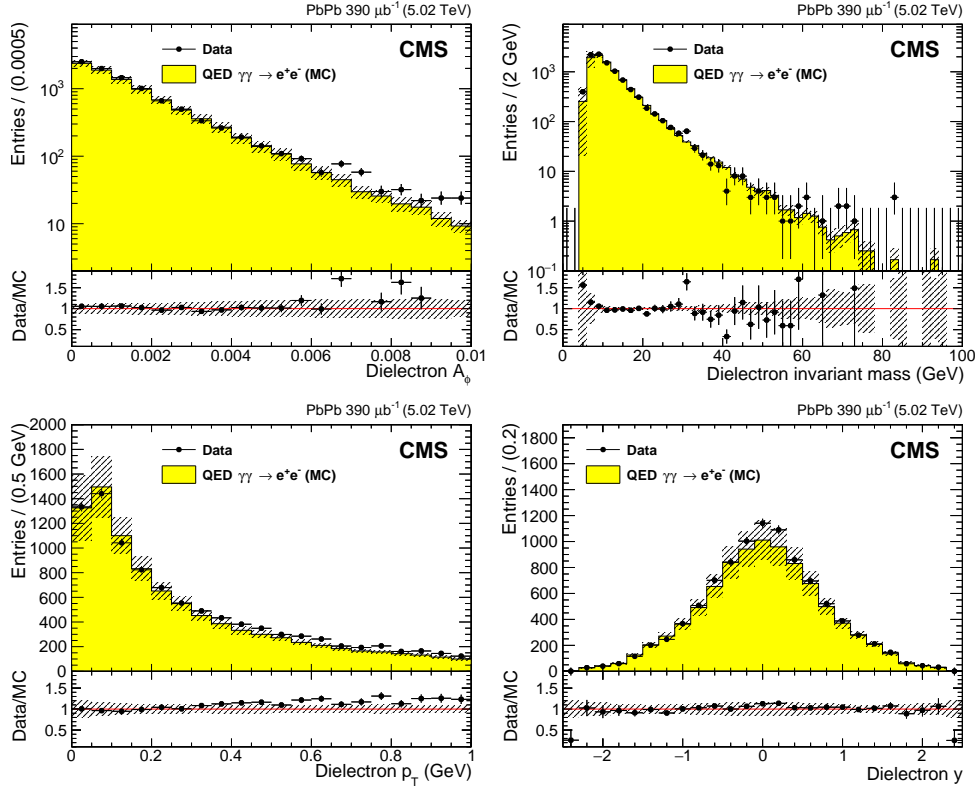


Figure 106: Comparison of data (circles) and MC expectation (histogram) for the exclusive  $e^+e^-$  events passing the selection criteria, as a function of dielectron acoplanarity (upper left), mass (upper right),  $p_T$  (lower left), and rapidity  $y$  (lower right). The error bars around the data points represent statistical uncertainties, while the hashed bands around the histograms represent the systematic and MC statistical uncertainties added in quadrature. The horizontal bars indicate the bin size. The ratio of the data to the MC expectation is shown in the lower panels. (Figures adapted from Ref. [548].)

having two photons (rather than electrons), each with  $E_T > 2 \text{ GeV}$  and  $|\eta| < 2.4$ , and having a diphoton invariant mass larger than  $5 \text{ GeV}$ . In the analysis, photons falling in the range  $1.444 < |\eta| < 1.566$ , corresponding to a gap region between the barrel and endcaps of the ECAL detector (discussed in Section 2.1), are missed. We observe 14 LbL scattering candidates, to be compared with the  $9.0 \pm 0.9$  (theo) STARLIGHT MC generator prediction for the LbL scattering signal. The (conservative) 10% uncertainty in the LbL theoretical prediction covers different implementations of the nonhadronic overlap condition for varying Pb radius and NN cross section values, as well as neglected NLO corrections. The overall data-to-simulation agreement is very good, given the small residual diphoton background:  $3.0 \pm 1.1$  (stat) from CEP and  $1.0 \pm 0.3$  (stat) from misidentified QED  $e^+e^-$  events.

Figure 107 compares the measured and simulated distributions for the single photon  $p_T$  and  $\eta$ , and for the diphoton invariant mass and  $p_T$ . Similarly to the measured yields, the kinematic distributions are also in agreement with the combination of the LbL scattering signal plus the background expectation. It should be noted that the overall diphoton cross section efficiency is approximately 20%, compared with about 10% for dielectrons. The lower efficiency results from each individual electron having a relatively large probability of losing energy by bremsstrahlung before reaching the ECAL, thereby causing some losses by not satisfying the trigger selection threshold.

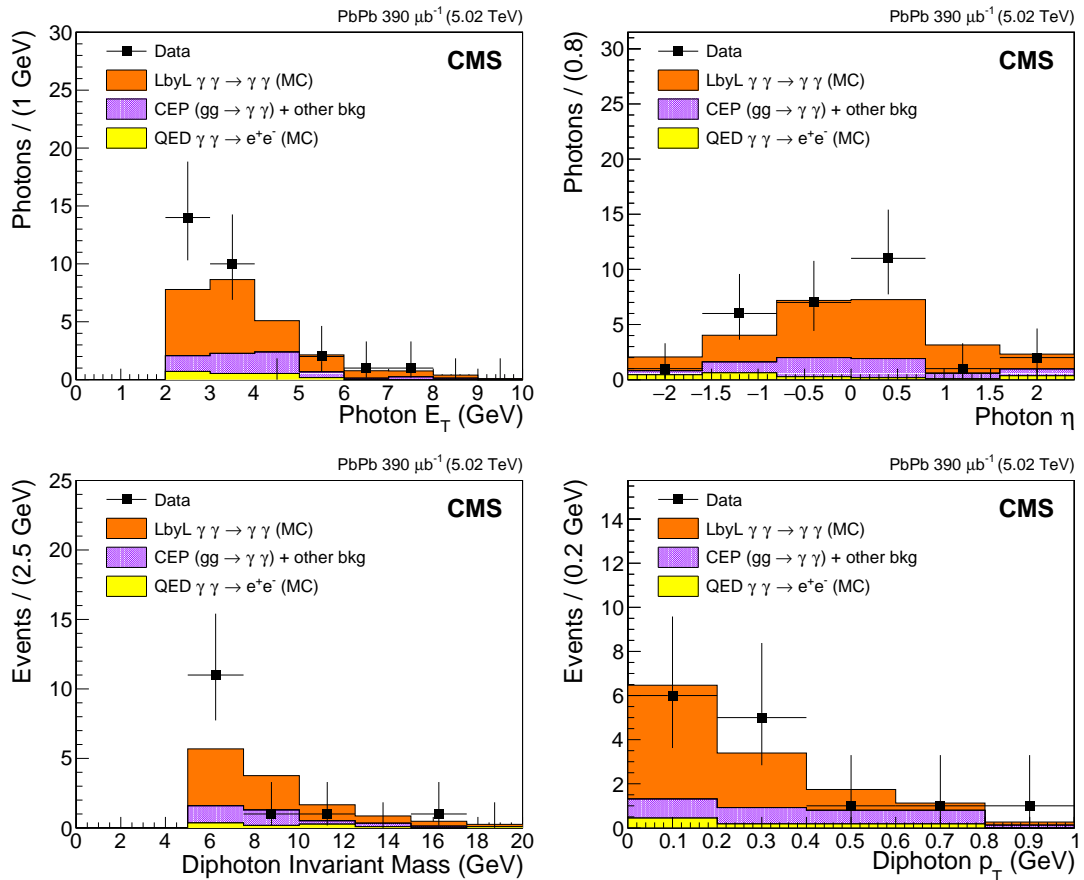


Figure 107: Distributions of the single photon  $E_T$  (upper left) and  $\eta$  (upper right), as well as diphoton invariant mass (lower left) and  $p_T$  (lower right), measured for the exclusive events passing the selection criteria (squares), compared to the expectations of LbL scattering signal (orange), QED  $e^+ e^-$  MC generator predictions (yellow), and the CEP background (light blue). The error bars indicate statistical uncertainties. (Figures adapted from Ref. [548].)

As noted in Ref. [549], the possibility of observing photon-induced  $\tau$  lepton production in UPC events at a HI collider was considered well before the LHC era [580]. Recently, theoretical studies have proposed that the kinematic properties of  $\tau$  lepton pairs produced in UPCs at the LHC can be used to constrain the electromagnetic couplings of the  $\tau$  lepton [581–583]. These constraints allow for fundamental tests of QED and searches for BSM physics. This has motivated the use of novel experimental approaches to observe this process, as undertaken in recent measurements by the ATLAS [584] and CMS [549] Collaborations.

Based on the 2015 PbPb data sample, CMS has observed  $\tau$  lepton pairs in UPC PbPb collisions,  $\gamma\gamma \rightarrow \tau^+\tau^-$ , in events that may contain excitations of the outgoing Pb ions. One  $\tau$  lepton ( $\tau_\mu$ ) is reconstructed through its decay to one muon and two neutrinos, while the other ( $\tau_{3\text{prong}}$ ) is reconstructed through its “3 pronged” decay into hadrons plus a neutrino [464]. A typical event display is shown in Fig. 101. This choice of final state offers a clean experimental signature, with the muon used for online selection and the hadronically decaying  $\tau$  candidate providing discrimination against dimuon photoproduction and thus providing an unambiguous reconstruction of the  $\tau$  lepton decay. Kinematic distributions showing the  $\gamma\gamma \rightarrow \tau^+\tau^-$  signal process, as well as the background model based on control samples in the data, are shown in Fig. 108. Good agreement is observed between the measured distributions and the sum of the signal simulation and background estimation.

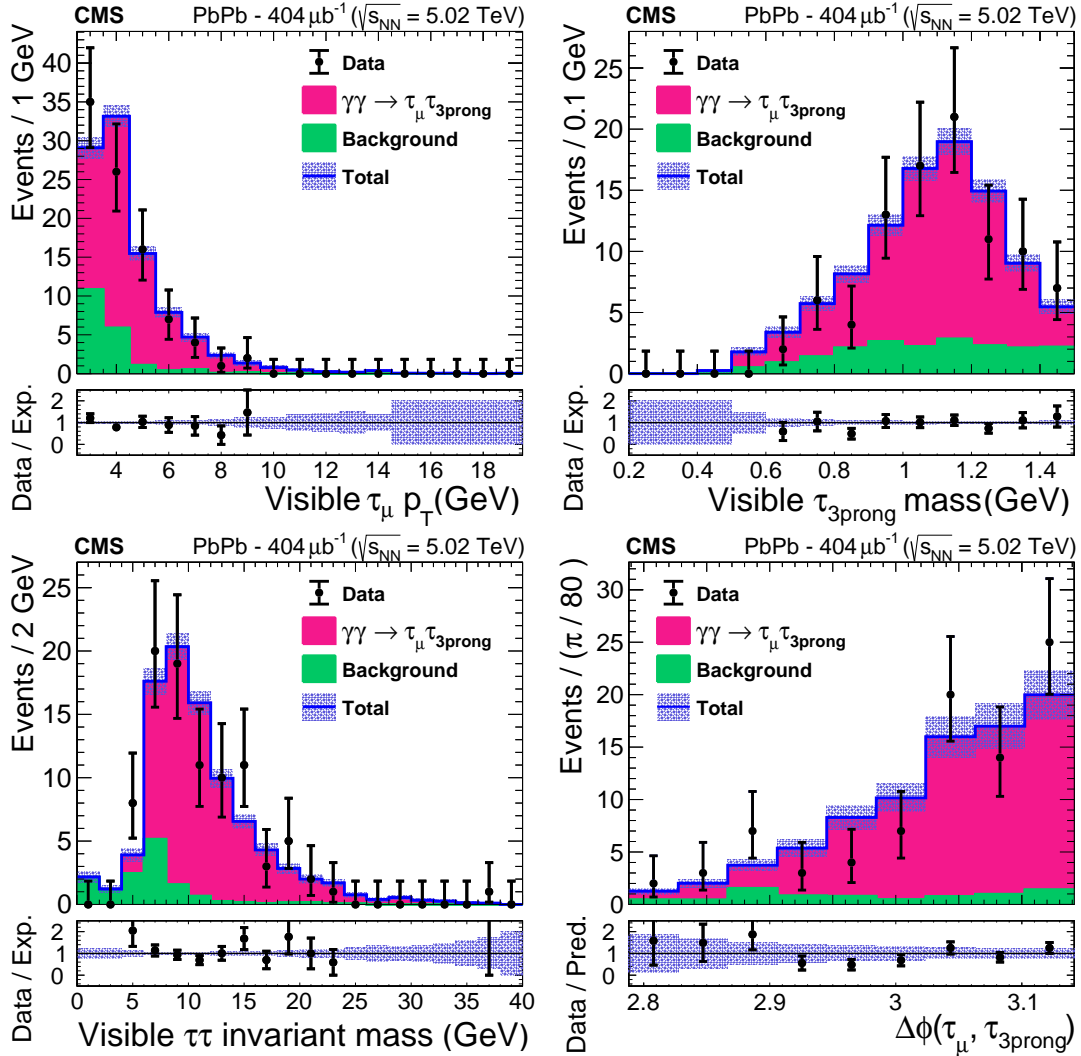


Figure 108: Transverse momentum of the muon originating from the  $\tau_\mu$  candidate (upper left). Invariant mass of the three pions forming the  $\tau_{3\text{prong}}$  candidate (upper right). Invariant mass of the  $\tau^+\tau^-$  system (lower left). The  $\Delta\phi(\tau_\mu, \tau_{3\text{prong}})$  azimuthal difference (lower right). In all plots, the signal component (magenta histogram) is stacked on top of the background component (green histogram). The sum of signal and background is displayed by a blue line and the shaded area shows the statistical uncertainty. The data are represented with black points and the uncertainty is statistical only. The lower panels show the ratios of data to the signal-plus-background prediction and the shaded bands represent the statistical uncertainty in the prefit expectation. (Figures adapted from Ref. [549].)

A maximum likelihood (binned) fit of the signal and background components is used for the signal extraction. The fit is performed on the distribution of the difference in azimuthal opening angle between the  $\tau_\mu$  and  $\tau_{3\text{prong}}$  candidates,  $\Delta\phi(\tau_\mu, \tau_{3\text{prong}})$ , exploiting the fact that the two signal  $\tau$  leptons are produced azimuthally back-to-back in UPCs. We measure  $77 \pm 12$   $\gamma\gamma \rightarrow \tau^+\tau^-$  signal events as the integral of the postfit signal component. The signal and background postfit  $\Delta\phi(\tau_\mu, \tau_{3\text{prong}})$  templates, along with the data, are also shown in Fig. 108 (lower right).

The measured fiducial cross section is shown in Fig. 109, in good agreement with LO QED predictions [581, 582]. The analytical calculation from Ref. [582] results in a cross section that is 20% higher than that found in Ref. [581]. This is explained in Ref. [582] as mainly stemming

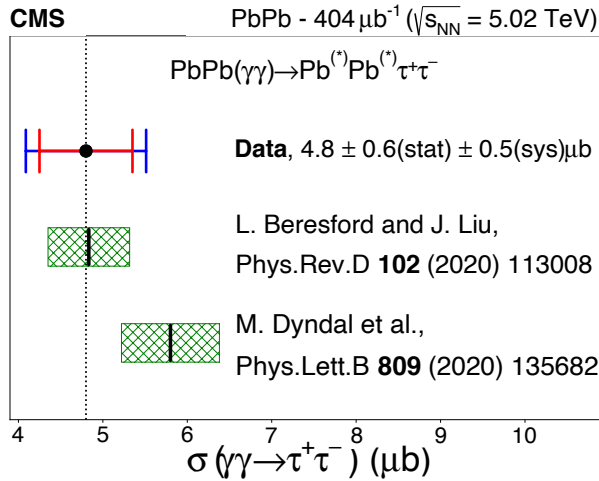


Figure 109: The  $\sigma(\gamma\gamma \rightarrow \tau^+\tau^-)$  cross section, measured in a fiducial phase space region at  $\sqrt{s_{\text{NN}}} = 5.02$  TeV. The theoretical predictions [581, 582] are computed with leading order accuracy in QED and are represented by the vertical solid lines, which can be compared with the vertical dotted line representing this measurement. The outer blue (inner red) error bars represent the total (statistical) uncertainties, whereas the green hatched bands correspond to the uncertainty in the theoretical predictions, as described in the text. The potential electromagnetic excitation of the outgoing Pb ions is denoted by (\*). (Figure adapted from Ref. [549].)

from the different requirements applied in the modeling of single-photon fluxes. In both cases, although further advancements in theory are needed for a proper uncertainty evaluation, a conservative uncertainty of 10% is reported, following the approach of Ref. [548].

#### 7.4 Exclusion limits on axion-like particle production and anomalous $\tau$ lepton magnetic moment

A contributing factor in the coupling of the lepton ( $\ell$ ) to the photon ( $\gamma$ ) is the anomalous magnetic moment  $a_\ell = (g - 2)_\ell/2$ , with the  $g$ -factor being the proportionality constant that relates the magnetic moment to the spin of the lepton. Although the predicted value of  $a_\tau$  is 0.00117721 (5), with the number in parentheses denoting the uncertainty in the last digit, its best measured value is  $-0.018 \pm 0.017$ , from the DELPHI Collaboration [585] (other existing limits on  $a_\tau$  can be found in Ref. [464]). The larger uncertainty in  $a_\tau$  compared to the measurements of  $a_\mu$  and  $a_e$  mainly results from the short  $\tau$  lepton lifetime, which is of the order of  $10^{-13}$  s, such that  $\tau$  leptons cannot be stored to measure their  $a_\tau$ -dependent precession in a magnetic field. A more precise  $a_\tau$  determination would facilitate tighter constraints on BSM physics models, in which additional particles with mass  $M$  contribute with terms typically proportional to  $(m_1/M)^2$ .

Thus, more recent calculations have evaluated the impact of BSM processes on the  $\gamma\gamma \rightarrow \tau^+\tau^-$  cross section. The BSM coupling variations in  $a_\tau$  can change the expected cross section and alter, e.g., the  $\tau$  lepton  $p_T$  spectrum [581, 582]. In Ref. [549], the dependence of the total  $\sigma(\gamma\gamma \rightarrow \tau^+\tau^-)$  on  $a_\tau$  [581] was used to extract a model-dependent value of  $a_\tau$  at the LHC, as shown in Fig. 110 at 68% CL. The projection to the integrated PbPb luminosity expected from the high-luminosity LHC program is also shown [586].

As noted in Ref. [548], the LbL process has been proposed as a particularly sensitive channel for studying BSM physics. Modifications of the LbL scattering rates can occur if, e.g., new heavy particles, such as magnetic monopoles, vector-like fermions or dark-sector particles, contribute

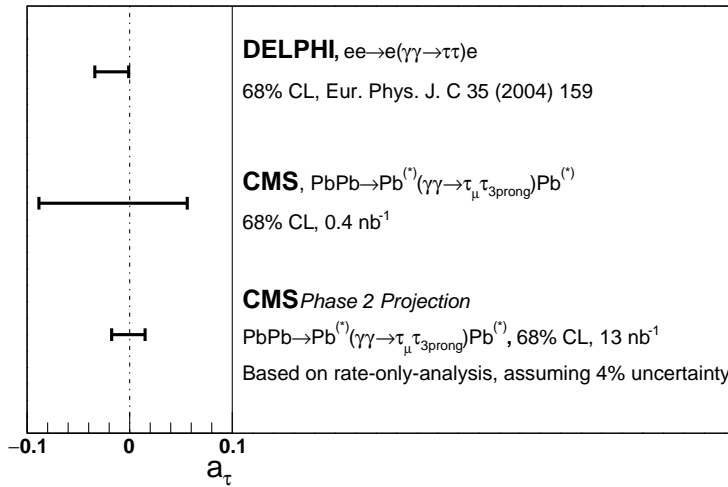


Figure 110: Comparison of the constraints on  $a_\tau$  at 68% CL from the analysis in Ref. [549] and the DELPHI experiment at LEP [585]. The projection to the integrated  $PbPb$  luminosity expected from the high-luminosity LHC program is included. (Figure adapted from Ref. [549].)

to the virtual corrections of the box depicted in Fig. 104 (left). Other new spin-even particles, such as ALPs [587] or gravitons [76, 588], can also contribute to the LbL scattering continuum or to new diphoton resonances. In addition, LbL cross sections are sensitive to Born–Infeld extensions of QED [589], and anomalous quartic gauge couplings [590].

The measured invariant mass distribution (Fig. 107, lower left) has been used to search for possible narrow diphoton resonances, such as pseudoscalar ALPs produced in the process  $\gamma\gamma \rightarrow a \rightarrow \gamma\gamma$ . All other processes, i.e., LbL, QED, and CEP, are considered as background in this search. Fully simulated STARLIGHT MC samples for ALP masses,  $m_a$ , ranging from 5 to 90 GeV are reconstructed. A binned maximum likelihood fit of the ALP signal and background contributions is performed on the data. A profile likelihood ratio is used as a test statistic based on the  $CL_s$  criterion [591, 592] to extract exclusion limits at 68 and 95% confidence levels (CL): first, in the  $\sigma(\gamma\gamma \rightarrow a \rightarrow \gamma\gamma)$  cross section; and then, in the  $g_{a\gamma}$  vs.  $m_a$  plane, where  $g_{a\gamma} \equiv 1/\Lambda$  is the ALP coupling to photons (with  $\Lambda$  being the energy scale associated with the underlying U(1) symmetry whose spontaneous breaking generates the ALP mass). Two scenarios are considered where the ALP couples to photons  $F^{\mu\nu}$  alone (shown in Fig. 111) or also to hypercharge. The derived constraints on the ALP mass and its coupling to photons in Fig. 111 are also compared to those obtained from various experiments (available up to the time of publication of Ref. [548]), assuming a 100% ALP decay branching fraction to diphotons. Despite the updated LbL measurement in Ref. [578] our exclusion limits still remain competitive over the  $m_a \approx 5\text{--}10 \text{ GeV}$  mass range [578], regardless of the sensitivity to the EM current alone or of extra ALP couplings to EW currents.

## 7.5 Summary of QED results and BSM searches with UPC

A broad range of photon-induced processes have been investigated using UPCs of lead ions at a center-of-mass energy per nucleon pair of 5.02 TeV. These studies span from standard QED tests to searches for BSM physics.

High-rate, exclusive, high-mass dilepton production ( $m_{l+1-} \gtrsim 5 \text{ GeV}$ ) from the 2018 data run is compared with QED expectations, providing a rigorous test of QED predictions. Rare processes, such as LbL scattering and  $\tau$  lepton production, have been explored to extend QED

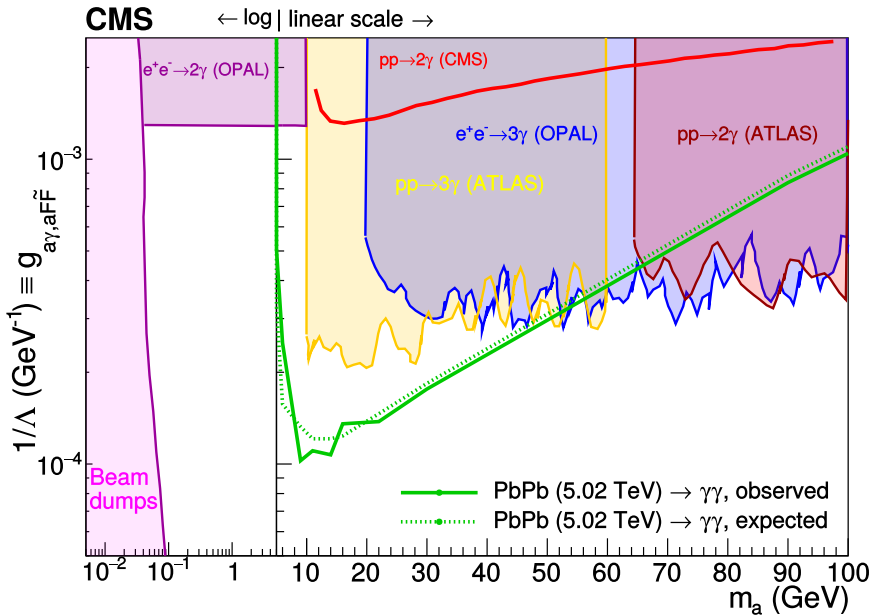


Figure 111: Exclusion limits at 95% CL in the ALP-photon coupling  $g_{a\gamma}$  vs. ALP mass  $m_a$  plane, for the operators  $a\tilde{F}\tilde{F}/4\Lambda$  assuming ALP coupling to photons only, derived in Refs. [587, 593] from measurements at beam dumps [594], in  $e^+e^-$  collisions at LEP 1 [593] and LEP 2 [595], and in  $pp$  collisions at the LHC [574, 596, 597], and compared to the limits obtained from Ref. [548]. (Figure adapted from Ref. [548].)

tests and to assess the potential of these channels to uncover BSM physics. The clean final-state signatures in these rare processes make such searches possible.

The CMS Collaboration conducted the first measurements of  $\gamma\gamma \rightarrow \mu^+\mu^-$  production as a function of forward neutron multiplicity in PbPb UPCs. A notable broadening of back-to-back azimuthal correlations was observed, increasing with the multiplicity of forward neutrons. This trend is qualitatively reproduced by a LO QED calculation that accounts for the influence of the impact parameter on the average  $p_T$  value of the photon. In the region of near back-to-back emission, the  $\gamma\gamma \rightarrow e^+e^-$  ratio shows good agreement between theory and data, confirming the quality of electromagnetic particle reconstruction and event selection criteria for exclusive QED production in PbPb UPCs.

Evidence for LbL scattering in PbPb UPC data was reported by CMS using data from 2015. The observed total yields and kinematic distributions align with expectations for the LbL scattering signal, with a small residual background primarily from misidentified exclusive dielectron and gluon-induced central exclusive processes. The exclusive diphoton invariant mass distribution was employed to set new exclusion limits on the production of pseudoscalar ALPs through the process  $\gamma\gamma \rightarrow a \rightarrow \gamma\gamma$ , covering the mass range of 5–90 GeV.

Additionally, CMS observed the production of  $\tau$  lepton pairs in PbPb UPCs using the 2015 data. Events featuring a final state with one muon and three charged hadrons were reconstructed, reaching a statistical significance exceeding five standard deviations with respect to the background-only expectation. The measured kinematical distributions and the extracted cross section both agree with LO QED predictions. From these measurements, a model-dependent value of the anomalous magnetic moment of the  $\tau$  lepton,  $a_\tau$ , was estimated, offering a novel experimental probe of  $a_\tau$  through heavy ion collisions at the LHC.

## 8 Summary

### 8.1 Discoveries and insights from the CMS heavy-ion physics program

This review presents the first comprehensive summary of results from the CMS heavy ion physics program using data collected during the first two running periods of the LHC: 2010–2013 and 2015–2018. After having successfully addressed many experimental challenges (Section 2), in particular thanks to major advances in the areas of online event selection and offline physics object reconstruction, CMS performed a series of measurements that covered and extended those initially anticipated (Section 1.4). Those experimental results, reviewed in the previous sections of this paper, covered several topics, including high-density quantum chromodynamics, precision quantum electrodynamics, and even novel searches for phenomena beyond the standard model.

These studies provide detailed macroscopic and microscopic probes of the quark-gluon plasma created at LHC energies, achieving the highest temperature and smallest baryon-chemical potential ever reached in a laboratory. The results have yielded groundbreaking insights across a wide range of quantum chromodynamics phenomena, representing some of the most important and novel findings in the history of the field. For example, CMS discovered that small collision systems, such as  $pp$  and  $pPb$ , can exhibit signs of collectivity, a phenomenon previously only associated with larger collision systems, such as  $PbPb$ . This discovery opened new avenues for understanding how fluidity and plasma-like properties emerge in QCD matter. Additionally, jet quenching measurements with fully reconstructed jets have set new standards, allowing us to experimentally assess medium modifications of entire parton showers beyond leading-hadron observables and to extract information about the medium response to hard probes. Studies of the nuclear modifications of the production yields of (fully reconstructed) beauty and charm hadrons, as well as of all five S-wave quarkonium states, including the rarely produced  $Y(3S)$ , have addressed long-standing questions in the field. Furthermore, evidence for gluon antishadowing and saturation, along with novel results from rare QED processes and beyond standard model searches, vastly expanded the scope of these studies. The three-dimensional evolution of the QGP has been explored, and signals of chiral magnetic effects have been excluded to a large extent. In the following paragraphs, we offer more details on these achievements, which highlight the significant contributions of CMS to the progress of our understanding of high-density QCD.

The study of the collectivity of charged hadrons in high-multiplicity  $pp$  and  $pPb$  collisions (Section 6) has provided the first observations of long-range correlations similar to those seen in HI collisions. The CMS Collaboration has offered further evidence of collectivity through multiparticle correlation and heavy-flavor meson analyses. The study of multiparticle correlations has been extended to smaller collision systems using ultraperipheral collisions, where the separation of the ions in the transverse plane strongly reduces the role of interactions mediated by quarks and gluons. One of the motivations for the small collision system studies was to search for evidence of jet quenching in these systems, to compare with the results obtained in collisions involving two heavy ions. Jet quenching effects have not been observed in  $pPb$  collisions.

The initial state of the nucleons and nuclei before a HI collision strongly influences the subsequent evolution of the created medium. The density of quarks and gluons within a nucleon, as a function of the fraction of the nucleon momentum ( $x$ ) carried by each parton and the squared transverse momentum transfer ( $Q^2$ ), is parameterized in terms of parton distribution functions. When the nucleon is embedded in a nucleus, this density is expressed as nuclear PDFs. Proton-lead collision data have been used to constrain the quark and gluon nuclear densities through

measurements of the cross section of electroweak gauge bosons, dijets, and top quark pairs (Section 3). Some of these results have been used as input to the latest nPDF fits, leading to a significant improvement in the precision across an extended phase space region. For studying the small- $x$  region, which is primarily driven by the evolution of the gluon density, the measurements of forward inclusive jet cross sections in pPb collisions and the cross sections for exclusive vector meson production in pPb and PbPb collisions have been used. As part of these studies, a technique has been developed to use forward neutron multiplicities in order to unfold the cross sections for exclusive vector meson production in the photon-nucleus frame, giving unprecedented access to the small- $x$  regime.

As expected, the LHC collaborations find a significant increase in the charged particle density and average transverse energy per charged particle compared to those found at RHIC energies, indicating a denser and hotter medium formed at the LHC. The CMS Collaboration has an extensive program for studying such bulk properties of the quark-gluon plasma in ultrarelativistic nuclear collisions and searching for novel phenomena (Section 4). Taking advantage of the wide pseudorapidity coverage of the CMS apparatus, long-range collective particle correlations (“flow”) are observed with unprecedented high precision. At the same time, factorization breaking in flow harmonics ( $v_n$ ) has been observed and studied for the first time by the CMS Collaboration and has been shown to have a strong sensitivity to the granularity of initial-state fluctuations. The observation of an  $\eta$ -dependent factorization breaking has provided sensitivity to the longitudinal dynamics of the QGP. In addition, the shape and size of the systems produced in different colliding systems and at various LHC energies were also investigated via femtoscopic correlation measurements. In relativistic HI collisions leading to QGP formation, the resulting medium may experience intense magnetic fields produced by the colliding ions. If net chiral (left- or right-handed) quarks are present, a localized current can be generated, leading to a charge separation known as the chiral magnetic effect and, as a separate process, a long-wavelength collective excitation known as a chiral magnetic wave. The CMS Collaboration has unambiguously shown that the CME and CMW signals are too small to be observed with the currently available data sample.

The experimental use of hard probes as a way to study the short-wavelength structure of the QGP has greatly advanced during the LHC Runs 1 and 2 (Section 5). With the initial studies, the depletion of particles with high transverse momentum observed in two-particle correlations, at BNL RHIC was confirmed to be the result of jet quenching with LHC measurements of dijet asymmetries using fully reconstructed jets. Further evidence comes from the suppression of jet and hadron yields in HI collisions compared to those expected by scaling up the results from pp collisions. The yield suppression is generally expressed in terms of the nuclear modification factor and can be associated with parton energy loss. Subsequent detailed studies of hadrons and jets have provided information regarding the path-length dependence of parton energy loss. The associated production of jets with electroweak bosons has made possible the determination of the absolute magnitude of the jet energy loss and these studies are now applied to test the survivor bias in inclusive jet samples. A multitude of measurements, including those of jet fragmentation functions and jet shapes, have established a qualitative picture in which quenching redistributes jet energy from the high- $p_T$  jet constituents to softer particles, and from small to large angles relative to the jet axis. Novel background subtraction algorithms and jet grooming techniques (which remove wide-angle soft radiation from a jet) allow the investigation of the early stages (early vacuum) of a parton shower in the QGP, well before its later medium-modified stage. These studies suggest that jet modifications can be sensitive to the earliest splittings in the evolution of the parton shower. However, further investigations are needed to properly account for a bias when selecting broader early-vacuum structures, and

hence more heavily quenched jet momenta.

The CMS Collaboration has also performed systematic studies of the mass dependence of quark energy loss by comparing the  $R_{AA}$  and  $v_2$  results for fully reconstructed light- and heavy-flavor (charm and beauty) hadrons over an unprecedentedly large  $p_T$  range: the production yields of both light and heavy (high- $p_T$ ) quarks are seemingly suppressed in the QGP, the dependence on the quark mass decreasing as  $p_T$  increases, as expected in the context of radiative energy loss. These studies led to unique measurements of B mesons in heavy ion collisions. The hadronization of heavy-flavor particles has also been examined in detail using various ratios of their yields, including, for the first time, details of the internal structure of exotic hadrons in the presence of the QGP.

The suppression patterns of the five S-wave quarkonia ( $J/\psi$ ,  $\psi(2S)$ , and  $Y(nS)$ ,  $n = 1\text{--}3$ ), never previously measured in a single experiment, strongly indicate that the nuclear suppression effects follow a sequential hierarchy reflecting the binding energy of the quarkonium state, as expected if the bound state is broken apart by the QGP medium.

In addition to nuclear hadronic interactions, electromagnetic interactions can also be studied in ultraperipheral collisions (Section 7) since heavy ions with energies of several TeV per nucleon can interact through very intense electromagnetic fields. The Lorentz factor of the Pb beam at the LHC determines the maximum quasireal photon energy of approximately 80 GeV, leading to photon-photon collisions of center-of-mass energies up to 160 GeV, i.e., similar to those reached at LEP 2 but with  $Z^4$  enhanced production cross sections. A broad range of precision SM and BSM processes has been studied in these photon-induced interactions, including exclusive high-mass dilepton ( $m_{1+1-} \gtrsim 5$  GeV) production as well as the rare processes of light-by-light scattering and  $\tau$  lepton production.

## 8.2 Future physics opportunities at CMS for high-density QCD measurements

The QCD theory, a cornerstone of the standard model, remains a crucial aspect in our understanding of the strong interaction, albeit with lingering questions. The large values of strong coupling ( $\alpha_S$ ) at low  $Q^2$  render the traditional small- $\alpha_S$  perturbation theory inapplicable, such that collective phenomena in nuclei are nonperturbative. However, a coordinated application of the QCD parton model for conventional hadrons, an effort to grasp the exotic hadron spectroscopy, and advances from lattice QCD calculations hold promise of a fundamentally improved understanding of the characteristics of nuclei and their interactions and how deconfinement arises.

Many unresolved questions remain regarding the precise nature of the initial state from which thermal QCD matter potentially emerges. How the parton density varies across the broad nuclear ( $x, Q^2$ ) phase space is still only partially known and, in particular, no unambiguous evidence has yet been found to mark the onset of parton saturation. Additionally, it is not yet quantitatively understood how the collective properties of the quark-gluon plasma emerge at a microscopic level from the interactions among the individual quarks and gluons that make up this medium. Therefore, a crucial aspect of nuclear studies is the exploitation of future opportunities for high-density QCD studies with ion and proton beams. This will allow for the study of cold nuclear matter effects, the onset of nuclear saturation, and the emergence of long-range correlations. Examination of high- $p_T$  hadrons, fully reconstructed jets, heavy quarkonia, open heavy-flavor particles, as well as novel tools [598] to investigate more detailed aspects [599] of jet quenching, will provide additional information about the strongly coupled QGP, complementing the bulk and collective observables of the soft sector. Long-term initiatives, such as the use of top quarks to unravel the intricacies of jet quenching at different time

scales of the QGP evolution, are in their early stages and are projected to rapidly progress with the increased luminosity anticipated in the LHC Run 3 (2022–2026) and beyond. A pilot run of oxygen-oxygen and proton-oxygen collisions will help answer the key prerequisite conditions for the onset of hot-medium effects [600]. It is also important to understand the level at which these effects could be phenomenologically limited by knowledge of nPDFs. At present, there is a lack of experimental oxygen data for comprehensive global nPDF fitting, underscoring the importance of proton-oxygen collisions in ensuring the accuracy of nPDFs for lighter ions. This also has far-reaching implications for modeling ultrahigh-energy (cosmic ray) phenomena, and is crucial for addressing significant unresolved questions in this field [601].

In addition to the larger luminosity, the detector upgrades planned for the CMS experiment in the LHC Run 4 (starting in year 2030) will significantly benefit the HI program. In particular, the increased  $\eta$  acceptance for charged particles resulting from tracker upgrades [602] will be very beneficial for bulk particle measurements. The upgraded Zero Degree Calorimeters [603] will further improve the existing triggering and identification of UPCs. The addition of time-of-flight particle identification capability, enabled by the Minimum Ionizing Particle Timing Detector [604], will allow identification between low-momentum charged hadrons, such as pions, kaons, and protons, which will improve the measurements of heavy-flavored particles and neutral strange hadrons, while improving the prospects for identified jet substructure measurements [605].

Proton-nucleus collisions have been an integral part of the LHC program since the 2011 and 2012 pilot runs. Within collinear factorization, constraints on our knowledge of the nuclear wave functions were extended at high  $Q^2$  using dijet, heavy gauge boson, and top quark production processes available for the first time in nuclear collisions. Further insights have been gained at lower  $Q^2$  with heavy-flavor production based on the assumption that the nuclear modification of their yields can be accurately incorporated in global analyses of nPDFs. In Run 2, the increased luminosity and detector improvements allowed for increased statistical precision, expanding the kinematic reach to encompass a broader range of accessible processes. Following the discoveries of collective-like effects in small collision systems, an order of magnitude higher integrated luminosity target for pPb collisions is set for Runs 3 and 4, including a large sample of pp collisions at the highest LHC energy, but with moderate pileup to reach the largest possible multiplicities over a full range of hadronic colliding systems.

The large PbPb integrated luminosity in Runs 3 and 4, coupled with high-accuracy theoretical QED calculations and several detector upgrades, will maximize the potential of UPC measurements. Collectively, these factors will broaden the phase space region and overall scope of physics exploration in the studies of low-mass resonances, the continuum, and heavy-flavor mesons in UPC events. The primary goal will be to cover a much wider range of masses: the expected spectrum obtainable by CMS for a  $13\text{ nb}^{-1}$  integrated luminosity run can extend to masses up to about 200 GeV, bridging the gap for BSM searches between PbPb and pp collisions (in the latter case, by employing the forward proton tagging technique) and overall extending the physics reach not only for (pseudo)scalar but also for tensor resonances [588]. Interestingly, these high-mass pairs correspond to two-photon interactions in, or in close proximity to the two nuclei, enhancing the effects owing to interactions with the medium and magnetic fields associated with the QGP. Lower masses should be accessible with looser requirements for track and electron  $p_T$  and their overall identification quality [606]. Exclusive dimuon production can offer a precision measurement of photon fluxes associated with ion beams, and as such can be used to constrain predictions for all other UPC processes. Additional LbL scattering data will also be crucial in determining the nature of newly discovered resonant structures, such as the  $X(6900)$  state [607].

Continuing the LHC HI physics program into the HL-LHC era [608, 609] offers the opportunity to collide intermediate-mass nuclei (e.g., oxygen and argon), facilitating the study of the initial stage of ion collisions, small- $x$  physics, and the determination of nPDFs. Furthermore, higher luminosities will allow vastly improved access to rare probes of the QGP. At the same time, it complements other key research efforts in the nuclear physics QCD community (e.g., ongoing efforts at RHIC [610] and the upcoming Electron-Ion Collider [611]), as well as technical developments in the high-energy and cosmic-ray [559] physics communities. Collectively, these initiatives will be pivotal in deepening our understanding of both QCD and QED, illuminating the intricate nature of matter in the early microseconds of the universe.

## Acknowledgments

We congratulate our colleagues in the CERN accelerator departments for the excellent performance of the LHC and thank the technical and administrative staffs at CERN and at other CMS institutes for their contributions to the success of the CMS effort. In addition, we gratefully acknowledge the computing centers and personnel of the Worldwide LHC Computing Grid and other centers for delivering so effectively the computing infrastructure essential to our analyses. Finally, we acknowledge the enduring support for the construction and operation of the LHC, the CMS detector, and the supporting computing infrastructure provided by the following funding agencies: the Armenian Science Committee, project no. 22rl-037; the Austrian Federal Ministry of Education, Science and Research and the Austrian Science Fund; the Belgian Fonds de la Recherche Scientifique, and Fonds voor Wetenschappelijk Onderzoek; the Brazilian Funding Agencies (CNPq, CAPES, FAPERJ, FAPERGS, and FAPESP); the Bulgarian Ministry of Education and Science, and the Bulgarian National Science Fund; CERN; the Chinese Academy of Sciences, Ministry of Science and Technology, the National Natural Science Foundation of China, and Fundamental Research Funds for the Central Universities; the Ministerio de Ciencia Tecnología e Innovación (MINCIENCIAS), Colombia; the Croatian Ministry of Science, Education and Sport, and the Croatian Science Foundation; the Research and Innovation Foundation, Cyprus; the Secretariat for Higher Education, Science, Technology and Innovation, Ecuador; the Estonian Research Council via PRG780, PRG803, RVTT3 and the Ministry of Education and Research TK202; the Academy of Finland, Finnish Ministry of Education and Culture, and Helsinki Institute of Physics; the Institut National de Physique Nucléaire et de Physique des Particules / CNRS, and Commissariat à l’Énergie Atomique et aux Énergies Alternatives / CEA, France; the Shota Rustaveli National Science Foundation, Georgia; the Bundesministerium für Bildung und Forschung, the Deutsche Forschungsgemeinschaft (DFG), under Germany’s Excellence Strategy – EXC 2121 “Quantum Universe” – 390833306, and under project number 400140256 - GRK2497, and Helmholtz-Gemeinschaft Deutscher Forschungszentren, Germany; the General Secretariat for Research and Innovation and the Hellenic Foundation for Research and Innovation (HFRI), Project Number 2288, Greece; the National Research, Development and Innovation Office (NKFIH), Hungary; the Department of Atomic Energy and the Department of Science and Technology, India; the Institute for Studies in Theoretical Physics and Mathematics, Iran; the Science Foundation, Ireland; the Istituto Nazionale di Fisica Nucleare, Italy; the Ministry of Science, ICT and Future Planning, and National Research Foundation (NRF), Republic of Korea; the Ministry of Education and Science of the Republic of Latvia; the Research Council of Lithuania, agreement No. VS-19 (LMTLT); the Ministry of Education, and University of Malaya (Malaysia); the Ministry of Science of Montenegro; the Mexican Funding Agencies (BUAP, CINVESTAV, CONACYT, LNS, SEP, and UASLP-FAI); the Ministry of Business, Innovation and Employment, New Zealand; the Pakistan Atomic Energy Commission; the Ministry of Education and Science and the National Science Center, Poland; the Fundação para a Ciência e a Tecnologia, grants CERN/FIS-PAR/0025/2019 and CERN/FIS-INS/0032/2019, Portugal; the Ministry of Education, Science and Technological Development of Serbia; MCIN/AEI/10.13039/501100011033, ERDF “a way of making Europe”, Programa Estatal de Fomento de la Investigación Científica y Técnica de Excelencia María de Maeztu, grant MDM-2017-0765, projects PID2020-113705RB, PID2020-113304RB, PID2020-116262RB and PID2020-113341RB-I00, and Plan de Ciencia, Tecnología e Innovación de Asturias, Spain; the Ministry of Science, Technology and Research, Sri Lanka; the Swiss Funding Agencies (ETH Board, ETH Zurich, PSI, SNF, UniZH, Canton Zurich, and SER); the Ministry of Science and Technology, Taipei; the Ministry of Higher Education, Science, Research and Innovation, and the National Science and Technology Development Agency of Thailand; the Scientific and Technical Research Council of Turkey, and Turkish Energy, Nuclear

and Mineral Research Agency; the National Academy of Sciences of Ukraine; the Science and Technology Facilities Council, UK; the US Department of Energy, and the US National Science Foundation.

Individuals have received support from the Marie-Curie program and the European Research Council and Horizon 2020 Grant, contract Nos. 675440, 724704, 752730, 758316, 765710, 824093, 101115353, 101002207, and COST Action CA16108 (European Union) the Leventis Foundation; the Alfred P. Sloan Foundation; the Alexander von Humboldt Foundation; the Belgian Federal Science Policy Office; the Fonds pour la Formation à la Recherche dans l’Industrie et dans l’Agriculture (FRIA-Belgium); the Agentschap voor Innovatie door Wetenschap en Technologie (IWT-Belgium); the F.R.S.-FNRS and FWO (Belgium) under the “Excellence of Science – EOS” – be.h project n. 30820817; the Beijing Municipal Science & Technology Commission, No. Z191100007219010; the Ministry of Education, Youth and Sports (MEYS) of the Czech Republic; the Shota Rustaveli National Science Foundation, grant FR-22-985 (Georgia); the Hungarian Academy of Sciences, the New National Excellence Program - ÚNKP, the NKFIH research grants K 131991, K 133046, K 138136, K 143460, K 143477, K 146913, K 146914, K 147048, 2020-2.2.1-ED-2021-00181, and TKP2021-NKTA-64 (Hungary); the Council of Scientific and Industrial Research, India; ICSC – National Research Center for High Performance Computing, Big Data and Quantum Computing and FAIR – Future Artificial Intelligence Research, funded by the EU NexGeneration program (Italy); the Latvian Council of Science; the Ministry of Education and Science, project no. 2022/WK/14, and the National Science Center, contracts Opus 2021/41/B/ST2/01369 and 2021/43/B/ST2/01552 (Poland); the Fundação para a Ciência e a Tecnologia, grant FCT CEECIND/01334/2018; the National Priorities Research Program by Qatar National Research Fund; the Programa Estatal de Fomento de la Investigación Científica y Técnica de Excelencia María de Maeztu, grant MDM-2017-0765 and projects PID2020-113705RB, PID2020-113304RB, PID2020-116262RB and PID2020-113341RB-I00, and Programa Severo Ochoa del Principado de Asturias (Spain); the Chulalongkorn Academic into Its 2nd Century Project Advancement Project, and the National Science, Research and Innovation Fund via the Program Management Unit for Human Resources & Institutional Development, Research and Innovation, grant B37G660013 (Thailand); the Kavli Foundation; the Nvidia Corporation; the SuperMicro Corporation; the Welch Foundation, contract C-1845; and the Weston Havens Foundation (USA).

## A Glossary

|        |  |
|--------|--|
| AA     | Ion-ion collision system                               |
| AGS    | Alternating Gradient Synchrotron                       |
| AJ     | Dijet asymmetry  |
| ALEPH  | Apparatus for LEP PHysics                              |
| ALICE  | A Large Ion Collider Experiment                        |
| ALP    | Axion Like Particles                                   |
| ATLAS  | A Toroidal LHC Apparatus                               |
| BDT    | Boosted Decision Tree                                  |
| BEC    | Bose–Einstein Correlations                             |
| BFKL   | Balitsky–Fadin–Kuraev–Lipatov                          |
| BNL    | Brookhaven National Laboratory                         |
| BRAHMS | Broad RAnge Hadron Magnetic Spectrometers              |
| BSC    | Beam Scintillation Counter                             |
| BSM    | Beyond the Standard Model                              |
| CASTOR | Centauro And STrange Object Research                   |
| CDF    | Collider Detector at Fermilab                          |
| CEP    | Central Exclusive Production                           |
| CERN   | European Organization for Nuclear Research             |
| CGC    | Color Glass Condensate                                 |
| CKF    | Combinatorial Kalman filter                            |
| CL     | Confidence Level                                       |
| CM     | Center of mass   |
| CME    | Chiral Magnetic Effect                                 |
| CMS    | Compact Muon Solenoid                                  |
| CMW    | Chiral Magnetic Wave                                   |
| CNM    | Cold Nuclear Matter                                    |
| CPU    | Central Processing Units                               |
| CS     | Constituent Subtraction                                |
| CSC    | Cathode Strip Chambers                                 |
| CSE    | Chiral Separation Effect                               |
| DAQ    | Data Acquisition                                       |
| DELPHI | DEtector with Lepton, Photon and Hadron Identification |
| DESY   | Deutsches Elektronen-Synchrotron                       |
| DGLAP  | Dokshitzer–Gribov–Lipatov–Altarelli–Parisi             |
| DT     | Drift Tubes  |
| DY     | Drell–Yan  |
| ECAL   | Electromagnetic Calorimeter                            |
| EM     | Electromagnetic  |
| EMC    | European Muon Collaboration                            |
| EMD    | Electromagnetic Dissociation                           |
| ESE    | Event Shape Engineering                                |
| ET     | Transverse Energy                                      |
| ETA    | Pseudorapidity   |
| EW     | Electroweak  |
| HCAL   | Hadron Hadronic Calorimeter                            |
| HERA   | Hadron-Electron Ring Accelerator                       |
| HF     | Forward Hadron Calorimeter                             |

---

|        |  |
|--------|--|
| HI     | Heavy Ions   |
| HLT    | High-Level Trigger   |
| HQ     | Heavy Quark  |
| ID     | Identification   |
| IP     | Impact Parameter   |
| ISR    | Initial-State Radiation  |
| KET    | Transverse Kinetic Energy  |
| LEP    | Large Electron–Positron Collider   |
| LHC    | Large Hadron Collider  |
| LO     | Leading order  |
| LPM    | Landau–Pomeranchuk–Migdal  |
| MB     | Minimum Bias   |
| MC     | Monte Carlo  |
| NAA    | Corresponding yield of the particle species of interest in AA collisions |
| NCQ    | Number Constituent Scaling   |
| NLO    | Next to Leading Order  |
| NN     | Nucleon Nucleon  |
| NNLL   | Next-to-Next-to-Leading Logarithmic                                      |
| NNLO   | Next-to-Next-to-Leading Order  |
| NPDF   | Nuclear PDFs   |
| NSD    | Non-Single-Diffractive   |
| OPAL   | Omni-Purpose Apparatus for LEP   |
| OS     | Opposite Sign  |
| PDFs   | Parton Distribution Functions  |
| PF     | Particle Flow  |
| PHENIX | Pioneering High Energy Nuclear Interaction eXperiment                    |
| PHOBOS | One of the initial suite of four detectors installed at RHIC             |
| POWHEG | Positive Weight Hardest Emission Generator                               |
| PP     | Proton-proton collision system   |
| PT     | Transverse Momentum  |
| PU     | Pileup   |
| PV     | Primary Vertex   |
| PYTHIA | Event generator  |
| QCD    | Quantum Chromodynamics   |
| QED    | Quantum Electrodynamics  |
| QGP    | Quark-Gluon Plasma   |
| RAA    | Nuclear Modification Factor  |
| RHIC   | Relativistic Heavy Ion Collider  |
| RMS    | Root-mean-squared  |
| RPC    | Resistive-Plate Chambers   |
| SM     | Standard Model   |
| SPS    | Super Proton Synchrotron   |
| SR     | Signal Region  |
| SS     | Same Sign  |
| STAR   | Solenoidal Tracker at RHIC   |
| STAT   | Statistical Uncertainty  |
| SYST   | Systematic Uncertainty   |
| TAA    | Nuclear Overlap Function   |
| TMVA   | Toolkit for Multivariate Data Analysis                                   |

|      |                            |
|------|----------------------------|
| UE   | Underlying Event           |
| UPC  | Ultraperipheral Collisions |
| VM   | Vector Meson               |
| ZDC  | Zero Degree Calorimeter    |
| ZEUS | Particle Detector at HERA  |

## References

- [1] CMS Collaboration, "The CMS experiment at the CERN LHC", *JINST* **3** (2008) S08004, doi:10.1088/1748-0221/3/08/S08004.
- [2] CMS Collaboration, "CMS: The Compact Muon Solenoid: Letter of intent for a general purpose detector at the LHC", 1992. <http://cds.cern.ch/record/290808>.
- [3] G. Baur et al., "Heavy ion physics programme in CMS", *Eur. Phys. J.* **32S2** (2004) 69, doi:10.1140/epjcd/s2003-01-0015-3.
- [4] CMS Collaboration, "CMS physics technical design report: Addendum on high density QCD with heavy ions", *J. Phys. G* **34** (2007) 2307, doi:10.1088/0954-3899/34/11/008.
- [5] R. Pasechnik and M. Šumbera, "Phenomenological review on quark-gluon plasma: Concepts vs. observations", *Universe* **3** (2017) 7, doi:10.3390/universe3010007, arXiv:1611.01533.
- [6] W. Busza, K. Rajagopal, and W. van der Schee, "Heavy ion collisions: The big picture, and the big questions", *Ann. Rev. Nucl. Part. Sci.* **68** (2018) 339, doi:10.1146/annurev-nucl-101917-020852, arXiv:1802.04801.
- [7] ALICE Collaboration, "The ALICE experiment – A journey through QCD", *Eur. Phys. J. C* **84** (2024) 813, arXiv:2211.04384.
- [8] ATLAS Collaboration, "The ATLAS experiment at the CERN Large Hadron Collider", *JINST* **3** (2008) S08003, doi:10.1088/1748-0221/3/08/S08003.
- [9] LHCb Collaboration, "The LHCb detector at the LHC", *JINST* **3** (2008) S08005, doi:10.1088/1748-0221/3/08/S08005.
- [10] C. A. Salgado et al., "Proton-nucleus collisions at the LHC: Scientific opportunities and requirements", *J. Phys. G* **39** (2012) 015010, doi:10.1088/0954-3899/39/1/015010, arXiv:1105.3919.
- [11] J. C. Collins and M. J. Perry, "Superdense matter: Neutrons or asymptotically free quarks?", *Phys. Rev. Lett.* **34** (1975) 1353, doi:10.1103/PhysRevLett.34.1353.
- [12] N. Cabibbo and G. Parisi, "Exponential hadronic spectrum and quark liberation", *Phys. Lett. B* **59** (1975) 67, doi:10.1016/0370-2693(75)90158-6.
- [13] J. Engels, F. Karsch, H. Satz, and I. Montvay, "High temperature SU(2) gluon matter on the lattice", *Phys. Lett. B* **101** (1981) 89, doi:10.1016/0370-2693(81)90497-4.
- [14] E. V. Shuryak, "Theory of hadronic plasma", *Sov. Phys. JETP* **47** (1978) 212.
- [15] HotQCD Collaboration, "Chiral crossover in QCD at zero and non-zero chemical potentials", *Phys. Lett. B* **795** (2019) 15, doi:10.1016/j.physletb.2019.05.013, arXiv:1812.08235.
- [16] S. Borsanyi et al., "QCD crossover at finite chemical potential from lattice simulations", *Phys. Rev. Lett.* **125** (2020) 052001, doi:10.1103/PhysRevLett.125.052001, arXiv:2002.02821.

[17] F. Gross et al., “50 years of Quantum Chromodynamics”, *Eur. Phys. J. C* **83** (2023) 1125, doi:10.1140/epjc/s10052-023-11949-2, arXiv:2212.11107.

[18] H. R. Schmidt and J. Schukraft, “The physics of ultrarelativistic heavy ion collisions”, *J. Phys. G* **19** (1993) 1705, doi:10.1088/0954-3899/19/11/006.

[19] U. W. Heinz and M. Jacob, “Evidence for a new state of matter: An assessment of the results from the CERN lead beam program”, 2000. arXiv:nucl-th/0002042.

[20] B. Muller and J. L. Nagle, “Results from the relativistic heavy ion collider”, *Ann. Rev. Nucl. Part. Sci.* **56** (2006) 93, doi:10.1146/annurev.nucl.56.080805.140556, arXiv:nucl-th/0602029.

[21] B. Muller, J. Schukraft, and B. Wyslouch, “First results from Pb+Pb collisions at the LHC”, *Ann. Rev. Nucl. Part. Sci.* **62** (2012) 361, doi:10.1146/annurev-nucl-102711-094910, arXiv:1202.3233.

[22] U. W. Heinz, “Concepts of heavy ion physics”, in *2nd CERN-CLAF school of high energy physics*, p. 165. 2004. arXiv:hep-ph/0407360.

[23] P. Braun-Munzinger and J. Stachel, “The quest for the quark-gluon plasma”, *Nature* **448** (2007) 302, doi:10.1038/nature06080.

[24] E. Shuryak, “Toward the theory of strongly coupled quark-gluon plasma”, *Prog. Theor. Phys. Suppl.* **168** (2007) 320, doi:10.1143/PTPS.168.320, arXiv:hep-ph/0703208.

[25] J. W. Harris and B. Müller, ““QGP Signatures” Revisited”, 2023. arXiv:2308.05743.

[26] BRAHMS Collaboration, “Quark gluon plasma and color glass condensate at RHIC? The perspective from the BRAHMS experiment”, *Nucl. Phys. A* **757** (2005) 1, doi:10.1016/j.nuclphysa.2005.02.130, arXiv:nucl-ex/0410020.

[27] PHENIX Collaboration, “Formation of dense partonic matter in relativistic nucleus-nucleus collisions at RHIC: Experimental evaluation by the PHENIX collaboration”, *Nucl. Phys. A* **757** (2005) 184, doi:10.1016/j.nuclphysa.2005.03.086, arXiv:nucl-ex/0410003.

[28] PHOBOS Collaboration, “The PHOBOS perspective on discoveries at RHIC”, *Nucl. Phys. A* **757** (2005) 28, doi:10.1016/j.nuclphysa.2005.03.084, arXiv:nucl-ex/0410022.

[29] STAR Collaboration, “Experimental and theoretical challenges in the search for the quark gluon plasma: The STAR Collaboration’s critical assessment of the evidence from RHIC collisions”, *Nucl. Phys. A* **757** (2005) 102, doi:10.1016/j.nuclphysa.2005.03.085, arXiv:nucl-ex/0501009.

[30] B. M. Mihalcea, V. S. Filinov, R. A. Syrovatka, and L. M. Vasilyak, “The physics and applications of strongly coupled coulomb systems (plasmas) levitated in electrodynamic traps”, *Physics Reports* **1016** (2023) 1, doi:10.1016/j.physrep.2023.03.004.

[31] C. Gale, S. Jeon, and B. Schenke, “Hydrodynamic modeling of heavy-ion collisions”, *Int. J. Mod. Phys. A* **28** (2013) 1340011, doi:10.1142/S0217751X13400113, arXiv:1301.5893.

- [32] U. Heinz and R. Snellings, "Collective flow and viscosity in relativistic heavy-ion collisions", *Ann. Rev. Nucl. Part. Sci.* **63** (2013) 123, doi:10.1146/annurev-nucl-102212-170540, arXiv:1301.2826.
- [33] J. E. Bernhard, J. S. Moreland, and S. A. Bass, "Bayesian estimation of the specific shear and bulk viscosity of quark-gluon plasma", *Nature Phys.* **15** (2019) 1113, doi:10.1038/s41567-019-0611-8.
- [34] N. Herrmann, J. P. Wessels, and T. Wienold, "Collective flow in heavy ion collisions", *Ann. Rev. Nucl. Part. Sci.* **49** (1999) 581, doi:10.1146/annurev.nucl.49.1.581.
- [35] H. Song, Y. Zhou, and K. Gajdosova, "Collective flow and hydrodynamics in large and small systems at the LHC", *Nucl. Sci. Tech.* **28** (2017) 99, doi:10.1007/s41365-017-0245-4, arXiv:1703.00670.
- [36] K. Dusling, W. Li, and B. Schenke, "Novel collective phenomena in high-energy proton–proton and proton–nucleus collisions", *Int. J. Mod. Phys. E* **25** (2016) 1630002, doi:10.1142/S0218301316300022, arXiv:1509.07939.
- [37] J. L. Nagle and W. A. Zajc, "Small system collectivity in relativistic hadronic and nuclear collisions", *Ann. Rev. Nucl. Part. Sci.* **68** (2018) 211, doi:10.1146/annurev-nucl-101916-123209, arXiv:1801.03477.
- [38] A. Accardi et al., "Hard probes in heavy ion collisions at the LHC: Jet physics", 2004. arXiv:hep-ph/0310274.
- [39] L. Apolinário, Y.-J. Lee, and M. Winn, "Heavy quarks and jets as probes of the QGP", *Prog. Part. Nucl. Phys.* **127** (2022) 103990, doi:10.1016/j.ppnp.2022.103990, arXiv:2203.16352.
- [40] G. Nijs and W. van der Schee, "Predictions and postdictions for relativistic lead and oxygen collisions with the computational simulation code Trajectum", *Phys. Rev. C* **106** (2022) 044903, doi:10.1103/PhysRevC.106.044903, arXiv:2110.13153.
- [41] C. Andrés et al., "Energy versus centrality dependence of the jet quenching parameter  $\hat{q}$  at RHIC and LHC: a new puzzle?", *Eur. Phys. J. C* **76** (2016) 475, doi:10.1140/epjc/s10052-016-4320-5, arXiv:1606.04837.
- [42] J. M. Jowett and M. Schaumann, "Overview of heavy ions in LHC Run 2", in *9th LHC Operations Evian Workshop*, p. 15. 2019.
- [43] J. M. Jowett et al., "First run of the LHC as a heavy ion collider", in *Proceedings of the 2nd International Particle Accelerator Conference (IPAC 2011)*, C. Petit-Jean-Genaz, ed., p. 1837. 2011.
- [44] J. M. Jowett et al., "Heavy ions in 2012 and the program up to 2022", in *Chamonix 2012 Workshop on LHC Performance*, CERN Yellow Reports: Conference Proceedings, p. 200, CERN. CERN, Geneva, 2012. doi:10.5170/CERN-2012-006.200.
- [45] J. Jowett et al., "Proton-nucleus collisions in the LHC", in *Proc. 4th International Particle Accelerator Conference*, p. MOODB201. 2013.
- [46] J. Jowett et al., "The 2015 heavy-ion run of the LHC", in *Proc. 7th International Particle Accelerator Conference*, p. TUPMW027. 2016. doi:10.18429/JACoW-IPAC2016-TUPMW027.

[47] J. Jowett et al., "The 2016 proton-nucleus run of the LHC", in *Proc. 8th International Particle Accelerator Conference*. 2017. doi:10.18429/JACoW-IPAC2017-TUPVA014.

[48] CMS Collaboration, "CMS luminosity measurement using nucleus-nucleus collisions at  $\sqrt{s_{\text{NN}}} = 5.02 \text{ TeV}$  in 2018", CMS Physics Analysis Summary CMS-PAS-LUM-18-001, 2022.

[49] CMS Collaboration, "CMS luminosity measurement using 2016 proton-nucleus collisions at  $\sqrt{s_{\text{NN}}} = 8.16 \text{ TeV}$ ", CMS Physics Analysis Summary CMS-PAS-LUM-17-002, 2018.

[50] J. Jowett et al., "The 2018 heavy-ion run of the LHC", in *Proc. 10th International Particle Accelerator Conference*, p. WEYYPLM2. 2019. doi:10.18429/JACoW-IPAC2019-WEYYPLM2.

[51] CMS Collaboration, "Performance of CMS muon reconstruction from proton-proton to heavy ion collisions", *JINST* **19** (2024) P09012, doi:10.1088/1748-0221/19/09/P09012, arXiv:2404.17377.

[52] B. Ducloué et al., "Nonlinear evolution in QCD at high-energy beyond leading order", *JHEP* **04** (2019) 081, doi:10.1007/JHEP04(2019)081, arXiv:1902.06637.

[53] D. G. d'Enterria, "Experimental tests of small- $x$  QCD", in *Proceedings of the 9th Workshop on Non-Perturbative Quantum Chromodynamics, 42th Rencontres de Moriond*, B. Mueller, M. A. Rotondo, and C.-I. Tan, eds., p. 17. 2007. arXiv:0706.4182.

[54] E. Iancu and R. Venugopalan, "The color glass condensate and high-energy scattering in QCD", in *Quark-gluon plasma 4*, R. C. Hwa and X.-N. Wang, eds., p. 249. 2003. arXiv:hep-ph/0303204. doi:10.1142/9789812795533\_0005.

[55] S. Abreu et al., "Heavy ion collisions at the lhc: Last call for predictions", in *Proc. Workshop on heavy ion collisions at the LHC: Last call for predictions*, p. 054001. 2008. arXiv:0711.0974. doi:10.1088/0954-3899/35/5/054001.

[56] N. Armesto, "Predictions for the heavy ion program at the Large Hadron Collider", in *Quark-gluon plasma 4*, R. C. Hwa and X.-N. Wang, eds., p. 375. 2010. arXiv:0903.1330. doi:10.1142/9789814293297\_0007.

[57] D. G. d'Enterria, "High- $p_T$  leading hadron suppression in nuclear collisions at  $\sqrt{s_{\text{NN}}} = 20\text{--}200 \text{ GeV}$ : Data versus parton energy loss models", *Eur. Phys. J. C* **43** (2005) 295, doi:10.1140/epjc/s2005-02332-8, arXiv:nucl-ex/0504001.

[58] M. Djordjevic and M. Gyulassy, "Where is the charm quark energy loss at RHIC?", *Phys. Lett. B* **560** (2003) 37, doi:10.1016/S0370-2693(03)00327-7, arXiv:nucl-th/0302069.

[59] C. Lourenço, "Open questions in quarkonium and electromagnetic probes", *Nucl. Phys. A* **783** (2007) 451, doi:10.1016/j.nuclphysa.2006.11.096, arXiv:nucl-ex/0612014.

[60] PHENIX Collaboration, "J/ $\psi$  suppression at forward rapidity in AuAu collisions at  $\sqrt{s_{\text{NN}}} = 200 \text{ GeV}$ ", *Phys. Rev. C* **84** (2011) 054912, doi:10.1103/PhysRevC.84.054912, arXiv:1103.6269.

- [61] M. Grabiak et al., "Electroweak physics at ultrarelativistic heavy ion colliders", *J. Phys. G* **15** (1989) 25, doi:10.1088/0954-3899/15/3/001.
- [62] K. Hencken, D. Trautmann, and G. Baur, "Photon-photon luminosities in relativistic heavy ion collisions at LHC energies", *Z. Phys. C* **68** (1995) 473, doi:10.1007/BF01620724, arXiv:nucl-th/9503004.
- [63] C. A. Bertulani and G. Baur, "Electromagnetic processes in relativistic heavy ion collisions", *Phys. Rept.* **163** (1988) 299, doi:10.1016/0370-1573(88)90142-1.
- [64] F. Krauss, M. Greiner, and G. Soff, "Photon and gluon induced processes in relativistic heavy ion collisions", *Prog. Part. Nucl. Phys.* **39** (1997) 503, doi:10.1016/S0146-6410(97)00049-5.
- [65] G. Baur, K. Hencken, and D. Trautmann, "Photon-photon physics in very peripheral collisions of relativistic heavy ions", *J. Phys. G* **24** (1998) 1657, doi:10.1088/0954-3899/24/9/003, arXiv:hep-ph/9804348.
- [66] G. Baur, "Physics opportunities in ultraperipheral heavy ion collisions at LHC", in *Proc. Workshop on Electromagnetic Probes of Fundamental Physics*, p. 183. 2001. arXiv:hep-ph/0112239.
- [67] C. A. Bertulani, S. R. Klein, and J. Nystrand, "Physics of ultraperipheral nuclear collisions", *Ann. Rev. Nucl. Part. Sci.* **55** (2005) 271, doi:10.1146/annurev.nucl.55.090704.151526, arXiv:nucl-ex/0502005.
- [68] A. J. Baltz, "The physics of ultraperipheral collisions at the LHC", *Phys. Rept.* **458** (2008) 1, doi:10.1016/j.physrep.2007.12.001, arXiv:0706.3356.
- [69] G. Baur et al., "Coherent gamma-gamma and gamma-A interactions in very peripheral collisions at relativistic ion colliders", *Phys. Rept.* **364** (2002) 359, doi:10.1016/S0370-1573(01)00101-6, arXiv:hep-ph/0112211.
- [70] A. A. Natale, "Resonance production in peripheral heavy ion collisions", *Mod. Phys. Lett. A* **9** (1994) 2075, doi:10.1142/S0217732394001933.
- [71] A. J. Baltz, S. R. Klein, and J. Nystrand, "Coherent vector meson photoproduction with nuclear breakup in relativistic heavy ion collisions", *Phys. Rev. Lett.* **89** (2002) 012301, doi:10.1103/PhysRevLett.89.012301, arXiv:nucl-th/0205031.
- [72] S. R. Klein and J. Nystrand, "Photoproduction of quarkonium in proton-proton and nucleus-nucleus collisions", *Phys. Rev. Lett.* **92** (2004) 142003, doi:10.1103/PhysRevLett.92.142003, arXiv:hep-ph/0311164.
- [73] K. J. Abraham, R. Laterveer, J. A. M. Vermaseren, and D. Zeppenfeld, "Higgs production by heavy ion scattering", *Phys. Lett. B* **251** (1990) 186, doi:10.1016/0370-2693(90)90251-Z.
- [74] D. d'Enterria and J.-P. Lansberg, "Study of Higgs boson production and its  $b\bar{b}$  decay in gamma-gamma processes in proton-nucleus collisions at the LHC", *Phys. Rev. D* **81** (2010) 014004, doi:10.1103/PhysRevD.81.014004, arXiv:0909.3047.
- [75] S. R. Klein, J. Nystrand, and R. Vogt, "Photoproduction of top in peripheral heavy ion collisions", *Eur. Phys. J. C* **21** (2001) 563, doi:10.1007/s100520100739, arXiv:hep-ph/0005157.

---

- [76] S. C. Ahern, J. W. Norbury, and W. J. Poyser, “Graviton production in relativistic heavy ion collisions”, *Phys. Rev. D* **62** (2000) 116001, doi:10.1103/PhysRevD.62.116001, arXiv:gr-qc/0009059.
- [77] A. A. Natale, “Glueballs in peripheral heavy ion collisions”, *Phys. Lett. B* **362** (1995) 177, doi:10.1016/0370-2693(95)01146-H, arXiv:hep-ph/9509280.
- [78] J. Rau, B. Muller, W. Greiner, and G. Soff, “Production of supersymmetric particles in ultrarelativistic heavy ion collisions”, *J. Phys. G* **16** (1990) 211, doi:10.1088/0954-3899/16/2/010.
- [79] L. D. Almeida, A. A. Natale, S. F. Novaes, and O. J. P. Eboli, “Nonstandard gamma gamma → lepton+ lepton- processes in relativistic heavy ion collisions”, *Phys. Rev. D* **44** (1991) 118, doi:10.1103/PhysRevD.44.118.
- [80] M. Greiner, M. Vidovic, and G. Soff, “Electromagnetic production of Higgs bosons, SUSY particles, glueballs and mesons in ultrarelativistic heavy ion collisions”, *Phys. Rev. C* **47** (1993) 2288, doi:10.1103/PhysRevC.47.2288.
- [81] CMS Collaboration, “Event displays of PbPb collision events in the CMS detector at the end of 2018”, 2018. <https://cds.cern.ch/record/2648517>.
- [82] CMS Collaboration, “Strategies and performance of the CMS silicon tracker alignment during LHC Run 2”, *Nucl. Instrum. Meth. A* **1037** (2022) 166795, doi:10.1016/j.nima.2022.166795, arXiv:2111.08757.
- [83] CMS Collaboration, “Description and performance of track and primary-vertex reconstruction with the CMS tracker”, *JINST* **9** (2014) P10009, doi:10.1088/1748-0221/9/10/P10009, arXiv:1405.6569.
- [84] Tracker Group of the CMS Collaboration, “The CMS Phase-1 pixel detector upgrade”, *JINST* **16** (2021) P02027, doi:10.1088/1748-0221/16/02/P02027, arXiv:2012.14304.
- [85] CMS Collaboration, “Track impact parameter resolution for the full pseudo rapidity coverage in the 2017 dataset with the CMS Phase-1 pixel detector”, CMS Detector Performance Summary CMS-DP-2020-049, 2020.
- [86] CMS Collaboration, “Performance of CMS muon reconstruction in pp collision events at  $\sqrt{s} = 7 \text{ TeV}$ ”, *JINST* **7** (2012) P10002, doi:10.1088/1748-0221/7/10/P10002, arXiv:1206.4071.
- [87] CMS Collaboration, “Performance of the CMS muon detector and muon reconstruction with proton-proton collisions at  $\sqrt{s} = 13 \text{ TeV}$ ”, *JINST* **13** (2018) P06015, doi:10.1088/1748-0221/13/06/P06015, arXiv:1804.04528.
- [88] CMS Collaboration, “Particle-flow reconstruction and global event description with the CMS detector”, *JINST* **12** (2017) P10003, doi:10.1088/1748-0221/12/10/P10003, arXiv:1706.04965.
- [89] CMS Collaboration, “Performance of photon reconstruction and identification with the CMS detector in proton-proton collisions at  $\sqrt{s} = 8 \text{ TeV}$ ”, *JINST* **10** (2015) P08010, doi:10.1088/1748-0221/10/08/P08010, arXiv:1502.02702.

[90] CMS Collaboration, “Electron and photon reconstruction and identification with the CMS experiment at the CERN LHC”, *JINST* **16** (2021) P05014, doi:10.1088/1748-0221/16/05/P05014, arXiv:2012.06888.

[91] CMS Collaboration, “ECAL 2016 refined calibration and Run 2 summary plots”, CMS detector performance summary, 2020.

[92] M. Cacciari, G. P. Salam, and G. Soyez, “The anti- $k_T$  jet clustering algorithm”, *JHEP* **04** (2008) 063, doi:10.1088/1126-6708/2008/04/063, arXiv:0802.1189.

[93] M. Cacciari, G. P. Salam, and G. Soyez, “FastJet user manual”, *Eur. Phys. J. C* **72** (2012) 1896, doi:10.1140/epjc/s10052-012-1896-2, arXiv:1111.6097.

[94] A. Giammanco, “The fast simulation of the CMS experiment”, *J. Phys. Conf. Ser.* **513** (2014) 022012, doi:10.1088/1742-6596/513/2/022012.

[95] S. Abdullin et al., “The fast simulation of the CMS detector at LHC”, *J. Phys. Conf. Ser.* **331** (2011) 032049, doi:10.1088/1742-6596/331/3/032049.

[96] CMS Collaboration, “Jet energy scale and resolution in the CMS experiment in pp collisions at 8 TeV”, *JINST* **12** (2017) P02014, doi:10.1088/1748-0221/12/02/P02014, arXiv:1607.03663.

[97] CMS Collaboration, “Precision luminosity measurement in proton-proton collisions at  $\sqrt{s} = 13$  TeV in 2015 and 2016 at CMS”, *Eur. Phys. J. C* **81** (2021) 800, doi:10.1140/epjc/s10052-021-09538-2, arXiv:2104.01927.

[98] CMS Collaboration, “CMS luminosity calibration for the pp reference run at  $\sqrt{s} = 5.02$  TeV”, CMS Physics Analysis Summary CMS-PAS-LUM-16-001, 2016.

[99] CMS Collaboration, “Luminosity measurement in proton-proton collisions at 5.02 TeV in 2017 at CMS”, CMS Physics Analysis Summary CMS-PAS-LUM-19-001, 2021.

[100] CMS Collaboration, “CMS: The TriDAS project. Technical design report, Vol. 1: The trigger systems”, 2000. <https://cds.cern.ch/record/706847>.

[101] CMS Collaboration, “Performance of the CMS Level-1 trigger in proton-proton collisions at  $\sqrt{s} = 13$  TeV”, *JINST* **15** (2020) P10017, doi:10.1088/1748-0221/15/10/P10017, arXiv:2006.10165.

[102] CMS Collaboration, “CMS: The TriDAS project. Technical design report, Vol. 2: Data acquisition and high-level trigger”, 2002. <http://cds.cern.ch/record/578006>.

[103] CMS Collaboration, “CMS technical design report for the level-1 trigger upgrade”, 2013. <https://cds.cern.ch/record/1556311>.

[104] Trigger and DAQ Groups of the CMS Collaboration, “The CMS high level trigger”, *Eur. Phys. J. C* **46** (2006) 605, doi:10.1140/epjc/s2006-02495-8, arXiv:hep-ex/0512077.

[105] CMS Collaboration, “CMS high level trigger”, technical report, CERN, 2007.

[106] CMS Collaboration, “Performance of the high-level trigger system at CMS in LHC run-2”, *IEEE Trans. Nucl. Sci.* **68** (2021) 2035, doi:10.1109/TNS.2021.3087618.

[107] S. M. Hasan, "Enhancing hadron jet reconstruction in the CMS Level-1 trigger using machine learning.". PhD thesis, Baylor U., 2022.

[108] CMS Collaboration, "Observation and studies of jet quenching in PbPb collisions at nucleon-nucleon center-of-mass energy  $\sqrt{s_{\text{NN}}} = 2.76 \text{ TeV}$ ", *Phys. Rev. C* **84** (2011) 024906, doi:10.1103/PhysRevC.84.024906, arXiv:1102.1957.

[109] CMS Collaboration, "Measurement of isolated photon production in pp and PbPb collisions at  $\sqrt{s_{\text{NN}}} = 2.76 \text{ TeV}$ ", *Phys. Lett. B* **710** (2012) 256, doi:10.1016/j.physletb.2012.02.077, arXiv:1201.3093.

[110] CMS Collaboration, "Multiplicity and transverse momentum dependence of two- and four-particle correlations in pPb and PbPb collisions", *Phys. Lett. B* **724** (2013) 213, doi:10.1016/j.physletb.2013.06.028, arXiv:1305.0609.

[111] CMS Collaboration, "Dependence on pseudorapidity and on centrality of charged hadron production in PbPb collisions at  $\sqrt{s_{\text{NN}}} = 2.76 \text{ TeV}$ ", *JHEP* **08** (2011) 141, doi:10.1007/JHEP08(2011)141, arXiv:1107.4800.

[112] CMS Collaboration, "The beam scintillation counter trigger system for CMS", CMS Detector Performance Summary, 2010.

[113] Z.-W. Lin et al., "A multi-phase transport model for relativistic heavy ion collisions", *Phys. Rev. C* **72** (2005) 064901, doi:10.1103/PhysRevC.72.064901, arXiv:nucl-th/0411110.

[114] I. P. Lokhtin and A. M. Snigirev, "A model of jet quenching in ultrarelativistic heavy ion collisions and high- $p_{\text{T}}$  hadron spectra at RHIC", *Eur. Phys. J. C* **45** (2006) 211, doi:10.1140/epjc/s2005-02426-3, arXiv:hep-ph/0506189.

[115] S. R. Klein et al., "STARLIGHT: A Monte Carlo simulation program for ultra-peripheral collisions of relativistic ions", *Comput. Phys. Commun.* **212** (2017) 258, doi:10.1016/j.cpc.2016.10.016, arXiv:1607.03838.

[116] S. Roesler, R. Engel, and J. Ranft, "Photoproduction off nuclei and point-like photon interactions. Part 2: Particle production", 1996. arXiv:hep-ph/9611379.

[117] T. Sjöstrand et al., "An introduction to PYTHIA8.2", *Comput. Phys. Commun.* **191** (2015) 159, doi:10.1016/j.cpc.2015.01.024, arXiv:1410.3012.

[118] GEANT4 Collaboration, "GEANT4—a simulation toolkit", *Nucl. Instrum. Meth. A* **506** (2003) 250, doi:10.1016/S0168-9002(03)01368-8.

[119] M. L. Miller, K. Reygers, S. J. Sanders, and P. Steinberg, "Glauber modeling in high energy nuclear collisions", *Ann. Rev. Nucl. Part. Sci.* **57** (2007) 205, doi:10.1146/annurev.nucl.57.090506.123020, arXiv:nucl-ex/0701025.

[120] C. Loizides, J. Kamin, and D. d'Enterria, "Improved Monte Carlo Glauber predictions at present and future nuclear colliders", *Phys. Rev. C* **97** (2018) 054910, doi:10.1103/PhysRevC.97.054910, arXiv:1710.07098. [Erratum: doi:10.1103/PhysRevC.99.019901].

[121] ALICE Collaboration, "Centrality dependence of the charged-particle multiplicity density at midrapidity in Pb-Pb collisions at  $\sqrt{s_{\text{NN}}} = 2.76 \text{ TeV}$ ", *Phys. Rev. Lett.* **106** (2011) 032301, doi:10.1103/PhysRevLett.106.032301, arXiv:1012.1657.

[122] PHOBOS Collaboration, “Importance of correlations and fluctuations on the initial source eccentricity in high-energy nucleus-nucleus collisions”, *Phys. Rev. C* **77** (2008) 014906, doi:10.1103/PhysRevC.77.014906, arXiv:0711.3724.

[123] T. Pierog et al., “EPOS LHC: Test of collective hadronization with data measured at the CERN Large Hadron Collider”, *Phys. Rev. C* **92** (2015) 034906, doi:10.1103/PhysRevC.92.034906, arXiv:1306.0121.

[124] X.-N. Wang and M. Gyulassy, “HIJING: A Monte Carlo model for multiple jet production in pp, pA and AA collisions”, *Phys. Rev. D* **44** (1991) 3501, doi:10.1103/PhysRevD.44.3501.

[125] CMS Collaboration, “Studies of dijet transverse momentum balance and pseudorapidity distributions in pPb collisions at  $\sqrt{s_{\text{NN}}} = 5.02 \text{ TeV}$ ”, *Eur. Phys. J. C* **74** (2014) 2951, doi:10.1140/epjc/s10052-014-2951-y, arXiv:1401.4433.

[126] CMS Collaboration, “Tracking and L1 trigger performance in 2018 and 2022 PbPb conditions”, CMS detector performance summary, 2023. CMS-DP-2023-011. <https://cds.cern.ch/record/2855333>.

[127] CMS Collaboration, “Charged-particle nuclear modification factors in XeXe collisions at  $\sqrt{s_{\text{NN}}} = 5.44 \text{ TeV}$ ”, *JHEP* **10** (2018) 138, doi:10.1007/JHEP10(2018)138, arXiv:1809.00201.

[128] CMS Collaboration, “Measurement of the elliptic anisotropy of charged particles produced in PbPb collisions at  $\sqrt{s_{\text{NN}}} = 2.76 \text{ TeV}$ ”, *Phys. Rev. C* **87** (2013) 014902, doi:10.1103/PhysRevC.87.014902, arXiv:1204.1409.

[129] CMS Collaboration, “Performance of the CMS muon trigger system in proton-proton collisions at  $\sqrt{s} = 13 \text{ TeV}$ ”, *JINST* **16** (2021) P07001, doi:10.1088/1748-0221/16/07/P07001, arXiv:2102.04790.

[130] Adam, W. and Frühwirth, R. and Strandlie, A. and Todorov, T., “Reconstruction of electrons with the Gaussian-sum filter in the CMS tracker at the LHC”, *J. Phys. G* **31** (2005) N9, doi:10.1088/0954-3899/31/9/n01.

[131] CMS Collaboration, “Energy calibration and resolution of the CMS electromagnetic calorimeter in pp collisions at  $\sqrt{s} = 7 \text{ TeV}$ ”, *JINST* **8** (2013) P09009, doi:10.1088/1748-0221/8/09/P09009, arXiv:1306.2016.

[132] CMS Collaboration, “Study of Z production in PbPb and pp collisions at  $\sqrt{s_{\text{NN}}} = 2.76 \text{ TeV}$  in the dimuon and dielectron decay channels”, *JHEP* **03** (2015) 022, doi:10.1007/JHEP03(2015)022, arXiv:1410.4825.

[133] CMS Collaboration, “Performance of electron reconstruction and selection with the CMS detector in proton-proton collisions at  $\sqrt{s} = 8 \text{ TeV}$ ”, *JINST* **10** (2015) P06005, doi:10.1088/1748-0221/10/06/P06005, arXiv:1502.02701.

[134] H. Voss, A. Höcker, J. Stelzer, and F. Tegenfeldt, “TMVA, the toolkit for multivariate data analysis with ROOT”, in *Proc. XIth International Workshop on Advanced Computing and Analysis Techniques in Physics Research (ACAT)*, p. 40. 2007. arXiv:physics/0703039. doi:10.22323/1.050.0040.

[135] CMS Collaboration, “The production of isolated photons in PbPb and pp collisions at  $\sqrt{s_{\text{NN}}} = 5.02 \text{ TeV}$ ”, *JHEP* **07** (2020) 116, doi:10.1007/JHEP07(2020)116, arXiv:2003.12797.

[136] M. Cacciari, “FastJet: A code for fast  $k_t$  clustering, and more”, in *Proc. Deep inelastic scattering, 14th International Workshop, DIS 2006*, p. 487. 2006. arXiv:hep-ph/0607071.

[137] CMS Collaboration, “Pileup mitigation at CMS in 13 TeV data”, *JINST* **15** (2020) P09018, doi:10.1088/1748-0221/15/09/P09018, arXiv:2003.00503.

[138] O. Kodolova, I. Vardanian, A. Nikitenko, and A. Oulianov, “The performance of the jet identification and reconstruction in heavy ions collisions with CMS detector”, *Eur. Phys. J. C* **50** (2007) 117, doi:10.1140/epjc/s10052-007-0223-9.

[139] ALICE Collaboration, “Azimuthal anisotropy of charged jet production in  $\sqrt{s_{\text{NN}}} = 2.76 \text{ TeV}$  Pb-Pb collisions”, *Phys. Lett. B* **753** (2016) 511, doi:10.1016/j.physletb.2015.12.047, arXiv:1509.07334.

[140] P. Berta, M. Spousta, D. W. Miller, and R. Leitner, “Particle-level pileup subtraction for jets and jet shapes”, *JHEP* **06** (2014) 92, doi:10.1007/JHEP06(2014)092, arXiv:hep-ex/1403.3108.

[141] P. Berta, L. Masetti, D. W. Miller, and M. Spousta, “Pileup and underlying event mitigation with iterative constituent subtraction”, *JHEP* **08** (2019) 175, doi:10.1007/JHEP08(2019)175, arXiv:1905.03470.

[142] CMS Collaboration, “Updates to constituent subtraction in heavy ions at CMS”, CMS detector performance summary, 2018. CMS-DP-2018-024. <http://cds.cern.ch/record/2621977>.

[143] CMS Collaboration, “First measurement of large area jet transverse momentum spectra in heavy-ion collisions”, *JHEP* **05** (2021) 284, doi:10.1007/JHEP05(2021)284, arXiv:2102.13080.

[144] D. d'Enterria and J. Rojo, “Quantitative constraints on the gluon distribution function in the proton from collider isolated-photon data”, *Nucl. Phys. B* **860** (2012) 311, doi:10.1016/j.nuclphysb.2012.03.003, arXiv:1202.1762.

[145] CMS Collaboration, “Measurement of prompt  $D^0$  meson azimuthal anisotropy in PbPb collisions at  $\sqrt{s_{\text{NN}}} = 5.02 \text{ TeV}$ ”, *Phys. Rev. Lett.* **120** (2018) 202301, doi:10.1103/PhysRevLett.120.202301, arXiv:1708.03497.

[146] CMS Collaboration, “Measurement of prompt  $D^0$  and  $\bar{D}^0$  meson azimuthal anisotropy and search for strong electric fields in PbPb collisions at  $\sqrt{s_{\text{NN}}} = 5.02 \text{ TeV}$ ”, *Phys. Lett. B* **816** (2021) 136253, doi:10.1016/j.physletb.2021.136253, arXiv:2009.12628.

[147] CMS Collaboration, “Probing charm quark dynamics via multiparticle correlations in Pb-Pb collisions at  $\sqrt{s_{\text{NN}}} = 5.02 \text{ TeV}$ ”, *Phys. Rev. Lett.* **129** (2022) 022001, doi:10.1103/PhysRevLett.129.022001, arXiv:2112.12236.

[148] CMS Collaboration, “Measurements of azimuthal anisotropy of nonprompt  $D^0$  mesons in PbPb collisions at  $\sqrt{s_{\text{NN}}} = 5.02 \text{ TeV}$ ”, *Phys. Lett. B* **850** (2024) 138389, doi:10.1016/j.physletb.2023.138389, arXiv:2212.01636.

[149] CMS Collaboration, "Evidence for top quark production in nucleus-nucleus collisions", *Phys. Rev. Lett.* **125** (2020) 222001, doi:10.1103/PhysRevLett.125.222001, arXiv:2006.11110.

[150] CMS Collaboration, "Identification of heavy-flavour jets with the CMS detector in pp collisions at 13 TeV", *JINST* **13** (2018) P05011, doi:10.1088/1748-0221/13/05/P05011, arXiv:1712.07158.

[151] G. Altarelli and G. Parisi, "Asymptotic freedom in parton language", *Nucl. Phys. B* **126** (1977) 298, doi:10.1016/0550-3213(77)90384-4.

[152] Y. L. Dokshitzer, "Calculation of the structure functions for deep inelastic scattering and  $e^+e^-$  annihilation by perturbation theory in quantum chromodynamics.", *Sov. Phys. JETP* **46** (1977) 641.

[153] V. N. Gribov and L. N. Lipatov, "Deep inelastic e p scattering in perturbation theory", *Sov. J. Nucl. Phys.* **15** (1972) 438.

[154] CMS Collaboration, "Observation of nuclear modifications in  $W^\pm$  boson production in pPb collisions at  $\sqrt{s_{_{NN}}} = 8.16$  TeV", *Phys. Lett. B* **800** (2020) 135048, doi:10.1016/j.physletb.2019.135048, arXiv:1905.01486.

[155] R. Boughezal et al., "Color singlet production at NNLO in MCFM", *Eur. Phys. J. C* **77** (2017) 7, doi:10.1140/epjc/s10052-016-4558-y, arXiv:1605.08011.

[156] S. Dulat et al., "New parton distribution functions from a global analysis of quantum chromodynamics", *Phys. Rev. D* **93** (2016) 033006, doi:10.1103/PhysRevD.93.033006, arXiv:1506.07443.

[157] K. J. Eskola, P. Paakkinen, H. Paukkunen, and C. A. Salgado, "EPPS16: Nuclear parton distributions with LHC data", *Eur. Phys. J. C* **77** (2017) 163, doi:10.1140/epjc/s10052-017-4725-9, arXiv:1612.057412110.13153.

[158] K. Kovarik et al., "nCTEQ15 - Global analysis of nuclear parton distributions with uncertainties in the CTEQ framework", *Phys. Rev. D* **93** (2016) 085037, doi:10.1103/PhysRevD.93.085037, arXiv:1509.00792.

[159] N. Armesto, "Nuclear shadowing", *J. Phys. G* **32** (2006) R367, doi:10.1088/0954-3899/32/11/R01, arXiv:hep-ph/0604108.

[160] CMS Collaboration, "Study of W boson production in pPb collisions at  $\sqrt{s_{_{NN}}} = 5.02$  TeV", *Phys. Lett. B* **750** (2015) 565, doi:10.1016/j.physletb.2015.09.057, arXiv:1503.05825.

[161] K. J. Eskola, P. Paakkinen, H. Paukkunen, and C. A. Salgado, "EPPS21: a global QCD analysis of nuclear PDFs", *Eur. Phys. J. C* **82** (2022) 413, doi:10.1140/epjc/s10052-022-10359-0, arXiv:2112.12462.

[162] A. Kusina et al., "Impact of LHC vector boson production in heavy ion collisions on strange PDFs", *Eur. Phys. J. C* **80** (2020) 968, doi:10.1140/epjc/s10052-020-08532-4, arXiv:2007.09100.

[163] R. Abdul Khalek, J. J. Ethier, J. Rojo, and G. van Weelden, "nNNPDF2.0: quark flavor separation in nuclei from LHC data", *JHEP* **09** (2020) 183, doi:10.1007/JHEP09(2020)183, arXiv:2006.14629.

[164] R. Abdul Khalek et al., “nNNPDF3.0: evidence for a modified partonic structure in heavy nuclei”, *Eur. Phys. J. C* **82** (2022) 507, doi:10.1140/epjc/s10052-022-10417-7, arXiv:2201.12363.

[165] I. Helenius, M. Walt, and W. Vogelsang, “NNLO nuclear parton distribution functions with electroweak-boson production data from the LHC”, *Phys. Rev. D* **105** (2022) 094031, doi:10.1103/PhysRevD.105.094031, arXiv:2112.11904.

[166] CMS Collaboration, “Study of Drell–Yan dimuon production in proton–lead collisions at  $\sqrt{s_{_{NN}}} = 8.16\text{ TeV}$ ”, *JHEP* **05** (2021) 182, doi:10.1007/JHEP05(2021)182, arXiv:2102.13648.

[167] S. Alioli, P. Nason, C. Oleari, and E. Re, “A general framework for implementing NLO calculations in shower Monte Carlo programs: the POWHEG BOX”, *JHEP* **06** (2010) 043, doi:10.1007/JHEP06(2010)043, arXiv:1002.2581.

[168] S. Alioli, P. Nason, C. Oleari, and E. Re, “NLO vector-boson production matched with shower in POWHEG”, *JHEP* **07** (2008) 060, doi:10.1088/1126-6708/2008/07/060, arXiv:0805.4802.

[169] CMS Collaboration, “Study of Z boson production in pPb collisions at  $\sqrt{s_{_{NN}}} = 5.02\text{ TeV}$ ”, *Phys. Lett. B* **759** (2016) 36, doi:10.1016/j.physletb.2016.05.044, arXiv:1512.06461.

[170] D. d’Enterria, K. Krajczár, and H. Paukkunen, “Top quark production in proton–nucleus and nucleus–nucleus collisions at LHC energies and beyond”, *Phys. Lett. B* **746** (2015) 64, doi:10.1016/j.physletb.2015.04.044, arXiv:1501.05879.

[171] CMS Collaboration, “Observation of top quark production in proton–nucleus collisions”, *Phys. Rev. Lett.* **119** (2017) 242001, doi:10.1103/PhysRevLett.119.242001, arXiv:1709.07411.

[172] M. Czakon, P. Fiedler, and A. Mitov, “Total top quark pair production cross section at hadron colliders through  $O(\alpha_S^4)$ ”, *Phys. Rev. Lett.* **110** (2013) 252004, doi:10.1103/PhysRevLett.110.252004, arXiv:1303.6254.

[173] J. M. Campbell and R. K. Ellis, “MCFM for the Tevatron and the LHC”, *Nucl. Phys. B Proc. Suppl.* **205-206** (2010) 10, doi:10.1016/j.nuclphysbps.2010.08.011, arXiv:1007.3492.

[174] J. L. Albacete et al., “Predictions for cold nuclear matter effects in pPb collisions at  $\sqrt{s_{_{NN}}} = 8.16\text{ TeV}$ ”, *Nucl. Phys. A* **972** (2018) 18, doi:10.1016/j.nuclphysa.2017.11.015, arXiv:1707.09973.

[175] D. de Florian, R. Sassot, P. Zurita, and M. Stratmann, “Global analysis of nuclear parton distributions”, *Phys. Rev. D* **85** (2012) 074028, doi:10.1103/PhysRevD.85.074028, arXiv:1112.6324.

[176] K. J. Eskola, H. Paukkunen, and C. A. Salgado, “EPS09: A new generation of NLO and LO nuclear parton distribution functions”, *JHEP* **04** (2009) 065, doi:10.1088/1126-6708/2009/04/065, arXiv:0902.4154.

[177] CMS Collaboration, “Constraining gluon distributions in nuclei using dijets in proton–proton and proton–lead collisions at  $\sqrt{s_{_{NN}}} = 5.02\text{ TeV}$ ”, *Phys. Rev. Lett.* **121** (2018) 062002, doi:10.1103/PhysRevLett.121.062002, arXiv:1805.04736.

[178] European Muon Collaboration, “The ratio of the nucleon structure functions  $F_{2,n}$  for iron and deuterium”, *Phys. Lett. B* **123** (1983) 275, doi:10.1016/0370-2693(83)90437-9.

[179] P. Paakkinen, K. Eskola, and H. Paukkunen, “Impact of CMS dijets in 5.02 TeV pPb and pp collisions on EPPS16 nuclear PDFs”, in *Proceedings of International Conference on Hard and Electromagnetic Probes of High-Energy Nuclear Collisions–PoS(HardProbes2018)*, D. d’Enterria, A. Morsch, and P. Crochet, eds., volume 345, p. 124. 2019. arXiv:1812.05438. doi:10.22323/1.345.0124.

[180] B. Alver, M. Baker, C. Loizides, and P. Steinberg, “The PHOBOS Glauber Monte Carlo”, 2008. arXiv:0805.4411.

[181] D. d’Enterria and C. Loizides, “Progress in the Glauber model at collider energies”, *Ann. Rev. Nucl. Part. Sci.* **71** (2021) 315, doi:10.1146/annurev-nucl-102419-060007, arXiv:2011.14909.

[182] P. Aurenche et al., “A new critical study of photon production in hadronic collisions”, *Phys. Rev. D* **73** (2006) 094007, doi:10.1103/PhysRevD.73.094007, arXiv:hep-ph/0602133.

[183] CMS Collaboration, “Study of W boson production in PbPb and pp collisions at  $\sqrt{s_{\text{NN}}} = 2.76$  TeV”, *Phys. Lett. B* **715** (2012) 66, doi:10.1016/j.physletb.2012.07.025, arXiv:1205.6334.

[184] CMS Collaboration, “Study of Z boson production in PbPb collisions at  $\sqrt{s_{\text{NN}}} = 2.76$  TeV”, *Phys. Rev. Lett.* **106** (2011) 212301, doi:10.1103/PhysRevLett.106.212301, arXiv:1102.5435.

[185] CMS Collaboration, “Constraints on the initial state of Pb-Pb collisions via measurements of Z-boson yields and azimuthal anisotropy at  $\sqrt{s_{\text{NN}}} = 5.02$  TeV”, *Phys. Rev. Lett.* **127** (2021) 102002, doi:10.1103/PhysRevLett.127.102002, arXiv:2103.14089.

[186] C. Loizides and A. Morsch, “Absence of jet quenching in peripheral nucleus–nucleus collisions”, *Phys. Lett. B* **773** (2017) 408, doi:10.1016/j.physletb.2017.09.002, arXiv:1705.08856.

[187] ALICE Collaboration, “ $W^\pm$ -boson production in p-Pb collisions at  $\sqrt{s_{\text{NN}}} = 8.16$  TeV and PbPb collisions at  $\sqrt{s_{\text{NN}}} = 5.02$  TeV”, *JHEP* **05** (2023) 036, doi:10.1007/JHEP05(2023)036, arXiv:2204.10640.

[188] ATLAS Collaboration, “Z boson production in Pb+Pb collisions at  $\sqrt{s_{\text{NN}}} = 5.02$  TeV measured by the ATLAS experiment”, *Phys. Lett. B* **802** (2020) 135262, doi:10.1016/j.physletb.2020.135262, arXiv:1910.13396.

[189] K. J. Eskola, I. Helenius, M. Kuha, and H. Paukkunen, “Shadowing in inelastic nucleon-nucleon cross section?”, *Phys. Rev. Lett.* **125** (2020) 212301, doi:10.1103/PhysRevLett.125.212301, arXiv:2003.11856.

[190] E. A. Kuraev, L. N. Lipatov, and V. S. Fadin, “The Pomeranchuk singularity in nonabelian gauge theories”, *Sov. Phys. JETP* **45** (1977) 199.

[191] I. I. Balitsky and L. N. Lipatov, “The Pomeranchuk singularity in quantum chromodynamics”, *Sov. J. Nucl. Phys.* **28** (1978) 822.

[192] L. N. Lipatov, "The bare pomeron in quantum chromodynamics", *Sov. Phys. JETP* **63** (1986) 904.

[193] V. S. Fadin and L. N. Lipatov, "BFKL pomeron in the next-to-leading approximation", *Phys. Lett. B* **429** (1998) 127, doi:10.1016/S0370-2693(98)00473-0, arXiv:hep-ph/9802290.

[194] I. Balitsky, "Operator expansion for high-energy scattering", *Nucl. Phys. B* **463** (1996) 99–160, doi:10.1016/0550-3213(95)00638-9, arXiv:hep-ph/9509348.

[195] I. Balitsky, "Factorization for high-energy scattering", *Phys. Rev. Lett.* **81** (1998) 2024–2027, doi:10.1103/PhysRevLett.81.2024, arXiv:hep-ph/9807434.

[196] I. Balitsky, "Factorization and high-energy effective action", *Phys. Rev. D* **60** (1999) 014020, doi:10.1103/PhysRevD.60.014020, arXiv:hep-ph/9812311.

[197] Y. V. Kovchegov, "Unitarization of the BFKL pomeron on a nucleus", *Phys. Rev. D* **61** (2000) 074018, doi:10.1103/PhysRevD.61.074018, arXiv:hep-ph/9905214.

[198] M. van de Klundert, "Search for gluon saturation in proton-lead collisions at  $\sqrt{s_{\text{NN}}} = 5.02 \text{ TeV}$  with the very forward CASTOR calorimeter at the CMS experiment". PhD thesis, University of Antwerp, 2018. CERN-THESIS-2018-087.

[199] S. Ostapchenko, "QGSJET-II: Towards reliable description of very high energy hadronic interactions", *Nucl. Phys. B Proc. Suppl.* **151** (2006) 143, doi:10.1016/j.nuclphysbps.2005.07.026, arXiv:hep-ph/0412332.

[200] A. van Hameren, "KaTie : For parton-level event generation with  $k_T$ -dependent initial states", *Comput. Phys. Commun.* **224** (2018) 371, doi:10.1016/j.cpc.2017.11.005, arXiv:1611.00680.

[201] J. L. Albacete, P. Guerrero Rodríguez, and Y. Nara, "Ultraforward particle production from color glass condensate and Lund fragmentation", *Phys. Rev. D* **94** (2016) 054004, doi:10.1103/PhysRevD.94.054004, arXiv:1605.08334.

[202] CMS Collaboration, "Measurement of inclusive very forward jet cross sections in proton-lead collisions at  $\sqrt{s_{\text{NN}}} = 5.02 \text{ TeV}$ ", *JHEP* **05** (2019) 043, doi:10.1007/JHEP05(2019)043, arXiv:1812.01691.

[203] H. Mäntysaari and H. Paukkunen, "Saturation and forward jets in proton-lead collisions at the LHC", *Phys. Rev. D* **100** (2019) 114029, doi:10.1103/PhysRevD.100.114029, arXiv:1910.13116.

[204] C. F. von Weizsäcker, "Radiation emitted in collisions of very fast electrons", *Z. Phys.* **88** (1934) 612, doi:10.1007/BF01333110.

[205] E. J. Williams, "Nature of the high-energy particles of penetrating radiation and status of ionization and radiation formulae", *Phys. Rev.* **45** (1934) 729, doi:10.1103/PhysRev.45.729.

[206] S. J. Brodsky et al., "Diffractive leptoproduction of vector mesons in QCD", *Phys. Rev. D* **50** (1994) 3134, doi:10.1103/PhysRevD.50.3134, arXiv:hep-ph/9402283.

[207] A. D. Martin, C. Nockles, M. G. Ryskin, and T. Teubner, "Small  $x$  gluon from exclusive J/psi production", *Phys. Lett. B* **662** (2008) 252, doi:10.1016/j.physletb.2008.02.067, arXiv:0709.4406.

[208] CMS Collaboration, “Measurement of exclusive  $\Upsilon$  photoproduction from protons in pPb collisions at  $\sqrt{s_{\text{NN}}} = 5.02 \text{ TeV}$ ”, *Eur. Phys. J. C* **79** (2019) 277, doi:10.1140/epjc/s10052-019-6774-8, arXiv:1809.11080.

[209] CMS Collaboration, “Measurement of exclusive  $\rho(770)^0$  photoproduction in ultraperipheral pPb collisions at  $\sqrt{s_{\text{NN}}} = 5.02 \text{ TeV}$ ”, *Eur. Phys. J. C* **79** (2019) 702, doi:10.1140/epjc/s10052-019-7202-9, arXiv:1902.01339.

[210] C. A. Flett et al., “How to include exclusive  $\text{J}/\psi$  production data in global PDF analyses”, *Phys. Rev. D* **101** (2020) 094011, doi:10.1103/PhysRevD.101.094011, arXiv:1908.08398.

[211] ALICE Collaboration, “Coherent  $\text{J}/\psi$  photoproduction in ultra-peripheral Pb-Pb collisions at  $\sqrt{s_{\text{NN}}} = 2.76 \text{ TeV}$ ”, *Phys. Lett. B* **718** (2013) 1273, doi:10.1016/j.physletb.2012.11.059, arXiv:1209.3715.

[212] ALICE Collaboration, “Charmonium and  $e^+e^-$  pair photoproduction at midrapidity in ultra-peripheral Pb-Pb collisions at  $\sqrt{s_{\text{NN}}} = 2.76 \text{ TeV}$ ”, *Eur. Phys. J. C* **73** (2013) 2617, doi:10.1140/epjc/s10052-013-2617-1, arXiv:1305.1467.

[213] CMS Collaboration, “Coherent  $\text{J}/\psi$  photoproduction in ultra-peripheral PbPb collisions at  $\sqrt{s_{\text{NN}}} = 2.76 \text{ TeV}$  with the CMS experiment”, *Phys. Lett. B* **772** (2017) 489, doi:10.1016/j.physletb.2017.07.001, arXiv:1605.06966.

[214] V. Guzey, M. Strikman, and M. Zhalov, “Disentangling coherent and incoherent quasielastic  $\text{J}/\psi$  photoproduction on nuclei by neutron tagging in ultraperipheral ion collisions at the LHC”, *Eur. Phys. J. C* **74** (2014) 2942, doi:10.1140/epjc/s10052-014-2942-z, arXiv:1312.6486.

[215] V. Guzey, E. Kryshen, M. Strikman, and M. Zhalov, “Evidence for nuclear gluon shadowing from the ALICE measurements of PbPb ultraperipheral exclusive  $\text{J}/\psi$  production”, *Phys. Lett. B* **726** (2013) 290, doi:10.1016/j.physletb.2013.08.043, arXiv:1305.1724.

[216] V. Guzey, E. Kryshen, and M. Zhalov, “Coherent photoproduction of vector mesons in ultraperipheral heavy ion collisions: Update for Run 2 at the CERN Large Hadron Collider”, *Phys. Rev. C* **93** (2016) 055206, doi:10.1103/PhysRevC.93.055206, arXiv:1602.01456.

[217] B. L. Berman and S. C. Fultz, “Measurements of the giant dipole resonance with monoenergetic photons”, *Rev. Mod. Phys.* **47** (1975) 713, doi:10.1103/RevModPhys.47.713.

[218] CMS Collaboration, “Observation of forward neutron multiplicity dependence of dimuon acoplanarity in ultraperipheral PbPb Collisions at  $\sqrt{s_{\text{NN}}} = 5.02 \text{ TeV}$ ”, *Phys. Rev. Lett.* **127** (2021) 122001, doi:10.1103/PhysRevLett.127.122001, arXiv:2011.05239.

[219] O. Surányi et al., “Performance of the CMS zero degree calorimeters in pPb collisions at the LHC”, *JINST* **16** (2021) P05008, doi:10.1088/1748-0221/16/05/P05008, arXiv:2102.06640.

[220] A. Łuszczak and W. Schäfer, “Coherent photoproduction of  $\text{J}/\psi$  in nucleus-nucleus collisions in the color dipole approach”, *Phys. Rev. C* **99** (2019) 044905, doi:10.1103/PhysRevC.99.044905, arXiv:1901.07989.

[221] CMS Collaboration, “Probing small Bjorken- $x$  nuclear gluonic structure via coherent  $J/\psi$  photoproduction in ultraperipheral PbPb collisions at  $\sqrt{s_{_{NN}}} = 5.02$  TeV”, *Phys. Rev. Lett.* **131** (2023) 262301, doi:10.1103/PhysRevLett.131.262301, arXiv:2303.16984.

[222] ALICE Collaboration, “Coherent  $J/\psi$  photoproduction at forward rapidity in ultra-peripheral Pb-Pb collisions at  $\sqrt{s_{_{NN}}} = 5.02$  TeV”, *Phys. Lett. B* **798** (2019) 134926, doi:10.1016/j.physletb.2019.134926, arXiv:1904.06272.

[223] H. Mäntysaari and B. Schenke, “Probing subnucleon scale fluctuations in ultraperipheral heavy ion collisions”, *Phys. Lett. B* **772** (2017) 832, doi:10.1016/j.physletb.2017.07.063, arXiv:1703.09256.

[224] J. Cepila, J. G. Contreras, and M. Krelina, “Coherent and incoherent  $J/\psi$  photonuclear production in an energy-dependent hot-spot model”, *Phys. Rev. C* **97** (2018) 024901, doi:10.1103/PhysRevC.97.024901, arXiv:1711.01855.

[225] D. Bendova, J. Cepila, J. G. Contreras, and M. Matas, “Photonuclear  $J/\psi$  production at the LHC: proton-based versus nuclear dipole scattering amplitudes”, *Phys. Lett. B* **817** (2021) 136306, doi:10.1016/j.physletb.2021.136306, arXiv:2006.12980.

[226] K. J. Eskola et al., “Exclusive  $J/\psi$  photoproduction in ultraperipheral Pb+Pb collisions at the CERN Large Hadron Collider calculated at next-to-leading order perturbative QCD”, *Phys. Rev. C* **106** (2022) 035202, doi:10.1103/PhysRevC.106.035202, arXiv:2203.11613.

[227] H. Mäntysaari and J. Penttala, “Complete calculation of exclusive heavy vector meson production at next-to-leading order in the dipole picture”, *JHEP* **08** (2022) 247, doi:10.1007/JHEP08(2022)247, arXiv:2204.14031.

[228] K. J. Eskola et al., “Next-to-leading order perturbative QCD predictions for exclusive  $J/\psi$  photoproduction in oxygen-oxygen and lead-lead collisions at energies available at the CERN Large Hadron Collider”, *Phys. Rev. C* **107** (2023) 044912, doi:10.1103/PhysRevC.107.044912, arXiv:2210.16048.

[229] L. D. Landau, “On the multiparticle production in high-energy collisions”, *Izv. Akad. Nauk Ser. Fiz.* **17** (1953) 51.

[230] PHENIX Collaboration, “Systematic studies of the centrality and  $\sqrt{s_{_{NN}}}$  dependence of the  $dE_T/d\eta$  and  $dN^{ch}/d\eta$  in heavy ion collisions at midrapidity”, *Phys. Rev. C* **71** (2005) 034908, doi:10.1103/PhysRevC.71.034908, arXiv:nucl-ex/0409015. [Erratum: doi:10.1103/PhysRevC.71.049901].

[231] CMS Collaboration, “Pseudorapidity distributions of charged hadrons in xenon-xenon collisions at  $\sqrt{s_{_{NN}}} = 5.44$  TeV”, *Phys. Lett. B* **799** (2019) 135049, doi:10.1016/j.physletb.2019.135049, arXiv:1902.03603.

[232] CMS Collaboration, “Measurement of the pseudorapidity and centrality dependence of the transverse energy density in PbPb collisions at  $\sqrt{s_{_{NN}}} = 2.76$  TeV”, *Phys. Rev. Lett.* **109** (2012) 152303, doi:10.1103/PhysRevLett.109.152303, arXiv:1205.2488.

[233] PHOBOS Collaboration, “System size, energy and centrality dependence of pseudorapidity distributions of charged particles in relativistic heavy ion collisions”, *Phys. Rev. Lett.* **102** (2009) 142301, doi:10.1103/PhysRevLett.102.142301, arXiv:0709.4008.

[234] PHOBOS Collaboration, "Charged-particle multiplicity and pseudorapidity distributions measured with the PHOBOS detector in Au+Au, Cu+Cu, d+Au, and p+p collisions at ultrarelativistic energies", *Phys. Rev. C* **83** (2011) 024913, doi:10.1103/PhysRevC.83.024913, arXiv:1011.1940.

[235] CMS Collaboration, "Transverse-momentum and pseudorapidity distributions of charged hadrons in pp collisions at  $\sqrt{s} = 7$  TeV", *Phys. Rev. Lett.* **105** (2010) 022002, doi:10.1103/PhysRevLett.105.022002, arXiv:1005.3299.

[236] CMS Collaboration, "Transverse-momentum and pseudorapidity distributions of charged hadrons in pp collisions at  $\sqrt{s} = 0.9$  and 2.36 TeV", *JHEP* **02** (2010) 041, doi:10.1007/JHEP02(2010)041, arXiv:1002.0621.

[237] ALICE Collaboration, "Charged-particle multiplicity measurement in proton-proton collisions at  $\sqrt{s} = 0.9$  and 2.36 TeV with ALICE at LHC", *Eur. Phys. J. C* **68** (2010) 89, doi:10.1140/epjc/s10052-010-1339-x, arXiv:1004.3034.

[238] UA5 Collaboration, "Scaling of pseudorapidity distributions at c.m. energies up to 0.9 TeV", *Z. Phys. C* **33** (1986) 1, doi:10.1007/BF01410446.

[239] UA1 Collaboration, "A study of the general characteristics of proton-antiproton collisions at  $\sqrt{s} = 0.2$  to 0.9 TeV", *Nucl. Phys. B* **335** (1990) 261, doi:10.1016/0550-3213(90)90493-W.

[240] CMS Collaboration, "Long-range and short-range dihadron angular correlations in central PbPb collisions at a nucleon-nucleon center of mass energy of 2.76 TeV", *JHEP* **07** (2011) 076, doi:10.1007/JHEP07(2011)076, arXiv:1105.2438.

[241] CMS Collaboration, "Centrality dependence of dihadron correlations and azimuthal anisotropy harmonics in PbPb collisions at  $\sqrt{s_{_{NN}}} = 2.76$  TeV", *Eur. Phys. J. C* **72** (2012) 2012, doi:10.1140/epjc/s10052-012-2012-3, arXiv:1201.3158.

[242] CMS Collaboration, "Measurement of higher-order harmonic azimuthal anisotropy in PbPb collisions at  $\sqrt{s_{_{NN}}} = 2.76$  TeV", *Phys. Rev. C* **89** (2014) 044906, doi:10.1103/PhysRevC.89.044906, arXiv:1310.8651.

[243] CMS Collaboration, "Studies of azimuthal dihadron correlations in ultra-central PbPb collisions at  $\sqrt{s_{_{NN}}} = 2.76$  TeV", *JHEP* **02** (2014) 088, doi:10.1007/JHEP02(2014)088, arXiv:1312.1845.

[244] CMS Collaboration, "Evidence for transverse momentum and pseudorapidity dependent event plane fluctuations in PbPb and pPb collisions", *Phys. Rev. C* **92** (2015) 034911, doi:10.1103/PhysRevC.92.034911, arXiv:1503.01692.

[245] CMS Collaboration, "Non-Gaussian elliptic-flow fluctuations in PbPb collisions at  $\sqrt{s_{_{NN}}} = 5.02$  TeV", *Phys. Lett. B* **789** (2019) 643, doi:10.1016/j.physletb.2018.11.063, arXiv:1711.05594.

[246] ALICE Collaboration, "Harmonic decomposition of two-particle angular correlations in Pb-Pb collisions at  $\sqrt{s_{_{NN}}} = 2.76$  TeV", *Phys. Lett. B* **708** (2012) 249, doi:10.1016/j.physletb.2012.01.060, arXiv:1109.2501.

[247] C. Shen, Z. Qiu, and U. Heinz, "Shape and flow fluctuations in ultracentral PbPb collisions at the energies available at the CERN Large Hadron Collider", *Phys. Rev. C* **92** (2015) 014901, doi:10.1103/PhysRevC.92.014901, arXiv:1502.04636.

---

- [248] D. T. Son and A. O. Starinets, "Viscosity, black holes, and quantum field theory", *Ann. Rev. Nucl. Part. Sci.* **57** (2007) 95,  
doi:10.1146/annurev.nucl.57.090506.123120, arXiv:0704.0240.
- [249] L. Yan, J.-Y. Ollitrault, and A. M. Poskanzer, "Azimuthal anisotropy distributions in high-energy collisions", *Phys. Lett. B* **742** (2015) 290,  
doi:10.1016/j.physletb.2015.01.039, arXiv:1408.0921.
- [250] R. S. Bhalerao, M. Luzum, and J.-Y. Ollitrault, "Understanding anisotropy generated by fluctuations in heavy-ion collisions", *Phys. Rev. C* **84** (2011) 054901,  
doi:10.1103/PhysRevC.84.054901, arXiv:1107.5485.
- [251] P. Romatschke and U. Romatschke, "Viscosity information from relativistic nuclear collisions: How perfect is the fluid observed at RHIC?", *Phys. Rev. Lett.* **99** (2007) 172301, doi:10.1103/PhysRevLett.99.172301, arXiv:0706.1522.
- [252] G. Giacalone, J. Noronha-Hostler, and J.-Y. Ollitrault, "Relative flow fluctuations as a probe of initial state fluctuations", *Phys. Rev. C* **95** (2017) 054910,  
doi:10.1103/PhysRevC.95.054910, arXiv:1702.01730.
- [253] CMS Collaboration, "Charged-particle angular correlations in XeXe collisions at  $\sqrt{s_{\text{NN}}} = 5.44 \text{ TeV}$ ", *Phys. Rev. C* **100** (2019) 044902,  
doi:10.1103/PhysRevC.100.044902, arXiv:1901.07997.
- [254] J. S. Moreland, J. E. Bernhard, and S. A. Bass, "Alternative ansatz to wounded nucleon and binary collision scaling in high-energy nuclear collisions", *Phys. Rev. C* **92** (2015) 011901, doi:10.1103/PhysRevC.92.011901, arXiv:1412.4708.
- [255] F. G. Gardim, F. Grassi, M. Luzum, and J.-Y. Ollitrault, "Breaking of factorization of two-particle correlations in hydrodynamics", *Phys. Rev. C* **87** (2013) 031901,  
doi:10.1103/PhysRevC.87.031901, arXiv:1211.0989.
- [256] U. Heinz, Z. Qiu, and C. Shen, "Fluctuating flow angles and anisotropic flow measurements", *Phys. Rev. C* **87** (2013) 034913,  
doi:10.1103/PhysRevC.87.034913, arXiv:1302.3535.
- [257] A. Dumitru, D. E. Kharzeev, E. M. Levin, and Y. Nara, "Gluon saturation in pA collisions at energies available at the CERN Large Hadron Collider: Predictions for hadron multiplicities", *Phys. Rev. C* **85** (2012) 044920,  
doi:10.1103/PhysRevC.85.044920, arXiv:1111.3031.
- [258] CMS Collaboration, "Principal-component analysis of two-particle azimuthal correlations in PbPb and pPb collisions at CMS", *Phys. Rev. C* **96** (2017) 064902,  
doi:10.1103/PhysRevC.96.064902, arXiv:1708.07113.
- [259] P. Bozek, W. Broniowski, and J. Moreira, "Torqued fireballs in relativistic heavy-ion collisions", *Phys. Rev. C* **83** (2011) 034911, doi:10.1103/PhysRevC.83.034911,  
arXiv:1011.3354.
- [260] B. Schenke and S. Schlichting, "3D glasma initial state for relativistic heavy ion collisions", *Phys. Rev. C* **94** (2016) 044907, doi:10.1103/PhysRevC.94.044907,  
arXiv:1605.07158.

[261] L. Yan and J.-Y. Ollitrault, “ $\nu_4, \nu_5, \nu_6, \nu_7$ : nonlinear hydrodynamic response versus LHC data”, *Phys. Lett. B* **744** (2015) 82, doi:10.1016/j.physletb.2015.03.040, arXiv:1502.02502.

[262] J. Qian, U. W. Heinz, and J. Liu, “Mode-coupling effects in anisotropic flow in heavy-ion collisions”, *Phys. Rev. C* **93** (2016) 064901, doi:10.1103/PhysRevC.93.064901, arXiv:1602.02813.

[263] D. Teaney and L. Yan, “Nonlinearities in the harmonic spectrum of heavy ion collisions with ideal and viscous hydrodynamics”, *Phys. Rev. C* **86** (2012) 044908, doi:10.1103/PhysRevC.86.044908, arXiv:1206.1905.

[264] J. Qian, U. Heinz, R. He, and L. Huo, “Differential flow correlations in relativistic heavy-ion collisions”, *Phys. Rev. C* **95** (2017) 054908, doi:10.1103/PhysRevC.95.054908, arXiv:1703.04077.

[265] G. Giacalone, L. Yan, and J.-Y. Ollitrault, “Nonlinear coupling of flow harmonics: Hexagonal flow and beyond”, *Phys. Rev. C* **97** (2018) 054905, doi:10.1103/PhysRevC.97.054905, arXiv:1803.00253.

[266] W. Zhao, H.-j. Xu, and H. Song, “Collective flow in 2.76 A TeV and 5.02 A TeV Pb+Pb collisions”, *Eur. Phys. J. C* **77** (2017) 645, doi:10.1140/epjc/s10052-017-5186-x, arXiv:1703.10792.

[267] S. McDonald et al., “Hydrodynamic predictions for Pb+Pb collisions at 5.02 TeV”, *Phys. Rev. C* **95** (2017) 064913, doi:10.1103/PhysRevC.95.064913, arXiv:1609.02958.

[268] CMS Collaboration, “Mixed higher-order anisotropic flow and nonlinear response coefficients of charged particles in PbPb collisions at  $\sqrt{s_{\text{NN}}} = 2.76$  and 5.02 TeV”, *Eur. Phys. J. C* **80** (2020) 534, doi:10.1140/epjc/s10052-020-7834-9, arXiv:1910.08789.

[269] M. A. Lisa, S. Pratt, R. Soltz, and U. Wiedemann, “Femtoscopy in relativistic heavy ion collisions”, *Ann. Rev. Nucl. Part. Sci.* **55** (2005) 357, doi:10.1146/annurev.nucl.55.090704.151533, arXiv:nucl-ex/0505014.

[270] R. Hanbury-Brown and R. Q. Twiss, “A new type of interferometer for use in radio astronomy”, *Phil. Magazine* **45** (1954) 663, doi:10.1080/14786440708520475.

[271] R. Hanbury-Brown and R. Q. Twiss, “Correlation between photons in two coherent beams of light”, *Nature* **177** (1956) 27, doi:10.1038/177027a0.

[272] R. Hanbury-Brown and R. Q. Twiss, “A test of a new type of stellar interferometer on Sirius”, *Nature* **178** (1956) 1046, doi:10.1038/1781046a0.

[273] G. Goldhaber et al., “Influence of Bose-Einstein statistics on the anti-proton proton annihilation process”, *Phys. Rev.* **120** (1960) 300, doi:10.1103/PhysRev.120.300. doi:10.1103/PhysRev.120.300.

[274] J. D. Bjorken, “Highly relativistic nucleus-nucleus collisions: The central rapidity region”, *Phys. Rev. D* **27** (1983) 140, doi:10.1103/PhysRevD.27.140.

[275] CMS Collaboration, “First measurement of Bose–Einstein correlations in proton-proton collisions at  $\sqrt{s} = 0.9$  and 2.36 TeV at the LHC”, *Phys. Rev. Lett.* **105** (2010) 032001, doi:10.1103/PhysRevLett.105.032001, arXiv:1005.3294.

[276] CMS Collaboration, “Measurement of Bose–Einstein correlations in pp collisions at  $\sqrt{s} = 0.9$  and 7 TeV”, *JHEP* **05** (2011) 029, doi:10.1007/JHEP05(2011)029, arXiv:1101.3518.

[277] CMS Collaboration, “Bose–Einstein correlations in pp, pPb, and PbPb collisions at  $\sqrt{s_{_{NN}}} = 0.9 - 7$  TeV”, *Phys. Rev. C* **97** (2018) 064912, doi:10.1103/PhysRevC.97.064912, arXiv:1712.07198.

[278] CMS Collaboration, “Bose–Einstein correlations of charged hadrons in proton-proton collisions at  $\sqrt{s} = 13$  TeV”, *JHEP* **03** (2020) 014, doi:10.1007/JHEP03(2020)014, arXiv:1910.08815.

[279] CMS Collaboration, “Two-particle Bose–Einstein correlations and their Lévy parameters in PbPb collisions at  $\sqrt{s_{_{NN}}} = 5.02$  TeV”, *Phys. Rev. C* **109** (2024) 024914, doi:10.1103/PhysRevC.109.024914, arXiv:2306.11574.

[280] T. Csorgo et al., “Bose–Einstein correlations for Levy stable source distributions”, *Eur. Phys. J. C* **36** (2004) 67, doi:10.1140/epjc/s2004-01870-9, arXiv:nucl-th/0310042.

[281] CMS Collaboration, “Observation of correlated azimuthal anisotropy Fourier harmonics in pp and pPb collisions at the LHC”, *Phys. Rev. Lett.* **120** (2018) 092301, doi:10.1103/PhysRevLett.120.092301, arXiv:1709.09189.

[282] A. Bzdak, B. Schenke, P. Tribedy, and R. Venugopalan, “Initial state geometry and the role of hydrodynamics in proton-proton, proton-nucleus and deuteron-nucleus collisions”, *Phys. Rev. C* **87** (2013) 064906, doi:10.1103/PhysRevC.87.064906, arXiv:nucl-th/1304.3403.

[283] L. McLerran, M. Praszalowicz, and B. Schenke, “Transverse momentum of protons, pions and kaons in high multiplicity pp and pA collisions: Evidence for the color glass condensate?”, *Nucl. Phys. A* **916** (2013) 210, doi:10.1016/j.nuclphysa.2013.08.008, arXiv:hep-ph/1306.2350.

[284] T. Csorgo and J. Zimanyi, “Pion interferometry for strongly correlated space-time and momentum space”, *Nucl. Phys. A* **517** (1990) 588, doi:10.1016/0375-9474(90)90220-G.

[285] L3 Collaboration, “Test of the  $\tau$ -model of Bose–Einstein correlations and reconstruction of the source function in hadronic Z-boson decay at LEP”, *Eur. Phys. J. C* **71** (2011) 1648, doi:10.1140/epjc/s10052-011-1648-8, arXiv:1105.4788.

[286] M. Chojnacki, W. Florkowski, and T. Csörgö, “Formation of hubble-like flow in little bangs”, *Phys. Rev. C* **71** (2005) 044902, doi:10.1103/PhysRevC.71.044902, arXiv:nucl-th/0410036.

[287] PHENIX Collaboration, “Bose–Einstein correlations of charged pion pairs in Au+Au collisions at  $\sqrt{s_{_{NN}}} = 200$  GeV”, *Phys. Rev. Lett.* **93** (2004) 152302, doi:10.1103/PhysRevLett.93.152302, arXiv:nucl-ex/0401003.

[288] STAR Collaboration, "Pion interferometry in Au+Au collisions at  $\sqrt{s_{\text{NN}}} = 200 \text{ GeV}$ ", *Phys. Rev. C* **71** (2005) 044906, doi:10.1103/PhysRevC.71.044906, arXiv:nucl-ex/0411036.

[289] STAR Collaboration, "Pion interferometry in Au+Au and Cu+Cu collisions at  $\sqrt{s_{\text{NN}}} = 62.4$  and  $200 \text{ GeV}$ ", *Phys. Rev. C* **80** (2009) 024905, doi:10.1103/PhysRevC.80.024905, arXiv:0903.1296.

[290] PHENIX Collaboration, "Systematic study of charged-pion and kaon femtoscopy in Au+Au collisions at  $\sqrt{s_{\text{NN}}} = 200 \text{ GeV}$ ", *Phys. Rev. C* **92** (2015) 034914, doi:10.1103/PhysRevC.92.034914, arXiv:1504.05168.

[291] M. Csanad, S. Lokos, and M. Nagy, "Expanded empirical formula for Coulomb final state interaction in the presence of Levy sources", *Phys. Part. Nucl.* **51** (2020) 238, doi:10.1134/S1063779620030089, arXiv:1910.02231.

[292] PHENIX Collaboration, "Levy-stable two-pion Bose-Einstein correlations in  $\sqrt{s_{\text{NN}}} = 200 \text{ GeV}$  Au+Au collisions", *Phys. Rev. C* **97** (2018) 064911, doi:10.1103/PhysRevC.97.064911, arXiv:1709.05649.

[293] R. L. Jaffe, "Perhaps a stable dihyperon", *Phys. Rev. Lett.* **38** (1977) 195, doi:10.1103/PhysRevLett.38.195.

[294] D. B. Kaplan and A. E. Nelson, "Kaon condensation in dense matter", *Nucl. Phys. A* **479** (1988) 273c, doi:10.1016/0375-9474(88)90442-3.

[295] J. Schaffner-Bielich, M. Hanauske, H. Stoecker, and W. Greiner, "Phase transition to hyperon matter in neutron stars", *Phys. Rev. Lett.* **89** (2002) 171101, doi:10.1103/PhysRevLett.89.171101, arXiv:astro-ph/0005490.

[296] K. Morita, T. Furumoto, and A. Ohnishi, "ΛΛ interaction from relativistic heavy-ion collisions", *Phys. Rev. C* **91** (2015) 024916, doi:10.1103/PhysRevC.91.024916, arXiv:1408.6682.

[297] CMS Collaboration, "K<sub>S</sub><sup>0</sup> and Λ(Λ̄) two-particle femtoscopic correlations in PbPb collisions at  $\sqrt{s_{\text{NN}}} = 5.02 \text{ TeV}$ ", 2023. arXiv:2301.05290. Submitted to PLB.

[298] D. Kharzeev, "Parity violation in hot QCD: Why it can happen, and how to look for it", *Phys. Lett. B* **633** (2006) 260, doi:10.1016/j.physletb.2005.11.075, arXiv:hep-ph/0406125.

[299] D. E. Kharzeev, L. D. McLerran, and H. J. Warringa, "The effects of topological charge change in heavy ion collisions: 'event by event P and CP violation'", *Nucl. Phys. A* **803** (2008) 227, doi:10.1016/j.nuclphysa.2008.02.298, arXiv:0711.0950.

[300] W. Li and G. Wang, "Chiral magnetic effects in nuclear collisions", *Ann. Rev. Nucl. Part. Sci.* **70** (2020) 293, doi:10.1146/annurev-nucl-030220-065203, arXiv:2002.10397.

[301] S. A. Voloshin, "Parity violation in hot QCD: How to detect it", *Phys. Rev. C* **70** (2004) 057901, doi:10.1103/PhysRevC.70.057901, arXiv:hep-ph/0406311.

[302] STAR Collaboration, "Observation of charge-dependent azimuthal correlations and possible local strong parity violation in heavy ion collisions", *Phys. Rev. C* **81** (2010) 054908, doi:10.1103/PhysRevC.81.054908, arXiv:0909.1717.

[303] CMS Collaboration, “Observation of long-range near-side angular correlations in proton-proton collisions at the LHC”, *JHEP* **09** (2010) 091, doi:10.1007/JHEP09(2010)091, arXiv:1009.4122.

[304] CMS Collaboration, “Measurement of long-range near-side two-particle angular correlations in pp collisions at  $\sqrt{s} = 13$  TeV”, *Phys. Rev. Lett.* **116** (2016) 172302, doi:10.1103/PhysRevLett.116.172302, arXiv:1510.03068.

[305] CMS Collaboration, “Evidence for collectivity in pp collisions at the LHC”, *Phys. Lett. B* **765** (2017) 193, doi:10.1016/j.physletb.2016.12.009, arXiv:1606.06198.

[306] CMS Collaboration, “Observation of long-range near-side angular correlations in proton-lead collisions at the LHC”, *Phys. Lett. B* **718** (2013) 795, doi:10.1016/j.physletb.2012.11.025, arXiv:1210.5482.

[307] CMS Collaboration, “Long-range two-particle correlations of strange hadrons with charged particles in pPb and PbPb collisions at LHC energies”, *Phys. Lett. B* **742** (2015) 200, doi:10.1016/j.physletb.2015.01.034, arXiv:1409.3392.

[308] CMS Collaboration, “Evidence for collective multiparticle correlations in p-Pb collisions”, *Phys. Rev. Lett.* **115** (2015) 012301, doi:10.1103/PhysRevLett.115.012301, arXiv:1502.05382.

[309] CMS Collaboration, “Observation of charge-dependent azimuthal correlations in p-Pb collisions and its implication for the search for the chiral magnetic effect”, *Phys. Rev. Lett.* **118** (2017) 122301, doi:10.1103/PhysRevLett.118.122301, arXiv:1610.00263.

[310] ALICE Collaboration, “Charge separation relative to the reaction plane in Pb-Pb collisions at  $\sqrt{s_{\text{NN}}} = 2.76$  TeV”, *Phys. Rev. Lett.* **110** (2013) 012301, doi:10.1103/PhysRevLett.110.012301, arXiv:1207.0900.

[311] CMS Collaboration, “Constraints on the chiral magnetic effect using charge-dependent azimuthal correlations in pPb and PbPb collisions at the CERN large hadron collider”, *Phys. Rev. C* **97** (2018) 044912, doi:10.1103/PhysRevC.97.044912, arXiv:1708.01602.

[312] B. Alver and G. Roland, “Collision geometry fluctuations and triangular flow in heavy-ion collisions”, *Phys. Rev. C* **81** (2010) 054905, doi:10.1103/PhysRevC.81.054905, arXiv:1003.0194. [Erratum: doi:10.1103/PhysRevC.82.039903].

[313] ATLAS Collaboration, “Measurement of event-plane correlations in  $\sqrt{s_{\text{NN}}} = 2.76$  TeV lead-lead collisions with the ATLAS detector”, *Phys. Rev. C* **90** (2014) 024905, doi:10.1103/PhysRevC.90.024905, arXiv:1403.0489.

[314] J. Schukraft, A. Timmins, and S. A. Voloshin, “Ultra-relativistic nuclear collisions: event shape engineering”, *Phys. Lett. B* **719** (2013) 394, doi:10.1016/j.physletb.2013.01.045, arXiv:1208.4563.

[315] Y. Burnier, D. E. Kharzeev, J. Liao, and H.-U. Yee, “Chiral magnetic wave at finite baryon density and the electric quadrupole moment of quark-gluon plasma in heavy ion collisions”, *Phys. Rev. Lett.* **107** (2011) 052303, doi:10.1103/PhysRevLett.107.052303, arXiv:1103.1307.

[316] D. E. Kharzeev and H.-U. Yee, “Chiral magnetic wave”, *Phys. Rev. D* **83** (2011) 085007, doi:10.1103/PhysRevD.83.085007, arXiv:1012.6026.

[317] D. E. Kharzeev, J. Liao, S. A. Voloshin, and G. Wang, “Chiral magnetic and vortical effects in high-energy nuclear collisions—A status report”, *Prog. Part. Nucl. Phys.* **88** (2016) 1, doi:10.1016/j.ppnp.2016.01.001, arXiv:1511.04050.

[318] CMS Collaboration, “Probing the chiral magnetic wave in pPb and PbPb collisions at  $\sqrt{s_{\text{NN}}} = 5.02$  TeV using charge-dependent azimuthal anisotropies”, *Phys. Rev. C* **100** (2019) 064908, doi:10.1103/PhysRevC.100.064908, arXiv:1708.08901.

[319] A. Bzdak and P. Bozek, “Contributions to the event-by-event charge asymmetry dependence for the elliptic flow of  $\pi^+$  and  $\pi^-$  in heavy-ion collisions”, *Phys. Lett. B* **726** (2013) 239, doi:10.1016/j.physletb.2013.08.003, arXiv:1303.1138.

[320] U. Gürsoy et al., “Charge-dependent flow induced by magnetic and electric fields in heavy ion collisions”, *Phys. Rev. C* **98** (2018) 055201, doi:10.1103/PhysRevC.98.055201, arXiv:1806.05288.

[321] A. Dubla, U. Gürsoy, and R. Snellings, “Charge-dependent flow as evidence of strong electromagnetic fields in heavy-ion collisions”, *Mod. Phys. Lett. A* **35** (2020) 2050324, doi:10.1142/S0217732320503241, arXiv:2009.09727.

[322] P. Braun-Munzinger, “Quarkonium production in ultra-relativistic nuclear collisions: Suppression versus enhancement”, *J. Phys. G* **34** (2007) S471, doi:10.1088/0954-3899/34/8/S36, arXiv:nucl-th/0701093.

[323] F.-M. Liu and S.-X. Liu, “Quark-gluon plasma formation time and direct photons from heavy ion collisions”, *Phys. Rev. C* **89** (2014) 034906, doi:10.1103/PhysRevC.89.034906, arXiv:1212.6587.

[324] S. K. Das et al., “Directed flow of charm quarks as a witness of the initial strong magnetic field in ultra-relativistic heavy ion collisions”, *Phys. Lett. B* **768** (2017) 260, doi:10.1016/j.physletb.2017.02.046, arXiv:1608.02231.

[325] PHENIX Collaboration, “Suppression of hadrons with large transverse momentum in central Au+Au collisions at  $\sqrt{s_{\text{NN}}} = 130$  GeV”, *Phys. Rev. Lett.* **88** (2002) 022301, doi:10.1103/PhysRevLett.88.022301, arXiv:nucl-ex/0109003.

[326] STAR Collaboration, “Centrality dependence of high  $p_{\text{T}}$  hadron suppression in Au+Au collisions at  $\sqrt{s_{\text{NN}}} = 130$  GeV”, *Phys. Rev. Lett.* **89** (2002) 202301, doi:10.1103/PhysRevLett.89.202301, arXiv:nucl-ex/0206011.

[327] ATLAS Collaboration, “Observation of a centrality-dependent dijet asymmetry in lead-lead collisions at  $\sqrt{s_{\text{NN}}} = 2.76$  TeV with the ATLAS detector at the LHC”, *Phys. Rev. Lett.* **105** (2010) 252303, doi:10.1103/PhysRevLett.105.252303, arXiv:1011.6182.

[328] CMS Collaboration, “Determination of jet energy calibration and transverse momentum resolution in CMS”, *JINST* **6** (2011) P11002, doi:10.1088/1748-0221/6/11/P11002, arXiv:1107.4277.

[329] CMS Collaboration, “Jet momentum dependence of jet quenching in PbPb collisions at  $\sqrt{s_{\text{NN}}} = 2.76$  TeV”, *Phys. Lett. B* **712** (2012) 176, doi:10.1016/j.physletb.2012.04.058, arXiv:1202.5022.

[330] CMS Collaboration, “Comparing transverse momentum balance of b jet pairs in pp and PbPb collisions at  $\sqrt{s_{\text{NN}}} = 5.02 \text{ TeV}$ ”, *JHEP* **03** (2018) 181,  
`doi:10.1007/JHEP03(2018)181`, `arXiv:1802.00707`.

[331] CMS Collaboration, “Measurement of transverse momentum relative to dijet systems in PbPb and pp collisions at  $\sqrt{s_{\text{NN}}} = 2.76 \text{ TeV}$ ”, *JHEP* **01** (2016) 006,  
`doi:10.1007/JHEP01(2016)006`, `arXiv:1509.09029`.

[332] CMS Collaboration, “Measurement of inclusive jet cross sections in pp and PbPb collisions at  $\sqrt{s_{\text{NN}}} = 2.76 \text{ TeV}$ ”, *Phys. Rev. C* **96** (2017) 015202,  
`doi:10.1103/PhysRevC.96.015202`, `arXiv:1609.05383`.

[333] K. C. Zapp, “JEWEL 2.0.0: directions for use”, *Eur. Phys. J. C* **74** (2014) 2762,  
`doi:10.1140/epjc/s10052-014-2762-1`, `arXiv:1311.0048`.

[334] R. Kunnawalkam Elayavalli and K. C. Zapp, “Medium response in JEWEL and its impact on jet shape observables in heavy ion collisions”, *JHEP* **07** (2017) 141,  
`doi:10.1007/JHEP07(2017)141`, `arXiv:1707.01539`.

[335] J. Casalderrey-Solana et al., “A hybrid strong/weak coupling approach to jet quenching”, *JHEP* **10** (2014) 019, `doi:10.1007/JHEP09(2014)019`,  
`arXiv:1405.3864`. [Erratum: `doi:10.1007/JHEP09(2015)175`].

[336] D. Pablos, “Jet suppression from a small to intermediate to large radius”, *Phys. Rev. Lett.* **124** (2020) 052301, `doi:10.1103/PhysRevLett.124.052301`, `arXiv:1907.12301`.

[337] B. Schenke, C. Gale, and S. Jeon, “MARTINI: An event generator for relativistic heavy-ion collisions”, *Phys. Rev. C* **80** (2009) 054913,  
`doi:10.1103/PhysRevC.80.054913`, `arXiv:0909.2037`.

[338] Y. He et al., “Interplaying mechanisms behind single inclusive jet suppression in heavy-ion collisions”, *Phys. Rev. C* **99** (2019) 054911,  
`doi:10.1103/PhysRevC.99.054911`, `arXiv:1809.02525`.

[339] Y. Tachibana, N.-B. Chang, and G.-Y. Qin, “Full jet in quark-gluon plasma with hydrodynamic medium response”, *Phys. Rev. C* **95** (2017) 044909,  
`doi:10.1103/PhysRevC.95.044909`, `arXiv:1701.07951`.

[340] N.-B. Chang and G.-Y. Qin, “Full jet evolution in quark-gluon plasma and nuclear modification of jet production and jet shape in Pb+Pb collisions at 2.76ATeV at the CERN Large Hadron Collider”, *Phys. Rev. C* **94** (2016) 024902,  
`doi:10.1103/PhysRevC.94.024902`, `arXiv:1603.01920`.

[341] N.-B. Chang, Y. Tachibana, and G.-Y. Qin, “Nuclear modification of jet shape for inclusive jets and  $\gamma$ -jets at the LHC energies”, *Phys. Lett. B* **801** (2020) 135181,  
`doi:10.1016/j.physletb.2019.135181`, `arXiv:1906.09562`.

[342] ALICE Collaboration, “Measurement of the radius dependence of charged-particle jet suppression in Pb-Pb collisions at  $\sqrt{s_{\text{NN}}} = 5.02 \text{ TeV}$ ”, *Phys. Lett. B* **849** (2024) 138412,  
`doi:10.1016/j.physletb.2023.138412`, `arXiv:2303.00592`.

[343] WA98 Collaboration, “Transverse mass distributions of neutral pions from Pb-208 induced reactions at 158-A-GeV”, *Eur. Phys. J. C* **23** (2002) 225,  
`doi:10.1007/s100520100886`, `arXiv:nucl-ex/0108006`.

[344] D. G. d'Enterria, "Indications of suppressed high- $p_T$  hadron production in nucleus-nucleus collisions at CERN-SPS", *Phys. Lett. B* **596** (2004) 32, doi:10.1016/j.physletb.2004.06.071, arXiv:nucl-ex/0403055.

[345] PHENIX Collaboration, "Neutral pion production with respect to centrality and reaction plane in Au+Au collisions at  $\sqrt{s_{\text{NN}}} = 200 \text{ GeV}$ ", *Phys. Rev. C* **87** (2013) 034911, doi:10.1103/PhysRevC.87.034911, arXiv:1208.2254.

[346] STAR Collaboration, "Transverse momentum and collision energy dependence of high  $p_T$  hadron suppression in Au+Au collisions at ultrarelativistic energies", *Phys. Rev. Lett.* **91** (2003) 172302, doi:10.1103/PhysRevLett.91.172302, arXiv:nucl-ex/0305015.

[347] NA49 Collaboration, "High transverse momentum hadron spectra at  $\sqrt{s_{\text{NN}}} = 17.3 \text{ GeV}$ , in Pb+Pb and p+p collisions, measured by CERN-NA49", *Phys. Rev. C* **77** (2008) 034906, doi:10.1103/PhysRevC.77.034906, arXiv:0711.0547.

[348] ALICE Collaboration, "Centrality dependence of charged particle production at large transverse momentum in Pb-Pb collisions at  $\sqrt{s_{\text{NN}}} = 2.76 \text{ TeV}$ ", *Phys. Lett. B* **720** (2013) 52, doi:10.1016/j.physletb.2013.01.051, arXiv:1208.2711.

[349] ATLAS Collaboration, "Measurement of charged-particle spectra in Pb+Pb collisions at  $\sqrt{s_{\text{NN}}} = 2.76 \text{ TeV}$  with the ATLAS detector at the LHC", *JHEP* **09** (2015) 050, doi:10.1007/JHEP09(2015)050, arXiv:1504.04337.

[350] CMS Collaboration, "Study of high- $p_T$  charged particle suppression in PbPb compared to pp collisions at  $\sqrt{s_{\text{NN}}} = 2.76 \text{ TeV}$ ", *Eur. Phys. J. C* **72** (2012) 1945, doi:10.1140/epjc/s10052-012-1945-x, arXiv:1202.2554.

[351] CMS Collaboration, "Charged-particle nuclear modification factors in PbPb and pPb collisions at  $\sqrt{s_{\text{NN}}} = 5.02 \text{ TeV}$ ", *JHEP* **04** (2017) 039, doi:10.1007/JHEP04(2017)039, arXiv:1611.01664.

[352] Y.-T. Chien et al., "Jet quenching from QCD evolution", *Phys. Rev. D* **93** (2016) 074030, doi:10.1103/PhysRevD.93.074030, arXiv:1509.02936.

[353] E. Bianchi et al., "The  $x$  and  $Q^2$  dependence of  $\hat{q}$ , quasi-particles and the JET puzzle", 2017. arXiv:1702.00481.

[354] J. Xu, J. Liao, and M. Gyulassy, "Bridging soft-hard transport properties of quark-gluon plasmas with CUJET3.0", *JHEP* **02** (2016) 169, doi:10.1007/JHEP02(2016)169, arXiv:1508.00552.

[355] J. Noronha-Hostler, B. Betz, J. Noronha, and M. Gyulassy, "Event-by-event hydrodynamics+jet energy loss: A solution to the  $R_{\text{AA}} \otimes v_2$  puzzle", *Phys. Rev. Lett.* **116** (2016) 252301, doi:10.1103/PhysRevLett.116.252301, arXiv:1602.03788.

[356] M. Gyulassy and X.-n. Wang, "Multiple collisions and induced gluon Bremsstrahlung in QCD", *Nucl. Phys. B* **420** (1994) 583, doi:10.1016/0550-3213(94)90079-5, arXiv:nucl-th/9306003.

[357] J. Casalderrey-Solana, Y. Mehtar-Tani, C. A. Salgado, and K. Tywoniuk, "New picture of jet quenching dictated by color coherence", *Phys. Lett. B* **725** (2013) 357, doi:10.1016/j.physletb.2013.07.046, arXiv:1210.7765.

[358] R. Baier et al., “Radiative energy loss of high energy quarks and gluons in a finite-volume quark-gluon plasma”, *Nucl. Phys. B* **483** (1997) 291, doi:10.1016/S0550-3213(96)00553-6, arXiv:hep-ph/9607355.

[359] C. Loizides, J. Nagle, and P. Steinberg, “Improved version of the PHOBOS Glauber Monte Carlo”, *SoftwareX* **1-2** (2015) 13, doi:10.1016/j.softx.2015.05.001, arXiv:1408.2549.

[360] F. Arleo and G. Falmagne, “Quenching of hadron spectra in XeXe and PbPb collisions at the LHC”, *PoS HardProbes2018* (2019) 075, doi:10.22323/1.345.0075, arXiv:1902.05032.

[361] CMS Collaboration, “Azimuthal anisotropy of charged particles with transverse momentum up to 100 GeV/c in PbPb collisions at  $\sqrt{s_{_{NN}}} = 5.02$  TeV”, *Phys. Lett. B* **776** (2018) 195, doi:10.1016/j.physletb.2017.11.041, arXiv:1702.00630.

[362] CMS Collaboration, “Azimuthal anisotropy of charged particles at high transverse momenta in PbPb collisions at  $\sqrt{s_{_{NN}}} = 2.76$  TeV”, *Phys. Rev. Lett.* **109** (2012) 022301, doi:10.1103/PhysRevLett.109.022301, arXiv:1204.1850.

[363] CMS Collaboration, “Azimuthal anisotropy of dijet events in PbPb collisions at  $\sqrt{s_{_{NN}}} = 5.02$  TeV”, *JHEP* **07** (2023) 139, doi:10.1007/JHEP07(2023)139, arXiv:2210.08325.

[364] CMS Collaboration, “Study of jet quenching with isolated-photon+jet correlations in PbPb and pp collisions at  $\sqrt{s_{_{NN}}} = 5.02$  TeV”, *Phys. Lett. B* **785** (2018) 14, doi:10.1016/j.physletb.2018.07.061, arXiv:1711.09738.

[365] CMS Collaboration, “Study of jet quenching with Z+jet correlations in Pb-Pb and pp collisions at  $\sqrt{s_{_{NN}}} = 5.02$  TeV”, *Phys. Rev. Lett.* **119** (2017) 082301, doi:10.1103/PhysRevLett.119.082301, arXiv:1702.01060.

[366] L. Apolinário, J. Barata, and G. Milhano, “On the breaking of Casimir scaling in jet quenching”, *Eur. Phys. J. C* **80** (2020) 586, doi:10.1140/epjc/s10052-020-8133-1, arXiv:2003.02893.

[367] J. Brewer, J. Thaler, and A. P. Turner, “Data-driven quark and gluon jet modification in heavy-ion collisions”, *Phys. Rev. C* **103** (2021) L021901, doi:10.1103/PhysRevC.103.L021901, arXiv:2008.08596.

[368] R. D. Field and R. P. Feynman, “A parametrization of the properties of quark jets”, *Nucl. Phys. B* **136** (1978) 1, doi:10.1016/0550-3213(78)90015-9.

[369] Fermilab-Serpukhov-Moscow-Michigan Collaboration, “Net charge in deep inelastic antineutrino - nucleon scattering”, *Phys. Lett. B* **91** (1980) 311, doi:10.1016/0370-2693(80)90456-6.

[370] J. P. Berge et al., “Quark jets from antineutrino interactions 1: Net charge and factorization in the quark jets”, *Nucl. Phys. B* **184** (1981) 13, doi:10.1016/0550-3213(81)90207-8.

[371] Aachen-Bonn-CERN-Munich-Oxford Collaboration, “Multiplicity distributions in neutrino - hydrogen interactions”, *Nucl. Phys. B* **181** (1981) 385, doi:10.1016/0550-3213(81)90532-0.

[372] Aachen–Bonn–CERN–Munich–Oxford Collaboration, “Charge properties of the hadronic system in  $\nu p$  and  $\bar{\nu} p$  interactions”, *Phys. Lett. B* **112** (1982) 88, doi:10.1016/0370-2693(82)90912-1.

[373] European Muon Collaboration, “Quark charge retention in final state hadrons from deep inelastic muon scattering”, *Phys. Lett. B* **144** (1984) 302, doi:10.1016/0370-2693(84)91825-2.

[374] Amsterdam-Bologna-Padua-Pisa-Saclay-Turin Collaboration, “Charged hadron multiplicities in high-energy anti-muon neutrino n and anti-muon neutrino p interactions”, *Z. Phys. C* **11** (1982) 283, doi:10.1007/BF01578279.

[375] R. Erickson et al., “Charge retention in deep inelastic electroproduction”, *Phys. Rev. Lett.* **42** (1979) 822, doi:10.1103/PhysRevLett.42.822. [Erratum: doi:10.1103/PhysRevLett.42.1246].

[376] H. T. Li and I. Vitev, “Jet charge modification in dense QCD matter”, *Phys. Rev. D* **101** (2020) 076020, doi:10.1103/PhysRevD.101.076020, arXiv:1908.06979.

[377] CMS Collaboration, “Measurement of quark- and gluon-like jet fractions using jet charge in PbPb and pp collisions at 5.02 TeV”, *JHEP* **07** (2020) 115, doi:10.1007/JHEP07(2020)115, arXiv:2004.00602.

[378] CMS Collaboration, “Evidence of b-jet quenching in PbPb collisions at  $\sqrt{s_{_{NN}}} = 2.76$  TeV”, *Phys. Rev. Lett.* **113** (2014) 132301, doi:10.1103/PhysRevLett.113.132301, arXiv:1312.4198. [Erratum: doi:10.1103/PhysRevLett.115.029903].

[379] ATLAS Collaboration, “Comparison of inclusive and photon-tagged jet suppression in 5.02 TeV Pb+Pb collisions with ATLAS”, *Phys. Lett. B* **846** (2023) 138154, doi:10.1016/j.physletb.2023.138154, arXiv:2303.10090.

[380] ATLAS Collaboration, “Measurement of the nuclear modification factor of b-jets in 5.02 TeV Pb+Pb collisions with the ATLAS detector”, *Eur. Phys. J. C* **83** (2023) 438, doi:10.1140/epjc/s10052-023-11427-9, arXiv:2204.13530.

[381] L. Apolinário, J. G. Milhano, G. P. Salam, and C. A. Salgado, “Probing the time structure of the quark-gluon plasma with top quarks”, *Phys. Rev. Lett.* **120** (2018) 232301, doi:10.1103/PhysRevLett.120.232301, arXiv:1711.03105.

[382] CMS Collaboration, “Measurement of jet fragmentation in PbPb and pp collisions at  $\sqrt{s_{_{NN}}} = 2.76$  TeV”, *Phys. Rev. C* **90** (2014) 024908, doi:10.1103/PhysRevC.90.024908, arXiv:1406.0932.

[383] X.-N. Wang, Z. Huang, and I. Sarcevic, “Jet quenching in the opposite direction of a tagged photon in high-energy heavy ion collisions”, *Phys. Rev. Lett.* **77** (1996) 231, doi:10.1103/PhysRevLett.77.231, arXiv:hep-ph/9605213.

[384] X.-N. Wang and Z. Huang, “Study medium induced parton energy loss in gamma+jet events of high-energy heavy ion collisions”, *Phys. Rev. C* **55** (1997) 3047, doi:10.1103/PhysRevC.55.3047, arXiv:hep-ph/9701227.

[385] X.-N. Wang and Y. Zhu, “Medium modification of  $\gamma$ -jets in high-energy heavy-ion collisions”, *Phys. Rev. Lett.* **111** (2013) 062301, doi:10.1103/PhysRevLett.111.062301, arXiv:1302.5874.

[386] J. Casalderrey-Solana et al., “Predictions for boson-jet observables and fragmentation function ratios from a hybrid strong/weak coupling model for jet quenching”, *JHEP* **03** (2016) 053, doi:10.1007/JHEP03(2016)053, arXiv:1508.00815.

[387] CMS Collaboration, “Observation of medium-induced modifications of jet fragmentation in Pb-Pb collisions at  $\sqrt{s_{\text{NN}}} = 5.02$  TeV using isolated photon-tagged jets”, *Phys. Rev. Lett.* **121** (2018) 242301, doi:10.1103/PhysRevLett.121.242301, arXiv:1801.04895.

[388] ZEUS Collaboration, “Measurement of jet shapes in high  $Q^2$  deep inelastic scattering at HERA”, *Eur. Phys. J. C* **8** (1999) 367, doi:10.1007/s100520050471, arXiv:hep-ex/9804001.

[389] H1 Collaboration, “Jets and energy flow in photon - proton collisions at HERA”, *Z. Phys. C* **70** (1996) 17, doi:10.1007/s002880050076, arXiv:hep-ex/9511012.

[390] D0 Collaboration, “Transverse energy distributions within jets in  $p\bar{p}$  collisions at  $\sqrt{s} = 1.8$  TeV”, *Phys. Lett. B* **357** (1995) 500, doi:10.1016/0370-2693(95)00889-S.

[391] CDF Collaboration, “A measurement of jet shapes in  $p\bar{p}$  collisions at  $\sqrt{s} = 1.8$  TeV”, *Phys. Rev. Lett.* **70** (1993) 713, doi:10.1103/PhysRevLett.70.713.

[392] ATLAS Collaboration, “Study of jet shapes in inclusive jet production in pp collisions at  $\sqrt{s} = 7$  TeV using the ATLAS detector”, *Phys. Rev. D* **83** (2011) 052003, doi:10.1103/PhysRevD.83.052003, arXiv:1101.0070.

[393] CMS Collaboration, “Modification of jet shapes in PbPb collisions at  $\sqrt{s_{\text{NN}}} = 2.76$  TeV”, *Phys. Lett. B* **730** (2014) 243, doi:10.1016/j.physletb.2014.01.042, arXiv:1310.0878.

[394] CMS Collaboration, “Correlations between jets and charged particles in PbPb and pp collisions at  $\sqrt{s_{\text{NN}}} = 2.76$  TeV”, *JHEP* **02** (2016) 156, doi:10.1007/JHEP02(2016)156, arXiv:1601.00079.

[395] CMS Collaboration, “Decomposing transverse momentum balance contributions for quenched jets in PbPb collisions at  $\sqrt{s_{\text{NN}}} = 2.76$  TeV”, *JHEP* **11** (2016) 055, doi:10.1007/JHEP11(2016)055, arXiv:1609.02466.

[396] CMS Collaboration, “Jet properties in PbPb and pp collisions at  $\sqrt{s_{\text{NN}}} = 5.02$  TeV”, *JHEP* **05** (2018) 006, doi:10.1007/JHEP05(2018)006, arXiv:1803.00042.

[397] CMS Collaboration, “In-medium modification of dijets in PbPb collisions at  $\sqrt{s_{\text{NN}}} = 5.02$  TeV”, *JHEP* **05** (2021) 116, doi:10.1007/JHEP05(2021)116, arXiv:2101.04720.

[398] Y.-T. Chien and I. Vitev, “Towards the understanding of jet shapes and cross sections in heavy ion collisions using soft-collinear effective theory”, *JHEP* **05** (2016) 023, doi:10.1007/JHEP05(2016)023, arXiv:1509.07257.

[399] J. Brewer, K. Rajagopal, A. Sadofyev, and W. Van Der Schee, “Evolution of the mean jet shape and dijet asymmetry distribution of an ensemble of holographic jets in strongly coupled plasma”, *JHEP* **02** (2018) 015, doi:10.1007/JHEP02(2018)015, arXiv:1710.03237.

[400] J. Casalderrey-Solana et al., “Angular structure of jet quenching within a hybrid strong/weak coupling model”, *JHEP* **03** (2017) 135, doi:10.1007/JHEP03(2017)135, arXiv:1609.05842.

[401] CMS Collaboration, “Jet shapes of isolated photon-tagged jets in Pb-Pb and pp collisions at  $\sqrt{s_{\text{NN}}} = 5.02 \text{ TeV}$ ”, *Phys. Rev. Lett.* **122** (2019) 152001, doi:10.1103/PhysRevLett.122.152001, arXiv:1809.08602.

[402] CMS Collaboration, “Using Z boson events to study parton-medium interactions in Pb-Pb collisions”, *Phys. Rev. Lett.* **128** (2022) 122301, doi:10.1103/PhysRevLett.128.122301, arXiv:2103.04377.

[403] J. G. Milhano and K. C. Zapp, “Origins of the di-jet asymmetry in heavy ion collisions”, *Eur. Phys. J. C* **76** (2016) 288, doi:10.1140/epjc/s10052-016-4130-9, arXiv:1512.08107.

[404] J. Brewer, A. Sadofyev, and W. van der Schee, “Jet shape modifications in holographic dijet systems”, *Phys. Lett. B* **820** (2021) 136492, doi:10.1016/j.physletb.2021.136492, arXiv:1809.10695.

[405] CMS Collaboration, “Measurement of the splitting function in pp and Pb-Pb collisions at  $\sqrt{s_{\text{NN}}} = 5.02 \text{ TeV}$ ”, *Phys. Rev. Lett.* **120** (2018) 142302, doi:10.1103/PhysRevLett.120.142302, arXiv:1708.09429.

[406] A. J. Larkoski, S. Marzani, G. Soyez, and J. Thaler, “Soft Drop”, *JHEP* **05** (2014) 146, doi:10.1007/JHEP05(2014)146, arXiv:1402.2657.

[407] CMS Collaboration, “Measurement of the groomed jet mass in PbPb and pp collisions at  $\sqrt{s_{\text{NN}}} = 5.02 \text{ TeV}$ ”, *JHEP* **10** (2018) 161, doi:10.1007/JHEP10(2018)161, arXiv:1805.05145.

[408] Y. L. Dokshitzer, V. A. Khoze, and S. I. Troian, “On specific QCD properties of heavy quark fragmentation (‘dead cone’)\”, *J. Phys. G* **17** (1991) 1602, doi:10.1088/0954-3899/17/10/023.

[409] CMS Collaboration, “Nuclear modification factor of  $D^0$  mesons in PbPb collisions at  $\sqrt{s_{\text{NN}}} = 5.02 \text{ TeV}$ ”, *Phys. Lett. B* **782** (2018) 474, doi:10.1016/j.physletb.2018.05.074, arXiv:1708.04962.

[410] CMS Collaboration, “Measurement of the  $B^\pm$  meson nuclear modification factor in Pb-Pb collisions at  $\sqrt{s_{\text{NN}}} = 5.02 \text{ TeV}$ ”, *Phys. Rev. Lett.* **119** (2017) 152301, doi:10.1103/PhysRevLett.119.152301, arXiv:1705.04727.

[411] CMS Collaboration, “Studies of beauty suppression via nonprompt  $D^0$  mesons in Pb-Pb collisions at  $Q^2 = 4 \text{ GeV}^2$ ”, *Phys. Rev. Lett.* **123** (2019) 022001, doi:10.1103/PhysRevLett.123.022001, arXiv:1810.11102.

[412] CMS Collaboration, “Measurement of prompt and nonprompt charmonium suppression in PbPb collisions at 5.02 TeV”, *Eur. Phys. J. C* **78** (2018) 509, doi:10.1140/epjc/s10052-018-5950-6, arXiv:1712.08959.

[413] CMS Collaboration, “Measurements of the azimuthal anisotropy of prompt and nonprompt charmonia in PbPb collisions at  $\sqrt{s_{\text{NN}}} = 5.02 \text{ TeV}$ ”, *JHEP* **10** (2023) 115, doi:10.1007/JHEP10(2023)115, arXiv:2305.16928.

[414] S. A. Voloshin, A. M. Poskanzer, A. Tang, and G. Wang, “Elliptic flow in the Gaussian model of eccentricity fluctuations”, *Phys. Lett. B* **659** (2008) 537, doi:10.1016/j.physletb.2007.11.043, arXiv:0708.0800.

[415] A. Bilandzic, R. Snellings, and S. Voloshin, “Flow analysis with cumulants: Direct calculations”, *Phys. Rev. C* **83** (2011) 044913, doi:10.1103/PhysRevC.83.044913, arXiv:1010.0233.

[416] B. Betz et al., “Cumulants and nonlinear response of high  $p_T$  harmonic flow at  $\sqrt{s_{NN}} = 5.02 \text{ TeV}$ ”, *Phys. Rev. C* **95** (2017) 044901, doi:10.1103/PhysRevC.95.044901, arXiv:1609.05171.

[417] B. Svetitsky, “Diffusion of charmed quarks in the quark-gluon plasma”, *Phys. Rev. D* **37** (1988) 2484, doi:10.1103/PhysRevD.37.2484.

[418] M. He, H. van Hees, and R. Rapp, “Heavy-quark diffusion in the quark-gluon plasma”, *Prog. Part. Nucl. Phys.* **130** (2023) 104020, doi:10.1016/j.ppnp.2023.104020, arXiv:2204.09299.

[419] X. Dong, Y.-J. Lee, and R. Rapp, “Open heavy-flavor production in heavy-ion collisions”, *Ann. Rev. Nucl. Part. Sci.* **69** (2019) 417, doi:10.1146/annurev-nucl-101918-023806, arXiv:1903.07709.

[420] Y. Xu et al., “Data-driven analysis for the temperature and momentum dependence of the heavy-quark diffusion coefficient in relativistic heavy-ion collisions”, *Phys. Rev. C* **97** (2018) 014907, doi:10.1103/PhysRevC.97.014907, arXiv:1710.00807.

[421] CMS Collaboration, “Studies of charm quark diffusion inside jets using PbPb and pp collisions at  $\sqrt{s_{NN}} = 5.02 \text{ TeV}$ ”, *Phys. Rev. Lett.* **125** (2020) 102001, doi:10.1103/PhysRevLett.125.102001, arXiv:1911.01461.

[422] CMS Collaboration, “Study of charm hadronization with prompt  $\Lambda_c^+$  baryons in proton-proton and lead-lead collisions at  $\sqrt{s_{NN}} = 5.02 \text{ TeV}$ ”, *JHEP* **01** (2024) 128, doi:10.1007/JHEP01(2024)128, arXiv:2307.11186.

[423] Andersson, Bo and Gustafson, G. and Ingelman, G. and Sjöstrand, T., “Parton fragmentation and string dynamics”, *Phys. Rept.* **97** (1983) 31, doi:10.1016/0370-1573(83)90080-7.

[424] V. Greco, C. M. Ko, and P. Levai, “Parton coalescence and anti-proton/pion anomaly at RHIC”, *Phys. Rev. Lett.* **90** (2003) 202302, doi:10.1103/PhysRevLett.90.202302, arXiv:nucl-th/0301093.

[425] R. J. Fries, V. Greco, and P. Sorensen, “Coalescence models for hadron formation from quark gluon plasma”, *Ann. Rev. Nucl. Part. Sci.* **58** (2008) 177, doi:10.1146/annurev.nucl.58.110707.171134, arXiv:0807.4939.

[426] J. Rafelski and B. Muller, “Strangeness production in the quark-gluon plasma”, *Phys. Rev. Lett.* **48** (1982) 1066, doi:10.1103/PhysRevLett.48.1066. [Erratum: doi:10.1103/PhysRevLett.56.2334].

[427] CMS Collaboration, “Measurement of  $B_s^0$  meson production in pp and PbPb collisions at  $\sqrt{s_{NN}} = 5.02 \text{ TeV}$ ”, *Phys. Lett. B* **796** (2019) 168, doi:10.1016/j.physletb.2019.07.014, arXiv:1810.03022.

[428] CMS Collaboration, "Observation of  $B_s^0$  mesons and measurement of the  $B_s^0/B^+$  yield ratio in PbPb collisions at  $\sqrt{s_{_{NN}}} = 5.02$  TeV", *Phys. Lett. B* **829** (2022) 137062, doi:10.1016/j.physletb.2022.137062, arXiv:2109.01908.

[429] CMS Collaboration, "Observation of the  $B_c^+$  meson in PbPb and pp collisions at  $\sqrt{s_{_{NN}}} = 5.02$  TeV and measurement of its nuclear modification factor", *Phys. Rev. Lett.* **128** (2022) 252301, doi:10.1103/PhysRevLett.128.252301, arXiv:2201.02659.

[430] CMS Collaboration, "Production of  $\Lambda_c^+$  baryons in proton-proton and lead-lead collisions at  $\sqrt{s_{_{NN}}} = 5.02$  TeV", *Phys. Lett. B* **803** (2020) 135328, doi:10.1016/j.physletb.2020.135328, arXiv:1906.03322.

[431] CMS Collaboration, "Evidence for  $X(3872)$  in Pb-Pb collisions and studies of its prompt production at  $\sqrt{s_{_{NN}}} = 5.02$  TeV", *Phys. Rev. Lett.* **128** (2022) 032001, doi:10.1103/PhysRevLett.128.032001, arXiv:2102.13048.

[432] J. R. Christiansen and P. Z. Skands, "String formation beyond leading colour", *JHEP* **08** (2015) 003, doi:10.1007/JHEP08(2015)003, arXiv:1505.01681.

[433] V. Minissale, S. Plumari, and V. Greco, "Charm hadrons in pp collisions at LHC energy within a coalescence plus fragmentation approach", *Phys. Lett. B* **821** (2021) 136622, doi:10.1016/j.physletb.2021.136622, arXiv:2012.12001v3.

[434] M. He and R. Rapp, "Charm-baryon production in proton-proton collisions", *Phys. Lett. B* **795** (2019) 117, doi:10.1016/j.physletb.2019.06.004, arXiv:1902.08889.

[435] M. He and R. Rapp, "Hadronization and charm-hadron ratios in heavy-ion collisions", *Phys. Rev. Lett.* **124** (2020) 042301, doi:10.1103/PhysRevLett.124.042301, arXiv:1905.09216v2.

[436] M. Benzke et al., "Prompt neutrinos from atmospheric charm in the general-mass variable-flavor-number scheme", *JHEP* **12** (2017) 021, doi:10.1007/JHEP12(2017)021, arXiv:1705.10386.

[437] B. Kniehl, G. Kramer, I. Schienbein, and H. Spiesberger, " $\Lambda_c^+$  production in pp collisions with a new fragmentation function", *Phys. Rev. D* **101** (2020) 114021, doi:10.1103/PhysRevD.101.114021, arXiv:2004.04213.

[438] LHCb Collaboration, "Measurement of  $f_s/f_u$  variation with proton-proton collision energy and B-meson Kinematics", *Phys. Rev. Lett.* **124** (2020) 122002, doi:10.1103/PhysRevLett.124.122002, arXiv:1910.09934.

[439] M. He, R. J. Fries, and R. Rapp, "Heavy flavor at the large hadron collider in a strong coupling approach", *Phys. Lett. B* **735** (2014) 445, doi:10.1016/j.physletb.2014.05.050, arXiv:1401.3817.

[440] S. Cao et al., "Charmed hadron chemistry in relativistic heavy-ion collisions", *Phys. Lett. B* **807** (2020) 133561, doi:10.1016/j.physletb.2020.133561, arXiv:1911.00456.

[441] J. Song, H.-h. Li, and F.-l. Shao, "New feature of low  $p_T$  charm quark hadronization in pp collisions at  $\sqrt{s} = 2.76$  TeV", *Eur. Phys. J. C* **78** (2018) 344, doi:10.1140/epjc/s10052-018-5817-x, arXiv:1801.09402.

[442] ExHIC Collaboration, “Studying exotic hadrons in heavy ion collisions”, *Phys. Rev. C* **84** (2011) 064910, doi:10.1103/PhysRevC.84.064910, arXiv:1107.1302.

[443] H. Zhang et al., “Deciphering the nature of  $X(3872)$  in heavy ion collisions”, *Phys. Rev. Lett.* **126** (2021) 012301, doi:10.1103/PhysRevLett.126.012301, arXiv:2004.00024.

[444] B. Wu, X. Du, M. Sibila, and R. Rapp, “ $X(3872)$  transport in heavy-ion collisions”, *Eur. Phys. J. A* **57** (2021) 122, doi:10.1140/epja/s10050-021-00435-6, arXiv:2006.09945. [Erratum: doi:10.1140/epja/s10050-021-00623-4].

[445] CMS Collaboration, “Measurement of the  $X(3872)$  production cross section via decays to  $J/\psi\pi^+\pi^-$  in  $pp$  collisions at  $\sqrt{s} = 7\text{ TeV}$ ”, *JHEP* **04** (2013) 154, doi:10.1007/JHEP04(2013)154, arXiv:1302.3968.

[446] ATLAS Collaboration, “Measurements of  $\psi(2S)$  and  $X(3872) \rightarrow J/\psi\pi^+\pi^-$  production in  $pp$  collisions at  $\sqrt{s} = 8\text{ TeV}$  with the ATLAS detector”, *JHEP* **01** (2017) 117, doi:10.1007/JHEP01(2017)117, arXiv:1610.09303.

[447] LHCb Collaboration, “Determination of the  $X(3872)$  meson quantum numbers”, *Phys. Rev. Lett.* **110** (2013) 222001, doi:10.1103/PhysRevLett.110.222001, arXiv:1302.6269.

[448] T. Matsui and H. Satz, “ $J/\psi$  suppression by quark-gluon plasma formation”, *Phys. Lett. B* **178** (1986) 416, doi:10.1016/0370-2693(86)91404-8.

[449] S. Digal, P. Petreczky, and H. Satz, “Quarkonium feed down and sequential suppression”, *Phys. Rev. D* **64** (2001) 094015, doi:10.1103/PhysRevD.64.094015, arXiv:hep-ph/0106017.

[450] F. Karsch, D. Kharzeev, and H. Satz, “Sequential charmonium dissociation”, *Phys. Lett. B* **637** (2006) 75, doi:10.1016/j.physletb.2006.03.078, arXiv:hep-ph/0512239.

[451] NA38 Collaboration, “ $J/\psi$ ,  $\psi(2S)$  and Drell–Yan production in S-U interactions at 200 GeV per nucleon”, *Phys. Lett. B* **449** (1999) 128, doi:10.1016/S0370-2693(99)00057-X.

[452] NA50 Collaboration, “Evidence for deconfinement of quarks and gluons from the  $J/\psi$  suppression pattern measured in  $\text{Pb}+\text{Pb}$  collisions at the CERN SPS”, *Phys. Lett. B* **477** (2000) 28, doi:10.1016/S0370-2693(00)00237-9.

[453] NA60 Collaboration, “ $J/\psi$  production in indium-indium collisions at 158 GeV/nucleon”, *Phys. Rev. Lett.* **99** (2007) 132302, doi:10.1103/PhysRevLett.99.132302.

[454] NA50 Collaboration, “ $J/\psi$  and  $\psi(2S)$  production and their normal nuclear absorption in proton-nucleus collisions at 400 GeV”, *Eur. Phys. J. C* **48** (2006) 329, doi:10.1140/epjc/s10052-006-0079-4, arXiv:nucl-ex/0612012.

[455] NA50 Collaboration, “Charmonium production and nuclear absorption in p-A interactions at 450 GeV”, *Eur. Phys. J. C* **33** (2004) 31, doi:10.1140/epjc/s2003-01539-y.

[456] E866/NuSea Collaboration, “Measurement of  $J/\psi$  and  $\psi(2S)$  suppression in p-A collisions at 800 GeV”, *Phys. Rev. Lett.* **84** (2000) 3256, doi:10.1103/PhysRevLett.84.3256, arXiv:nucl-ex/9909007.

[457] PHENIX Collaboration, “Measurement of the relative yields of  $\psi(2S)$  to  $J/\psi$  mesons produced at forward and backward rapidity in p+p, p+Al, p+Au, and  ${}^3\text{He}+\text{Au}$  collisions at  $\sqrt{s_{\text{NN}}} = 200$  GeV”, *Phys. Rev. C* **95** (2017) 034904, doi:10.1103/PhysRevC.95.034904, arXiv:1609.06550.

[458] C. Lourenço, R. Vogt, and H. Wöhri, “Energy dependence of  $J/\psi$  absorption in proton-nucleus collisions”, *JHEP* **02** (2009) 014, doi:10.1088/1126-6708/2009/02/014, arXiv:0901.3054.

[459] PHENIX Collaboration, “Measurement of  $\psi(2S)$  nuclear modification at backward and forward rapidity in p+p, p+Al, and p+Au collisions at  $\sqrt{s_{\text{NN}}} = 200$  GeV”, *Phys. Rev. C* **105** (2022) 064912, doi:10.1103/PhysRevC.105.064912, arXiv:2202.03863.

[460] LHCb Collaboration, “Charmonium production in p+Ne collisions at  $\sqrt{s_{\text{NN}}} = 68.5$  GeV”, *Eur. Phys. J. C* **83** (2023) 625, doi:10.1140/epjc/s10052-023-11608-6, arXiv:2211.11645.

[461] LHCb Collaboration, “Study of  $\chi_b$  meson production in pp collisions at  $\sqrt{s} = 7$  and 8 TeV and observation of the decay  $\chi_b(3P) \rightarrow Y(3S)\gamma$ ”, *Eur. Phys. J. C* **74** (2014) 3092, doi:10.1140/epjc/s10052-014-3092-z, arXiv:1407.7734.

[462] P. Faccioli, C. Lourenço, M. Araújo, and J. Seixas, “Universal kinematic scaling as a probe of factorized long-distance effects in high-energy quarkonium production”, *Eur. Phys. J. C* **78** (2018) 118, doi:10.1140/epjc/s10052-018-5610-x, arXiv:1802.01102.

[463] J. Boyd, S. Thapa, and M. Strickland, “Transverse momentum dependent feed-down fractions for bottomonium production”, *Phys. Rev. D* **108** (2023) 094024, doi:10.1103/PhysRevD.108.094024, arXiv:2307.03841.

[464] R. L. Workman et al., “Review of particle physics”, *PTEP* **2022** (2022) 083C01, doi:10.1093/ptep/ptac097.

[465] P. Faccioli, C. Lourenço, J. Seixas, and H. Wöhri, “Study of  $\psi(2S)$  and  $\chi_c$  decays as feed-down sources of  $J/\psi$  hadro-production”, *JHEP* **10** (2008) 004, doi:10.1088/1126-6708/2008/10/004, arXiv:0809.2153.

[466] J.-P. Lansberg, “New observables in inclusive production of quarkonia”, *Phys. Rept.* **889** (2020) 1, doi:10.1016/j.physrep.2020.08.007, arXiv:1903.09185.

[467] R. L. Thews, M. Schroedter, and J. Rafelski, “Enhanced  $J/\psi$  production in deconfined quark matter”, *Phys. Rev. C* **63** (2001) 054905, doi:10.1103/PhysRevC.63.054905, arXiv:hep-ph/0007323.

[468] P. Braun-Munzinger and J. Stachel, “(Non)thermal aspects of charmonium production and a new look at  $J/\psi$  suppression”, *Phys. Lett. B* **490** (2000) 196, doi:10.1016/S0370-2693(00)00991-6, arXiv:nucl-th/0007059.

[469] P. Faccioli and C. Lourenço, “The fate of quarkonia in heavy-ion collisions at LHC energies: a unified description of the sequential suppression patterns”, *Eur. Phys. J. C* **78** (2018) 731, doi:10.1140/epjc/s10052-018-6216-z, arXiv:1809.10488.

[470] CMS Collaboration, “Observation of the  $\Upsilon(3S)$  meson and suppression of  $\Upsilon$  states in  $\text{PbPb}$  collisions at  $\sqrt{s_{\text{NN}}} = 5.02 \text{ TeV}$ ”, 2023. arXiv:2303.17026. Submitted to PRL.

[471] CMS Collaboration, “Relative modification of prompt  $\psi(2S)$  and  $\text{J}/\psi$  yields from  $\text{pp}$  to  $\text{PbPb}$  collisions at  $\sqrt{s_{\text{NN}}} = 5.02 \text{ TeV}$ ”, *Phys. Rev. Lett.* **118** (2017) 162301, doi:10.1103/PhysRevLett.118.162301, arXiv:1611.01438.

[472] CMS Collaboration, “Measurement of nuclear modification factors of  $\Upsilon(1S)$ ,  $\Upsilon(2S)$ , and  $\Upsilon(3S)$  mesons in  $\text{PbPb}$  collisions at  $\sqrt{s_{\text{NN}}} = 5.02 \text{ TeV}$ ”, *Phys. Lett. B* **790** (2019) 270, doi:10.1016/j.physletb.2019.01.006, arXiv:1805.09215.

[473] CMS Collaboration, “Fragmentation of jets containing a prompt  $\text{J}/\psi$  meson in  $\text{PbPb}$  and  $\text{pp}$  collisions at  $\sqrt{s_{\text{NN}}} = 5.02 \text{ TeV}$ ”, *Phys. Lett. B* **825** (2022) 136842, doi:10.1016/j.physletb.2021.136842, arXiv:2106.13235.

[474] D. d’Enterria et al., “Estimates of hadron azimuthal anisotropy from multiparton interactions in proton-proton collisions at  $\sqrt{s} = 14 \text{ TeV}$ ”, *Eur. Phys. J. C* **66** (2010) 173, doi:10.1140/epjc/s10052-009-1232-7, arXiv:0910.3029.

[475] L. Cunqueiro, J. Dias de Deus, and C. Pajares, “Nuclear like effects in proton-proton collisions at high energy”, *Eur. Phys. J. C* **65** (2010) 423, doi:10.1140/epjc/s10052-009-1215-8, arXiv:0806.0523.

[476] K. Werner, F.-M. Liu, and T. Pierog, “Parton ladder splitting and the rapidity dependence of transverse momentum spectra in deuteron-gold collisions at the BNL Relativistic Heavy Ion Collider”, *Phys. Rev. C* **74** (2006) 044902, doi:10.1103/PhysRevC.74.044902, arXiv:hep-ph/0506232.

[477] M. Gyulassy and X.-N. Wang, “HIJING 1.0: A Monte Carlo program for parton and particle production in high energy hadronic and nuclear collisions”, *Comput. Phys. Commun.* **83** (1994) 307, doi:10.1016/0010-4655(94)90057-4, arXiv:nucl-th/9502021.

[478] R. Xu, W.-T. Deng, and X.-N. Wang, “Nuclear modification of high- $p_{\text{T}}$  hadron spectra in high-energy  $\text{p}+\text{A}$  collisions”, *Phys. Rev. C* **86** (2012) 051901, doi:10.1103/PhysRevC.86.051901, arXiv:1204.1998.

[479] S. Roesler, R. Engel, and J. Ranft, “The Monte Carlo event generator DPMJET-III”, in *Proc. Advanced Monte Carlo for radiation physics, particle transport simulation and applications. Conference, MC2000, Lisbon, Portugal, October 23-26, 2000*, p. 1033. 2000. arXiv:hep-ph/0012252. doi:10.1007/978-3-642-18211-2\_166.

[480] ALICE Collaboration, “Pseudorapidity density of charged particles in  $\text{pPb}$  collisions at  $\sqrt{s_{\text{NN}}} = 5.02 \text{ TeV}$ ”, *Phys. Rev. Lett.* **110** (2013) 032301, doi:10.1103/PhysRevLett.110.032301, arXiv:1210.3615.

[481] E178 Collaboration, “Experimental study of multiparticle production in hadron-nucleus interactions at high energy”, *Phys. Rev. D* **22** (1980) 13, doi:10.1103/PhysRevD.22.13.

[482] NA35 Collaboration, “Charged particle production in proton, deuteron, oxygen and sulphur nucleus collisions at 200 GeV per nucleon”, *Eur. Phys. J. C* **2** (1998) 643, doi:10.1007/s100529800867, arXiv:hep-ex/9711001.

[483] PHOBOS Collaboration, "Pseudorapidity distribution of charged particles in d+Au collisions at  $\sqrt{s_{\text{NN}}} = 200 \text{ GeV}$ ", *Phys. Rev. Lett.* **93** (2004) 082301, doi:10.1103/PhysRevLett.93.082301, arXiv:nucl-ex/0311009.

[484] PHENIX Collaboration, "Transverse energy production and charged-particle multiplicity at midrapidity in various systems from  $\sqrt{s_{\text{NN}}} = 7.7$  to  $200 \text{ GeV}$ ", *Phys. Rev. C* **93** (2016) 024901, doi:10.1103/PhysRevC.93.024901, arXiv:1509.06727.

[485] PHENIX Collaboration, "Measurements of azimuthal anisotropy and charged-particle multiplicity in d+Au collisions at  $\sqrt{s_{\text{NN}}} = 200, 62.4, 39$ , and  $19.6 \text{ GeV}$ ", *Phys. Rev. C* **96** (2017) 064905, doi:10.1103/PhysRevC.96.064905, arXiv:1708.06983.

[486] NA50 Collaboration, "Scaling of charged particle multiplicity in Pb-Pb collisions at SPS energies", *Phys. Lett. B* **530** (2002) 43, doi:10.1016/S0370-2693(02)01353-9.

[487] STAR Collaboration, "Multiplicity distribution and spectra of negatively charged hadrons in Au+Au collisions at  $\sqrt{s_{\text{NN}}} = 130 \text{ GeV}$ ", *Phys. Rev. Lett.* **87** (2001) 112303, doi:10.1103/PhysRevLett.87.112303, arXiv:nucl-ex/0106004.

[488] BRAHMS Collaboration, "Charged particle densities from Au+Au collisions at  $\sqrt{s_{\text{NN}}} = 130 \text{ GeV}$ ", *Phys. Lett. B* **523** (2001) 227, doi:10.1016/S0370-2693(01)01333-8, arXiv:nucl-ex/0108016.

[489] BRAHMS Collaboration, "Pseudorapidity distributions of charged particles from Au+Au collisions at the maximum RHIC energy,  $\sqrt{s_{\text{NN}}} = 200 \text{ GeV}$ ", *Phys. Rev. Lett.* **88** (2002) 202301, doi:10.1103/PhysRevLett.88.202301, arXiv:nucl-ex/0112001.

[490] PHENIX Collaboration, "Centrality dependence of charged particle multiplicity in Au-Au collisions at  $\sqrt{s_{\text{NN}}} = 130 \text{ GeV}$ ", *Phys. Rev. Lett.* **86** (2001) 3500, doi:10.1103/PhysRevLett.86.3500, arXiv:nucl-ex/0012008.

[491] PHOBOS Collaboration, "Charged-particle multiplicity near midrapidity in central Au+Au collisions at  $\sqrt{s_{\text{NN}}} = 56$  and  $130 \text{ GeV}$ ", *Phys. Rev. Lett.* **85** (2000) 3100, doi:10.1103/PhysRevLett.85.3100, arXiv:hep-ex/0007036.

[492] PHOBOS Collaboration, "Charged-particle pseudorapidity density distributions from Au+Au collisions at  $\sqrt{s_{\text{NN}}} = 130 \text{ GeV}$ ", *Phys. Rev. Lett.* **87** (2001) 102303, doi:10.1103/PhysRevLett.87.102303, arXiv:nucl-ex/0106006.

[493] PHOBOS Collaboration, "Significance of the fragmentation region in ultrarelativistic heavy-ion collisions", *Phys. Rev. Lett.* **91** (2003) 052303, doi:10.1103/PhysRevLett.91.052303, arXiv:nucl-ex/0210015.

[494] ALICE Collaboration, "Charged-particle multiplicity density at midrapidity in central Pb-Pb collisions at  $\sqrt{s_{\text{NN}}} = 2.76 \text{ TeV}$ ", *Phys. Rev. Lett.* **105** (2010) 252301, doi:10.1103/PhysRevLett.105.252301, arXiv:1011.3916.

[495] ATLAS Collaboration, "Measurement of the centrality dependence of the charged particle pseudorapidity distribution in lead-lead collisions at  $\sqrt{s_{\text{NN}}} = 2.76 \text{ TeV}$  with the ATLAS detector", *Phys. Lett. B* **710** (2012) 363, doi:10.1016/j.physletb.2012.02.045, arXiv:1108.6027.

[496] STAR Collaboration, “Identified particle production, azimuthal anisotropy, and interferometry measurements in Au+Au collisions at  $\sqrt{s_{\text{NN}}} = 9.2 \text{ GeV}$ ”, *Phys. Rev. C* **81** (2010) 024911, doi:10.1103/PhysRevC.81.024911, arXiv:0909.4131.

[497] STAR Collaboration, “Systematic measurements of identified particle spectra in pp, d+Au, and Au+Au collisions at the STAR detector”, *Phys. Rev. C* **79** (2009) 034909, doi:10.1103/PhysRevC.79.034909, arXiv:0808.2041.

[498] UA5 Collaboration, “Particle multiplicities in pp interactions at  $\sqrt{s} = 540 \text{ GeV}$ ”, *Phys. Lett. B* **121** (1983) 209, doi:10.1016/0370-2693(83)90916-4.

[499] CDF Collaboration, “Pseudorapidity distributions of charged particles produced in  $\bar{p}p$  interactions at  $\sqrt{s} = 630$  and  $1800 \text{ GeV}$ ”, *Phys. Rev. D* **41** (1990) 2330, doi:10.1103/PhysRevD.41.2330.

[500] Aachen-CERN-Heidelberg-Munich Collaboration, “Charged particle multiplicity distributions in pp collisions at ISR energies”, *Nucl. Phys. B* **129** (1977) 365, doi:10.1016/0550-3213(77)90122-5.

[501] CMS Collaboration, “Pseudorapidity distribution of charged hadrons in proton-proton collisions at  $\sqrt{s} = 13 \text{ TeV}$ ”, *Phys. Lett. B* **751** (2015) 143, doi:10.1016/j.physletb.2015.10.004, arXiv:1507.05915.

[502] CMS Collaboration, “Study of the inclusive production of charged pions, kaons, and protons in pp collisions at  $\sqrt{s} = 0.9, 2.76$ , and  $7 \text{ TeV}$ ”, *Eur. Phys. J. C* **72** (2012) 2164, doi:10.1140/epjc/s10052-012-2164-1, arXiv:1207.4724.

[503] ALICE Collaboration, “Centrality dependence of  $\pi$ , K, p production in Pb-Pb collisions at  $\sqrt{s_{\text{NN}}} = 2.76 \text{ TeV}$ ”, *Phys. Rev. C* **88** (2013) 044910, doi:10.1103/PhysRevC.88.044910, arXiv:1303.0737.

[504] CMS Collaboration, “Multiplicity and rapidity dependence of strange hadron production in pp, pPb, and PbPb collisions at the LHC”, *Phys. Lett. B* **768** (2017) 103, doi:10.1016/j.physletb.2017.01.075, arXiv:1605.06699.

[505] CMS Collaboration, “Centrality and pseudorapidity dependence of the transverse energy density in pPb collisions at  $\sqrt{s_{\text{NN}}} = 5.02 \text{ TeV}$ ”, *Phys. Rev. C* **100** (2019) 024902, doi:10.1103/PhysRevC.100.024902, arXiv:1810.05745.

[506] S. A. Voloshin, A. M. Poskanzer, and R. Snellings, “Collective phenomena in non-central nuclear collisions”, *Landolt-Bornstein* **23** (2010) 293, doi:10.1007/978-3-642-01539-7\_10, arXiv:0809.2949.

[507] STAR Collaboration, “Centrality dependence of charged hadron and strange hadron elliptic flow from  $\sqrt{s_{\text{NN}}} = 200 \text{ GeV}$  Au+Au collisions”, *Phys. Rev. C* **77** (2008) 054901, doi:10.1103/PhysRevC.77.054901, arXiv:0801.3466.

[508] L. Yan and J.-Y. Ollitrault, “Universal fluctuation-driven eccentricities in proton-proton, proton-nucleus and nucleus-nucleus collisions”, *Phys. Rev. Lett.* **112** (2014) 082301, doi:10.1103/PhysRevLett.112.082301, arXiv:1312.6555.

[509] CMS Collaboration, “Multiparticle correlation studies in pPb collisions at  $\sqrt{s_{\text{NN}}} = 8.16 \text{ TeV}$ ”, *Phys. Rev. C* **101** (2020) 014912, doi:10.1103/PhysRevC.101.014912, arXiv:1904.11519.

[510] CMS Collaboration, “Correlations of azimuthal anisotropy Fourier harmonics with subevent cumulants in pPb collisions at  $\sqrt{s_{_{NN}}} = 8.16 \text{ TeV}$ ”, *Phys. Rev. C* **103** (2021) 014902, doi:10.1103/PhysRevC.103.014902, arXiv:1905.09935.

[511] J. Jia, M. Zhou, and A. Trzupek, “Revealing long-range multiparticle collectivity in small collision systems via subevent cumulants”, *Phys. Rev. C* **96** (2017) 034906, doi:10.1103/PhysRevC.96.034906, arXiv:1701.03830.

[512] ATLAS Collaboration, “Measurement of the correlation between flow harmonics of different order in lead-lead collisions at  $\sqrt{s_{_{NN}}} = 2.76 \text{ TeV}$  with the ATLAS detector”, *Phys. Rev. C* **92** (2015) 034903, doi:10.1103/PhysRevC.92.034903, arXiv:1504.01289.

[513] ALICE Collaboration, “Correlated event-by-event fluctuations of flow harmonics in Pb-Pb collisions at  $\sqrt{s_{_{NN}}} = 2.76 \text{ TeV}$ ”, *Phys. Rev. Lett.* **117** (2016) 182301, doi:10.1103/PhysRevLett.117.182301, arXiv:1604.07663.

[514] Z. Xu and C. Greiner, “Shear viscosity in a gluon gas”, *Phys. Rev. Lett.* **100** (2008) 172301, doi:10.1103/PhysRevLett.100.172301, arXiv:0710.5719.

[515] A. Bzdak and G.-L. Ma, “Elliptic and triangular flow in p+Pb and peripheral Pb+Pb collisions from parton scatterings”, *Phys. Rev. Lett.* **113** (2014) 252301, doi:10.1103/PhysRevLett.113.252301, arXiv:1406.2804.

[516] A. Dumitru et al., “The ridge in proton-proton collisions at the LHC”, *Phys. Lett. B* **697** (2011) 21, doi:10.1016/j.physletb.2011.01.024, arXiv:1009.5295.

[517] K. Dusling and R. Venugopalan, “Azimuthal collimation of long range rapidity correlations by strong color fields in high multiplicity hadron-hadron collisions”, *Phys. Rev. Lett.* **108** (2012) 262001, doi:10.1103/PhysRevLett.108.262001, arXiv:1201.2658.

[518] G. Giacalone, B. Schenke, and C. Shen, “Observable signatures of initial state momentum anisotropies in nuclear collisions”, *Phys. Rev. Lett.* **125** (2020) 192301, doi:10.1103/PhysRevLett.125.192301, arXiv:2006.15721.

[519] A. Baty, P. Gardner, and W. Li, “Novel observables for exploring QCD collective evolution and quantum entanglement within individual jets”, *Phys. Rev. C* **107** (2023) 064908, doi:10.1103/PhysRevC.107.064908, arXiv:2104.11735.

[520] STAR Collaboration, “Measurement of  $D^0$  azimuthal anisotropy at midrapidity in Au+Au collisions at  $\sqrt{s_{_{NN}}} = 200 \text{ GeV}$ ”, *Phys. Rev. Lett.* **118** (2017) 212301, doi:10.1103/PhysRevLett.118.212301, arXiv:1701.06060.

[521] ALICE Collaboration, “Azimuthal anisotropy of D meson production in Pb-Pb collisions at  $\sqrt{s_{_{NN}}} = 2.76 \text{ TeV}$ ”, *Phys. Rev. C* **90** (2014) 034904, doi:10.1103/PhysRevC.90.034904, arXiv:1405.2001.

[522] ALICE Collaboration, “D-meson azimuthal anisotropy in midcentral Pb-Pb collisions at  $\sqrt{s_{_{NN}}} = 5.02 \text{ TeV}$ ”, *Phys. Rev. Lett.* **120** (2018) 102301, doi:10.1103/PhysRevLett.120.102301, arXiv:1707.01005.

[523] CMS Collaboration, “Elliptic flow of charm and strange hadrons in high-multiplicity pPb collisions at  $\sqrt{s_{_{NN}}} = 8.16 \text{ TeV}$ ”, *Phys. Rev. Lett.* **121** (2018) 082301, doi:10.1103/PhysRevLett.121.082301, arXiv:1804.09767.

[524] CMS Collaboration, “Observation of prompt  $J/\psi$  meson elliptic flow in high-multiplicity  $p\text{Pb}$  collisions at  $\sqrt{s_{\text{NN}}} = 8.16 \text{ TeV}$ ”, *Phys. Lett. B* **791** (2019) 172, doi:10.1016/j.physletb.2019.02.018, arXiv:1810.01473.

[525] CMS Collaboration, “Studies of charm and beauty hadron long-range correlations in  $\text{pp}$  and  $\text{pPb}$  collisions at LHC energies”, *Phys. Lett. B* **813** (2021) 136036, doi:10.1016/j.physletb.2020.136036, arXiv:2009.07065.

[526] X. Du and R. Rapp, “In-medium charmonium production in proton-nucleus collisions”, *JHEP* **03** (2019) 015, doi:10.1007/JHEP03(2019)015, arXiv:1808.10014.

[527] D. Molnar and S. A. Voloshin, “Elliptic flow at large transverse momenta from quark coalescence”, *Phys. Rev. Lett.* **91** (2003) 092301, doi:10.1103/PhysRevLett.91.092301, arXiv:nucl-th/0302014.

[528] R. J. Fries, B. Muller, C. Nonaka, and S. A. Bass, “Hadronization in heavy ion collisions: recombination and fragmentation of partons”, *Phys. Rev. Lett.* **90** (2003) 202303, doi:10.1103/PhysRevLett.90.202303, arXiv:nucl-th/0301087.

[529] STAR Collaboration, “Particle type dependence of azimuthal anisotropy and nuclear modification of particle production in  $\text{Au+Au}$  collisions at  $\sqrt{s_{\text{NN}}} = 200 \text{ GeV}$ ”, *Phys. Rev. Lett.* **92** (2004) 052302, doi:10.1103/PhysRevLett.92.052302, arXiv:nucl-ex/0306007.

[530] STAR Collaboration, “Mass, quark-number, and  $\sqrt{s_{\text{NN}}}$  dependence of the second and fourth flow harmonics in ultra-relativistic nucleus-nucleus collisions”, *Phys. Rev. C* **75** (2007) 054906, doi:10.1103/PhysRevC.75.054906, arXiv:nucl-ex/0701010.

[531] PHENIX Collaboration, “Scaling properties of azimuthal anisotropy in  $\text{Au+Au}$  and  $\text{Cu+Cu}$  collisions at  $\sqrt{s_{\text{NN}}} = 200 \text{ GeV}$ ”, *Phys. Rev. Lett.* **98** (2007) 162301, doi:10.1103/PhysRevLett.98.162301, arXiv:nucl-ex/0608033.

[532] C. Zhang et al., “Elliptic flow of heavy quarkonia in  $\text{pA}$  collisions”, *Phys. Rev. Lett.* **122** (2019) 172302, doi:10.1103/PhysRevLett.122.172302, arXiv:1901.10320.

[533] C. Zhang et al., “Collectivity of heavy mesons in proton-nucleus collisions”, *Phys. Rev. D* **102** (2020) 034010, doi:10.1103/PhysRevD.102.034010, arXiv:2002.09878.

[534] A. Badea et al., “Measurements of two-particle correlations in  $e^+e^-$  collisions at 91 GeV with ALEPH archived data”, *Phys. Rev. Lett.* **123** (2019) 212002, doi:10.1103/PhysRevLett.123.212002, arXiv:1906.00489.

[535] Y.-C. Chen et al., “Long-range near-side correlation in  $e^+e^-$  collisions at 183-209 GeV with ALEPH archived data”, *Phys. Lett. B* **856** (2024) 138957, arXiv:2312.05084.

[536] Belle Collaboration, “Measurement of two-particle correlations of hadrons in  $e^+e^-$  collisions at Belle”, *Phys. Rev. Lett.* **128** (2022) 142005, doi:10.1103/PhysRevLett.128.142005, arXiv:2201.01694.

[537] Belle Collaboration, “Two-particle angular correlations in  $e^+e^-$  collisions to hadronic final states in two reference coordinates at Belle”, *JHEP* **03** (2023) 171, doi:10.1007/JHEP03(2023)171, arXiv:2206.09440.

[538] ZEUS Collaboration, “Two-particle azimuthal correlations as a probe of collective behaviour in deep inelastic ep scattering at HERA”, *JHEP* **04** (2020) 070, doi:10.1007/JHEP04(2020)070, arXiv:1912.07431.

[539] ZEUS Collaboration, “Azimuthal correlations in photoproduction and deep inelastic ep scattering at HERA”, *JHEP* **12** (2021) 102, doi:10.1007/JHEP12(2021)102, arXiv:2106.12377.

[540] CMS Collaboration, “Measurement of prompt and nonprompt  $J/\psi$  production in pp and pPb collisions at  $\sqrt{s_{_{NN}}} = 5.02$  TeV”, *Eur. Phys. J. C* **77** (2017) 269, doi:10.1140/epjc/s10052-017-4828-3, arXiv:1702.01462.

[541] CMS Collaboration, “Nuclear modification of Y states in pPb collisions at  $\sqrt{s_{_{NN}}} = 5.02$  TeV”, *Phys. Lett. B* **835** (2022) 137397, doi:10.1016/j.physletb.2022.137397, arXiv:2202.11807.

[542] CMS Collaboration, “Investigation into the event-activity dependence of Y(nS) relative production in proton-proton collisions at  $\sqrt{s} = 7$  TeV”, *JHEP* **11** (2020) 001, doi:10.1007/JHEP11(2020)001, arXiv:2007.04277.

[543] A. Huss et al., “Predicting parton energy loss in small collision systems”, *Phys. Rev. C* **103** (2021) 054903, doi:10.1103/PhysRevC.103.054903, arXiv:2007.13758.

[544] CMS Collaboration, “Measurement of inclusive jet production and nuclear modifications in pPb collisions at  $\sqrt{s_{_{NN}}} = 5.02$  TeV”, *Eur. Phys. J. C* **76** (2016) 372, doi:10.1140/epjc/s10052-016-4205-7, arXiv:1601.02001.

[545] CMS Collaboration, “Measurements of the charm jet cross section and nuclear modification factor in pPb collisions at  $\sqrt{s_{_{NN}}} = 5.02$  TeV”, *Phys. Lett. B* **772** (2017) 306, doi:10.1016/j.physletb.2017.06.053, arXiv:1612.08972.

[546] G. Baur et al., “Hot topics in ultraperipheral ion collisions”, in *Workshop on Electromagnetic Probes of Fundamental Physics*, p. 235. 2002. arXiv:hep-ex/0201034. doi:10.1142/9789812704214\_0025.

[547] R. Engel, M. A. Braun, C. Pajares, and J. Ranft, “Diffraction dissociation, an important background to photon-photon collisions via heavy ion beams at LHC”, *Z. Phys. C* **74** (1997) 687, doi:10.1007/s002880050432, arXiv:hep-ph/9605227.

[548] CMS Collaboration, “Evidence for light-by-light scattering and searches for axion-like particles in ultraperipheral PbPb collisions at  $\sqrt{s_{_{NN}}} = 5.02$  TeV”, *Phys. Lett. B* **797** (2019) 134826, doi:10.1016/j.physletb.2019.134826, arXiv:1810.04602.

[549] CMS Collaboration, “Observation of  $\tau$  lepton pair production in ultraperipheral lead-lead collisions at  $\sqrt{s_{_{NN}}} = 5.02$  TeV”, *Phys. Rev. Lett.* **131** (2023) 151803, doi:10.1103/PhysRevLett.131.151803, arXiv:2206.05192.

[550] C. N. Azevedo, V. P. Goncalves, and B. D. Moreira, “Double particle production in ultraperipheral PbPb collisions at the Large Hadron Collider and Future Circular Collider”, *Eur. Phys. J. A* **59** (2023) 193, doi:10.1140/epja/s10050-023-01114-4, arXiv:2306.05519.

[551] D. d’Enterria and A. Snigirev, “Double, triple, and  $n$ -parton scatterings in high-energy proton and nuclear collisions”, *Adv. Ser. Direct. High Energy Phys.* **29** (2018) 159, doi:10.1142/9789813227767\_0009, arXiv:1708.07519.

[552] A. Esposito, C. A. Manzari, A. Pilloni, and A. D. Polosa, “Hunting for tetraquarks in ultraperipheral heavy ion collisions”, *Phys. Rev. D* **104** (2021) 114029, doi:10.1103/PhysRevD.104.114029, arXiv:2109.10359.

[553] R. Fariello, D. Bhandari, C. A. Bertulani, and F. S. Navarra, “Two- and three-photon fusion into charmonium in ultraperipheral nuclear collisions”, *Phys. Rev. C* **108** (2023) 044901, doi:10.1103/PhysRevC.108.044901, arXiv:2306.10642.

[554] ATLAS Collaboration, “Observation of centrality-dependent acoplanarity for muon pairs produced via two-photon scattering in Pb+Pb collisions at  $\sqrt{s_{\text{NN}}} = 5.02$  TeV with the ATLAS detector”, *Phys. Rev. Lett.* **121** (2018) 212301, doi:10.1103/PhysRevLett.121.212301, arXiv:1806.08708.

[555] C. G. Roldao and A. A. Natale, “Photon-photon and pomeron-pomeron processes in peripheral heavy ion collisions”, *Phys. Rev. C* **61** (2000) 064907, doi:10.1103/PhysRevC.61.064907, arXiv:nucl-th/0003038.

[556] J. Thomas et al., “Parton distribution functions probed in ultraperipheral collisions at the CERN Large Hadron Collider”, 2016. arXiv:1603.01919.

[557] X. Cid Vidal et al., “Report from Working Group 3: Beyond the Standard Model physics at the HL-LHC and HE-LHC”, *CERN Yellow Rep. Monogr.* **7** (2019) 585, doi:10.23731/CYRM-2019-007.585, arXiv:1812.07831.

[558] R. Bruce et al., “New physics searches with heavy ion collisions at the CERN Large Hadron Collider”, *J. Phys. G* **47** (2020) 060501, doi:10.1088/1361-6471/ab7ff7, arXiv:1812.07688.

[559] D. d’Enterria et al., “Opportunities for new physics searches with heavy ions at colliders”, *J. Phys. G* **50** (2023) 050501, doi:10.1088/1361-6471/acc197, arXiv:2203.05939.

[560] S. Fichet et al., “Probing new physics in diphoton production with proton tagging at the Large Hadron Collider”, *Phys. Rev. D* **89** (2014) 114004, doi:10.1103/PhysRevD.89.114004, arXiv:1312.5153.

[561] M. Begel et al., “Precision QCD, hadronic structure and forward QCD, heavy ions: Report of energy frontier topical groups 5, 6, 7 submitted to Snowmass 2021”, 2022. arXiv:2209.14872.

[562] H.-S. Shao and D. d’Enterria, “Gamma-UPC: automated generation of exclusive photon-photon processes in ultraperipheral proton and nuclear collisions with varying form factors”, *JHEP* **09** (2022) 248, doi:10.1007/JHEP09(2022)248, arXiv:2207.03012.

[563] R. Bruce et al., “First observations of beam losses due to bound-free pair production in a heavy ion collider”, *Phys. Rev. Lett.* **99** (2007) 144801, doi:10.1103/PhysRevLett.99.144801, arXiv:0706.2292.

[564] A. J. Baltz, Y. Gorbunov, S. R. Klein, and J. Nystrand, “Two-photon interactions with nuclear breakup in relativistic heavy ion collisions”, *Phys. Rev. C* **80** (2009) 044902, doi:10.1103/PhysRevC.80.044902, arXiv:0907.1214.

[565] STAR Collaboration, “Low- $p_T$   $e^+e^-$  pair production in Au+Au collisions at  $\sqrt{s_{_{NN}}} = 200$  GeV and U+U collisions at  $\sqrt{s_{_{NN}}} = 193$  GeV at STAR”, *Phys. Rev. Lett.* **121** (2018) 132301, doi:10.1103/PhysRevLett.121.132301, arXiv:1806.02295.

[566] W. Zha, J. D. Brandenburg, Z. Tang, and Z. Xu, “Initial transverse-momentum broadening of Breit–Wheeler process in relativistic heavy-ion collisions”, *Phys. Lett. B* **800** (2020) 135089, doi:10.1016/j.physletb.2019.135089, arXiv:1812.02820.

[567] C. Li, J. Zhou, and Y.-J. Zhou, “Impact parameter dependence of the azimuthal asymmetry in lepton pair production in heavy ion collisions”, *Phys. Rev. D* **101** (2020) 034015, doi:10.1103/PhysRevD.101.034015, arXiv:1911.00237.

[568] R.-j. Wang, S. Pu, and Q. Wang, “Lepton pair production in ultraperipheral collisions”, *Phys. Rev. D* **104** (2021) 056011, doi:10.1103/PhysRevD.104.056011, arXiv:2106.05462.

[569] G. Baur, K. Hencken, and D. Trautmann, “Electron-positron pair production in relativistic heavy ion collisions”, *Phys. Rep.* **453** (2007) 1, doi:10.1016/j.physrep.2007.09.002, arXiv:0706.0654.

[570] ATLAS Collaboration, “Exclusive dimuon production in ultraperipheral Pb+Pb collisions at  $\sqrt{s_{_{NN}}} = 5.02$  TeV with ATLAS”, *Phys. Rev. C* **104** (2021) 024906, doi:10.1103/PhysRevC.104.024906, arXiv:2011.12211.

[571] J. D. Brandenburg et al., “Acoplanarity of QED pairs accompanied by nuclear dissociation in ultra-peripheral heavy ion collisions”, 2020. arXiv:2006.07365.

[572] D. d'Enterria and G. G. da Silveira, “Observing light-by-light scattering at the Large Hadron Collider”, *Phys. Rev. Lett.* **111** (2013) 080405, doi:10.1103/PhysRevLett.111.080405, arXiv:1305.7142. [Erratum: doi:10.1103/PhysRevLett.116.129901].

[573] CMS Collaboration, “Exclusive photon-photon production of muon pairs in proton-proton collisions at  $\sqrt{s} = 7$  TeV”, *JHEP* **01** (2012) 052, doi:10.1007/JHEP01(2012)052, arXiv:1111.5536.

[574] CMS Collaboration, “Search for exclusive or semi-exclusive photon pair production and observation of exclusive and semi-exclusive electron pair production in pp collisions at  $\sqrt{s} = 7$  TeV”, *JHEP* **11** (2012) 080, doi:10.1007/JHEP11(2012)080, arXiv:1209.1666.

[575] L. A. Harland-Lang, “Exciting ions: A systematic treatment of ultraperipheral heavy ion collisions with nuclear breakup”, *Phys. Rev. D* **107** (2023) 093004, doi:10.1103/PhysRevD.107.093004, arXiv:2303.04826.

[576] M. Klusek-Gawenda, P. Lebiedowicz, and A. Szczurek, “Light-by-light scattering in ultraperipheral Pb-Pb collisions at energies available at the CERN Large Hadron Collider”, *Phys. Rev. C* **93** (2016) 044907, doi:10.1103/PhysRevC.93.044907, arXiv:1601.07001.

[577] ATLAS Collaboration, “Evidence for light-by-light scattering in heavy-ion collisions with the ATLAS detector at the LHC”, *Nature Phys.* **13** (2017) 852, doi:10.1038/nphys4208, arXiv:1702.01625.

[578] ATLAS Collaboration, “Measurement of light-by-light scattering and search for axion-like particles with  $2.2 \text{ nb}^{-1}$  of Pb+Pb data with the ATLAS detector”, *JHEP* **03** (2021) 243, doi:10.1007/JHEP03(2021)243, arXiv:2008.05355. [Erratum: doi:10.1007/JHEP11(2021)050].

[579] G. K. Krintiras et al., “Light-by-light scattering cross-section measurements at the LHC”, *Acta Phys. Polon. Supp.* **16** (2023) 123, doi:10.5506/APhysPolBSupp.16.1-A123.

[580] F. del Aguila, F. Cornet, and J. I. Illana, “The possibility of using a large heavy ion collider for measuring the electromagnetic properties of the  $\tau$  lepton”, *Phys. Lett. B* **271** (1991) 256, doi:10.1016/0370-2693(91)91309-J.

[581] L. Beresford and J. Liu, “New physics and  $\tau g - 2$  using LHC heavy ion collisions”, *Phys. Rev. D* **102** (2020) 113008, doi:10.1103/PhysRevD.102.113008, arXiv:1908.05180. [Erratum: doi:10.1103/PhysRevD.106.039902].

[582] M. Dyndal, M. Klusek-Gawenda, M. Schott, and A. Szczurek, “Anomalous electromagnetic moments of  $\tau$  lepton in  $\gamma\gamma \rightarrow \tau^+\tau^-$  reaction in PbPb collisions at the LHC”, *Phys. Lett. B* **809** (2020) 135682, doi:10.1016/j.physletb.2020.135682, arXiv:2002.05503.

[583] N. Burmasov, E. Kryshen, P. Bühler, and R. Lavicka, “Feasibility studies of  $\tau$  lepton anomalous magnetic moment measurements in ultraperipheral collisions at the LHC”, *Phys. Part. Nucl.* **54** (2023) 590, doi:10.1134/S1063779623040111.

[584] ATLAS Collaboration, “Observation of the  $\gamma\gamma \rightarrow \tau\tau$  process in Pb+Pb collisions and constraints on the  $\tau$ -lepton anomalous magnetic moment with the ATLAS detector”, *Phys. Rev. Lett.* **131** (2023) 151802, doi:10.1103/PhysRevLett.131.151802, arXiv:2204.13478.

[585] DELPHI Collaboration, “Study of  $\tau$  pair production in photon-photon collisions at LEP and limits on the anomalous electromagnetic moments of the  $\tau$  lepton”, *Eur. Phys. J. C* **35** (2004) 159, doi:10.1140/epjc/s2004-01852-y, arXiv:hep-ex/0406010.

[586] CMS Collaboration, “Snowmass white paper contribution: Physics with the Phase-2 ATLAS and CMS detectors”, CMS Physics Analysis Summary CMS-PAS-FTR-22-001, 2022.

[587] S. Knapen, T. Lin, H. K. Lou, and T. Melia, “Searching for axion-like particles with ultraperipheral heavy ion collisions”, *Phys. Rev. Lett.* **118** (2017) 171801, doi:10.1103/PhysRevLett.118.171801, arXiv:1607.06083.

[588] D. d'Enterria et al., “Collider constraints on massive gravitons coupling to photons”, *Phys. Lett. B* **846** (2023) 138237, doi:10.1016/j.physletb.2023.138237, arXiv:2306.15558.

[589] J. Ellis, N. E. Mavromatos, and T. You, “Light-by-light scattering constraint on Born-Infeld theory”, *Phys. Rev. Lett.* **118** (2017) 261802, doi:10.1103/PhysRevLett.118.261802, arXiv:1703.08450.

[590] E. Chapon, C. Royon, and O. Kepka, “Anomalous quartic  $WW\gamma\gamma$ ,  $ZZ\gamma\gamma$ , and trilinear  $WW\gamma$  couplings in two-photon processes at high luminosity at the LHC”, *Phys. Rev. D* **81** (2010) 074003, doi:10.1103/PhysRevD.81.074003, arXiv:0912.5161.

[591] A. L. Read, “Presentation of search results: The  $CL_s$  technique”, *J. Phys. G* **28** (2002) 2693, doi:10.1088/0954-3899/28/10/313.

[592] T. Junk, “Confidence level computation for combining searches with small statistics”, *Nucl. Instrum. Meth. A* **434** (1999) 435, doi:10.1016/S0168-9002(99)00498-2, arXiv:hep-ex/9902006.

[593] J. Jaeckel and M. Spannowsky, “Probing MeV to 90 GeV axion-like particles with LEP and LHC”, *Phys. Lett. B* **753** (2016) 482, doi:10.1016/j.physletb.2015.12.037, arXiv:1509.00476.

[594] B. Döbrich et al., “ALPtraum: ALP production in proton beam dump experiments”, *JHEP* **02** (2016) 018, doi:10.1007/JHEP02(2016)018, arXiv:1512.03069.

[595] OPAL Collaboration, “Multiphoton production in  $e^-e^+$  collisions at  $\sqrt{s} = 181$  to 209 GeV”, *Eur. Phys. J. C* **26** (2003) 331, doi:10.1140/epjc/s2002-01074-5, arXiv:hep-ex/0210016.

[596] ATLAS Collaboration, “Search for scalar diphoton resonances in the mass range 65-600 GeV with the ATLAS detector in pp collision data at  $\sqrt{s} = 8$  TeV”, *Phys. Rev. Lett.* **113** (2014) 171801, doi:10.1103/PhysRevLett.113.171801, arXiv:1407.6583.

[597] ATLAS Collaboration, “Search for new phenomena in events with at least three photons collected in pp collisions at  $\sqrt{s} = 8$  TeV with the ATLAS detector”, *Eur. Phys. J. C* **76** (2016) 210, doi:10.1140/epjc/s10052-016-4034-8, arXiv:1509.05051.

[598] H. A. Andrews et al., “Novel tools and observables for jet physics in heavy ion collisions”, *J. Phys. G* **47** (2020) 065102, doi:10.1088/1361-6471/ab7cbc, arXiv:1808.03689.

[599] C. Andres et al., “Resolving the scales of the quark-gluon plasma with energy correlators”, *Phys. Rev. Lett.* **130** (2023) 262301, doi:10.1103/PhysRevLett.130.262301, arXiv:2209.11236.

[600] J. Brewer, A. Mazeliauskas, and W. van der Schee, “Opportunities of OO and pO collisions at the LHC”, 2021. arXiv:2103.01939.

[601] J. Albrecht et al., “The muon puzzle in cosmic-ray induced air showers and its connection to the Large Hadron Collider”, *Astrophys. Space Sci.* **367** (2022) 27, doi:10.1007/s10509-022-04054-5, arXiv:2105.06148.

[602] CMS Collaboration, “The Phase-2 upgrade of the CMS tracker”, technical report, 2017. doi:10.17181/CERN.QZ28.FLHW.

[603] R. Longo (for the ATLAS and CMS Collaborations), “Joint ATLAS/CMS ZDC upgrade project for the high-luminosity LHC”, *EPJ Web Conf.* **276** (2023) 05003, doi:10.1051/epjconf/202327605003.

[604] CMS Collaboration, “A MIP timing detector for the CMS Phase-2 upgrade”, technical report, CERN, 2019.

[605] CMS Collaboration, “New opportunities of heavy ion physics with CMS-MTD at the HL-LHC”, technical report, 2021.

- [606] CMS Collaboration, “Performance of physics objects with low transverse momentum using ultraperipheral pbpb collisions at 5.36 tev in 2023”, CMS Detector Performance Summary CMS-DP-2024/011, 2024.
- [607] V. Biloshytskyi et al., “Two-photon decay of  $X(6900)$  from light-by-light scattering at the LHC”, *Phys. Rev. D* **106** (2022) L111902, doi:10.1103/PhysRevD.106.L111902, arXiv:2207.13623.
- [608] Z. Citron et al., “Report from Working Group 5: Future physics opportunities for high-density QCD at the LHC with heavy-ion and proton beams”, *CERN Yellow Rep. Monogr.* **7** (2019) 1159, doi:10.23731/CYRM-2019-007.1159, arXiv:1812.06772.
- [609] P. Achenbach et al., “The present and future of QCD”, 2023. arXiv:2303.02579.
- [610] Program Advisory Committee (Brookhaven National Laboratory), “Recommendations of the nuclear and particle physics program”, 2023.  
<https://www.bnl.gov/npp/docs/2023-npp-pac-recommendations.pdf>.
- [611] A. Accardi et al., “Electron Ion Collider: The next QCD frontier: Understanding the glue that binds us all”, *Eur. Phys. J. A* **52** (2016) 268, doi:10.1140/epja/i2016-16268-9, arXiv:1212.1701.

## B The CMS Collaboration

### Yerevan Physics Institute, Yerevan, Armenia

A. Hayrapetyan, A. Tumasyan<sup>1</sup> 

### Institut für Hochenergiephysik, Vienna, Austria

W. Adam , J.W. Andrejkovic, T. Bergauer , S. Chatterjee , K. Damanakis , M. Dragicevic , P.S. Hussain , M. Jeitler<sup>2</sup> , N. Krammer , A. Li , D. Liko , I. Mikulec , J. Schieck<sup>2</sup> , R. Schöfbeck , D. Schwarz , M. Sonawane , S. Templ , W. Waltenberger , C.-E. Wulz<sup>2</sup> 

### Universiteit Antwerpen, Antwerpen, Belgium

M.R. Darwish<sup>3</sup> , T. Janssen , P. Van Mechelen 

### Vrije Universiteit Brussel, Brussel, Belgium

E.S. Bols , J. D'Hondt , S. Dansana , A. De Moor , M. Delcourt , H. El Faham , S. Lowette , I. Makarenko , D. Müller , S. Tavernier , M. Tytgat<sup>4</sup> , G.P. Van Onsem , S. Van Putte , D. Vannerom 

### Université Libre de Bruxelles, Bruxelles, Belgium

B. Clerbaux , A.K. Das, G. De Lentdecker , H. Evard , L. Favart , P. Gianneios , D. Hohov , J. Jaramillo , A. Khalilzadeh, F.A. Khan , K. Lee , M. Mahdavikhorrami , A. Malara , S. Paredes , L. Thomas , M. Vanden Bemden , C. Vander Velde , P. Vanlaer 

### Ghent University, Ghent, Belgium

M. De Coen , D. Dobur , Y. Hong , J. Knolle , L. Lambrecht , G. Mestdach, K. Mota Amarilo , C. Rendón , A. Samalan, K. Skovpen , N. Van Den Bossche , J. van der Linden , L. Wezenbeek 

### Université Catholique de Louvain, Louvain-la-Neuve, Belgium

A. Benecke , A. Bethani , G. Bruno , C. Caputo , C. Delaere , I.S. Donertas , A. Giammanco , Sa. Jain , V. Lemaitre, J. Lidrych , P. Mastrapasqua , K. Mondal , T.T. Tran , S. Wertz 

### Centro Brasileiro de Pesquisas Fisicas, Rio de Janeiro, Brazil

G.A. Alves , E. Coelho , C. Hensel , T. Menezes De Oliveira , A. Moraes , P. Rebello Teles , M. Soeiro

### Universidade do Estado do Rio de Janeiro, Rio de Janeiro, Brazil

W.L. Aldá Júnior , M. Alves Gallo Pereira , M. Barroso Ferreira Filho , H. Brandao Malbouisson , W. Carvalho , J. Chinellato<sup>5</sup>, E.M. Da Costa , G.G. Da Silveira<sup>6</sup> , D. De Jesus Damiao , S. Fonseca De Souza , R. Gomes De Souza, J. Martins<sup>7</sup> , C. Mora Herrera , L. Mundim , H. Nogima , J.P. Pinheiro , A. Santoro , A. Sznajder , M. Thiel , A. Vilela Pereira 

### Universidade Estadual Paulista, Universidade Federal do ABC, São Paulo, Brazil

C.A. Bernardes<sup>6</sup> , L. Calligaris , T.R. Fernandez Perez Tomei , E.M. Gregores , I. Maietto Silverio , P.G. Mercadante , S.F. Novaes , B. Orzari , Sandra S. Padula 

### Institute for Nuclear Research and Nuclear Energy, Bulgarian Academy of Sciences, Sofia, Bulgaria

A. Aleksandrov , G. Antchev , R. Hadjiiska , P. Iaydjiev , M. Misheva , M. Shopova , G. Sultanov 

**University of Sofia, Sofia, Bulgaria**A. Dimitrov , L. Litov , B. Pavlov , P. Petkov , A. Petrov , E. Shumka **Instituto De Alta Investigación, Universidad de Tarapacá, Casilla 7 D, Arica, Chile**S. Keshri , S. Thakur **Beihang University, Beijing, China**T. Cheng , T. Javaid , L. Yuan **Department of Physics, Tsinghua University, Beijing, China**Z. Hu , J. Liu, K. Yi<sup>8,9</sup> **Institute of High Energy Physics, Beijing, China**G.M. Chen<sup>10</sup> , H.S. Chen<sup>10</sup> , M. Chen<sup>10</sup> , F. Iemmi , C.H. Jiang, A. Kapoor<sup>11</sup> , H. Liao , Z.-A. Liu<sup>12</sup> , R. Sharma<sup>13</sup> , J.N. Song<sup>12</sup>, J. Tao , C. Wang<sup>10</sup>, J. Wang , Z. Wang<sup>10</sup>, H. Zhang **State Key Laboratory of Nuclear Physics and Technology, Peking University, Beijing, China**A. Agapitos , Y. Ban , A. Levin , C. Li , Q. Li , Y. Mao, S.J. Qian , X. Sun , D. Wang , H. Yang, L. Zhang , C. Zhou **Guangdong Provincial Key Laboratory of Nuclear Science and Guangdong-Hong Kong Joint Laboratory of Quantum Matter, South China Normal University, Guangzhou, China**S. Yang **Sun Yat-Sen University, Guangzhou, China**Z. You **University of Science and Technology of China, Hefei, China**K. Jaffel , N. Lu **Nanjing Normal University, Nanjing, China**G. Bauer<sup>14</sup>**Institute of Modern Physics and Key Laboratory of Nuclear Physics and Ion-beam Application (MOE) - Fudan University, Shanghai, China**X. Gao<sup>15</sup> , D. Leggat, H. Okawa **Zhejiang University, Hangzhou, Zhejiang, China**Z. Lin , C. Lu , M. Xiao **Universidad de Los Andes, Bogota, Colombia**C. Avila , D.A. Barbosa Trujillo, A. Cabrera , C. Florez , J. Fraga , J.A. Reyes Vega**Universidad de Antioquia, Medellin, Colombia**J. Mejia Guisao , F. Ramirez , M. Rodriguez , J.D. Ruiz Alvarez **University of Split, Faculty of Electrical Engineering, Mechanical Engineering and Naval Architecture, Split, Croatia**D. Giljanovic , N. Godinovic , D. Lelas , A. Sculac **University of Split, Faculty of Science, Split, Croatia**M. Kovac , T. Sculac **Institute Rudjer Boskovic, Zagreb, Croatia**P. Bargassa , V. Brigljevic , B.K. Chitroda , D. Ferencek , K. Jakovcic, S. Mishra , A. Starodumov<sup>16</sup> , T. Susa 

**University of Cyprus, Nicosia, Cyprus**

A. Attikis , K. Christoforou , S. Konstantinou , J. Mousa , C. Nicolaou, F. Ptochos , P.A. Razis , H. Rykaczewski, H. Saka , A. Stepennov 

**Charles University, Prague, Czech Republic**

M. Finger , M. Finger Jr. , A. Kveton 

**Escuela Politecnica Nacional, Quito, Ecuador**

E. Ayala 

**Universidad San Francisco de Quito, Quito, Ecuador**

E. Carrera Jarrin 

**Academy of Scientific Research and Technology of the Arab Republic of Egypt, Egyptian Network of High Energy Physics, Cairo, Egypt**

H. Abdalla<sup>17</sup> , Y. Assran<sup>18,19</sup> 

**Center for High Energy Physics (CHEP-FU), Fayoum University, El-Fayoum, Egypt**

A. Lotfy , M.A. Mahmoud 

**National Institute of Chemical Physics and Biophysics, Tallinn, Estonia**

K. Ehataht , M. Kadastik, T. Lange , S. Nandan , C. Nielsen , J. Pata , M. Raidal , L. Tani , C. Veelken 

**Department of Physics, University of Helsinki, Helsinki, Finland**

H. Kirschenmann , K. Osterberg , M. Voutilainen 

**Helsinki Institute of Physics, Helsinki, Finland**

S. Bharthuar , E. Brücke , F. Garcia , K.T.S. Kallonen , R. Kinnunen, T. Lampén , K. Lassila-Perini , S. Lehti , T. Lindén , L. Martikainen , M. Myllymäki , M.m. Rantanen , H. Siikonen , E. Tuominen , J. Tuominiemi 

**Lappeenranta-Lahti University of Technology, Lappeenranta, Finland**

P. Luukka , H. Petrow 

**IRFU, CEA, Université Paris-Saclay, Gif-sur-Yvette, France**

M. Besancon , F. Couderc , M. Dejardin , D. Denegri, J.L. Faure, F. Ferri , S. Ganjour , P. Gras , G. Hamel de Monchenault , V. Lohezic , J. Malcles , J. Rander, A. Rosowsky , M.Ö. Sahin , A. Savoy-Navarro<sup>20</sup> , P. Simkina , M. Titov , M. Tornago 

**Laboratoire Leprince-Ringuet, CNRS/IN2P3, Ecole Polytechnique, Institut Polytechnique de Paris, Palaiseau, France**

C. Baldenegro Barrera , F. Beaudette , A. Buchot Perraguin , P. Busson , A. Cappati , C. Charlot , M. Chiusi , F. Damas , O. Davignon , A. De Wit , B.A. Fontana Santos Alves , S. Ghosh , A. Gilbert , R. Granier de Cassagnac , A. Hakimi , B. Harikrishnan , L. Kalipoliti , G. Liu , J. Motta , M. Nguyen , C. Ochando , L. Portales , R. Salerno , J.B. Sauvan , Y. Sirois , A. Tarabini , E. Vernazza , A. Zabi , A. Zghiche 

**Université de Strasbourg, CNRS, IPHC UMR 7178, Strasbourg, France**

J.-L. Agram<sup>21</sup> , J. Andrea , D. Apparue , D. Bloch , J.-M. Brom , E.C. Chabert , C. Collard , S. Falke , U. Goerlach , C. Grimault, R. Haeberle , A.-C. Le Bihan , M. Meena , G. Saha , M.A. Sessini , P. Van Hove 

**Institut de Physique des 2 Infinis de Lyon (IP2I ), Villeurbanne, France**

S. Beauceron , B. Blancon , G. Boudoul , N. Chanon , J. Choi , D. Contardo 

P. Depasse , C. Dozen<sup>22</sup> , H. El Mamouni, J. Fay , S. Gascon , M. Gouzevitch , C. Greenberg , G. Grenier , B. Ille , I.B. Laktineh, M. Lethuillier , L. Mirabito, S. Perries, A. Purohit , M. Vander Donckt , P. Verdier , J. Xiao 

### Georgian Technical University, Tbilisi, Georgia

I. Lomidze , T. Toriashvili<sup>23</sup> , Z. Tsamalaidze<sup>16</sup> 

### RWTH Aachen University, I. Physikalisches Institut, Aachen, Germany

V. Botta , L. Feld , K. Klein , M. Lipinski , D. Meuser , A. Pauls , N. Röwert , M. Teroerde 

### RWTH Aachen University, III. Physikalisches Institut A, Aachen, Germany

S. Diekmann , A. Dodonova , N. Eich , D. Eliseev , F. Engelke , J. Erdmann , M. Erdmann , P. Fackeldey , B. Fischer , T. Hebbeker , K. Hoepfner , F. Ivone , A. Jung , M.y. Lee , F. Mausolf , M. Merschmeyer , A. Meyer , S. Mukherjee , D. Noll , F. Nowotny, A. Pozdnyakov , Y. Rath, W. Redjeb , F. Rehm, H. Reithler , U. Sarkar , V. Sarkisovi , A. Schmidt , A. Sharma , J.L. Spah , A. Stein , F. Torres Da Silva De Araujo<sup>24</sup> , L. Vigilante, S. Wiedenbeck , S. Zaleski

### RWTH Aachen University, III. Physikalisches Institut B, Aachen, Germany

C. Dziwok , G. Flügge , W. Haj Ahmad<sup>25</sup> , T. Kress , A. Nowack , O. Pooth , A. Stahl , T. Ziemons , A. Zott 

### Deutsches Elektronen-Synchrotron, Hamburg, Germany

H. Aarup Petersen , M. Aldaya Martin , J. Alimena , S. Amoroso, Y. An , S. Baxter , M. Bayatmakou , H. Becerril Gonzalez , O. Behnke , A. Belvedere , S. Bhattacharya , F. Blekman<sup>26</sup> , K. Borras<sup>27</sup> , A. Campbell , A. Cardini , C. Cheng , F. Colombina , S. Consuegra Rodríguez , G. Correia Silva , M. De Silva , G. Eckerlin, D. Eckstein , L.I. Estevez Banos , O. Filatov , E. Gallo<sup>26</sup> , A. Geiser , A. Giraldi , V. Guglielmi , M. Guthoff , A. Hinzmann , A. Jafari<sup>28</sup> , L. Jeppe , N.Z. Jomhari , B. Kaech , M. Kasemann , C. Kleinwort , R. Kogler , M. Komm , D. Krücker , W. Lange, D. Leyva Pernia , K. Lipka<sup>29</sup> , W. Lohmann<sup>30</sup> , R. Mankel , I.-A. Melzer-Pellmann , M. Mendizabal Morentin , A.B. Meyer , G. Milella , A. Mussgiller , L.P. Nair , A. Nürnberg , Y. Otarid, J. Park , D. Pérez Adán , E. Ranken , A. Raspereza , B. Ribeiro Lopes , J. Rübenach, A. Saggio , M. Scham<sup>31,27</sup> , S. Schnake<sup>27</sup> , P. Schütze , C. Schwanenberger<sup>26</sup> , D. Selivanova , K. Sharko , M. Shchedrolosiev , R.E. Sosa Ricardo , D. Stafford , F. Vazzoler , A. Ventura Barroso , R. Walsh , Q. Wang , Y. Wen , K. Wichmann, L. Wiens<sup>27</sup> , C. Wissing , Y. Yang , A. Zimermann Castro Santos 

### University of Hamburg, Hamburg, Germany

A. Albrecht , S. Albrecht , M. Antonello , S. Bein , L. Benato , S. Bollweg, M. Bonanomi , P. Connor , M. Eich, K. El Morabit , Y. Fischer , C. Garbers , E. Garutti , A. Grohsjean , J. Haller , H.R. Jabusch , G. Kasieczka , P. Keicher , R. Klanner , W. Korcari , T. Kramer , V. Kutzner , F. Labe , J. Lange , A. Lobanov , C. Matthies , A. Mehta , L. Moureaux , M. Mrowietz, A. Nigamova , Y. Nissan, A. Paasch , K.J. Pena Rodriguez , T. Quadfasel , B. Raciti , M. Rieger , D. Savoiu , J. Schindler , P. Schleper , M. Schröder , J. Schwandt , M. Sommerhalder , H. Stadie , G. Steinbrück , A. Tews, M. Wolf 

### Karlsruher Institut fuer Technologie, Karlsruhe, Germany

S. Brommer , M. Burkart, E. Butz , T. Chwalek , A. Dierlamm , A. Droll, N. Faltermann , M. Giffels , A. Gottmann , F. Hartmann<sup>32</sup> , R. Hofsaess , M. Horzela , U. Husemann , J. Kieseler , M. Klute , R. Koppenhöfer , J.M. Lawhorn , M. Link,

A. Lintuluoto , S. Maier , S. Mitra , M. Mormile , Th. Müller , M. Neukum, M. Oh , E. Pfeffer , M. Presilla , G. Quast , K. Rabbertz , B. Regnery , N. Shadskiy , I. Shvetsov , H.J. Simonis , M. Toms , N. Trevisani , R.F. Von Cube , M. Wassmer , S. Wieland , F. Wittig, R. Wolf , X. Zuo 

**Institute of Nuclear and Particle Physics (INPP), NCSR Demokritos, Aghia Paraskevi, Greece**

G. Anagnostou, G. Daskalakis , A. Kyriakis , A. Papadopoulos<sup>32</sup>, A. Stakia 

**National and Kapodistrian University of Athens, Athens, Greece**

P. Kontaxakis , G. Melachroinos, A. Panagiotou, I. Papavergou , I. Paraskevas , N. Saoulidou , K. Theofilatos , E. Tziaferi , K. Vellidis , I. Zisopoulos 

**National Technical University of Athens, Athens, Greece**

G. Bakas , T. Chatzistavrou, G. Karapostoli , K. Kousouris , I. Papakrivopoulos , E. Siamarkou, G. Tsipolitis , A. Zacharopoulou

**University of Ioánnina, Ioánnina, Greece**

K. Adamidis, I. Bestintzanos, I. Evangelou , C. Foudas, C. Kamtsikis, P. Katsoulis, P. Kokkas , P.G. Kosmoglou Kioseoglou , N. Manthos , I. Papadopoulos , J. Strologas 

**HUN-REN Wigner Research Centre for Physics, Budapest, Hungary**

M. Bartók<sup>33</sup> , C. Hajdu , D. Horvath<sup>34,35</sup> , K. Márton, F. Sikler , V. Veszpremi 

**MTA-ELTE Lendület CMS Particle and Nuclear Physics Group, Eötvös Loránd University, Budapest, Hungary**

M. Csanád , K. Farkas , M.M.A. Gadallah<sup>36</sup> , Á. Kadlecsik , P. Major , K. Mandal , G. Pásztor , A.J. Rádl<sup>37</sup> , G.I. Veres 

**Faculty of Informatics, University of Debrecen, Debrecen, Hungary**

P. Raics, B. Ujvari , G. Zilizi 

**HUN-REN ATOMKI - Institute of Nuclear Research, Debrecen, Hungary**

G. Bencze, S. Czellar, J. Molnar, Z. Szillasi

**Karoly Robert Campus, MATE Institute of Technology, Gyongyos, Hungary**

T. Csorgo<sup>37</sup> , F. Nemes<sup>37</sup> , T. Novak 

**Panjab University, Chandigarh, India**

J. Babbar , S. Bansal , S.B. Beri, V. Bhatnagar , G. Chaudhary , S. Chauhan , N. Dhingra<sup>38</sup> , A. Kaur , A. Kaur , H. Kaur , M. Kaur , S. Kumar , K. Sandeep , T. Sheokand, J.B. Singh , A. Singla 

**University of Delhi, Delhi, India**

A. Ahmed , A. Bhardwaj , A. Chhetri , B.C. Choudhary , A. Kumar , A. Kumar , M. Naimuddin , K. Ranjan , S. Saumya 

**Saha Institute of Nuclear Physics, HBNI, Kolkata, India**

S. Baradia , S. Barman<sup>39</sup> , S. Bhattacharya , S. Dutta , S. Dutta, S. Sarkar

**Indian Institute of Technology Madras, Madras, India**

M.M. Ameen , P.K. Behera , S.C. Behera , S. Chatterjee , P. Jana , P. Kalbhor , J.R. Komaragiri<sup>40</sup> , D. Kumar<sup>40</sup> , P.R. Pujahari , N.R. Saha , A. Sharma , A.K. Sikdar , S. Verma 

**Tata Institute of Fundamental Research-A, Mumbai, India**

S. Dugad, M. Kumar , G.B. Mohanty , P. Suryadevara

**Tata Institute of Fundamental Research-B, Mumbai, India**

A. Bala , S. Banerjee , R.M. Chatterjee, R.K. Dewanjee<sup>41</sup> , M. Guchait , Sh. Jain , A. Jaiswal, S. Karmakar , S. Kumar , G. Majumder , K. Mazumdar , S. Parolia , A. Thachayath 

**National Institute of Science Education and Research, An OCC of Homi Bhabha National Institute, Bhubaneswar, Odisha, India**

S. Bahinipati<sup>42</sup> , C. Kar , D. Maity<sup>43</sup> , P. Mal , T. Mishra , V.K. Muraleedharan Nair Bindhu<sup>43</sup> , K. Naskar<sup>43</sup> , A. Nayak<sup>43</sup> , P. Sadangi, P. Saha , S.K. Swain , S. Varghese<sup>43</sup> , D. Vats<sup>43</sup> 

**Indian Institute of Science Education and Research (IISER), Pune, India**

S. Acharya<sup>44</sup> , A. Alpana , S. Dube , B. Gomber<sup>44</sup> , B. Kansal , A. Laha , B. Sahu<sup>44</sup> , S. Sharma , K.Y. Vaish 

**Isfahan University of Technology, Isfahan, Iran**

H. Bakhshiansohi<sup>45</sup> , E. Khazaie<sup>46</sup> , M. Zeinali<sup>47</sup> 

**Institute for Research in Fundamental Sciences (IPM), Tehran, Iran**

S. Chenarani<sup>48</sup> , S.M. Etesami , M. Khakzad , M. Mohammadi Najafabadi 

**University College Dublin, Dublin, Ireland**

M. Grunewald 

**INFN Sezione di Bari<sup>a</sup>, Università di Bari<sup>b</sup>, Politecnico di Bari<sup>c</sup>, Bari, Italy**

M. Abbrescia<sup>a,b</sup> , R. Aly<sup>a,c,49</sup> , A. Colaleo<sup>a,b</sup> , D. Creanza<sup>a,c</sup> , B. D'Anzi<sup>a,b</sup> , N. De Filippis<sup>a,c</sup> , M. De Palma<sup>a,b</sup> , A. Di Florio<sup>a,c</sup> , W. Elmetenawee<sup>a,b,49</sup> , L. Fiore<sup>a</sup> , G. Iaselli<sup>a,c</sup> , M. Louka<sup>a,b</sup> , G. Maggi<sup>a,c</sup> , M. Maggi<sup>a</sup> , I. Margjeka<sup>a,b</sup> , V. Mastrapasqua<sup>a,b</sup> , S. My<sup>a,b</sup> , S. Nuzzo<sup>a,b</sup> , A. Pellecchia<sup>a,b</sup> , A. Pompili<sup>a,b</sup> , G. Pugliese<sup>a,c</sup> , R. Radogna<sup>a</sup> , G. Ramirez-Sanchez<sup>a,c</sup> , D. Ramos<sup>a</sup> , A. Ranieri<sup>a</sup> , L. Silvestris<sup>a</sup> , F.M. Simone<sup>a,b</sup> , Ü. Sözbilir<sup>a</sup> , A. Stamerra<sup>a</sup> , R. Venditti<sup>a</sup> , P. Verwilligen<sup>a</sup> , A. Zaza<sup>a,b</sup> 

**INFN Sezione di Bologna<sup>a</sup>, Università di Bologna<sup>b</sup>, Bologna, Italy**

G. Abbiendi<sup>a</sup> , C. Battilana<sup>a,b</sup> , D. Bonacorsi<sup>a,b</sup> , L. Borgonovi<sup>a</sup> , R. Campanini<sup>a,b</sup> , P. Capiluppi<sup>a,b</sup> , A. Castro<sup>a,b</sup> , F.R. Cavallo<sup>a</sup> , M. Cuffiani<sup>a,b</sup> , G.M. Dallavalle<sup>a</sup> , T. Diotalevi<sup>a,b</sup> , F. Fabbri<sup>a</sup> , A. Fanfani<sup>a,b</sup> , D. Fasanella<sup>a,b</sup> , P. Giacomelli<sup>a</sup> , L. Giommi<sup>a,b</sup> , L. Guiducci<sup>a,b</sup> , S. Lo Meo<sup>a,50</sup> , L. Lunerti<sup>a,b</sup> , S. Marcellini<sup>a</sup> , G. Masetti<sup>a</sup> , F.L. Navarria<sup>a,b</sup> , A. Perrotta<sup>a</sup> , F. Primavera<sup>a,b</sup> , A.M. Rossi<sup>a,b</sup> , T. Rovelli<sup>a,b</sup> , G.P. Siroli<sup>a,b</sup> 

**INFN Sezione di Catania<sup>a</sup>, Università di Catania<sup>b</sup>, Catania, Italy**

S. Costa<sup>a,b,51</sup> , A. Di Mattia<sup>a</sup> , R. Potenza<sup>a,b</sup> , A. Tricomi<sup>a,b,51</sup> , C. Tuve<sup>a,b</sup> 

**INFN Sezione di Firenze<sup>a</sup>, Università di Firenze<sup>b</sup>, Firenze, Italy**

P. Assiouras<sup>a</sup> , G. Barbagli<sup>a</sup> , G. Bardelli<sup>a,b</sup> , B. Camaiani<sup>a,b</sup> , A. Cassese<sup>a</sup> , R. Ceccarelli<sup>a</sup> , V. Ciulli<sup>a,b</sup> , C. Civinini<sup>a</sup> , R. D'Alessandro<sup>a,b</sup> , E. Focardi<sup>a,b</sup> , T. Kello<sup>a</sup> , G. Latino<sup>a,b</sup> , P. Lenzi<sup>a,b</sup> , M. Lizzo<sup>a</sup> , M. Meschini<sup>a</sup> , S. Paoletti<sup>a</sup> , A. Papanastassiou<sup>a,b</sup> , G. Sguazzoni<sup>a</sup> , L. Viliani<sup>a</sup> 

**INFN Laboratori Nazionali di Frascati, Frascati, Italy**

L. Benussi , S. Bianco , S. Meola<sup>52</sup> , D. Piccolo 

**INFN Sezione di Genova<sup>a</sup>, Università di Genova<sup>b</sup>, Genova, Italy**P. Chatagnon<sup>a</sup> , F. Ferro<sup>a</sup> , E. Robutti<sup>a</sup> , S. Tosi<sup>a,b</sup> **INFN Sezione di Milano-Bicocca<sup>a</sup>, Università di Milano-Bicocca<sup>b</sup>, Milano, Italy**A. Benaglia<sup>a</sup> , G. Boldrini<sup>a,b</sup> , F. Brivio<sup>a</sup> , F. Cetorelli<sup>a</sup> , F. De Guio<sup>a,b</sup> , M.E. Dinardo<sup>a,b</sup> , P. Dini<sup>a</sup> , S. Gennai<sup>a</sup> , R. Gerosa<sup>a,b</sup> , A. Ghezzi<sup>a,b</sup> , P. Govoni<sup>a,b</sup> , L. Guzzi<sup>a</sup> , M.T. Lucchini<sup>a,b</sup> , M. Malberti<sup>a</sup> , S. Malvezzi<sup>a</sup> , A. Massironi<sup>a</sup> , D. Menasce<sup>a</sup> , L. Moroni<sup>a</sup> , M. Paganoni<sup>a,b</sup> , D. Pedrini<sup>a</sup> , B.S. Pinolini<sup>a</sup> , S. Ragazzi<sup>a,b</sup> , T. Tabarelli de Fatis<sup>a,b</sup> , D. Zuolo<sup>a</sup> **INFN Sezione di Napoli<sup>a</sup>, Università di Napoli 'Federico II'<sup>b</sup>, Napoli, Italy; Università della Basilicata<sup>c</sup>, Potenza, Italy; Scuola Superiore Meridionale (SSM)<sup>d</sup>, Napoli, Italy**S. Buontempo<sup>a</sup> , A. Cagnotta<sup>a,b</sup> , F. Carnevali<sup>a,b</sup> , N. Cavallo<sup>a,c</sup> , F. Fabozzi<sup>a,c</sup> , A.O.M. Iorio<sup>a,b</sup> , L. Lista<sup>a,b,53</sup> , P. Paolucci<sup>a,32</sup> , B. Rossi<sup>a</sup> , C. Sciacca<sup>a,b</sup> **INFN Sezione di Padova<sup>a</sup>, Università di Padova<sup>b</sup>, Padova, Italy; Università di Trento<sup>c</sup>, Trento, Italy**R. Ardino<sup>a</sup> , P. Azzi<sup>a</sup> , N. Bacchetta<sup>a,54</sup> , M. Benettoni<sup>a</sup> , D. Bisello<sup>a,b</sup> , P. Bortignon<sup>a</sup> , G. Bortolato<sup>a,b</sup> , A. Bragagnolo<sup>a,b</sup> , R. Carlin<sup>a,b</sup> , P. Checchia<sup>a</sup> , T. Dorigo<sup>a</sup> , F. Gasparini<sup>a,b</sup> , U. Gasparini<sup>a,b</sup> , E. Lusiani<sup>a</sup> , M. Margoni<sup>a,b</sup> , F. Marini<sup>a</sup> , M. Migliorini<sup>a,b</sup> , J. Pazzini<sup>a,b</sup> , P. Ronchese<sup>a,b</sup> , R. Rossin<sup>a,b</sup> , F. Simonetto<sup>a,b</sup> , G. Strong<sup>a</sup> , M. Tosi<sup>a,b</sup> , A. Triossi<sup>a,b</sup> , S. Ventura<sup>a</sup> , H. Yarar<sup>a,b</sup> , M. Zanetti<sup>a,b</sup> , P. Zotto<sup>a,b</sup> , A. Zucchetta<sup>a,b</sup> , G. Zumerle<sup>a,b</sup> **INFN Sezione di Pavia<sup>a</sup>, Università di Pavia<sup>b</sup>, Pavia, Italy**S. Abu Zeid<sup>a,55</sup> , C. Aimè<sup>a,b</sup> , A. Braghieri<sup>a</sup> , S. Calzaferri<sup>a</sup> , D. Fiorina<sup>a</sup> , P. Montagna<sup>a,b</sup> , V. Re<sup>a</sup> , C. Riccardi<sup>a,b</sup> , P. Salvini<sup>a</sup> , I. Vai<sup>a,b</sup> , P. Vitulo<sup>a,b</sup> **INFN Sezione di Perugia<sup>a</sup>, Università di Perugia<sup>b</sup>, Perugia, Italy**S. Ajmal<sup>a,b</sup> , G.M. Bilei<sup>a</sup> , D. Ciangottini<sup>a,b</sup> , L. Fanò<sup>a,b</sup> , M. Magherini<sup>a,b</sup> , G. Mantovani<sup>a,b</sup> , V. Mariani<sup>a,b</sup> , M. Menichelli<sup>a</sup> , F. Moscatelli<sup>a,56</sup> , A. Rossi<sup>a,b</sup> , A. Santocchia<sup>a,b</sup> , D. Spiga<sup>a</sup> , T. Tedeschi<sup>a,b</sup> **INFN Sezione di Pisa<sup>a</sup>, Università di Pisa<sup>b</sup>, Scuola Normale Superiore di Pisa<sup>c</sup>, Pisa, Italy; Università di Siena<sup>d</sup>, Siena, Italy**P. Asenov<sup>a,b</sup> , P. Azzurri<sup>a</sup> , G. Bagliesi<sup>a</sup> , R. Bhattacharya<sup>a</sup> , L. Bianchini<sup>a,b</sup> , T. Boccali<sup>a</sup> , E. Bossini<sup>a</sup> , D. Bruschini<sup>a,c</sup> , R. Castaldi<sup>a</sup> , M.A. Ciocci<sup>a,b</sup> , M. Cipriani<sup>a,b</sup> , V. D'Amante<sup>a,d</sup> , R. Dell'Orso<sup>a</sup> , S. Donato<sup>a</sup> , A. Giassi<sup>a</sup> , F. Ligabue<sup>a,c</sup> , D. Matos Figueiredo<sup>a</sup> , A. Messineo<sup>a,b</sup> , M. Musich<sup>a,b</sup> , F. Palla<sup>a</sup> , A. Rizzi<sup>a,b</sup> , G. Rolandi<sup>a,c</sup> , S. Roy Chowdhury<sup>a</sup> , T. Sarkar<sup>a</sup> , A. Scribano<sup>a</sup> , P. Spagnolo<sup>a</sup> , R. Tenchini<sup>a</sup> , G. Tonelli<sup>a,b</sup> , N. Turini<sup>a,d</sup> , A. Venturi<sup>a</sup> , P.G. Verdini<sup>a</sup> **INFN Sezione di Roma<sup>a</sup>, Sapienza Università di Roma<sup>b</sup>, Roma, Italy**P. Barria<sup>a</sup> , C. Basile<sup>a,b</sup> , M. Campana<sup>a,b</sup> , F. Cavallari<sup>a</sup> , L. Cunqueiro Mendez<sup>a,b</sup> , D. Del Re<sup>a,b</sup> , E. Di Marco<sup>a</sup> , M. Diemoz<sup>a</sup> , F. Errico<sup>a,b</sup> , E. Longo<sup>a,b</sup> , P. Meridiani<sup>a</sup> , J. Mijuskovic<sup>a,b</sup> , G. Organtini<sup>a,b</sup> , F. Pandolfi<sup>a</sup> , R. Paramatti<sup>a,b</sup> , C. Quaranta<sup>a,b</sup> , S. Rahatlou<sup>a,b</sup> , C. Rovelli<sup>a</sup> , F. Santanastasio<sup>a,b</sup> , L. Soffi<sup>a</sup> **INFN Sezione di Torino<sup>a</sup>, Università di Torino<sup>b</sup>, Torino, Italy; Università del Piemonte Orientale<sup>c</sup>, Novara, Italy**N. Amapane<sup>a,b</sup> , R. Arcidiacono<sup>a,c</sup> , S. Argiro<sup>a,b</sup> , M. Arneodo<sup>a,c</sup> , N. Bartosik<sup>a</sup> , R. Bellan<sup>a,b</sup> , A. Bellora<sup>a,b</sup> , C. Biino<sup>a</sup> , C. Borca<sup>a,b</sup> , N. Cartiglia<sup>a</sup> , M. Costa<sup>a,b</sup> , R. Covarelli<sup>a,b</sup> , N. Demaria<sup>a</sup> , L. Finco<sup>a</sup> , M. Grippo<sup>a,b</sup> , B. Kiani<sup>a,b</sup> , F. Legger<sup>a</sup> 

F. Luongo<sup>a,b</sup> , C. Mariotti<sup>a</sup> , L. Markovic<sup>a,b</sup> , S. Maselli<sup>a</sup> , A. Mecca<sup>a,b</sup> , E. Migliore<sup>a,b</sup> , M. Monteno<sup>a</sup> , R. Mulargia<sup>a</sup> , M.M. Obertino<sup>a,b</sup> , G. Ortona<sup>a</sup> , L. Pacher<sup>a,b</sup> , N. Pastrone<sup>a</sup> , M. Pelliccioni<sup>a</sup> , M. Ruspa<sup>a,c</sup> , F. Siviero<sup>a,b</sup> , V. Sola<sup>a,b</sup> , A. Solano<sup>a,b</sup> , A. Staiano<sup>a</sup> , C. Tarricone<sup>a,b</sup> , D. Trocino<sup>a</sup> , G. Umoret<sup>a,b</sup> , E. Vlasov<sup>a,b</sup> 

**INFN Sezione di Trieste<sup>a</sup>, Università di Trieste<sup>b</sup>, Trieste, Italy**

S. Belforte<sup>a</sup> , V. Candelise<sup>a,b</sup> , M. Casarsa<sup>a</sup> , F. Cossutti<sup>a</sup> , K. De Leo<sup>a,b</sup> , G. Della Ricca<sup>a,b</sup> 

**Kyungpook National University, Daegu, Korea**

S. Dogra , J. Hong , C. Huh , B. Kim , D.H. Kim , J. Kim, H. Lee, S.W. Lee , C.S. Moon , Y.D. Oh , M.S. Ryu , S. Sekmen , Y.C. Yang 

**Department of Mathematics and Physics - GWNU, Gangneung, Korea**

M.S. Kim 

**Chonnam National University, Institute for Universe and Elementary Particles, Kwangju, Korea**

G. Bak , P. Gwak , H. Kim , D.H. Moon 

**Hanyang University, Seoul, Korea**

E. Asilar , D. Kim , T.J. Kim , J.A. Merlin

**Korea University, Seoul, Korea**

S. Choi , S. Han, B. Hong , K. Lee, K.S. Lee , S. Lee , J. Park, S.K. Park, J. Yoo 

**Kyung Hee University, Department of Physics, Seoul, Korea**

J. Goh , S. Yang 

**Sejong University, Seoul, Korea**

H. S. Kim , Y. Kim, S. Lee

**Seoul National University, Seoul, Korea**

J. Almond, J.H. Bhyun, J. Choi , W. Jun , J. Kim , S. Ko , H. Kwon , H. Lee , J. Lee , J. Lee , B.H. Oh , S.B. Oh , H. Seo , U.K. Yang, I. Yoon 

**University of Seoul, Seoul, Korea**

W. Jang , D.Y. Kang, Y. Kang , S. Kim , B. Ko, J.S.H. Lee , Y. Lee , I.C. Park , Y. Roh, I.J. Watson 

**Yonsei University, Department of Physics, Seoul, Korea**

S. Ha , H.D. Yoo 

**Sungkyunkwan University, Suwon, Korea**

M. Choi , M.R. Kim , H. Lee, Y. Lee , I. Yu 

**College of Engineering and Technology, American University of the Middle East (AUM), Dasman, Kuwait**

T. Beyrouty 

**Riga Technical University, Riga, Latvia**

K. Dreimanis , A. Gaile , G. Pikurs, A. Potrebko , M. Seidel , V. Veckalns<sup>57</sup> 

**University of Latvia (LU), Riga, Latvia**

N.R. Strautnieks 

**Vilnius University, Vilnius, Lithuania**M. Ambrozas , A. Juodagalvis , A. Rinkevicius , G. Tamulaitis **National Centre for Particle Physics, Universiti Malaya, Kuala Lumpur, Malaysia**N. Bin Norjoharuddeen , I. Yusuff<sup>58</sup> , Z. Zolkapli**Universidad de Sonora (UNISON), Hermosillo, Mexico**J.P. Barajas Ibarria, J.F. Benitez , A. Castaneda Hernandez , H.A. Encinas Acosta, L.G. Gallegos Maríñez, M. León Coello , J.A. Murillo Quijada , A. Sehrawat , L. Valencia Palomo **Centro de Investigacion y de Estudios Avanzados del IPN, Mexico City, Mexico**G. Ayala , H. Castilla-Valdez , H. Crotte Ledesma, E. De La Cruz-Burelo , I. Heredia-De La Cruz<sup>59</sup> , R. Lopez-Fernandez , C.A. Mondragon Herrera, A. Sánchez Hernández **Universidad Iberoamericana, Mexico City, Mexico**C. Oropeza Barrera , M. Ramírez García **Benemerita Universidad Autonoma de Puebla, Puebla, Mexico**I. Bautista , I. Pedraza , H.A. Salazar Ibarguen , C. Uribe Estrada **University of Montenegro, Podgorica, Montenegro**I. Bubanja , N. Raicevic **University of Canterbury, Christchurch, New Zealand**P.H. Butler **National Centre for Physics, Quaid-I-Azam University, Islamabad, Pakistan**A. Ahmad , M.I. Asghar, A. Awais , M.I.M. Awan, H.R. Hoorani , W.A. Khan **AGH University of Krakow, Faculty of Computer Science, Electronics and Telecommunications, Krakow, Poland**V. Avati, L. Grzanka , M. Malawski **National Centre for Nuclear Research, Swierk, Poland**H. Bialkowska , M. Bluj , B. Boimska , M. Górski , M. Kazana , M. Szleper , P. Zalewski **Institute of Experimental Physics, Faculty of Physics, University of Warsaw, Warsaw, Poland**K. Bunkowski , K. Doroba , A. Kalinowski , M. Konecki , J. Krolkowski , A. Muhammad **Warsaw University of Technology, Warsaw, Poland**K. Pozniak , W. Zabolotny **Laboratório de Instrumentação e Física Experimental de Partículas, Lisboa, Portugal**M. Araujo , D. Bastos , C. Beirão Da Cruz E Silva , A. Boletti , M. Bozzo , T. Camporesi , G. Da Molin , P. Faccioli , M. Gallinaro , J. Hollar , N. Leonardo , T. Niknejad , A. Petrilli , M. Pisano , J. Seixas , J. Varela , J.W. Wulff **Faculty of Physics, University of Belgrade, Belgrade, Serbia**P. Adzic , P. Milenovic **VINCA Institute of Nuclear Sciences, University of Belgrade, Belgrade, Serbia**M. Dordevic , J. Milosevic , V. Rekovic**Centro de Investigaciones Energéticas Medioambientales y Tecnológicas (CIEMAT),**

**Madrid, Spain**

M. Aguilar-Benitez, J. Alcaraz Maestre , Cristina F. Bedoya , M. Cepeda , M. Cerrada , N. Colino , B. De La Cruz , A. Delgado Peris , A. Escalante Del Valle , D. Fernández Del Val , J.P. Fernández Ramos , J. Flix , M.C. Fouz , O. Gonzalez Lopez , S. Goy Lopez , J.M. Hernandez , M.I. Josa , D. Moran , C. M. Morcillo Perez , Á. Navarro Tobar , C. Perez Dengra , A. Pérez-Calero Yzquierdo , J. Puerta Pelayo , I. Redondo , D.D. Redondo Ferrero , L. Romero, S. Sánchez Navas , L. Urda Gómez , J. Vazquez Escobar , C. Willmott

**Universidad Autónoma de Madrid, Madrid, Spain**

J.F. de Trocóniz 

**Universidad de Oviedo, Instituto Universitario de Ciencias y Tecnologías Espaciales de Asturias (ICTEA), Oviedo, Spain**

B. Alvarez Gonzalez , J. Cuevas , J. Fernandez Menendez , S. Folgueras , I. Gonzalez Caballero , J.R. González Fernández , E. Palencia Cortezon , C. Ramón Álvarez , V. Rodríguez Bouza , A. Soto Rodríguez , A. Trapote , C. Vico Villalba , P. Vischia 

**Instituto de Física de Cantabria (IFCA), CSIC-Universidad de Cantabria, Santander, Spain**

S. Bhowmik , S. Blanco Fernández , J.A. Brochero Cifuentes , I.J. Cabrillo , A. Calderon , J. Duarte Campderros , M. Fernandez , G. Gomez , C. Lasosa García , C. Martinez Rivero , P. Martinez Ruiz del Arbol , F. Matorras , P. Matorras Cuevas , E. Navarrete Ramos , J. Piedra Gomez , L. Scodellaro , I. Vila , J.M. Vizan Garcia 

**University of Colombo, Colombo, Sri Lanka**

M.K. Jayananda , B. Kailasapathy<sup>60</sup> , D.U.J. Sonnadara , D.D.C. Wickramarathna 

**University of Ruhuna, Department of Physics, Matara, Sri Lanka**

W.G.D. Dharmaratna<sup>61</sup> , K. Liyanage , N. Perera , N. Wickramage 

**CERN, European Organization for Nuclear Research, Geneva, Switzerland**

D. Abbaneo , C. Amendola , E. Auffray , G. Auzinger , J. Baechler, D. Barney , A. Bermúdez Martínez , M. Bianco , B. Bilin , A.A. Bin Anuar , A. Bocci , C. Botta , E. Brondolin , C. Caillol , G. Cerminara , N. Chernyavskaya , D. d'Enterria , A. Dabrowski , A. David , A. De Roeck , M.M. Defranchis , M. Deile , M. Dobson , L. Forthomme , G. Franzoni , W. Funk , S. Giani, D. Gigi, K. Gill , F. Glege , L. Gouskos , M. Haranko , J. Hegeman , B. Huber , V. Innocente , T. James , P. Janot , O. Kaluzinska , S. Laurila , P. Lecoq , E. Leutgeb , C. Lourenço , B. Maier , L. Malgeri , M. Mannelli , A.C. Marini , M. Matthewman, F. Meijers , S. Mersi , E. Meschi , V. Milosevic , F. Monti , F. Moortgat , M. Mulders , I. Neutelings , S. Orfanelli, F. Pantaleo , G. Petrucciani , A. Pfeiffer , M. Pierini , D. Piparo , H. Qu , D. Rabady , G. Reales Gutiérrez, M. Rovere , H. Sakulin , S. Scarfi , C. Schwick, M. Selvaggi , A. Sharma , K. Shchelina , P. Silva , P. Sphicas<sup>62</sup> , A.G. Stahl Leiton , A. Steen , S. Summers , D. Treille , P. Tropea , A. Tsirou, D. Walter , J. Wanczyk<sup>63</sup> , J. Wang, S. Wuchterl , P. Zehetner , P. Zejdl , W.D. Zeuner

**PSI Center for Neutron and Muon Sciences, Villigen, Switzerland**

T. Bevilacqua<sup>64</sup> , L. Caminada<sup>64</sup> , A. Ebrahimi , W. Erdmann , R. Horisberger , Q. Ingram , H.C. Kaestli , D. Kotlinski , C. Lange , M. Missiroli<sup>64</sup> , L. Noehte<sup>64</sup> , T. Rohe 

**ETH Zurich - Institute for Particle Physics and Astrophysics (IPA), Zurich, Switzerland**

T.K. Arrestad , K. Androsov<sup>63</sup> , M. Backhaus , A. Calandri , C. Cazzaniga 

K. Datta [ID](#), A. De Cosa [ID](#), G. Dissertori [ID](#), M. Dittmar, M. Donegà [ID](#), F. Eble [ID](#), M. Galli [ID](#), K. Gedia [ID](#), F. Glessgen [ID](#), C. Grab [ID](#), D. Hits [ID](#), W. Lustermann [ID](#), A.-M. Lyon [ID](#), R.A. Manzoni [ID](#), M. Marchegiani [ID](#), L. Marchese [ID](#), C. Martin Perez [ID](#), A. Mascellani<sup>63</sup> [ID](#), F. Nesi-Tedaldi [ID](#), F. Pauss [ID](#), V. Perovic [ID](#), S. Pigazzini [ID](#), C. Reissel [ID](#), T. Reitenspiess [ID](#), B. Ristic [ID](#), F. Riti [ID](#), R. Seidita [ID](#), J. Steggemann<sup>63</sup> [ID](#), D. Valsecchi [ID](#), R. Wallny [ID](#)

**Universität Zürich, Zurich, Switzerland**

C. Amsler<sup>65</sup> [ID](#), P. Bärtschi [ID](#), D. Brzhechko, M.F. Canelli [ID](#), K. Cormier [ID](#), J.K. Heikkilä [ID](#), M. Huwiler [ID](#), W. Jin [ID](#), A. Jofrehei [ID](#), B. Kilminster [ID](#), S. Leontsinis [ID](#), S.P. Liechti [ID](#), A. Macchiolo [ID](#), P. Meiring [ID](#), U. Molinatti [ID](#), A. Reimers [ID](#), P. Robmann, S. Sanchez Cruz [ID](#), M. Senger [ID](#), F. Stäger [ID](#), Y. Takahashi [ID](#), R. Tramontano [ID](#)

**National Central University, Chung-Li, Taiwan**

C. Adloff<sup>66</sup>, D. Bhowmik, C.M. Kuo, W. Lin, P.K. Rout [ID](#), P.C. Tiwari<sup>40</sup> [ID](#), S.S. Yu [ID](#)

**National Taiwan University (NTU), Taipei, Taiwan**

L. Ceard, Y. Chao [ID](#), K.F. Chen [ID](#), P.s. Chen, Z.g. Chen, A. De Iorio [ID](#), W.-S. Hou [ID](#), T.h. Hsu, Y.w. Kao, R. Khurana, G. Kole [ID](#), Y.y. Li [ID](#), R.-S. Lu [ID](#), E. Paganis [ID](#), X.f. Su [ID](#), J. Thomas-Wilsker [ID](#), L.s. Tsai, H.y. Wu, E. Yazgan [ID](#)

**High Energy Physics Research Unit, Department of Physics, Faculty of Science, Chulalongkorn University, Bangkok, Thailand**

C. Asawatangtrakuldee [ID](#), N. Srimanobhas [ID](#), V. Wachirapusanand [ID](#)

**Çukurova University, Physics Department, Science and Art Faculty, Adana, Turkey**

D. Agyel [ID](#), F. Boran [ID](#), Z.S. Demiroglu [ID](#), F. Dolek [ID](#), I. Dumanoglu<sup>67</sup> [ID](#), E. Eskut [ID](#), Y. Guler<sup>68</sup> [ID](#), E. Gurpinar Guler<sup>68</sup> [ID](#), C. Isik [ID](#), O. Kara, A. Kayis Topaksu [ID](#), U. Kiminsu [ID](#), G. Onengut [ID](#), K. Ozdemir<sup>69</sup> [ID](#), A. Polatoz [ID](#), B. Tali<sup>70</sup> [ID](#), U.G. Tok [ID](#), S. Turkcapar [ID](#), E. Uslan [ID](#), I.S. Zorbakir [ID](#)

**Middle East Technical University, Physics Department, Ankara, Turkey**

M. Yalvac<sup>71</sup> [ID](#)

**Bogazici University, Istanbul, Turkey**

B. Akgun [ID](#), I.O. Atakisi [ID](#), E. Gülmез [ID](#), M. Kaya<sup>72</sup> [ID](#), O. Kaya<sup>73</sup> [ID](#), S. Tekten<sup>74</sup> [ID](#)

**Istanbul Technical University, Istanbul, Turkey**

A. Cakir [ID](#), K. Cankocak<sup>67,75</sup> [ID](#), Y. Komurcu [ID](#), S. Sen<sup>76</sup> [ID](#)

**Istanbul University, Istanbul, Turkey**

O. Aydilek<sup>25</sup> [ID](#), S. Cerci<sup>70</sup> [ID](#), V. Epshteyn [ID](#), B. Hacisahinoglu [ID](#), I. Hos<sup>77</sup> [ID](#), B. Kaynak [ID](#), S. Ozkorucuklu [ID](#), O. Potok [ID](#), H. Sert [ID](#), C. Simsek [ID](#), C. Zorbilmez [ID](#)

**Yildiz Technical University, Istanbul, Turkey**

B. Isildak<sup>78</sup> [ID](#), D. Sunar Cerci<sup>70</sup> [ID](#)

**Institute for Scintillation Materials of National Academy of Science of Ukraine, Kharkiv, Ukraine**

A. Boyaryntsev [ID](#), B. Grynyov [ID](#)

**National Science Centre, Kharkiv Institute of Physics and Technology, Kharkiv, Ukraine**

L. Levchuk [ID](#)

**University of Bristol, Bristol, United Kingdom**

D. Anthony [ID](#), J.J. Brooke [ID](#), A. Bundred [ID](#), F. Bury [ID](#), E. Clement [ID](#), D. Cussans [ID](#), H. Flacher [ID](#), M. Glowacki, J. Goldstein [ID](#), H.F. Heath [ID](#), L. Kreczko [ID](#), S. Paramesvaran [ID](#)

L. Robertshaw, S. Seif El Nasr-Storey, V.J. Smith , N. Stylianou<sup>79</sup> , K. Walkingshaw Pass, R. White 

**Rutherford Appleton Laboratory, Didcot, United Kingdom**

A.H. Ball, K.W. Bell , A. Belyaev<sup>80</sup> , C. Brew , R.M. Brown , D.J.A. Cockerill , C. Cooke , K.V. Ellis, K. Harder , S. Harper , M.-L. Holmberg<sup>81</sup> , J. Linacre , K. Manolopoulos, D.M. Newbold , E. Olaiya, D. Petyt , T. Reis , A.R. Sahasransu , G. Salvi , T. Schuh, C.H. Shepherd-Themistocleous , I.R. Tomalin , T. Williams 

**Imperial College, London, United Kingdom**

R. Bainbridge , P. Bloch , C.E. Brown , O. Buchmuller, V. Cacchio, C.A. Carrillo Montoya , G.S. Chahal<sup>82</sup> , D. Colling , J.S. Dancu, I. Das , P. Dauncey , G. Davies , J. Davies, M. Della Negra , S. Fayer, G. Fedi , G. Hall , M.H. Hassanshahi , A. Howard, G. Iles , M. Knight , J. Langford , J. León Holgado , L. Lyons , A.-M. Magnan , S. Malik, M. Mieskolainen , J. Nash<sup>83</sup> , M. Pesaresi , B.C. Radburn-Smith , A. Richards, A. Rose , K. Savva , C. Seez , R. Shukla , A. Tapper , K. Uchida , G.P. Uttley , L.H. Vage, T. Virdee<sup>32</sup> , M. Vojinovic , N. Wardle , D. Winterbottom 

**Brunel University, Uxbridge, United Kingdom**

K. Coldham, J.E. Cole , A. Khan, P. Kyberd , I.D. Reid 

**Baylor University, Waco, Texas, USA**

S. Abdullin , A. Brinkerhoff , B. Caraway , E. Collins , J. Dittmann , K. Hatakeyama , J. Hiltbrand , B. McMaster , M. Saunders , S. Sawant , C. Sutantawibul , J. Wilson 

**Catholic University of America, Washington, DC, USA**

R. Bartek , A. Dominguez , C. Huerta Escamilla, A.E. Simsek , R. Uniyal , A.M. Vargas Hernandez 

**The University of Alabama, Tuscaloosa, Alabama, USA**

B. Bam , R. Chudasama , S.I. Cooper , S.V. Gleyzer , C.U. Perez , P. Rumerio<sup>84</sup> , E. Usai , R. Yi 

**Boston University, Boston, Massachusetts, USA**

A. Akpinar , D. Arcaro , C. Cosby , Z. Demiragli , C. Erice , C. Fangmeier , C. Fernandez Madrazo , E. Fontanesi , D. Gastler , F. Golf , S. Jeon , I. Reed , J. Rohlf , K. Salyer , D. Sperka , D. Spitzbart , I. Suarez , A. Tsatsos , S. Yuan , A.G. Zecchinelli 

**Brown University, Providence, Rhode Island, USA**

G. Benelli , X. Coubez<sup>27</sup> , D. Cutts , M. Hadley , U. Heintz , J.M. Hogan<sup>85</sup> , T. Kwon , G. Landsberg , K.T. Lau , D. Li , J. Luo , S. Mondal , M. Narain<sup>†</sup> , N. Pervan , S. Sagir<sup>86</sup> , F. Simpson , M. Stamenkovic , X. Yan , W. Zhang 

**University of California, Davis, Davis, California, USA**

S. Abbott , J. Bonilla , C. Brainerd , R. Breedon , H. Cai , M. Calderon De La Barca Sanchez , M. Chertok , M. Citron , J. Conway , P.T. Cox , R. Erbacher , F. Jensen , O. Kukral , G. Mocellin , M. Mulhearn , D. Pellett , W. Wei , Y. Yao , F. Zhang 

**University of California, Los Angeles, California, USA**

M. Bachtis , R. Cousins , A. Datta , G. Flores Avila , J. Hauser , M. Ignatenko , M.A. Iqbal , T. Lam , E. Manca , A. Nunez Del Prado, D. Saltzberg , V. Valuev 

**University of California, Riverside, Riverside, California, USA**

R. Clare , J.W. Gary , M. Gordon, G. Hanson , W. Si , S. Wimpenny<sup>†</sup> 

**University of California, San Diego, La Jolla, California, USA**

J.G. Branson , S. Cittolin , S. Cooperstein , D. Diaz , J. Duarte , L. Giannini , J. Guiang , R. Kansal , V. Krutelyov , R. Lee , J. Letts , M. Masciovecchio , F. Mokhtar , S. Mukherjee , M. Pieri , M. Quinnan , B.V. Sathia Narayanan , V. Sharma , M. Tadel , E. Vourliotis , F. Würthwein , Y. Xiang , A. Yagil 

**University of California, Santa Barbara - Department of Physics, Santa Barbara, California, USA**

A. Barzdukas , L. Brennan , C. Campagnari , J. Incandela , J. Kim , A.J. Li , P. Masterson , H. Mei , J. Richman , U. Sarica , R. Schmitz , F. Setti , J. Sheplock , D. Stuart , T. Vámi , S. Wang 

**California Institute of Technology, Pasadena, California, USA**

A. Bornheim , O. Cerri, A. Latorre, J. Mao , H.B. Newman , M. Spiropulu , J.R. Vlimant , C. Wang , S. Xie , R.Y. Zhu 

**Carnegie Mellon University, Pittsburgh, Pennsylvania, USA**

J. Alison , S. An , M.B. Andrews , P. Bryant , M. Cremonesi, V. Dutta , T. Ferguson , A. Harilal , C. Liu , T. Mudholkar , S. Murthy , P. Palit , M. Paulini , A. Roberts , A. Sanchez , W. Terrill 

**University of Colorado Boulder, Boulder, Colorado, USA**

J.P. Cumalat , W.T. Ford , A. Hart , A. Hassani , G. Karathanasis , E. MacDonald, N. Manganelli , A. Perloff , C. Savard , N. Schonbeck , K. Stenson , K.A. Ulmer , S.R. Wagner , N. Zipper 

**Cornell University, Ithaca, New York, USA**

J. Alexander , S. Bright-Thonney , X. Chen , D.J. Cranshaw , J. Fan , X. Fan , D. Gadkari , S. Hogan , P. Kotamnives, J. Monroy , M. Oshiro , J.R. Patterson , J. Reichert , M. Reid , A. Ryd , J. Thom , P. Wittich , R. Zou 

**Fermi National Accelerator Laboratory, Batavia, Illinois, USA**

M. Albrow , M. Alyari , O. Amram , G. Apollinari , A. Apresyan , L.A.T. Bauerick , D. Berry , J. Berryhill , P.C. Bhat , K. Burkett , J.N. Butler , A. Canepa , G.B. Cerati , H.W.K. Cheung , F. Chlebana , G. Cummings , J. Dickinson , I. Dutta , V.D. Elvira , Y. Feng , J. Freeman , A. Gandrakota , Z. Gecse , L. Gray , D. Green, A. Grummer , S. Grünendahl , D. Guerrero , O. Gutsche , R.M. Harris , R. Heller , T.C. Herwig , J. Hirschauer , L. Horyn , B. Jayatilaka , S. Jindariani , M. Johnson , U. Joshi , T. Klijnsma , B. Klima , K.H.M. Kwok , S. Lammel , D. Lincoln , R. Lipton , T. Liu , C. Madrid , K. Maeshima , C. Mantilla , D. Mason , P. McBride , P. Merkel , S. Mrenna , S. Nahm , J. Ngadiuba , D. Noonan , V. Papadimitriou , N. Pastika , K. Pedro , C. Pena<sup>87</sup> , F. Ravera , A. Reinsvold Hall<sup>88</sup> , L. Ristori , E. Sexton-Kennedy , N. Smith , A. Soha , L. Spiegel , S. Stoynev , J. Strait , L. Taylor , S. Tkaczyk , N.V. Tran , L. Uplegger , E.W. Vaandering , A. Whitbeck , I. Zoi 

**University of Florida, Gainesville, Florida, USA**

C. Aruta , P. Avery , D. Bourilkov , L. Cadamuro , P. Chang , V. Cherepanov , R.D. Field, E. Koenig , M. Kolosova , J. Konigsberg , A. Korytov , K. Matchev , N. Menendez , G. Mitselmakher , K. Mohrman , A. Muthirakalayil Madhu , N. Rawal , D. Rosenzweig , S. Rosenzweig , J. Wang 

**Florida State University, Tallahassee, Florida, USA**

T. Adams [ID](#), A. Al Kadhim [ID](#), A. Askew [ID](#), S. Bower [ID](#), R. Habibullah [ID](#), V. Hagopian [ID](#), R. Hashmi [ID](#), R.S. Kim [ID](#), S. Kim [ID](#), T. Kolberg [ID](#), G. Martinez, H. Prosper [ID](#), P.R. Prova, M. Wulansatiti [ID](#), R. Yohay [ID](#), J. Zhang

**Florida Institute of Technology, Melbourne, Florida, USA**

B. Alsufyani [ID](#), M.M. Baarmand [ID](#), S. Butalla [ID](#), T. Elkafrawy<sup>55</sup> [ID](#), M. Hohlmann [ID](#), R. Kumar Verma [ID](#), M. Rahmani, E. Yanes

**University of Illinois Chicago, Chicago, Illinois, USA**

M.R. Adams [ID](#), A. Baty [ID](#), C. Bennett, R. Cavanaugh [ID](#), R. Escobar Franco [ID](#), O. Evdokimov [ID](#), C.E. Gerber [ID](#), D.J. Hofman [ID](#), J.h. Lee [ID](#), D. S. Lemos [ID](#), A.H. Merrit [ID](#), C. Mills [ID](#), S. Nanda [ID](#), G. Oh [ID](#), B. Ozek [ID](#), D. Pilipovic [ID](#), R. Pradhan [ID](#), T. Roy [ID](#), S. Rudrabhatla [ID](#), M.B. Tonjes [ID](#), N. Varelas [ID](#), Z. Ye [ID](#), J. Yoo [ID](#)

**The University of Iowa, Iowa City, Iowa, USA**

M. Alhusseini [ID](#), D. Blend, K. Dilsiz<sup>89</sup> [ID](#), L. Emediato [ID](#), G. Karaman [ID](#), O.K. Köseyan [ID](#), J.-P. Merlo, A. Mestvirishvili<sup>90</sup> [ID](#), J. Nachtman [ID](#), O. Neogi, H. Ogul<sup>91</sup> [ID](#), Y. Onel [ID](#), A. Penzo [ID](#), C. Snyder, E. Tiras<sup>92</sup> [ID](#)

**Johns Hopkins University, Baltimore, Maryland, USA**

B. Blumenfeld [ID](#), L. Corcodilos [ID](#), J. Davis [ID](#), A.V. Gritsan [ID](#), L. Kang [ID](#), S. Kyriacou [ID](#), P. Maksimovic [ID](#), M. Roguljic [ID](#), J. Roskes [ID](#), S. Sekhar [ID](#), M. Swartz [ID](#)

**The University of Kansas, Lawrence, Kansas, USA**

A. Abreu [ID](#), L.F. Alcerro Alcerro [ID](#), J. Anguiano [ID](#), P. Baringer [ID](#), A. Bean [ID](#), Z. Flowers [ID](#), D. Grove [ID](#), J. King [ID](#), G. Krintiras [ID](#), M. Lazarovits [ID](#), C. Le Mahieu [ID](#), J. Marquez [ID](#), N. Minafra [ID](#), M. Murray [ID](#), M. Nickel [ID](#), M. Pitt [ID](#), S. Popescu<sup>93</sup> [ID](#), C. Rogan [ID](#), C. Royon [ID](#), R. Salvatico [ID](#), S. Sanders [ID](#), C. Smith [ID](#), Q. Wang [ID](#), G. Wilson [ID](#)

**Kansas State University, Manhattan, Kansas, USA**

B. Allmond [ID](#), A. Ivanov [ID](#), K. Kaadze [ID](#), A. Kalogeropoulos [ID](#), D. Kim, Y. Maravin [ID](#), J. Natoli [ID](#), D. Roy [ID](#), G. Sorrentino [ID](#)

**Lawrence Livermore National Laboratory, Livermore, California, USA**

F. Rebassoo [ID](#), D. Wright [ID](#)

**University of Maryland, College Park, Maryland, USA**

A. Baden [ID](#), A. Belloni [ID](#), Y.M. Chen [ID](#), S.C. Eno [ID](#), N.J. Hadley [ID](#), S. Jabeen [ID](#), R.G. Kellogg [ID](#), T. Koeth [ID](#), Y. Lai [ID](#), S. Lascio [ID](#), A.C. Mignerey [ID](#), S. Nabili [ID](#), C. Palmer [ID](#), C. Papageorgakis [ID](#), M.M. Paranjpe, L. Wang [ID](#)

**Massachusetts Institute of Technology, Cambridge, Massachusetts, USA**

J. Bendavid [ID](#), I.A. Cali [ID](#), M. D'Alfonso [ID](#), J. Eysermans [ID](#), C. Freer [ID](#), G. Gomez-Ceballos [ID](#), M. Goncharov, G. Grossi, P. Harris, D. Hoang, D. Kovalskyi [ID](#), J. Krupa [ID](#), L. Lavezzi [ID](#), Y.-J. Lee [ID](#), K. Long [ID](#), A. Novak [ID](#), C. Paus [ID](#), D. Rankin [ID](#), C. Roland [ID](#), G. Roland [ID](#), S. Rothman [ID](#), G.S.F. Stephans [ID](#), Z. Wang [ID](#), B. Wyslouch [ID](#), T. J. Yang [ID](#)

**University of Minnesota, Minneapolis, Minnesota, USA**

B. Crossman [ID](#), B.M. Joshi [ID](#), C. Kapsiak [ID](#), M. Krohn [ID](#), D. Mahon [ID](#), J. Mans [ID](#), B. Marzocchi [ID](#), S. Pandey [ID](#), M. Revering [ID](#), R. Rusack [ID](#), R. Saradhy [ID](#), N. Schroeder [ID](#), N. Strobbe [ID](#), M.A. Wadud [ID](#)

**University of Mississippi, Oxford, Mississippi, USA**

L.M. Cremaldi [ID](#)

**University of Nebraska-Lincoln, Lincoln, Nebraska, USA**

K. Bloom , D.R. Claes , G. Haza , J. Hossain , C. Joo , I. Kravchenko , J.E. Siado , W. Tabb , A. Vagnerini , A. Wightman , F. Yan , D. Yu 

**State University of New York at Buffalo, Buffalo, New York, USA**

H. Bandyopadhyay , L. Hay , I. Iashvili , A. Kharchilava , M. Morris , D. Nguyen , S. Rappoccio , H. Rejeb Sfar, A. Williams 

**Northeastern University, Boston, Massachusetts, USA**

G. Alverson , E. Barberis , J. Dervan , Y. Haddad , Y. Han , A. Krishna , J. Li , M. Lu , G. Madigan , R. McCarthy , D.M. Morse , V. Nguyen , T. Orimoto , A. Parker , L. Skinnari , B. Wang , D. Wood 

**Northwestern University, Evanston, Illinois, USA**

S. Bhattacharya , J. Bueghly, Z. Chen , S. Dittmer , K.A. Hahn , Y. Liu , Y. Miao , D.G. Monk , M.H. Schmitt , A. Taliercio , M. Velasco

**University of Notre Dame, Notre Dame, Indiana, USA**

G. Agarwal , R. Band , R. Bucci, S. Castells , A. Das , R. Goldouzian , M. Hildreth , K.W. Ho , K. Hurtado Anampa , T. Ivanov , C. Jessop , K. Lannon , J. Lawrence , N. Loukas , L. Lutton , J. Mariano, N. Marinelli, I. Mcalister, T. McCauley , C. Mcgrady , C. Moore , Y. Musienko<sup>16</sup> , H. Nelson , M. Osherson , A. Piccinelli , R. Ruchti , A. Townsend , Y. Wan, M. Wayne , H. Yockey, M. Zarucki , L. Zygalia 

**The Ohio State University, Columbus, Ohio, USA**

A. Basnet , B. Bylsma, M. Carrigan , L.S. Durkin , C. Hill , M. Joyce , M. Nunez Ornelas , K. Wei, B.L. Winer , B. R. Yates 

**Princeton University, Princeton, New Jersey, USA**

F.M. Addesa , H. Bouchamaoui , P. Das , G. Dezoort , P. Elmer , A. Frankenthal , B. Greenberg , N. Haubrich , G. Kopp , S. Kwan , D. Lange , A. Loeliger , D. Marlow , I. Ojalvo , J. Olsen , A. Shevelev , D. Stickland , C. Tully 

**University of Puerto Rico, Mayaguez, Puerto Rico, USA**

S. Malik 

**Purdue University, West Lafayette, Indiana, USA**

A.S. Bakshi , V.E. Barnes , S. Chandra , R. Chawla , S. Das , A. Gu , L. Gutay, M. Jones , A.W. Jung , D. Kondratyev , A.M. Koshy, M. Liu , G. Negro , N. Neumeister , G. Paspalaki , S. Piperov , V. Scheurer, J.F. Schulte , M. Stojanovic , J. Thieman , A. K. Virdi , F. Wang , W. Xie 

**Purdue University Northwest, Hammond, Indiana, USA**

J. Dolen , N. Parashar , A. Pathak 

**Rice University, Houston, Texas, USA**

D. Acosta , T. Carnahan , K.M. Ecklund , P.J. Fernández Manteca , S. Freed, P. Gardner, F.J.M. Geurts , W. Li , O. Miguel Colin , B.P. Padley , R. Redjimi, J. Rotter , E. Yigitbasi , Y. Zhang 

**University of Rochester, Rochester, New York, USA**

A. Bodek , P. de Barbaro , R. Demina , J.L. Dulemba , A. Garcia-Bellido , O. Hindrichs , A. Khukhunaishvili , N. Parmar , P. Parygin<sup>94</sup> , E. Popova<sup>94</sup> , R. Taus 

**The Rockefeller University, New York, New York, USA**

K. Goulianos [id](#)

**Rutgers, The State University of New Jersey, Piscataway, New Jersey, USA**

B. Chiarito, J.P. Chou [id](#), S.V. Clark [id](#), Y. Gershtein [id](#), E. Halkiadakis [id](#), M. Heindl [id](#), C. Houghton [id](#), D. Jaroslawski [id](#), O. Karacheban<sup>30</sup> [id](#), I. Laflotte [id](#), A. Lath [id](#), R. Montalvo, K. Nash, H. Routray [id](#), S. Salur [id](#), S. Schnetzer, S. Somalwar [id](#), R. Stone [id](#), S.A. Thayil [id](#), S. Thomas, J. Vora [id](#), H. Wang [id](#)

**University of Tennessee, Knoxville, Tennessee, USA**

H. Acharya, D. Ally [id](#), A.G. Delannoy [id](#), S. Fiorendi [id](#), S. Higginbotham [id](#), T. Holmes [id](#), A.R. Kanuganti [id](#), N. Karunarathna [id](#), L. Lee [id](#), E. Nibigira [id](#), S. Spanier [id](#)

**Texas A&M University, College Station, Texas, USA**

D. Aebi [id](#), M. Ahmad [id](#), O. Bouhali<sup>95</sup> [id](#), R. Eusebi [id](#), J. Gilmore [id](#), T. Huang [id](#), T. Kamon<sup>96</sup> [id](#), H. Kim [id](#), S. Luo [id](#), R. Mueller [id](#), D. Overton [id](#), D. Rathjens [id](#), A. Safonov [id](#)

**Texas Tech University, Lubbock, Texas, USA**

N. Akchurin [id](#), J. Damgov [id](#), V. Hegde [id](#), A. Hussain [id](#), Y. Kazhykarim, K. Lamichhane [id](#), S.W. Lee [id](#), A. Mankel [id](#), T. Peltola [id](#), I. Volobouev [id](#)

**Vanderbilt University, Nashville, Tennessee, USA**

E. Appelt [id](#), Y. Chen [id](#), S. Greene, A. Gurrola [id](#), W. Johns [id](#), R. Kunnawalkam Elayavalli [id](#), A. Melo [id](#), F. Romeo [id](#), P. Sheldon [id](#), S. Tuo [id](#), J. Velkovska [id](#), J. Viinikainen [id](#)

**University of Virginia, Charlottesville, Virginia, USA**

B. Cardwell [id](#), B. Cox [id](#), J. Hakala [id](#), R. Hirosky [id](#), A. Ledovskoy [id](#), C. Neu [id](#), C.E. Perez Lara [id](#)

**Wayne State University, Detroit, Michigan, USA**

P.E. Karchin [id](#)

**University of Wisconsin - Madison, Madison, Wisconsin, USA**

A. Aravind [id](#), S. Banerjee [id](#), K. Black [id](#), T. Bose [id](#), S. Dasu [id](#), I. De Bruyn [id](#), P. Everaerts [id](#), C. Galloni, H. He [id](#), M. Herndon [id](#), A. Herve [id](#), C.K. Koraka [id](#), A. Lanaro, R. Loveless [id](#), J. Madhusudanan Sreekala [id](#), A. Mallampalli [id](#), A. Mohammadi [id](#), S. Mondal, G. Parida [id](#), L. Pétré [id](#), D. Pinna, A. Savin, V. Shang [id](#), V. Sharma [id](#), W.H. Smith [id](#), D. Teague, H.F. Tsoi [id](#), W. Vetens [id](#), A. Warden [id](#)

**Authors affiliated with an international laboratory covered by a cooperation agreement with CERN**

G. Gavrilov [id](#), V. Golovtcov [id](#), Y. Ivanov [id](#), V. Kim<sup>97</sup> [id](#), P. Levchenko<sup>98</sup> [id](#), V. Murzin [id](#), V. Oreshkin [id](#), D. Sosnov [id](#), V. Sulimov [id](#), L. Uvarov [id](#), A. Vorobyev<sup>†</sup>, T. Aushev [id](#)

**Authors affiliated with an institute formerly covered by a cooperation agreement with CERN**

S. Afanasiev [id](#), D. Budkouski [id](#), I. Golutvin [id](#), I. Gorbunov [id](#), V. Karjavine [id](#), V. Korenkov [id](#), A. Lanev [id](#), A. Malakhov [id](#), V. Matveev<sup>97</sup> [id](#), V. Palichik [id](#), V. Perelygin [id](#), M. Savina [id](#), V. Shalaev [id](#), S. Shmatov [id](#), S. Shulha [id](#), V. Smirnov [id](#), O. Teryaev [id](#), N. Voityshin [id](#), B.S. Yuldashev<sup>99</sup>, A. Zarubin [id](#), I. Zhizhin [id](#), Yu. Andreev [id](#), A. Dermenev [id](#), S. Gnninenko [id](#), N. Golubev [id](#), A. Karneyeu [id](#), D. Kirpichnikov [id](#), M. Kirsanov [id](#), N. Krasnikov [id](#), I. Tlisova [id](#), A. Toropin [id](#), V. Gavrilov [id](#), N. Lychkovskaya [id](#), A. Nikitenko<sup>100,101</sup> [id](#), V. Popov [id](#), A. Zhokin [id](#), R. Chistov<sup>97</sup> [id](#), M. Danilov<sup>97</sup> [id](#), S. Polikarpov<sup>97</sup> [id](#), V. Andreev [id](#), M. Azarkin [id](#), M. Kirakosyan, A. Terkulov [id](#), A. Belyaev [id](#), E. Boos [id](#), A. Ershov [id](#), A. Gribushin [id](#), L. Khein [id](#), O. Kodolova<sup>101</sup> [id](#), V. Korotkikh, O. Lukina [id](#), S. Obraztsov [id](#), S. Petrushanko [id](#), V. Savrin [id](#), A. Snigirev [id](#), I. Vardanyan [id](#), V. Blinov<sup>97</sup>, T. Dimova<sup>97</sup> [id](#)

A. Kozyrev<sup>97</sup> , O. Radchenko<sup>97</sup> , Y. Skovpen<sup>97</sup> , V. Kachanov , S. Slabospitskii ,  
 A. Uzunian , A. Babaev , V. Borshch , D. Druzhkin<sup>102</sup> , E. Tcherniaev , V. Chekhovsky,  
 V. Makarenko 

†: Deceased

<sup>1</sup>Also at Yerevan State University, Yerevan, Armenia

<sup>2</sup>Also at TU Wien, Vienna, Austria

<sup>3</sup>Also at Institute of Basic and Applied Sciences, Faculty of Engineering, Arab Academy for Science, Technology and Maritime Transport, Alexandria, Egypt

<sup>4</sup>Also at Ghent University, Ghent, Belgium

<sup>5</sup>Also at Universidade Estadual de Campinas, Campinas, Brazil

<sup>6</sup>Also at Federal University of Rio Grande do Sul, Porto Alegre, Brazil

<sup>7</sup>Also at UFMS, Nova Andradina, Brazil

<sup>8</sup>Also at Nanjing Normal University, Nanjing, China

<sup>9</sup>Now at The University of Iowa, Iowa City, Iowa, USA

<sup>10</sup>Also at University of Chinese Academy of Sciences, Beijing, China

<sup>11</sup>Also at China Center of Advanced Science and Technology, Beijing, China

<sup>12</sup>Also at University of Chinese Academy of Sciences, Beijing, China

<sup>13</sup>Also at China Spallation Neutron Source, Guangdong, China

<sup>14</sup>Now at Henan Normal University, Xinxiang, China

<sup>15</sup>Also at Université Libre de Bruxelles, Bruxelles, Belgium

<sup>16</sup>Also at an institute formerly covered by a cooperation agreement with CERN

<sup>17</sup>Also at Cairo University, Cairo, Egypt

<sup>18</sup>Also at Suez University, Suez, Egypt

<sup>19</sup>Now at British University in Egypt, Cairo, Egypt

<sup>20</sup>Also at Purdue University, West Lafayette, Indiana, USA

<sup>21</sup>Also at Université de Haute Alsace, Mulhouse, France

<sup>22</sup>Also at Department of Physics, Tsinghua University, Beijing, China

<sup>23</sup>Also at Tbilisi State University, Tbilisi, Georgia

<sup>24</sup>Also at The University of the State of Amazonas, Manaus, Brazil

<sup>25</sup>Also at Erzincan Binali Yildirim University, Erzincan, Turkey

<sup>26</sup>Also at University of Hamburg, Hamburg, Germany

<sup>27</sup>Also at RWTH Aachen University, III. Physikalisches Institut A, Aachen, Germany

<sup>28</sup>Also at Isfahan University of Technology, Isfahan, Iran

<sup>29</sup>Also at Bergische University Wuppertal (BUW), Wuppertal, Germany

<sup>30</sup>Also at Brandenburg University of Technology, Cottbus, Germany

<sup>31</sup>Also at Forschungszentrum Jülich, Juelich, Germany

<sup>32</sup>Also at CERN, European Organization for Nuclear Research, Geneva, Switzerland

<sup>33</sup>Also at Institute of Physics, University of Debrecen, Debrecen, Hungary

<sup>34</sup>Also at HUN-REN ATOMKI - Institute of Nuclear Research, Debrecen, Hungary

<sup>35</sup>Now at Universitatea Babes-Bolyai - Facultatea de Fizica, Cluj-Napoca, Romania

<sup>36</sup>Also at Physics Department, Faculty of Science, Assiut University, Assiut, Egypt

<sup>37</sup>Also at HUN-REN Wigner Research Centre for Physics, Budapest, Hungary

<sup>38</sup>Also at Punjab Agricultural University, Ludhiana, India

<sup>39</sup>Also at University of Visva-Bharati, Santiniketan, India

<sup>40</sup>Also at Indian Institute of Science (IISc), Bangalore, India

<sup>41</sup>Also at Birla Institute of Technology, Mesra, Mesra, India

<sup>42</sup>Also at IIT Bhubaneswar, Bhubaneswar, India

<sup>43</sup>Also at Institute of Physics, Bhubaneswar, India

<sup>44</sup>Also at University of Hyderabad, Hyderabad, India

<sup>45</sup>Also at Deutsches Elektronen-Synchrotron, Hamburg, Germany

<sup>46</sup>Also at Department of Physics, Isfahan University of Technology, Isfahan, Iran

<sup>47</sup>Also at Sharif University of Technology, Tehran, Iran

<sup>48</sup>Also at Department of Physics, University of Science and Technology of Mazandaran, Behshahr, Iran

<sup>49</sup>Also at Helwan University, Cairo, Egypt

<sup>50</sup>Also at Italian National Agency for New Technologies, Energy and Sustainable Economic Development, Bologna, Italy

<sup>51</sup>Also at Centro Siciliano di Fisica Nucleare e di Struttura Della Materia, Catania, Italy

<sup>52</sup>Also at Università degli Studi Guglielmo Marconi, Roma, Italy

<sup>53</sup>Also at Scuola Superiore Meridionale, Università di Napoli 'Federico II', Napoli, Italy

<sup>54</sup>Also at Fermi National Accelerator Laboratory, Batavia, Illinois, USA

<sup>55</sup>Also at Ain Shams University, Cairo, Egypt

<sup>56</sup>Also at Consiglio Nazionale delle Ricerche - Istituto Officina dei Materiali, Perugia, Italy

<sup>57</sup>Also at Riga Technical University, Riga, Latvia

<sup>58</sup>Also at Department of Applied Physics, Faculty of Science and Technology, Universiti Kebangsaan Malaysia, Bangi, Malaysia

<sup>59</sup>Also at Consejo Nacional de Ciencia y Tecnología, Mexico City, Mexico

<sup>60</sup>Also at Trincomalee Campus, Eastern University, Sri Lanka, Nilaveli, Sri Lanka

<sup>61</sup>Also at Saegis Campus, Nugegoda, Sri Lanka

<sup>62</sup>Also at National and Kapodistrian University of Athens, Athens, Greece

<sup>63</sup>Also at Ecole Polytechnique Fédérale Lausanne, Lausanne, Switzerland

<sup>64</sup>Also at Universität Zürich, Zurich, Switzerland

<sup>65</sup>Also at Stefan Meyer Institute for Subatomic Physics, Vienna, Austria

<sup>66</sup>Also at Laboratoire d'Annecy-le-Vieux de Physique des Particules, IN2P3-CNRS, Annecy-le-Vieux, France

<sup>67</sup>Also at Near East University, Research Center of Experimental Health Science, Mersin, Turkey

<sup>68</sup>Also at Konya Technical University, Konya, Turkey

<sup>69</sup>Also at Izmir Bakircay University, Izmir, Turkey

<sup>70</sup>Also at Adiyaman University, Adiyaman, Turkey

<sup>71</sup>Also at Bozok Universitetesi Rektörlüğü, Yozgat, Turkey

<sup>72</sup>Also at Marmara University, Istanbul, Turkey

<sup>73</sup>Also at Milli Savunma University, Istanbul, Turkey

<sup>74</sup>Also at Kafkas University, Kars, Turkey

<sup>75</sup>Now at Istanbul Okan University, Istanbul, Turkey

<sup>76</sup>Also at Hacettepe University, Ankara, Turkey

<sup>77</sup>Also at Istanbul University - Cerrahpasa, Faculty of Engineering, Istanbul, Turkey

<sup>78</sup>Also at Yildiz Technical University, Istanbul, Turkey

<sup>79</sup>Also at Vrije Universiteit Brussel, Brussel, Belgium

<sup>80</sup>Also at School of Physics and Astronomy, University of Southampton, Southampton, United Kingdom

<sup>81</sup>Also at University of Bristol, Bristol, United Kingdom

<sup>82</sup>Also at IPPP Durham University, Durham, United Kingdom

<sup>83</sup>Also at Monash University, Faculty of Science, Clayton, Australia

<sup>84</sup>Also at Università di Torino, Torino, Italy

<sup>85</sup>Also at Bethel University, St. Paul, Minnesota, USA

<sup>86</sup>Also at Karamanoğlu Mehmetbey University, Karaman, Turkey

<sup>87</sup>Also at California Institute of Technology, Pasadena, California, USA

<sup>88</sup>Also at United States Naval Academy, Annapolis, Maryland, USA

<sup>89</sup>Also at Bingol University, Bingol, Turkey

<sup>90</sup>Also at Georgian Technical University, Tbilisi, Georgia

<sup>91</sup>Also at Sinop University, Sinop, Turkey

<sup>92</sup>Also at Erciyes University, Kayseri, Turkey

<sup>93</sup>Also at Horia Hulubei National Institute of Physics and Nuclear Engineering (IFIN-HH), Bucharest, Romania

<sup>94</sup>Now at another institute formerly covered by a cooperation agreement with CERN

<sup>95</sup>Also at Texas A&M University at Qatar, Doha, Qatar

<sup>96</sup>Also at Kyungpook National University, Daegu, Korea

<sup>97</sup>Also at another institute formerly covered by a cooperation agreement with CERN

<sup>98</sup>Also at Northeastern University, Boston, Massachusetts, USA

<sup>99</sup>Also at Institute of Nuclear Physics of the Uzbekistan Academy of Sciences, Tashkent, Uzbekistan

<sup>100</sup>Also at Imperial College, London, United Kingdom

<sup>101</sup>Now at Yerevan Physics Institute, Yerevan, Armenia

<sup>102</sup>Also at Universiteit Antwerpen, Antwerpen, Belgium